

Project: PNII-ID-PCE-2012-4-0299

Project title: “Nuclear astrophysics studies at IFIN-HH” NUCASTRO

Final report October 2016

1. Introduction

This is the final report for the project identified above, written in September-October 2016, after 3 years since the beginning of its financing. The project was submitted in April 2012, announced on Nov. 7, 2012 as evaluated with 98 out of 100 points, but its financing started only on Sept 2, 2013 for 27 months and with financial cuts at 27/36 of initial funding, then extended and ending with 38 months duration, slightly longer than originally proposed, but with reduced finances as described above. It has the internal IFIN-HH nr. PNII 27/2013 and some documents may identify it with this number. This final report includes language and figures from the previous intermediate reports of Dec. 2013, Dec. 2014 and Dec. 2015, and normally so.

Due to a late start and financial truncation, some of the objectives will obviously not be as stated in the original proposal [1]. Moreover, after only 3 months of regular financing in 2013, the funds for the project were cut to about 55% of those scheduled for 2014 and got a 10 months extension into 2016. This lead the Project Director (PD) (or Principal Investigator - PI), to a reassessment of program's objectives and in particular of the use of funds. Funds in this project had to be, at points, complemented with funds from other projects. These are clearly shown where the case, and in the financial documents. While the project followed and fulfilled the proposed objectives of 2012, some changes from the original proposal may have occurred also due to the natural evolution of science in the 4.5 years from its inception and due to the unforeseeable circumstances, normal when large international collaborations are involved.

The report is structured as follows: a general report on the objectives of this Nuclear Astrophysics (NA) project is given in Sect. 2, followed by comprehensive reports of the 3 years activity per subject, rather than in chronological order. The material is structured in order of efforts and results: it begins with a report on the direct measurements of 2014-2016 using IFIN-HH's new 3 MV tandetron accelerator and the ultra-low background laboratory in the salt mine of Slanic in Sect. 3, then on the studies using indirect methods: beta-delayed proton emission with the new ASTROBOX2 detector at TAMU in Sect. 4, progress on the use of breakup of Rare Ion Beams (RIB) and Trojan Horse Method as indirect measurements in Nuclear Astrophysics in Sect. 5, theory work the Optical Model Potentials for use the reliable predictions of nucleus-nucleus collisions in Sect. 6. The activities connected with two Carpathians Summer Schools of Physics, the 2014 (CSSP14) and 2016 (CSSP16) editions (rather than a single one foreseen in the original project) are summarized in Sect. 7. Sect. 8 is a list of publications and of participations at conferences of the group for 2013-2016. Conclusions are summarized in Sect. 9. Appendix 1 has the Content pages of the volume of Proceedings of CSSP14 and Appendix 2 contains the Program of CSSP16. Pdf files of the publications are appended at the very end of the report.

2. General report

This report will start from part *C. Project description* from the proposal of April 2012 [1] and use the convention that those parts are always included in *italics*, to distinguish them from the body of the report.

The project had two motivations, as declared in part *C1. Introduction to project's problematic*:

- *the intent of the project director to return to Romania after a 19 years stay and work in the United States.*
- *to start ... a **group** working in **nuclear astrophysics** and the present proposal is to establish an initial funding for exploratory research in this area. This is the second, the scientific motivation of this proposal.*

Both goals were fulfilled, as **the program director works for over 4 years in IFIN-HH** as Senior Researcher 1 (CS1 in Romanian) and **has established a Nuclear Astrophysics Group (NAG)** working in the Department of Nuclear Physics of the institute. It consists now of four young research assistants, in addition to the PD himself and a theoretician at CS1 (top) level (dr. F. Carstoiu, working in the Department of Theoretical Physics- DFT). See the rest of the report for argumentation.

I find that the best approach for this final report is to start from the objectives, as stated in Sec. C2 of the proposal. I add numbers to each objective, (per paragraph, not present in the original) to help referring to each one later in the Section.

C2. Objectives

The concrete objectives of the proposal are:

- **C2.1** *Start a research group in the Department of Nuclear Physics (DFN) of IFIN-HH. That will start with the return of the project director. Search for a suitable candidate for a second permanent position in the group, at CS3 or CS2 level. Search will focus on existing IFIN personnel. Attract two graduate students in the group in 2013 and after.*
- **C2.2** *Start work on the physics of the project. Collaboration with dr. F. Carstoiu of DFT who will be involved 15% of his time in this project will continue on the subject of theory of breakup reactions at intermediate energies. Of prime and immediate concern will be the calculations for the experiments at the RIBF of RIKEN, Japan, scheduled for 2013.*
- **C2.3** *Continue work on projects started earlier while at my TAMU position. Of prime importance will be the THM experiments with the group from Catania. The continuation of the $^{16}\text{O}+^{12}\text{C}$ experiment started by the Dec. 2010 experiment at the IFIH tandem accelerator. Second, move to IFIN the experiment NiCAR approved by the LNS Catania PAC in 2011, in case the Sicilian accelerator will not work. For these to happen a new, improved goniometric system to measure angles in the existing reaction chamber with better accuracy will be developed.*
- **C2.4** *Will complete the current collaboration with the CEA Saclay and CERN groups for the design and construction of a new version of the AstroBox detector built while at TAMU. The new detector will have a better beam efficiency and a better energy resolution for the low energy protons from β -delayed proton emission. Experiments will be proposed at TAMU to test the detector in 2013. After the tests of 2013,*

proposals will be made to use it at CERN's HIE-ISOLDE facility. Very short lived exotic species can be obtained at ISOLDE, but current energies of reaccelerated beams make impractical their implantation in AstroBox.

- **C2.5** *In 2013 the experiment RIBF13 approved by the RIKEN PAC at SAMURAI should take place. The preparations for this experiment (reactions with two different radioactive beams at 2 energies on light and heavy targets) will take a large part of the time. Part of the data will be analyzed in IFIN in 2014 and after.*
- **C2.6** *In the summer of 2014 a new edition of the Carpathian Summer School of Physics, the 5th under the title "Exotic Nuclei and Nuclear/Particle Astrophysics. From nuclei to stars" will be organized. The organization will start one year earlier. Only seed funds for the school are asked for in this project, the rest will be sought later from internal and international bodies.*

C2.1 The PD returned to IFIN-HH in June 2012, as CS1 (Senior Researcher 1), more than a year before the start of financing for this project. A few month after, he could secure other funds from the institute to start hiring for the group.

- Dr. D. Chesneanu, CS (Research Scientist) at the time of hiring in Feb 2013, CS3 (Research Scientist 3) working as a post-doc for 2013 till 2014, when she moved from the institute.

Later six students were hired for part-time positions:

- Vicentiu Iancu - master student; in Aug. 2014 he left for France for an ELI-NP fellowship;
- Iustinian Focsa - undergraduate student preparing his diploma thesis with me to June 2015; master student 2015-2016;
- Sebastian Toma - PhD student, joined in Sept. 2013 and moved to another project in 2014;

From the beginning of 2015 I have three more research assistants in the NAG:

- Alexandra Chilug
- Dana Tudor
- Ionut-Catalin Stefanescu.

All three have master degrees in physics and the first two became PhD students at the University of Bucharest in Sept 2016 under joint supervision from me and profs. Alexandrina Petrovici and Vlad Avrigeanu, respectively.

Two sophomore students (undergraduates) have joined the group recently (fall 2016), but are not financed from this project.

C2.2 The collaboration with dr. Carstoiu, which lasts for over 20 years, continued. PD and dr. Carstoiu continued working together on subjects from this project or on related projects. Of prime and immediate concern was to finalize by publication work which was done earlier, either at Texas A&M University or elsewhere. This resulted in 7 papers in 2013-2016 [2-8].

Calculations for a proposed experiment at RIBF of RIKEN, Japan, were made and a proposal was submitted to the Dec. 2014 PAC of RIBF. The joint proposal NP1412-SAMURAI29R1 of IFIN-HH, Texas A&M University (TAMU), Louisiana State University (LSU), Washington University at St. Louis (WU), MO, ATOMKI Debrecen and RIKEN, Wako, with L. Trache as spokesperson was approved by the PAC and given A priority. We are also

involved in 3 other proposals of our above-named collaborators, but we aren't the leading institution thereof. Details about the preparation of this package of experiments later.

C2.3 We continued working on subjects started earlier. As per the proposal, we continued to work on using the Trojan Horse Method (THM) with the group of prof. Claudio Spitaleri from the University of Catania and INFN-LNS, Catania, Italy. We did participate in one experiment with the Italian group at the LNS tandem in July 2013 and we had one experiment at the Bucharest tandem in June 2014. In preparation of the latter we had to make extensive adaptations to an existing large diameter target chamber. These changes were included in the proposal of this project and were done in collaboration with the DAT staff, but had to be supported with other funds. Both experiments were successful. Data were being analyzed by the Catania group. One of the students in our group, Iustinian Focsa, wrote a diploma thesis on the subject of Trojan Horse Method, defended successfully in June 2015. A preliminary report of these efforts was presented at conferences and published in Ref. 9.

C2.4 Another topic in which we have expertise is that of the study of resonances important in radiative proton capture using the inverse phenomenon of beta-delayed proton decay (βp). While at Texas A&M University we have pioneered this type of research. Currently we have the design for a new version of the detector, named ASTROBOX2, which was already realized, mounted and tested at TAMU [10]. It was tested in beam in two experiments, one in April 2015 and one very recently, Oct. 13-21, 2016. An European version is now under construction in IFIN-HH and at Saclay, with the main and most sensitive part, the micromegas array, made and tested off-line. Funds from other projects will be needed to complete its construction. I will get back to this in the next sections of the report. From the experience with this type of micromegas detection a notable spin-off is an upgrade of the focal plane detector of the MDM spectrometer at TAMU [11].

C2.5 Breakup experiment at RIKEN. In the contracted project it was re-scheduled for 2017. This did not take place yet. One reason is our lack of funding in most of 2013 for this purpose. Another, more important, is that the radioactive beam facility RIBF at RIKEN, Wako, Japan, functions only for a very limited time each year (5 months or so), for financial and energy reasons, especially after the catastrophic earthquake and tsunami of March 11, 2011. A proposal (code NP0906-RIBF13) in which breakup in nuclear and Coulomb fields was proposed for ^9C , ^{17}F and ^{27}P , all with NA motivation, was previously approved by the RIBF PAC, but expired. We had to prepare, in cooperation with our collaborators from Japan, USA, Italy and France, a renewal of this proposal. Importantly:

- due to scarcity of the beam time, we reduced the study to one projectile only, ^9C , for which the science case is stronger.
- We will use the newly commissioned spectrometer SAMURAI instead of the ZeroDegree spectrometer. SAMURAI gives by far better conditions. I have also worked for the last 4 years, in collaboration with groups from four US universities and our Japanese colleagues, for developing the detector system and associated electronics in front of SAMURAI, right after the target station. This proposal was presented at the RIBF PAC on Dec. 12th, 2014, in Wako and was approved. It has the

code NP1412-SAMURAI29R1. In addition we are partners in breakup proposals which were inspired by our earlier work [12-15], codes NP1412-SAMURAI25R1, NP1412-SAMURAI28 and NP1412-SAMURAI24, lead by groups from ATOMKI, Hungary, Louisiana State University, USA, and RIKEN Nishina Center, Japan, respectively. All four experiments are planned to be scheduled for beam in fall 2017. They share the same experimental setup, and are proposed to be done in one campaign.

C2.6 We have organized successfully the 2014 edition of the Carpathian Summer School of Physics. The event has taken place between July 13-26, 2014 in Sinaia, Romania, as proposed in this project. The proceedings were published in the prestigious American Institute of Physics Conference Series as volume 1645 [16].

Moreover, in 2015-2016, we have worked to organize the next edition (27th) of the Carpathian Summer School of Physics, which took place, again successfully in Sinaia, June 26 – July 9, 2016. The PD was one of the co-chairs of the meeting and the junior members of NAG were crucial in the flawless organization of the event. The volume of its Proceedings is under preparation at the time of this report and it is again under contract with the AIP Publishing.

One important addition to the objectives as stated in the 2012 proposal is the inclusion of a strong component of the activities of the NAGroup “at home”: direct measurements. Only foreseen and briefly mentioned at the time of the original proposal, in 2013 and 2014 it became clear that doing direct measurements for nuclear astrophysics may be a possibility afforded by the newly installed 3 MV tandetron accelerator of IFIN-HH [17], which was just installed at the time. The idea of coupling it with the use of the ultra-low background laboratory IFIN-HH has in the salt mine at Slanic-Prahova turned out to be a valuable one that made the group competitive in this field. The accelerator tests of 2013 and the experiments of 2014, 2015 and 2016 proved the idea correct: this combination makes the group competitive for direct measurements with alpha particle and light ion beams. The plans of NAG and the objectives of the project were adjusted to include these activities that could be done “home”. These “home experiments” turned out also to be an excellent training opportunity for the young students in the group. The main emphasis was on the experiment $^{13}\text{C}+^{12}\text{C}$, which was done with groups from China and from the departments of IFIN-HH DAT, DFNA and DFVM. While most of the new equipment needed for these experiments was financed from other resources, the human resources needed for this endeavor were financed from NUCASTRO. Preliminary results were communicated and published [18-20].

Another dimension of the work done under this project was that of the presentation of our results to the scientific community of our peers. Both PD and the younger members of the group participated in several conferences and nuclear astrophysics schools where we presented our work and its results. As a result, I appreciate that we are already a valuable and valued member of world’s nuclear astrophysics community.

3. Direct measurements for NA in IFIN-HH

3.1 Direct measurements for NA at the 3 MV tandetron of IFIN-HH

With the final goal of establishing a solid line of research in nuclear astrophysics (NA) at the Bucharest accelerators and laboratories of IFIN-HH, we have performed in 2013 and 2014 experiments to check the limits of one method that seems appropriate and for which the institute had or could acquire installations: the activation method following NA direct measurements. We used for irradiation the new 3 MV tandetron accelerator. It was tested in 2013 that this accelerator can provide good intensities for alpha particles and light ions, and that these intensities are stable for long experiments, as those direct NA measurements tend to be. We noted that while there are many small proton accelerators used specifically for NA, some underground (like LUNA in LNGS, Gran Sasso, Italy or DIANE project in USA) not many accelerators for alpha and light ions are dedicated to NA direct measurements. This could be the niche of our laboratory. In 2014 we tested this accelerator's possibilities, together with the existing low and ultralow background laboratories of IFIN-HH, situated above ground and underground, respectively, for activation measurements. We have chosen the $^{13}\text{C}+^{12}\text{C}$ reaction, which leads to an activation appropriate for our tests: ^{24}Na , formed by fusion followed by one proton evaporation. First tests were done in the period May-June 2014 and then full experiments were carried out in Oct. 2014, Oct. 2015 and May 2016. We studied the $^{12}\text{C}+^{13}\text{C}$ fusion reaction in the energy range $E_{\text{c.m.}} = 2.3 - 5.3$ MeV using the activation method and prompt gamma-rays spectroscopy. Activities of irradiated targets measured both in the underground and surface laboratories allowed to determine the limit of detection of cross sections to be of the order of 1-3 nb [18] (later we reached 90 pb! [19]). By increasing the intensity it would be possible to gain a factor of 10 in sensitivity and by using β - γ coincidences, another factor of 10 (the evaluation of 2014). However, this implied a good cooling of the graphite targets. Calibrations and measurements performed in identical or similar conditions allowed us to reduce the uncertainties associated with the experimental data corresponding with range $E_{\text{c.m.}} = 2.5$ -5.3 MeV below 20%, and to determine the cross section for the $^{12}\text{C}+^{13}\text{C}$ process at an energy as low as $E_{\text{c.m.}} = 2.3$ MeV. Essentially, we found that we could increase the sensitivity of these measurements by about a factor 100 compared with best world results.

3.2 Experiments in IFIN-HH to determine reaction cross sections for the $^{13}\text{C}+^{12}\text{C}$ system through direct measurements at very low energies

The actual measurements were done together with a group from IMP Lanzhou, and CAS Beijing, China. The data obtained are now fully analysed and we can say that they confirm the assessments from the initial tests, and that the measurements were already taken to energies lower than any measured before in the world. We shall report here on this part more thoroughly, as it was for the group the one type of experiments that could be done in own facilities and was the school for the preparations of the young members of the group and a benchmark for its increasing maturity. The first experiments were carried out in May-June and Sept-Oct 2014 and preliminary reports on those results were presented and published [18, 19]. After we analyzed, in collaboration with our colleagues from IMP China, we decided to continue the experiment in the fall of 2015 to strengthen the absolute values of the measured activation cross sections and to go even at lower energies that we reached last year (5.2 MeV in laboratory frame). During 2015's experiment a total of 36 targets were irradiated at

different beam energies in steps of 0.2 MeV between $E(^{13}\text{C})=4.6\text{--}11$ MeV (in laboratory frame).

The NA motivation of the experiment is simple: the real reaction of interest is $^{12}\text{C}+^{12}\text{C}$, for carbon burning in massive stars. However, the study of that reaction in the region of the Gamow window proved to be very difficult. Not only that the cross sections become very small below the Coulomb barrier, but it varies a lot due to numerous resonances (molecular states) found in the excitation function. There is no easy way to extrapolate the results down into the region of interest. On the contrary, for the systems with one or two extra neutrons, $^{13}\text{C}+^{12}\text{C}$ and $^{13}\text{C}+^{13}\text{C}$, the cross section varies smoothly and it turns out that their behavior predicts well the top of the resonances for $^{12}\text{C}+^{12}\text{C}$ (Fig. 3.1. The modified astrophysical S-factor S^* is defined as: $S^*(E) = \sigma(E)Ee^{\frac{87.21}{\sqrt{E}}+0.46E}$). Therefore, a study of one of these systems down into the Gamow window could prove useful for understanding the reaction dynamics at these low energies. We are doing this for $^{13}\text{C}+^{12}\text{C}$. It has the advantage that one of the open channels in the fusion-evaporation process, the proton evaporation channel, leads to activation, ^{24}Na , which has a half-time $T_{1/2}=15.0$ hr, adequate for de-activation measurements in IFIN-HH's ultra-low background laboratory “ μBq ” (microBequerel). The travel time to that location is about 2.5 hr, but the gain in background is enormous: the count rate from natural radioactivity in the shielded Ge detector below ground is 4000 times smaller compared with the rate in the same detector unshielded above ground [21–22].

The first measurements were done in Sept–Oct 2014, and were confirming the potential of the method. After the irradiation of graphite targets with ^{13}C beam from the 3 MV tandetron (irradiations of various durations of time, depending of the energy), the resulting activities were measured either in the GammaSpec laboratory of IFIN-HH, situated above ground in the immediate vicinity of the accelerator, in the underground laboratory, or in both (where possible, for cross check). From these activities we have determined the activation cross sections as function of energy using the thick-target procedure.

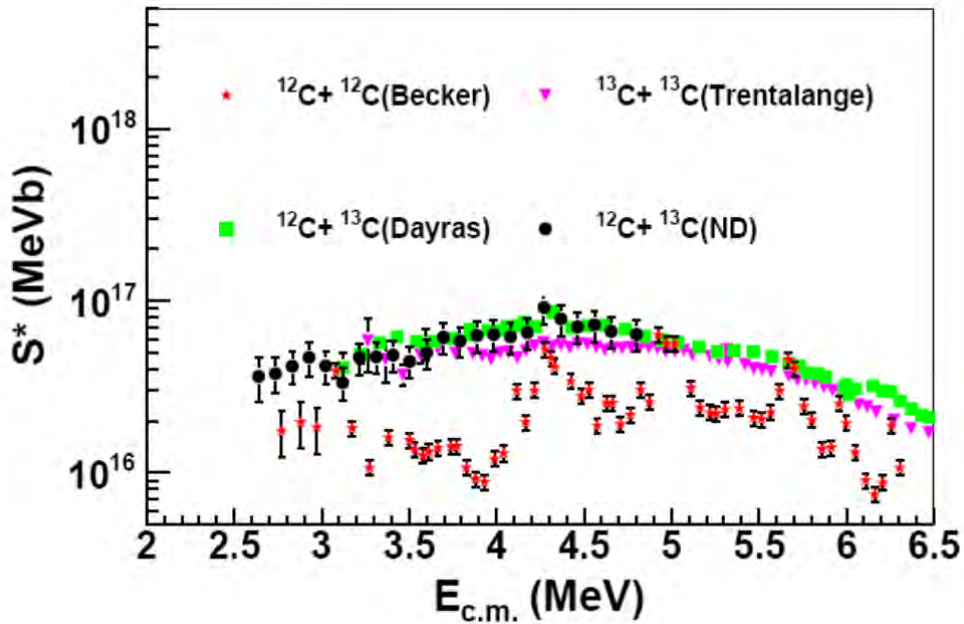


Figure 1. Modified astrophysical S^* factor for C+C reactions.

For 2015-2016 we proposed at the “Spring Campaign of experiments 2015” PAC at IFIN-HH the experiment “Measurement of $^{13}\text{C}+^{12}\text{C}$ fusion cross section at deep sub-barrier energies in IFIN-HH”, which was approved with highest priority was and performed again in collaboration with our colleagues from IMP China in October 2015. Our objectives for the proposed experiment were to:

- A. Certify the absolute values of the cross section s measured by further testing calibrations.
- B. Determine the relative contribution of the channels: activation vs. total cross section at a few energies by measuring prompt gamma rays and activation gamma rays.
- C. Extend the measurements to lower energies using the microBq lab.
- D. Use of beta-gamma coincidences to further clean the background in the spectra with the aim of going to even lower energies than those foreseen with the current method.

For this objectives we had requested 26 days for beam time at 3MV Tandem Accelerator:

- 1 day for in-beam γ -ray measurements
- 14 days for decay measurements
- 11 days for trying the β - γ coincidence measurements.

However, as we only had allocated 15 days for beam time, therefore we could do all planned experiments A-C, but could not perform all the β - γ coincidence measurements (D). We could only test the procedure and determine the efficiency we can attain for it in our laboratory and with the detectors, electronics and data acquisition systems available. Therefore, in May 2016 we (NAG without the Chinese collaborators) have re-measured some of the data at higher energies (up to 11 MeV beam energy) to check for inconsistencies that seemed to occur in the normalization of some of the points measured. These flows were fixed. Measurements were done for prompt gamma-rays and for some activation.

$^{13}\text{C}+^{12}\text{C}$ experimental arrangement and procedure at 3 MV Tandem Accelerator. Measurements, data collected and results

After initial tests of accelerator performances, like beam intensities, stability of beam energies and intensities for long periods of time, and of the logistics involved by irradiations and de-activation measurements at separate locations, we confirmed that we could be competitive for reactions induced by alphas and light ions [18].

During the experiment, the ^{13}C beam in the laboratory energy range of $E_{\text{Lab}} = 11 - 4.6$ MeV ($E_{\text{cm}} = 5.28 - 2.21$ MeV), with steps of 0.2 MeV, impinged on 1.5 mm thick natural carbon targets. Intensities in the range of 0.02-15 μA were used in different runs.

We have made a number of activation and measurements. In total 36 targets were irradiated at different energies and we went down to the lowest energy ever reached of 4.6 MeV in laboratory frame where the cross section was 90 pb (in absolute value).

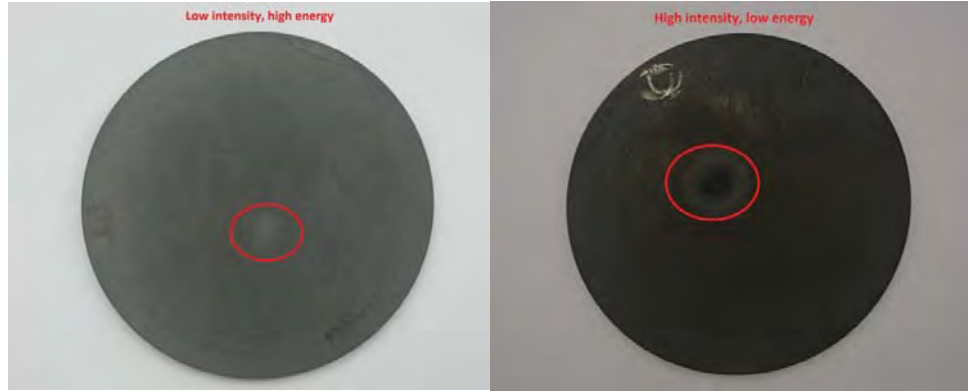


Figure 2. Examples of beam marks on targets irradiated at different energies and different beam currents

The experiment contained two parts: one of on-line and one of offline measurements. During the prompt gamma-rays measurements we were able to see the open channels for this reaction.

For activation (the proton evaporation channel) we measured the two gamma rays of ^{24}Mg .

Preparation of experimental set-up

The resonances from the $^{13}\text{C}+^{12}\text{C}$ fusion reaction make it very difficult to measure in the Gamow window, so to be able to test the predictive power of various models and establish a reliable upper limit for the cross section, we studied the $^{13}\text{C}+^{12}\text{C}$ fusion cross section at deep sub-barrier energies. The machine has a maximum voltage of 3.2 MV, and it can run as low as 200 kV. During tests we have proven that the accelerator has high and stable beam current in the range of tens of μA for the prolific negative ions (^{12}C , ^{13}C , ^{28}Si , ^{197}Au) and we consider it suitable for α and light ion beams (0.2-1 MeV per nucleon).

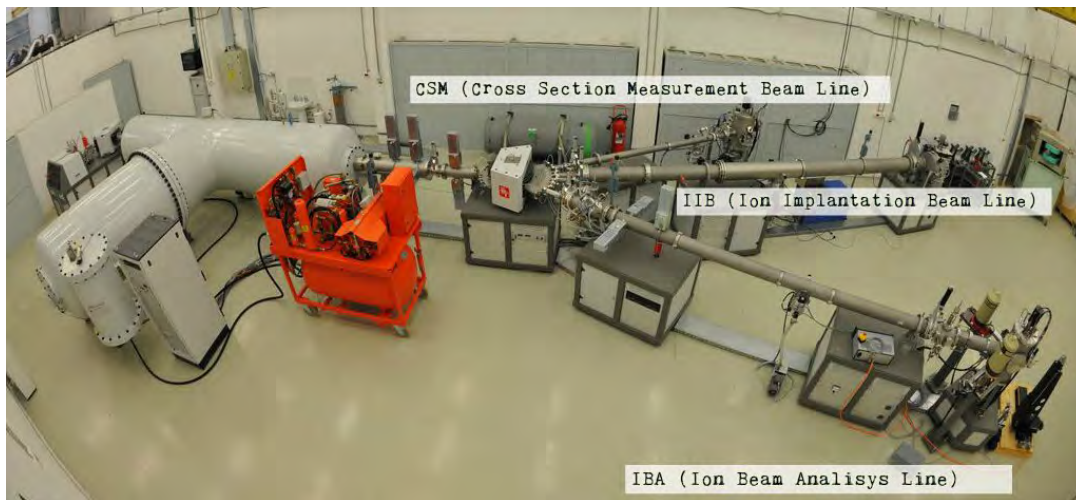


Figure 3. The 3 MV Tandatron Accelerator at IFIN-HH [17].

The reaction we chose $^{13}\text{C}+^{12}\text{C}$ has the advantage that leads to an activation product with a half-life allowing for the transportation and efficient de-activation measurement. Therefore, one of our interests was focused on the proton evaporation channel $^{12}\text{C} (^{13}\text{C}, p)^{24}\text{Na}$ and the other one on the prompt gamma-rays measurements, because we were able to use one HPGe

detector with relative efficiency of 100% placed at 55° in extension of the reaction chamber of accelerator Cross Section Measurements line. The irradiation chamber was electrically isolated, acting as a Faraday cup for current integration.

Prompt gamma rays measurements

The objectives of in-beam measurements were:

- to determine the relative contributions of open reaction channels to the total reaction cross section

- to verify the proton cross section obtained thru in-beam and activation measurements.

We have started the experiment by performing energy and efficiency calibration of the HPGe detector used in-beam. For calibration we used the following calibrated radioactive sources: ^{133}Ba , ^{152}Eu and ^{60}Co .

Exit channel	$E_\gamma[\text{keV}]$	ϵ_γ
$\rightarrow ^{21}\text{Ne}+\alpha$	350.7	0.182%
$\rightarrow ^{23}\text{Na}+\text{pn}$	439.9	0.199%
$\rightarrow ^{24}\text{Ne}+\text{p}$	472.2	0.205%
$\rightarrow ^{24}\text{Mg}+\text{n}$	1368.63	0.287%

where ϵ_γ is the photo-peak detection efficiency.

We measured the prompt gamma-rays during the irradiation with a ^{13}C beam on 1.5 mm thick natural carbon targets. The prompt emission spectra were measured using a spectroscopy system consisting of a coaxial high-purity germanium (HPGe) detector, signal amplifier and a multichannel analyzer. The experimental set-up is shown in Figure 5. The HPGe detector used is a 100% efficiency (relative to a standard 3"x 3" NaI crystal) detector. The detector was placed at 55° in extension of the reaction chamber of accelerator Cross Section Measurements line at 13 cm distance of Faraday cup. The radioactive sources and the targets were placed in an iron flange of 2.3 cm thickness. The HPGe detector was shielded along its length and on the front face with 5 cm thick lead bricks.



Figure 5. HPGe detector 100% relative efficiency placed at 55° at the reaction chamber.

For prompt gamma ray measurements we were able to analyze only the spectra of irradiated targets at beam energies higher than 6.4 MeV (laboratory frame) because the

background inside the accelerator hall is too high and due to the small values of reaction cross-section. The difference between two different beam energies can be seen in Figure 7.

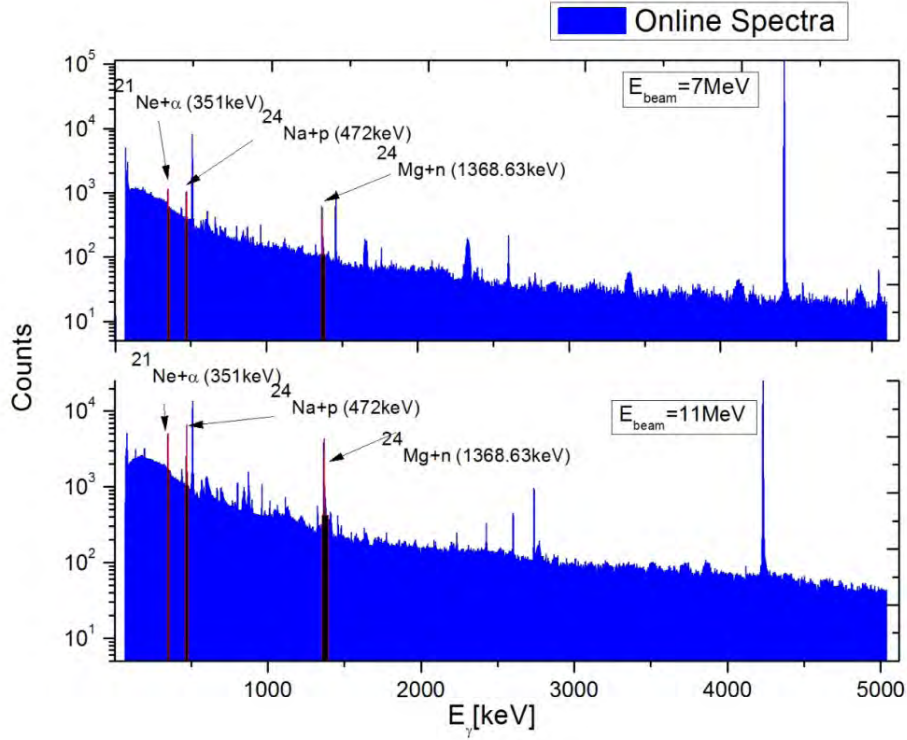


Figure 6. A typical γ -ray spectrum obtained with a ^{13}C beam on a natural carbon target. The origins of the prominent transitions are indicated by the associated light particle evaporated from the compound nucleus.

We have succeeded to measure and analyze the proton, neutron, alpha and deuterium evaporation exit channels independently and to compare the relative agreement for these four cases and this fact is an important feature of the present method for deducing absolute total cross sections.

We calculated the corresponding yields for each open channel which helped us to see the contribution of each channel at the total reaction cross section. For computing the yields we took into account the beam current (time integration of the beam current in order to obtain the total charge which hits the targets), irradiation time, the photo-peak efficiency for selected gamma rays and charge state. Starting from these we obtained the projectile numbers using Eq.1

$$N_p = \frac{Q(C)}{e \cdot q} \quad (1)$$

where $Q(C)$ =total charge and q =charge state

The peak area was obtained using RadWare code. ($N_{\gamma\text{det}}$) (Figure 7)

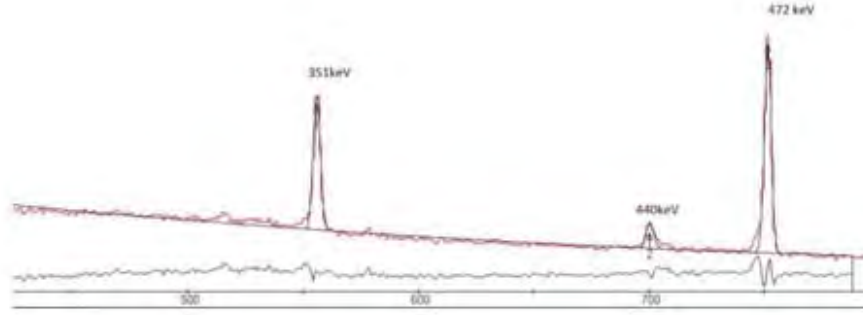


Figure 7. Net area of the photopeak obtained by using RadWare [23]

The yield of each opened reaction channel were calculated using Eq.2:

$$Y_{chx}(E) = \frac{N_{ydet}}{\varepsilon_Y \cdot N_p} \quad (2)$$

For determination of density of nuclei in target, we used the Physical Calculator tool of LISE++ program to obtain the range of energy loss of the ^{13}C nuclei in graphite [24]. The density of nuclei in target can be calculated using Eq.3:

$$N_t = \frac{N_A \cdot \Delta R}{A_t} \quad (3)$$

where N_A is the Avogadro Number, ΔR is the difference in range between 2 consecutive energies (mg/cm^2) and A_t is the mass number of target.

In Figure 9 you can observe the obtained values of yields for each opened reaction channel: for alpha evaporation channel we take into account the 350.7 keV gamma ray, for pn channel/deuteron channel [the same ^{23}Na] – the 439.9 keV gamma ray, for proton evaporation channel – 472.2 keV and the gamma ray for neutron evaporation channel is 1368.63 keV.

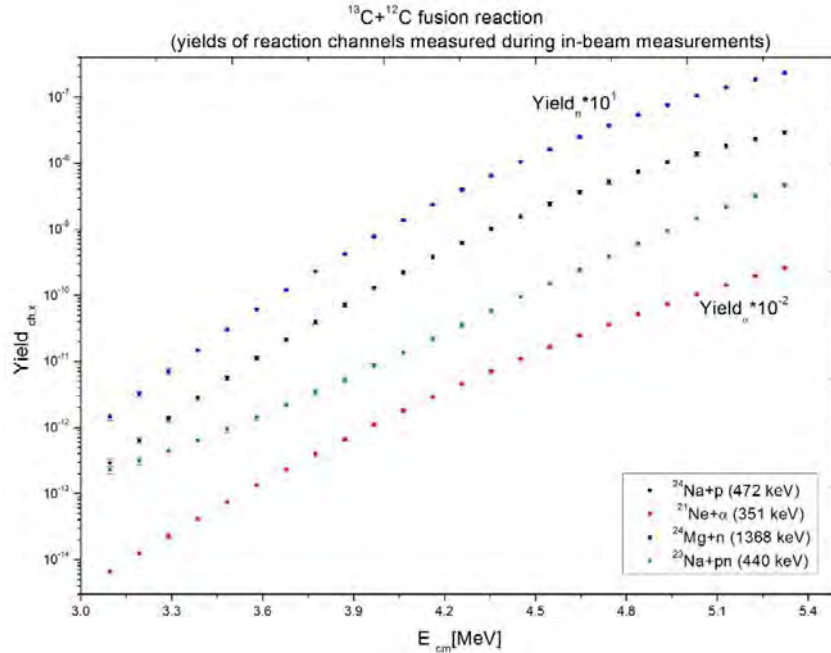


Figure 8. Measured yields for each open channels.

After this step, we can obtain the cross section of each open reaction channel (Eq.4) . As a results I will represent our values in comparison with Dayras et al. [25].

$$\sigma(\tilde{E}) = \frac{Y_{chx}(E+\Delta E) - Y_{chx}(E)}{N_t} \cdot 10^{24} b \quad (4)$$

where N_t is the number density of target nuclei present in the target and Y is the yield.

In the following graphs a comparison is made between absolute values of cross section of each reaction obtain during our experiments and Dayras values of cross section obtained during in-beam measurements [25].

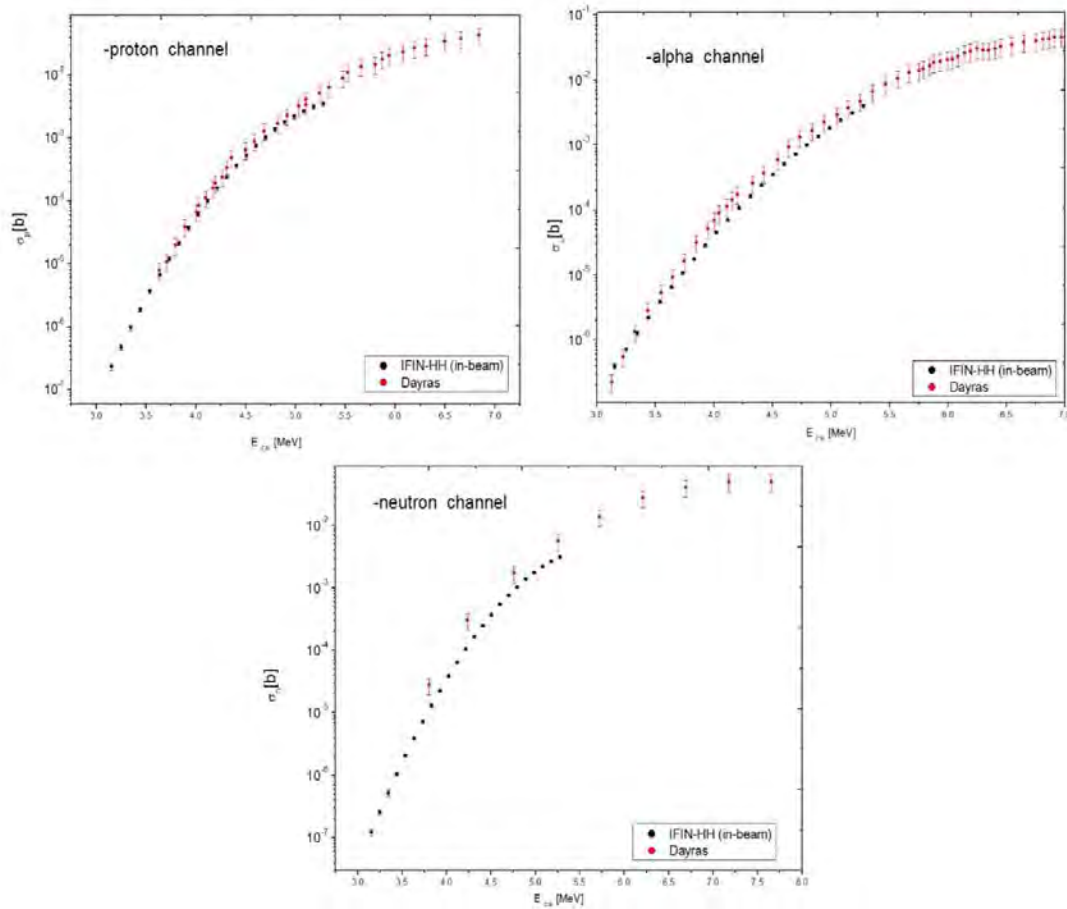


Figure 9. The absolute values of cross section for each reaction channel.

The final step of data analysis will consist of Hauser-Feshbach calculations to find the correction factors for summing and branching ratio of each reaction channel in order to obtain the fusion cross section. The values of Ref. 25 used in the previous graphs are corrected with these factors. So the comparisons between values obtained during this experiment and Dayras experiment [25] is not final.

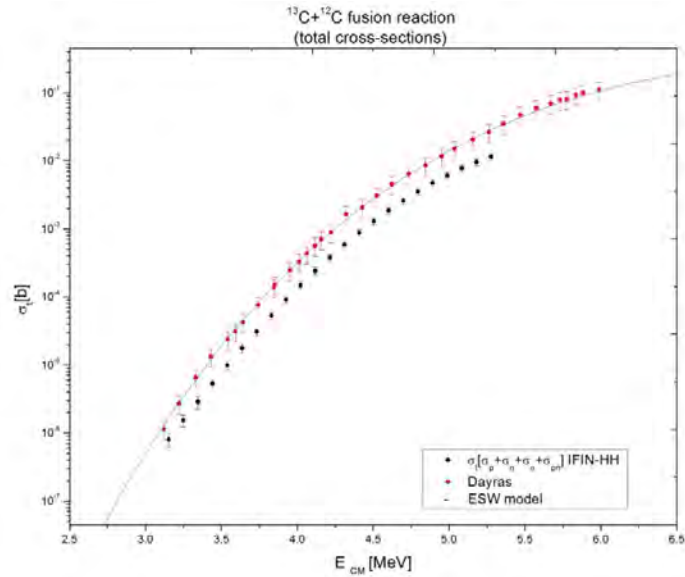


Figure 10. The total fusion cross section.

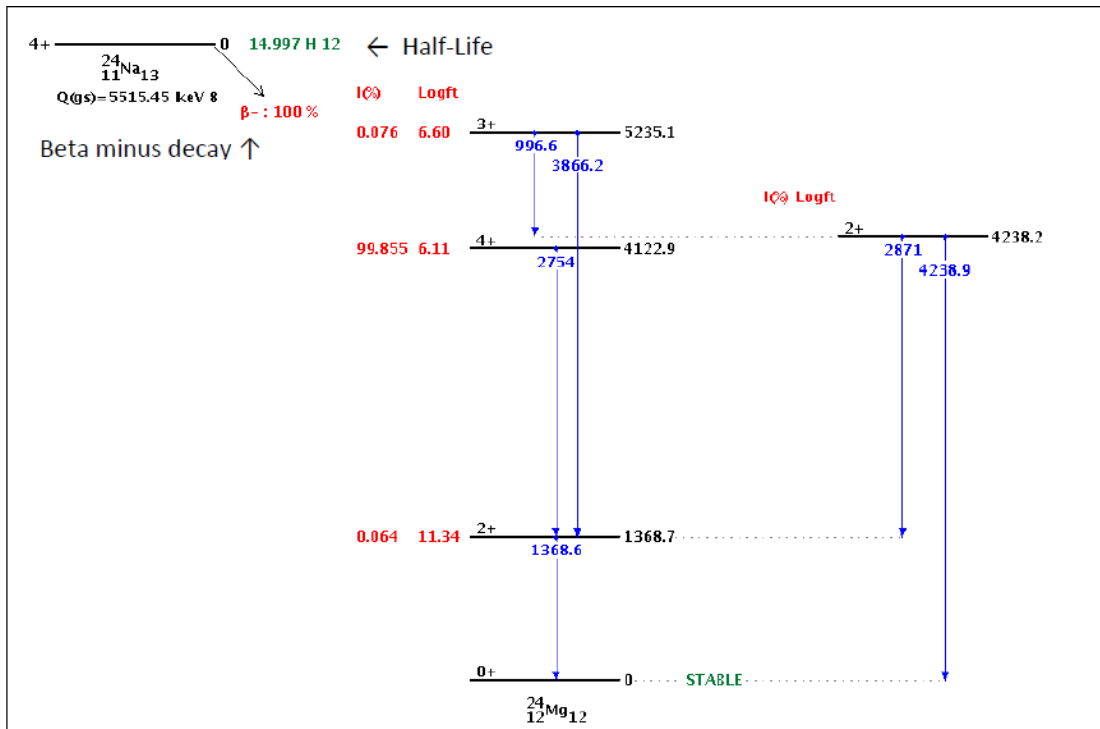


Figure 11. The decay scheme of ^{24}Na . Note the around 99.9% beta decay branch with half-life of 15 hours to the 4+ state of ^{24}Mg , and then to the ground state via the emission of two gamma rays of energies 2754 keV and 1368.63 keV.

Activation measurements

Thick target yield for the $^{12}\text{C} (^{13}\text{C}, p)^{24}\text{Na}$ fusion reaction was determined through the measurement of the gamma-ray yield following the beta-decay of ^{24}Na ($T_{1/2}=15$ h) at the low

background laboratory GammaSpec (at ground level in IFIN-HH), in NAG's own setup and in the ultra-low background laboratory μ Bq in Unirea salt mine at Slanic (Figure 12). At μ Bq a significant reduction of radiation background compared with GammaSpec and NAG occurs (as you can see in Figure 13).

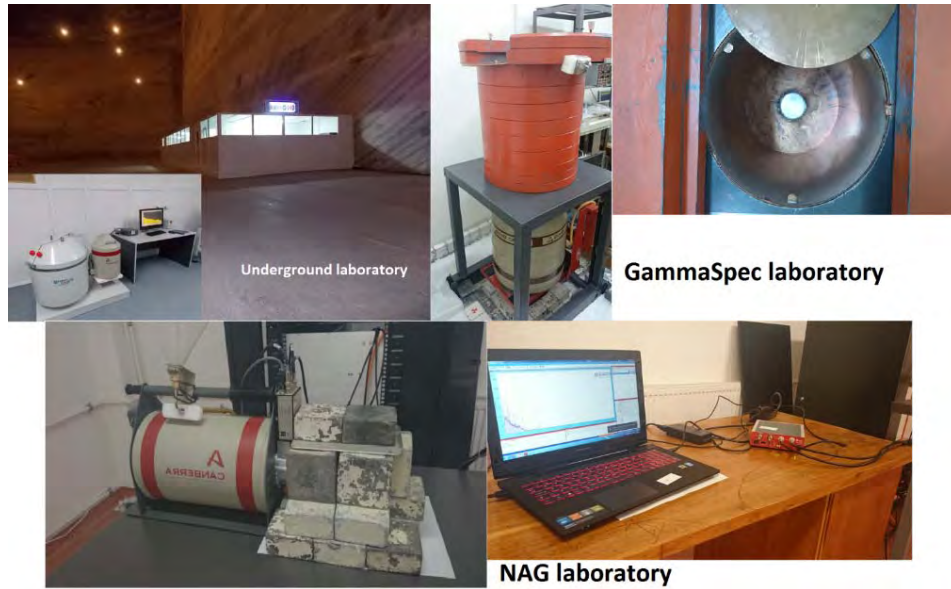


Figure 12. GammaSpec, NAG and μ Bq Laboratories.

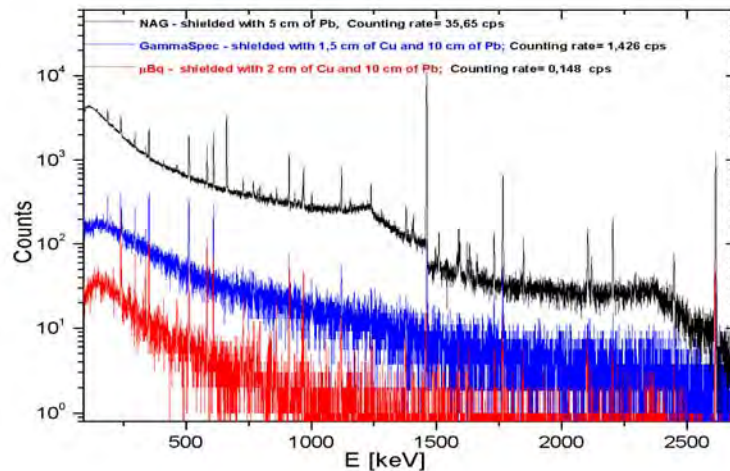


Figure 13. Comparison between collected background from laboratories (NAG, GammaSpec and μ Bq).

In these laboratories the cascading gamma rays (1369 and 2754 keV) were detected with shielded HPGGe detectors with 100% relative efficiency (at NAG), 30% (at GammaSpec) and 120% (at μ Bq in the salt mine). To calibrate the detectors in efficiency we used sources with well known activities, like: ^{153}Eu , ^{133}Ba , ^{60}Co , ^{137}Cs , ^{241}Am (Figure 14).

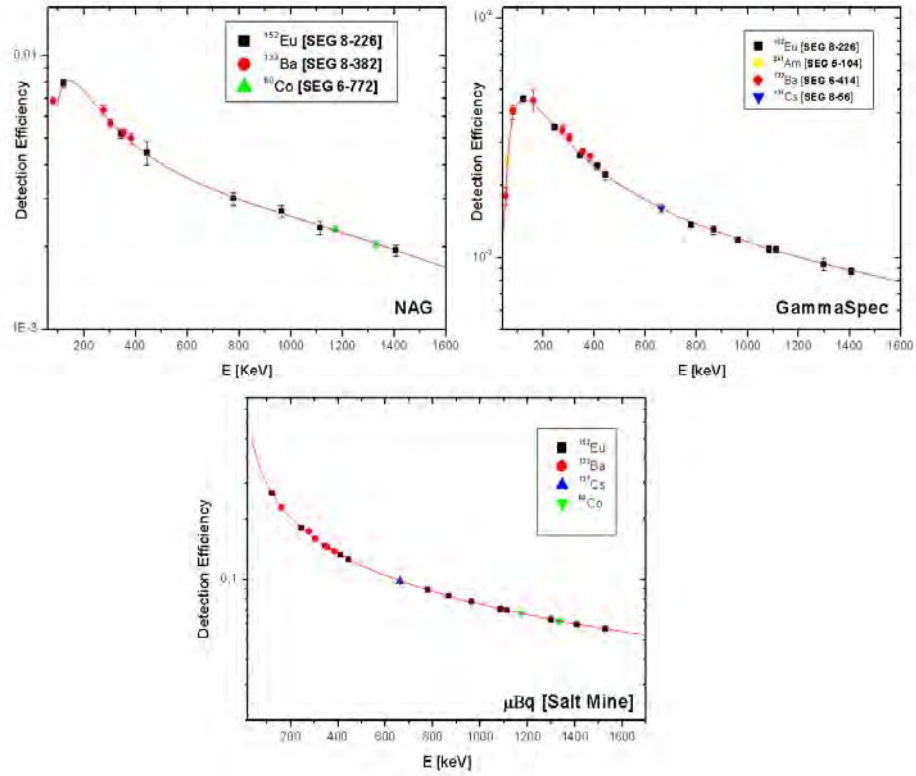


Figure 14. Detection efficiency curves.

The targets which were irradiated at energies $E_{\text{beam}} \geq 5.8$ MeV (in lab. frame) were measured at GammaSpec and at NAG laboratories because of the too high background for such measurements. For energies between 5.8-4.6 MeV (in lab. frame) the samples were measured in μBq Laboratory. After that, the $^{12}\text{C}(^{13}\text{C}, p)^{24}\text{Na}$ cross sections were calculated starting from the experimental yield:

$$Y(E) = \int_0^E \sigma(E) \frac{dx}{dE} \frac{N_A}{A_t} dE$$

where:

$$\frac{dx}{dE} = \text{Range} \left(\frac{g}{\text{cm}^2} \right)$$

➤ Firstly, we have calculated the activity at the end of irradiation as follows:

$$\Lambda_{\text{end irr}} = \frac{\text{Area}}{\varepsilon \cdot P \cdot t_{\text{meas}}} \cdot \frac{1}{(F_{\text{decay meas}} \cdot F_{\text{cooling}})}$$

$$F_{\text{decay meas}} = \frac{1 - e^{-\lambda t_{\text{irr}}}}{\lambda \cdot t_{\text{irr}}}$$

$$F_{\text{cooling}} = e^{-\lambda \cdot \Delta t}$$

where:

ε = detection efficiency;

$t_{meas.}$ = measuring time;

Δt = waiting time (between stop irradiation to start measurement);

P= gamma ray intensity (probability);

t_{irr} = irradiation time.

➤ Secondly the thick target yield (Fig. 15):

$$Yield = \frac{\frac{\Lambda_{end\ irr}}{\lambda}}{\frac{[I * \Delta t]}{q * e}}$$

where: $I * \Delta t$ = beam current integrated in time (corrected stepwise for decay during irradiation).

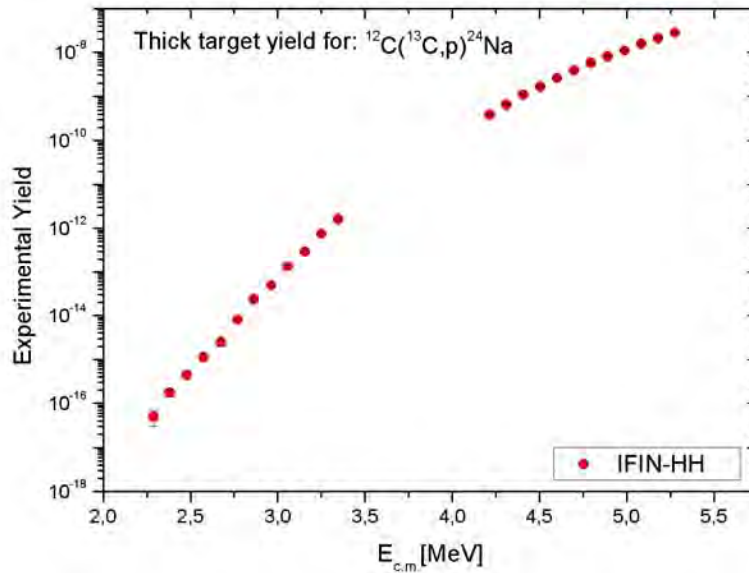


Figure 15. Experimental thick target yield for the proton evaporation channel.

➤ At the end we have calculated the cross section (see Fig. 16):

➤

$$\sigma(\tilde{E}) = \frac{Y(E+\Delta E) - Y(E)}{n_t} \cdot 10^{24} b$$

with:

ΔE = 0.2 MeV [in laboratory frame];

n_t = is the number density of target nuclei present in the target [nuclei/cm²].

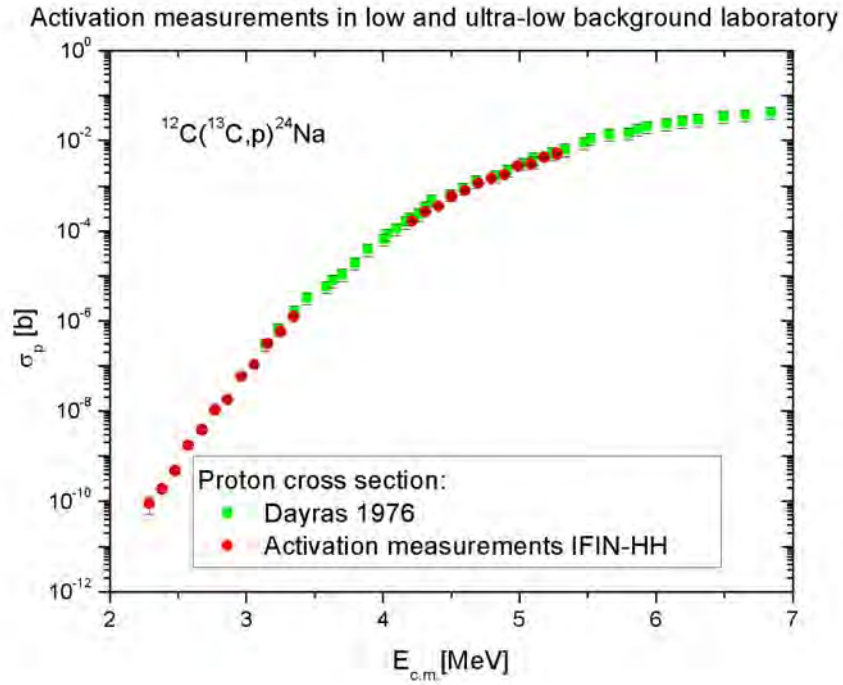


Figure 16. Cross section of the $^{12}\text{C}(^{13}\text{C},p)^{24}\text{Na}$ reaction obtained from activation measurements (red circles). Comparison with previous measurements (green squares) [25] is shown.

Conclusions:

- Measurements at GammaSpec, NAG and at μBq are consistent in absolute values.
- Yield_p from activation are consistent with Yield_p from in-beam measurements, for the overlap energies.

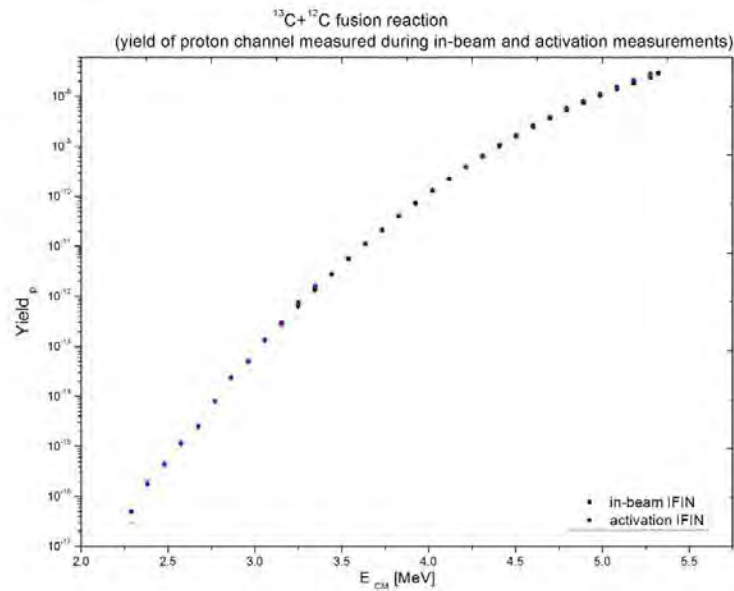


Figure 17. Comparison between yield of proton channel measured during in-beam and activation measurements

- Our σ_p fit values of σ_p by Dayras.

- σ_{tot} not yet final; σ_p , σ_n , σ_α , σ_d , - final absolute values from in-beam.

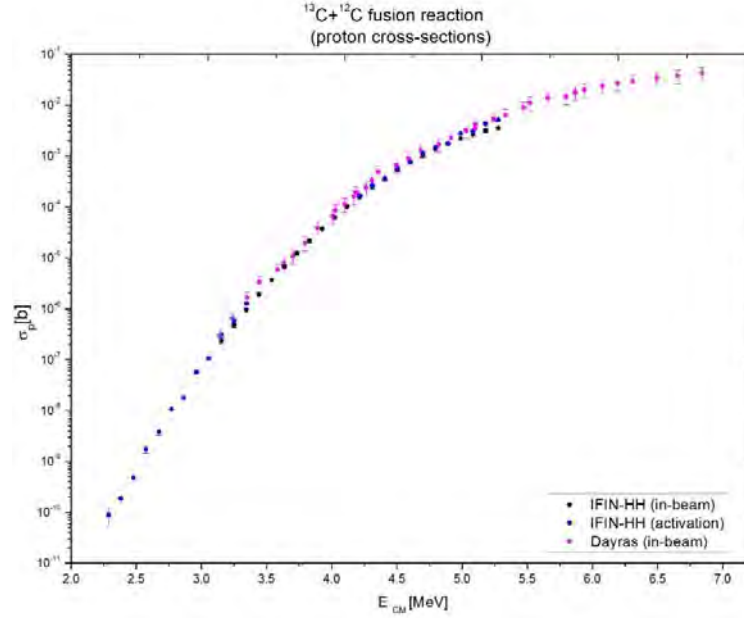


Figure 18. Comparison between proton cross sections values from this experiment and Ref. 25.

4. Indirect methods. Beta-delayed proton decay experiments

4.1 The method: study of resonances

While at Texas A&M University I also started to work on obtaining data for the resonant contributions in radiative proton capture reactions from the spectroscopy of those resonances. In particular I started program to study the spectroscopy of states populated by β -delayed proton emission (βp). This is useful for cases where the proton capture is dominated by low-energy resonances. The resonant capture of protons is a two-step process where the proton incident on a nucleus populates first a metastable state in the compound nucleus (1st step) that then de-excites (2nd step) by gamma-ray emission. The corresponding astrophysical reaction rates are given by the properties of the narrow, isolated resonances only: spin and parity, energy and resonant strength $\omega\gamma$ [26]. To study these resonances at astrophysical energies by direct measurements is not always easy or even possible. An alternative is to populate the same metastable states and determine their spectroscopic properties by other means. One way is the decay spectroscopy: we chose an exotic nucleus that will beta-decay to these same states. Important conditions must be met:

- (i) $Q_{\text{EC}} > S_p$, to have enough energy to populate states above the proton threshold in the daughter, and

- (ii) that the spin and parity selection rules allow to populate the states that are the important resonances.

The relation between these decay spectroscopy studies and the proton capture reactions that occur through narrow, isolated resonances in stellar environments is presented in Figure 4.1 below. We will discuss here only the basics of the experiments, using material from the report of 2014, with emphasis on the best studied case: βp -decay of ^{23}Al . Beta-delayed proton decay of ^{31}Cl and ^{27}P were also studied thru experiments at Texas A&M University, Cyclotron Institute and most of the data were analysed during this project, but I do not refer to them here. In particular, very recently, in October 2016 we carried out an experiment for the study of β -delayed proton decay of ^{31}Cl at TAMU, experiment that appears to be successful, but is too soon to talk about those data in this report. We have used the ASTROBOX2 detector described below, detector developed and built jointly with physicists from TAMU, CEA/IRFU Saclay and CERN.

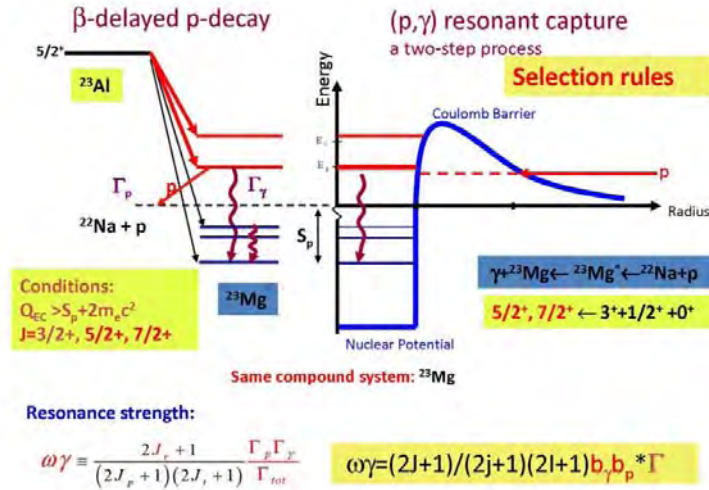


Figure 19. Schematic presentation of the relation allowing the use of beta-delayed proton decay in resonant proton capture.

4.2 The experimental technique. βp -decay of ^{23}Al

We have studied ^{23}Al β -decay before [27] using β - γ coincidence techniques. Secondary beam rates of about 4000 pps and >90% purity were obtained with the MARS spectrometer [28], by far the best yet in literature. The states populated in ^{23}Mg above the proton threshold at $S_p=7580$ keV can decay by proton emission. They are resonances in the proton capture reaction $^{22}\text{Na}(p,\gamma)^{23}\text{Mg}$, crucially important for the depletion of ^{22}Na in ONe novae. We studied these by new methods. The novelty of our approach consist in that that instead of the usual technique of separating the unstable nucleus, depositing it on/in a surface and then measuring its decay with an external detector (like in the measurements of the Jyväskylä group), we chose to implant the unstable ^{23}Al nuclei in the middle of a detector and then measured its decay. A setup consisting of a thin Si double-sided strip detector (DSSD) (p-detector, 65 μm , 16x16 strips, type W1-65 from Micron Semiconductor Ltd., UK) and a thick Si detector (β -detector, 1 mm) was used in the first experiment. A HPGe detector outside the

chamber has detected the γ -rays. We have pulsed the beam from the cyclotron, implanting the source nuclei in the thin Si detector (for about 2 lifetimes), and then switched the beam off (same duration) and measured simultaneously β -p and β - γ coincidences. In order to reduce to a minimum and control the implantation depth we have restricted the momentum spread of the incoming ^{23}Al nuclei to about $\pm 0.25\%$ and the beam rate to about 500 pps. This has been done by closing down the momentum defining slits in MARS. The implantation depth was controlled using a rotating energy-degrader aluminium foil in front of the Si telescope. Implantation distributions of the order of 17 μm deep were obtained (established by simulations, which were confirmed by the proton spectra obtained). After β -decay to excited states of the daughter nucleus either gamma or proton decay follows. All protons emitted with energies below 1.5 MeV stop in the thin Si strip detector and give sharp peaks. The positrons (emitted before) leave a small signal of continuum spectrum in the same thin detector that adds to the proton signal to produce a skewing of the proton peaks on the high energy side and degrade the resolution. For those (majority) cases where gamma rays are emitted instead, the positrons give a large background at low energies in the p-detector. To reduce this background and the degradation of the resolution it was essential to make the proton detector as thin as possible, reduce the volume of the detector as much as possible (narrow strips) and have a narrow distribution of the stopped beam in the middle of the detector. Almost half of the emitted positrons end up in the thick detector behind and trigger the acquisition when a gamma ray or a proton signal arrives in coincidence. Data on the β -delayed proton decay of ^{23}Al existed before, but were obtained with less intense sources and at times were contradictory. The most remarkable result is that we have located the most important resonance in the $^{22}\text{Na}(p,\gamma)$ reaction at $E_{\text{cm}}=207$ keV and we were able to measure both its proton and gamma-branching, a rare, if not unique case (published elsewhere [29, 30]). Another remarkable result of the current measurement was obtained while implanting ^{21}Mg in the middle of the p-detector. With a production rate of about 1 pps, we could obtain a reasonable spectrum in about 8 hrs of experiment. This shows the sensitivity and selectivity of our method. In a later stage we went with an even thinner detector: a 45 μm thick 24x24 strips, 24x24 mm^2 , BB2-45 type detector also from Micron Semiconductor.

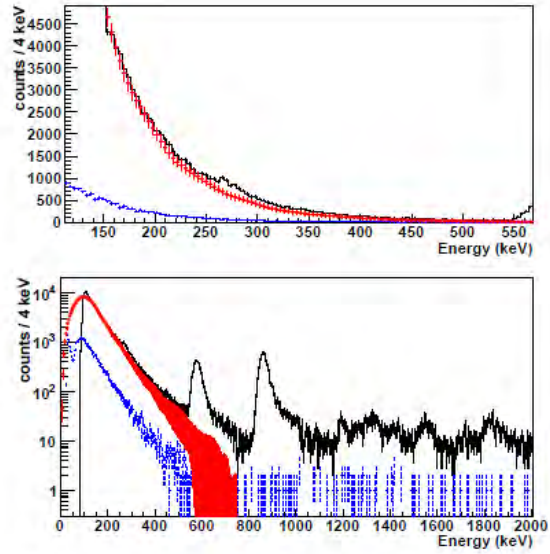


FIG. 7: (Color online) Full collected statistics for the ^{23}Al data (black, solid) and the ^{22}Mg data (blue, dashed). The energy is the total measured decay energy. Smoothed ^{22}Mg spectrum, scaled to match the ^{23}Al spectrum at 150 keV is shown with red dots and corresponding uncertainties. Upper panel shows only the low energy part where the proton group at ~ 270 keV is clearly visible on top of the β background, whereas the lower panel shows the total spectra.

Figure 20. Spectra from the β p-decays measured with a 65mm thin Si detector. From Ref. [30].

4.3 Astrobox 1, results and the new Astrobox2 detector

However remarkable our results using detectors as thin as possible (65 μm , then 45 μm) were, the measurements suffered from a very high background in the region of low energy protons, below 400 keV, e.g., due to the continuum signal left in the Si detectors by the overwhelming number of positrons, present at each decay. While protons have branchings of $10^{-3} - 10^{-4}$ or even lower. In order to diminish this background we chose a detection medium less sensitive to positrons: gas (P5 or P10). In the same time, we chose a technique which allows significant signals from so low energy deposits: the so called micromegas [31]. The detector was named ASTROBOX1 (Figure 2) and the technique was successfully applied to the case of ^{23}Al and published in 2013 [32].

Figure 21. Picture of AstroBox1 from pre-experiment setup. Beam enters perpendicular on cylinder axis.



As in the case of Si detectors, the incoming radioactive specie is stopped in the middle of the (gas) detector by bombardment using the same energy degrader as before (“implantation mode”), then the beam is stopped and the detector goes into a “measuring mode”, characterized by a higher gain and high resolution. A spectrum obtained with the Si detector is shown in Figure 20 and for comparison one with Astrobox1 in Figure 23. It is obvious that the continuum background due to positrons was reduced down to energies below 80-100 keV, making Astrobox1 ideal for the study of proton resonances in the region $E_p=100\text{-}400$ keV, where they occur in most astrophysical (p, γ) processes.

However, we considered that this detector can be improved and a newer, more elaborate design was conceived in the last years: Astrobox2. The active part of the detector has a rectangular geometry, better for the geometry of the experiment. It is shown in Figure 5. At this moment the detector was built by a collaborative effort: micromegas at Bucharest-CERN-Saclay, the body of the detector at TAMU, the electronics in Bucharest, the gas handling system at TAMU. It was assembled in Oct. 2014 at Texas A&M University, where it was also tested with sources. The results show that it works in the expected parameters. The first in-beam test was possible in April 2015 with beam from the K500 superconducting cyclotron of TAMU, with our participation. The test was very successful. However, the next beam time was only possible in October 2016.

4.4 Construction and tests off-line and in-beam of the detector AstroBox2 (AB2) at Texas A&M University

Above we discussed in the design of a new version of a detector to measure β -delayed proton emission, of its micromegas component – the main active part of the detector, and have shown its use for measuring very low energy protons, as well as the connection between these measurements and the determination of astrophysical reaction rates for proton induced reaction rates dominated by resonances. We will only describe briefly the detector built and

the test measurements done at the Cyclotron Institute, Texas A&M University, in College Station, TX.

The active part of the detector, the micromegas, was built for us by a group at CERN, the inventors of such devices. The body of the detector was designed by my former student and current post-doc in Texas, dr. A. Saastamoinen. Its design and realization was actively pursued by us and by our collaborator from CEA/IRFU Saclay, France, dr. E. Pollacco. Schematically it is shown in Figure 5. The detector was put together in the fall 2014 and spring of 2015 and on April 20-28, 2015, we had beams for tests of the detector. The main difference from AstroBox 1 [32] is that it does have a geometry that is more appropriate to the geometry of the beam and its stopping in the gas of the detector. Another difference is that it has 29 separated pads and correspondingly 29 signals, compared with 3 only for AstroBox 1 (AB1).

Figure 22. layout of the micromegas in Astrobox2.

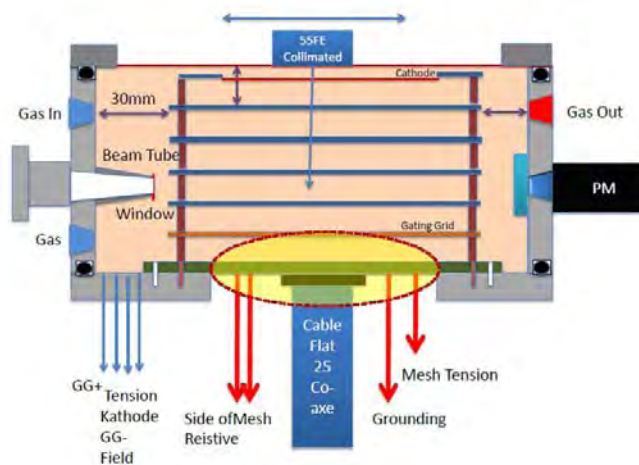
The tests that were done in April 2015, were:

- a) Off-beam tests using ^{55}Fe and ^{241}Am sources
- b) In-beam commissioning of the detector using a ^{25}Si radioactive beam separated by the MARS spectrometer. The radioactive specie we used, ^{25}Si , is very

appropriate for a test of a new proton detector, as it is a good, well known, β -delayed proton emitter with a large βp -branching. It was produced at a reasonable rate from a primary beam of ^{28}Si at 40 MeV/nucleon on a ^{27}Al solid target. The result was actually a cocktail of secondary beams, a benefit for the identification of the beam in AB2.

- c) In-beam measurements for the ^{23}Al secondary beam, which is the main focus of the physics for these measurements.

The first two parts of the tests went very well, and the commissioning of the AB2 detector was a success [10]. So appeared to be the last measurement (c), for which we reserved the last 4 days of the experiment. The primary beam of ^{24}Mg at 45 MeV/nucleon was delivered successfully to us on Friday April 24, and the next day the secondary beam of ^{23}Al was selected and was stopped in the middle of the AB2. All seemed to work well for us and it was only a matter of 2 more days of active beamtime to obtain the desired statistics. Unfortunately, Sunday April 26 a thunderstorm hit the city and produced a blackout that has stopped the cyclotron. The measurement could not be restarted and was incomplete.



After the full analysis of the data, the collaboration decided that the test of the new detector was successful and a new experiment was scheduled for Oct. 13-21, 2016. At the time of writing this report the experiment still goes on. The first part, consisting from the off-line tests of AB2, from the calibration using ^{25}Si β p emitter as described above (parts a) and b)), the production, separation and implantation of ^{31}Cl (equivalent to c) above) were successful and the measurement goes on as I type. Unfortunately it will be too late for these data to be included in this report.

4.1.3 Isospin mixing in ^{23}Al

Aside from the interest for studying the resonances important for nuclear astrophysics, there is another subject of high physics interest in these measurements: isospin mixing. It was detailed in the 2014 report and I will include that here, as it may extend from ^{23}Al to ^{31}Cl . Isospin mixing is not directly related to NA, but is interesting as it was enticing us to complete the spectroscopy of β p-decay of ^{23}Al and seek better detection techniques, like those with Astrobox1 and 2. Simply put it goes like that:

- as in β -decays where this is energetically possible, the isospin $T=3/2$, $J^\pi=5/2^+$ g.s. of ^{23}Al populates very well the isobar analog state (IAS) in the daughter nucleus ^{23}Mg . It has $T=3/2$, not $T=1/2$ as all neighboring excited states in ^{23}Mg . We located it at $E_{\text{exc}}=7803$ keV by measuring its $\log ft=3.31(3)$, fully consistent with a pure Fermi transition. It is only 16 keV higher in excitation energy than another state of regular isospin at $E_{\text{exc}}=7787$ keV, of spin $J^\pi=5/2^+$ or $7/2^+$ (most probably $7/2^+$).
- Proton decay of the IAS is isospin forbidden to

$^{22}\text{Na}^*+p$, $T=1/2$ states, but an experiment of the famous Berkeley group in the 90's claimed to have identified that decay, which would only take place due to an isospin mixing in the IAS which is 50 times stronger than expected from best nuclear structure calculations [33].

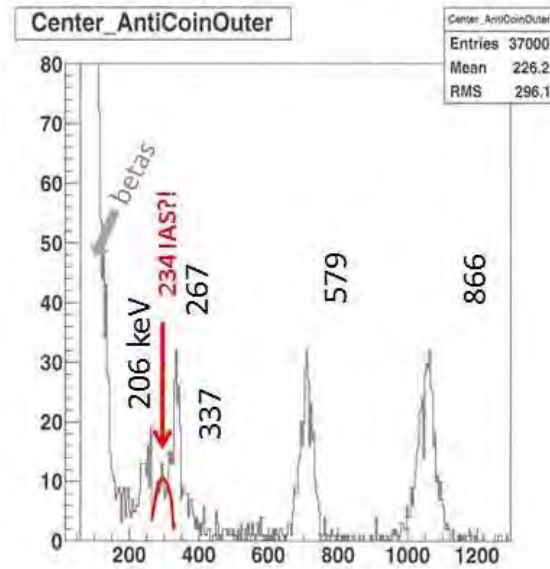


Figure 23. Spectrum taken with the Astrobox1 detector [32].

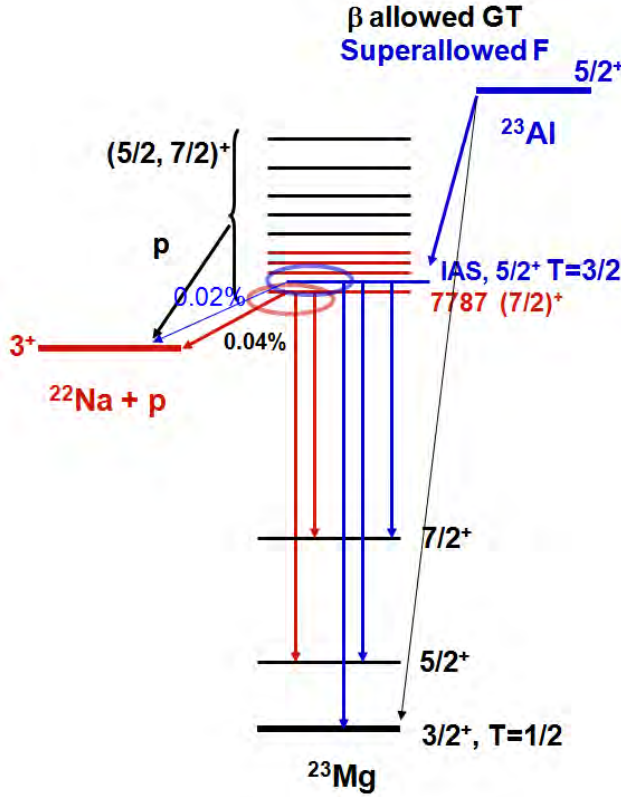


Figure 24. Scheme of ^{23}Al β - and βp -decay.

better results for our future measurements with Astrobox2. Further uncertainty, both in calculations and in the interpretation is due to the uncertain spin of the lower state. A spin $J^\pi=7/2^+$, the most probable, simplifies the interpretation, but a $J^\pi=5/2^+$ spin complicates it, as even small mixing matrix elements between these two states are much more difficult to control and reproduce by calculations.

Another remarkable result is that for some states in ^{23}Al the proton branchings measured are as low as 10^{-4} , result pointing to the sensitivity of the detection method. While it may be too soon to mention, we have hopes that a similar situation may occur in ^{31}Cl : the proton decay line of the IAS is at even lower energy (150 keV) and less abundant, but it seems that it will be within the sensitivity of AB2 and we have hopes to detect it, or place a limit on its branching..

Our β - γ measurements [27] and those with ^{23}Al implanted in Si detectors have shown that the measurements of the Berkeley group at low energies were wrong, but even our measurements with ^{23}Al implanted in thin Si detectors could not establish a good limit of the isospin mixing due to the strong background at low proton energies due to competitive positron signals (figure 20). We found though that the lower $T=1/2$ state at $E_{\text{exc}}=7787$ keV decays by proton emission and by gamma emission [27]. However, our Astrobox1 measurements could find the very small peak in the proton spectrum (Figure 23) and from its relative intensity that decay is fully consistent with a very small isospin mixing, of the order of that calculated using best sd-shell parameters of BA

Brown [34]. This result is not yet fully published, in expectation of even

5 Other indirect methods in Nuclear Astrophysics. Breakup and THM

5.1 RIBF experiment at RIKEN: the breakup of ^9C

Beginning in 2001 we have proposed a novel indirect method for nuclear astrophysics: the use of nuclear breakup of loosely bound proton rich nuclei [12,13]. At the time we (PD and

dr. Carstoiu as leading authors) proposed to use existing breakup data to determine the ANC (Asymptotic Normalization Coefficients) for the breakup of nuclei $Y \rightarrow X + p$ and from there to evaluate the astrophysical S-factors for radiative proton capture reactions $X(p, \gamma)Y$. Important NA reactions data like S_{17} [12,13] and S_{18} [35] were evaluated using data from literature. Later a dedicated experiment at GANIL was used to obtain NA data for the reactions $^{22}\text{Mg}(p, \gamma)^{23}\text{Al}$ [14] and $^{23}\text{Al}(p, \gamma)^{24}\text{Si}$ [15].

A further proposal to use nuclear and Coulomb breakup was sent to RIKEN, in collaboration with Japanese, US and European groups. Proposal NP1412-SAMURAI29R1 was presented to the PAC of RIKEN RIBF in Dec. 2014 and was approved.

The motivation for the experiment is nuclear astrophysics. The current knowledge of the rate of the $^8\text{B}(p, \gamma)^9\text{C}$ reaction in stellar conditions is not complete and is no hope to determine it, now or ever, by other means than by indirect methods. Below I use parts of the proposal to describe the work done/proposed.

1. Physics Motivation, Purpose of the experiment.

The main motivation of this proposal is nuclear astrophysics (NA). The current knowledge of the rate of the $^8\text{B}(p, \gamma)^9\text{C}$ reaction in stellar conditions is contradictory at best and there is no hope to determine it, now or ever, by other means than by indirect methods. This reaction gives a possible path to the hot pp chain pp -IV at high temperatures and away from it toward a rapid alpha process rap I at high temperatures and densities and therefore is important in understanding nucleosynthesis in super-massive hot stars in the early universe, including possible bypasses of the 3α -process.

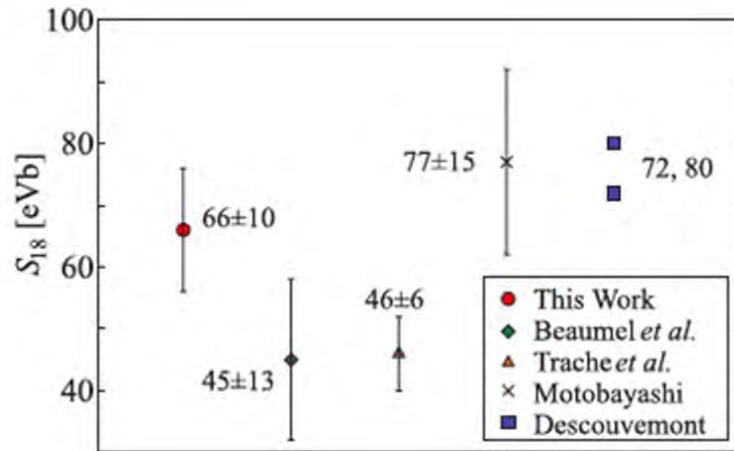


Figure 25. The values of current $S_{18}(0)$ as from different experiments and methods.

Our best hope at the determination of the astrophysical factor S_{18} at low energies is by using the $^9\text{C} \rightarrow ^8\text{B} + p$ breakup. We proposed to use a combination of nuclear and Coulomb dissociation measurements (on a light target – Be or C and on a heavy target – Pb,

respectively) at two energies (100 and 300 MeV/nucleon) to extract structure information which will allow to evaluate the radiative proton capture cross section at low energies and from there the reaction rate.

Also, and not least important, we propose an exclusive study of the reaction, which may allow a better understanding of the reaction mechanism. The high probability of two-proton breakup ${}^9\text{C} \rightarrow {}^7\text{Be} + 2\text{p}$ for this projectile makes it a good case to learn about the complex reaction mechanisms involved. Such an understanding may allow for a better theoretical description of the reactions and more accurate calculations of the momentum and angular distributions, a crucial step in using indirect methods for nuclear astrophysics.

Not negligibly, the reaction proposed is the easiest among the p-HI experiments being planned at this point with SAMURAI and will be a good start for the use of the Si detector system in front of SAMURAI as it results in a smaller dynamical range and an easier particle identification and less kinematic focus.

Nuclear breakup: from the momentum distributions and the absolute -1p breakup cross sections of ${}^9\text{C}$ on a light target we will extract the Asymptotic Normalization Coefficient (ANC) [36] of the wave function of the last bound proton around the ${}^8\text{B}$ core and from it will evaluate S_{18} . This is possible because both processes, nuclear breakup and radiative proton capture, are peripheral and only the asymptotic part of the wave function contributes. The method was used successfully in the past to evaluate astrophysical S-factors for ${}^7\text{Be}(p,\gamma){}^8\text{B}$ [12, 13], ${}^{22}\text{Mg}(p,\gamma){}^{23}\text{Al}$ [14], ${}^{23}\text{Al}(p,\gamma){}^{24}\text{Si}$ [15], etc. It was also used for the case of this projectile, but from less certain data existent in the literature at the time [35]. The method avoids the uncertainties related to the poor knowledge of the nuclear interior, including that of the precise geometry of the proton binding potential. Details of the theoretical calculations and a discussion of extracting ANC and their use in NA are also presented in Refs. 12 and 35. Calculated momentum distributions of the core are shown in Fig. 26 below. Notice that there are now ab-initio state-of-the-art calculations of overlap functions in light nuclei using the Variational Monte Carlo method [37], which have recently been used to compare data to nuclear breakup reaction calculations [38].

Coulomb breakup: is one of the earliest indirect methods used in nuclear astrophysics to evaluate radiative capture cross sections and consist in measuring the inverse reaction in a field of virtual photons created by the fast projectile moving in the strong Coulomb field of the target [39, 40]. The complexities arising from the need to disentangle the contribution of different multipoles call for careful angular distribution measurements. This will be possible with SAMURAI and the detector setup in front of it.

Exploratory calculations of the interplay between the different mechanisms causing proton breakup (nuclear, direct Coulomb and recoil Coulomb) have shown a possible enhancement of the cross section due to interference effects with respect to the simple incoherent sum [38]. Furthermore the interaction of the core ^8B with the target is expected to show anomalies with respect to the strong absorption model usually adopted.

Reaction mechanism study: The existence of the SAMURAI spectrometer at this time, with its larger momentum and angular acceptances and the detection system in front of it, will allow for better and exclusive measurements now. The Si detector system will allow to simultaneously identify the protons broken from the projectile and the remnant core, their positions at two different planes behind the target and, therefore, the reconstruction of the reaction kinematics. For these, the Si strip detector system and the associated PA+ASIC electronics [41] that the authors of this proposal worked to design and build, need to have extreme capabilities in terms of number of channels, dynamic range and counting rate. *The light(er) HI involved in this particular reactions are however less demanding on the system and we deem it “good start” in the p-HI program planned at SAMURAI.*

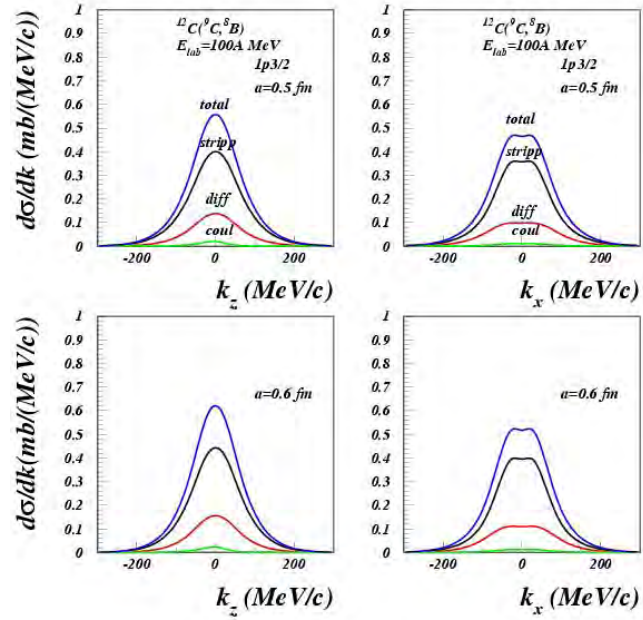


Figure 26. Calculated momentum distributions from 1p-breakup of ^9C at 100 MeV/u on a C target. Calculations with two different geometries of the binding potential for the last proton are shown (see text for details).

In addition to data for nuclear astrophysics, we expect the proposed studies to bring significant contributions to the understanding of the reaction mechanisms at these energies and to the development of theoretical reaction models and codes. As is always the case for indirect methods, such understanding is crucial to obtain reliable nuclear astrophysics data. We will make an explicit goal of these experiments to obtain data that help to test and improve our current breakup reaction calculations. We will determine the stripping and diffraction parts of the breakup cross sections, the contribution of two-step processes and will disentangle configuration mixing in the projectile. We will use different approaches for the reaction mechanisms and test different effective nucleon-nucleon interactions. Both in nuclear structure and reaction theories, special attention needs to be given to the study of the approximations made and of the different effective nucleon-nucleon interactions used to calculate the proton-target and core-target interactions. In the case of a Be and Pb target state-of-the-art optical potentials [42-45] exist that would allow for comparison of the results. The Hilbert space used in the reaction models is often not fully antisymmetrized under the

exchange of identical nucleons, and this affects the short-range form and normalization of the relevant wave functions. It also means that a full set of core excitations after nucleon removal is not easy to calculate. These problems could be solved by using a complete set of correlated many-body wave functions for the bound and continuum states. Another major concern in reactions with unstable nuclei at energies of several hundred MeV/nucleon is the role of relativistic corrections. Kinematic effects are easy and straightforward to include in the calculations. However, dynamical effects are not easy (Ref. 38 and references therein) and require a major theoretical effort, which is part of this project. Unifying reaction and continuum structure models as described above is essential. The role of continuum states in reactions with short-lived unstable nuclei has been a major area of theoretical study in recent years. Together with the developments of the continuum in nuclear structure, a proper study of properties of the continuum in nuclear reactions with unstable nuclei will be necessary.

To summarize:

^9C projectiles from fragmentation of a ^{16}O primary beam will be separated by BigRIPS and will impinge on the target at the target location of SAMURAI.

For *nuclear breakup* at this moment we favor a C target, but metallic Be targets are also considered if C targets will show non-uniformities.

For *Coulomb breakup* a Pb target will be used. Both targets (C and Pb) will be measured sequentially at 300 MeV/nucleon. After the reaction, the beam remnant and the reaction products will enter the Si tracking detector setup where they will be detected at two different positions behind the target. Then they will be bent by SAMURAI and measured in the detector system at the back.

The detector DALI will be coupled easily into the measurement. SAMURAI-DALI coincidences will be useful in disentangling the population of ^7Be g.s. and first excited state as final states in the two-proton breakup case (there is no need for it for $^9\text{C} \rightarrow ^8\text{B} + \text{p}$).

Main strong points of the proposal (as seen by the authors):

- *Nuclear astrophysics*: the determination of S_{18} astrophysical S-factor for the radiative proton capture on ^8B , a reaction important for nucleosynthesis in massive stars in the early Universe. Only possible through indirect methods like the proposed ones.
- *Inclusive measurements* will allow reaction mechanism studies and give good data for serious checks of the associated reaction theories. The nuclear (exclusive) breakup measurements provide information on nuclear breakup contribution (to the Coulomb dissociation results) in their higher multipole (essentially E2 or $l=2$) . Note that $l=1$ (E1) nuclear excitation should be negligible compared with the dominant (for direct capture) dipole Coulomb excitation.
- In earlier studies this E2 (relative) contribution in the case of ^8B Coulomb dissociation is still not converging in, say, 10% level. If it is large, a part of discrepancy between earlier Coulomb dissociation and ANC results could be interpreted.

- *Good start experiment* for a p-HI series of experiments at SAMURAI.

At the rate of ^9C secondary beam which RIBF will provide, good statistics will be acquired in short time of full and correct functioning of the setup. We estimate that 1.5 days will be sufficient to measure at each energy for the two targets. Most of this comes from the condition of coincidence gamma-particles which will disentangle the 2p-breakup to the first excited state of ^7Be from that of its g.s.

2. Experimental conditions

Below the experimental setup is sketched. The top view of the experimental setup at SAMURAI facility and which SAMURAI standard detectors will be used are shown in figures below. They show experimental setup and trajectories of charged particles from different breakup channels ($^8\text{B}+p$ and $^7\text{Be}+2p$) at different beam energies (100 and 300 MeV/nucleon).

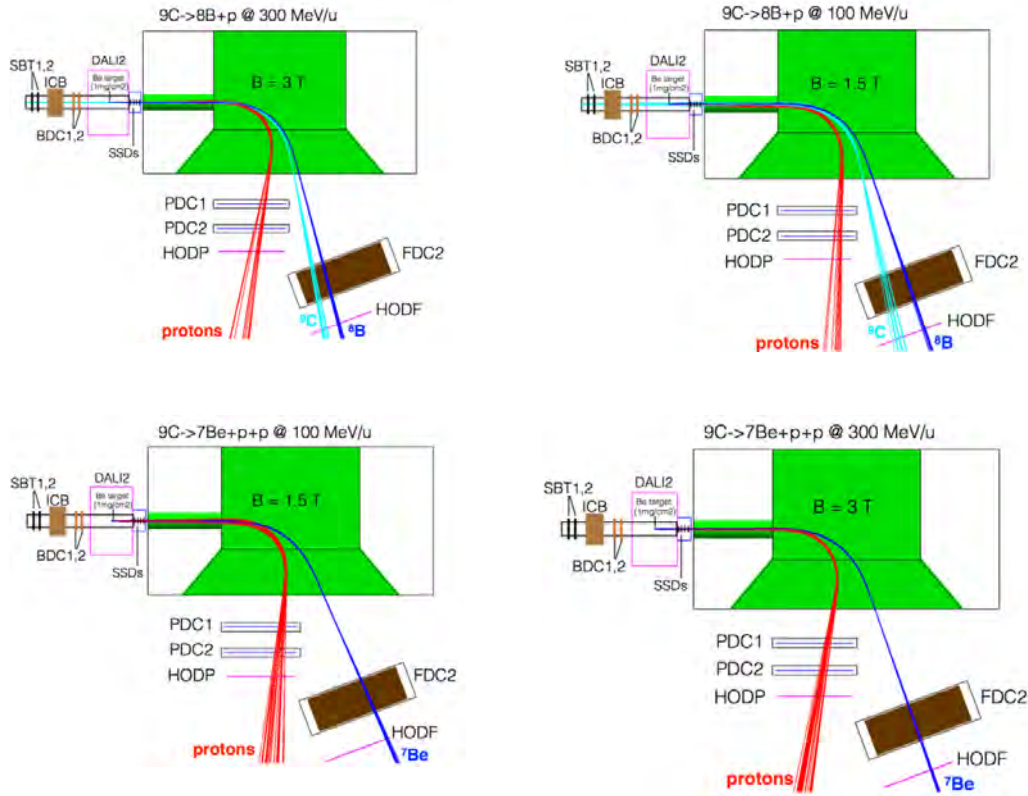


Figure 27. proposed setups (see text for details).

Standard tracking system will be used before the target as shown in the figure 27. ICB is in principle obsolete and can be removed since the charge of incoming light isotopes can be effectively measured by plastic scintillators SBT1 and SBT2. DALI2 might be replaced by

CATANA detector if available. Behind the SAMURAI, charge of the heavy fragment will be measured in HODF.

SAMURAI will be rotated by 90 degrees and filled with helium gas. Two field settings will be used: ~ 1.5 T and ~ 3 T due to the two beam energies 100 MeV/u and 300 MeV/u respectively.

Thick targets will be used.

Potential difficulties:

- No difficulties are expected with the production and separation of the secondary beam.
- Difficulties may occur due to the fact that the non-interacted beam will pass fully through the Si strip detectors at the front of SAMURAI. This will lead to a large rate of useless events and to a large number of delta-electrons from the first detectors into the next.

At this point the authors acknowledge that the latter is not a point very clear to us and was tested in a HIMAC experiment Feb. 2015. In case these factors will show to have a big impact, we'll consider a solution with a hole for the beam in the center. Such detectors are considered at this time and their impact on the final results will be simulated.

3. Readiness

All components to be used are ready, but some of them have not been tested yet in an assembled configuration in which they would work together. The detector system between the target and the front of SAMURAI proper has not been fully tested at the energies proposed here and the chamber is not yet completed (but will be by the time proposed). Its conceptual design is included in Fig. 28. Comprehensive tests will be done in the HIMAC experiment mentioned above and scheduled for February 2015. In particular we shall see how we can protect the detectors from delta-electrons emitted from the beam passing through the detectors and what rates we can safely handle.

Simulations for this setup were being made. Some were communicated and published [46].

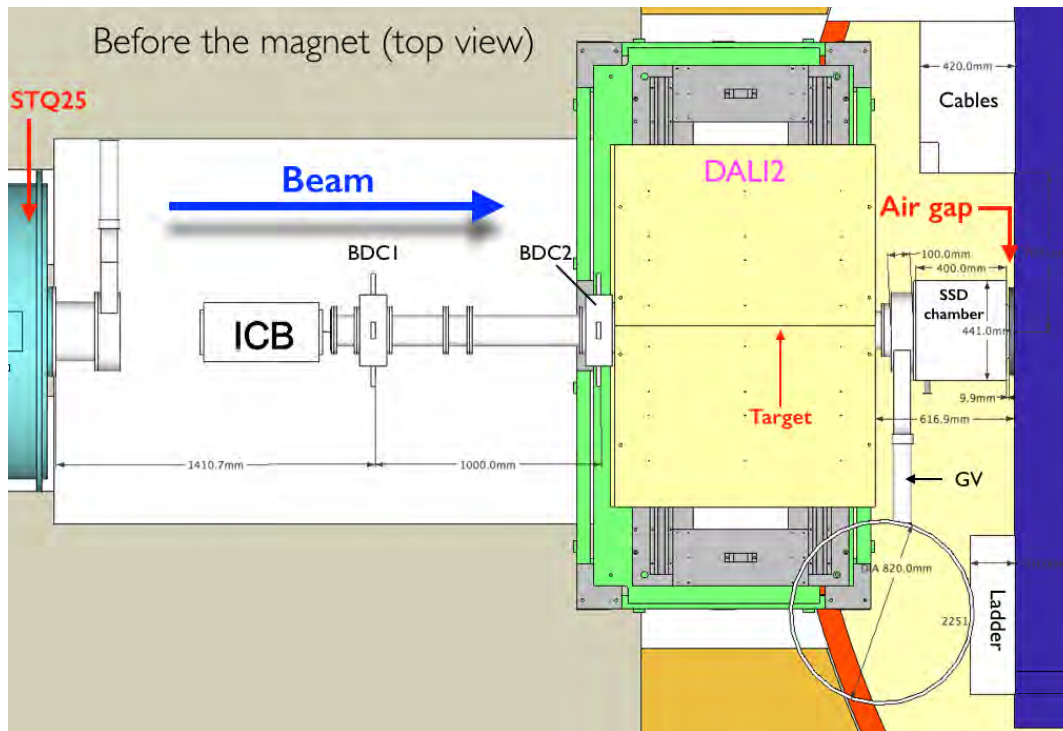


Figure 28. Conceptual design of the vacuum chamber in front of SAMURAI.

In February 2015 a test experiment was carried out at the HIMAC accelerator in Chiba, Japan, for the detector assembly prepared to be used for the 9C breakup experiment proposed and approved by the PAC of the RIBF (Radioactive Ion Beam facility) of RIKEN, Japan. The test was done together with the collaborating groups from RIKEN, Louisiana State University, Washington University in St. Louis and Texas A&M University. The main subject of the tests was the newly designed and built dual gain integrated preamplifiers. The test was successful. While it is part of the program of this project, the proposal and the participation at these tests was financed from another grant, therefore I will skip the details of the experiments and the results.

At this time, given the importance of the subject and of the experiment, we are also contemplating the addition of a plan B: the use of a tracking system between the target and SAMURAI, which does not take the secondary unreacted beam through the detectors, bypassing, therefore, one of the main complications. Our solution is based on S4-type detectors, produced by Micron Semiconductor. These detectors have a hole in the middle, which could accommodate the RIBF secondary beam, and have circles and sectors with sufficient granularity to allow for attaining the relative angle sensitivity that the experiments are requesting. The electronics would be the same as for the Plan A that use GLAST-type detectors by Hamamatsu. The complete simulations for this setup is to be made in the next few months in Bucharest.

5.2 Trojan Horse Method measurements for the $^{12}\text{C}+^{12}\text{C}$ system

Trojan Horse Method is a splendid indirect method for NA, which cannot be easily described here. It is pursued by the group of prof. Claudio Spitaleri from the University of Catania and INFN LNS, group that has shown with multiple examples its usefulness. They have proposed and test measurements were done in Bucharest, at the 9 MV FN tandem accelerator together with us to check if the reaction $^{12}\text{C} + ^{12}\text{C}$ can be studied using the Trojan Horse Method. The NA motivation is the same reaction as for our $^{13}\text{C}+^{12}\text{C}$ direct measurements described in Sec. 3. The reaction proposed was $^{12}\text{C}(^{16}\text{O}, \alpha^{20}\text{Ne})\alpha$. The test was done using an ^{16}O beam on ^{12}C targets. The beam was delivered on the beamline no. 4 (at 0 degree) in the large target chamber existent there. The setup was used before in Bucharest, but this time the reaction chamber was much improved. The test aimed at deciding if the method could work in this combination beam-target. Unfortunately the answer was NO = the projectile ^{16}O does not have a clear cluster structure in its ground state (a $^{12}\text{C}+\alpha$ clusterisation) to allow for the quasi-free reaction mechanism [9]. The experiment is not useful to study $^{12}\text{C}+^{12}\text{C}$ at low energies, but spectroscopic information was obtained and will be published (in a separate experiment the Catania group found the reaction with ^{14}N projectile would work!). However, we have a student that has written a diploma on the THM and is continuing toward a master thesis on similar subjects.

6 Optical Model Potentials for nucleus-nucleus collisions

We have a long-term program to understand and describe nucleus-nucleus collisions in terms of one interaction potential, the optical model potential (OMP). The PD has worked on the problem for almost two decades with dr. F. Carstoiu. The motivation is that a good understanding of all phenomena occurring in the elastic nucleus-nucleus scattering, which are used typically to extract OMP, and the interpretation of the origin of different aspects, including the well know potential ambiguities, are of crucial importance for finding and justifying the procedures used for predicting nucleus-nucleus OMP in the era of radioactive nuclear beams (RNB) (see ours based on double folding in Ref. 47). The reliability of these potentials is crucial in the correct description of a number of reactions, from elastic to transfer, to breakup, at energies ranging from a few to a few hundred MeV/nucleon. Of particular interest for us is to support the absolute values of the calculated cross sections for reactions used in indirect methods for nuclear astrophysics, see references [2-4] for the most recent results. The procedure was established in its main lines in the works of the last years of the past millennium when a large number of systematic and extended measurements of elastic scattering of p-shell nuclei were measured at Texas A&M University and were compared with doubly-folded potentials computed using various effective nucleon-nucleon interactions. A carefully tuned procedure was established by our first publication in 2000 [47] and extended a few times later. It was shown along the years that the potentials predicted by this procedure could explain or predict elastic scattering of loosely bound RNB. The best results were obtained with the JLM effective interaction which works at energies around 10 MeV/nucleon with only a renormalization of the real and imaginary parts by $N_R \sim 0.4$ and $N_I = 1.0$. A rather large renormalization of the real part of the potential was necessary at lower

energies, but it was shown that it tends to unity at larger energies (>50 MeV/nucleon). and could be extended to higher energies.

In this framework, the two senior researchers involved in this project treated in three related papers published in Romanian Journal of Physics [6-8] the case of heavy ion orbiting, one of the phenomena found over the years to occur is special cases of elastic scattering. While the consensus is that this phenomenon is well understood semi-classically, it is not well documented by specific examples. We do not extent the discussion here, but attach the pdf files of the submitted articles.

7. The Carpathian Summer Schools of Physics

7.1 Carpathian Summer School of Physics 2014

The Carpathian Summer School of Physics 2014 was organized in Sinaia, July 13-26, 2014. It was the 26th edition of a tradition that begun in 1964 and the 5th in the series dedicated to nuclear and particle astrophysics, in relation to nuclei and to physics of exotic nuclei in particular. This is already a 50 years tradition. Therefore we also (modestly) celebrated the jubilee of the Carpathian schools this year. The title of the event was:

"Exotic Nuclei and Nuclear/Particle Astrophysics (V). From Nuclei to Stars"

and was in the series with the same title organized in Mamaia (2005) and Sinaia (2007, 2010 and 2012). It was hosted again in Sinaia, on the facilities of hotel "International". The Carpathian school is part of the European Network of Nuclear Astrophysics Schools (ENNAS), together with the **European Summer School on Experimental Nuclear Astrophysics, ESSENA** (Santa Tecla, Italy) and the **Russbach School on Nuclear Astrophysics, RSNA** (Russbach am Pass Gschütt, Austria). In agreement with those schools' organizers, we created an established network of periodic events that responds to the need of preparing and educating the younger generations of physicists in the cross disciplinary fields of nuclear physics and astrophysics. The organizers were, as in the past 5 editions:

"Horia Hulubei" National Institute for Physics and Nuclear Engineering (IFIN-HH)
Bucharest and
Cyclotron Institute, Texas A&M University (TAMU), College Station, Texas, USA.

As in the past editions also, the **first week** of the event had a school-like format defined by a series of courses 1- 2 hours each. It was being aimed at graduate students, post-docs and young researchers. About 55 students from the host country, the surrounding regions and all countries attended. A number of stipends (22) to cover the local expenses for students were available and established following the rules spelled out in our announcements. The **second week** had a conference-like format, closer to the past format of all Carpathian schools, with 1 hour invited lectures. Students and young researchers gave 20 min. short communications, both weeks.

The sessions of CSSP14 covered the following topics, set by the organizers after consultation with the other directors of ENNAS and advice from an extended International Advisory Committee:

- **Exotic nuclei**
- **Nuclear physics with RIBs**
- **Nuclear physics for astrophysics**
- **Neutron stars and EOS**
- **Issues in nuclear astrophysics & nucleosynthesis**
- **Stellar evolution. Compact stars and supernovae**
- **Neutrino physics**
- **Astroparticle physics**
- **Stellar and laser induced plasmas**
- **Physics at ELI-NP**

We intended to bring to this audience news about the **Extreme Light Infrastructure – Nuclear Physics (ELI-NP)**, the newest and most important scientific project that happens in the host country and the region. Therefore, Thursday-Friday July 17-18 the school included the *International Conference “ELI-NP. Status and Perspectives”*.

A special outreach day was being planned for **Saturday July 19th**. The morning session gathered lectures addressing a broader audience like that of prof. K.-L. Kratz, 2014's Bethe prize winner, and the charming lectures of S. Bishop (a nuclear physicist) and R. Egli (a geologist) on looking in the depth of the planetary ocean for signs of a supernova explosion in the past in our galactic neighbourhood (the problem of ^{60}Fe)! The afternoon session was held in a, by now traditional, round table format. The subject chosen this year was:

“CERN at 60 and the internationalization of science”

The day was honoured by the presence of prof. Rolf Heuer, director general of CERN, prof. Tudor Prisecaru, MEN state secretary, other officials of the host country involved in the research policy and in the management of research and higher education, by CERN, FAIR, and ELI officials, scientists working at CERN, FAIR and ELI-NP, politicians and representatives of media invited to join the CSSP14 participants in open discussions on the above subject. The session was followed by the school's banquet that evening and by the school excursion(s) on Sunday, July 20th. A short overview of the interventions at this session and the lecture of professor Heuer are included in Part III of this volume.

Sponsors of the school were *the two organizing institutions*, the *Romanian Ministry of National Education (MEN)*, ENSAR through *the ATHENA network*, the *Nuclear Astrophysics Virtual Institute (NAVI)* and the exhibitors *iGroup*, *CAEN* and *Canberra*. The event was endorsed by the European Physical Society, through its Nuclear Physics Board. Most of the participants were supported by their respective institutions, a fact which contributed to existence and the success of the school and which makes these institutions be our sponsors too.

We have attracted at the peak of participation on Saturday-Sunday July 19-20, approximately 120 people, of which 52 from outside Romania. There were 59 lecturers who gave 65 lectures in the two weeks. As organizer of the latest 5 editions of the school with this title, I can say that this was probably the most successful, in terms of number and quality of participants and lectures/debates. I mention that we had 31 communications from students and young researchers, compared to 19 in the previous edition (CSSP12).

Due to reduction of funds for 2014, we avoided using resources from this project and used only 4,521 RON for Carpathian school's organization. Most of the funds were attracted from outside: 10,000 euro from ATHENA, a network of ENSAR, 5,000 euros from NAVI, 4,600 euros from exhibitors CAEN, iGroup and Canberra and 7,500 RON for the Ministry of National Education, Bucharest. In our integrated financial report to MEN, we evaluated that the total cost of the event was 234,060 RON, not including the expenses of the participants who use own institutions' funds for accommodation and meals.

The volume of the Proceedings is published with the American Institute of Physics, New York [16]. In its 450 pages it contains 30 lectures and 30 communications. It was published online before the end of the year 2014, and in print at the beginning of 2015. We include in Appendix 1 the Content pages of the volume of these Proceedings.

7.2 Carpathian Summer School of Physics 2016

For part of 2015 and first half of 2016, the PD and the young members of NAG were working on the organization of the 2016 edition of the Carpathian Summer School of Physics. It took place in the same location, Sinaia, and was partly financed from this project. Other sponsors were ANCSI, ENSAR2, plus 7 private sponsors.

The title of the event was:

"Exotic Nuclei and Nuclear/Particle Astrophysics (VI). Physics with small accelerators"

and was the 6th in the latest series with the same title, again part of ENNAS (European Network of Nuclear Astrophysics Schools). This year we added additional flavour to the event through the explicit inclusion of subjects related to physics with small accelerators, fundamental or applied research subjects.

We remained faithful to the successful format of the latest editions: the **first week** of the event was closer to a school-like format defined by a series of courses up to 2-4 hours each, aimed at graduate students, post-docs and young researchers. The **second week** had a conference-like format, with 1 hour invited lectures. Students and young researchers gave 20 min. short communications.

For this edition "**Horia Hulubei**" National Institute for Physics and Nuclear Engineering (IFIN-HH) Bucharest-Magurele was the sole organizer of the school.

Topics announced were similar to the ones in 2014, but included applications explicitly:

- **Exotic nuclei**
- **Nuclear physics with RIBs**
- **Nuclear physics for astrophysics**
- **Stellar evolution. Compact stars and supernovae**
- **Astroparticle physics**
- **Stellar and laser induced plasmas**

- **Physics at ELI-NP**
- **Applications at small accelerators**
- **Nuclear astrophysics with small accelerators**
- **Instrumentation**
- **Accelerators for medical treatments, radioisotope production and industrial applications**

Students from Romania, from the surrounding regions and all countries were invited to attend. A limited number of stipends to cover the local expenses for students were available. In total there were 126 participants:

- 53 invited lecturers
- 55 students, who presented 23 oral communications.

Two days (31 June-1 July) have been reserved for the special sessions “ELI-NP. Status and Perspectives”. Saturday July 2 we had the traditional outreach session with the subject “JINR Dubna at 60 and the internationalization of science”, which was honored by the participation of Prof. Mikhail Itkis, deputy director of JINR Dubna, Prof. B. Sharkov, scientific director of FAIR Darmstadt, prof. K. Langanke, scientific director of GSI Darmstadt, prof. I.I. Ursu, vice-president of ANCSI, Bucharest, other guests from Romanian academia, public and media representatives.

Between June 30 and July 2 a number of exhibits were open in the framework of the school: “JINR at 60” and exhibits from the 7 sponsors.

CSSP16 was unanimously appreciated as a success, both for the quality of science and organization. It was recommended:

- To continue this school with a new edition in 2018
- To continue its affiliation with ENNAS
- The future editions to concentrate on physics at FAIR and ELI-NP.

The Proceedings of CSSP16 will be published again with the prestigious “AIP Conference Proceedings” series of the American Institute of Physics. At the time of this report the volume is under contract, but still under preparation (with deadline in November 28, 2016).

8. List of publications and conferences

8.1 List of publications for PD and the NAG 2013-2016

According to the ISI Thomson-Reuters Web of Science, the PD has published in 2013-2016 a number of 22 articles and conference papers, with >30 citations. Of which at least 16 publications are related to this project.

Here is the **list of publications**:

Livius Trache and the Nuclear Astrophysics Group 2013-2016

1. Trache, Livius, in INTERNATIONAL SUMMER SCHOOL FOR ADVANCED STUDIES DYNAMICS OF OPEN NUCLEAR SYSTEMS (PREDEAL12) Book Series: Journal of Physics Conference Series Volume: 413 Article Number: 012025 Published: 2013
Nuclear astrophysics with exotic nuclei and rare ion beams
2. Pollacco, E.; Trache, L.; Simmons, E.; et al.
NUCLEAR INSTRUMENTS & METHODS IN PHYSICS RESEARCH SECTION A-ACCELERATORS SPECTROMETERS DETECTORS AND ASSOCIATED EQUIPMENT Volume: 723 Pages: 102-108 Published: SEP 21 2013
AstroBox: A novel detection system for very low-energy protons from beta-delayed proton decay
3. Al-Abdullah, T.; Carstoiu, F.; Chen, X.; et al. **Phys. Rev. C** **89**, 025809 Published: FEB 26 2014
Astrophysical reaction rate for $F-17(p,\gamma)Ne-18$ from the transfer reaction $C-13(O-17,O-18)C-12$
4. Al-Abdullah, T.; Carstoiu, F.; Gagliardi, C. A.; et al. , **Phys. Rev. C** **89**, 064602 Published: JUN 5 2014
Peripheral elastic and inelastic scattering of $O-17,O-18$ on light targets at 12 MeV/nucleon
5. Carstoiu, F.; Al-Abdullah, T.; Gagliardi, C. A.; et al. in Trache, L., Chesneanu, D, Ur, CA (eds) EXOTIC NUCLEI AND NUCLEAR/PARTICLE ASTROPHYSICS (V). FROM NUCLEI TO STARS, AIP Conf. Proc., vol. 1645, p. 39-51, 2015
Peripheral elastic and inelastic scattering of $O-17,O-18$ on light targets at 12 MeV/nucleon
6. Chesneanu, D.; Trache, L., Margineanu, R.; Pantelica, Ghita, D, Straticiuc M, Burducea I.; Blebea-Apostu, A. M., Gomoiu, C. M., Tang, X., in Trache, L., Chesneanu, D, Ur, CA (eds) EXOTIC NUCLEI AND NUCLEAR/PARTICLE ASTROPHYSICS (V). FROM NUCLEI TO STARS, AIP Conf. Proc., vol. 1645, p. 311, 2015
Investigating $C-13+C-12$ Reaction by the Activation Method. Sensitivity Tests
7. F. Carstoiu, M. Lassaut, L. Trache and V. Balanica, **Rom. J. Phys.** vol. **61**, 400 (2016)
Heavy Ion Orbiting and Regge Poles (I)
8. Zhang, NT, Tang, XD, Chen, H, Chesneanu, D, Straticiuc, M, Trache, L, Burducea, I , Li, KA, Li, YJ, Ghita, DG, Margineanu, R , Pantelica, A, Gomoiu, C, in Liu, WP e.a. (eds.) "13TH INTERNATIONAL SYMPOSIUM ON ORIGIN OF MATTER AND EVOLUTION OF GALAXIES (OMEG2015)", **Eur Phys J Web of Conferences**, vol. **109** (2016)
Fusion cross section of $C-12+C-13$ at sub-barrier energies
9. Pizzone, RG; Roeder, BT; McCleskey, M; Trache, L; Tribble, RE; Spitaleri; Bertulani, CA; Cherubini; Gulino M; Indelicato, I; La Cognata, M; Lamia, L; Rapisarda, GG; Sparta, R, **Eur. Phys. J. A** **52**, 24 (2016)
Trojan Horse measurement of the $F-18(p, \alpha)O-15$ astrophysical $S(E)$ -factor
10. Saastamoinen, A.; Pollacco, E.; Roeder, B. T.; et al. **NIM B** **376** (2016)357.
AstroBox2-detector for low-energy particle detection

11. Spiridon A., Pollacco E., Roeder B.T. et al, **NIM B 376** (2016)364
Upgrade of the TAMU MDM-focal plane detector with MicroMegas technology
12. Trache Livius, in C. Spitaleri, L. Lamia and G.R. Pizzone (eds.), Proceedings of the 8th European Summer School of Physics on Experimental Nuclear Astrophysics (Santa Tecla School), **J. of Phys: Conf Series**, vol. **703** (2016) 012011
Nuclear Astrophysics at IFIN-HH
13. D. Tudor, A.I. Chilug, M. Straticiuc, L. Trache et al., in C. Spitaleri, L. Lamia and G.R. Pizzone (eds.), Proceedings of the 8th European Summer School of Physics on Experimental Nuclear Astrophysics (Santa Tecla School), **J. of Phys: Conf Series**, vol. **703** (2016) 012028.
Experimental study of the $^{13}\text{C}+^{12}\text{C}$ fusion reaction at deep sub-barrier energies
14. F. Carstoiu, M. Lassaut, L. Trache, V. Balanica, **Rom. J. Phys.**, vol. **61**, 857-874 (2016).
Heavy Ion Orbiting and Regge Poles (II)
15. F. Carstoiu, M. Lassaut, L. Trache, V. Balanica, **Rom. J. Phys.**, vol. **61**, 1180-1197 (2016).
Heavy Ion Orbiting and Regge Poles (III)
16. V. Panin et al., **Nucl. Phys. Review** **28**, (2015) 9
New generation of experiments for the investigation of stellar (p,γ) reaction rates using SAMURAI
17. A. Saastamoinen, A. Kankainen and L. Trache, **Eur. Phys. J. Plus**, **131**, 272 (2016)
Beta-decay of ^{31}Cl : an indirect probe of the $^{30}\text{P}(p, \gamma)^{31}\text{S}$ reaction. Present status and future perspectives
18. G. Rapisarda et al. **J. of Phys: Conf Series**, vol. **703** (2016), 012024.
Study of $^{16}\text{O}(^{12}\text{C},\alpha)^{20}\text{Ne}$ for the investigation of carbon-carbon fusion reaction via the Trojan Horse Method

Books:

1. **L. Trache, D. Chesneanu and C.A. Ur (eds.)**
Exotic Nuclei and Nuclear/Particle Astrophysics (V). From Nuclei to stars: Carpathian Summer School of Physics 2014
American Institute of Physics Conference Proceedings, vol. 1645, Melville, New York, 2015.
<http://dx.doi.org/10.1063/v1645.frontmatter>

8.2 Participation to conferences, schools and workshops in NA

A number of participations of members of our group in conferences, schools or workshops were related directly to creating and improving the visibility of NA research at IFIN-HH, the very subject of this proposals. This is the case mostly for the seniors of the group, in particular of my-self, as PD. The juniors and students were participating to learn, mostly, but they also have communicated group's latest results. As such, the project director was invited in 2013 - 2016 to several conferences, meetings, workshops and schools dedicated to nuclear astrophysics or related to it. Several of those were financed from this project, but not all. In particular I was asked to talk or lecture about the use of indirect methods in Nuclear Astrophysics using radioactive nuclear beams. I indicate them in the list below, specifying the website where the material was/is posted, when available or known to me:

- 10th Russbach Winter school on nuclear astrophysics, in Russbach, Austria. March 2013. Invited lecture: "Decay spectroscopy for nuclear astrophysics". <http://russbachwks.sciencesconf.org/resource/page/id/12>
- The EURISOL User Group Topical Meeting, Krakow, July 1-3 2013, <http://eurisol.ifj.edu.pl/>. Invited talk: "Rare isotope production and ELI-NP".
- International Workshop in Nuclear Dynamics in honor of prof. J.B. Natowitz, Texas A&M University, College Station, TX, USA. Aug. 22-25, 2013.
- The APS town meeting at NSCL, East Lansing, MI, USA. 25 Aug. 2013.
- 2nd International workshop on quasi-free scattering with Radioactive-Ion Beams, QFS13, Azores Islands, Portugal. Sept. 15-21, 2013. Invited talk: "Experiments on Direct Reactions with Light Radioactive Beams [for nuclear structure, reaction mechanisms and nuclear astrophysics]". <http://cfnul.cii.fc.ul.pt/events/QFS-RB13/>.
- 7th European Summer School on Experimental Nuclear Astrophysics, St. Tecla, Italy. Sep. 15-25, 2013. Invited lecture: "Decay spectroscopy for nuclear astrophysics and conditions created by one ExtremeLy hot Infrastructure for Nuclear astroPhysics". <https://agenda.infn.it/conferenceDisplay.py?confId=5302>
- ECOS-LINCE Workshop, University of Huelva (Spain), 30-31 October, 2013; invited talk: "Nuclear astrophysics using high intensity stable beams". <http://indico.cern.ch/event/263009/?ovw=True>
- Texas Symposium on Relativistic Cosmology, Dallas, TX, USA. Dec. 9-13, 2013. Invited NA session talk. "*Nuclear Physics for Astrophysics: from the Laboratory to the Stars*".
- 11th Russbach Winter school on nuclear astrophysics, in Russbach, Austria. March 9-15, 2014. Invited lecture: "[Nuclear astrophysics at ELI-NP](http://russbachwks2014.sciencesconf.org/)".
- Final ATHENA workshop at Villa Vigoni on Lake Como, Italy. May 13-16, 2014. Invited lecture "*Indirect methods in nuclear astrophysics using RIBs*"
- Nuclei in Cosmos NIC XIII school, Debrecen, Hungary. June-July 2014. Invited lectures: "Experimental nuclear astrophysics (stable beam experiments)". <http://www.atomki.hu/nic2014school/program.html>
- International Olympiad Astronomy & Astrophysics, Universitatea "Stefan cel Mare" Suceava, Romania. Invited talk at outreach event: "*Chemical origin of chemical elements*", Aug. 4th, 2014.
- APS town meeting on the new Long Range Plan, Texas A&M University, College Station, TX, USA. Aug. 2014.
- ECT* workshop Nuclear Physics and Astrophysics of Neutron-Star Mergers and Supernovae, and the Origin of R-Process Elements" Trento, Italy, Sep. 8-12, 2014. Invited talk and organizer. <http://www.ectstar.eu/node/788>
- Notre Dame-Europe Symposium on Nuclear Science and Society, London, Oct. 27-29, 2014. Invited talk: "*Study and preservation of cultural heritage with atomic and nuclear techniques at IFIN-HH Bucharest*". <http://isnap.nd.edu/events/NSS2014/>.
- 12th Russbach Winter school on nuclear astrophysics, in Russbach, Austria. March 11-14, 2015. Invited lecture "*Nuclear astrophysics with Radioactive Ion Beams*".

- International Conference ISTROS 2015, Casta-Papiernica, Slovakia. Invited lecture on Nuclear Astrophysics.
- International Workshop “Weakly Bound Exotic Nuclei”, Natal, Brasil, May 23-30, 2015. Invited talk “*Nuclear Astrophysics with Radioactive Ion Beams*”.
- Gordon Research Conference “Confluence of Structure and Reactions”, in New London, NH, SUA, May 31-June 6, 2015. Invited talk.
- Shanghai, China – invited talk at SINAP: “Nuclear Astrophysics and IFIN-HH”, June 2015.
- Nucleus-Nucleus Conference 2015, Catania, Italy, member of International Advisory Committee.
- EuNPC Groningen, The Netherlands, Aug. 31 – Sep 3, 2015. Co-author several presentations.
- International Conference “Processes in Isotopes and Molecules”, Cluj-Napoca, Romania, Sept. 23-25, 2015. Invited talk “*Isotopes and molecules in current nuclear physics*”
- European School on Experimental Nuclear Astrophysics, St. Tecla, Italy, Sep 13-20, 2015. Lecture invitata: “Nuclear Astrophysics at IFIN-HH Bucharest”.
- 13th Russbach Winter school on nuclear astrophysics, in Russbach, Austria. March 6-12, 2016. Invited lecture “*Indirect Methods in Nuclear Astrophysics*” .
- ECT* workshop “Three-body systems in reactions with rare isotopes”, October 3-7, 2016, Trento, Italy. Invited talk “**Breakup of ^9C : what can we learn? Inclusive and exclusive breakup of ^9C in nuclear and Coulomb fields for $S_{18} - ^8\text{B}(p,g)^9\text{C}$** ”

Dr. Daniela Chesneanu has participated and presented communications at the 7th European Summer School on Experimental Nuclear Astrophysics, St. Tecla, Italy. Sep. 23-25, 2013 and at the Carpathian Summer School of Physics 2014.

The students of the group attended schools on our research subjects: the JINR Dubna school in Borovets, Bulgaria in 2014 (V. Iancu and I. Focsa) and in 2015 (A. Chilug and D. Tudor), and the CSSP14 and CSSP16, Sinaia.

Physicists Chilug Alexandra and Tudor Dana attended the JINR Dubna school in Borovets, Bulgaria, 2015 and at the 8th European Summer School on Experimental Nuclear Astrophysics, St. Tecla, Italy. Sep. 13-20, 2015. Tudor Dana has presented our experimental results on “Measurement of $^{13}\text{C}+^{12}\text{C}$ fusion cross section at deep sub-barrier energies in IFIN-HH” at the 8th European Summer School on Experimental Nuclear Astrophysics, St. Tecla, Italy. Sep. 13-20, 2015. They also presented communications at CSSP16 and are working hard for the completion of the volume of CSSP16 Proceedings.

9. Conclusions

From the above report and documents attached, we conclude that the objectives for the 3 years of this project were fulfilled in both spirit and letter. It may be that some of the activities proposed over 4.5 years ago could not be done in their last and smallest letter, due to the fact that they are affected not only by local parameters (availability of personnel and funds), but by external ones, like availability of beam time at large RNB facilities (RIBF at

RIKEN, Japan and MARS at TAMU, USA), and possibly, by shifts in the short term tactics, while keeping the focus of the strategy of research: nuclear astrophysics in IFIN-HH.

A number of activities and achievements related to the main scientific motivation of this project must be outlined here. They are related to the constant work to obtain, then increase, the visibility of a nuclear group working in nuclear astrophysics in IFIN-HH. These were on two directions, intertwined in fact:

- Creating and testing the experimental capabilities for nuclear astrophysics in Bucharest. This was done by experiments at the 9 MV tandem, but especially at the new 3 MV tandetron of IFIN-HH and the ultra-low background laboratory in a salt mine.
- Creating and promoting the visibility of the NA research in IFIN-HH, and promotion of the potential in European context, which should attract outside users for our facilities (and allow therefore, for justified reciprocity, our participation in experiments at foreign facilities). This was done by participation to a number of international conferences, schools and workshops, in particular of the PD, who used his existing prestige and recognition from the previous decades of activity in this field of research.

The results of this project allowed us to file two new project proposals covering the next 2-3 years, one dealing with the indirect methods for nuclear astrophysics using RNB at foreign facilities (NAIRIB), project which was already accepted and financed this month, and one (NUCASTRO2) dealing with direct measurements at IFIN-HH's own facilities, which is still under evaluation.

Bibliography

- [1] L. Trache – Project proposal, April 2012. File C Descrierea proiectului.pdf.
- [2] T. Al-Abdullah, **F. Carstoiu**, X. Chen, H. L. Clark, C. A. Gagliardi, Y.-W. Lui, A. Mukhamedzhanov, G. Tabacaru, Y. Tokimoto, L. Trache, R. E. Tribble, and Y. Zhai, **Phys. Rev. C** **89**, 025809 (2014).
- [3] M. McCleskey, A. M. Mukhamedzhanov, L. Trache, R. E. Tribble, A. Banu, V. Eremenko, V. Z. Goldberg, Y.-W. Lui, E. McCleskey, B. T. Roeder, A. Spiridon, **F. Carstoiu**, V. Burjan, Z. Hons, and I. J. Thompson, **Phys. Rev. C** **89**, 044605 (2014).
- [4] T. Al-Abdullah, **F. Carstoiu**, C. A. Gagliardi, G. Tabacaru, L. Trache, and R. E. Tribble, **Phys. Rev. C** **89**, 064602 (2014).
- [5] Carstoiu, F.; Al-Abdullah, T.; Gagliardi, C. A.; et al. in Trache, L., Chesneanu, D, Ur, CA (eds) EXOTIC NUCLEI AND NUCLEAR/PARTICLE ASTROPHYSICS (V). FROM NUCLEI TO STARS, AIP Conf. Proc., vol. 1645, p. 39-51, 2015
- [6] F. Carstoiu, M. Lassaut, L. Trache and V. Balanica, **Romanian Journal of Physics**, vol. **61**, 400 (2016).
- [7] F. Carstoiu, M. Lassaut, L. Trache, V. Balanica, **Rom. J. Phys.**, vol. **61**, 857-874 (2016).
- [8] F. Carstoiu, M. Lassaut, L. Trache, V. Balanica, **Rom. J. Phys.**, vol. **61**, 1180-1197 (2016).
- [9] G. Rapisarda et al. **J. of Phys: Conf Series**, vol. **703** (2016), 012024
- [10] A. Saastamoinen; Pollacco, E.; Roeder, B. T.; et al. **NIM B** **376** (2016)357.
- [11] A. Spiridon, Pollacco E., Roeder B.T. et al, **NIM B** **376** (2016)364
- [12] L. Trache, F. Carstoiu, CA Gagliardi and RE Tribble, **Phys. Rev. Lett.** **87**, 271102 (2001).
- [13] L. Trache, F. Carstoiu, CA Gagliardi and RE Tribble, **Phys. Rev. C** **69**, 032802 (2004).
- [14] A. Banu et al., **Phys. Rev. C** **84**, 015803.
- [15] A. Banu et al., **Phys. Rev. C** **86**, 015806.
- [16] L. Trache, D. Chesneanu and C.A. Ur (eds.), *Exotic Nuclei and Nuclear/Particle Astrophysics (V). From Nuclei to stars: Carpathian Summer School of Physics 2014* American Institute of Physics Conference Proceedings, vol. 1645, Melville, New York, 2015. <http://dx.doi.org/10.1063/v1645.frontmatter>
- [17] I. Burducea, M. Straticiuc, D.G. Ghita, D.V. Mosu, C.I. Calinescu, N.C. Podaru, D.J.W. Mous, I. Ursu, N.V. Zamfir, **Nuclear Instruments and Methods in Physics Research B** **359**, 1219, 2015.

- [18] D. Chesneanu, L. Trache, R. Margineanu, A. Pantelica, D. Ghita, M. Straticiuc, I. Burducea, A.M. Blebea-Apostu, C.M. Gomoiu and X. Tang, in the above Proc. CSSP14
- [19] D. Tudor, A.I. Chilug, M. Straticiuc, L. Trache et al., in C. Spitaleri, L. Lamia and G.R. Pizzone (eds.), Proceedings of the 8th European Summer School of Physics on Experimental Nuclear Astrophysics (Santa Tecla School), **J. of Phys: Conf Series**, vol. **703** (2016) 012028.
- [20] Zhang, NT, Tang, XD, Chen, H, Chesneanu, D, Straticiuc, M, Trache, L, Burducea, I, Li, KA, Li, YJ, Ghita, DG, Margineanu, R, Pantelica, A, Gomoiu, C, in Liu, WP e.a. (eds.) “13TH INTERNATIONAL SYMPOSIUM ON ORIGIN OF MATTER AND EVOLUTION OF GALAXIES (OMEG2015)”, **Eur Phys J Web of Conferences**, vol. **109** (2016)
- [21] R. M. Margineanu, C. Simion, S. Bercea, O.G. Dului, D. Gheorghiu, A. Stochioiu and M. Matei, **Appl. Radiat. Isot.** **66**, 1501(2008)
- [22] R. M. Margineanu et al., **Appl. Radiat. Isot.** **67** (2009) 759–761
- [23] <http://radware.phy.ornl.gov>
- [24] <http://lise.nscl.msu.edu/lise.html>
- [25] R.A.Dayras, R.G. Stokstad, Z.E.Switkowski and R.M.Wieland, **Nucl. Phys. A****625**, 152-188, 1976
- [26] C. Rolfs and W.S. Rodney, *Cauldrons in the Cosmos*, University of Chicago Press, 1988.
- [27] V.E. Jacob et al., **Phys. Rev. C** **74**, (2006).
- [28] R.E. Tribble et al., **Nucl. Instr. Meth. A** **285**, 441 (1991).
- [29] L. Trache et al., AIP Conf. Proc. **1409**, 67 (2011); doi: 10.1063/1.3664152
- [30] A. Saastamoinen, L. Trache et al., **Phys. Rev. C** **83**, 045808 (2011).
- [31] Y. Giomataris *et al.*, **Nucl. Instr. und Meth. in Phys. Res. A** **376** (1996) 29-35
- [32] E. Pollacco, L. Trache et al., **Nucl. Instr. Meth. Phys. Res. A** **723**, 102 (2013).
- [33] R. J. Tighe, J. C. Batchelder, D. M. Moltz, T. J. Ognibene, M. W. Rowe, J. Cerny, and B. A. Brown, **Phys. Rev. C** **52**, R2298 (1995).
- [34] M. Horoi, private communication
- [35] L. Trache, F. Carstoiu, CA Gagliardi and RE Tribble, **Phys. Rev. C** **66**, 035801 (2002)
- [36] A.M. Mukhamedzanov, C.A. Gagliardi and R.E. Tribble, **Phys. Rev. C** **63**, 024612.
- [37] R. B. Wiringa, <http://www.phy.anl.gov/theory/research/overlap/>
- [38] C.A.Bertulani, **Phys. Rev. Lett.** **94**, 072701 (2005); K. Ogata and C.A. Bertulani, **Prog. Phys.** **77** (2014) 106901.

- [39] G. Baur, CA Bertulani and H. Rebel, **Nucl. Phys. A****458**, 188 (1986).
- [40] T. Motobayashi et al., **Phys. Rev. Lett.** **73**, 2680 (1994).
- [41] G.I. Engel et al., **NIM A** **652**, 462 (2011).
- [42] A. Bonaccorso, R. J. Charity, R. Kumar, G. Salvioni, proceedings of the CSSP 2014, Sinaia, July 2014.
- [43] A. Bonaccorso, and R. J. Charity, **Phys. Rev. C** **89**, 024619 (2014).
- [44] C. Mahaux and R. Sartor, **Adv. Nucl. Phys.** **20**, 1 (1991).
- [45] A. Bonaccorso, F. Carstoiu and R.J. Charity, **Phys. Rev. C** **94**, 034604 (2016)
- [46] V. Panin et al., **Nucl. Phys. Review** **28**, (2011) 9.
- [47] L. Trache et al. **Phys. Rev. C** **61**, 024612 (2000).

Consideram ca obiectivele acestei faze au fost integral indeplinite.

Responsabil Proiect
Dr. Livius Trache

Responsabil Etapa
Dr. Livius Trache



Front Matter for Volume 1645

Citation: [AIP Conference Proceedings 1645](#), frontmatter (2015); doi: 10.1063/v1645.frontmatter

View online: <http://dx.doi.org/10.1063/v1645.frontmatter>

View Table of Contents: <http://scitation.aip.org/content/aip/proceeding/aipcp/1645?ver=pdfcov>

Published by the [AIP Publishing](#)

Articles you may be interested in

[Back Matter for Volume 1645](#)

AIP Conf. Proc. **1645**, backmatter (2015); 10.1063/v1645.backmatter

[Front Matter for Volume 1417](#)

AIP Conf. Proc. **1417** (2011); 10.1063/v1417.frontmatter

[Front Matter for Volume 1409](#)

AIP Conf. Proc. **1409** (2011); 10.1063/v1409.frontmatter

[Front Matter for Volume 1402](#)

AIP Conf. Proc. **1402** (2011); 10.1063/v1402.frontmatter

[Front Matter for Volume 888](#)

AIP Conf. Proc. **888** (2007); 10.1063/v888.frontmatter



Exotic Nuclei and Nuclear/ Particle Astrophysics (V). From Nuclei to Stars

Carpathian Summer School of Physics 2014



Sinaia, Romania

13–26 July 2014

Editors

Livius Trache, Daniela Chesneanu and Calin Alexandru Ur

AIP | Proceedings

proceedings.aip.org

AIP Proceedings: A name your community will know and respect

40 years' experience • 100,000+ papers • 1,500+ volumes

A world-class proceedings service for all events: From workshops to the largest international conference

- Online-only proceedings
- Optional printed copies or CDs for participants
- Rapid online and print publication

Our wealth of experience and expertise will ensure an outstanding publication experience.

Publication fees which work with your budget

- **Simple online publication fees:** Completely independent of page counts, publish substantial papers at no extra cost.
- **Options for online access:** 1-year conference access or select perpetual open access for the entire community.

Flexibility in the printed medium

Choose from these options to print all papers or just a selection of articles from the conference:



Conference collection

- Printed copies containing all papers published in the online proceedings.
- For editors who want to reproduce all online papers for their participants.



Selected papers

- Printed copies containing a selection of papers chosen by the editors.
- Choose to print just the best work, avoid the cost of printing everything.



Workshops and summer schools

- Printed copies designed especially for summer schools and workshops.
- Visibility and identity for events publishing tutorials and reviews.

Get a proposal for your proceedings in 3 simple steps

Step 1.

Obtain a proceedings questionnaire by writing to us at confproc@aip.org or download from proceedings.aip.org

Step 2.

Fill in the questionnaire with details of your conference and return it to confproc@aip.org

Step 3.

We'll review the questionnaire and your requirements and write to confirm if we can offer a proposal.



proceedings.aip.org



Exotic Nuclei and Nuclear/Particle Astrophysics (V). From Nuclei to Stars

Carpathian Summer School of Physics 2014

Sinaia, Romania

13–26 July 2014

Editors

Livius Trache

Daniela Chesneanu

“Horia Hulubei” Institute for Physics and Nuclear Engineering, Bucharest-Magurele, Romania

Calin Alexandru Ur

“Horia Hulubei” Institute for Physics and Nuclear Engineering, Bucharest-Magurele, Romania

Extreme Light Infrastructure – Nuclear Physics, Bucharest-Magurele, Romania

All papers have been peer reviewed.

Sponsoring Organizations

Ministry of National Education

ATHENA network of ENSAR

Nuclear Astrophysics Virtual Institute

Endorsed by the European Physical Society

iGroup

CAEN

Canberra



Melville, New York, 2015
AIP Proceedings

Volume 1645

To learn more about AIP Proceedings visit <http://proceedings.aip.org>

Editors

Livius Trache

Daniela Chesneanu

“Horia Hulubei” Institute for Physics

and Nuclear Engineering

Str. Reactorului no. 30

P.O. Box MG-6

Bucharest-Magurele, Romania

E-mail: livius.trache@nipne.ro

chesneanu@nipne.ro

Calin Alexandru Ur

“Horia Hulubei” Institute for Physics

and Nuclear Engineering

Str. Reactorului no. 30

P.O. Box MG-6

Bucharest-Magurele, Romania

Extreme Light Infrastructure – Nuclear Physics

P.O. Box MG-6

Bucharest-Magurele, Romania

E-mail: calin.ur@eli-np.ro

Authorization to photocopy items for internal or personal use, beyond the free copying permitted under the 1978 U.S. Copyright Law (see statement below), is granted by the AIP Publishing LLC for users registered with the Copyright Clearance Center (CCC) Transactional Reporting Service, provided that the base fee of \$30.00 per copy is paid directly to CCC, 222 Rosewood Drive, Danvers, MA 01923, USA: <http://www.copyright.com>. For those organizations that have been granted a photocopy license by CCC, a separate system of payment has been arranged. The fee code for users of the Transactional Reporting Services is: 978-0-7354-1284-2/15/\$30.00



© 2015 AIP Publishing LLC

No claim is made to original U.S. Government works.

Permission is granted to quote from the AIP Conference Proceedings with the customary acknowledgment of the source. Republication of an article or portions thereof (e.g., extensive excerpts, figures, tables, etc.) in original form or in translation, as well as other types of reuse (e.g., in course packs) require formal permission from AIP Publishing and may be subject to fees. As a courtesy, the author of the original proceedings article should be informed of any request for republication/reuse. Permission may be obtained online using RightsLink. Locate the article online at <http://proceedings.aip.org>, then simply click on the RightsLink icon/“Permissions/Reprints” link found in the article abstract. You may also address requests to: AIP Publishing Office of Rights and Permissions, Suite 300, 1305 Walt Whitman Road, Melville, NY 11747-4300, USA; Fax: 516-576-2450; Tel.: 516-576-2268; E-mail: rights@aip.org.

ISBN 978-0-7354-1284-2

ISSN 0094-243X

Printed in the United States of America

AIP Conference Proceedings, Volume 1645
Exotic Nuclei and Nuclear/Particle Astrophysics (V). From Nuclei to Stars
Carpathian Summer School of Physics 2014

Table of Contents

Conference Organization	1
 Preface: Carpathian Summer School of Physics 2014 Livius Trache, Daniela Chesneanu, and Calin Alexandru Ur	3
 List of Summer Schools of Physics Held in the Carpathians	7
 Conference Pictures	11
 Carpathian Summer School of Physics 2014: Conference Program	15
 PART I: INVITED LECTURES	
1. Exotic Nuclei - Structure and Reactions	
Isospin-symmetry-breaking effects in $A \sim 70$ nuclei within beyond-mean-field approach A. Petrovici and O. Andrei	21
 Knockout beyond the dripline A. Bonaccorso, R. J. Charity, R. Kumar, and G. Salvioni	30
 Peripheral elastic and inelastic scattering of $^{17,18}\text{O}$ on light targets at 12 MeV/nucleon F. Carstoiu, T. Al-Abdullah, C. A. Gagliardi, and L. Trache	39
 Recent results and open questions on collective type phenomena from A-A to pp collisions M. Petrovici, C. Andrei, I. Berceanu, A. Bercuci, A. Herghelegiu, and A. Pop	52

2. Equation of State and Compact Stars

Introduction to neutron stars James M. Lattimer	61
Hyperons and neutron stars Isaac Vidaña	79
Strangeness driven phase transitions in compressed baryonic matter and their relevance for neutron stars and core collapsing supernovae Ad. R. Raduta, F. Gulminelli, and M. Oertel	86
Neutron-star matter within the energy-density functional theory and neutron-star structure A. F. Fantina, N. Chamel, J. M. Pearson, and S. Goriely	92
3. Nucleosynthesis	
Weak-interaction processes in core-collapse supernovae K. Langanke	101
Relevance of β-delayed neutron data for reactor, nuclear physics and astrophysics applications Karl-Ludwig Kratz	109
And there was light C. A. Bertulani	121
Heavy element production in the early galaxy Mounib F. El Eid	132
4. Nuclear Physics for Astrophysics	
On reaction mechanisms involved in the deuteron-induced surrogate reactions M. Avrigeanu, V. Avrigeanu, and C. Măniulescu	139
Enhanced α-particle optical potential at low energies, for the mass range $A \sim 45$-209 V. Avrigeanu, M. Avrigeanu, and C. Măniulescu	148
Applications of the Trojan Horse method in nuclear astrophysics Claudio Spitaleri	157

Light elements burning reaction rates at stellar temperatures as deduced by the Trojan Horse measurements L. Lamia, C. Spitaleri, M. La Cognata, S. Palmerini, S. M. R. Puglia, and M. L. Sergi	167
LUNA: Nuclear astrophysics underground A. Best	173
5. Cosmic Rays and Astroparticles	
Cosmic muons, as messengers from the Universe I. M. Brancus and H. Rebel	178
New cosmic rays experiments in the underground laboratory of IFIN-HH from Slanic Prahova, Romania Bogdan Mitrica, Denis Stanca, Iliana Brancus, Romul Margineanu, Ana-Maria Blebea-Apostu, Claudia Gomoiu, Alexandra Saftoiu, Gabriel Toma, Heinigerd Rebel, Andreas Haungs, Octavian Sima, Alexandru Gherghel-Lascu, and Mihai Niculescu-Oglinzanu	188
News about vs Irina Mocioiu	197
6. Physics at ELI-NP. Nuclear Physics with Lasers	
Implementation status of the extreme light infrastructure - nuclear physics (ELI-NP) project S. Gales and N. V. Zamfir	201
From laser particle acceleration to the synthesis of extremely neutron rich isotopes via the novel fission-fusion mechanism P. G. Thirolf	210
High power femtosecond lasers at ELI-NP Razvan Dabu	219
Perspectives for neutron and gamma spectroscopy in high power laser driven experiments at ELI-NP F. Negoita, M. Gugiu, H. Petrascu, C. Petrone, D. Pietreanu, J. Fuchs, S. Chen, D. Higginson, L. Vassura, F. Hannachi, M. Tarisien, M. Versteegen, P. Antici, D. Balabanski, S. Balascuta, M. Cernaianu, I. Dancus, S. Gales, L. Neagu, C. Petcu, M. Risca, M. Toma, E. Turcu, and D. Ursescu	228
7. Physics at ELI-NP. Nuclear Physics with Gamma Beams	
Gamma beam system at ELI-NP Calin Alexandru Ur	237

Physics with gamma-beams and charged particle detectors: I) Nuclear structure	
II) Nuclear astrophysics	
Moshe Gai	246
New scintillator materials for future and present facilities	
Franco Camera and Agnese Giaz	253
Contemporary research with nuclear resonance fluorescence at the S-DALINAC	
M. Zweidinger, T. Beck, J. Beller, U. Gayer, L. Mertes, H. Pai, N. Pietralla, P. Ries, C. Romig, and V. Werner	259
Mass and isospin dependence of the dipole response in a microscopic transport approach	
V. Baran, M. Colonna, M. Di Toro, A. Croitoru, and A. I. Nicolin	267
PART II: COMMUNICATIONS	
Relativistic mean-field model with energy dependent self-energies	
S. Antic and S. Typel	276
Fragmentation potential for the superheavy element ^{296}Lv	
D. Aranghel and A. Sandulescu	282
X_{max}^μ vs. N^μ from extensive air showers as estimator for the mass of primary UHECR's. Application for the Pierre Auger Observatory	
Nicusor Arsene and Octavian Sima	286
Sub-saturation matter in compact stars: Nuclear modelling in the framework of the extended Thomas-Fermi theory	
François Aymard, Francesca Gulminelli, and Jérôme Margueron	291
A conceptual design of an electron spectrometer for ELI-NP	
S. Balascuta and I. C. E. Turcu	296
3D reconstruction of nuclear reactions using GEM TPC with planar readout	
Jan Stefan Białowicz	301

Development of a Monte Carlo code for the data analysis of the $^{18}\text{F}(p,\alpha)^{15}\text{O}$ reaction at astrophysical energies	
A. Caruso, S. Cherubini, C. Spitaleri, V. Crucillà, M. Gulino, M. La Cognata, L. Lamia, G. Rapisarda, S. Romano, M.L. Sergi, S. Kubono, H. Yamaguchi, S. Hayakawa, Y. Wakabayashi, N. Iwasa, S. Kato, T. Komatsubara, T. Teranishi, A. Coc, F. Hammache, and N. de Séréville	306
Investigating $^{13}\text{C}+^{12}\text{C}$ reaction by the activation method. Sensitivity tests	
Daniela Chesneanu, L. Trache, R. Margineanu, A. Pantelica, D. Ghita, M. Straticiuc, I. Burducea, A. M. Blebea-Apostu, C. M. Gomoiu, and X. Tang	311
The mass-radius relationship of massive compact stars	
Partha Roy Chowdhury	317
Geant4 simulations on Compton scattering of laser photons on relativistic electrons	
D. Filipescu, H. Utsunomiya, I. Gheorghe, T. Glodariu, O. Tesileanu, T. Shima, K. Takahisa, and S. Miyamoto	322
Absolute photoneutron cross sections of Sm isotopes	
I. Gheorghe, H. Utsunomiya, D. Filipescu, T. Glodariu, H.-T. Nyhus, T. Renstrøm, O. Tesileanu, T. Shima, K. Takahisa, and S. Miyamoto	327
Refined lateral energy correction functions for the KASCADE-Grande experiment based on Geant4 simulations	
A. Gherghel-Lascu, W. D. Apel, J. C. Arteaga-Velázquez, K. Bekk, M. Bertaina, J. Blümer, H. Bozdog, I. M. Brancus, E. Cantoni, A. Chiavassa, F. Cossavella, K. Daumiller, V. de Souza, F. Di Pierro, P. Doll, R. Engel, J. Engler, B. Fuchs, D. Fuhrmann, H. J. Gils, R. Glasstetter, C. Grupen, A. Haungs, D. Heck, J. R. Hörandel, D. Huber, T. Huege, K.-H. Kampert, D. Kang, H. O. Klages, K. Link, P. Łuczak, H. J. Mathes, H. J. Mayer, J. Milke, B. Mitrica, C. Morello, J. Oehlschläger, S. Ostapchenko, N. Palmieri, M. Petcu, T. Pierog, H. Rebel, M. Roth, H. Schieler, S. Schoo, F. G. Schröder, O. Sima, G. Toma, G. C. Trinchero, H. Ulrich, A. Weindl, J. Wochele, and J. Zabierowski	332
Effect of $^{12}\text{C}+^{12}\text{C}$ reaction & convective mixing on the progenitor mass of ONe white dwarfs	
Ghina M. Halabi and Mounib El Eid	339
The fusion-fission process in the reaction $^{34}\text{S}+^{186}\text{W}$ near the interaction barrier	
I. M. Harca, S. Dmitriev, J. Itkis, E. M. Kozulin, G. Knyazheva, T. Loktev, K. Novikov, F. Azaiez, A. Gottardo, I. Matea, D. Verney, G. Chubarian, F. Hanappe, J. Piot, C. Schmitt, W. H. Trzaska, and E. Vardaci	344
Space-atmospheric interactions of energetic cosmic rays	
Paula Gina Isar	349

Calibration of photo sensors for the space-based cosmic ray telescope JEM-EUSO Michael Karus	353
Production and dosimetry of simultaneous therapeutic photons and electrons beam by linear accelerator: A Monte Carlo study Navid Khledi, Azim Arbabi, Dariush Sardari, Mohammad Mohammadi, and Ahmad Ameri	358
Properties of low-lying intruder states in ^{34}Al and ^{34}Si populated in the beta-decay of ^{34}Mg R. Lică, F. Rotaru, F. Negoită, S. Grévy, N. Mărginean, Ph. Desagne, T. Stora, C. Borcea, R. Borcea, S. Călinescu, J. M. Daugas, D. Filipescu, I. Kuti, L. M. Fraile, S. Franchoo, I. Gheorghe, D. G. Ghită, R. Mărginean, C. Mihai, P. Mourface, P. Morel, J. Mrazek, A. Negret, D. Pietreanu, T. Sava, D. Sohler, M. Stănoiu, I. Stefan, R. Șuvăilă, S. Toma, and C. A. Ur	363
Reducing the uncertainties in particle therapy C. Oancea, K. N. Shipulin, G. V. Mytsin, and Y. I. Luchin	367
Positron production at extreme light infrastructure – nuclear physics (ELI-NP) A. Oprisa, S. Balascuta, and C. A. Ur	372
The AGB star nucleosynthesis in the light of the recent $^{17}\text{O}(\text{p},\alpha)^{14}\text{N}$ and $^{18}\text{O}(\text{p},\alpha)^{15}\text{N}$ reaction rate determinations S. Palmerini, M. L. Sergi, M. La Cognata, L. Lamia, R. G. Pizzone, and C. Spitaleri	377
Study of the $^{10}\text{B}(\text{p},\alpha)^7\text{Be}$ reaction through the indirect Trojan Horse method S. M. R. Puglia, C. Spitaleri, L. Lamia, S. Romano, V. Burjan, N. Carlin, L. Chengbo, M. G. Del Santo, V. Kroha, Z. Hons, B. Irgaziev, M. La Cognata, J. Mrazek, A. Mukhamedzhanov, M. G. Munhoz, R. G. Pizzone, W. Qungang, G. G. Rapisarda, Z. Shu-Hua, M. L. Sergi, E. Somoryai, F. Souza, A. Szanto de Toledo, G. Tabacaru, A. Tumino, Y. Wakabayashi, and H. Yamaguchi	382
β-delayed α decay of ^{16}N and the $^{12}\text{C}(\alpha,\gamma)^{16}\text{O}$ cross section at astrophysical energies: A new experimental approach S. Sanfilippo, S. Cherubini, S. Hayakawa, A. Di Pietro, P. Figuera, M. Gulino, M. La Cognata, M. Lattuada, C. Spitaleri, H. Yamaguchi, D. Kahl, T. Nakao, S. Kubono, Y. Wakabayashi, T. Hashimoto, N. Iwasa, Y. Okoda, K. Ushio, T. Teranishi, M. Mazzocco, C. Signorini, D. Torresi, J. Y. Moon, T. Komatsubara, P. S. Lee, K. Y. Chae, and M. S. Gwak	387
THM determination of the 65 keV resonance strength intervening in the $^{17}\text{O}(\text{p},\alpha)^{14}\text{N}$ reaction rate M. L. Sergi, C. Spitaleri, S. V. Burjan, S. Cherubini, A. Coc, M. Gulino, F. Hammache, Z. Hons, B. Irgaziev, G. G. Kiss, V. Kroha, M. La Cognata, L. Lamia, A. Mukhamedzhanov, R. G. Pizzone, S. M. R. Puglia, G. G. Rapisarda, S. Romano, N. de Séréville, E. Somorjai, and A. Tumino	392

Elastic scattering measurements for the system ${}^7\text{Be}+{}^{28}\text{Si}$ at 17.2 MeV	
O. Sgouros, A. Pakou, D. Pierroutsakou, M. Mazzocco, L. Acosta, X. Aslanoglou, A. Boiano, C. Boiano, J. Grebosz, N. Keeley, M. La Commara, G. Marquez-Duran, I. Martel, C. Parascandolo, K. Rusek, A. M. Sánchez-Benítez, C. Signorini, V. Soukeras, E. Stiliaris, E. Strano, I. Strojek, and D. Torresi	397
Impact of nuclear fission on r-process nucleosynthesis and origin of solar r-process elements	
Shota Shibagaki, Toshitaka Kajino, Grant J. Mathews, and Satoshi Chiba	402
Elastic scattering for the system ${}^6\text{Li}+p$ at near barrier energies with MAGNEX	
V. Soukeras, A. Pakou, F. Cappuzzello, L. Acosta, C. Agodi, N. Alamanos, M. Bondi, D. Carbone, M. Cavallaro, A. Cunsolo, M. De Napoli, A. Di Pietro, J. P. Fernández-García, P. Figuera, M. Fisichella, A. Foti, N. Keeley, G. Marquez-Duran, I. Martel, M. Mazzocco, D. Nicolosi, D. Pierroutsakou, K. Rusek, O. Sgouros, E. Stiliaris, E. Strano, and D. Torresi	406
Interacting supernovae and supernova impostors: Evidence of incoming supernova explosions?	
L. Tartaglia	410
Strong field physics and QED experiments with ELI-NP 2×10^{14}W laser beams	
I. C. E. Turcu, S. Balascuta, F. Negoita, D. Jaroszynski, and P. McKenna	416
Cosmic rays muon flux measurements at Belgrade shallow underground laboratory	
N. Veselinović, A. Dragić, D. Maletić, D. Joković, M. Savić, R. Banjanac, V. Udovičić, and I. Aničin	421
PART III: OUTREACH ACTIVITIES AND CLOSING	
The outreach sessions	
Livius Trache	426
CERN and 60 years of science for peace	
Rolf-Dieter Heuer	430
Closing Remarks and List of Awards	437
List of Participants	439

Organized by

“Horia Hulubei” National Institute for Physics and Nuclear Engineering (IFIN-HH), Bucharest-Magurele, Romania and
Texas A&M University (TAMU), College Station, Texas, USA

Sponsored also by

Ministry of National Education, Bucharest, Romania
ATHENA network of ENSAR
Nuclear Astrophysics Virtual Institute, Germany (NAVI)
Endorsed by the European Physical Society
iGroup
CAEN
Canberra

International Advisory Committee:

<i>M. Ahmed (Duke)</i>	<i>T. Motobayashi (Tokyo)</i>
<i>T. Aumann (Darmstadt)</i>	<i>N. Pietralla (Darmstadt)</i>
<i>F. Azaiez (Orsay)</i>	<i>Zs. Podolyak (Surrey)</i>
<i>C. Bertulani (Commerce, TX)</i>	<i>H. Rebel (Karlsruhe)</i>
<i>S. Bishop (Munich)</i>	<i>W. Sandner (Berlin)</i>
<i>M. El Eid (Beirut)</i>	<i>H. Schatz (East Lansing)</i>
<i>F. Ferroni (Rome)</i>	<i>A. Smirnov (Trieste)</i>
<i>Z. Fulop (Debrecen)</i>	<i>B. Sherrill (East Lansing)</i>
<i>F. Gulminelli (Caen)</i>	<i>O. Sorlin (Caen)</i>
<i>M. Hass (Rehovot)</i>	<i>C. Spitaleri (Catania)</i>
<i>J. Jose (Barcelona)</i>	<i>T. Tajima (Irvine)</i>
<i>T. Kajino (Tokyo)</i>	<i>M. Wiescher (Notre Dame)</i>
<i>K.-L. Kratz (Mainz)</i>	<i>N. V. Zamfir (Bucharest)</i>
<i>K. Langanke (Darmstadt)</i>	

Organizing Committee:

Livius Trache *and* Robert Tribble: *chairs*
Daniela Chesneanu *and* Calin Alexandru Ur: *scientific secretaries*
Dan Cozma, Nicu Marginean *and* Denis Stanca (IFIN-HH), Gabriel Tabacaru, Antti Saastamoinen *and* Alexandra Spiridon (TAMU): *members*

Technical Secretariat:

Alexandra Olteanu – financial director
Denisa Cranganu

LIST OF SUMMER SCHOOLS OF PHYSICS HELD IN THE CARPATHIANS*

Along the times, different names were used for the summer schools of physics organized in the Carpathians: Predeal International SSP, Brasov SSP and Carpathian SSP. Here, to the best of our current knowledge, the history of these schools, including the names of the organizers and the published Proceedings:

1964 - According to oral tradition: a session organized by IFA where V.G. Soloviev (JINR Dubna, USSR) attended as sole foreign lecturer.

There is a large gap here in our memory ...

1974 - *Proceedings of the International School on Nuclear Physics - Predeal, Romania, September 1974*, editor: A. Ciocanel et al. Editura Academiei RSR, Bucharest, Romania, 1976. 446 pp.

1976 - *“Heavy Ion Physics” Predeal International Summer School - Predeal, Romania, Sep. 1976*, editors: Valentin Ceausescu, I. A. Dorobantu. Central Institute of Physics Publ., Bucharest, Romania, 1977. 589 pp.

1978 - *“Heavy Ion Physics” Proceedings - Predeal International School 1978*, editors: A. Berinde, V. Ceausescu, I.A. Dorobantu. Central Institute of Physics Publ., Bucharest, Romania, 1978. 1219 pp.

1979. *“Recent Advances in Statistical Mechanics” Proceedings - Brasov International School, Aug. – Sep. 1979*, editor: A. Corciovei, Central Institute of Physics Publ., Bucharest, Romania, 1980.

1980 – *“Critical Phenomena In Heavy Ion Physics”, Brasov International School, 1980*. Organizing Committee: directors: M. Petrascu, A.A. Raduta, scientific secretaries: G. Stratan, V. Zoran. *Proceedings* - Central Institute Of Physics Publ., Bucharest, Romania, 1982. 1124 pp.

1981 - *“Gauge Theories: Fundamental Interactions and Rigorous Results” Proceedings - International Summer School of Theoretical Physics Poiana Brasov, Romania “*. Organizers: V Ceausescu, G. Costache and V. Georgescu. Editors: P. Dita, V. Georgescu and R. Purice, published in “Progress in Physics”, vol 5, “Critical Phenomena”, Basel, Stuttgart: Boston Birkhauser, 1982. ISBN 3-7643-3095-3.

1982 – *“Nuclear Collective Dynamics” - Lectures of the 1982 International Summer School Of Nuclear Physics Poiana Brasov, Romania, 26 August - 7 September 1982*, editors: D. Bucurescu, V. Ceausescu, N.V. Zamfir, World Scientific Publishing, Singapore, 1983.

1983 - *“Critical Phenomena” – Proceedings of the Brasov School Conference.* Organizers: V Ceausescu, G. Costache and V. Georgescu. Editors: V. Ceausescu, G. Costache and V. Georgescu published in *“Progress in Physics”*, vol 11, *“Critical Phenomena”*, Basel, Stuttgart: Birkhauser Boston, 438 pp, 1985. ISBN 3-7643-3289-1.

1984 - *“Atomic and Nuclear Heavy Ion Interactions” - proceedings of the 15th Course of the Brasov International School in Physics, Poiana Brasov, Romania, August 28 - September 8, 1984.*

First Part: *“Atomic Physics”*, editors: Al Berinde, I.A. Dorobantu, V. Zoran , Central Institute of Physics Publ., Bucharest, Romania, 1986. 482 pp.

Second Part: *“Nuclear Physics”*, editors: G. Semenescu, I.A. Dorobantu, N.V. Zamfir. Central Institute of Physics Publ., Bucharest, Romania, 1986. 761 pp.

1986 - Poiana Brasov International Summer School of Physics.

“Symmetries and Semiclassical Features of Nuclear Dynamics” . Invited Lectures of the 1986 International Summer School Held at Poiana Brasov, Romania, September 1-13, 1986. Series: Lecture Notes in Physics, Vol. 279, Raduta, A.A. (Ed.), Springer Verlag, Berlin, 1987. ISBN 978-3-540-17926-9.

1988 - *“Recent Advances In Nuclear Physics” - Lectures of the 1988 International Summer School Of Nuclear Physics, August 30th - September 9th, 1988, Poiana Brasov, Romania,* editors: M. Petrovici, N.V. Zamfir, World Scientific, Singapore, 1989. 537 pp.

1990 – *“Nuclear Structure Recent Advances In Nuclear Structure” – Proceedings - Predeal, Romania, August 28th - September 8th 1990,* editors: D. Bucurescu, G. Cata-Danil, N.V. Zamfir, World Scientific, Singapore, 1991. 514 pp.

1991 - *“New Trends in Theoretical and Experimental Nuclear Physics” – Proceedings - Predeal International Summer School of Physics, Predeal, Romania, Aug 26th – Sep 7th 1991,* editors: A.A. Raduta, D.S. Delion, I.I. Ursu, World Scientific, Singapore, New Jersey, London, Hong Kong, 1992. ISBN 981-02-0906-1C

1992 - Predeal International summer school of physics, NATO Advanced Study Institute, Org: V. Zoran, A Calboreanu., L. Trache, V. Florescu.

“Topics in Atomic and Nuclear Collisions” Proceedings of a NATO ASI held in Predeal, Romania, August 31-September 11, 1992. Series: Nato Science Series B, Vol. 321 Remaud, B.; Calboreanu, A.; Zoran, V. (Eds.), Springer Verl., Berlin, 1994, 478pp. ISBN 978-0-306-44662-7

1995 – *“Collective Motion And Nuclear Dynamics” – Proceedings - Predeal International Summer School, August 28th - September 9th , 1995, Predeal, Romania,*

editors: A.A.Raduta, D. Bucurescu, D.S.Delion, I.I. Ursu. World Scientific, Singapore, 1996. 571 pp. ISBN 98102252882.

1998 Predeal International Summer School.

“Structure and Stability of Nucleon and Nuclear Systems”. *Proceedings of Predeal International Summer School, Predeal, Romania*. AA Raduta, II Ursu and S Stoica (eds.), World Scientific, Singapore, 1999. ISBN-10: 981023774X.

2000 - *Predeal International Summer School of Physics: “Nuclei far from stability and Astrophysics”*. Organizers: DN Poenaru and H. Rebel, directors. 28.08- 08.09 2000. Proc of NATO Advanced Study Institute on “Nuclei Far from Stability and Astrophysics”, eds. DN Poenaru, H. Rebel and J. Wentz. NATO Science series, II Mathematics, Physics and Chemistry, vol. 17. Kluwer Academic Publishers, Dordrecht, Boston, London, 2001.

2005 – *“Exotic Nuclei and Nuclear/Particle Astrophysics” – Proceedings - Carpathian Summer School of Physics 2005, Mamaia-Constanta, Romania, June 13th – June 24th* , 2005, editors: S. Stoica, L. Trache and R. Tribble, New Jersey: World Scientific Publishing Co. Pte. Ltd., 484 pp, 2006. ISBN 981-270-007-2

2006 – *“Collective Motion And Phase Transitions In Nuclear Systems” - Proceedings - The Predeal International Summer School In Nuclear Physics, Predeal, Romania August 28th - September 9th* , 2006, Editors: A.A. Raduta; V. Baran; A.C. Gheorghe; I. Ursu , World Scientific Publ., Singapore, 2007. 672 pp. ISBN 9789812700834

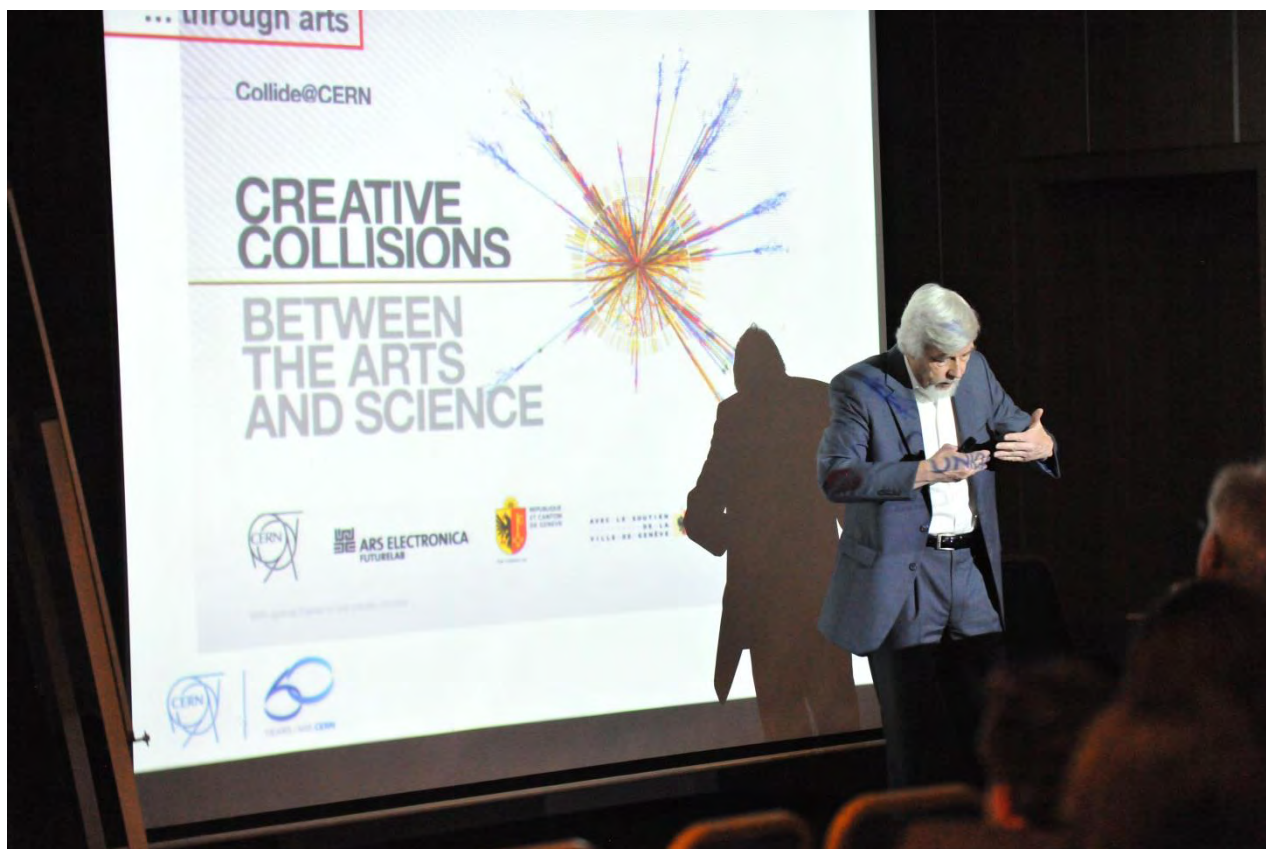
2007 – *“Exotic Nuclei and Nuclear/Particle Astrophysics (II)” – Proceedings: The Carpathian Summer School of Physics 2007, Sinaia, Romania, August 20th – 31st* , 2007, editors: L. Trache and S. Stoica. American Institute of Physics (AIP), Conference Proceedings, vol. 972, Melville, New York, 2008. 617pp. ISBN 978-0-7354-0490-8, ISSN 0094-243X.

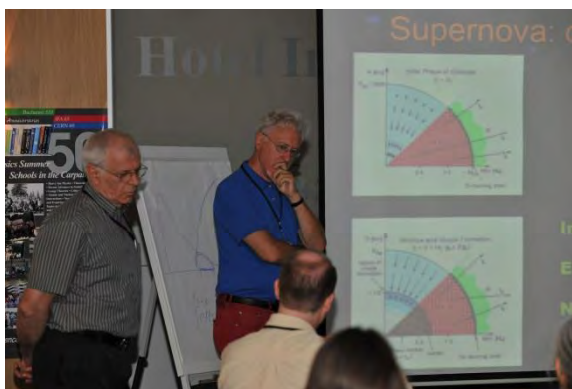
2010 – *“Exotic Nuclei and Nuclear/Particle Astrophysics (III) – From Nuclei to Stars” Proceedings - Carpathian Summer School of Physics 2010, Sinaia, Romania, June 20th – July 3rd* , 2010. Editors: L. Trache, S. Stoica and A. Smirnov; American Institute of Physics (AIP), Conference Proceedings, vol. 1304, Melville, New York, 2010. ISBN 978-0-7354-0859-3, ISSN 0094-243X.

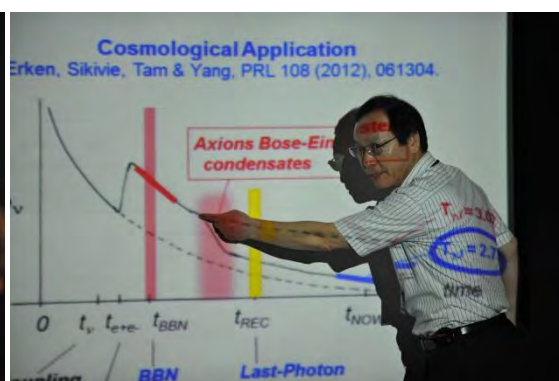
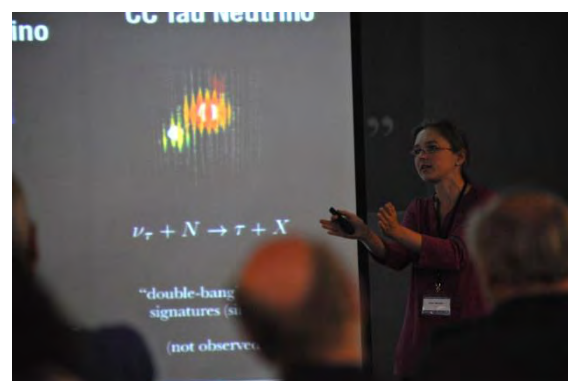
2012 – *“Exotic Nuclei and Nuclear/Particle Astrophysics (IV) – From Nuclei to Stars” Proceedings - Carpathian Summer School of Physics 2012, Sinaia, Romania, June 20th – July 3rd* , 2012. Editors: Livius Trache and Paula Gina Isar; American Institute of Physics (AIP), Conference Proceedings, vol. 1498, Melville, New York, 2012. ISBN 978-0-7354-1112-8, ISSN 0094-243X.

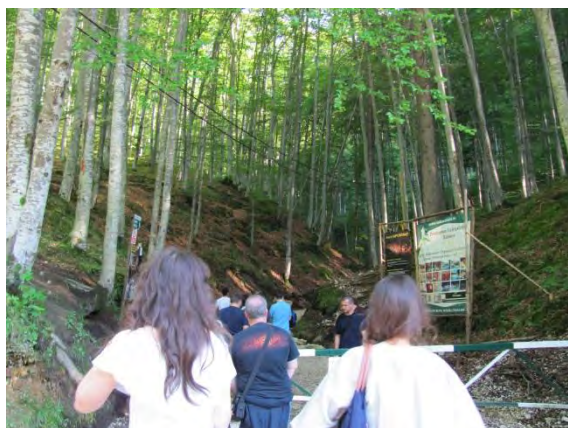
2014 – “*Exotic Nuclei and Nuclear/Particle Astrophysics (V) – From Nuclei to Stars*”
Proceedings - Carpathian Summer School of Physics 2014, Sinaia, Romania, July 13th – 26th, 2014. Editors: Livius Trache, Daniela Chesneanu and Calin Alexandru Ur; American Institute of Physics (AIP), Conference Proceedings, Melville, New York, to be published.

**This list was compiled by Livius Trache with assistance from Ion I. Ursu, Denise Cranganu and Adriana Mihai. If you have any suggestions, or further information, please write at dir.sci@nipne.ro. Thanks!*









Carpathian Summer School of Physics 2014

Conference Program

Sunday, July 13th , 2014	16.00-Registration of participants 20.00- Welcome Party
--	--

Monday, July 14th , 2014	
<i>Introduction (I)</i> Chair: Livius Trache	
9:00 - 9:15	Opening
9:15 - 9:55	<i>C. Bertulani (I)</i> : Quasi-Free Scattering and Knockout Reactions with Rare Isotopes
9:55 - 10:50	<i>M.C. Wiescher (I)</i> : Nuclear Astrophysics – Challenges at Threshold Energies
10:50 - 11:10	Coffee break
11:10 - 12:00	<i>K. Langanke (I)</i> : Core collapse supernovae - from the view of a nuclear theorist
12:00 - 12:50	<i>B.S. Meyer (I)</i> : Synthesis of Radioactive Nuclei and Secondary Supernova Machine
13:00 - 15:00	Lunch
<i>Afternoon Session</i> Chair: Karlheinz Langanke	
15:00 - 15:50	<i>R. Diehl</i> : Gamma Ray Astronomy: Lessons from cosmic radioactive nuclei
15:50 - 16:10	Coffee break
16:10 - 17:05	<i>J. Lattimer (I)</i> : Introduction to Neutron stars I
17:05 - 18:00	<i>I. Mocoiu</i> : News about nus
18:00 - 18:15	<i>M. Karus</i> : Calibration of Photo Sensors for the Space-Based Cosmic Ray Telescope JEM-EUS
18:15 - 18:30	<i>M. Holl</i> : Quasi-Free Scattering from Relativistic Neutron-Deficient Carbon
18:30 - 18:45	<i>A. Slemer</i> : Advanced Stellar Evolution and Related Nucleosynthesis

Tuesday, July 15th , 2014	
<i>Introduction (II)</i> Chair: Carlos Bertulani	
9:00 - 9:55	<i>K-L Kratz (I)</i> : Astrophysical, observational and nuclear-structure aspects of r-process nucleosynthesis
9:55 - 10:50	<i>M.C. Wiescher (II)</i> : Nuclear Astrophysics – challenges at threshold energies
10:50 - 11:10	Coffee break
11:10 - 12:00	<i>T. Kajino</i> : Big-Bang and Supernova Neutrinos and Nucleosynthesis
12:00 - 12:50	<i>B.S. Meyer (II)</i> : Synthesis of Radioactive Nuclei and Secondary Supernova Machine
13:00 - 15:00	Lunch
<i>Afternoon Session</i> Chair: Dan Cozma	
15:00 - 15:50	<i>K. Langanke (II)</i> : Core collapse supernovae- from the view of a nuclear theorist
15:50 - 16:10	Coffee break
16:10 - 17:05	<i>J. Lattimer (II)</i> : Introduction to Neutron Stars II
17:05 - 18:00	<i>C. Bertulani (II)</i> : Two-photon and photonuclear collisions at the Large Hadron Collider at

	CERN
18:00 - 18:15	<i>A. Saastamoinen</i> : Study of excited states of ^{35}Ar through β -decay of ^{35}K for nucleosynthesis in novae and X-ray bursts
18:15 - 18:30	<i>L. Tartaglia</i> : Interacting supernovae and supernova impostors: evidence of incoming SN explosions?
18:30 - 18:45	<i>I. Gheorghe</i> : Absolute photoneutron cross sections of Sm isotopes
18:45 - 19:00	<i>R. Lica</i> : Properties of low-lying intruder states in ^{34}Al and ^{34}Si from the beta-decay of ^{34}Mg

Wednesday, July 16th, 2014	
<i>EOS and compact stars</i>	
Chair: James M. Lattimer	
9:00 - 9:55	<i>F. Gulminelli</i> : Sub-saturation equation of state for Core-Collapse Supernovae and Neutron Stars
9:55 - 10:50	<i>A. Fantina</i> : Neutron-star matter within the energy-density functional theory and neutron-star structure
10:50 - 11:10	Coffee break
11:10 - 12:00	<i>C. Providência</i> : The symmetry energy: the inner crust and strangeness of neutron stars
12:00 - 12:50	<i>T. Aumann</i> : The dipole response and neutron-skin of nuclei and the symmetry energy
13:00 - 15:00	Lunch
<i>Afternoon Session</i>	
Chair: Francesca Gulminelli	
15:00 - 15:50	<i>I. Vidana</i> : Hyperons and Neutrons Stars
15:50 - 16:10	Coffee break
16:10 - 17:05	<i>Ad. Raduta</i> : Strangeness driven phase transitions in compressed baryonic matter and their relevance for neutron stars and core collapsing supernovae
17:05 - 18:00	<i>I. Sagert</i> : Quark matter in compact stars
18:00 - 18:15	<i>S. Antic</i> : Relativistic mean-field model with energy dependent self-energies
18:15 - 18:30	<i>T. Aymard</i> : Sub-saturation matter in Compact Stars : nuclear modelling in the framework of the Extended Thomas-Fermi theory
18:30 - 18:45	<i>A. Horvat</i> : Collective Excitations in Nuclei Away from the Valley of Stability

Thursday, July 17th, 2014	
<i>ELI-NP session</i>	
Chair: Nicolae Victor Zamfir	
9:00 - 9:55	<i>N.V. Zamfir</i> : Extreme Light Infrastructure – Nuclear Physics (ELI-NP) Status and Perspectives
9:55 - 10:50	<i>S. Gales</i> : Nuclear Science and Applications with next generation of High Power Lasers and Brilliant Low Energy Gamma Beams at ELI-NP
10:50 - 11:10	Coffee break
11:10 - 12:00	<i>D.L. Balabanski</i> : Nuclear Physics Experiments at the ELI-NP Facility
12:00 - 12:50	<i>C.A. Ur</i> : Gamma Beam System at ELI-NP
13:00 - 15:00	Lunch
<i>Afternoon Session</i>	
Chair: Calin A. Ur	
15:00 - 15:50	<i>M. Gai</i> : Physics with Gamma-Beams and Charged Particle Detectors: I Nuclear Structure

15:50 - 16:10	Coffee break
16:10 - 17:05	<i>M. Gai</i> : Physics with Gamma-Beams and Charged Particle Detectors: II Nuclear Astrophysics
17:05 - 18:00	<i>M. Zweidinger</i> : Contemporary Research with Nuclear Resonance Fluorescence at the S-DALINAC
18:00 - 18:30	<i>D. Filipescu</i> : Geant4 simulations on Compton scattering of laser photons on relativistic electrons

Friday, July 18th, 2014	
<i>ELI-NP session</i> Chair: Sydney Gales	
9:00 - 9:55	<i>G. Mourou</i> : Zepto-Physics at ELI-NP
9:55 - 10:50	<i>R. Dabu</i> : Ultrahigh intensity lasers based on chirped pulse amplification technique
10:50 - 11:10	Coffee break
11:10 - 12:00	<i>R. Dabu</i> : High Power femtosecond lasers at ELI-NP
12:00 - 12:50	<i>P.G. Thirolf</i> : From laser particle acceleration to the synthesis of the extremely neutron rich isotopes via the novel fission-fusion mechanism
13:00 - 14:30	Lunch
<i>Afternoon Session</i> Chair: Dimiter Balabanski	
14:30 - 15:20	<i>P.G. Thirolf</i> : From laser particle acceleration to the synthesis of the extremely neutron rich isotopes via the novel fission-fusion mechanism
15:20 - 15:50	<i>E. Turcu</i> : High Field QED Experiments with ELI-NP 2x10PW Laser
15:50 - 16:10	Coffee break
16:10 - 17:05	<i>V. Baran</i> : Mass and Isospin Dependence of the Dipole Response in a Microscopic Transport Model Approach
17:05 - 18:00	<i>A. Bonasera</i> : Nuclear Physics Using Lasers
18:00-18:55	<i>F. Negoita</i> : Perspectives for neutron and gamma spectroscopy in high power laser driven experiments at ELI-NP

Saturday, July 19th, 2014	
<i>Outreach day</i> Chair: Michael Wiescher	
9:00 - 9:55	<i>A. Haungs (I)</i> : At the Doorway to Astroparticle Astronomy
9:55 - 10:50	<i>S. Bishop</i> : Search for Supernova-produced ⁶⁰ Fe in the Earths Fossil Record
10:50 - 11:10	Coffee break
11:10 - 12:00	<i>R. Egli</i> : From supernova to terrestrial dirt: a journey between astrophysics, biology and geophysics
12:00 - 12:30	<i>K-L Kratz (II)</i> : Astrophysical, observational and nuclear-structure aspects of r-process nucleosynthesis
12:30 - 13:30	Lunch
13:30 Round table: CERN at 60. And the internationalization of science	
15:50 - 16:10	Coffee break
16:10 - 17:05	Round table: continued
19:00 on	BANQUET

Sunday July 20– Excursions: Hiking and bus trip choice; start at 9am

Monday, July 21st, 2014	
Astroparticles	
Chair: Marilena Avrigeanu	
9:00 - 9:50	<i>A. Haungs (II)</i> : The Pierre Auger Observatory: highlights and future prospects
10:00 - 10:50	<i>I. Brâncuş</i> : Cosmic Muons as Messengers from the Universe
10:50 - 11:10	Coffee break
11:10 - 12:00	<i>O.Sima</i> : The KASCADE-Grande Experiment
12:00 - 12:50	<i>B.Mitrică</i> : New cosmic rays experiments in the underground laboratory of IFIN-HH from Slănic Prahova, Romania
13:00 - 15:00	Lunch
Exotic decays	
Chair: Octavian Sima	
15:00 - 15:50	<i>M.Pfutzner</i> : Charge-particle spectroscopy with the Optical TPC
15:50 - 16:10	Coffee break
16:10 - 17:05	<i>M.Horoi</i> : Search for physics beyond the Standard Model in double-beta decay
17:05 - 18:00	<i>L.V.Grigorenko</i> : Few-body dynamics on the driplines
18:00 - 18:15	<i>N.Arsene</i> : X_{\max}^{U} vs. N_{μ} from Extensive Air Showers as estimator for the mass of primary UHECR's. Application for the Pierre Auger Observatory
18:15 - 18:30	<i>A.Gherghel-Lascu</i> : Refined Lateral Energy Correction Functions for the KASCADE-GRANDE Experiment Based on GEANT4 Simulations
18:30 - 18:45	<i>M.Niculescu</i> : Underground cosmic muon detector based on SiPM , optic fibers and plastic scintillators
18:45-19:00	<i>C.Costache</i> : RDDS lifetime measurements using the ROSPHERE spectrometer: The case of ^{119}Te

Tuesday, July 22nd, 2014	
Nuclear Reactions	
Chair: Thoru Motobayashi	
9:00 – 9:50	<i>A.Bonaccorso</i> : Knockout beyond the dripline
10:00 - 10:50	<i>T.Uesaka</i> : Mass measurement of r-process nuclei at RIBF
10:50 - 11:10	Coffee break
11:10 - 12:00	<i>F.Camera (I)</i> : New scintillator materials for future and present facilities
12:00 - 12:50	<i>V.Iacob</i> : From estimates of the order of magnitude to precise measurements: The superallowed beta decays
13:00 - 15:00	Lunch
Exotic Nuclei	
Chair: Vladilen Goldberg	
15:00 - 15:50	<i>F.Camera (II)</i> : New scintillator materials for future and present facilities
15:50 - 16:10	Coffee break
16:10 - 17:05	<i>F.Carstoiu</i> : Peripheral reactions with $^{17,18}\text{O}$ at 12MeV/nucleon <i>M. Avrigeanu</i> : On reaction mechanism involved in the deuteron-induced surrogate reactions on actinides
17:05 - 17:20	<i>D.Chesneanu</i> : Investigating $^{12}\text{C}+^{13}\text{C}$ reaction using high resolution gamma ray spectroscopy
17:20 - 17:35	<i>N.Veselinovic</i> : CR muon flux measurements at Belgrade shallow underground laboratory

17:35 – 17:50	<i>O.Sgouros</i> : Elastic scattering of the system ${}^7\text{Be}+{}^{28}\text{Si}$ at 17.2MeV
18:00 - 18:15	<i>V.Soukeras</i> : Elastic scattering of the system ${}^6\text{Li} + \text{p}$ at near barrier energies with MAGNEX
18:15 – 18:30	<i>A.Caruso</i> : ${}^{18}\text{F} + \text{p}$ at astrophysical energies
18:30 – 18:45	<i>I.Harca</i> : Investigation of shell effects in fusion-fission and quasifission processes in the reaction ${}^{34}\text{S} + {}^{186}\text{W}$

Wednesday, July 23rd, 2014

Morning Session Chair: Vlad Avrigeanu	
9:00 - 9:55	<i>T. Motobayashi</i> : Nuclear astrophysics studies at RIKEN RIBF
10:00 - 10:50	<i>A.Parikh</i> : Important and significant: lies the experimentalist told me
10:50 - 11:10	Coffee break
11:10 - 12:00	<i>A. Petrovici</i> : Isospin-symetry-breaking effects in A~70 nuclei within beyond-mean-field approach
12:00 - 12:50	<i>M. Petrovici</i> : Recent results and open questions on collective type phenomena from A+A to p+p collisions
13:00 - 15:00	Lunch
Free afternoon	

Thursday, July 24th, 2014

Nuclear astrophysics Chair: Claudio Spitalieri	
9:00 - 9:50	<i>M.El Eid</i> : Heavy Element Synthesis in the Early Galaxy
10:00 - 10:50	<i>P.Woods</i> : Measurements for Explosive Nuclear Astrophysics
10:50 - 11:10	Coffee break
11:10 - 12:00	<i>C.Lederer</i> : Neutron induced reactions in Nuclear Astrophysics
12:00 - 12:50	<i>V. Avrigeanu</i> : Enhanced α -particle optical model potential at low energies for the mass range A~40-209
13:00 - 15:00	Lunch
Afternoon Session: Chair: Vlad Avrigeanu	
15:00 - 15:50	<i>V.Goldberg</i> : Recently developed approaches to calculate nuclear structure need tests by novel experimental methods
15:50 - 16:10	Coffee break
16:10 – 16:25	<i>J.S. Bihalowicz</i> : 3D reconstruction of nuclear reaction using GEM TPC with planar readout
16:25 - 16:40	<i>B.Chesca</i> : Ultra-sensitive superconducting detectors of the radiative decay of cosmic background neutrinos
16:40-16:55	<i>A.Cvetinovic</i> : Large electron screening effect in ${}^1\text{H}({}^7\text{Li},\alpha){}^4\text{He}$ and ${}^2\text{H}({}^{19}\text{F},\text{n}){}^{20}\text{Ne}$ reactions in different environments
17:05-17:20	<i>G.M. Halabi</i> : Effect of ${}^{12}\text{C}+{}^{12}\text{C}$ Fusion Reaction & Convective Mixing on the Progenitor Mass of ONe White Dwarfs
17:20-17:35	<i>S.Shibagaki</i> : Roles of Fission, Neutron Star Mergers and Supernovae in R-Process Nucleosynthesis
17:35-17:50	<i>S. Balascuta</i> : The conceptual design of the Electron Spectrometer for the High Field Physics experiments at ELI-NP

17:50-18:05	<i>S.Sanfillipo</i> : β -delayed α -decay of ^{16}N and the $^{12}\text{C}(\alpha,\gamma)^{16}\text{O}$ cross-section at astrophysical energies
18:05-18:20	<i>P.R.Chowdhury</i> : The Equation of State for Nuclear Matter at Extreme and Compact Star Properties

Friday, July 25th, 2014	
Morning Session	
Chair: Mounib El Eid	
9:00 - 9:50	<i>C.Spitalieri(I)</i> : Nuclear Astrophysics with the Trojan Horse Method
10:00 - 10:50	<i>C.Spitalieri(II)</i> : Nuclear Astrophysics with the Trojan Horse Method
10:50 - 11:10	Coffee break
11:10 - 12:00	<i>L.Lamia</i> : Light elements burning reaction rates at stellar temperatures as deduced by the Trojan Horse measurements
12:00 - 12:50	<i>A.Best</i> : LUNA: Underground nuclear astrophysics
13:00 - 15:00	Lunch
Afternoon Session	
Chair: Livius Trache	
15:00 -15:15	<i>S.Puglia</i> : Study of the $^{10}\text{B}(\text{p},\alpha)^7\text{Be}$ reaction through the Trojan Horse Method
15:15-15:30	<i>M.L. Sergi</i> : Recent THM determination of the 65 keV resonance strength intervening in the $^{17}\text{O}(\text{p},\alpha)^{14}\text{N}$ reaction rate
15:30-15:45	<i>S.Palmerini</i> : The RGB and AGB star nucleosynthesis in the light of the recent $^{18}\text{O}(\text{p},\alpha)^{15}\text{N}$ and $^{17}\text{O}(\text{p},\alpha)^{14}\text{N}$ reaction rate determinations
15:45 - 16:10	Coffee break
16:10-16:25	<i>C.Oancea</i> : Reducing the Uncertainties in Particle Therapy
16:25-16:40	<i>N.Kahledi</i> : Production and dosimetry of simultaneous therapeutic photons and electrons beam by linear accelerator: a monte carlo study
16:40-16:55	<i>P.Isar</i> : Space-atmospheric interactions of ultra-high energy cosmic rays
17:05 - 18:00	Closing

Saturday, July 26th, 2014	9.00 - Departure
---	------------------

Carpathian Summer School of Physics 2016
Exotic Nuclei and Nuclear/Particle Astrophysics (VI). Physics with small accelerators
June 26th – July 9th, 2016, Sinaia, Romania
Program

Monday, June 27th, 2016		<i>Physics with small accelerators</i>
Morning Session: Opening <i>Chair: L. Trache</i>		
09:00 - 09:15	<i>Opening</i>	
09:15 - 09:55	L. Trache: <i>Opening Session</i>	
09:55 - 10:50	M. Horoi: <i>Nuclear structure and weak probes</i>	
10:50 - 11:10	<i>Coffee break</i>	
11:10 - 12:00	A. Mackova: <i>Ion beams provided by small accelerators for material synthesis and characterization</i>	
12:00 - 12:50	B. Constantinescu: <i>Archaeometry with PIXE at small accelerators</i>	
13:00 - 15:00	<i>Lunch</i>	
Afternoon Session <i>Chair: D. Ghita</i>		
15:00 - 15:50	M. Straticiuc: <i>Particle Accelerators: Multi-tools for Science, Education and Technology</i> I. Burducea: <i>Ion Beam Analysis - Applications in Materials Science</i>	
15:50 - 16:10	<i>Coffee break</i>	
16:10 - 17:05	C. Granja: <i>Position-sensitive coincidence detection of nuclear reaction products at Prague VdG accelerator</i>	
17:05 - 18:00	M. Nistor: <i>The composition – property relationship of oxide thin films using Rutherford Backscattering Spectrometry</i>	
18:00 - 18:55	<i>Communications</i>	

Tuesday, June 28th, 2016		<i>AMS</i>
Morning Session <i>Chair: Stan-Sion</i>		
09:00 - 09:55	W. Kutschera : (I) <i>Exploring the World with Accelerator Mass Spectrometry</i>	
09:55 - 10:50	W. Kutschera: (II) <i>Exploring the World with Accelerator Mass Spectrometry</i>	
10:50 - 11:10	<i>Coffee break</i>	
11:10 - 12:00	H. A. Synal: <i>Progress in Accelerator Mass Spectrometry</i>	
12:00 - 12:50	T. Sava: <i>ROAMS – Status of the new Bucharest AMS center</i>	
13:00 - 15:00	<i>Lunch</i>	
Afternoon Session <i>Chair: Z. Fulop</i>		
15:00 - 15:50	N. Palincas: <i>Radiocarbon Dating in Archaeology as Interdisciplinary Approach</i>	
15:50 - 16:10	<i>Coffee break</i>	
16:10 - 17:05	S. Sion: <i>Physics with light nuclei at small accelerators</i>	
17:05 - 18:00	<i>Communications</i>	
18:00 - 18:55	<i>Communications</i>	


Wednesday, June 29th, 2016		<i>Physics with small accelerators</i>
Morning Session		
<i>Chair: T. Sava</i>		
09:00 - 09:55	Z. Fulop: <i>The Atomki Accelerator Centre</i>	
09:55 - 10:50	S. Tamas: <i>Underground Nuclear Astrophysics</i>	
10:50 - 11:10	<i>Coffee break</i>	
11:10 - 12:00	A. Jokinen: <i>Nuclear and applied research at JYFL Accelerator Laboratory</i>	
12:00 - 12:50	D. S. Delion: <i>Proton-neutron correlations above 100Sn</i>	
13:00 - 15:00	<i>Lunch</i>	
Afternoon Session		<i>Exotic nuclei</i>
<i>Chair: D. S. Delion</i>		
15:00 - 15:50	E. Pollacco: <i>Drift towards time projection chambers in Nuclear Physics.</i>	
15:50 - 16:10	<i>Coffee break</i>	
16:10 - 17:05	C. Sotty: <i>Nuclear physics experiments with Plunger and Fast-Timing technique.</i>	
17:05 - 18:00	<i>Communications</i>	
18:00 - 18:55	<i>Communications</i>	

Thursday, June 30 th , 2016		ELI-NP session
Morning Session		
Chair: F. Negoita		
09:00 - 09:55	S. Gales: From Technical Design reports to Implementation phase. Status and Perspectives.	
09:55 - 10:50	R. Dabu: High power, high contrast hybrid femtosecond laser systems	
10:50 - 11:10	Coffee break	
11:10 - 12:00	A. Bonasera: Nuclear Physics Using Lasers	
12:00 - 12:50	M. Boca: Elementary processes in the presence of super-intense laser fields; beyond perturbative QED	
13:00 - 15:00	Lunch	
Afternoon Session		
Chair: D. Balabanski		
15:00 - 15:50	D. Neely: Laser driven particle accelerators	
15:50 - 16:10	Coffee break	
16:10 - 17:05	D. Stutman: X-ray and XUV phase-contrast diagnostics for ELI-NP	
17:05 - 18:00	F. Negoita: Nuclear Physics using High Power Laser System of ELI-NP	
18:00 - 18:55	Communications	

Friday, July 1 st , 2016		ELI-NP session
Morning Session		
Chair: S. Gales		
09:00 - 09:55	C. Matei: How to Prepare an Experiment using the Gamma Beam System at ELI-NP	
09:55 - 10:50	D. Balabanski: Highlights of the experimental program with brilliant gamma beams at ELI-NP	
10:50 - 11:10	Coffee break	
11:10 - 12:00	D. Filipescu: Neutron multiplicity sorting in photo-neutron reactions. Revisiting gamma strength functions database.	
12:00 - 12:50	V. Baran: The macroscopic structure of pygmy dipole resonance	
13:00 - 15:00	Lunch	
Afternoon Session		
Chair: D. Stutman		
15:00 - 15:50	S. Miyamoto: Laser Compton Scattering Gamma-ray Beam Generation and Applications	
15:50 - 16:10	Coffee break	
16:10 - 17:05	M. Fujiwara: Medical Isotope Production via photonuclear reactions	
17:05 - 18:00	O. Tesileanu: Combined laser-gamma beam experiments at ELI-NP	
Saturday, July 2 nd , 2016		Outreach day
Morning Session		
Chair:		
09:00 - 09:55	P.J. Woods:	
09:55 - 10:50	M. G. Itkis: SHE research at JINR Dubna	
10:50 - 11:10	Coffee break	
11:10 - 12:00	S. Bishop: Time-Resolved Two Million Year Old Supernova Activity . Discovered in the Earth's Microfossil Record	
12:00 - 12:50	T. Jull: Radiocarbon dating methods and applications to environmental studies	
12:30 – 13:30	Lunch	
13:30 Round table: JINR at 60		
15:00 - 15:50	M. G. Itkis, B. Sharkov	
15:50 - 16:10	Coffee break	
16:10 - 17:05	Round table	
19:00	Banquet	

Monday, July 4 th , 2016		Astroparticles
Morning Session		
Chair: Ad. Vd Berg		
09:00 - 09:50	A. Haungs: <i>Status of JEM-EUSO and its Test Experiments</i>	
10:00 - 10:50	K. Kampert:	
10:50 - 11:10	Coffee break	
11:10 - 12:00	I. Brancus: <i>Romanian contribution in Pierre Auger Observatory</i>	
12:00 - 12:50	A. Gladyshev:	
13:00 - 15:00	Lunch	
New Facilities		
Chair: K. Langanke		
15:00 - 15:50	V. Kolesnikov: <i>Prospects for the study of the properties of dense nuclear matter at the NICA heavy-ion complex at JINR (Dubna)</i>	
15:50 - 16:10	Coffee break	
16:10 - 17:05	D. Nicmorus: <i>FAIR exploring the nature of matter and its evolution</i>	
17:05 - 18:00	T. Motobayashi: <i>Manifestation and Latency of Nuclear Magic Numbers</i>	
18:00 – 18:55	Communications	

Tuesday, July 5 th , 2016		<i>Nuclear astrophysics</i>
Morning Session		
<i>Chair: K-L. Kratz</i>		
09:00 - 09:50	K. Langanke: <i>Neutrino-nucleus reactions and their role for supernova dynamics and nucleosynthesis</i>	
10:00 - 10:50	C. Spitaleri:	
10:50 - 11:10	<i>Coffee break</i>	
11:10 - 12:00	A. Tumino: <i>The $^{12}\text{C}(^{12}\text{C},\alpha)^{20}\text{Ne}$ and $^{12}\text{C}(^{12}\text{C},p)^{23}\text{N}$ reactions at the Gamow peak</i>	
12:00 - 12:50	C. Bertulani: <i>Searching for Pigmy resonances</i>	
13:00 - 15:00	<i>Lunch</i>	
Afternoon Session		
<i>Chair: M. Hass</i>		
15:00 - 15:50	K-L. Kratz: <i>Nuclear-data input to the solar-system r-process: The case of beta-decay properties</i>	
15:50 - 16:10	<i>Coffee break</i>	
16:10 - 17:05	A. Haungs: <i>25 years of KASCADE and KASCADE-Grande Experiments. Achievements in Cosmic Ray Physics</i>	
17:05 - 18:00	<i>Communications</i>	
18:00 - 18:55	<i>Communications</i>	

Wednesday, July 6 th , 2016		Astroparticles
Morning Session		
Chair: K-H. Kampert		
09:00 - 09:50	Ad. Berg : <i>Detection of cosmic rays at the Pierre Auger Observatory using the Auger Engineering Radio Array (AERA)</i>	
10:00 - 10:50	I. Mocioiu: <i>Neutrinos and New Interactions</i>	
10:50 - 11:10	Coffee break	
11:10 - 12:00	R. Diehl: (I) <i>Cosmic gamma ray line spectroscopy in the MeV regime: radioactivities and positron annihilation</i>	
12:00 - 12:50	R. Diehl: (II) <i>Supernova explosion diagnostics with cosmic gamma ray lines</i>	
13:00 - 13:50	C. Borcea: <i>Proton beta decay in a colliding system</i>	
13:50 – 15:00	Lunch	
Sinaia’s trails or excursion		
15:00 - 15:50		
15:50 - 16:10		
16:10 - 17:05		
17:05 - 18:00		

Thursday, July 7 th , 2016		Exotic nuclei
Morning Session		
Chair: C. Bertulani		
09:00 - 09:50	M. Petrovici: From p+p to A+A ultrarelativistic collisions	
10:00 - 10:50	A. Petrovici: Shape coexistence effects on stellar weak interaction rates of proton-rich nuclei within beyond-mean-field approach	
10:50 - 11:10	Coffee break	
11:10 - 12:00	S. Shlomo: A novel method for determining the mean-field directly from the single particle matter density: Application to the measured charge density difference between the isotones ²⁰⁶ Pb– ²⁰⁵ Tl	
12:00 - 12:50	Bao An Li: Symmetry Energy of Neutron-Rich Matter and its Astrophysical Impacts	
13:00 - 15:00	Lunch	
Afternoon Session		
Chair:		
15:00 - 15:50	M. Gai: Using Stars to measure the Universe	
15:50 - 16:10	Coffee break	
16:10 - 17:05	T. Jull: Applications of cosmogenic nuclides to extraterrestrial materials	
17:05 - 18:00	S. Bishop: Time-Resolved Two Million Year Old Supernova Activity . Discovered in the Earth’s Microfossil Record	

Friday, July 8th, 2016**Morning Session***Chair:*

09:00 - 09:50

V. Avrigeanu: *Uncertainties of alpha-particle optical-potential assessment around and below the Coulomb barrier*

10:00 - 10:50

M. Gai: *Nuclear Astrophysics With Charged Particle Detection at the ELI-NP*

10:50 - 11:10

Coffee break

11:10 - 12:00

M. Hass: *Probing fundamental interactions by an Electrostatic Ion Beam Trap and by an Atom MOT Trap*

12:00 - 12:50

B. Mitrica: *Modern cosmic rays muon detectors developed in IFIN-HH*

13:00 - 15:00

*Lunch***Afternoon Session***Closing**Chair: L. Trache*

15:00 - 15:50

15:50 - 16:10

Coffee break

16:10 - 17:05

17:05 - 18:00

Saturday, July 9th, 2016

09:00

Departures

Nuclear astrophysics with exotic nuclei and rare ion beams

Livius Trache

Cyclotron Institute, Texas A&M University, College Station, TX 77843, USA, and
“Horia Hulubei” National Institute for Physics and Nuclear Engineering, Bucharest-
Magurele, Romania

E-mail: livius_trache@tamu.edu, or livius.trache@nipne.ro

Abstract. Nuclear astrophysics has become a major motivation for nuclear physics research in the latest few decades. The quests to understand grand scale cosmic phenomena, the origin of elements and isotopes, the sources of energy in stars, were advanced by studies at the microscopic scale of nuclei. Advances in the production, separation and acceleration of unstable nuclei lead not only to new knowledge in the structure of nuclei and nuclear matter, but also have revolutionized nuclear physics for astrophysics. I will review some of the many contributions that nuclear astrophysics made to our fundamental knowledge, and then will describe a few indirect methods used in nuclear astrophysics using radioactive beams, concentrating on those used by the groups I work with.

1. Introduction

I need to start not merely by thanking the organizers for inviting me here, but also by “justifying” my presence here at this school that celebrates the 80th year of life of prof. Aurel Sandulescu! He was, and is, a theoretician in nuclear physics! And I am an experimentalist! Most of the speakers before me are reputed theoreticians, his collaborators, or experimentalists working in fields where prof. Sandulescu made important contributions. And I am neither! However, he was my diploma advisor, most probably the only experimentalist to claim this qualification! He may or may not remember, but I do remember very well: I was for 3 months in Dubna for my diplomawork, in the Laboratory for Nuclear Reactions (today the Flerov Laboratory), where he was at the time deputy director. We had long conversations at the time: I was learning “deep inelastic collisions” (DIC) from their discoverer, dr. V.V. Volkov; he was “munching” at the time the idea of cluster radioactivity. I said munching, and I believe it is not the wrong word, because they were mostly physical images prof. Sandulescu was using to try to figure out the phenomena, not equations or existing models. And the idea of the double nuclear system used at the time in DIC, a dynamical nuclear system at temperature $T \neq 0$, was probably encouraging his ideas about cluster decay from $T=0$ systems. I wish him good health and a long, productive life!

Going into the subject of my lecture: after attending the lectures of the first days I realized that I have to rethink and retool my own presentation! I am the first, and the only one for some time, talking about *nuclear astrophysics* (NA). Even though the actual subject is better called ‘*nuclear physics for astrophysics*’, a brief introduction in nuclear astrophysics is in order. I will start by making a few general considerations about the contributions of nuclear astrophysics to fundamental science, to our

understanding of the Universe in general. Contributions made in the last 100, or 60 years, but more so in the last few decades. Given the many students in the audience, I find that going directly into the details of the subject to which the title refers specifically would be counter-productive! These should also be good starting points for discussions with “the adults” in the audience. Second, I will introduce the domain we call nuclear physics for astrophysics (NPA), including its specific vocabulary and main problems (very low energies on nuclear scale, very low cross sections and reactions involving in many cases unstable nuclei, far from stability). Third, I will go into the subject of the indirect methods for nuclear astrophysics using rare ion beams (RIB). I will insist on a few only and will use mostly examples from I studies I was participating.

The above was the structure of the lecture. For this paper I will retain some of the points made in the general, introductory discussion. I will treat only briefly the second part, as those can be found in many books, or lectures at other conferences. And I will review the third part, with only one example for each of the methods treated. References to which I send throughout should be good reading to cover some of the details missing here, for those students wanting to go deeper into the subject.

2. Nuclear Astrophysics

As essentially a fundamental science, in addition to so many practical applications that it brought us, Nuclear Physics (NP) was from its beginnings taking a front place in the human endeavour of understanding of the Universe. Our Universe! It was and continues to be part in understanding its composition, its dynamics, its origins and history, and possibly, its future. Some of these advances were made through its branch which we call *nuclear astrophysics*. Here is a short, non-exhaustive, list of the important successes of nuclear astrophysics:

- **Nuclear physics for astrophysics** – is increasingly motivation for NP research:
 - We know that nuclei are the fuel of the stars
 - Origin of chemical elements: nucleosynthesis = a large series of nuclear reactions & elemental/isotopic abundances are indelible fingerprints of cosmic processes. We need better nuclear data to have convincing quantitative descriptions of various scenarios.
- **Big successes of NA:**
 - **BBN** (Big Bang Nucleosynthesis) – is a quantitative, parameter free theory explaining the formation of the lightest elements. Alternatively, we should say that BBN theory was the first to determine that fundamental parameter of the standard model which is the baryon-to-photon ratio η . CMB (Cosmic Microwave Background) studies later confirmed the value and decreased the error bar! BBN theory lead also to the demonstration that there are 3 types of neutrinos, before the 3rd type was discovered.
 - **Heavier elements were created in stars** through a number of complex processes.
 - **Solar reactions are basically understood** (pp-chains, CNO cycle, solar neutrinos, neutrino oscillations...)
 - Nucleosynthesis is an **on-going** process!
 - We (quasi-) understand **novae, XRB, neutron stars** ...,
 - but not the super-novae – mechanisms, quantitative description, etc...

We study our Universe through observations, but also through experiments in the laboratory. It is actually considered that cosmology went from the realm of philosophy and speculation into that of science when physicists started to use nuclear physics data to model the genesis of chemical elements (Bethe and Critchfield, 1938 [1]; Alpher, Bethe and Gamow, 1948 [2]) and compare their quantitative predictions with the observations. Since then, many and fundamental advances were made, a large and rich spectrum of new astrophysical observations was added to our knowledge, and for their interpretation more detailed nuclear and particle data were necessary. Isotopic abundances, available from astronomical observations, are unique fingerprints of the evolution of stars. Sir A. Edington was the first to suggest that nuclei only can hold the key to the production of solar energy. In the 1920s and

'30s the hypothesis was advanced that nuclear reactions are the source of the solar energy, the very source that made and makes possible life on Earth, our life. It was only possible to explain the origin of the solar energy when nuclear processes started to be understood in the 1930s. The detailed mechanisms of this energy production could only be described, in part yet, much later with the advance of *nuclear physics for astrophysics*, or *nuclear astrophysics* (NA). Because nuclear reactions could not happen at the measured temperature of the solar spectrum! One can say that only in the early '70s the existence of the nuclear reactions was proved by the detection of solar neutrinos originating from the much hotter interior of the Sun. This was a joint achievement of *nuclear astrophysics*, *nuclear chemistry* and *astroparticle physics*.

Nuclei are the fuel of the stars! And all chemical elements in the Universe as we know it were produced in processes that we call generically nucleosynthesis. Nucleosynthesis occurred in various stages of the evolution of the Universe, in various places and in different types of events: Big Bang Nucleosynthesis (BBN) or later stellar evolution, far away or around us, explosive or steady burning. And we have firm evidence collected in the latter decades that nucleosynthesis happens today, even in our own galaxy, close to where we live. We also know today that the nuclear processes occurring in stars are not only the source of energy for cosmic processes, but also that nucleosynthesis gives us unique and indelible fingerprints of these processes. Many nucleosynthesis scenarios exist today. Some were formulated for some time, beginning with the seminal works by Burbidge, Burbidge, Fowler & Hoyle, 1957 [3] and independently by Cameron, 1957 [4]: Big Bang Nucleosynthesis (BBN), Inhomogeneous Big Bang Nucleosynthesis (IBBN), the s-process, the r-process, the rp-process, etc., and some are newer proposals. The possibilities to check the detailed predictions of specific models occurred only recently, with the availability of more and better astrophysical observations, of more nuclear data, of advances in understanding the dynamics of non-equilibrium processes, and of increased computing power. It turns out that an important component of all these nucleosynthesis model calculations is represented by the data for the nuclear processes involved. Only good nuclear physics data permit to make definite, quantitative predictions that can be checked against the ever increasing observational data sought and obtained by astrophysicists. This is the object of the nuclear physics for astrophysics, a subject that is most often called *nuclear astrophysics*. It does not deal with the specificities of the dynamics of different stellar processes, but only with the nuclear reactions involved, in particular with how we obtain these data from direct or indirect measurements. However, more recently the modeling of stellar processes and the dynamics of stars came closer and closer to the realm of interest of nuclear physicists and there is increased synergy of the two fields.

There are thousands of nuclear reactions and nuclear processes that occur in stars. Some are very important, some are less important and some are irrelevant in one type of process, while becoming important in another, depending on the conditions of the particular process: composition, densities and temperatures involved. There are also many nucleosynthesis processes, and our knowledge about them differs.

It is an important success of physics in general that we can describe now the **primordial abundances** (in BBN) over ten orders of magnitude. This description is parameter free after the baryon-to-photon ratio was determined independently and quite exactly $\eta_{WMAP}=6.19(15)*10^{-10}$ from the measurement of the Cosmic Microwave Background using 7-year WMAP data. Only the abundance of ${}^7\text{Li}$ is not exactly matching the observations and remains "the Li puzzle of BBN" (see Fig. 1). It is not clear now if this is due to the existing nuclear reaction data, to the list of 11 reactions important being incomplete, or is due to observational problems.

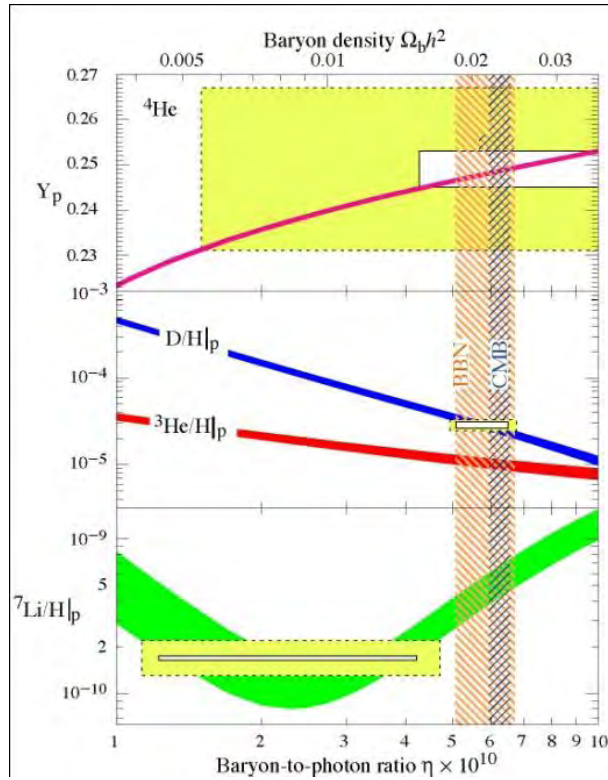


Figure 1 The abundances of ^4He , D , ^3He , and ^7Li as predicted by the standard Big Bang Nucleosynthesis, as function of the baryon-to-photon ratio η . The vertical bands show the η values given by the CMB and by the BBN. Boxes indicate the observed light isotopes abundances ($\pm 1\sigma$, and $\pm 2\sigma$ errors). From Ref. [5].

Closer to home, we have a good understanding of how our **Sun** works. Nuclear astrophysics measurements provide currently good data for most of the reactions important in Sun: those in the pp-I and pp-II chains responsible for most of the energy production and those in the CNO cycle. And for the $^3\text{He}(^4\text{He}, \gamma)^7\text{Be}$ and $^7\text{Be}(p, \gamma)^8\text{B}$ reactions at the end of the pp-III chain (Figure 2, right), reactions crucial for the evaluation of the solar neutrino production. However, the cross sections accuracies of around 5% called for by the current Standard Solar Model are not met in all cases. Much progress was made lately through the work of the underground facility LUNA at Gran Sasso National Laboratory, in Italy, where for the first time cross sections were measured into the energies in the Gamow peak. See for these the lecture of M. Junker at the recent Sinaia Carpathian School [6]. The “solar neutrino puzzle”= the discrepancy between the number of solar neutrinos produced and measured on Earth, lead to the discovery of neutrino oscillations, and implicitly to the proof for neutrino mass, and all current revolution in neutrino physics (see, e.g [7]).

Jointly nuclear astrophysics and observational astrophysics have also proven that **nucleosynthesis is an on-going process** in the Universe: it happened at various evolution stages in the past, but is still happening now. This very important concept has been proven by the gamma-ray space-based telescopes like COMPTEL and INTEGRAL, through the identification of characteristic gamma-rays emitted following the β -decay of long-lived isotopes like ^{26}Al ($T_{1/2}=0.7$ My) or ^{60}Fe ($T_{1/2}=1.5$ My), or not so long-lived ones, like ^{44}Ti ($T_{1/2}=60$ y) or ^{22}Na ($T_{1/2}=2.6$ y). The detection of gamma-rays originating from ^{26}Al , with a lifetime considerably shorter than that of the Universe, or of that of our Galaxy, was the first proof that nucleosynthesis is an on-going process. (*Note: this is a common statement! However, we should not forget that He was first identified in Sun’s spectra, and*

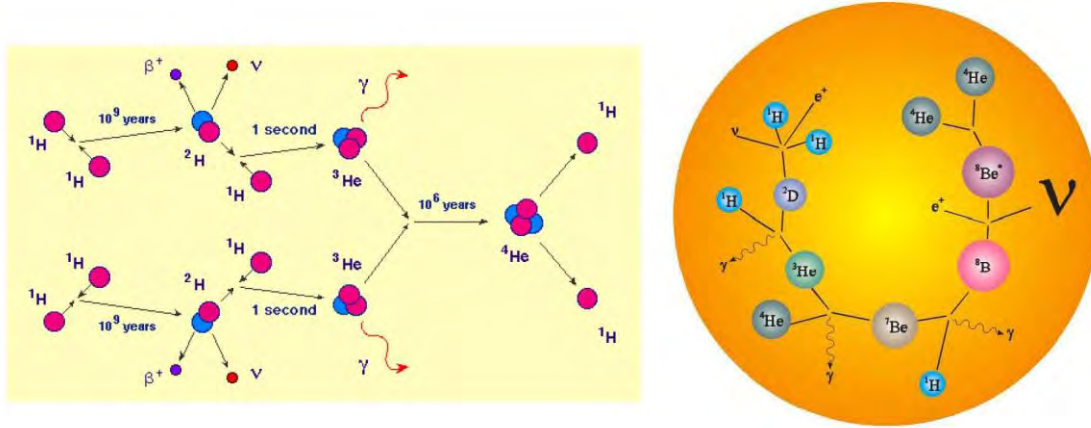


Figure 2 The reactions in the pp-chains taking place in Sun and producing most of the energy (pp-I left) and most of the observed neutrinos (pp-III, right).

the element Tc ($Z=43$), which does not have a stable element, was also first identified in stellar spectra). Figure x of Ref. [8] presents schematically the nuclear process involved and a sky map of the measured distribution of ^{26}Al sources. The distributions of sources can give information not only about the location of the nucleosynthesis sites, but also of the dynamics of mixing of the matter in the galaxy by measuring distributions for sources of various lifetimes. However, we do not have yet a precise and quantitative understanding of the nuclear processes leading to the production of these isotopes. Nor of the transport dynamics of the matter ejected from the underlying cosmic processes and more nuclear physics data are needed.

We can presently describe relatively well **H- and He-burning** in some environments like novae and X-Ray Bursters (XRB) and we have models for various types of **supernovae** (SN), more or less successful, but we do not know major things, for example the cosmic environments of the **s- and r-processes** [8]. We should say here that these processes account, each, for the production of about 50% of the chemical elements heavier than Fe, essential for life and our own existence. The origin of these heavy elements is considered one of the greatest unanswered questions of contemporary physics. The least we know today about the formation of heavier elements through the repeated absorption of neutrons at high neutron densities and high temperatures, the so called r-process. It is not clear what the exact path of these reactions is because we do not know key elements like the lifetimes of very neutron-rich nuclei or their neutron absorption cross sections. And for sure we do not know the exact location of the neutron dripline for medium and heavy elements. As this is dominantly a fast chain of reactions, followed by decays, it may not be needed to know all reactions precisely, but currently we have very limited knowledge even about the crucial ones at the waiting points at $N=82$ and $N=126$ shell closures. For many of the reactions involved the uncertainties are a few orders of magnitude! Therefore, much more work is needed before we fully understand and describe stellar nucleosynthesis and it is to be expected that the new facilities will bear answers to some of the above questions and to new ones that will appear.

3. Introduction to Nuclear Physics for Astrophysics

A number of particularities occur when we talk about nuclear data needed to describe reactions taking place in stars or in stellar environments. *Cross sections* are needed, but for practical reasons, in cases where barrier penetrations are important, it is helpful to introduce the *astrophysical S-factors*. In fact,

what the nucleosynthesis modelists are using are *reaction rates*, averaging cross sections' contributions over the whole energy ranges in gases at the appropriate energies. The weighing with the Maxwell-distributions lead to the so called *Gamow peak*, which specifies for what energies we would actually need to know/measure reactions cross sections. In reactions we can have *direct* and *resonant contributions*, etc... Discussions of these notions and their precise definitions can be found in books (like [9], e.g.) and in some previous lectures [10]. I will not repeat them in print, here.

4. Indirect methods for nuclear astrophysics with RIBs

The use of indirect methods in nuclear astrophysics is prompted by the difficulties that one encounters in attempting to make direct nuclear astrophysics measurements. Direct experiments mean trying to measure exactly the reactions that happen in stars, in those exact conditions (targets and projectiles, energies, charge states, etc...). The main difficulties arise because:

- Stars are cold! Compared with the energies typical in our nuclear physics laboratories, the energies of the partners in stars are very small (10s-100s keV) and the corresponding cross sections, in particular when charged particles are involved, are very small, therefore difficult to measure.
- In stars many reaction partners are unstable nuclei, and some are so short-lived that even with the recent advances in the rare isotope production they are not available, or not easily available, for the exact projectile-target combination at the energies they have in stars.

We have to resort to indirect methods. Several such methods are known in literature, some dedicated and labelled as such, some not. All these experiments are done at laboratory energies (1-10-100 MeV/nucleon) to extract nuclear structure information. This nuclear structure information is then used for nuclear astrophysics, that is, to evaluate reaction cross sections at low energies (10s-100s keV) and the resulting reaction rates at appropriate stellar temperatures. There are two steps here where theoretical calculations occur, and these calculations need to be seriously tested, well parameterized if necessary, using a large variety of data. For this, the use of good quality data with stable beams is still crucial. I want to stress this, because even if common sense, it is too many times overlooked and neglected.

In this lecture I will present three of these indirect methods:

1. One-nucleon transfer reactions (the ANC method)
2. Breakup reactions at intermediate energies
3. Decay spectroscopy. Beta-delayed gamma and proton decays.

In all three cases they are being used to evaluate reaction rates for radiative proton capture, with the difference that the first two are applied to find the continuum (non-resonant) component of the reaction cross sections, while the latter is used for resonant capture.

This being a school, I will not attempt below to be exhaustive in the description of the methods, but rather to be illustrative. I will also prefer to use relevant cases as illustrations, not necessarily 'newest' data. All of the examples will be from work done in the group I am working at Texas A&M University, even though many groups in the world have by now accepted these methods and are using them.

4.1 One-nucleon transfer reactions (the ANC method)

A direct transfer reaction is characterized by the rearrangement of only a few nucleons during a fast process. From the early days of nuclear physics, nucleon transfer reactions were the tool to study the single-particle degrees of freedom of nuclei and were crucial in establishing our current understanding of the structure of nuclei. Typically, spectra of final states and angular distributions were measured. Due to the direct character of the interaction, the tool of choice for the description of transfer reactions was the Born Approximation, either in the Plane Wave (PWBA), or the Distorted Wave (DWBA) form. By comparing the shape of the measured angular distributions with DWBA, the quantum numbers nlj of the single-particle orbitals involved could be determined, and by comparing the

absolute values of experimental cross sections with those calculated, the spectroscopic factors S_{nlj} were found for the states populated. The spectroscopic factor is proportional to the "probability" that a many-body system is found in a given configuration. In the case we are talking about, single particle orbitals nlj , the classical definition (from Macfarlane and French, 1960 to Bohr and Mottelson, 1969 etc...) relates the spectroscopic factors to the occupation number for the nlj orbital in question. One nuclear state may present several spectroscopic factors: e.g. the ground state (g.s.) of ${}^8\text{B}$ has $S(p_{3/2})$, $S(p_{1/2})$... related to the probability that the last proton is bound around the g.s. of the ${}^7\text{Be}$ core in a $1p_{3/2}$, or a $1p_{1/2}$ orbital. The determination of spectroscopic factors from one-nucleon transfer reactions was and is crucial in building our current understanding of the fermionic degrees of freedom in nuclei and their coupling to other types of excitations. The Asymptotic Normalization Coefficient (ANC) method is an indirect NA method introduced by our group more than a decade ago to determine astrophysical S-factors for the non-resonant component of radiative proton capture at low energies (tens or hundreds of keV) from one-proton transfer reactions involving complex nuclei at laboratory energies (about 10 MeV/u) [10]. The method was explained in detail in many previous publications, I summarize the main ideas below.

We can choose peripheral proton transfer reactions to extract the ANCs, which can be used to evaluate (p, γ) cross sections important in different types of H-burning processes. The idea behind it is that in peripheral processes it is sufficient to know the overlap integral at large distances, and this is given by a known Whittaker function times a normalization coefficient C_{nlj} , to be determined by experiment. Figure also stresses the importance of having good and reliable optical model potentials (OMP) to make the DWBA calculations, a problem I will not discuss here.

The technique was used in several experiments of this type; I will mention one of the latest studies, on the ${}^{12}\text{N}(p,\gamma){}^{13}\text{O}$ proton capture reaction at stellar energies. It uses the proton transfer reaction ${}^{14}\text{N}({}^{12}\text{N}, {}^{13}\text{O}){}^{13}\text{C}$ with a ${}^{12}\text{N}$ beam at 12 MeV/u [11]. Figure 3 below, also the image of a slide shown during the lecture, summarizes the whole process. Going from bottom left, clockwise: we have measured the elastic scattering and the one-proton transfer using a ${}^{12}\text{N}$ beam produced and separated with the MARS spectrometer [12] at Texas A&M University. The elastic scattering data (lower left corner) were used to determine the OMP needed in the DWBA calculations for transfer. The ANC for the system ${}^{13}\text{O} \rightarrow {}^{12}\text{N}+p$ was extracted from the transfer data (top left) after which was used to evaluate the non-resonant component of the astrophysical S-factor for the radiative proton capture ${}^{12}\text{N}(p,\gamma){}^{13}\text{O}$ and the corresponding reaction rate as a function of stellar temperature (top right). Finally, the astrophysical consequences are shown in a plot (bottom right) which shows the region of density-temperature where the capture process competes with its competitor (β -decay), in first stars. For comparison, the curves from literature before our data were measured are shown. There is a big change from the original estimates (dashed curves) based on theoretical estimates only.

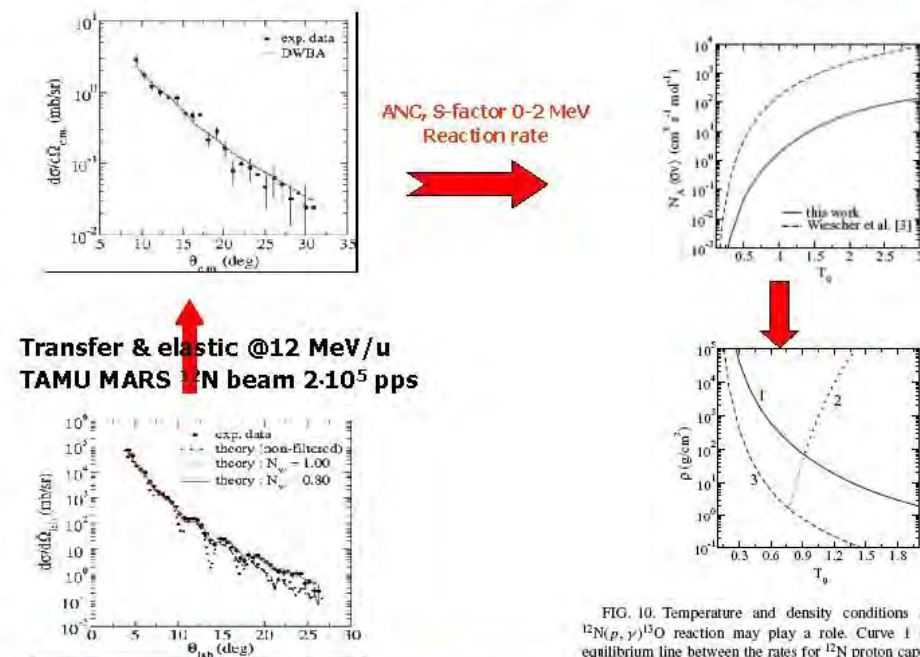
A variation of the ANC method uses one-neutron transfer reactions to obtain information about the mirror nuclei, for example studying the ${}^{13}\text{C}({}^7\text{Li}, {}^8\text{Li}){}^{12}\text{C}$ reaction to determine the ANC for ${}^8\text{Li}$ which we then translate into the corresponding structure information (the proton ANC) for its mirror ${}^8\text{B}$ and from there $S_{17}(0)$ for the reaction important in the neutrino production in Sun ${}^7\text{Be}(p,\gamma){}^8\text{B}$ [4]. We did this using the mirror symmetry of these nuclei: the similarity of their wave functions, expressed best by the identity of the neutron and proton spectroscopic factors for the same nlj orbital in the two nuclei $S_p(nlj)=S_n(nlj)$ (of course, the radial wave functions are not identical!). The experiment using these concepts and the results were published in Ref. [13].

I mentioned before that in order to extract data, either the spectroscopic factors, or the ANCs, the experiments have to be compared with calculations, and in the above conditions, the knowledge of the optical potentials is crucial. We established a procedure based on double folding, starting from an effective nucleon-nucleon interaction we call JLM. Florin Carstoiu of Bucharest was instrumental in this work. I will not insist on all these here, but I send you to literature [14].

4.2 Breakup reactions at intermediate energies

Work done in the last decade in several laboratories has demonstrated that one-nucleon removal reactions (or breakup reactions) can be a good and reliable spectroscopic tool. In a typical experiment a loosely bound projectile at energies above the Fermi energy impinges on a target and loses one nucleon. The momentum distributions (parallel and/or transversal) of the remaining core measured after reaction give information about the momentum distribution of the removed nucleon in the wave function of the ground state of the projectile.

$^{14}\text{N}(^{12}\text{N}, ^{13}\text{O})$ proton-transfer react \Rightarrow $^{12}\text{N}(p, \gamma)^{13}\text{O}$ (rap I, II proc)



A. Banu et al, Phys Rev C 79, 025805 (2009)

FIG. 10. Temperature and density conditions at which the $^{12}\text{N}(p, \gamma)^{13}\text{O}$ reaction may play a role. Curve 1 represents the equilibrium line between the rates for ^{12}N proton capture and ^{12}N β decay. Curve 3 illustrates the same result as determined from Ref. [3]. Curve 2 shows the line of equal strength between the rate of the ^{12}N radiative proton capture to ^{13}O and the rate for the inverse process, ^{13}O photodisintegration. See text for details.

Figure 3. Summary of how elastic and one-proton transfer data measured with secondary RIB (left side) are transformed in nuclear astrophysics information (right side).

The shape of the momentum distributions allows determining the quantum numbers nlj of the s.p. wave function (unambiguously only l is determined; shell model systematics are needed for the others). It was shown in Ref. 15 that on a large range of projectile energies breakup reactions are peripheral and, therefore, the breakup cross sections can be used to extract asymptotic normalization coefficients. For this to be true, we need, again, careful and reliable reaction model calculations. They need to reproduce all available data from such measurements if they are to be believed. This is a very important point, which I stressed in the lecture. The method to use breakup reaction for nuclear astrophysics was first applied in [15,16] to the breakup of ^8B to determine $S_{17}(0)$. All available breakup data, on targets from C to Pb and at energies from 27 MeV/u to 1400 MeV/u were used to determine the ANC for $^8\text{B} \rightarrow ^7\text{Be} + p$. Different reaction models and different nucleon-nucleon effective interactions were used. Consistent ANCs values were obtained, with an overall uncertainty estimated at about 10%. This is a very good agreement, a fact that validates both the $S_{17}(0)$ adopted in the neutrino production calculations pertinent to what was called the “solar neutrino puzzle” before the neutrino oscillations were demonstrated, and the validity of indirect methods in NA.

Another example is the breakup of ^{23}Al and ^{24}Si at intermediate energies [17,18]. The first is a good example as it takes a case where several configurations contribute to make the ground state of the projectile. The participating configurations were disentangled using the detection of gamma-rays from the de-excitation of the remaining core after a proton is removed from the projectile moving at 50-60 MeV/nucleon. It also shows how it is important to combine the results of this nuclear breakup reaction to evaluate the continuum contribution to the reaction rate with those of Coulomb breakup of the same projectile to evaluate the contribution of the resonant part. It is treated in the paper by A. Banu *et al.* and I refer the reader to it [17].

4.3 Decay spectroscopy. Beta-delayed gamma and proton decays.

Among the indirect methods, a large class is the spectroscopy of resonances, in general (transfer reactions, gamma-ray in-beam spectroscopy, decay spectroscopy, etc...). These resonances are meta-stable states in the compound nuclear system produced in reaction as an intermediate step. To evaluate the corresponding contributions to the reaction rates (for narrow, isolated resonances) it is sufficient to determine the location of the resonances (E_r) and their resonance strengths ($\omega\gamma$):

$$\langle\sigma v\rangle_{res} = \left(\frac{2\pi}{\mu kT}\right)^{3/2} \hbar^2 \omega\gamma \exp\left(-\frac{E_r}{kT}\right)$$

These may be obtained by studying the spectroscopic properties of the corresponding meta-stable states, populated through another, more convenient method. The decay spectroscopy is one such method: instead of measuring radiative proton capture (p,γ) one can study the inverse of its first step, the proton decay of the same state. The states populated by beta-delayed proton decay: in the same compound nucleus, states above the proton threshold are populated by β -decay, and then they decay emitting a proton. This happens if the selection rules for (p,γ) and βp allow for the population of the same states (energy and spin-parity selection rules). One can determine that way the energy of the resonance, determine or restrict the spins and parity and determine the branching ratios. This simple connection is schematically presented in figure 1 of Ref. [] for the case of the $^{22}\text{Na}(p,\gamma)^{23}\text{Mg}$ radiative proton capture: we aim at populating and study states in the ^{23}Mg daughter nucleus following the β -decay of ^{23}Al . The selection rules allow that: s-wave radiative capture involves $J^\pi=5/2^+$ and $7/2^+$ states; beta-decay populates predominantly positive parity states with spins 3/2, 5/2 and 7/2. Figure 1, a slide from the actual lecture, underlines that we need to locate the resonances and determine their properties (spin and parity and partial widths). Similar situations for the other two proton capture in our list, which we study through the decay of ^{27}P and ^{31}Cl , respectively. I will skip these in favor of sending the reader to the recent papers describing these experiments, the equipment and experimental methods involved, and their results [20,21].

5 Conclusions

After a brief review of nuclear astrophysics most important contributions to our understanding of the Universe, I showed that in many cases we need to use indirect methods to obtain data leading to the evaluation of stellar reaction rates. Three methods involving rare ion beams are described: one-nucleon transfer (the ANC method), nuclear breakup at intermediate energies and decay spectroscopy.

Acknowledgements

All of the examples used in this paper are based on work done along the years with my colleagues from the Cyclotron Institute at Texas A&M University: R.E. Tribble, A.M. Mukhamedzhanov, A. Banu (now at J. Madison University, Harrisonburg, VA, USA), B. Roeder, M. McCleskey, E. Simmons, and A. Spiridon. F. Carstoiu of IFIN-HH Bucharest very beneficially collaborated with us over many years on the reaction theory of subjects touched here. E. Pollacco (CEA/IRFU Saclay)

collaborated on the beta-delayed proton-decay spectroscopy. I thank them all. The original articles or planned publications are cited throughout this paper. The work presented in this paper was supported by U.S. Department of Energy under Grant No. DE-FG03-93ER40773.

References

- [1] C.L. Crichfield and H. Bethe 1938, *Phys. Rev.* **248**, 862(L).
- [2] R. Alpher, H. Bethe. and G. Gamov 1948, *Phys. Rev.* **73**, 803.
- [3] E.M. Burbidge, B.R. Burbidge, W.A. Fowler W and F. Hoyle 1957, *Rev Mod. Phys.* **29**, 547.
- [4] A.G.W. Cameron 1957, *Pub. Astron. Soc. Pac.* **6**, 201.
- [5] Particle Data Group (<http://pdg.lbl.gov/2010>).
- [6] J.N. Bahcall and M.H. Pinsonneault 2004, *Phys. Rev. Lett.* **92**, 121301.
- [7] R. Diehl et al. 2006, *Nature* **439**, 45. doi:10.1038/nature04364.
- [8] K.-L. Kratz 2008, in “Exotic Nuclei and Nuclear/Particle Astrophysics (II)”, Proc. CSSP07, Sinaia, Romania, eds. L. Trache and S. Stoica, AIP Conf Proceedings, vol. **972**, Melville, New York, p. 298.
- [9] C. Rolfs and W.S. Rodney 1988, *Cauldrons in the Cosmos*, University of Chicago Press.
- [10] A.M. Mukhamedzhanov, C.A. Gagliardi and R.E. Tribble 2001, *Phys. Rev. C* **63**, 024612.
- [11] A. Banu et al. 2009, *Phys. Rev. C* **79**, 025805.
- [12] R.E. Tribble et al. 1991, *Nucl. Instr. Meth. A* **285**, 441.
- [13] E.G. Adelberger et al. 1998, *Rev. Mod. Phys.* **70**, 1265; ibidem 2010, **83**, 195.
- [14] L. Trache et al. 2003, *Phys. Rev. C* **67**, 062801(R).
- [15] L. Trache et al. 2000, *Phys. Rev. C* **61**, 024612; F. Carstoiu et al. 2004, *Phys. Rev. C* **70**, 054610.
- [16] L. Trache, F. Carstoiu, C.A. Gagliardi and R.E. Tribble 2001, *Phys. Rev. Lett.* **87**, 271102.
- [17] L. Trache, F. Carstoiu, C.A. Gagliardi and R.E. Tribble 2004, *Phys.Rev. C* **69**, 032802(R).
- [18] A. Banu et al. 2010, *Phys. Rev. C* **84**, 015803.
- [19] A. Banu et al. 2012, *Phys. Rev. C* **86**, 015806.
- [20] A. Saastamoinen et al. 2011, *Phys. Rev. C* **83**, 045808.
- [21] A. Saastamoinen et al. 2012, *Nuclear Instruments and Methods A* **698**, in press.

AstroBox: a new detection system for very low-energy protons from β -delayed proton decay

E. Pollacco¹, L. Trache², E. Simmons², A. Spiridon², M. McCleskey², B.T. Roeder², R.E. Tribble², G. Pascovici³, Marc Riallot¹, Jean Philippe Mols¹, Mariam Kebbiri¹

¹ *IRFU, CEA Saclay, Gif-sur-Yvette, France*

² *Cyclotron Institute, Texas A&M University, College Station, TX 77843-3366, USA*

³ *Institut fuer Kernphysik der Universitaet zu Koeln, D-50937 Koeln, Germany*

Abstract

An instrument we call AstroBox, was developed to perform low energy proton spectroscopy from β -delayed proton emitters of interest for astrophysics studies. Energetic precursor nuclei are identified and stopped in a gas volume. After decay, the electrons drift in an electric field and are further amplified by employing a Micro Pattern Gas Amplifier Detector, MPGAD. It was tested in-beam using the β -delayed proton-emitter ^{23}Al produced and separated with the Momentum Achromat Recoil Spectrometer (MARS). Off-beam proton spectra have no or low β background down to ~ 100 keV and we found a resolution of ~ 15 keV (fwhm) for lines at $E_p=206$ and 267 keV. Lines with βp -branching as low as 0.02% are observed. The device gives also a good mass and charge resolution for energetic heavy ions measured in-beam.

Version of 12/05/2012 @ 22:07

1. Introduction. Nuclear astrophysics motivation

In many radiative proton capture reactions $X(p,\gamma)Y$ important in steady or explosive H-burning in stars or stellar environments, the resonant parts are dominant or play a major role. In such cases the reaction rates can be evaluated based on information about the resonances involved: their location and their resonance strength [1]. This information can be obtained by indirect methods: the same metastable states in the compound system Y^* are populated and studied. Among the indirect methods is that of decay spectroscopy: excited states in nucleus Y are populated from β -decay and their decay is further observed. Beta-delayed proton emission (βp) from exotic nuclei was observed to occur in proton-rich nuclei (precursors P) which have sufficiently large Q -value to significantly populate excited states above the proton binding energy in the daughter nucleus Y ($Q_\beta > S_p$). These states may decay further either by gamma-ray or by proton emission. If these decays are $P \rightarrow Y^* \rightarrow X + p$, then the excited states in Y^* can be resonances of interest in the $X(p,\gamma)Y$ capture. Provided, of course, that the selection rules for (p,γ) and βp allow for the population of the same states in the compound system Y (energy and spin-parity selection rules). One can determine through proton spectroscopy the energy of the resonances, restrict the spins and parity (maybe even determine them) and determine the branching ratios.

¹ Email: epollacco@cea.fr

However, experimentally this is not simple. Stars are “cold”, relative to the nuclear energies. In phenomena like novae or X-ray bursts (XRB) the temperatures involved are $T=0.1-0.4$ GK and up to 1 GK, respectively. For these temperatures the range of energies that contribute most to the reaction rates (the Gamow window) are low, of the order of a few 100s keV at most: 100-400 keV for the first case, up to ~ 800 keV in the latter (numbers are given here for captures on *sd*-shell nuclei $A=20-30$). These raise two considerable experimental problems for the observation of very low-energy protons from β -delayed proton decay. The first is related to the need to avoid energy losses of the emitted protons before entering the active area of the detector. To do this we chose to implant the source in the detector itself. The second one comes from the fact that the lower the energy of the metastable states above the proton threshold, the lower the probability for the proton emission: the gamma-ray branching becomes dominant; due to Coulomb barrier penetration the dependence is exponential. It results that these low energy protons have also a small branching. For their observation we need detectors with very high sensitivity. In the case of sources implanted in the detector, that involves a low sensitivity to the betas emitted in the first step of the decay process.

A good deal of success was achieved earlier [2,3] at Texas A&M University by implanting the precursor nuclei in very thin Si strip detectors, but the region of energies below 3-400 keV remained elusive as the measured spectra were dominated by a large continuum background resulting from the energy losses of the positrons copiously dominating the protons in the same energy region. We show here how we better solve these two problems by using a gas detector that has two stages. Gas reduces the sensitivity to the positrons emitted and pushes the background further down in energy. The second stage is a high gain gas amplifier based on MPGAD [4] which assures a good gain for protons while maintaining a good resolution.

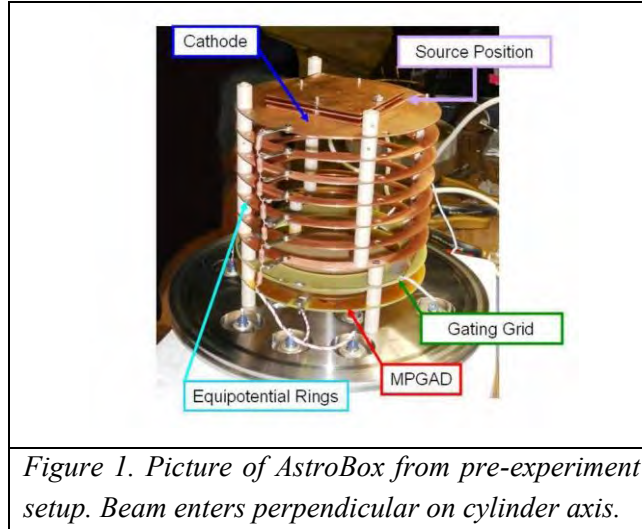
We built a detector we call AstroBox that was tested for the beta-delayed proton decay of ^{23}Al . A low β background is obtained since protons and positrons have very different ranges and ionization in the active gas medium. The paper describes the detector and its performance with radioactive sources in Section 2. Section 3 describes the first tests with radioactive beams and gives its performances. The conclusions are summarized in Sec. 4. Parts of this work were presented or mentioned before at conferences [5,6].

2. AstroBox

2.1 The AstroBox detector

AstroBox is, basically, a cylindrical gas detector with a few of channels. A photograph of the assembly is shown in [fig. 1](#). A CAD drawing of it is given in [fig. 2a](#) and a scheme showing its elements and voltages are given in [fig. 2b](#). The detector is housed in a stainless steel cylindrical chamber (not shown) with ports to allow for beam entry through a vacuum tight aramica window 50 μm thick and for chamber evacuation and gas flow. Two further ports can carry vacuum tight Kapton window to allow for X-ray sources to be placed. The design of the detector allows for the beam or sources to enter axially or perpendicularly with respect to its

symmetry axis. The main components inside the chamber are: cathode, equipotential rings, gating grid, GG, and gas amplifier, MPGAD (Figs. 1 and 2b). Geometrically these elements are stacked equally spaced. By setting the voltages given in [fig 2b](#), a uniform field is set up in the active volume between the cathode and the gas amplifier. The GG has a grid stretched to cover part of the central area (100 μm diameter wire with 2 mm pitch) and has a functionality described below. The MPGAD is a Micromegas structure [4] and is the main element of AstroBox. It consists of a gold plated anode divided into five areas (fig.3b) on a PCB. Inter-pad distance is 300 μm . A nickel mesh (thickness 18 μm) is stretched over the anode and kept at a uniform distance (128 μm) from the anode by placing insulating pods spaced regularly every 5 mm. Amplification of the electrons entering the mesh-pad volume occurs by reaching a very high electric field strength (approximately 30-40 kV/cm) in the 128 μm amplification zone. The optimum transmission of the electrons through the mesh is obtained with biases noted in [fig 2b](#). The manufacture, signal formation and performance of this device are described in detail in ref. [MPGAD#2](#).



The gas used was a standard mixture of Ar and methane in various proportions (P5 or P10). The gas employed in the result shown herein is P5 with high purity (< 5 ppm O_2 and H_2O). The pressure $p=800$ torr was selected to ensure the gas purity in case of leaks. A continuous refreshing of the gas was kept at 8.5 L/hr. The density of the gas was monitored to be stable during the run at $<0.1\%$. The gas handling system is based on a MKS unit with slow control [9]. The choice of materials employed and design were such as to minimize possible contamination of the gas from the low vapor pressure material or trapped gases. A clean environment was obtained flowing the gas through for two days before use.

Bias power supplies on the mesh and anode pads were from an Ortec Quad Bias Supply 710 and from two Ortec 549 (0-5kV) bias supply units for the Cathode and the GG [10]. Filtering of the bias input to detectors was employed. Signals from the anode pads were fed into 142a/b Ortec pre-amplifiers followed by a classical fast-slow set-up. The trigger is given by signals firing a

leading edge discriminator on the central pad. The ADCs from all channels were read for a given trigger. For the tests shown herein, three electronic chains were set-up and hence the four side pads were summed into two channels, S1 and S2. The cathode was biased at a fixed negative voltage of 1.8 kV to give a drift velocity of **4 cm/ μ s (to check)**. The mean calculated lateral diffuseness (sigma) was approximately 1.2 mm.

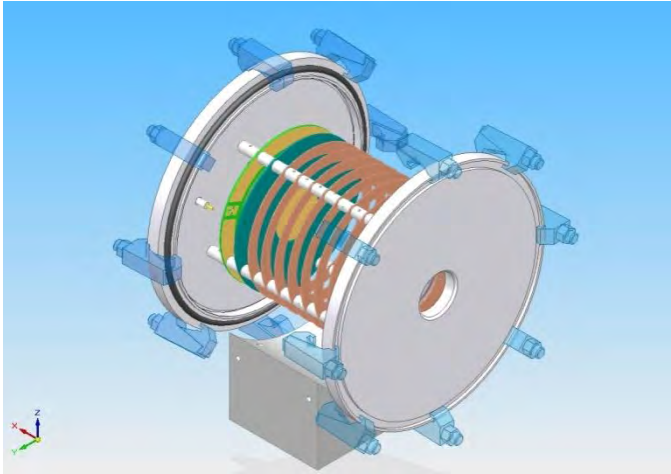


Figure 2a. Schematic drawing of AstroBox.

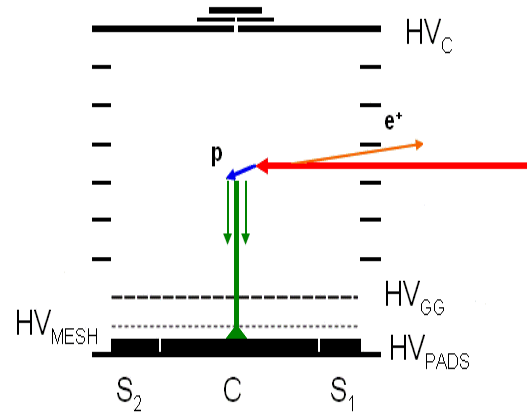


Fig. 2b Schematic representation of the detector and how it works. The MPGAD is at the bottom;

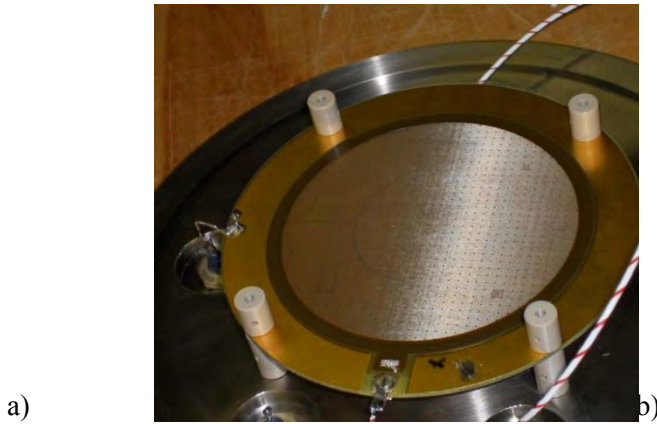
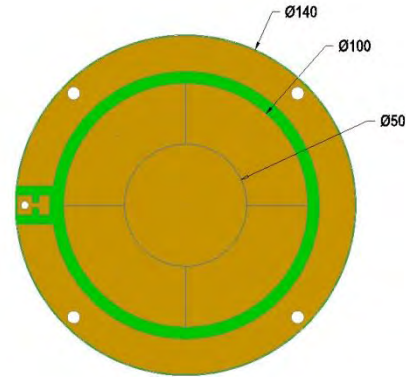


Figure 3 (a) Picture of the micromesh sitting on top of the anode.



(b) Schematic drawing of the anode pads.

The functionality of AstroBox is similar to that of a TPC: electrons from the ionization of the gas, created by particles losing energy in the active volume drift towards the GG and then onto the gas amplifier. By placing appropriate bias on the GG, the drifted electrons are collected or

partially collected on the MPGAD. For close to 100% transmission of the drifted electrons the grid is set at 0 V. The GG is opaque at +200 V.

The energy loss in the active gas volume from the stopping beam may be very high ($>50\text{MeV}$) compared to the required dynamic range (50 to 4000 keV) to measure low energy protons. Hence a large number of electrons could reach the anode when the beam enters and stops in AstroBox. To avoid spark damage to the MPGAD and contain the dynamic range for proton-decay measurements, the beam is pulsed with beam-on for implantation and beam-off for the measurement. The GG high voltage is synchronized with the beam to remove a large fraction of the electrons when the beam is on, and be transparent when the beam is off. With the beam off the bias is set to 0 V. To do this a simple but effective circuit based on **GG 1** transistor was devised for this function. Since transistors at negative voltage were not accessible the anode had to be placed on a positive voltage. Rise and decay time of the GG are typically 300 μsec . By adjusting the GG bias we could get the system to detect both the beam and the high energy part of the proton spectrum during beam-on. That was useful for beam particle counting, important for normalization.

2.2 Simulations of the Implantation and Detector Response

Detailed Monte Carlo simulations of the AstroBox detector were carried out prior to the construction of the detector to study how it would function in a typical experiment. These simulations were made with the GEANT4 toolkit [11] using the standard packages for the energy loss of charged particles and a custom physics model to generate the β -delayed proton decay of our test case, ^{23}Al . Two important aspects of the test experiment were studied: the implantation of the high energy ^{23}Al ions into the AstroBox chamber and also the expected response of the detector for detection of positrons vs. protons during the ^{23}Al decay at beam-off.

For the simulations of the ^{23}Al ion implantation, it was assumed that the ^{23}Al ions are produced in the manner described above. Thus, the calculations were carried out assuming that a secondary beam of 40 MeV/u ^{23}Al ions with momentum distribution $\Delta p/p = \pm 0.25\%$ that passed through a rotatable Al degrader, a 50 μm Aramica window, and finally into the detector chamber itself with P5 gas (95% Argon, 5% Methane) at $p=800$ torr. The rotation angle of the Al degrader was adjusted such that the ^{23}Al ions were stopped close to the center of the AstroBox detector. The resulting distribution of the stopped ions along the central axis of the detector is shown in **figure 4**. The simulation showed that it is possible to stop $\sim 85\%$ of the ions inside the active gas volume associated with the central pad of the MPGAD. The main contributions to the width of the distribution were shown to be the initial momentum spread of the beam and the energy straggling of the ions as they pass through the Al degrader, entrance window and the gas.

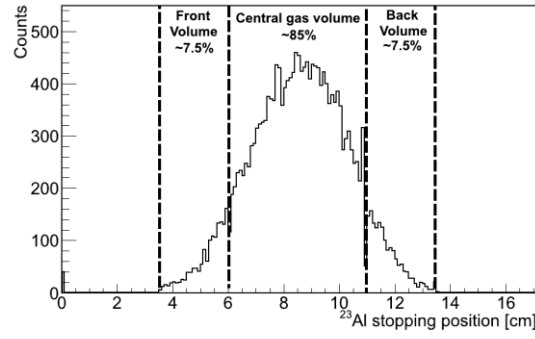


Figure 4. – Monte Carlo simulation of the distribution of the ^{23}Al ions inside AstroBox.

For the simulations of the AstroBox detector response to the positrons and protons from ^{23}Al decay, separate calculations were carried out. In this case, the ^{23}Al ions were placed inside AstroBox with the distribution calculated above. Then, the ^{23}Al nuclei were allowed to decay at random positions within this distribution. The result of this simulation is shown in Sec. 3 for 2×10^5 events. The calculations indicated that for P5 gas at $p=800$ torr, maximum energy deposited by the positrons in central active gas volume was around 100 keV, with most of the positrons depositing less energy. The calculations also showed that the protons from ^{23}Al decay with energies between 200-300 keV should be clearly visible and well-separated from the positron background. This represents a substantial improvement over the previous measurements with implantation into silicon detectors where careful background subtraction was needed. The simulations used best available proton decay data, as extracted from the studies with very thin Si detectors [3].

Finally, the detection efficiency of AstroBox for protons of various energies was simulated. The efficiency depended on both the energy of the protons and the size of the expected distribution after the implantation. The results of these simulations assuming P5 gas at $p=800$ torr and the simulated ^{23}Al distribution above are shown in figure 5. As the entire ^{23}Al distribution fits within the sum of the inner and outer active volumes, the proton detection efficiency is close to 100% for proton energies below ~ 1000 keV. Beyond 1000 keV, the path length of the protons in the gas is > 2 cm, allowing some of the protons to exit the active gas volumes of the detector and thus reduce the efficiency. This effect is more pronounced if only the central active gas volume is considered. In this case, the efficiency is limited to $\sim 84\%$ even for low energy protons because some of the ^{23}Al ions are not inside this volume when stopped. Also, the detection efficiency decays rapidly to near 0 for proton energies above 1000 keV as the path length of the protons is larger than the diameter of the central volume. The efficiency can be improved by increasing the gas pressure (increasing the gas also reduces the size of distribution of the

ions inside the detector) at the cost of also increasing the contributions of the positrons to the energy loss spectrum.

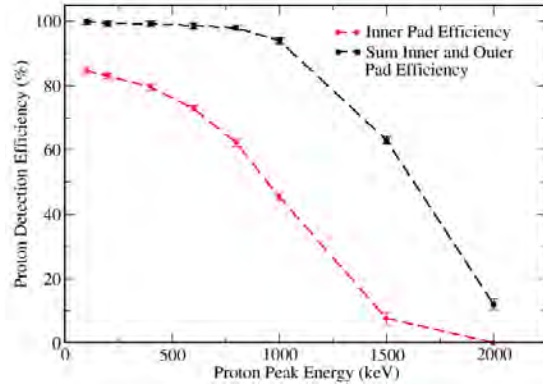
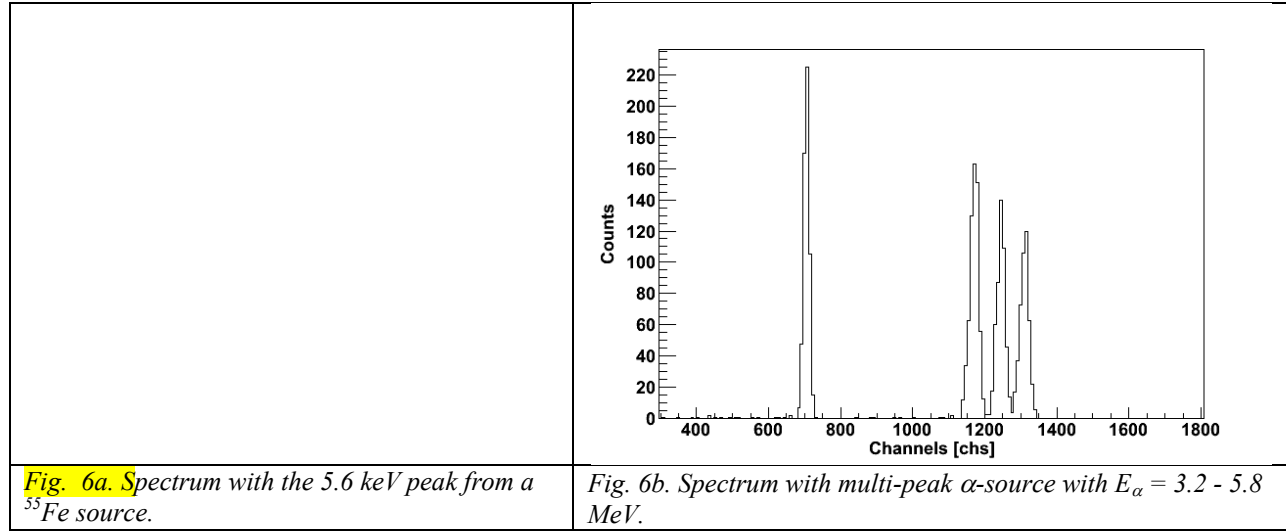


Figure 5. – Simulated proton detection efficiency in AstroBox with the initial ion distribution given in Figure ? above. See text for discussion.

2.3 Tests with sources

To establish the functionality of AstroBox an X-rays ^{55}Fe source and mixed alpha sources were employed. The ^{55}Fe source viewed the active volume through one of the side ports having a Kapton window. A typical spectrum from the central pad is given in [fig. 6a](#) and shows that the resolution for the 5.9 keV peak after subtraction of the 6.5 keV peak is 11% (FWHM). The escape peak at 3 keV is clearly seen. Amplification for such spectra was typically of the order of 10^4 . The alpha source was a mixture of ^{148}Gd , ^{239}Pu , ^{241}Am and ^{244}Cm isotopes covering a range between 3.2 and 5.8 MeV alphas. To obtain a clean spectrum the source was set on the cathode employing two 1 mm diameter collimators with a 3 mm spacer (visible on top of fig. 1). Spectrum from this source is given in [fig. 6b](#). The typical energy resolution is 2.5% (FWHM) at the alpha lines of ^{241}Am . The observed integrated non-linearity over the 2.6 MeV range is less than 1%.

The tests were done both in Saclay and at TAMU.



3. In-beam tests

3.1 Production and separation of ^{23}Al

The in-beam tests of the AstroBox were done at the Cyclotron Institute, Texas A&M University. A primary beam of ^{24}Mg at 45 MeV/nucleon was generated from the K500 superconducting cyclotron. It impinged on a hydrogen target at LN_2 temperature at $p=2$ atm. The Momentum Achromat Recoil Spectrometer (MARS) [12] was used to separate a radioactive beam of ^{23}Al with up to 4000 pps intensity (at $\Delta p/p = \pm 0.6\%$) and 90% purity. The procedure and the resulting parameters were similar with those described in Ref. [Iacob 2006]. We chose this particular nucleus because of its astrophysical significance and because we had previously studied it by implantation in thin silicon Double Sided Strip Detectors (DSSD) [3]. Following the results from that study, there were still particular questions about the low-energy region below $E_p=400$ keV, exactly the region of interest for nuclear astrophysics. The major difficulty when using DSSD was the large background at low energies due to betas (Fig. 7 of Ref. 3). Another reason to choose ^{23}Al is that its total proton branchings from beta decay is around 1.26%, not too large, but not exceedingly small, and because it has two easily recognizable proton lines at $E_p=558$ and 829 keV, energies where AstroBox has a good efficiency.

Attached to the MARS backend was a degrader chamber, followed by AstroBox separated by a 50 μm aramica window. The degrader chamber contains a rotating Al foil 625 μm thick, in vacuum. By adjusting the angle of the foil with respect to the beam, the energy of the resulting beam is degraded from 40 MeV/nucleon so that the ^{23}Al stops above the central pad in AstroBox.

The beam enters the AstroBox chamber perpendicular to the cylinder axis. In order to implant the nuclei in the centre region (the active volume) the angle of the rotating Al energy degrader foil was fine tuned. For this we had to operate the system in two modes:

- an “implantation-control mode”,
- a “ βp measurement mode”.

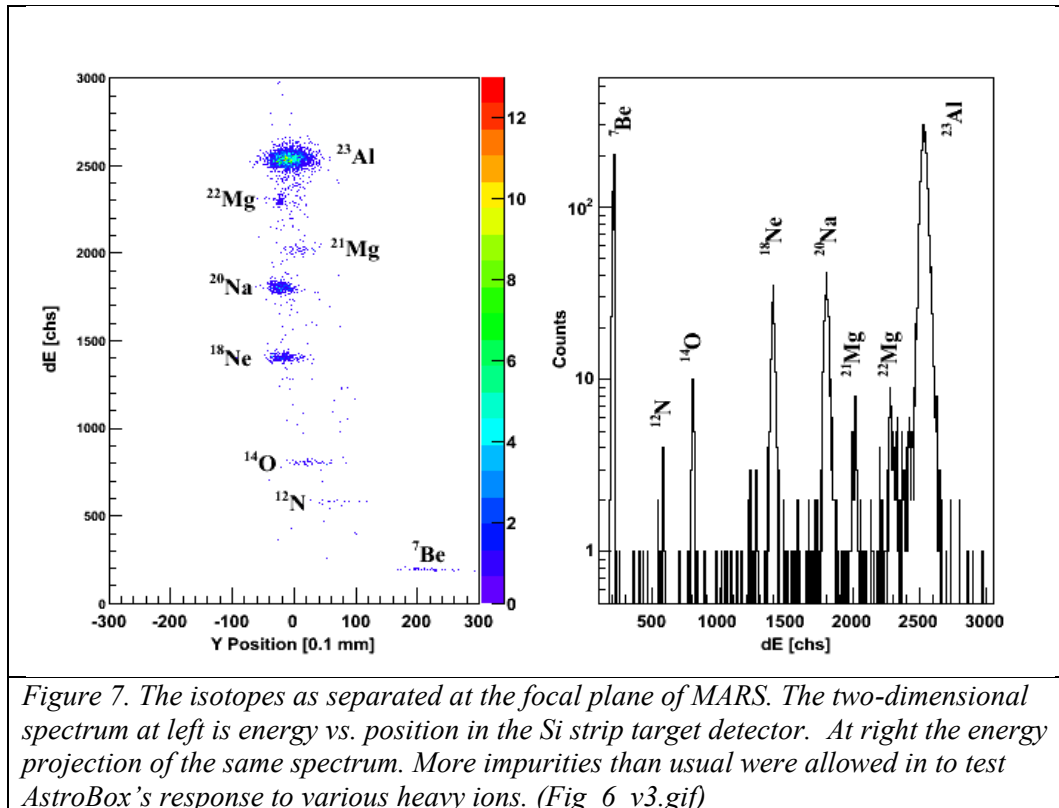
In the implantation-control mode a) we tuned the detector gain to an appropriate dynamic range to be able to measure the energy losses of the heavy ions in the gas (up to 100 MeV total). The beam was not (macro-) pulsed.

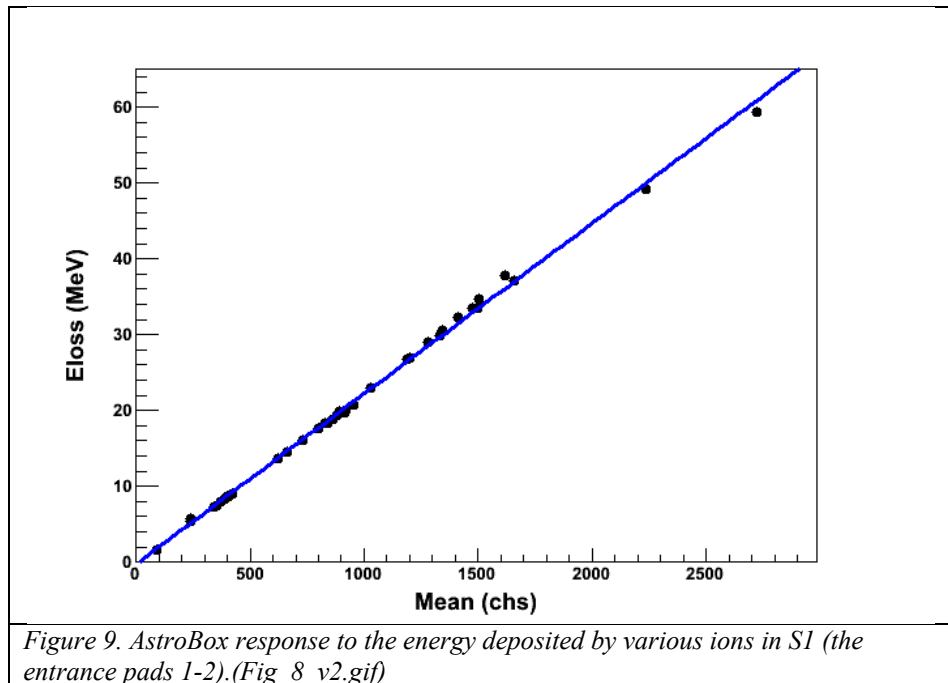
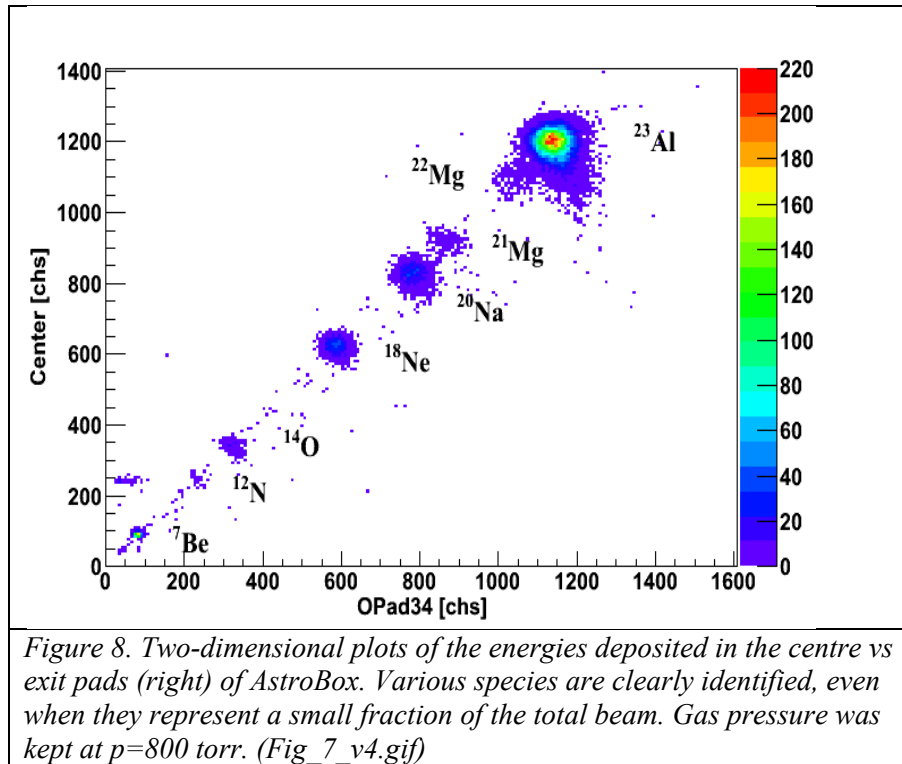
For the measurement for β -delayed protons, mode b), we tuned the detector gain for a smaller dynamic range: 0-4 MeV. The beam from the cyclotron was pulsed in this case: we irradiated for 1000 ms (implantation time), then turned the beam off, paused briefly (move time=7 ms), then measured for 994 ms (measurement time). The gating grid was biased at 0 V for full transparency (measurement time) and +600 V for full opacity (implantation time). This was done in order to protect the detectors from the large drifted charge deposits created by the HI's during implantation. The bias on the mesh was also fixed at +225 V, whereas the voltage on the detection pads was varied to determine the optimum value.

3.2 Detector response to heavy ions

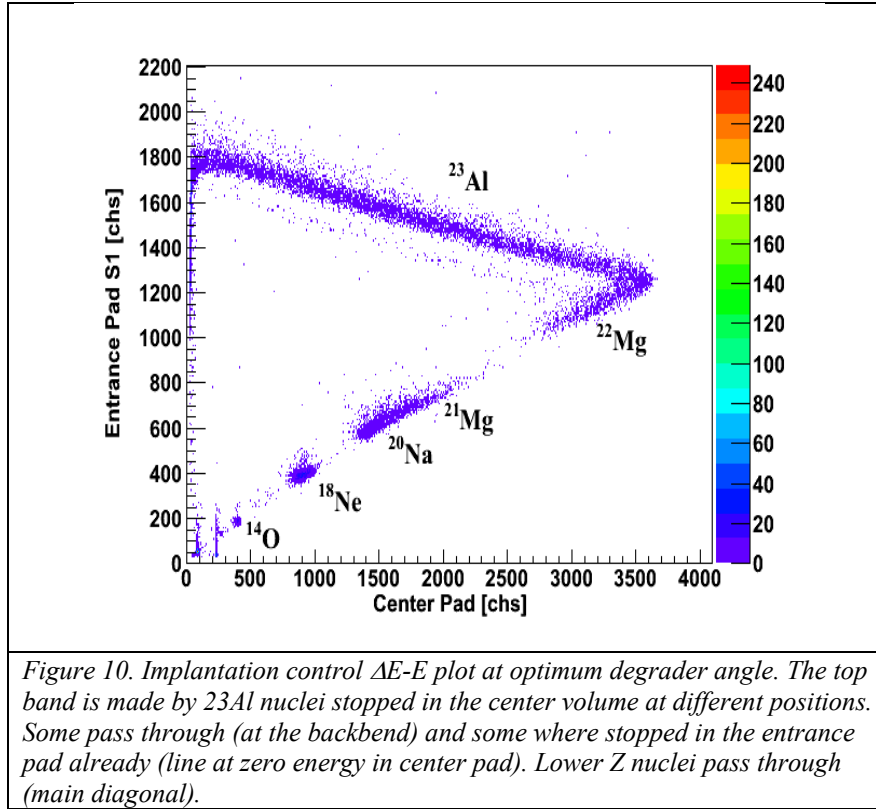
While our goal was to study the low energy protons we also needed to study the heavy ions during the initial implantation (mode a). This led us to find the characteristic response of the detector to energetic heavy ions. To do that we used the secondary beam as before, but tuned MARS such that we increased somewhat the impurities content in the beam cocktail (essentially by opening wider the admittance slits at the front of MARS and the selection slits at the end of it). The momentum slits of MARS were kept narrow, at ± 0.4 cm, such that we had a momentum acceptance $\Delta p/p = \pm 0.25\%$, with a corresponding decrease of the rate at around 800 pps. Such we obtained a cocktail of 8 different ion species with $Z=4-13$, different energies and very different relative intensities. The composition of the beam cocktail is shown in Figure 7, which is taken with the MARS target detector, a position sensitive Si strip detector (type X1-300 by Micron Semiconductor Ltd. [MSL catalogue]). The left panel shows the two-dimensional distribution energy-position and the right one is a projection on the energy axis allowing better figuring the relative intensities of the species in the cocktail. They vary from $\sim 70\%$ (^{23}Al) to $<1\%$ ($^{21,22}\text{Mg}$ 0.7%, ^{12}N 0.13%). We then dropped the target detector out of the beam and let the beam in AstroBox. We had S_1 (2 entrance quarters connected), centre, and S_2 (2 exit quarters connected) signals to work with, basically giving two ΔE -E detector setups. In Figure 8 a two-dimensional spectrum Centre pad vs exit pads S_2 is shown. With the Al degrader foil normal to the beam (zero degrees), the ions pass through the detector and the signals registered correspond to energy losses. We can see a clear separation of all components of the beam: ^{22}Mg and ^{23}Al are well separated in spite of a ratio 1:100 for their intensities. The resolution is $\sim 2-3\%$ (fwhm) for the main component (^{23}Al) for energy losses 25-55 MeV (obtained by rotating the Al degrader foil). This 5% include all the contributions: the resolution of the secondary beam ($\sim 1\%$ in energy), the straggling in and the non-uniformities of the Al degrader foil and in the gas before entering the active volume of the detector, as well as the different lengths of the paths inside the volumes covered by the pads – due to their circular geometry. The detector response is also found to be linear: in Figure 9 we plot the response (channel position) vs the energy loss of the

ions at different angles of the degrader foil (therefore different energies entering the detector's active volumes). These energy losses were evaluated with the code SRIM [13] using the known thickness of the degrader, of the aramica window, the geometry of the pads and the composition and pressure of the gas in the detector. Therefore, any deviations from linearity may be also due to this evaluation procedure. The plot shows that we do not seem to have important charge density induced non-linearity.





In the implantation-control mode by rotating Al energy degrader we slowed the beam down until it was stopped in the centre of the detector. We determined when that happened by looking at plots of energy loss in the centre pad versus energy loss in the outer pads.



We had three energy loss detector signals and we could make a complex analysis. In **Figure 10** we plot the two dimensional spectra of the energy loss in the centre pad versus the energy loss in the entrance pads and the exit pads, respectively. Most of the ^{23}Al beam is stopped in the detector volume on top of the centre pad (as identified by the thick region in the left picture, after the back bending) while the lower Z impurities (of the same magnetic rigidity) are punching through into the regions covered by the exit pads and further. Some ^{23}Al stop in the entrance pads (left: the part on the main diagonal before the back bending) and some are stopping in the exit pads (the top line in the picture on right). The fraction not stopped above the centre pad amounts to **16%**, in agreement with the results of the GEANT4 simulations.

After determining the degrader angle for best central implantation, we switched to the “ βp measurement mode”. The beam from the cyclotron was pulsed and we only have measured with beam-off and the detector voltages were adjusted to have a dynamic range of 0-4 MeV in the detector. During beam-on, for 1 sec, we implanted and the gating grid was on, becoming opaque, to protect the detector. During beam off, also for about 1 sec, the grid was off allowing full transparency and we measured the decay of ^{23}Al .

3.3 Beta-delayed protons. Analysis and results

In the present ^{23}Al case only β -delayed gamma decay (to which the detector is practically transparent) and β -delayed proton decay is possible. Therefore particle identification is not

required. The spectra measured in each pad are proton spectra with distortions from the accompanying betas. The spectra obtained can be of three categories. There are events where the projected proton track is contained within the central pad C and trigger only it, events which trigger only the side pads, S_1 or S_2 , and events where the track is shared between the central pad and the one of the surrounding pads, CUS_1 or CUS_2 . Events S_1 or S_2 , as well as S_1US_2 type events are not discussed herein.

The division between the event classes may be somewhat blurred because it depends upon the detection and detection thresholds. Electronic thresholds were set as low as about 30 keV. For C the proton peaks have a line shape that is distorted by the accompanying β^+ ionization of the gas and the threshold effects. The line shape of the event-by-event added spectra ($C+S_1$ and $C+S_2$) is in addition also a function of the calibration. As with regards the energy calibration, the proton fully stopped energy deposit regime in Argon ($E_p < 1\text{MeV}$) is not amply understood. The principal factors that could govern the energy calibration are the non-linear effects in the drift and amplification volumes. The processes of signal formation could also give rise to non-linear response. Electronics does not add significant contribution and can be corrected for. To evaluate the line distortions and deviations from linearity we compare the proton spectra data collected from double sided silicon detectors [3]. Lines from alpha and X-ray sources are too far in energy and could not be used in this work. The resolution as a function of proton energy should be governed by the stochastic effects and hence should vary like $E_p^{-1/2}$. We note that in comparing calibration runs with ^{55}Fe and alpha emitting sources as well as beam data this relationship is not necessarily withheld. Results are extracted and compared.

A proton spectrum is given in fig. 11a as detected by the centre pad after approximately 2 hours of statistics and ^{23}Al intensity of 500 Hz, with an anticoincidence condition with the outer pad. The spectrum was calibrated employing a pulser and the higher energy peaks associated at 579 and 866 keV [ref. 3]. The estimated error in the 267 keV peak position is 11 keV and consistent with errors evaluated in Ref. 3. At low energy the 206 keV peak is well separated. Peak resolution is of the order of 5% (FWHM). The line shape effects are not sticking and significantly well reproduced by the simulation. The major advantage seen here is tremendous reduction in the β^+ background, with respect to equivalent spectrum in Ref. 3. The reduction is very dependent on energy and can reach one in thousands. The beta background drops at a level comparable to the height of the proton peak at 206 keV for a beta energy loss around 80-100 keV. Again the simulation gives a good reproduction of the beta background.

In fig 11b the CUS_1 is given and shows the linear sharing of the track. Similar 2-D for CUS_2 is available. Again, through a calibration of the S_1 and S_2 spectra by employing the known peaks in ^{23}Al (ref. 3) and pulse generator, the spectra from S_1UC , S_2UC and C were summed to give fig. 10.

To evaluate the efficiency the incident beam is assumed to be uniformly distributed over the time window and the proton life time corrections in one beam cycles is introduced. The counting of the incident ions is performed by placing windows for the ions that do not stop in the active volume (as noted in section 3.2). The number of ions of interest is counted burst-by-burst from the ion composition of beam for the beam entering AstoBox at higher energies. By counting the protons in the following decay window, the branching ratios are evaluated per beam burst and cumulative value obtained. Dead-time corrections for the DAQ are not made here and could have been easily done. However the trigger

One issue that came up and complicated the analysis was the implantation distribution. It looked like it was not restricted to the central area. The edges were actually in the outer region. Furthermore, some protons were emitted on a path that had them lose energy in both detection regions. Figure 6 illustrates that. Each line corresponds to one of the energy peaks visible in Figure 5, except that here protons leave part of that energy in one pad and part of it in the other. For a complete analysis, we had to take these protons into account as well.

A raw proton spectrum can be seen in [Figure 12](#) as detected by the centre pad after ~2 hours of statistics with an anticoincidence condition with the outer pad. Peak resolution is ~7% and the beta background threshold is down to ~80 keV. Even at low energy the peaks were well separated and we could see some other features that may or may not be other peaks. One issue that came up and complicated the analysis was the implantation distribution. It looked like it was not restricted to the central area. The edges were actually in the outer region. Furthermore, some protons were emitted on a path that had them lose energy in both detection regions. Figure 6 illustrates that. Each line corresponds to one of the energy peaks visible in Figure 5, except that here protons leave part of that energy in one pad and part of it in the other. For a complete analysis, we had to take these protons into account as well.

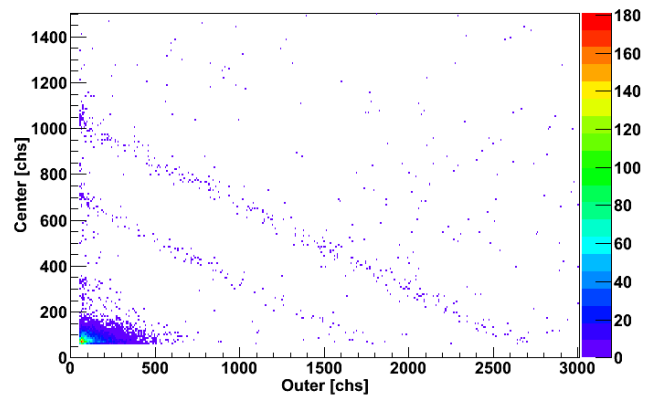
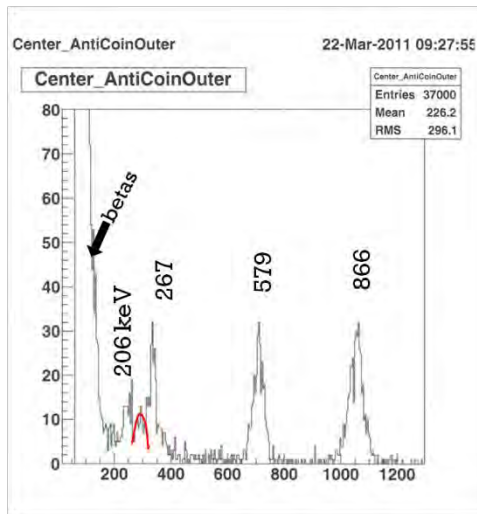
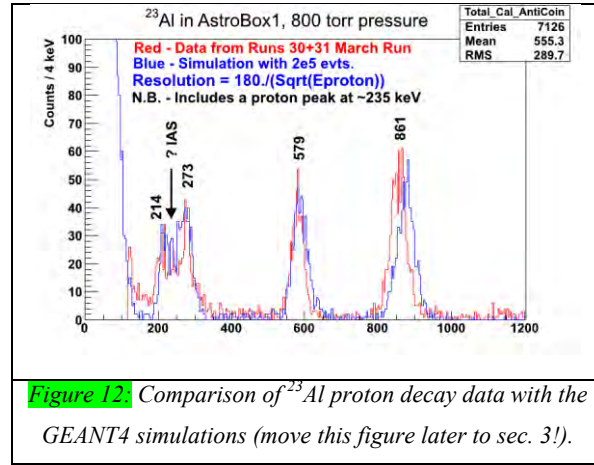


Figure 11a. Spectrum obtained from the anticoincidence of the centre with outer pad

Figure 11b. Centre vs Outer histogram



4. Conclusions

A detector was built, which can measure very low energy protons from β -delayed proton decays. It can measure proton energies down to 100 keV or lower, an energy range of interest for studies motivated by nuclear astrophysics. Its performances are due to a combination of three factors:

- The exotic nuclei are implanted inside the detector itself (= no windows or dead layers for the protons emitted)
- Uses gas as primary detection medium (= low sensitivity to positrons).
- Uses a MPGAD to ensure high amplification factors with a good resolution.

We find out that while the detector allows to measure record low proton energies from βp , it is efficient in a rather narrow range up to 600-1000 keV. It is not an universal tool for proton decay studies, but a good one for the energy range relevant in the spectroscopy of resonances from radiative proton capture reactions of importance in nuclear astrophysics. It may need to be combined with measurements with other detectors or methods to provide the complete picture of the decay process: with Si detectors for proton energies >1000 keV and with Ge detectors to determine proton-to-gamma decay branchings for the same state (resonance) in the daughter nucleus.

In the test measurements we used a ^{23}Al secondary beam at 40 A MeV produced and separated with MARS. We could reduce the β -background in the proton spectra below 100 keV, measure proton peaks around $E_p=200$ keV with 5% resolution and with β -branchings as low as 0.02%.

Further optimizations and design improvements are possible, including those that would make the detector a true TPC and/or would lower further the proton energies within reach and its sensitivity.

We found also that the detector has good resolution for heavy ions that would deposit several tens of MeV and could serve as good energy loss detectors valuable in particle identification schemes.

References

- [1] C. Rolfs and W. Rodney, *Cauldrons in the Cosmos*, Univ. of Chicago Press, Chicago, 1988.
- [2] L. Trache *et al.*, in *Proc. 10th Symposium on Nuclei in the Cosmos, July 27-Aug 1, 2008, Mackinac Island, MI*, **PoS (NIC X) 163**.
- [3] A. Saastamoinen *et al.*, *Phys. Rev. C* **83**, 045808 (2011).
- [4] Y. Giomataris *et al.*, *Nucl. Instr. und Meth. in Phys. Res. A* **376** (1996) 29-35
- [5] L. Trache *et al.*, in *Proc. Intern. Conf. Nuclear Physics for Astrophysics V, Apr. 3-8, 2011, Eilat, Israel*. L. Trache *et al.*, in *Proc. Fourth International Conference on Proton-emitting Nuclei (PROCON2011)*, Bordeaux, France, 6-10 June 2011, ed. B. Blank, AIP Conf. Series, vol. 1409, Melville, NY, 2011; A. Saastamoinen *et al.*, *ibidem*.
- [6] Alexandra Spiridon *et al.*, in *Proceedings 6th European School on Experimental NuclearAstrophysics*, **PoS (ENAS 6)038**.
- [7] V.E. Jacob *et al.*, *Phys.Rev. C* **74**, 045810 (2006).
- [8] MPGAD#2
- [9] <http://www.mksinst.com>
- [10] <http://www.ortec-online.com/Solutions/modular-electronic-instruments.aspx>
- [11] <http://geant4.web.cern.ch/geant4>
- [12] R.E. Tribble *et al.*, *Nucl. Instr. Meth. A* **285**, 441 (1991).
- [13] J. F. Ziegler and J. P. Biersack and M. D. Ziegler (2008). *SRIM - The Stopping and Range of Ions in Matter*. SRIM Co. [ISBN 0-9654207-1-X](https://doi.org/10.1306/96542071-X)

Astrophysical reaction rate for $^{17}\text{F}(p,\gamma)^{18}\text{Ne}$ from the transfer reaction $^{13}\text{C}(^{17}\text{O},^{18}\text{O})^{12}\text{C}$

T. Al-Abdullah,^{1,2,*} F. Carstoiu,³ X. Chen,^{1,†} H. L. Clark,¹ C. A. Gagliardi,¹ Y.-W. Lui,¹ A. Mukhamedzhanov,¹ G. Tabacaru,¹ Y. Tokimoto,¹ L. Trache,^{1,3} R. E. Tribble,¹ and Y. Zhai^{1,‡}

¹*Cyclotron Institute, Texas A&M University, College Station, Texas 77843-3366, USA*

²*Physics Department, The Hashemite University, Zarqa 13115, Jordan*

³*National Institute for Physics and Nuclear Engineering Horia Hulubei, Bucharest, Romania*

(Received 23 August 2013; revised manuscript received 27 January 2014; published 26 February 2014)

The asymptotic normalization coefficients of the bound states $J^\pi = (0_1^+, 2_1^+, 4_1^+, 2_2^+)$ in ^{18}O are extracted from the peripheral neutron transfer reaction $^{13}\text{C}(^{17}\text{O},^{18}\text{O})^{12}\text{C}$. They are then converted to their mirror states in ^{18}Ne , which are further used to evaluate the astrophysical S factor for the proton capture reaction $^{17}\text{F}(p,\gamma)^{18}\text{Ne}$. The elastic-scattering cross sections have been measured in both incoming and outgoing channels in order to extract the optical potentials needed for distorted-wave-Born-approximation calculations. The S factor is found to be $S_{1-17}(0) = 2.17 \pm 0.37$ keV b. The contribution of the direct capture rate to this reaction is estimated, and its consequences on the production of ^{18}F at stellar energies in ONe novae are discussed.

DOI: 10.1103/PhysRevC.89.025809

PACS number(s): 21.10.Jx, 26.30.-k, 25.70.Hi, 27.30.+t

I. INTRODUCTION

Nucleosynthesis of elements in ONe white dwarf (WD) novae produces several sources of γ -ray lines. Among them is the positron-electron annihilation in the nova envelope, which leads to a strong line at 511 keV and a continuum below it. It is believed that ^{13}N ($t_{1/2} = 9.965$ min) and ^{18}F ($t_{1/2} = 109.77$ min) are the main contributors to the production of observable positron annihilation radiation [1]. Because of the short lifetime of ^{13}N , the decay of ^{18}F is more important since its γ -ray photons are emitted when the envelope starts to be transparent [1–3]. According to the ONe novae models, when the temperature in the burning shell reaches $T_9 \sim 0.2$ – 0.4 , the main nuclear activity to produce ^{18}F is driven by a β decay following the proton capture reaction $^{17}\text{F}(p,\gamma)^{18}\text{Ne}$ [4]. This is an important reaction that is interesting to be studied to understand the 511-keV line after the explosion. The rate of this reaction may influence the abundances of ^{18}F , ^{18}Ne , ^{17}F , and ^{15}O and may explain the transition sequence from the HCNO cycle to the NeNa cycle [5].

The nuclear structure of ^{18}Ne is related to the configurations and the binding energy of the levels in the mirror nucleus ^{18}O taking into account the Coulomb energies. Shell-model calculations assume a $2s$ or $1d$ nucleon coupled to the single-particle $5/2^+$, $1/2^+$, and $3/2^+$ levels of ^{17}F and ^{17}O , respectively. Comparison of the nuclear structure of the mirror nuclei for the low-lying states (2_1^+ , 4_1^+ , 0_2^+ , 2_2^+ , 2_3^+ , 0_3^+ , 3_1^+) shows that their excitation energies are very similar as reported in Ref. [6]. The rate of the $^{17}\text{F}(p,\gamma)^{18}\text{Ne}$ reaction has been estimated by applying several theoretical methods and experimental measurements. It is determined as a sum of the direct capture terms, including the bound states 0_1^+ , 2_1^+ , 4_1^+ , 0_2^+ , 2_2^+ and of a resonant contribution due to the states located

just above $^{17}\text{F} + p$ threshold, such as 1_1^- , 3_1^+ , and 0_3^+ [7,8]. Wiescher, Görres, and Thielmann noticed that the $J^\pi = 3_1^+$ level in ^{18}Ne may greatly influence the thermonuclear reaction rate [9]. Recent experiments have obtained precise information about the energy of the 3_1^+ level [10,11]. Averaging their results with weights gives $E_x = 4.525(3)$ MeV, and its total width $\Gamma_p = 18(3)$ keV. Estimates of the reaction rate show that the resonant capture to the 3_1^+ state dominates the rate only at $T_9 > 0.5$ [10], which is an appropriate temperature for explosive events such as x-rays bursts and supernovae. The direct reaction measurement for $^{17}\text{F}(p,\gamma)^{18}\text{Ne}$ at ORNL determined the resonant strength. It shows that astrophysical importance of the resonant contribution is increased by a factor of 10 over the direct contribution at $T_9 = 0.5$ – 1.0 [12]. A slight complication occurs from the fact that ^{18}Ne is an even- Z nucleus, and its states can have more than one proton orbital involved. There are five proton bound states in ^{18}Ne and direct radiative proton capture can proceed via any and all of them. The nuclear cross section shows that the $^{17}\text{F}(p,\gamma)^{18}\text{Ne}$ reaction will be dominated by direct capture to the lowest-energy $J^\pi = 2^+$ states, mainly $E_x(2_1^+) = 1.887$ MeV and $E_x(2_2^+) = 3.616$ MeV [7].

The importance of the direct capture to the bound states in ^{18}Ne has not been resolved to date. Because of the difficulties of obtaining information from experiments with radioactive beams, we use here the asymptotic normalization coefficients (ANCs) [13] as an alternative technique to evaluate this direct capture reaction rate. The spectroscopic factors for mirror states are the same [14,15], so the ANC method can be applied to the mirror nucleus ^{18}O to extract the ANCs for the $E_x(2_1^+) = 1.982$ MeV and $E_x(2_2^+) = 3.920$ MeV states and then convert them to their corresponding states in ^{18}Ne . Measurements of $^{17}\text{O}(d,p)^{18}\text{O}$ [16] found that the wave functions for the $E_x(2_1^+)$ is an admixture of $(d_{5/2})^2$ and $(d_{5/2}s_{1/2})$ configurations with the spectroscopic factors 0.83 and 0.21, respectively. Similarly, the spectroscopic factors for $E_x(2_2^+)$ are 0.66 and 0.35 for the $(d_{5/2})^2$, or briefly (dd), and $(d_{5/2}s_{1/2})$, or (ds), configurations, respectively. A 25% uncertainty was estimated for these spectroscopic values [16]. The results were obtained

*abdullatq@gmail.com

[†]Present address: Department of Chemistry, Washington University at St. Louis, MO, USA.

[‡]Present address: Cooper Medical School of Rowan University, NJ, USA.

TABLE I. The parameters of the Woods-Saxon optical model potentials obtained from the analysis of the elastic-scattering data for $^{17}\text{O} + ^{13}\text{C}$ and $^{18}\text{O} + ^{12}\text{C}$.

Channel	Pot	V (MeV)	W (MeV)	r_V (fm)	r_W (fm)	a_V (fm)	a_W (fm)	χ^2	σ_R (mb)	J_V (MeV fm ³)	R_V (fm)	J_W (MeV fm ³)	R_W (fm)
$^{17}\text{O} + ^{13}\text{C}$	1	96.14	25.93	0.90	1.13	0.84	0.68	6.90	1662	215	4.64	96	4.98
	2	188.40	24.95	0.72	1.12	0.94	0.69	4.62	1667	271	4.44	92	4.99
	3	248.75	26.36	0.69	1.13	0.90	0.66	4.53	1659	318	4.27	99	4.97
$^{18}\text{O} + ^{12}\text{C}$	4	89.18	25.24	0.88	1.16	0.88	0.68	5.12	1712	197	4.69	103	5.09
	6	195.40	25.59	0.68	1.16	0.96	0.67	6.39	1702	257	4.40	104	5.07
	7	295.82	26.00	0.60	1.16	0.95	0.67	7.54	1696	297	4.20	106	5.06
	8	374.41	26.19	0.58	1.16	0.90	0.68	9.78	1695	334	4.01	107	5.07

with the aid of distorted-wave Born approximation (DWBA) calculations by fixing the geometric parameters of the Woods-Saxon potential for the radius, $r_0 = 1.25$ fm, and diffuseness, $a = 0.65$ fm.

A brief description of the experiments and the extraction of the optical potentials are presented in Sec. II. That is followed in Sec. III by the analysis of the transfer reaction data to measure the ANC's. These are finally used in model calculations to estimate and discuss the reaction rate in Sec. IV. The conclusions are summarized in Sec. V.

II. THE EXPERIMENTS

The experiments carried out were the peripheral neutron transfer reaction $^{13}\text{C}(^{17}\text{O}, ^{18}\text{O})^{12}\text{C}$ and the associated elastic scatterings in both entrance and exit channels (a rarely possible situation with nucleus-nucleus reactions). They were carried out with two separate 12 MeV/nucleon ^{17}O and ^{18}O beams from the K500 superconducting cyclotron at Texas A&M University. Each beam was transported through the beam analysis system to the scattering chamber of the multipole-dipole-multipole (MDM) magnetic spectrometer [17], where it interacted with 100- $\mu\text{g}/\text{cm}^2$ targets. The Oxford detector [18] was used in the focal plane to observe the reaction products. We have measured the neutron pickup from ^{13}C ($S_n = 4.95$ MeV) and the elastic scattering to determine the optical model parameters (OMPs) for the incoming and outgoing channels. First, the ^{17}O beam bombarded a ^{13}C target. The elastic-scattering angular distribution was measured for the spectrometer angles 4° – 25° in the laboratory system. The $4^\circ \times 1^\circ$ wide-opening mask and an angle mask consisting of five narrow ($\Delta\theta = 0.1^\circ$) slits were used for each spectrometer angle to double check the absolute values of the cross section and the quality of the angle calibration. Fine-tuned RAYTRACE [19] calculations were used to reconstruct the position of particles in the focal plane and the scattering angle at the target. The instrumental setup, including the focal plane detector, and the procedure for energy and angle calibrations are identical to that described in Ref. [20]. Second, the ^{12}C target was bombarded by an ^{18}O beam with 216 MeV of total laboratory energy. The elastic-scattering cross section was measured at 4° – 22° spectrometer angles. The angular resolution, $\Delta\theta_{\text{res}}$, of the detector in both cases was, on average, 0.31° in the center-of-mass frame and the focal plane position resolution was better than 1 mm. The absolute values of cross sections

were determined using a careful integration of beam charge in a Faraday cup and the measurement of target thicknesses from energy loss of α particles from sources and from the beam. The procedures are detailed in Ref. [20] and the uncertainties are specified throughout the text.

Using reduced χ^2 as a criterion to get the best fit of the elastic-scattering data, three distinct families of potentials with standard Woods-Saxon (WS) volume form factors were obtained for $^{17}\text{O} + ^{13}\text{C}$ scattering and four sets for the $^{18}\text{O} + ^{12}\text{C}$ case. Their parameters are presented in Table I, where only central potential terms have been included (see Ref. [21] and references therein). All of the potentials give relatively small χ^2 , but only those with the smallest values for entrance and exit channels, potentials 3 and 4, respectively, are adopted in the DWBA calculations of the neutron transfer reaction, while the others are used to determine the uncertainty in the choice of the OMP for either channel. The elastic-scattering fits with those potentials are plotted in Fig. 1. The pattern is characteristic for strong

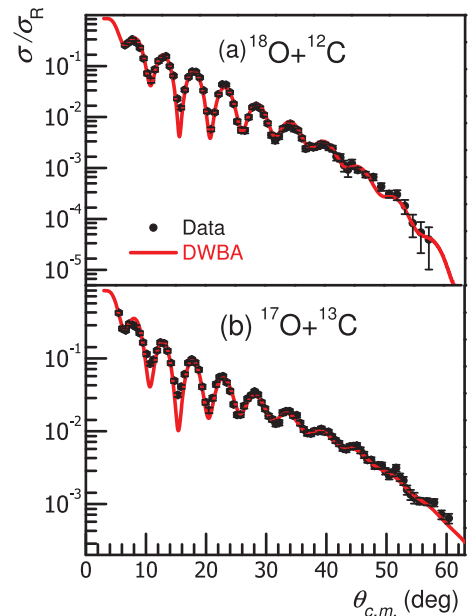


FIG. 1. (Color online) Angular distributions for the elastic-scattering data (filled circles) for (a) $^{18}\text{O} + ^{12}\text{C}$ and (b) $^{17}\text{O} + ^{13}\text{C}$ at 12 MeV/nucleon. The solid curves are calculations with the best-fit optical potentials from Table I.

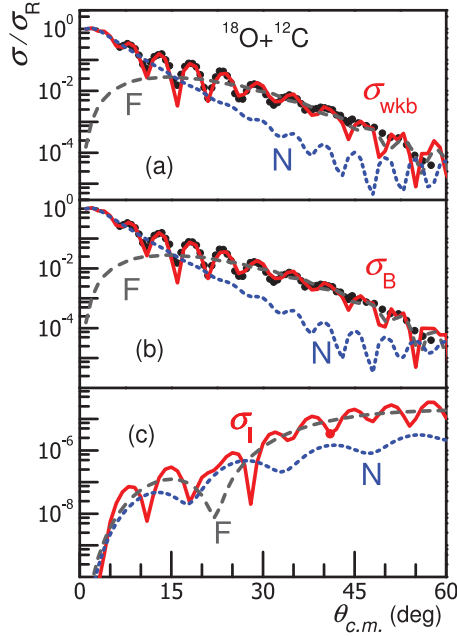


FIG. 2. (Color online) (a) Semiclassical (WKB) analysis of the cross section based on the parameter set 4, Table I. (b) The barrier (σ_B) and (c) the internal barrier (σ_I) are further decomposed into far (F) and near side (N) components, which are indicated by dashed and dotted lines, respectively.

absorption with Fraunhofer oscillations at forward angles and a smoothly decaying cross section at larger angles due to far-side dominance. The peripherality of the reaction was checked by performing a detailed Wentzel-Kramers-Brillouin (WKB) analysis according to the Brink-Takigawa prescription [22]. The barrier and internal barrier component of the semiclassical scattering amplitude are shown in Fig. 2 for $^{18}\text{O} + ^{12}\text{C}$. The barrier component which accounts for the flux reflected at the most external turning point of the potential fully accounts for the total cross section in the measured angular range, while the internal barrier component is negligibly small. The reaction is completely peripheral. Similar results were obtained for the case of the $^{17}\text{O} + ^{13}\text{C}$ elastic data at same energy $E = 12$ MeV/nucleon and are not shown explicitly here. The results of the analysis are shown in Table I.

III. ASYMPTOTIC NORMALIZATION COEFFICIENTS

The neutron transfer reaction $^{13}\text{C}(^{17}\text{O}, ^{18}\text{O})^{12}\text{C}$ has been measured in the laboratory frame for the spectrometer angles 4° – 11° , which is equivalent to 10° – 26° in the center of mass. The ground state and the excited states $J^\pi = 0_1^+$, 2_1^+ , 4_1^+ , and 2_2^+ of ^{18}O were observed. Extracting information for the first $J^\pi = 0_1^+$ and 2_1^+ ($E = 1.982$ MeV) states is straightforward. However, due to the energy resolution of the detector, $\Delta E_{\text{res}} = 350$ keV, an overlap exists between the tails of 4_1^+ ($E = 3.555$ MeV) and 2_2^+ ($E = 3.920$ MeV). Populating the 1_1^- excited state ($E^* = 4.456$ MeV) in ^{18}O and the parasitic reaction $^{13}\text{C}(^{17}\text{O}, ^{18}\text{O})^{12}\text{C}^*$ are also present. The positions of their peaks are strongly overlapped and interfere slightly with the 2_2^+ peak. To solve the problem, RAYTRACE was used to do an

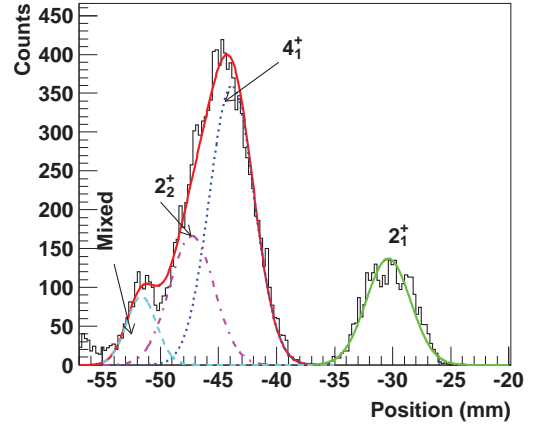


FIG. 3. (Color online) The multi-Gaussian fit used to extract the angular distributions for the excited states in ^{18}O when the spectrometer angle is at 4° . The solid curve represents the overlapped states beside the well-separated 2_1^+ state. The curves for the 4_1^+ , 2_2^+ , and the mixed state are plotted using dotted, dash-dotted, and dashed peaks, respectively. See the text for the explanation of the left most peak.

energy calibration for the first few low-lying states in ^{18}O and their expected positions along the dispersive x axis in the focal plane of the detector. Using the information about the full width at half maximum of the 2_1^+ peak and the determined positions of the other states of interest in ^{18}O , a multi-Gaussian macro was written to extract the angular distribution of the inelastic transfer reactions. Two main constraints are included in the macro, the separation between the 2_2^+ and 4_1^+ positions and the width of their corresponding peaks for each spectrometer angle, as illustrated in Fig. 3. The contribution of the 0_2^+ excited state at 3.634 MeV has been estimated. Its angular distribution was calculated and then rescaled by its relevant spectroscopic factor 0.28 reported in Ref. [16]. Comparing its cross section with those measured for 4_1^+ and 2_2^+ gives a ratio of $\frac{1}{40}$ and $\frac{1}{19}$, respectively. Including these ratios in the macro to search for 0_2^+ , the fit did not show any significant change for the integration of the peaks shown in Fig 3. Therefore, the contribution of the 0_2^+ is dropped out from our determinations, but an additional uncertainty of 2.5% and 1% are added to the values of the ANC's for 4_1^+ and 2_2^+ , respectively. The position spectra in the focal plane were produced from the data with the $4^\circ \times 1^\circ$ wide-mask with eight 0.5° gates on the reconstructed target angle, and the measurements at 4° , 6° , and 8° allowed a self-consistency check of the data for at least two bins.

The angular distributions for $J^\pi = 0_1^+$ and 4_1^+ are shown in Fig. 4, and those for 2_1^+ and 2_2^+ states are shown in Fig. 5. Taking into consideration the shell-model configurations [16], the ANC for each 2^+ state is determined using

$$\frac{d\sigma}{d\Omega} = \frac{C_{p_{1/2}}^2(^{13}\text{C})}{b_{p_{1/2}}^2(^{13}\text{C})} \times \left\{ C_{d_{5/2}}^2(^{18}\text{O}) \frac{\sigma_{d_{5/2}}^{\text{DWBA}}}{b_{d_{5/2}}^2(^{18}\text{O})} + C_{s_{1/2}}^2(^{18}\text{O}) \frac{\sigma_{s_{1/2}}^{\text{DWBA}}}{b_{s_{1/2}}^2(^{18}\text{O})} \right\}, \quad (1)$$

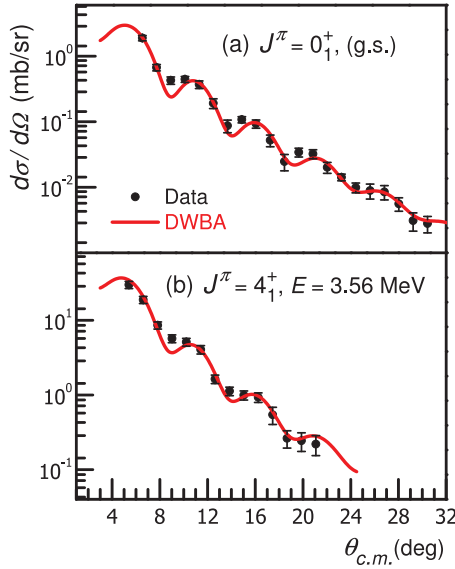


FIG. 4. (Color online) The angular distributions for populating (a) the ground state and (b) 4^+ excited state of ^{18}O . The points are the experimental data, while the solid curves are the DWBA cross sections obtained from PTOLEMY.

where $C_{p_{1/2}}^2(^{13}\text{C})$ represents the ANC for the other vertex of the reaction. b_{nlj} is the single-particle ANC and its value is obtained from the ratio between the normalized single-particle bound-state neutron wave function for a specific orbital and the corresponding Hankel function at radii greater than 5.0 fm. The ANCs for the 0_1^+ and 4_1^+ states are extracted using only the

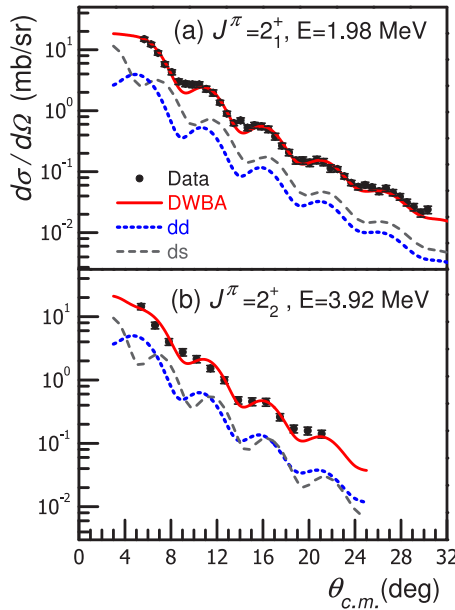


FIG. 5. (Color online) The cross section values for transfer reactions to the (a) 2_1^+ and (b) 2_2^+ states in ^{18}O . The DWBA calculations, drawn with solid curves, are the sum of the (dd) and (ds) lines. The angular distribution for the (dd) (dots) and (ds) (dashes) configurations of the 2^+ states are reduced by a factor of 5 to show their contributions.

first term of the equation. The peripherality of the reaction was checked by studying the influence of changing the geometries of the WS neutron binding potential in ^{18}O , $r_0 = 1.1\text{--}1.3$ fm and $a = 0.50\text{--}0.65$, on the ANC and spectroscopic factor values. We found that its ANC varies by less than 4% around its mean value, while its spectroscopic factor differs by more than 25%, demonstrating that only the asymptotic part of the wave function contributes in the DWBA calculations and the reaction is peripheral at 12 MeV/nucleon beam energy. The ANC of the ground state of ^{13}C , $C_{p_{1/2}}^2 = 2.31 \pm 0.08 \text{ fm}^{-1}$, has been found in Ref. [23]. This value is needed in Eq. (1) to extract the ANCs for the ground state and excited states in ^{18}O . The main uncertainties in the values of the ANCs for $^{17}\text{O} + n \rightarrow ^{18}\text{O}$ are due to the (3%) in the $C_{p_{1/2}}^2(^{13}\text{C})$, (7.5%) in the thickness of the target, almost (3%) statistical errors, and (4%) due to Gaussian fit for nearby states. The uncertainties in the selection of the optical potential sets for each reaction channel, and the WS geometry of the neutron binding potential used in the DWBA calculation, are not the same for all configurations, but their average values are (2.5%) and (3.5%), respectively. The total uncertainty is around 10%.

The ANCs for the 2_1^+ state were obtained by normalizing the calculated DWBA angular distributions for (dd) and (ds) configurations simultaneously to the data. Ratio of the spectroscopic factors for these $\ell = 0$ to $\ell = 2$ in the (2_1^+) state is 0.21 ± 0.03 , which agrees with the measured ratio 0.22 ± 0.05 reported in Refs. [16,24]. Weighing the calculations by χ^2 gives $C_{d_{5/2}}^2(2_1^+) = 2.10 \pm 0.23 \text{ fm}^{-1}$ and $C_{s_{1/2}}^2(2_1^+) = 5.77 \pm 0.63 \text{ fm}^{-1}$. In contrast, the ANCs for 2_2^+ were obtained by fixing the ratio between the spectroscopic factors for the (dd) and (ds) components to the measured value 0.53 ± 0.08 from Ref. [16]. Then, the normalizing procedure, using Eq. (1), was performed with one degree of freedom that is related to the (dd) configuration. This procedure added 2% and 11% to the (dd) and (ds) uncertainties, respectively. The extracted ANCs are $C_{d_{5/2}}^2(2_2^+) = 0.45 \pm 0.06 \text{ fm}^{-1}$ and $C_{s_{1/2}}^2(2_2^+) = 4.11 \pm 0.62 \text{ fm}^{-1}$. For the 0_1^+ and 4_1^+ states we found that their (dd) spectroscopic factors are 1.50 ± 0.13 and 1.31 ± 0.14 , while the measured values reported in Ref. [16] are 1.22 ± 0.31 and 1.57 ± 0.39 , respectively. The ANCs for the 0_1^+ state is $C_{d_{5/2}}^2(0_1^+) = 8.18 \pm 0.76 \text{ fm}^{-1}$ and for the 4_1^+ is $C_{d_{5/2}}^2(4_1^+) = 1.31 \pm 0.16 \text{ fm}^{-1}$.

IV. THE $^{17}\text{F}(p,\gamma)^{18}\text{Ne}$ REACTION RATE

The ANCs of the bound states in ^{18}Ne are determined from those of their corresponding states in the mirror nucleus ^{18}O using the equality of the spectroscopic factors, which leads to the relation $C_{nlj}^2(^{18}\text{Ne}) = [b_{nlj}^2(^{18}\text{Ne})/b_{nlj}^2(^{18}\text{O})]C_{nlj}^2(^{18}\text{O})$. The single-particle ANC, b , in ^{18}Ne was calculated for a proton bound in a WS potential with the same geometry, $r_0 = 1.25$ fm and $a = 0.65$ fm, and the same spin-orbit interaction that were used for a neutron bound in ^{18}O . Only the depth of the central potential was adjusted to reproduce the experimental proton separation energy for each state in ^{18}Ne . The values obtained by this procedure for the depth of the nuclear potential are similar to those of the nuclear potentials found for ^{18}O . This is a very good confirmation of the charge symmetry assumption

TABLE II. The single-particle orbitals and the ANCs of the low-lying levels in ^{18}O and ^{18}Ne .

J^π	Orbital	$C_{\ell j}^2(^{18}\text{O}) \text{ (fm}^{-1}\text{)}$	$C_{\ell j}^2(^{18}\text{Ne}) \text{ (fm}^{-1}\text{)}$
0_1^+	$1d_{5/2}$	8.18 ± 0.76	12.2 ± 1.2
2_1^+	$1d_{5/2}$	2.10 ± 0.23	2.85 ± 0.32
	$2s_{1/2}$	5.77 ± 0.63	14.9 ± 2.1
4_1^+	$1d_{5/2}$	1.31 ± 0.16	2.73 ± 0.35
2_2^+	$1d_{5/2}$	0.45 ± 0.06	2.46 ± 0.33
	$2s_{1/2}$	4.11 ± 0.62	117 ± 20

made here. The ANCs obtained for the four bound states in ^{18}Ne are listed in Table II. However, using a three-body model, a symmetry breaking in mirror ANCs for ^{18}O and ^{18}Ne is estimated [25]. While this breaking is about 3% for all (dd) configurations, it can be inaccurate up to 12% for the (ds) configurations of the $2_{1,2}^+$ states. Since this variation is very large in comparison with any other calculations on mirror states, the adopted uncertainty for (ds) case is 9%. This mismatch contributes less than the uncertainties of the extracted ANCs in ^{18}Ne but it has been included.

Finally, using these nuclear structure data—the ANCs in Table II—the contributions to the astrophysical S factor for the $^{17}\text{F}(p, \gamma)^{18}\text{Ne}$ direct capture to each bound state were calculated using R -matrix approach. The proton binding WS potential was fixed using $r_0 = 1.25$ fm and $a = 0.65$ fm. Only the $E1$ electromagnetic transitions and p and f waves are considered when calculating the direct capture contributions. The S factors as a function of the center-of-mass energy for the $J^\pi = 0_1^+, 2_1^+, 4_1^+$, and 2_2^+ states of ^{18}Ne are plotted in Fig. 6, where $S(E)$ for the 2_1^+ and 2_2^+ states is the sum of their (dd) and (ds) components. It should be noted that the $(1d_{5/2}2s_{1/2})_{2^+}$ component contributes most in the proton capture. This is easy to understand due to the lack of a centrifugal barrier for the $2s_{1/2}$ orbital in the final state which extends further from the core into the asymptotic region where the proton capture happens. The figure shows that the transitions to

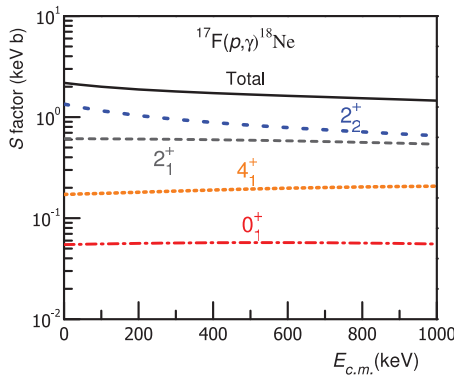


FIG. 6. (Color online) The S -factor components of the $^{17}\text{F}(p, \gamma)^{18}\text{Ne}$ reaction. $S(0)$ of the $J^\pi = 2_2^+$ state (large dotted line) makes the major contribution and is almost 50% larger than the 2_1^+ contribution (dashed line). The other components due to $J^\pi = 4_1^+$ (small dotted line) and $J^\pi = 0_1^+$ (dash-dotted line) are one order of magnitude smaller than the major one.

$J^\pi = 2_{1,2}^+$ dominate the direct capture reaction rate over the other contributions, and the $J^\pi = 2_2^+$ state makes the larger contribution at all energies. The estimated S factors at zero energy for the $0_1^+, 2_1^+, 4_1^+$ and 2_2^+ are, respectively, 0.06 ± 0.01 , 0.61 ± 0.11 , 0.17 ± 0.03 , and 1.34 ± 0.24 keV b. The variations in the S values are calculated using the ANCs' uncertainties given in Table II and the dependence of the R -matrix approach on the channel radius. The total S factor (in keV b) as a function of E (in keV) is well fit by

$$S_{1-17}(0) = 2.17 - 1.76 \times 10^{-3} E + 1.98 \times 10^{-6} E^2 - 9.4 \times 10^{-10} E^3. \quad (2)$$

The value of the total S factor at zero energy is $S_{1-17}(0) = 2.17 \pm 0.37$ keV b, which is 25% lower than $S(0) = 2.9 \pm 0.4$ keV b computed by García *et al.* [7]. However, there are significant differences when we compare our results with model-dependent calculations by Dufour and Descouvemont [26] and Chatterjee *et al.* [27]. Dufour used a microscopic two-cluster, two-channel generator coordinate method (GCM) with Volkov nuclear NN potential. Despite the attempt to correct the Gaussian behavior of the generator function at large intercluster distances, the usage of the Volkov potential overestimates the calculated ANCs, see Table 4 of Ref. [26], compared to our experimental ones, and sometimes quite significantly. It reflects the well-known fact that microscopically calculated ANCs are very sensitive to the choice of the NN potential, and the Volkov potential is not the best choice. Therefore, the calculated S factor due to $E1$ transition is $S(0) = 3.5$ keV b, 60% higher than ours. The other approach by Chatterjee slightly differs. The calculated ANCs in the framework of the shell model embedded in the continuum are comparable to our ANCs, except for the (ds) configuration of the 2_2^+ state which is almost two times larger. However, their $S(0)$ due to $E1$ transition is about 0.65 keV b, almost 3 times smaller than our estimate. Although Chatterjee increased the reaction rate by giving more contributions to $M1$ transition over $E1$ [27], his total S factor is still small. As a double check, we recalculated the S factor at low energies using the RADCAP code [28] and the results obtained by the R -matrix calculations were successfully reproduced.

Using the central energy of the Gamow peak for $p + ^{17}\text{F}$, $E_o = 0.52T_9^{2/3}$ MeV, and $\tau = \frac{18.03}{T_9^{1/3}}$, the effective S factor in terms of T_9 is given by

$$S_{\text{eff}}(T_9) = 2.17 \left[1 + 0.023 T_9^{1/3} - 4.20 \times 10^{-4} T_9^{2/3} - 6.80 \times 10^{-5} T_9 + 2.45 \times 10^{-7} T_9^{4/3} + 1.01 \times 10^{-7} T_9^{5/3} \right], \quad (3)$$

TABLE III. The parameters used to calculate the resonance reaction rate.

$E_{c.m.} \text{ (keV)}$	J^π	$\Gamma_\gamma \text{ (meV)}$	$\omega\gamma \text{ (meV)}$	Ref.
597 ± 5	1_1^-	15(3)	3.8(8)	[7]
599.8 ± 2	3_1^+	56(38)	33(22)	[10,12]
665 ± 5	0_3^+	1.0(2)	0.08(2)	[7]

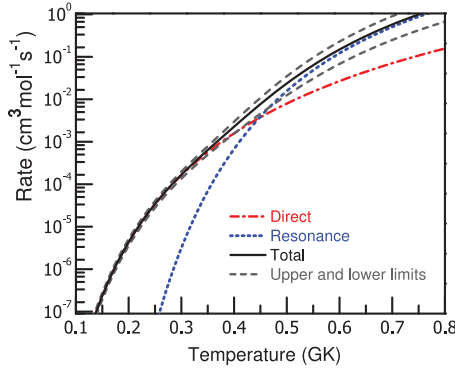


FIG. 7. (Color online) The direct (dash-dots) and resonant (dots) capture-rate contributions to the $^{17}\text{F}(p,\gamma)^{18}\text{Ne}$ reaction. The direct capture strongly dominates the rate for temperatures in ONe novae; $T_9 < 0.5$. The upper and lower limits of the total rate are indicated by dashed lines.

where $S_{\text{eff}}(T_9)$ is in keV b. With this equation, the estimated direct capture reaction rate for $^{17}\text{F}(p,\gamma)^{18}\text{Ne}$ is

$$N_A \langle \sigma v \rangle = 51 \tau^2 S_{\text{eff}}(T_9) e^{-\tau} \left[\frac{\text{cm}^3}{\text{mole s}} \right], \quad (4)$$

where N_A is Avogadro's number and $\langle \sigma v \rangle$ is the reaction rate per particle. The total direct capture rate has been estimated. The uncertainty in the reaction rate is dominated by the 17% overall uncertainty of the extracted ANCs. Thus, we evaluated the direct capture reaction rate of $^{17}\text{F}(p,\gamma)^{18}\text{Ne}$ through the measurement of the ANCs in the mirror nuclear system. In units of $\text{cm}^3 \text{mole}^{-1} \text{s}^{-1}$, the indirect capture through the resonance states given in Table III was calculated using

$$N_A \langle \sigma v \rangle_r = \frac{1.540 \times 10^{11}}{(\mu T_9)^{3/2}} \sum_i \omega \gamma_i e^{-11.605 E_{R_i} / T_9}, \quad (5)$$

where μ is the reduced mass in amu, E_{R_i} are the center-of-mass energies, and the $\omega \gamma_i$ are the strengths of the resonances in MeV. A comparison between the two rates is illustrated in Fig. 7. The present results show that the thermonuclear reaction rate is dominated by the direct capture component by one to four orders of magnitude over the resonant contribution for the relevant temperature range $T_9 = 0.2$ – 0.4 in ONe novae.

TABLE IV. The direct, resonant and total reaction rates in $\text{cm}^3 \text{mole}^{-1} \text{s}^{-1}$ for $^{17}\text{F}(p,\gamma)^{18}\text{Ne}$. The upper and lower limits were calculated including the measured uncertainties.

T_9	Direct	Resonance	Total	Upper	Lower
0.1	2.28×10^{-9}	1.19×10^{-25}	2.28×10^{-9}	2.64×10^{-9}	1.91×10^{-9}
0.2	4.35×10^{-6}	5.35×10^{-11}	4.35×10^{-6}	5.04×10^{-6}	3.65×10^{-6}
0.3	1.64×10^{-4}	3.16×10^{-6}	1.67×10^{-4}	1.95×10^{-4}	1.39×10^{-4}
0.4	1.59×10^{-3}	6.77×10^{-4}	2.27×10^{-3}	2.94×10^{-3}	1.59×10^{-3}
0.5	7.92×10^{-3}	1.57×10^{-2}	2.36×10^{-2}	3.47×10^{-2}	1.26×10^{-2}
0.6	2.68×10^{-2}	1.21×10^{-1}	1.48×10^{-1}	2.28×10^{-1}	6.84×10^{-2}
0.7	7.06×10^{-2}	5.05×10^{-1}	5.76×10^{-1}	9.02×10^{-1}	2.50×10^{-1}
0.8	1.57×10^{-1}	1.43×10^0	1.59×10^0	2.51×10^0	6.73×10^{-1}
0.9	3.06×10^{-1}	3.16×10^0	3.46×10^0	5.48×10^0	1.45×10^0
1.0	5.44×10^{-1}	5.84×10^0	6.39×10^0	1.01×10^1	2.66×10^0

Our direct reaction rate is, on average, 17% lower than García's [7] calculations for temperatures less than $T_9 = 0.4$. The $\pm 17\%$ uncertainty covers the central values of the previous calculations, but it is more important because it is evaluated from measured values that provides a significant reduction in the uncertainty of the rate. In Table IV, we present the contributions from both resonant and nonresonant terms to the total reaction rate. The upper and lower limits are calculated depending on the variations extracted from measurements and their sequences are shown in Fig. 7. The resultant total rate is almost 15% lower than recent estimates by Chippis [12].

No new nucleosynthesis calculations were made here, but we can use the analysis that Parete-Koon *et al.* [29] made of the astrophysical consequences of four different rates available at the time, analysis spurned by the then recent identification of the 3_1^+ state in ^{18}Ne , the resonance considered to give the largest contribution to the resonant capture. The present new rate for the $^{17}\text{F}(p,\gamma)^{18}\text{Ne}$ reaction is slow and is very close to the ORNL rate in the direct part and identical in the resonant part. This implies that the analysis made there for the ORNL rate should hold [12]. In comparison with Bardayan [10] and Chippis [12], our rate predicts higher abundances of ^{17}O and ^{17}F in the hottest zones of $1.25 M_\odot$ and $1.35 M_\odot$ novae.

Although the overall uncertainty of $^{17}\text{F}(p,\gamma)^{18}\text{Ne}$ is of the order of 50%, but it is still the most important reaction to consider for its influence on the production of ^{18}F . Measuring the strength of the 665-keV resonance from $^{18}\text{F}(p,\gamma)^{19}\text{Ne}$ shows that it has almost no role in the destruction of ^{18}F within the relevant temperature regime associated with ONe novae [30]. Direct measurement of the $^{17}\text{O}(p,\gamma)^{18}\text{F}$ at Gamow energies using the two narrow resonances 66 and 183 keV gives a reduction in the synthesis of ^{18}O and ^{18}F by 10% [31].

V. CONCLUSIONS

In conclusion, we have measured the neutron transfer reaction $^{13}\text{C}(^{17}\text{O},^{18}\text{O})^{12}\text{C}$ and the elastic scattering for $^{17}\text{O} + ^{13}\text{C}$ and $^{18}\text{O} + ^{12}\text{C}$. The OMPs (of the WS shape) were obtained to be used in DWBA analysis, as precise description of the input and exit channels of the transfer reaction. The

peripherality of the reaction mechanism was studied using a semiclassical method and from proving that the ANC's are independent of the geometries of the neutron-binding potential. The ANC's of the bound states of ^{18}O were extracted and transposed to their mirror states in ^{18}Ne to determine the S factor for the $^{17}\text{F}(p, \gamma)^{18}\text{Ne}$ reaction. We found that its reaction rate is dominated by direct capture to the 2_1^+ and 2_2^+ states in ^{18}Ne . As far as we know, this is the first time the direct capture reaction using measured ANC's has been evaluated. Our rate is slow and implies more production of ^{18}F in 1.25 M_\odot novae. Direct measurements, if possible using (probably) ^{17}F radioactive nuclear beams in inverse kinematics, may clarify the importance of direct capture for

the rate of the $^{17}\text{F}(p, \gamma)^{18}\text{Ne}$ reaction rate in novae. Indirect methods measurements like the Coulomb or nuclear breakup of ^{18}Ne may give some useful information for its ground state (ANC) and be compared with the one extracted here using its ^{18}O mirror.

ACKNOWLEDGMENTS

This work was supported in part by the U.S. Department of Energy under Grant No. DE-FG02-93ER40773 and DE-FG52-06NA26207, NSF under Grant No. PHY-0852653, the Robert A. Welch Foundation under Grant No. A-1082, and by CNCSIS (Romania) Grant No. PN-II-PCE-55/2011.

-
- [1] J. Gómez-Gomar, M. Hernanz, J. José, and J. Isern, *Mon. Not. R. Astron. Soc.* **296**, 913 (1998).
 - [2] M. J. Harris, J. E. Naya, B. J. Teegarden, T. L. Cline, N. Gehrels, D. M. Palmer, R. Ramaty, and H. Seifert, *Astrophys. J.* **522**, 424 (1999).
 - [3] J. José, M. Hernanz, and C. Iliadis, *Nucl. Phys. A* **777**, 550 (2006).
 - [4] A. Coc, M. Hernanz, J. José, and J. Thibaud, *Astron. Astrophys.* **357**, 561 (2000).
 - [5] R. K. Wallace and S. E. Woosley, *Astrophys. J. Suppl. Ser.* **45**, 389 (1981).
 - [6] R. Sherr and H. T. Fortune, *Phys. Rev. C* **58**, 3292 (1998).
 - [7] A. García, E. G. Adelberger, P. V. Magnus, D. M. Markoff, K. B. Swartz, M. S. Smith, K. I. Hahn, N. Bateman, and P. D. Parker, *Phys. Rev. C* **43**, 2012 (1991).
 - [8] K. I. Hahn, A. García, E. G. Adelberger, P. V. Magnus, A. D. Bacher, N. Bateman, G. P. A. Berg, J. C. Blackmon, A. E. Champagne, B. Davis *et al.*, *Phys. Rev. C* **54**, 1999 (1996).
 - [9] M. Wiescher, J. Görres, and F.-K. Thielemann, *Astrophys. J.* **326**, 384 (1988).
 - [10] D. W. Bardayan, J. C. Blackmon, C. R. Brune, A. E. Champagne, A. A. Chen, J. M. Cox, T. Davinson, V. Y. Hansper, M. A. Hofstee, B. A. Johnson *et al.*, *Phys. Rev. Lett.* **83**, 45 (1999).
 - [11] Y. Parpottas, S. M. Grimes, S. Al-Quraishi, C. R. Brune, T. N. Massey, J. E. O'Donnell, J. E. Oldendick, A. Salas, and R. T. Wheeler, *Phys. Rev. C* **72**, 025802 (2005).
 - [12] K. A. Chipps, D. W. Bardayan, J. C. Blackmon, K. Y. Chae, U. Greife, R. Hatarik, R. L. Kozub, C. Matei, B. H. Moazen, C. D. Nesaraja *et al.*, *Phys. Rev. Lett.* **102**, 152502 (2009).
 - [13] H. M. Xu, C. A. Gagliardi, R. E. Tribble, A. M. Mukhamedzhanov, and N. K. Timofeyuk, *Phys. Rev. Lett.* **73**, 2027 (1994).
 - [14] L. Trache, A. Azhari, F. Carstoiu, H. L. Clark, C. A. Gagliardi, Y.-W. Lui, A. M. Mukhamedzhanov, X. Tang, N. Timofeyuk, and R. E. Tribble, *Phys. Rev. C* **67**, 062801(R) (2003).
 - [15] N. K. Timofeyuk, R. C. Johnson, and A. M. Mukhamedzhanov, *Phys. Rev. Lett.* **91**, 232501 (2003).
 - [16] T. K. Li, D. Dehnhard, R. E. Brown, and P. J. Ellis, *Phys. Rev. C* **13**, 55 (1976).
 - [17] D. M. Pringle, W. N. Catford, J. S. Winfield, D. G. Lewis, N. A. Jelley, K. W. Allen, and J. H. Coupland, *Nucl. Instrum. Methods A* **245**, 230 (1986).
 - [18] J. S. Winfield, D. M. Pringle, W. N. Catford, D. G. Lewis, N. A. Jelley, and K. W. Allen, *Nucl. Instrum. Methods A* **251**, 297 (1986).
 - [19] S. Kowalski and H. A. Enge, computer code raytrace (unpublished), University of Oxford, England, UK, 1986.
 - [20] A. M. Mukhamedzhanov, V. Burjan, F. Carstoiu, J. Cepjek, H. L. Clark, C. A. Gagliardi, Y.-W. Lui, V. Kroha, L. Trache, R. E. Tribble *et al.*, *Phys. Rev. C* **56**, 1302 (1997).
 - [21] F. Carstoiu, L. Trache, R. E. Tribble, and C. A. Gagliardi, *Phys. Rev. C* **70**, 054610 (2004).
 - [22] D. M. Brink and N. Takigawa, *Nucl. Phys. A* **279**, 159 (1977).
 - [23] T. Al-Abdullah, F. Carstoiu, X. Chen, H. L. Clark, C. Fu, C. A. Gagliardi, Y.-W. Lui, A. Mukhamedzhanov, G. Tabacaru, Y. Tokimoto *et al.*, *Phys. Rev. C* **81**, 035802 (2010).
 - [24] R. L. Lawson, F. J. D. Serduke, and H. T. Fortune, *Phys. Rev. C* **14**, 1245 (1976).
 - [25] N. K. Timofeyuk and I. J. Thompson, *Phys. Rev. C* **78**, 054322 (2008).
 - [26] M. Dufour and P. Descouvemont, *Nucl. Phys. A* **730**, 316 (2004).
 - [27] R. Chatterjee, J. Okołowicz, and M. Płoszajczak, *Nucl. Phys. A* **764**, 528 (2006).
 - [28] C. A. Bertulani, *Comput. Phys. Commun.* **156**, 123 (2003).
 - [29] S. Parete-Koon, W. R. Hix, M. S. Smith, S. Starrfield, D. W. Bardayan, M. W. Guidry, and A. Mezzacappa, *Astrophys. J.* **598**, 1239 (2003).
 - [30] C. Akers, A. M. Laird, B. R. Fulton, C. Ruiz, D. W. Bardayan, L. Buchmann, G. Christian, B. Davids, L. Erikson, J. Fallis *et al.*, *Phys. Rev. Lett.* **110**, 262502 (2013).
 - [31] D. A. Scott, A. Cacioli, A. D. Leva, A. Formicola, M. Aliotta, M. Anders, D. Bemmerer, C. Broggini, M. Campeggio, P. Corvisiero *et al.*, *Phys. Rev. Lett.* **109**, 202501 (2012).

Peripheral elastic and inelastic scattering of $^{17,18}\text{O}$ on light targets at 12 MeV/nucleonT. Al-Abdullah,^{1,2} F. Carstoiu,^{3,*} C. A. Gagliardi,¹ G. Tabacaru,¹ L. Trache,^{1,3} and R. E. Tribble¹¹Cyclotron Institute, Texas A&M University, College Station, Texas 77843, USA²Physics Department, The Hashemite University, Zarqa, Jordan³National Institute for Physics and Nuclear Engineering Horia Hulubei, Bucharest, Romania

(Received 7 April 2014; revised manuscript received 12 May 2014; published 5 June 2014)

A study of interaction of neutron-rich oxygen isotopes $^{17,18}\text{O}$ with light targets has been undertaken in order to determine the optical potentials needed for the transfer reaction $^{13}\text{C}(^{17,18}\text{O},^{12}\text{C})$. Optical potentials in both incoming and outgoing channels have been determined in a single experiment. This transfer reaction was used to infer the direct capture rate to the $^{17}\text{F}(p,\gamma)^{18}\text{Ne}$ which is essential to estimate the production of ^{18}F at stellar energies in ONe novae. The success of the asymptotic normalization coefficient (ANC) as indirect method for astrophysics is guaranteed if the reaction mechanism is peripheral and the distorted wave Born approximation cross-section calculations are warranted and stable against the optical model potential (OMP) used. We demonstrate the stability of the ANC method and the OMP results by using good-quality elastic and inelastic-scattering data with stable beams before extending the procedures to rare-ion beams. The peripherality of our reaction is inferred from a semiclassical decomposition of the total-scattering amplitude into barrier and internal barrier components. Comparison between elastic scattering of ^{17}O , ^{18}O , and ^{16}O projectiles is made.

DOI: [10.1103/PhysRevC.89.064602](https://doi.org/10.1103/PhysRevC.89.064602)

PACS number(s): 25.70.Bc, 25.70.Hi, 24.10.Ht

I. INTRODUCTION

The $^{17}\text{F}(p,\gamma)^{18}\text{Ne}$ reaction is important for understanding nucleosynthesis in novae and plays a role in determining if radioactive nuclei with characteristic γ -ray signatures are produced in sufficient yield to be observed by γ -ray satellites. The reaction rate is expected to be dominated by the direct-capture cross section at nova temperatures and influences the abundances of ^{15}O , ^{17}F , ^{18}F , and ^{18}Ne [1]. The rate also determines the $^{17}\text{O}/^{18}\text{O}$ ratio that is produced and explains the transition sequence from the HCNO cycle to the rp process [2].

The importance of direct capture to the bound states in ^{18}Ne has been recently estimated by our team [3]. Because of the difficulties of obtaining information from experiments with radioactive beams, the asymptotic normalization coefficients (ANCs) as an alternative technique to determine this direct-capture reaction rate has been used. The spectroscopic factors for the major components of the lowest-lying states in mirror nuclei are the same, so the ANC method can be applied to the mirror nucleus ^{18}O and can be used to extract the ANCs for the ground state and the $E_x(2_1^+) = 1.982$ MeV and $E_x(2_2^+) = 3.920$ MeV states and convert them to their corresponding states in ^{18}Ne . The primary goal of the experiment was the measurement of the peripheral neutron transfer reaction $^{13}\text{C}(^{17,18}\text{O},^{12}\text{C})$. Optical potentials in the incoming and outgoing channels have been obtained by measuring elastic-scattering angular distributions $^{17}\text{O} + ^{13}\text{C}$ and $^{18}\text{O} + ^{12}\text{C}$ at 12 MeV/nucleon incident energy. The quality of the obtained potentials has been also checked from inelastic scattering to selected states in $^{17}\text{O}^*$ and $^{18}\text{O}^*$. Since

the ANC method assumes the peripherality of the reaction mechanism, we discuss here rather extensively this issue by decomposing semiclassically the total scattering amplitude into barrier and internal barrier subcomponents. We show that the internal barrier subcomponent, which corresponds to the flux penetrating the barrier, gives a negligibly small contribution to the total cross section, and thus the reaction is peripheral. The elastic scattering $^{17}\text{O} + ^{13}\text{C}$ includes a weakly bound target. A difficulty in obtaining the optical-model (OM) parameters in this type of reactions may arise due to the competition between the increased refractive power of the real potential and increased absorption at the nuclear surface. The well-known existence of many ambiguities in the optical-model parameters extracted from elastic scattering can raise questions about the reliability and accuracy of these determinations.

Previously, $^{18}\text{O} + ^{12}\text{C}$ elastic scattering at barrier energies was measured by Robertson *et al.* [4], by Szilner *et al.* [5], and by Rudchik *et al.* [6] at some 5–7 MeV/nucleon. Fresnel scattering of ^{18}O on ^{28}Si was measured by Mermaz *et al.* [7] at 56 MeV. For the $^{17}\text{O} + ^{13}\text{C}$ reaction, the data are rather scarce: we identified a single fusion study and poor elastic angular distributions at barrier energies [8]. The main conclusion of these studies was that the interaction of $^{17,18}\text{O}$ nuclei with light targets is slightly more absorptive compared with that of the closed-shell nucleus ^{16}O and that no significant effects due to the neutron excess were identified.

In Sec. II we give a short description of the experiment. Elastic scattering data and the derivation of the OM potentials are discussed in Sec. III. The semiclassical Wenzel–Kramers–Brillouin (WKB) method is used in Sec. IV to decompose the total-scattering amplitude into barrier and internal barrier components. Inelastic angular distributions to selected states in $^{18}\text{O}^*$ and $^{17}\text{O}^*$ are discussed in Sec. V. Our conclusions are summarized in Sec. VI.

*carstoiu@theory.nipne.ro

II. EXPERIMENT

The primary goal of the experiment was the measurement of the transfer reaction $^{13}\text{C}(^{17}\text{O}, ^{18}\text{O})^{12}\text{C}$ at 12 MeV/nucleon. In addition, elastic scattering in both incoming and outgoing channels as well as inelastic scattering to selected states in ^{17}O and ^{18}O were measured.

The experiment was carried out with two separate ^{17}O and ^{18}O beams from the K500 superconducting cyclotron at Texas A&M University. Each beam was transported through the beam-analysis system to the scattering chamber of the multipole-dipole-multipole (MDM) magnetic spectrometer [9], where it interacted with $100\ \mu\text{g}/\text{cm}^2$ self-supporting targets.

First, the ^{17}O beam impinged on the ^{13}C target enriched up to 99%. We continuously monitored the excitation of the 4.44 MeV state in ^{12}C in order to estimate the carbon deposition during the exposure and found a negligibly small contribution. The elastic-scattering angular distribution was measured for the spectrometer angles 4° – 25° in the laboratory system. Fine tuned RAYTRACE [10] calculations were used to reconstruct the position of particles in the focal plane and the scattering angle at the target. A $4^\circ \times 1^\circ$ wide-opening mask and an angle mask consisting of five narrow ($\Delta\theta = 0.1^\circ$) slits were used for each spectrometer angle to double-check the absolute values of the cross section and the quality of the angle calibration. The instrumental setup, including the focal-plane detector and processes for energy and angle calibrations, is identical to that described in Ref. [11]. Second, the ^{12}C target was bombarded by the ^{18}O beam with 216 MeV total

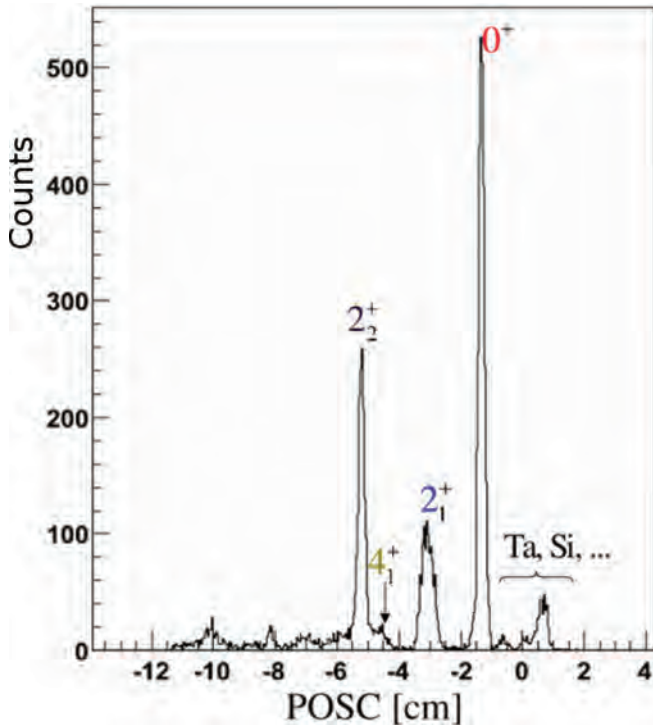


FIG. 1. (Color online) Low-lying spectrum of ^{18}O versus particle position in the focal plane, measured at the spectrometer angle of 4° . The peaks at the right of the elastic peak are due to Si and Ta contaminants in the target.

laboratory energy. The elastic-scattering cross section was measured at 4° – 22° spectrometer angles.

The angular resolution $\Delta\theta_{\text{res}}$ of the detector in both cases was on average 0.31° in the c.m. frame and the position resolution was better than 1 mm. The low-lying spectrum of ^{18}O as a function of the position in the focal plane is shown in Fig. 1. The spectrum is taken at the spectrometer angle of 4° . The peaks corresponding to elastic scattering and to inelastic transitions to the 2_1^+ and 2_2^+ excited states were observed with sufficient statistics over the whole angular range to obtain good angular distributions. Small amounts of heavy impurities in the target, most likely Ta and Si, dominate the spectrum at small angles (below $\theta_{\text{lab}} = 3^\circ$). The absolute values of the cross section were determined by a careful integration of beam charge in a Faraday cup and the measurement of target thickness from the energy loss was done by using alpha particles from sources and the beam. The overall normalization of data was also extensively checked by comparing the data at the most forward angles with the optical-model calculation. At these angles the cross section is less sensitive to the nuclear potential. The main uncertainties in the data are due to 7.5% in the target thickness and 3% statistical errors. The average normalization error was less than 3%.

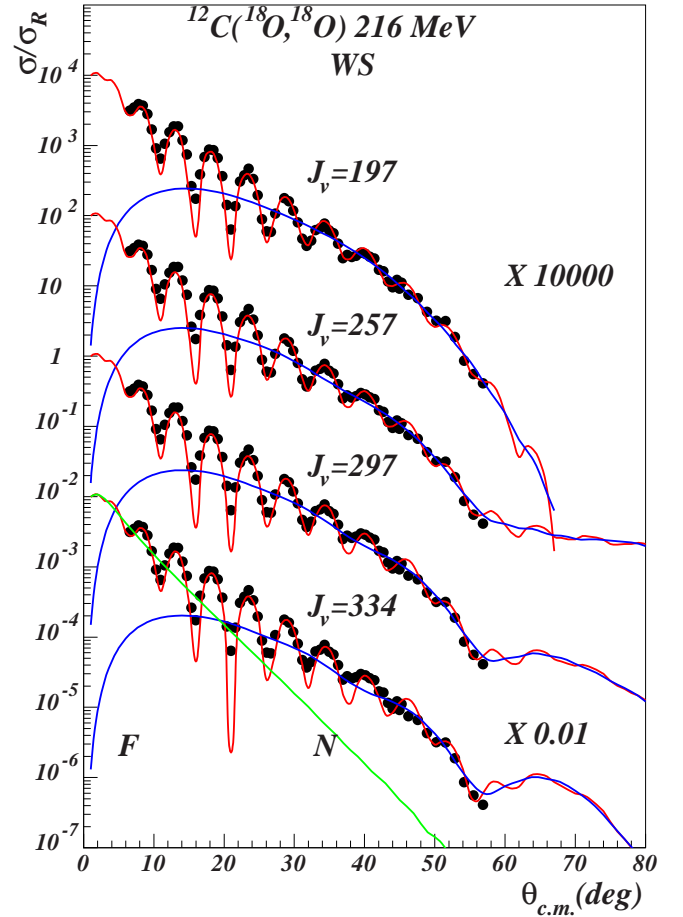


FIG. 2. (Color online) Cross section and far-side or near-side (F or N) decomposition of the scattering amplitude for WS potentials in Table I. Each calculation is identified by its real volume integral J_v and shifted by factors X to increase the visibility.

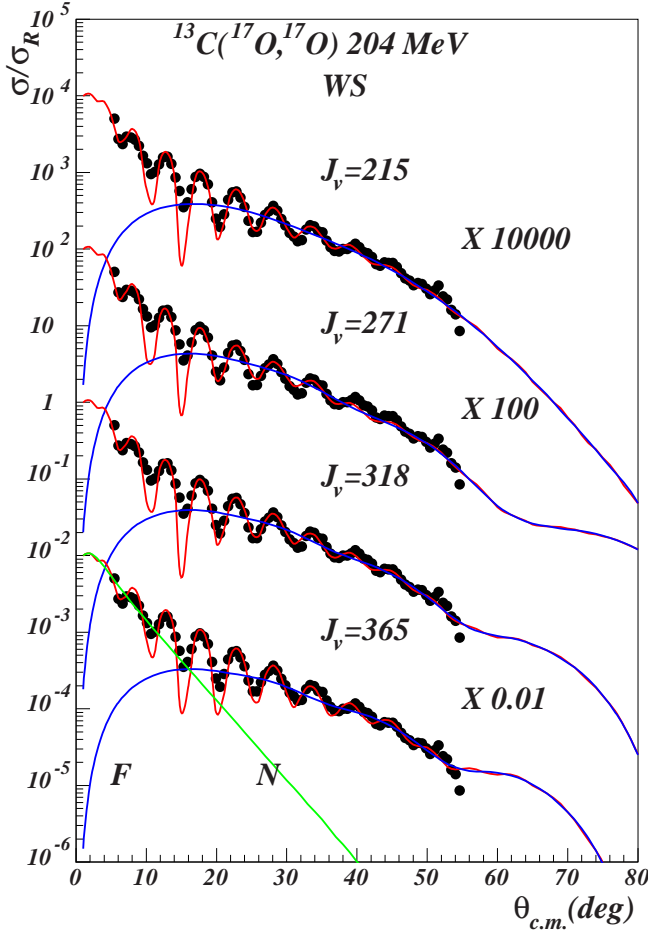


FIG. 3. (Color online) Cross sections and F or N decomposition for the WS potentials of Table I. The far-side component shows an Airy oscillation which moves to forward angles with increased real volume integral.

III. ELASTIC SCATTERING

A. Woods–Saxon form factors

The measured elastic-scattering data at $E_{\text{lab}} = 216$ and 204 MeV are shown in Figs. 2 and 3. The data are first analyzed

TABLE I. Discrete solutions obtained with WS form factors for $^{18}\text{O} + ^{12}\text{C}$ at 216 MeV and $^{17}\text{O} + ^{13}\text{C}$ at 204 MeV. The line labeled PP9 is a WS phase equivalent of the JLM1 solution.

Pot.	V MeV	W MeV	r_V fm	r_W fm	a_V fm	a_W fm	χ^2	σ_R mb	J_V MeV fm ³	R_V fm	J_W MeV fm ³	R_W fm
$^{18}\text{O} + ^{12}\text{C}$ at 216 MeV												
PP5	89.18	25.24	0.88	1.16	0.88	0.68	5.12	1712	197	4.69	103	5.09
PP6	195.40	25.59	0.68	1.16	0.96	0.67	6.39	1702	257	4.40	104	5.07
PP7	295.82	26.00	0.60	1.16	0.95	0.67	7.54	1696	297	4.20	106	5.06
PP8	374.41	26.19	0.58	1.16	0.90	0.68	9.78	1695	334	4.01	107	5.06
PP9	75.68	26.16	0.89	1.15	0.93	0.66	5.31	1677	178	4.85	104	5.02
$^{17}\text{O} + ^{13}\text{C}$ at 204 MeV												
T1	94.69	26.91	0.91	1.13	0.84	0.67	4.47	1659	215	4.67	99	4.96
T2	188.40	24.95	0.72	1.12	0.94	0.69	4.62	1667	271	4.44	92	4.99
T3	248.75	26.36	0.69	1.13	0.90	0.66	4.53	1659	318	4.27	99	4.97
T4	275.49	25.63	0.73	1.15	0.81	0.65	5.90	1660	365	4.11	100	5.00

by using optical potentials with conventional Woods–Saxon (WS) form factors for the nuclear term, supplemented with a Coulomb potential generated by a uniform charge distribution with a reduced radius fixed to $r_c = 1$ fm. No preference has been found for volume or surface-localized absorption and throughout the paper only volume absorption is considered. In the absence of any spin-dependent observables, spin-orbit or tensor interactions have been ignored. Ground-state reorientation couplings have been neglected also. The potential is defined by six parameters specifying the depth and geometry of the real and imaginary terms, with the standard notations; the same as used in Ref. [13]. The number N of data points is quite large and, consequently, the usual goodness of fit criteria (χ^2) normalized to N has been used.

Using the strength of the real component of the optical potential as a control parameter, a grid search procedure revealed a number of discrete solutions. Their parameters are presented in Table I. All of the potentials give relatively small χ^2 , but only those with the smallest values for entrance and exit channels, potential T1 and PP5, respectively, were adopted in the distorted wave Born approximation (DWBA) calculations of the neutron transfer reaction [3], while the others were used to determine the uncertainty in the choice of the OMP in either channel. The ambiguity in the optical potential has two main sources: the limited range of the measured angles and the strong absorption. When the strong absorption dominates the reaction mechanism, then the interaction is sensitive only to the surface and several phase-equivalent optical potentials will appear. The patterns shown in Figs. 2 and 3 show rapid oscillation at forward angles followed by a smooth falloff at intermediate angles. Assuming pure Fraunhofer scattering at forward angles, we extract a grazing angular momentum $\ell_g \approx 36$ from the angular spacing $\Delta\theta = \pi/(\ell_g + 1/2)$. The corresponding grazing distance is quite large, $R_g \approx 7$ fm, much larger than the distance of touching configuration. We systematically find diffuse real potentials ($a_V \approx 0.9$ fm). This effect may be tentatively attributable to the neutron excess. We find also quite constant volume integrals and rms radii for the imaginary component. As a consequence the total reaction cross section seems to be a well-defined observable. Weighted average values from Tables I and II are $\sigma_R = 1713 \pm 35$ mb

TABLE II. Unique solutions obtained with folding form factors for $^{18}\text{O} + ^{12}\text{C}$ at 216 MeV and $^{17}\text{O} + ^{13}\text{C}$ at 204 MeV.

Pot.	N_V	N_W	t_V	t_W	χ^2	σ_R mb	J_V MeV fm ³	R_V fm	J_W MeV fm ³	R_W fm
$^{18}\text{O} + ^{12}\text{C}$ at 216 MeV										
M3YZR	0.37	0.20	0.88	0.80	10.72	1812	163	4.60	86	5.06
M3YFR	0.33	0.21	0.88	0.86	8.15	1737	164	4.68	103	4.83
GOGNY1	0.28	0.18	0.89	0.87	7.27	1707	158	4.70	103	4.83
GOGNY3	0.37	0.21	0.91	0.84	7.39	1767	158	4.69	89	5.08
JLM1	0.33	0.93	0.87	0.86	6.87	1675	178	4.55	109	4.80
JLM3	0.36	1.02	0.86	0.85	6.75	1708	180	4.56	102	4.85
$^{17}\text{O} + ^{13}\text{C}$ at 204 MeV										
M3YZR	0.46	0.22	0.91	0.85	5.24	1742	203	4.48	95	4.80
M3YFR	0.38	0.18	0.93	0.86	5.16	1738	196	4.52	94	4.87
GOGNY1	0.32	0.15	0.94	0.85	5.74	1748	188	4.53	88	4.99
GOGNY3	0.41	0.20	0.95	0.87	6.03	1729	186	4.53	88	4.97
JLM1	0.35	0.72	0.89	0.84	6.06	1691	196	4.47	84	4.96
JLM3	0.37	0.80	0.88	0.83	5.63	1719	192	4.49	81	5.00

and $\sigma_R = 1699 \pm 36$ mb for $^{18}\text{O} + ^{12}\text{C}$ and $^{17}\text{O} + ^{13}\text{C}$ reactions, respectively. The larger the real volume integral, the smaller reduced radius r_V is required to match the data and the far-side component becomes more structured. For the largest real volume integral, an Airy oscillation forward to a primary rainbow becomes apparent. Usually, the dominance of the far-side component beyond the Fraunhofer crossover is interpreted as a signature of refractive effects due to a strongly attractive real potential and weak absorption. We will show below that the strong absorption is still the dominant reaction mechanism.

A comparison with the scattering of the tightly bound nucleus ^{16}O is in order. Experimental data [12] and our

calculation for $^{16}\text{O} + ^{12}\text{C}$ at 11.3 MeV/nucleon are displayed in Fig. 4. We did not find any reasonable WS solution with $J_V < 300$ MeV fm³ and so the solution with the lowest acceptable real volume integral is plotted. Since the potential is strong, the far-side component of the cross section is much more structured. While the Fraunhofer (diffractive) part at forward angles is similar to our reactions, strong refractive effects appear at $\theta > 40^\circ$ as deep Airy oscillations.

B. Folding form factors

In the following we discuss the ability of the folding model to describe our data. We start by a quite simple model in which the spin-isospin independent form factor of the optical model potential (OMP) is given by the double folding integral

$$V_{\text{fold}}(R) = \int d\vec{r}_1 d\vec{r}_2 \rho_1(r_1) \rho_2(r_2) v_{\text{M3Y}}(s), \quad (1)$$

where v_{M3Y} is the M3Y parametrization of the G matrix obtained from the Paris NN interaction [14], and $\vec{s} = \vec{r}_1 + \vec{R} - \vec{r}_2$ is the NN separation distance. For the reaction $^{17}\text{O} + ^{13}\text{C}$ we add the small isovector component arising from the non-negligible neutron skin present in both interacting partners. The Coulomb component of the optical potential is calculated by replacing the nuclear single-particle (s.p.) densities with proton densities and using $v_{\text{Coul}}(s) = e^2/s$ as effective interaction. The small effect arising from finite proton size is ignored. In the simplest version of this model, dubbed here as M3YZR, the knock-on exchange component is simulated by a zero-range potential with a slightly energy-dependent strength,

$$J_{00}(E) = -276(1 - 0.005E/A). \quad (2)$$

We keep the number of fitting parameters at the minimum level and take the OMP in the form

$$U(R) = N_V V(R, t_V) + i N_W V(R, t_W), \quad (3)$$

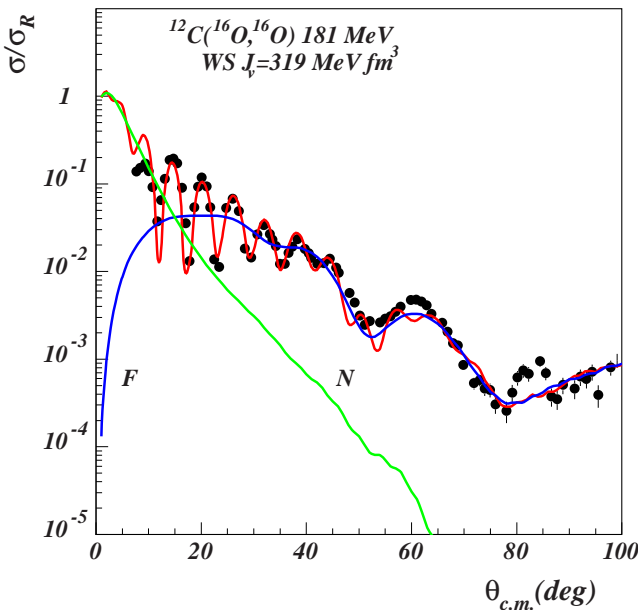


FIG. 4. (Color online) Elastic scattering $^{16}\text{O} + ^{12}\text{C}$ at 11.3 MeV/nucleon. The real part of the WS optical potential is much stronger and the far-side component shows several deep Airy oscillations. Experimental data are taken from Ref. [12].

where N_V and N_W are normalization constants and t_V and t_W are range parameters defined by the scaling transformation

$$V(R, t) \rightarrow t^3 V_{\text{fold}}(tR). \quad (4)$$

This transformation conserves the volume integral of the folding potential and modifies the radius as

$$\langle R^2 \rangle_V = \frac{1}{t^2} \langle R^2 \rangle_{\text{fold}} \quad (5)$$

Thus the strength of the form factor is controlled by the parameters N_V and N_W . Note that the transformation in Eq. (4) ensures that only the rms radius of the bare folding potential is changed. This is in line with the original prescription of Ref. [15] which proposed a smearing procedure in terms of a normalized Gaussian function. We found that the transformation in Eq. (4) is more efficient. Based on Eq. (5) one may estimate in an average way the importance of the dynamic polarization potential (DPP) and finite range effects. Throughout this paper we use single particle densities obtained from a spherical Hartree-Fock (HF + BCS) calculation based on the density functional of Beiner and Lombard [16]. The obtained rms charge radii are very close to the experimental values [17] and the model predicts a neutron skin $\Delta r = r_n - r_p$ of 0.1, 0.18, and 0.1 fm for ^{13}C , ^{18}O , ^{17}O , respectively. The calculated neutron rms radii are 2.84 and 2.76 fm for ^{18}O and ^{17}O , in good agreement with the values extracted by Khoa *et al.* [18] from the high-energy interaction cross section. Note that for the weakly bound ^{13}C ($S_n = 4.9$ MeV) this model predicts a small occupation probability for the neutron $2s_{1/2}$ level of $v_{2s_{1/2}}^2 = 0.0016$ but this has a small influence on the tail of the s.p. density. A more elaborate calculation leads to a nonlocal knock-on exchange kernel [19],

$$U_{\text{ex}}(\vec{R}^+, \vec{R}^-) = \mu^3 v_{\text{ex}}(\mu R^-) \int d\vec{X}_1 \rho_1(X_1) \hat{j}_1 \times \left(k_{f1}(X_1) \frac{(A_1 - 1)A_2}{A_1 + A_2} R^- \right) \rho_2(|\vec{R}^+ - \vec{X}_1|) \times \hat{j}_1 \left(k_{f2}|\vec{R}^+ - \vec{X}_1| \right) \frac{(A_2 - 1)A_1}{A_1 + A_2} R^- \Big), \quad (6)$$

where A_1 and A_2 are mass numbers, μ is the reduced mass of the system, k_{f1} and k_{f2} are Fermi momenta, R^+ and R^- are the usual nonlocal coordinates, and v_{ex} is the exchange component of the interaction including the long-range one-pion exchange potential (OPEP) tail. Equation 6 already shows that the nonlocality is small and behaves as $\sim \mu^{-1}$. In the lowest order of the Perey-Saxon approximation, the local equivalent of the nonlocal kernel is obtained by solving the nonlinear equation

$$U_L(R) = 4\pi \int d\vec{r}_1 d\vec{r}_2 \rho_1(r_1) \rho_2(r_2) \times \int s^2 ds v_{\text{ex}}(s) \hat{j}_1[k_{f1}(r_1) \beta_1 s] \hat{j}_1[k_{f2}(r_1) \beta_2 s] \times j_0 \left[\frac{1}{\mu} K(R) s \right] \delta(\vec{r}_2 - \vec{r}_1 + \vec{R}). \quad (7)$$

Above $\beta_i = (A_i - 1)/A_i$ are recoil corrections, $\hat{j}_1(x) = 3j_1(x)/x$ and j_0 and j_1 are spherical Bessel functions. The

local Fermi momenta k_f are evaluated in an extended Thomas-Fermi approximation [20]. We have explored also the extended Slater approximation for the mixed densities of Campi and Bouyssy [21] but did not obtain substantial improvements over the usual Slater approximation. The local momentum for the relative motion is given by

$$K^2(R) = \frac{2\mu}{\hbar^2} [E_{\text{c.m.}} - U_D(R) - U_L(R)], \quad (8)$$

where U_D is the total direct component of the potential including the Coulomb term. In Eq. (8) we assumed a purely real local momentum of the relative motion since the absorptive component of the OMP is small compared with the real part. The effective mass correction [22] $\mu^*/\mu = 1 - \partial U / \partial E$ is of the order of a few percent for our systems and is absorbed in the renormalization parameter N_W . Some tens of iterations are needed to solve Eq. (7) in order to obtain a precision of 10^{-7} in the entire radial range ($R_{\text{max}} = 25$ fm). Calculations with the finite-range model are dubbed M3YFR.

Neglecting the spin-orbit component, the Gogny NN effective interaction can be expressed as a sum of a central, finite-range term and a zero-range density-dependent term

$$v(\vec{r}_{12}) = \sum_{i=1}^2 (W_i + B_i P_\sigma - H_i P_\tau - M_i P_\sigma P_\tau) e^{-r_{12}^2/\mu_i^2} + t_3(1 + P_\sigma) \rho^\alpha(\vec{R}_{12}) \delta(\vec{r}_{12}), \quad (9)$$

where $\vec{r}_{12} = \vec{r}_1 - \vec{r}_2$, $\vec{R}_{12} = (\vec{r}_1 + \vec{r}_2)/2$, and standard notations have been used for parameter strengths and spin-isospin exchange operators. The strengths parameters and the ranges are taken from Ref. [23]. The isoscalar and isovector components of the effective interaction are constructed in the standard way. The interest in this interaction resides in its excellent description (at the HF level) of the saturation properties of the nuclear matter in line with a modern estimate from isoscalar giant monopole [24] or dipole resonance [25] studies. Antisymmetrization of the density-dependent term is trivial, so that the sum of direct and exchange term reads

$$v_D^\rho(r_{12}) + v_{\text{ex}}^\rho(r_{12}) = \frac{3t_3}{4} \rho^\alpha \delta(\vec{r}_{12}). \quad (10)$$

The local equivalent of the finite-range knock-on exchange is calculated with Eq. (7). Two approximations were used for the overlap density:

$$\rho = [\rho_1(r_1) \rho_2(r_2)]^{1/2}, \quad (11)$$

and

$$\rho = \frac{1}{2} [\rho_1(r_1) + \rho_2(r_2)]. \quad (12)$$

The first approximation (11) has the merit that the overlap density goes to zero when one of the interacting nucleons is far from the bulk. In Eq. (12) a factor 1/2 was introduced such that the overlap density does not exceed the equilibrium density for normal nuclear matter. At large-density overlaps, the fusion and other inelastic processes are dominant and the elastic-scattering amplitude is negligibly small. The calculated OM potentials are dubbed GOGNY1 and GOGNY3, respectively. Both definitions represent crude approximations of the overlap

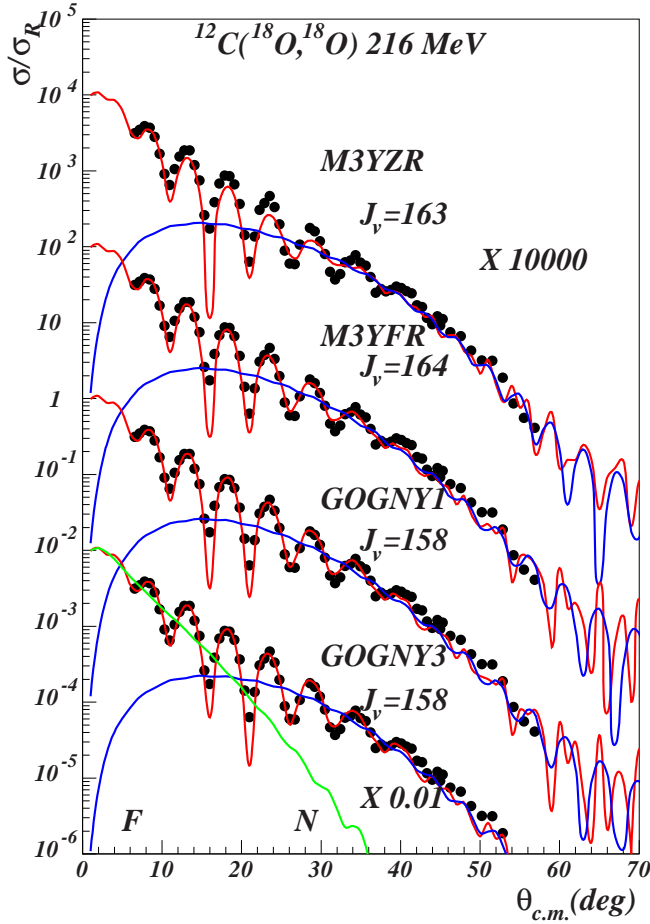


FIG. 5. (Color online) Cross section calculated with folding form factors by using the M3Y and GOGNY models. The real volume integral is indicated on each curve. The far-side–near-side components of the cross section are denoted by F or N. Experimental data and calculation have been shifted by factor X to increase visibility.

density but are widely used to estimate the density-dependence effects in the folding model.

We further examine the density-dependence effects by using the nuclear matter approach of Jeukenne, Lejeune, and Mahaux (JLM) [15], which incorporates a complex, energy- and density-dependent parametrization of the NN effective interaction obtained in a Brueckner Hartree–Fock approximation from the Reid soft-core NN potential. The systematic study [13] of the elastic scattering between p -shell nuclei at energies around 10 MeV/nucleon leads to the surprising result that, on average, the imaginary part of the folded JLM potential was perfectly adequate to describe such reactions and did not need any renormalization ($N_W = 1.00 \pm 0.09$), while the real component needed a substantial renormalization, in line with other effective interactions used in folding models. We examine here to which extent this feature is conserved for tightly bound nuclei in the d shell in the presence of a small neutron excess. Exchange effects are included in this model at the level of N-target interaction. Calculations with this model are dubbed JLM1 and JLM3, depending on which definition we use for the overlap density [Eqs. (11) and (12), respectively].

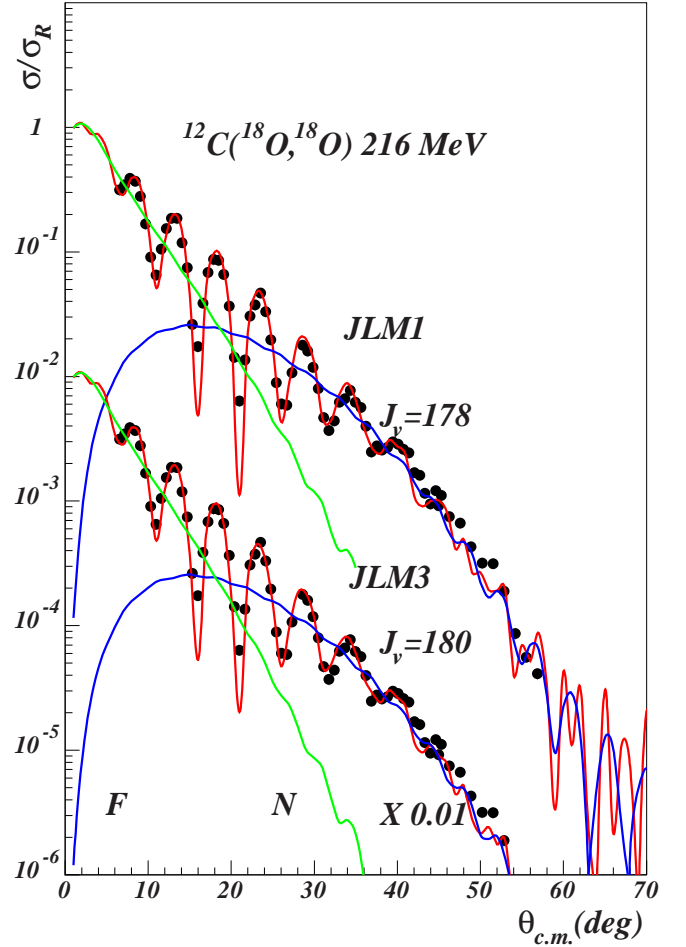


FIG. 6. (Color online) The same as in Fig. 5 but for the JLM model.

A grid search on the real volume integral reveals a unique solution for all six versions of the effective interaction, see Table II and Figs. 5–8. The folding model validates only the solution with the lowest real volume integral found with the WS parametrization. Averaging over all six folding calculations, we find $J_V = 167 \pm 9$ MeV fm³ for ¹⁸O and $J_V = 194 \pm 5$ MeV fm³ for ¹⁷O, and so the interaction of ¹⁷O is slightly more refractive. Again, imaginary volume integrals are quite small, pointing to some transparency of the potential. Corrections due to the finite-range effects are quite large: of the order of $\Delta R \approx 0.5$ fm for the real potential and much larger for the imaginary potential. The folding calculation reproduces perfectly the diffractive pattern at forward angles and the Fraunhofer F or N crossover always produces an interference maximum. Beyond the crossover the far-side component decays quite smoothly and shows some glory effects at $\theta > 60^\circ$.

More information can be extracted from Fig. 9, where we plot the spectral gradient (or relative cross section) [26],

$$E(q) = 2[\sigma_1(q) - \sigma_2(q)]/[\sigma_1(q) + \sigma_2(q)], \quad (13)$$

where σ_1 and σ_2 denote the differential cross sections for ¹⁸O and ¹⁷O, respectively, and q is the momentum transfer. The calculation is done with the JLM3 model, since the Glauber

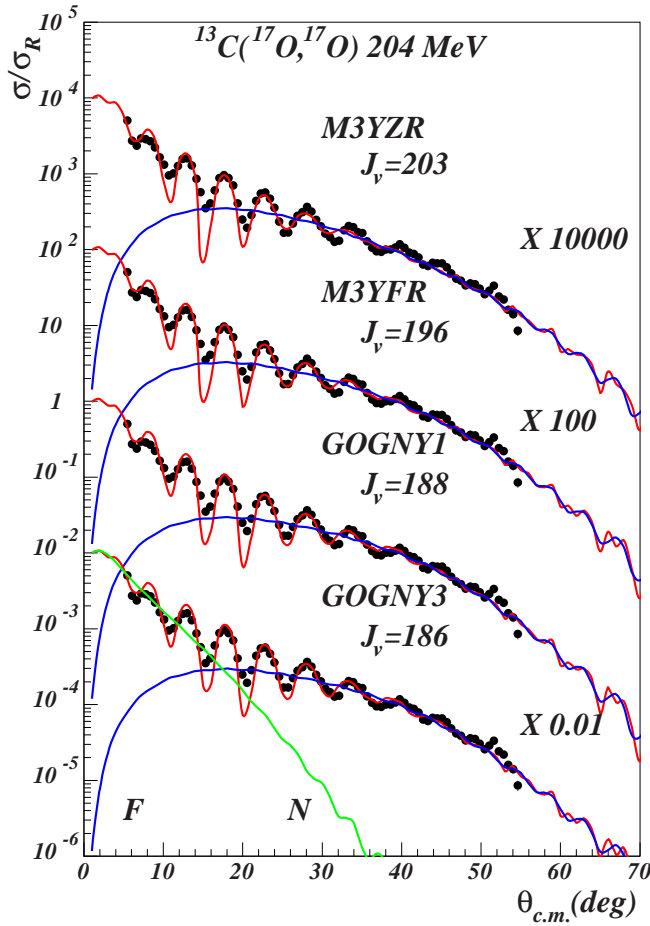


FIG. 7. (Color online) Cross section and F or N decomposition with folding form factors. Parameters are taken from Table II.

model is questionable at this low energy. The pattern in Fig. 9 confirms the diffractive character of our reactions and an intricate interference effect arising from the variation in the radius of optical model potential and its surface thickness. The disagreement at low momentum transfer arises mostly from the lack of long-range correlation in the HF + BCS model for open shell nuclei. At this point we want to make a comment on the role of the dynamic polarization potential for nuclei with neutron excess over the closed shell. A close examination of the results in Table II shows that we have obtained consistent results for all effective interactions used in the folding model. Our results confirm the conjecture that one can extract from the elastic scattering at best only the low momenta of the interaction (volume integrals and rms radii). Corrections in the range parameters are large especially for the imaginary component of the optical potential. We found substantial renormalization for the real part of the optical potential; on average, $N_V = 0.36 \pm 0.05$, in line with the previous study [13]. This can be easily understood: the bare folding form factor has a volume integral around $J_V \approx 450 \text{ MeV fm}^3$, while the data requires precise values around $160\text{--}190 \text{ MeV fm}^3$. Note that the renormalization of the imaginary component in the JLM model is again quite close to unity. Although the density dependence in the GOGNY and JLM effective

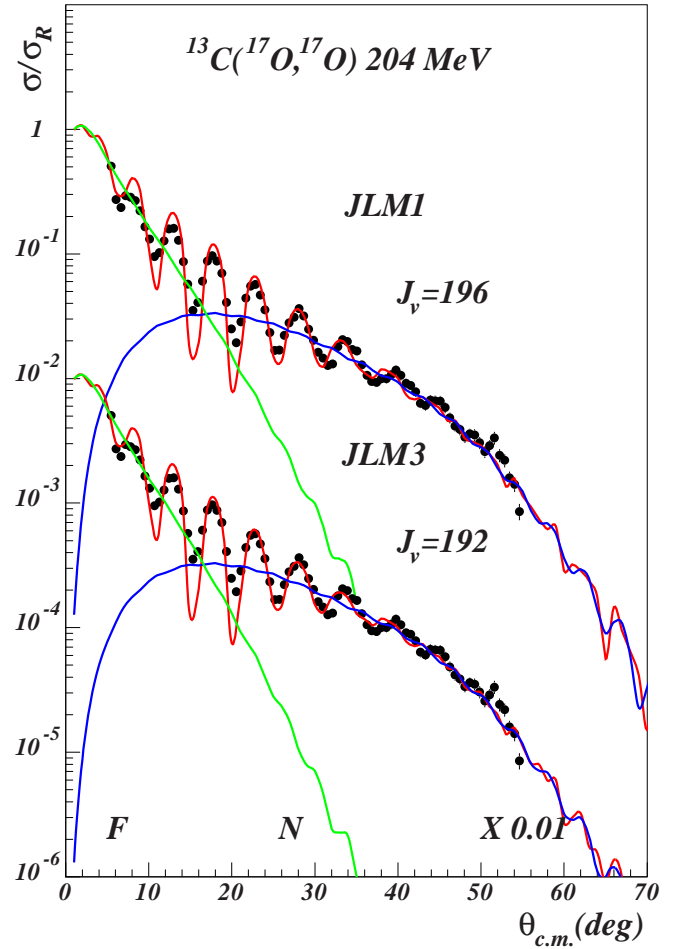


FIG. 8. (Color online) Cross section and F or N decomposition using the JLM form factors.

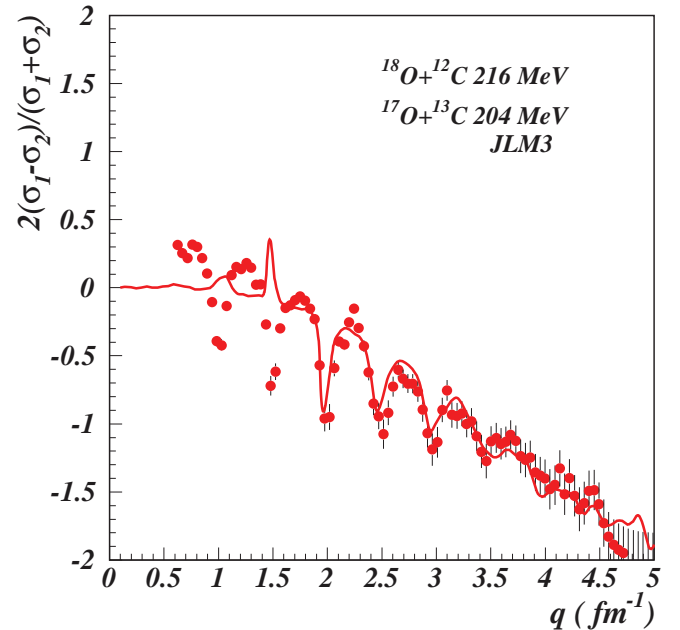


FIG. 9. (Color online) Relative cross section for the elastic scattering $^{18}\text{O} + ^{12}\text{C}$ and $^{17}\text{O} + ^{13}\text{C}$ reactions as a function of momentum transfer is compared with the JLM3 model.

interactions is very different, one cannot disentangle between the two models for the overlap density based on the present data, since both of them give identical results.

IV. SEMICLASSICAL BARRIER AND INTERNAL BARRIER AMPLITUDES

Once we have established the main features of the average OM potential, we turn now to study the reaction mechanism by using semiclassical methods.

The semiclassical uniform approximation for the scattering amplitude of Brink and Takigawa [27] is well adapted to describe situations in which the scattering is controlled by at most three active, isolated, complex turning points. An approximate multireflection series expansion of the scattering function can be obtained, the terms of which have the same simple physical meaning as in the exact Debye expansion for the scattering of light on a spherical well. The major interest in this theory comes from the fact that it can give precious information on the response of a nuclear system to the nuclear interior.

We take as an example the potential PP9 in Table I which is a WS phase equivalent to the JLM1 optical potential. We discard the absorptive term and define the effective potential as

$$V_{\text{eff}}(r) = V(r) + \frac{\hbar^2}{2\mu} \frac{\lambda^2}{r^2}, \quad \lambda = \ell + \frac{1}{2}, \quad (14)$$

where the Langer prescription has been used for the centrifugal term. This guarantees the correct behavior of the semiclassical wave function at the origin. Then we calculate the deflection function,

$$\Theta(\lambda) = \pi - 2 \int_{r_1}^{\infty} \frac{\sqrt{\frac{\hbar^2}{2\mu} \lambda^2 - V(r)}}{r^2 \sqrt{E_{\text{c.m.}} - V_{\text{eff}}}} dr, \quad (15)$$

where r_1 is the outer zero of the square root, i.e., the radius of closest approach to the scatterer, and μ is the reduced mass. Note that, with the replacement $\hbar\lambda = b\sqrt{2\mu E}$, Eq. (15) becomes identical with the classical deflection function $\Theta(b)$, where b is the impact parameter. The result is shown in Fig. 10. The behavior of $\Theta(\lambda)$ is the one expected for an attractive nuclear potential. The nuclear rainbow angle is $\theta_R \approx 36^\circ$. All the measured angular range is classically illuminated and only a few points were measured in the dark side. This explains partially the ambiguities found with the WS form factors.

However, this simple calculation does not provide too much information about the interference effects of the corresponding semiclassical trajectories. Going into the complex r plane, we search for complex turning points, i.e., the complex roots of the quantity $E_{\text{c.m.}} - V_{\text{eff}} - iW$. This is an intricate numerical problem because, for a WS optical potential, the turning points are located near the potential singularities and there are an infinite number of such poles. The situation for integer angular momenta is depicted in Fig. 11. Active turning points are located near the poles of the real form factor. Inactive turning points are located quite far from the real axis and give negligibly small contribution to the total S matrix. We observe an ideal situation with three, well isolated turning points for each partial wave. The multireflection expansion of

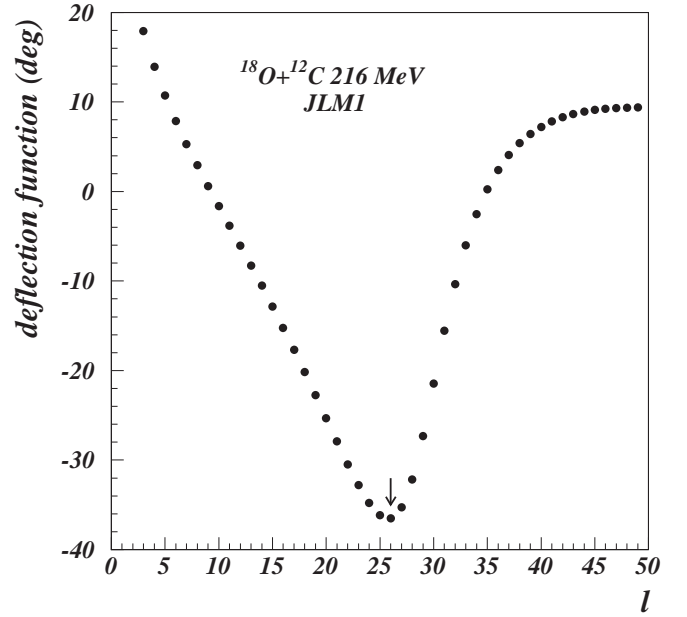


FIG. 10. Classical deflection function for the WS potential equivalent to JLM1. The rainbow angle is $\theta_R = 36^\circ$. The entire measured angular range is illuminated.

the scattering function in the Brink–Takigawa approach reads

$$S_{\text{WKB}}(\ell) = \sum_{q=0}^{\infty} S_q(\ell), \quad (16)$$

where

$$S_0(\ell) = \frac{\exp(2i\delta_1^\ell)}{N(S_{21}/\pi)}, \quad (17)$$

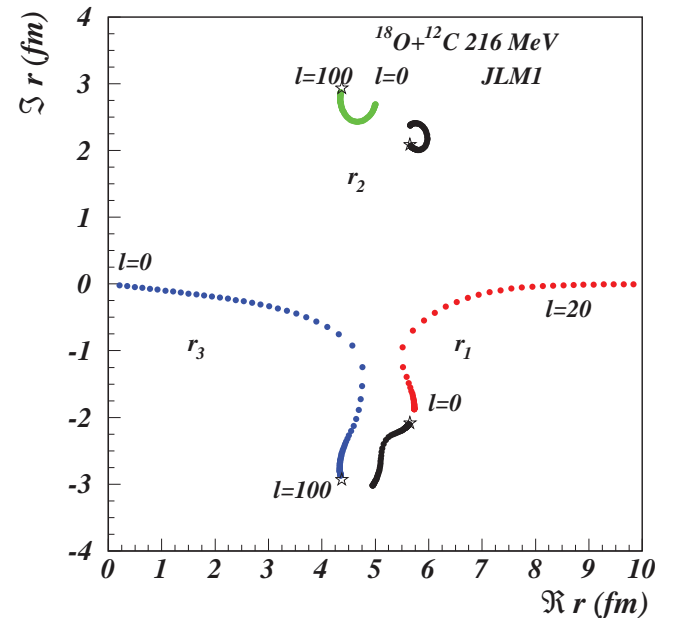


FIG. 11. (Color online) Complex turning points for the WS potential equivalent to JLM1. The stars denote the complex poles of the potential.

and for $q \neq 0$,

$$S_q(\ell) = (-)^{q+1} \frac{\exp[2i(qS_{32} + S_{21} + \delta_1^\ell)]}{N^{q+1}(S_{21}/\pi)}. \quad (18)$$

In these equations, δ_1^ℓ is the WKB (complex) phase shift corresponding to the turning point r_1 , $N(z)$ is the barrier penetrability factor

$$N(z) = \frac{\sqrt{2\pi}}{\Gamma(z + \frac{1}{2})} \exp(z \ln z - z), \quad (19)$$

and S_{ij} is the action integral calculated between turning points r_i and r_j ,

$$S_{ij} = \int_{r_i}^{r_j} dr \left\{ \frac{2\mu}{\hbar^2} [E_{c.m.} - V_{\text{eff}} - iW] \right\}^{1/2}. \quad (20)$$

S_{21} and S_{32} are independent of the integration path provided they lie on the first Riemann sheet and collision with potential poles is avoided. Each term in Eq. (16) has a simple physical interpretation. The first term (the barrier term, denoted also S_B) retains contributions from trajectories reflected at the barrier, not penetrating the internal region. The q th term corresponds to trajectories refracted q times in the nuclear interior with $q - 1$ reflections at the barrier turning point r_2 . Summation of terms $q \geq 1$ can be recast into a single term,

$$S_I = \frac{\exp[2i(S_{32} + S_{21} + \delta_1^\ell)]}{[N(S_{21})]^2} \frac{1}{1 + \exp(2iS_{32})/[N(S_{21}/\pi)]}, \quad (21)$$

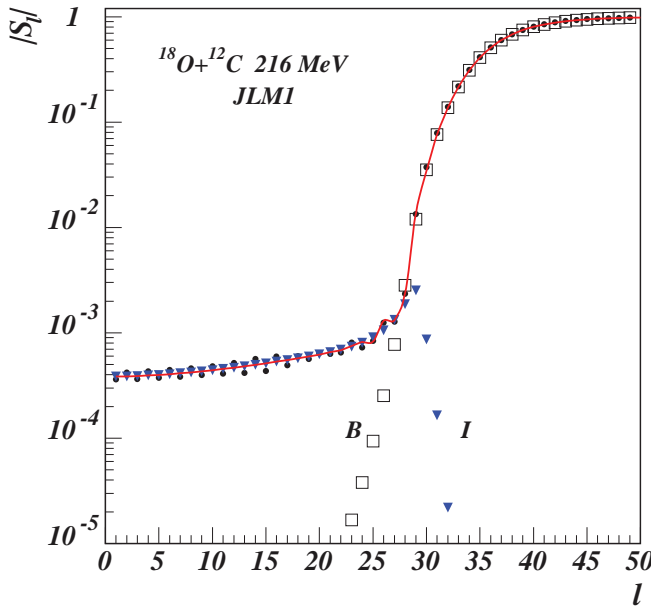


FIG. 12. (Color online) Semiclassical absorption profile for the WS potential equivalent to JLM1. The barrier and internal barrier components of the S matrix are shown by open squares and triangles, respectively. The barrier component is typical for strong absorption. The black dots denote the exact quantum result for the same potential and the line is a spline interpolation of the WKB S matrix.

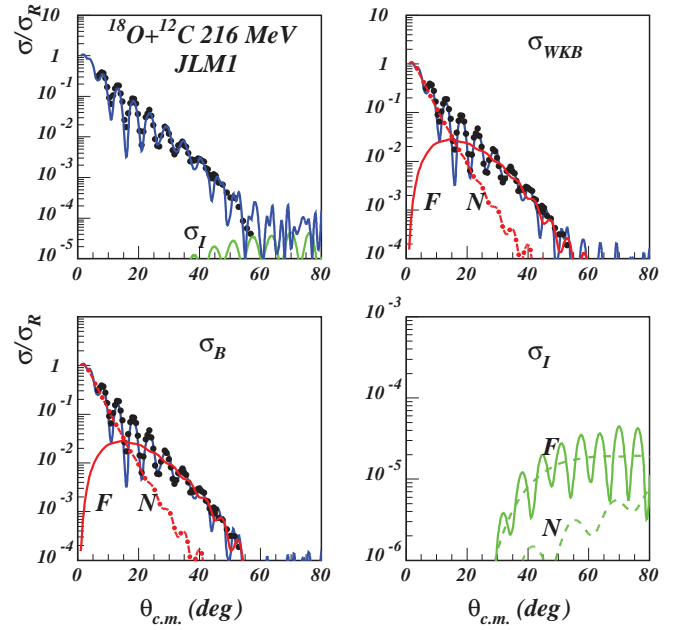


FIG. 13. (Color online) Semiclassical calculation of the cross section based on the WS potential equivalent to JLM1. The WKB scattering amplitude is further decomposed into barrier (σ_B) and internal barrier (σ_I) components. The internal barrier component is negligibly small in the measured angular range. The reaction is peripheral.

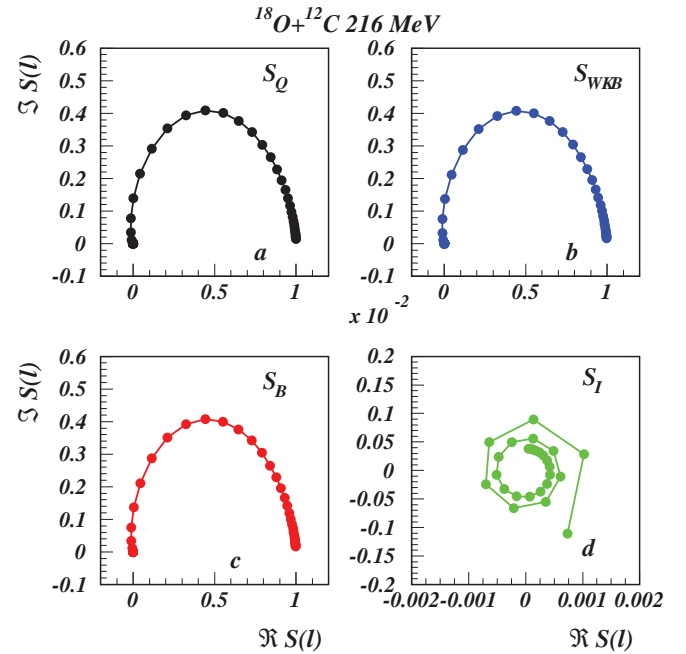


FIG. 14. (Color online) Argand diagram for the semiclassical S matrix based on the WS potential equivalent to JLM1. The barrier trajectory [panel (c)] is identical to the exact quantum result [panel (a)]. The small internal barrier component [panel (d)] shows a hint of an orbiting effect or the presence of Regge poles, but these are too far from the real axis to have noticeable effect in the total cross section.

and is known as the internal barrier scattering function. The last factor in Eq. (21), the enhancement factor, is responsible for the multiple reflections of the wave within the potential pocket. When the absorption in the nuclear interior is large, the enhancement factor reduces to unity. Since the semiclassical scattering function is decomposed additively, $S_{\text{WKB}} = S_B + S_I$, the corresponding total-scattering amplitude is decomposed likewise as $f_{\text{WKB}} = f_B + f_I$ and, conveniently, the corresponding barrier and internal barrier angular distributions are calculated as $\sigma_B = |f_B|^2$ and $\sigma_I = |f_I|^2$ by using the usual angular-momentum expansion of the amplitudes.

The poles of the semiclassical S matrix are given by

$$N(i\epsilon) + e^{2iS_{32}} = 0, \quad \epsilon = -\frac{i}{\pi} S_{21}. \quad (22)$$

Semiclassical Regge poles of Eq. (22) are too far from the real axis to have a noticeable influence on the total cross section. The accuracy of the semiclassical calculation has been checked by comparing the barrier and internal barrier absorption profiles with the exact quantum-mechanical result in Fig. 12. One observes that the semiclassical B/I (barrier/inner barrier) expansion is an *exact* decomposition of

the quantum result. They are virtually identical at the scale of the figure. The internal component gets significant values up to the grazing angular momentum ($\ell_g = 36$) and is negligibly small beyond this value. The barrier component resembles a strong absorption profile and this justifies the interpretation that it corresponds to the part of the flux not penetrating into the nuclear interior. Second, the B/I components are almost decoupled in the angular-momentum space and therefore they will contribute in different angular ranges.

Semiclassical cross sections are compared with the data in Fig. 13. Better insight into this technique is obtained by further decomposing the B/I components into far and near (BF/BN and IF/IN) subcomponents. Clearly, the barrier component dominates the entire measured angular range. Fraunhofer diffractive oscillations appear as the result of BF and BN interference. At large angles, the internal contribution is negligible and the reaction is peripheral.

The Argand diagrams corresponding to the B/I decomposition is displayed in Fig. 14. The barrier amplitude [Fig. 14(c)] is almost identical with the exact quantum result [Fig. 14(a)] while the internal barrier component shows a nice orbiting effect, but the corresponding dynamical content $S_I(\ell)$ is too small to have any sizable effect in the total cross section.

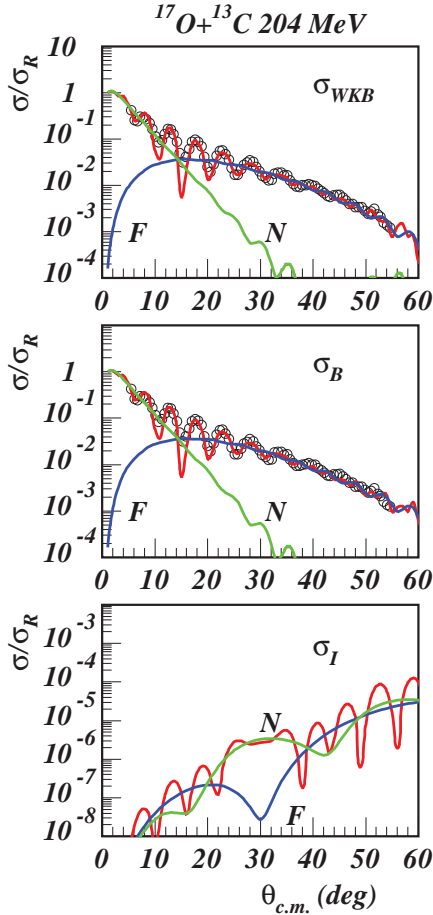


FIG. 15. (Color online) Semiclassical (WKB) calculation of the cross section based on the T1 potential (see Table I). The barrier component match perfectly the data in the entire angular range, while the internal barrier component is negligibly small.

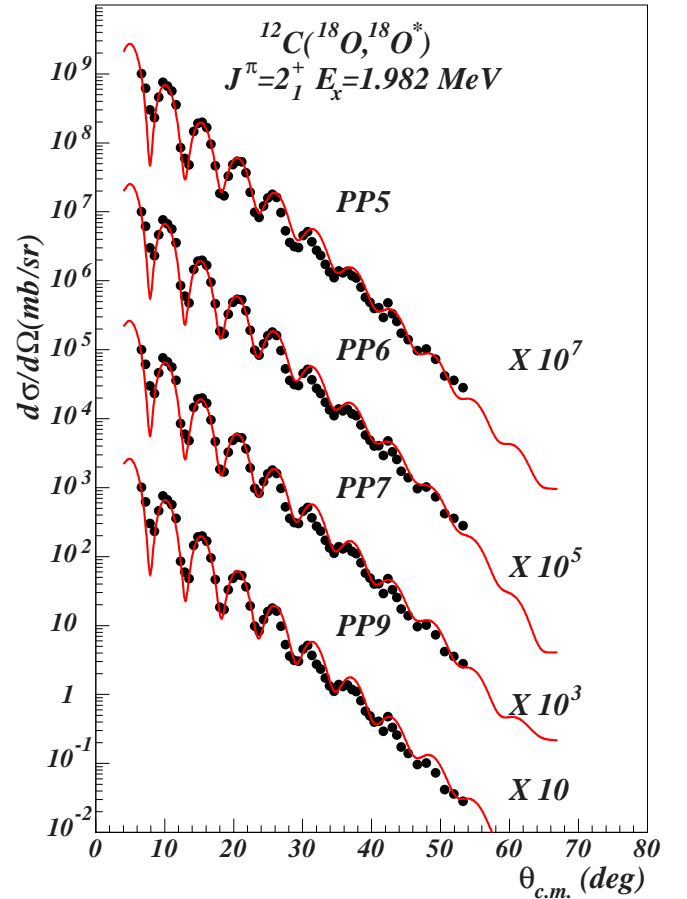


FIG. 16. (Color online) Inelastic cross section to 2_1^+ (1.982 MeV) state in ^{18}O . The DWBA calculation is based on the potentials in Table I.

A similar analysis was performed for the reaction $^{17}\text{O} + ^{13}\text{C}$ based on the WS potential (parameter set T1 in Table I). Again we find that the WKB cross section is identical with the exact quantum result based on the same potential. The barrier component match perfectly the data in the entire angular range, while the internal barrier component gives negligible contribution; see Fig. 15. Thus the peripherality character of our reactions is completely demonstrated.

V. INELASTIC TRANSITIONS

We examine in this section the ability of our optical potentials to describe the measured data for inelastic transitions to selected states in ^{18}O ($J^\pi = 2_1^+$, $E_x = 1.982$ MeV; Fig. 16 and $J^\pi = 2_2^+$, $E_x = 3.92$ MeV; Fig. 17) and two transitions in ^{17}O ($J^\pi = \frac{5}{2}^-$, $E_x = 3.843$ MeV; Fig. 18 and $J^\pi = \frac{1}{2}^+$, $E_x = 6.36$ MeV; Fig. 19).

The pattern of our data shows a clear diffractive character since they obey fairly well the Blair phase rule [28] and therefore a standard DWBA should be an appropriate approach. The deformation table [29] indicates a quadrupole deformation $\beta_2 = 0.107$ for ^{18}O . The systematic by Raman *et al.* [30] gives a value of 0.355(8). Since the DWBA cross

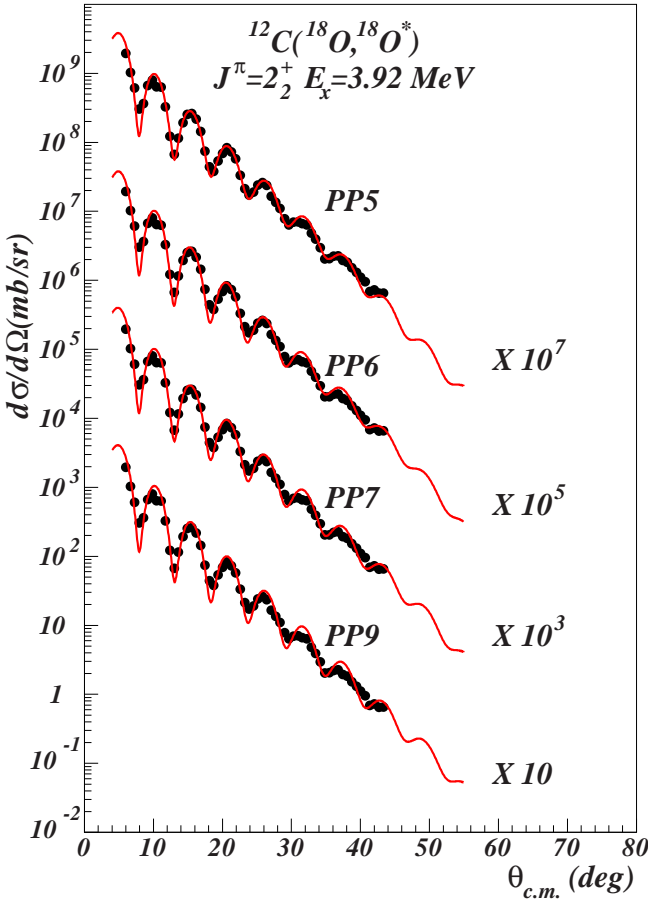


FIG. 17. (Color online) Inelastic cross section to 2_2^+ (3.92 MeV) state in ^{18}O . The DWBA calculation is based on the potentials in Table I.

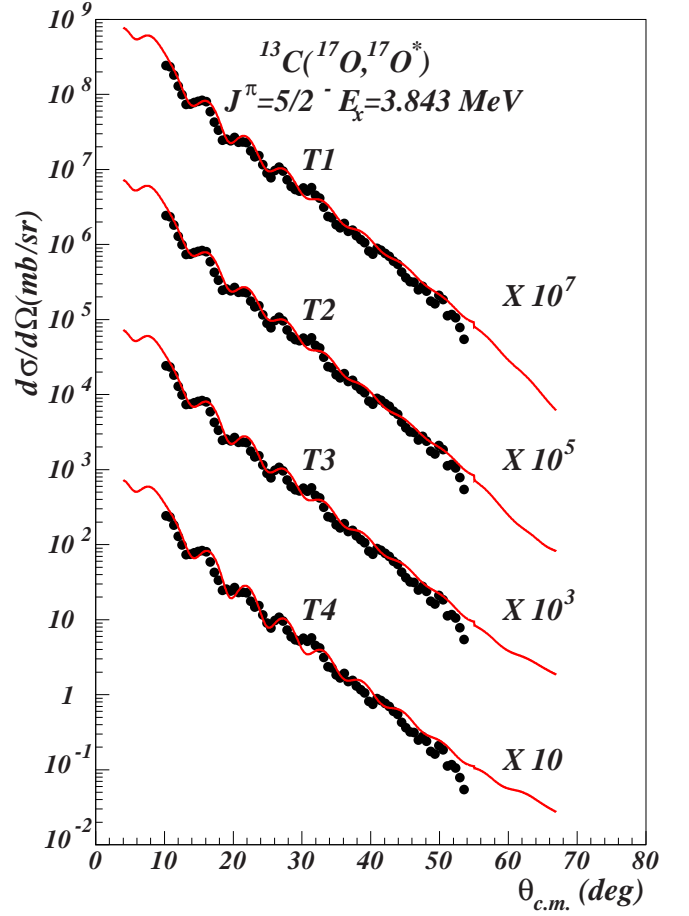


FIG. 18. (Color online) Inelastic cross section to $5/2^-$ (3.84 MeV) state in ^{17}O . The DWBA calculation is based on the potentials in Table I.

section scales with β_2^2 , we execute a number of calculations using $\beta_2 = 0.015$ – 0.6 , chosen rather arbitrarily in the range of suggested values. DWUCK4 and FRESKO give identical shapes for these values using the usual form factor for inelastic transitions $V_\lambda = -\frac{\delta_\lambda}{\sqrt{4\pi}} \frac{dU}{dr}$ where δ_λ is the deformation length and U is the potential. Optimum deformation parameters were obtained by averaging over various optical potentials and different angular ranges in the angular distributions. The scaled calculations that match the data are shown in Figs. 16 and 17 and the optimum deformation parameters are given in Table III.

The shape of the calculated cross section is virtually identical for all the potentials at the scale of the figure. This proves once again that our potentials are almost phase equivalent, small differences appearing only at large angles

TABLE III. Average deformation obtained from inelastic scattering.

Nucleus	J^π	β_λ
^{17}O	$5/2^-$	0.66 ± 0.03
^{17}O	$1/2^+$	0.19 ± 0.01
^{18}O	2_1^+	0.38 ± 0.04
^{18}O	2_2^+	0.52 ± 0.05

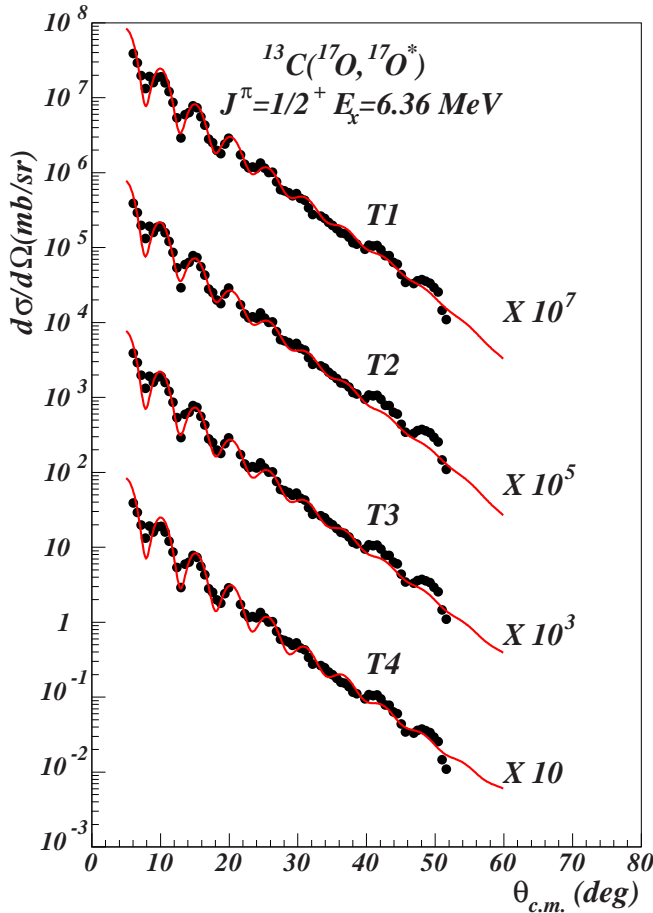


FIG. 19. (Color online) Inelastic cross section to $1/2^+$ (6.36 MeV) state in ^{17}O . The DWBA calculation is based on the potentials in Table I.

much beyond the measured angular range. Remarkably, the calculation with the PP9 parameter set, which is a WS potential phase equivalent to JLM1 folding potential describes the data as well as the other parameter sets. The situation is similar for the other folding potentials. Thus we have obtained a consistent description of both the elastic and inelastic cross section by using a large palette of optical potentials.

The pattern of the measured transitions in ^{17}O is quite different. The cross section decays almost exponentially at large angles with small amplitude wiggles. The experimental study by Cunsolo *et al.* [31] using a three-particle transfer reaction showed that the low-lying negative-parity state in ^{17}O , $J^\pi = \frac{5}{2}^-, E_x = 3.843$ MeV is a member of ^{16}O $K^+\alpha$ -rotational band coupled to a $p_{1/2}$ neutron, and thus has a pure $4p$ - $3h$ configuration. The state $J^\pi = \frac{1}{2}^+, E_x = 6.36$ MeV,

located only 3 keV below the α threshold in ^{17}O is weakly populated in the reaction $^{13}\text{C}(^6\text{Li}, d)^{17}\text{O}$ [32]. This state is astrophysically important since it is considered the main source of the $^{13}\text{C}(\alpha, n)^{16}\text{O}$ reaction-rate uncertainty. According to Cunsolo *et al.* [33] this state has a dominant $3p$ - $2h$ structure and belongs to a $(sd)^3$, $T = 1/2$ ^{17}O rotational band. Repeating the procedure used for ^{18}O , we obtain a satisfactory description of our data with the deformation parameters given in Table III; see Figs. 18 and 19.

VI. CONCLUSIONS

We have measured elastic-scattering cross sections for $^{18}\text{O} + ^{12}\text{C}$ and $^{17}\text{O} + ^{13}\text{C}$ at 12 MeV/nucleon as well as the inelastic transition to selected states in $^{18}\text{O}^*$ and $^{17}\text{O}^*$ in order to determine the optical potentials needed to study the one-neutron pickup reaction $^{13}\text{C}(^{17}\text{O}, ^{18}\text{O})^{12}\text{C}$. Optical potentials in both incoming and outgoing channels were extracted from a standard analysis using Woods–Saxon form factors. Analysis in terms of semimicroscopic double folding form factors, using six different approximations for the NN effective interactions, helped us to eliminate the ambiguities found with WS potentials. Thus a unique solution emerged from the analysis, which is quite surprising when the reaction mechanism is dominated by strong absorption. We found that the neutron excess over the closed d shell leads to a less-refractive interaction as compared with the closed-shell nucleus ^{16}O . We found that the absorptive component of the JLM is adequate for the d -shell heavy-ion interaction. The well-known Gogny effective interaction, designed mainly for HFB calculations, gives excellent results for scattering provided that the knock-on exchange and isovector components are properly included. A detailed semiclassical analysis in terms of barrier and internal barrier amplitudes of Brink and Takigawa demonstrated that the flux penetrating the barrier has negligible contribution to the total cross section, and thus the reactions are peripheral. This provides a complete justification for the use of ANC method to extract spectroscopic information from the transfer reaction.

ACKNOWLEDGMENTS

This work was supported in part by the US Department of Energy under Grants No. DE-FG02-93ER40773 and No. DE-FG52-06NA26207, the NSF under Grant No. PHY-0852653, the Robert A. Welch Foundation under Grant No. A-1082, and by CNCSIS (Romania) Grants No. PN-II-PCE-55/2011 and No. PN-II-ID-PCE-0299/2012. T.A.-A. thanks the Hashemite University for support. We thank V. Balanica for technical support and to Dr. Roland Lombard and Dr. Vlad Avrigeanu for correspondence.

- [1] A. García, E. G. Adelberger, P. V. Magnus, D. M. Markoff, K. B. Swartz, M. S. Smith, K. I. Hahn, N. Bateman, and P. D. Parker, *Phys. Rev. C* **43**, 024601 (1991).
- [2] R. K. Wallace and S. E. Woosley, *Astrophys. J., Suppl. Ser.* **45**, 389 (1981).

- [3] T. Al-Abdullah, F. Carstoiu, X. Chen, H. L. Clark, C. A. Gagliardi, Y.-W. Lui, A. Mukhamedzhanov, G. Tabacaru, Y. Tokimoto, L. Trache, R. E. Tribble, and Y. Zhai, *Phys. Rev. C* **89**, 025809 (2014).
- [4] B. C. Robertson, J. T. Sample, D. R. Goosman, K. Nagatani, and K. W. Jones, *Phys. Rev. C* **4**, 2176 (1971).

- [5] S. Szilner, M. P. Nicoli, Z. Basrak, R. M. Freeman, F. Haas, A. Morsad, M. E. Brandan, and G. R. Satchler, *Phys. Rev. C* **64**, 064614 (2001).
- [6] A. T. Rudchik *et al.*, *Eur. Phys. J. A* **44**, 221 (2010).
- [7] M. C. Mermaz, M. A. G. Fernandes, A. Greiner, B. T. Kim, and N. Lisbona, *Phys. Rev. C* **19**, 794 (1979).
- [8] B. Heusch, C. Beck, J. P. Coffin, P. Engelstein, R. M. Freeman, G. Guillaume, F. Haas, and P. Wagner, *Phys. Rev. C* **26**, 542 (1982).
- [9] D. M. Pringle, W. N. Catford, J. S. Winfield, D. G. Lewis, N. A. Jelley, K. W. Allen, and J. H. Coupland, *Nucl. Instrum. Methods Phys. Res., Sect. A* **245**, 230 (1986).
- [10] S. Kowalski and H. A. Enge, computer code RAYTRACE (unpublished) (1986).
- [11] A. M. Mukhamedzhanov, H. L. Clark, C. A. Gagliardi, Y.-W. Lui, L. Trache, R. E. Tribble, H. M. Xu, X. G. Zhou, V. Burjan, J. Ceppek, V. Kroha, and F. Carstoiu, *Phys. Rev. C* **56**, 1302 (1997).
- [12] Yu. A. Glukhov, S. A. Goncharov, A. S. Dem'yanova, A. A. Ogloblin, M. V. Rozhkov, V. P. Rudakov, and V. Trashka, *Izv. Ross. Akad. Nauk, Ser. Fiz.* **65**, 647 (2001) (Russian).
- [13] L. Trache, A. Azhari, H. L. Clark, C. A. Gagliardi, Y.-W. Lui, A. M. Mukhamedzhanov, R. E. Tribble, and F. Carstoiu, *Phys. Rev. C* **61**, 024612 (2000).
- [14] N. Anantaraman, H. Toki, and G. F. Bertsch, *Nucl. Phys. A* **398**, 269 (1983).
- [15] J. P. Jeukenne, A. Lejeune, and C. Mahaux, *Phys. Rev. C* **16**, 80 (1977).
- [16] M. Beiner and R. J. Lombard, *Ann. Phys. (NY)* **86**, 262 (1974).
- [17] I. Angeli, *Acta Phys. Hung. New Ser.: Heavy Ion Phys.* **8**, 23 (1998).
- [18] D. T. Khoa, H. S. Than, T. H. Nam, M. Grasso, and N. V. Giai, *Phys. Rev. C* **69**, 044605 (2004).
- [19] F. Carstoiu and M. Lassaut, *Nucl. Phys. A* **597**, 269 (1996).
- [20] Dao T. Khoa, *Phys. Rev. C* **63**, 034007 (2001).
- [21] X. Campi and A. Bouyssy, *Phys. Lett. B* **73B**, 263 (1978).
- [22] J. W. Negele and K. Yazaki, *Phys. Rev. Lett.* **47**, 71 (1981).
- [23] D. Gogny, in *Proceedings of International Conference on Nuclear Physics, Munich*, edited by J. de Boer and H. J. Mang (Springer Verlag, Berlin, 1973), Vol. 1, p. 48.
- [24] D. H. Youngblood, H. L. Clark, and Y.-W. Lui, *Phys. Rev. Lett.* **82**, 691 (1999).
- [25] G. Colo, N. Van Giai, P. F. Bortignon, and M. R. Quaglia, *Phys. Lett. B* **485**, 362 (2000).
- [26] J. P. Auger and R. J. Lombard, *Phys. Lett. B* **90B**, 200 (1980).
- [27] D. M. Brink and N. Takigawa, *Nucl. Phys. A* **279**, 159 (1977).
- [28] J. S. Blair, *Phys. Rev.* **115**, 928 (1959).
- [29] P. Möller, J. R. Nix, W. D. Myers, and W. J. Swiatecki, *At. Data Nucl. Data Tables* **59**, 185 (1995).
- [30] S. Raman, C. W. Nestor, Jr., and P. Tikkanen, *At. Data Nucl. Data Tables* **78**, 1 (2001).
- [31] A. Cunsolo, A. Foti, G. Immé, G. Pappalardo, G. Raciti, and N. Saunier, *Phys. Rev. C* **24**, 2127 (1981).
- [32] S. Kubono, K. Abe, S. Kato, T. Teranishi, M. Kurokawa, X. Liu, N. Imai, K. Kumagai, P. Strasser, M. H. Tanaka, Y. Fuchi, C. S. Lee, Y. K. Kwon, L. Lee, J. H. Ha, and Y. K. Kim, *Phys. Rev. Lett.* **90**, 062501 (2003).
- [33] A. Cunsolo, A. Foti, G. Immé, G. Pappalardo, and G. Raciti, *Phys. Lett. B* **124**, 439 (1983).

Peripheral elastic and inelastic scattering of $^{17,18}\text{O}$ on light targets at 12 MeV/nucleon

F. Carstoiu, T. Al-Abdullah, C. A. Gagliardi, and L. Trache

Citation: [AIP Conference Proceedings](#) **1645**, 39 (2015); doi: 10.1063/1.4909558

View online: <http://dx.doi.org/10.1063/1.4909558>

View Table of Contents: <http://scitation.aip.org/content/aip/proceeding/aipcp/1645?ver=pdfcov>

Published by the [AIP Publishing](#)

Articles you may be interested in

[Elastic \$^3\text{He}\$ -transfer Reaction of \$^6\text{He}\$ on the \$^9\text{Be}\$ Target at 25 MeV/nucleon](#)

[AIP Conf. Proc.](#) **865**, 16 (2006); 10.1063/1.2398822

[Erratum: "Measurements of thick target neutron yields and shielding studies using beams of 4 He , 12 C , and 16 O at 155 MeV/nucleon from the K 1200 cyclotron at the National Superconducting Cyclotron Laboratory" \[Rev. Sci. Instrum. 70, 2314 \(1999\)\]](#)

[Rev. Sci. Instrum.](#) **72**, 1600 (2001); 10.1063/1.1338484

[Measurements of thick target neutron yields and shielding studies using beams of 4 He, 12 C and 16 O at 155 MeV/nucleon from the K1200 cyclotron at the National Superconducting Cyclotron Laboratory](#)

[Rev. Sci. Instrum.](#) **70**, 2314 (1999); 10.1063/1.1149757

[Fragment decay in \$^{12}\text{C}+^{197}\text{Au}\$ from 30 to 100 MeV/nucleon](#)

[AIP Conf. Proc.](#) **250**, 409 (1992); 10.1063/1.42028

[K-- \$^{12}\text{C}\$ elastic scattering at 800 MeV/C](#)

[AIP Conf. Proc.](#) **54**, 714 (1979); 10.1063/1.31970

Peripheral elastic and inelastic scattering of $^{17,18}\text{O}$ on light targets at 12 MeV/nucleon

F. Carstoiu*, T. Al-Abdullah[†], C.A. Gagliardi** and L. Trache**

*National Institute for Physics and Nuclear Engineering Horia Hulubei, Bucharest, Romania

[†]Physics Department, The Hashemite University, Zarqa, Jordan

**Cyclotron Institute, Texas A&M University, College Station, Texas 77843, USA

Abstract. The elastic and inelastic scattering of $^{17,18}\text{O}$ with light targets has been undertaken at 12 MeV/nucleon in order to determine the optical potentials needed for the transfer reaction $^{13}\text{C}(^{17,18}\text{O},^{12}\text{C})$. Optical potentials in both incoming and outgoing channels have been determined in a single experiment. This transfer reaction was used to infer the direct capture rate to the $^{17}\text{F}(p,\gamma)^{18}\text{Ne}$ which is essential to estimate the production of ^{18}F at stellar energies in ONe novae. We demonstrate the stability of the ANC method and OMP results using good quality elastic and inelastic scattering data with stable beams. The peripherality of our reaction is inferred from a semiclassical decomposition of the total scattering amplitude into barrier and internal barrier components. Comparison between elastic scattering of ^{17}O , ^{18}O and ^{16}O projectiles is made.

Keywords: Woods-Saxon potential, folding potentials, WKB.

PACS: 25.70.Bc, 25.70.Hi, 24.10.Ht.

INTRODUCTION

The $^{17}\text{F}(p,\gamma)^{18}\text{Ne}$ reaction is important for understanding nucleosynthesis in novae and plays a role in determining if radioactive nuclei with characteristic gamma-ray signature are produced in sufficient yield to be observed by gamma-ray satellites. The reaction rate is expected to be dominated by direct-capture cross section at nova temperatures and influences the abundances of ^{15}O , ^{17}F , ^{18}F and ^{18}Ne [1]. The rate also determines the $^{17}\text{O}/^{18}\text{O}$ ratio that is produced and explains the transition sequence from the HCNO cycle to the *rp*-process [2]. The primary goal of the experiment was the measurement of the peripheral neutron transfer reaction $^{13}\text{C}(^{17,18}\text{O},^{12}\text{C})$. Optical potentials in the incoming and outgoing channels have been obtained by measuring elastic scattering angular distributions $^{17}\text{O}+^{13}\text{C}$ and $^{18}\text{O}+^{12}\text{C}$ at 12 MeV/nucleon incident energy. The quality of the obtained potentials has been also checked from inelastic scattering to selected states in $^{17}\text{O}^*$ and $^{18}\text{O}^*$. Since the ANC method assumes the peripherality of the reaction mechanism, we discuss here rather extensively this issue by decomposing semiclassically the total scattering amplitude into barrier and internal barrier subcomponents. We show that the internal barrier subcomponent, which corresponds to the flux penetrating the barrier, gives negligible small contribution to the total cross section, and thus the reaction is peripheral. The elastic scattering $^{17}\text{O}+^{13}\text{C}$ includes a weakly bound target.

Previously, $^{18}\text{O}+^{12}\text{C}$ elastic scattering at barrier energies was measured by Robertson *et al.* [3], by Szilner *et al.* [4] and Rudchik *et al.* [5] at some 5-7 MeV/nucleon. Fresnel scattering of ^{18}O on ^{28}Si was measured by Mermaz *et al.* [6] at 56 MeV. For the $^{17}\text{O}+^{13}\text{C}$ reaction the data are rather scarce, we identified a single fusion study and poor elastic angular distributions at barrier energies [7]. The main conclusion of these studies was that the interaction of $^{17,18}\text{O}$ nuclei with light targets is slightly more absorptive compared with that of the closed shell nucleus ^{16}O and that no significant effects due to the neutron excess were identified.

In Sec. II we give a short description of the experiment. Elastic scattering data and the derivation of the OM potentials are discussed in Sec. III. The semiclassical (WKB) method is used in Sec IV to decompose the total scattering amplitude into barrier and internal barrier components. Inelastic angular distributions to selected states in $^{18}\text{O}^*$ and $^{17}\text{O}^*$ are discussed in Sec. V. Our conclusions are summarized in Sec. VI.

THE EXPERIMENT

The experiment was carried out with two separate ^{17}O and ^{18}O beams from K500 superconducting cyclotron at Texas A&M University. Each beam was transported through the beam analysis system to the scattering chamber of the

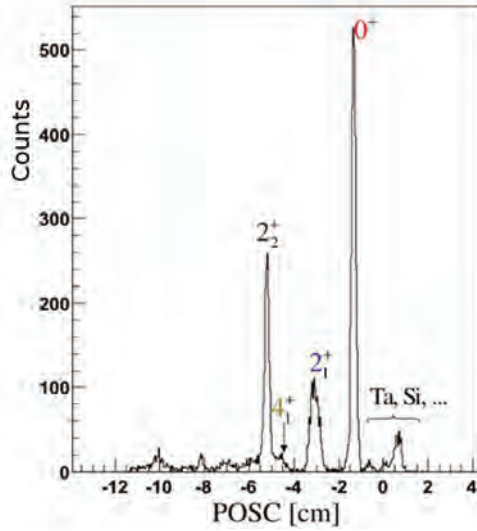


FIGURE 1. (Color online) Low-lying spectrum of ^{18}O versus the particle position in the focal plane, measured at the spectrometer angle of 4° . The peaks at the right of the elastic peak are due to Si and Ta contaminants in the target.

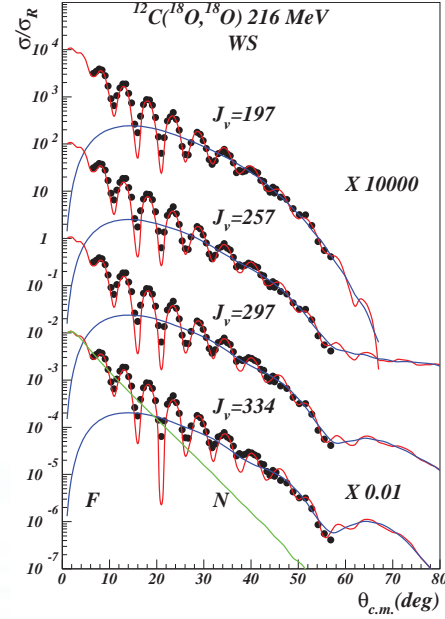


FIGURE 2. (Color online) Cross section and far side/near side (F/N) decomposition of the scattering amplitude for WS potentials in Table 1. Each calculation is identified by its real volume integral J_V and shifted by factors X to increase the visibility.

multipole-dipole-multipole (MDM) magnetic spectrometer [8], where it interacted with $100 \mu\text{g}/\text{cm}^2$ self-supporting targets.

First, the ^{17}O beam impinged on ^{13}C target enriched up to 99%. We continuously monitored the excitation of the 4.44 MeV state in ^{12}C in order to estimate the carbon deposition during the exposure and found negligible small contribution. The elastic scattering angular distribution was measured for the spectrometer angles 4° - 25° in the laboratory system. Fine tuned RAYTRACE [9] calculations were used to reconstruct the position of particles in the focal plane and the scattering angle at the target. A $4^\circ \times 1^\circ$ wide-opening mask and an angle mask consisting of five narrow ($\Delta\theta = 0.1^\circ$) slits were used for each spectrometer angle to double-check the absolute values of the cross section and the quality of the angle calibration. The instrumental setup, including the focal plane detector, and processes for energy and angle calibrations, are identical to that described in Ref. [10]. Second, the ^{12}C target was bombarded by ^{18}O beam with 216 MeV total laboratory energy. The elastic scattering cross section was measured at 4° - 22° spectrometer angles.

ELASTIC SCATTERING

Woods-Saxon formfactors

The measured elastic scattering data at $E_{lab}=216$ and 204 MeV are shown in Figs. 2 and 3. The data are first analyzed using optical potentials with conventional Woods-Saxon (WS) form factors for the nuclear term, supplemented with a Coulomb potential generated by a uniform charge distribution with a reduced radius fixed to $r_c=1$ fm. No preference has been found for volume or surface localized absorption and throughout the paper only volume absorption is considered. In the absence of any spin dependent observables, spin-orbit or tensor interactions have been ignored. Ground state reorientation couplings have been neglected also. The potential is defined by six parameters specifying the depth and geometry of the real and imaginary terms, with the standard notations, the same as used in Ref. [11]. The number of data points N is quite large, and consequently the usual goodness of fit criteria (χ^2) normalized to N has been used.

Using the strength of the real component of the optical potential as a control parameter, a grid search procedure

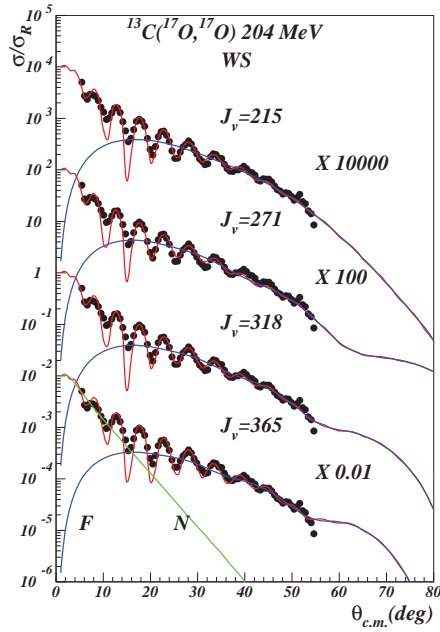


FIGURE 3. (Color online) Cross sections and F/N decomposition for the WS potentials Table 1. The far side component shows Airy oscillation which moves to forward angles with increased value of the real volume integral.

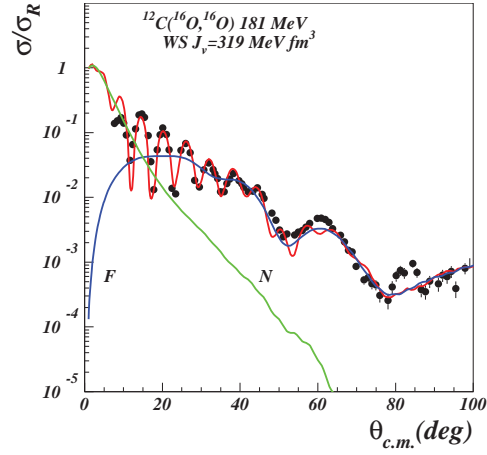


FIGURE 4. (Color online) Elastic scattering $^{16}\text{O}+^{12}\text{C}$ at 11.3 MeV/nucleon. The real part of the WS optical potential is much stronger and the far side component shows several deep Airy oscillations. Experimental data are taken from [12].

TABLE 1. Discrete solutions obtained with WS form factors for $^{18}\text{O}+^{12}\text{C}$ at 216 MeV and $^{17}\text{O}+^{13}\text{C}$ at 204 MeV. The line labeled PP9 is a WS phase equivalent of the JLM1 solution.

pot	V MeV	W MeV	r_V fm	r_W fm	a_V fm	a_W fm	χ^2	σ_R mb	J_V MeV fm ³	R_V fm	J_W MeV fm ³	R_W fm
$^{18}\text{O}+^{12}\text{C}$ at 216 MeV												
PP5	89.18	25.24	0.88	1.16	0.88	0.68	5.12	1712	197	4.69	103	5.09
PP6	195.40	25.59	0.68	1.16	0.96	0.67	6.39	1702	257	4.40	104	5.07
PP7	295.82	26.00	0.60	1.16	0.95	0.67	7.54	1696	297	4.20	106	5.06
PP8	374.41	26.19	0.58	1.16	0.90	0.68	9.78	1695	334	4.01	107	5.06
PP9	75.68	26.16	0.89	1.15	0.93	0.66	5.31	1677	178	4.85	104	5.02
$^{17}\text{O}+^{13}\text{C}$ at 204 MeV												
T1	94.69	26.91	.91	1.13	.84	.67	4.47	1659	215	4.67	99	4.96
T2	188.40	24.95	.72	1.12	.94	.69	4.62	1667	271	4.44	92	4.99
T3	248.75	26.36	.69	1.13	.90	.66	4.53	1659	318	4.27	99	4.97
T4	275.49	25.63	.73	1.15	.81	.65	5.90	1660	365	4.11	100	5.00

revealed a number of discrete solutions. Their parameters are presented in Table 1. The ambiguity in the optical potential has two main sources: the limited range of the measured angles and the strong absorption. When the strong absorption dominates the reaction mechanism, then the interaction is sensitive only to the surface and several phase equivalent optical potentials will appear. The patterns shown in Figs 2 and 3 show rapid oscillation at forward angles followed by a smooth fall-off at intermediate angles. Assuming pure Fraunhofer scattering at forward angles, we extract a grazing angular momentum $\ell_g \approx 36$ from the angular spacing $\Delta\theta = \pi/(\ell_g + 1/2)$. The corresponding grazing distance is quite large, $R_g \approx 7$ fm, much larger than the distance of touching configuration. We systematically find diffuse real potentials ($a_V \approx 0.9$ fm). This effect may be tentatively attributable to the neutron excess. We find also quite constant volume integrals and *rms* radii for the imaginary component. As a consequence the total reaction cross section seems to be a well defined observable. Weighted average values from Table 1 and Table 2 are $\sigma_R = 1713 \pm 35$ mb and

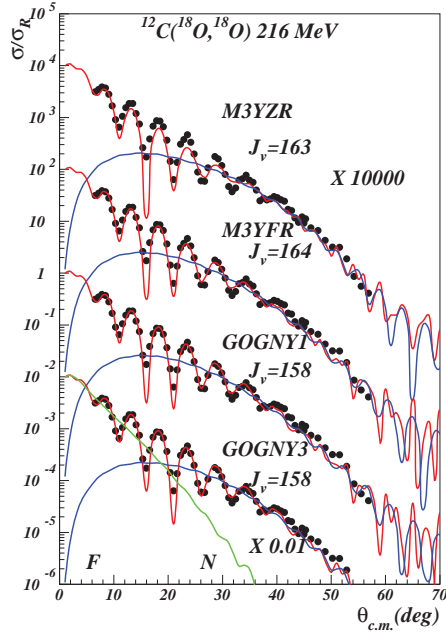


FIGURE 5. (Color online) Cross section calculated with folding form factors using the M3Y and GOGNY models. The real volume integral is indicated on each curve. The far side/near side components of the cross section are denoted by F/N. Experimental data and calculation have been shifted by factor X to increase visibility.

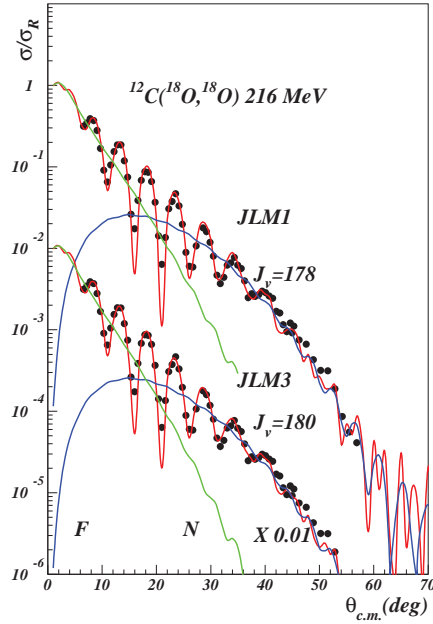


FIGURE 6. (Color online) The same as in Fig.5 but for the JLM model.

$\sigma_R = 1699 \pm 36$ mb for $^{18}\text{O}+^{12}\text{C}$ and $^{17}\text{O}+^{13}\text{C}$ reactions respectively. For the largest real volume integral an Airy oscillation forward to a primary rainbow becomes apparent. Usually, the dominance of the far-side component beyond the Fraunhofer crossover is interpreted as a signature of refractive effects due to a strongly attractive real potential and weak absorption. We will show below that the strong absorption is still the dominant reaction mechanism.

A comparison with the scattering of the tightly bound nucleus ^{16}O is in order. Experimental data [12] and our calculation for $^{16}\text{O}+^{12}\text{C}$ at 11.3 MeV/nucleon are displayed in Fig. 4. We did not find any reasonable WS solution with $J_V < 300$ MeV fm³ and so the solution with the lowest acceptable real volume integral is plotted. Since the potential is strong, the far-side component of the cross section is much more structured. While the Fraunhofer (diffractive) part at forward angles is similar to our reactions, strong refractive effects appear at $\theta > 40^\circ$ as deep Airy oscillations.

Folding formfactors

In the following we discuss the ability of the folding model to describe our data. We start by a quite simple model in which the spin-isospin independent formfactor of the OMP is given by the double folding integral,

$$V_{fold}(R) = \int d\vec{r}_1 d\vec{r}_2 \rho_1(r_1) \rho_2(r_2) v_{M3Y}(s) \quad (1)$$

where v_{M3Y} is the M3Y parametrization of the G-matrix obtained from the Paris NN interaction [13], and $\vec{s} = \vec{r}_1 + \vec{R} - \vec{r}_2$ is the NN separation distance. For the reaction $^{17}\text{O}+^{13}\text{C}$ we add the small isovector component arising from the nonnegligible neutron skin present in both interacting partners. The Coulomb component of the optical potential is calculated by replacing the nuclear s.p. densities with proton densities and using $v_{coul}(s) = e^2/s$ as effective interaction. The small effect arising from finite proton size is ignored. In the simplest version of this model, dubbed here as

TABLE 2. Unique solutions obtained with folding form factors for $^{18}\text{O}+^{12}\text{C}$ at 216 MeV and $^{17}\text{O}+^{13}\text{C}$ at 204 MeV.

pot	N_V	N_W	t_V	t_W	χ^2	σ_R mb	J_V MeV fm ³	R_V fm	J_W MeV fm ³	R_W fm
$^{18}\text{O}+^{12}\text{C}$ at 216 MeV										
M3YZR	0.37	0.20	0.88	0.80	10.72	1812	163	4.60	86	5.06
M3YFR	0.33	0.21	0.88	0.86	8.15	1737	164	4.68	103	4.83
GOGNY1	0.28	0.18	0.89	0.87	7.27	1707	158	4.70	103	4.83
GOGNY3	0.37	0.21	0.91	0.84	7.39	1767	158	4.69	89	5.08
JLM1	0.33	0.93	0.87	0.86	6.87	1675	178	4.55	109	4.80
JLM3	0.36	1.02	0.86	0.85	6.75	1708	180	4.56	102	4.85
$^{17}\text{O}+^{13}\text{C}$ at 204 MeV										
M3YZR	0.46	0.22	0.91	0.85	5.24	1742	203	4.48	95	4.80
M3YFR	0.38	0.18	0.93	0.86	5.16	1738	196	4.52	94	4.87
GOGNY1	0.32	0.15	0.94	0.85	5.74	1748	188	4.53	88	4.99
GOGNY3	0.41	0.20	0.95	0.87	6.03	1729	186	4.53	88	4.97
JLM1	0.35	0.72	0.89	0.84	6.06	1691	196	4.47	84	4.96
JLM3	0.37	0.80	0.88	0.83	5.63	1719	192	4.49	81	5.00

M3YZR, the knockon exchange component is simulated by a zero range potential with a slightly energy dependent strength,

$$J_{00}(E) = -276(1 - 0.005E/A) \quad (2)$$

We keep the number of fitting parameters at the minimum level and take the OMP in the form,

$$U(R) = N_V V(R, t_V) + iN_W V(R, t_W) \quad (3)$$

where $N_{V,W}$ are normalization constants and $t_{V,W}$ are range parameters defined by the scaling transformation,

$$V(R, t) \rightarrow t^3 V_{fold}(tR) \quad (4)$$

This transformation conserves the volume integral of the folding potential and modifies the radius as,

$$\langle R^2 \rangle_V = \frac{1}{t^2} \langle R^2 \rangle_{fold} \quad (5)$$

Thus the strength of the formfactor is controlled by the parameters $N_{V,W}$. Note that the transformation in Eq. (4) ensures that only the *rms* radius of the bare folding potential is changed. Based on Eq. (5) one may estimate in an average way the importance of the dynamic polarization potential (DPP) and finite range effects. Throughout this paper we use single particle densities obtained from a spherical Hartree-Fock (HF+BCS) calculation based on the density functional of Beiner and Lombard [15]. The obtained *rms* charge radii are very close to the experimental values [16] and the model predicts a neutron skin $\Delta r = r_n - r_p$ of 0.1, 0.18 and 0.1 fm for ^{13}C , ^{18}O , ^{17}O respectively. The calculated neutron *rms* radii are 2.84 and 2.76 fm for ^{18}O , ^{17}O in good agreement with the values extracted by Khoa *et al.* [17] from high energy interaction cross section. Note that for the weakly bound ^{13}C ($S_n = 4.9$ MeV) this model predicts a small occupation probability for the neutron $2s_{1/2}$ level of $v_{2s_{1/2}}^2 = 0.0016$ but this has a small influence on the tail of the s.p. density. A more elaborate calculation leads to a nonlocal knockon exchange kernel [18],

$$U_{ex}(\vec{R}^+, \vec{R}^-) = \mu^3 v_{ex}(\mu R^-) \int d\vec{X}_1 \rho_1(X_1) \hat{j}_1(k_{f1}(X_1) \frac{(A_1 - 1)A_2}{A_1 + A_2} R^-) \times \rho_2(|\vec{R}^+ - \vec{X}_1|) \hat{j}_1(k_{f2}(|\vec{R}^+ - \vec{X}_1|) \frac{(A_2 - 1)A_1}{A_1 + A_2} R^-) \quad (6)$$

where $A_{1,2}$ are mass numbers, μ is the reduced mass of the system, $k_{f1,2}$ are Fermi momenta, $R^{+,-}$ are the usual nonlocal coordinates and v_{ex} is the exchange component of the interaction including the long range OPEP tail.

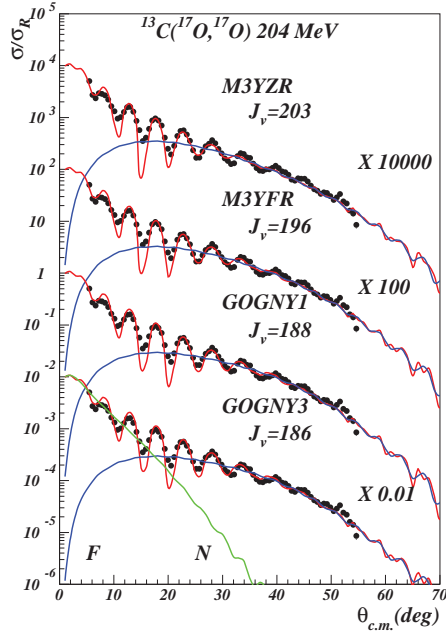


FIGURE 7. (Color online) Cross section and F/N decomposition with folding form factors. Parameters are taken from Table 2.

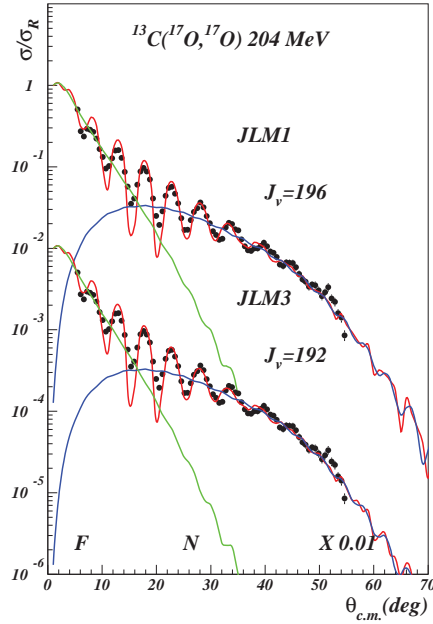


FIGURE 8. (Color online) Cross section and F/N decomposition using the JLM form factors

Eq. (6) already shows that the nonlocality is small and behaves as $\sim \mu^{-1}$. In the lowest order of the Perey-Saxon approximation, the local equivalent of the nonlocal kernel is obtained by solving the nonlinear equation,

$$U_L(R) = 4\pi \int d\vec{r}_1 d\vec{r}_2 \rho_1(r_1) \rho_2(r_2) \int s^2 ds v_{ex}(s) \hat{j}_1(k_{f1}(r_1) \beta_1 s) \hat{j}_1(k_{f2}(r_1) \beta_2 s) j_0\left(\frac{1}{\mu} K(R) s\right) \delta(\vec{r}_2 - \vec{r}_1 + \vec{R}) \quad (7)$$

Above $\beta_i = (A_i - 1)/A_i$ are recoil corrections, $\hat{j}_1(x) = 3j_1(x)/x$ and $j_{0,1}$ are spherical Bessel functions. The local Fermi momenta k_f are evaluated in an extended Thomas-Fermi approximation [19]. The local momentum for the relative motion is given by,

$$K^2(R) = \frac{2\mu}{\hbar^2} (E_{c.m.} - U_D(R) - U_L(R)) \quad (8)$$

where U_D is the total direct component of the potential including the Coulomb term. In Eq. (8) we assumed a purely real local momentum of the relative motion since the absorptive component of the OMP is small compared with the real part. The effective mass correction [21], $\frac{\mu^*}{\mu} = 1 - \frac{\partial U}{\partial E}$ is of the order of a few percent for our systems and is absorbed in the renormalization parameter N_W . Calculations with finite range model are dubbed M3YFR.

Neglecting the spin-orbit component, the Gogny NN effective interaction can be expressed as a sum of a central, finite range term and a zero range density dependent term,

$$v(\vec{r}_{12}) = \sum_{i=1}^2 (W_i + B_i P_\sigma - H_i P_\tau - M_i P_\sigma P_\tau) e^{-\frac{r_{12}^2}{\mu_i^2}} + t_3 (1 + P_\sigma) \rho^\alpha(\vec{R}_{12}) \delta(\vec{r}_{12}) \quad (9)$$

where $\vec{r}_{12} = \vec{r}_1 - \vec{r}_2$, $\vec{R}_{12} = (\vec{r}_1 + \vec{r}_2)/2$ and standard notations have been used for parameter strengths and spin-isospin exchange operators. The strengths parameters and the ranges are taken from [22]. Antisymmetrization of the density

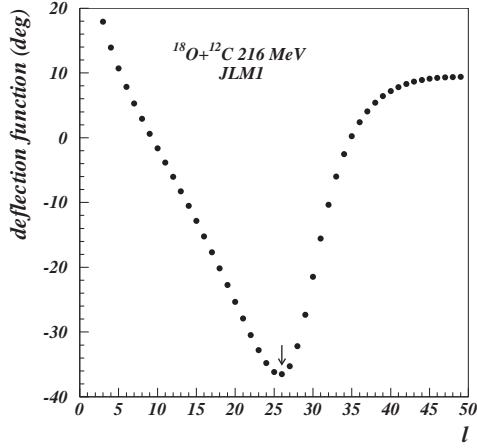


FIGURE 9. Classical deflection function for the WS potential equivalent to JLM1. The rainbow angle is $\theta_R = 36^\circ$. The entire measured angular range is illuminated.

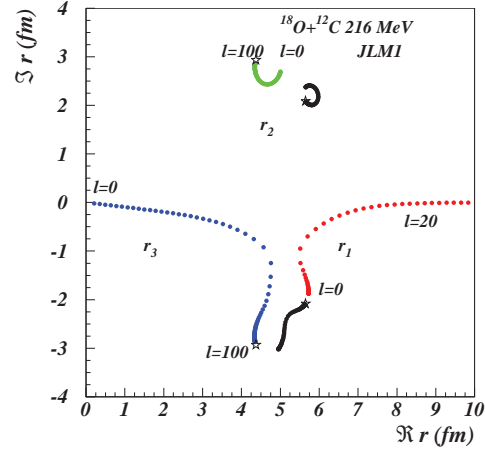


FIGURE 10. (Color online) Complex turning points for the WS potential equivalent to JLM1. The stars denote the complex poles of the potential.

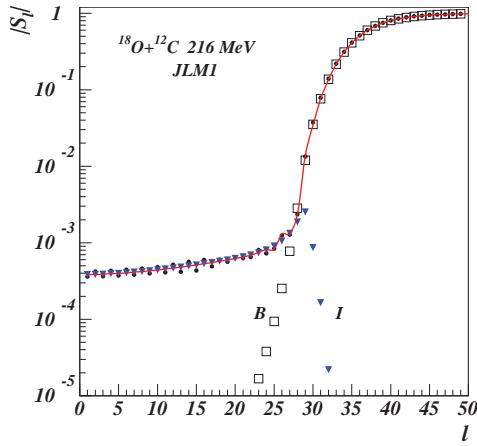


FIGURE 11. (Color online) Semiclassical absorption profile for the WS potential equivalent to JLM1. The barrier and internal barrier components of the S-matrix are shown by open squares and triangles respectively. The barrier component is typical for strong absorption. The black dots denote the exact quantum result for the same potential and the line is a spline interpolation of the WKB S-matrix.

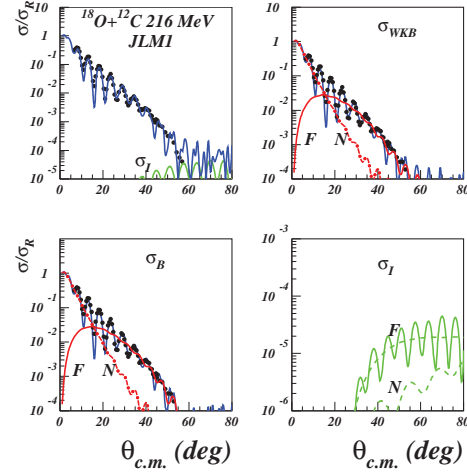


FIGURE 12. (Color online) Semiclassical calculation of the cross section based on the WS potential equivalent to JLM1. The WKB scattering amplitude is further decomposed into barrier (σ_B) and internal barrier (σ_I) components. The internal barrier component is negligible small in the measured angular range. The reaction is peripheral.

dependent term is trivial, so that the sum of direct and exchange term reads,

$$v_D^\rho(r_{12}) + v_{ex}^\rho(r_{12}) = \frac{3t_3}{4} \rho^\alpha \delta(\vec{r}_{12}) \quad (10)$$

The local equivalent of the finite range knockon exchange is calculated with Eq. (7). Two approximations were used for the overlap density,

$$\rho = (\rho_1(r_1)\rho_2(r_2))^{1/2} \quad (11)$$

and

$$\rho = \frac{1}{2}(\rho_1(r_1) + \rho_2(r_2)) \quad (12)$$

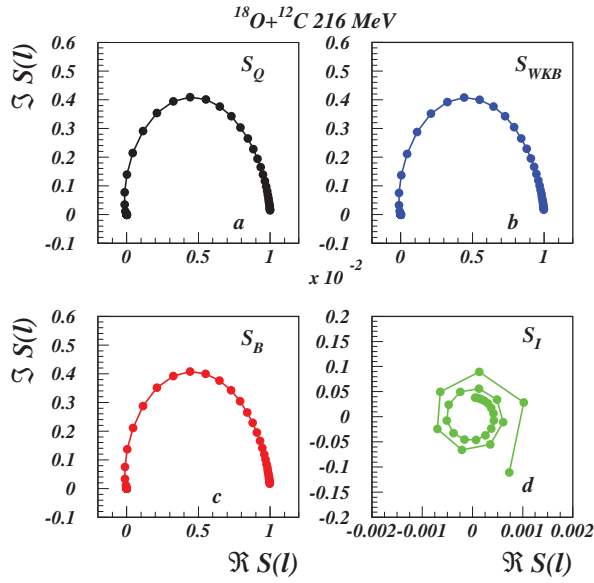


FIGURE 13. (Color online) Argand diagram for the semiclassical S-matrix based on the WS potential equivalent to JLM1. The barrier trajectory (panel c) is identical to the exact quantum result (panel a). The small internal barrier component (panel d) shows a hint of an orbiting effect or the presence of Regge poles, but these are too far from the real axis to have noticeable effect in the total cross section.

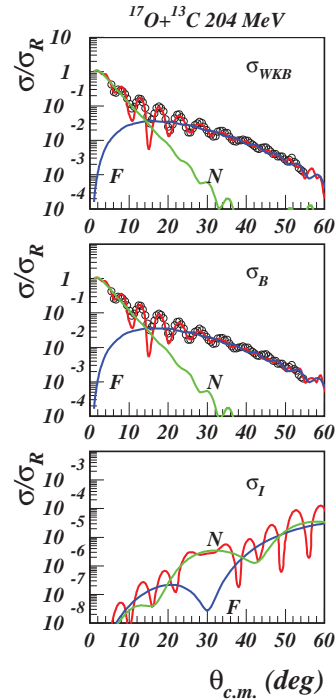


FIGURE 14. Semiclassical (WKB) calculation of the cross section based on the T1 potential Table 1. The barrier component match perfectly the data in the entire angular range, while the internal barrier component is negligibly small.

The calculated OM potentials are dubbed GOGNY1 and GOGNY3 respectively. Both definitions represent crude approximations of the overlap density but are widely used in the estimation of the density dependence effects in the folding model.

We further examine the density dependence effects by using the nuclear matter approach of Jeukenne, Lejeune and Mahaux (JLM) [14] which incorporates a complex, energy and density dependent parametrization of the NN effective interaction obtained in a Brueckner Hartree-Fock approximation from the Reid soft core NN potential. The systematic study [11] of the elastic scattering between p -shell nuclei at energies around 10 MeV/nucleon leads to the surprising result that on average, the imaginary part of the folded JLM potential was perfectly adequate to describe such reactions and did not need any renormalization ($N_W = 1.00 \pm 0.09$), while the real component needed a substantial renormalization, in line with other effective interactions used in folding models. We examine here to which extent this feature is conserved for tightly bound nuclei in the d shell in the presence of a small neutron excess. Exchange effects are included in this model at the level of N-target interaction. Calculations with this model are dubbed JLM1 and JLM3, depending on which definition we use for the overlap density (Eqs.(11) and (12) respectively).

A grid search on the real volume integral reveals a unique solution for all six versions of the effective interaction, see Table 2 and Figs 5, 6, 7 and 8. The folding model validates only the solution with the lowest real volume integral found with the WS parametrization. Averaging over all six folding calculations, we find $J_V = 167 \pm 9$ MeV fm³ for ¹⁸O and $J_V = 194 \pm 5$ MeV fm³ for ¹⁷O and so the interaction of ¹⁷O is slightly more refractive. Again imaginary volume integrals are quite small pointing to a some transparency of the potential. Correction due to the finite range effects are quite large, of the order of $\Delta R \approx 0.5$ fm for the real potential and much larger for the imaginary potential. The folding calculation reproduces perfectly the diffractive pattern at forward angles and the Fraunhofer F/N crossover produces always an interference maximum. Beyond the cross-over the far-side component decays quite smoothly and shows some glory effects at $\theta > 60^\circ$.

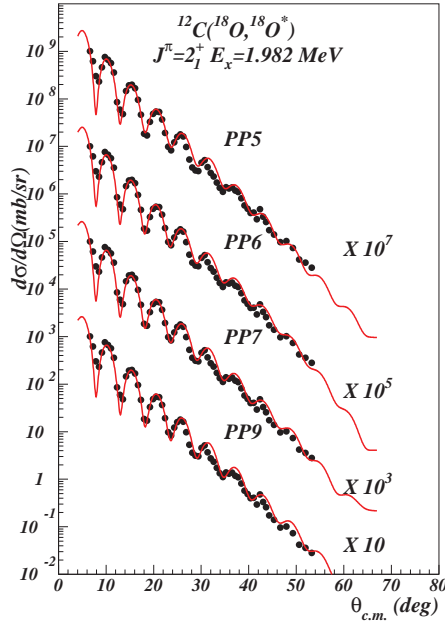


FIGURE 15. (Color online) Inelastic cross section to 2_1^+ (1.982 MeV) state in ^{18}O . The DWBA calculation is based on the potentials in Table 1.

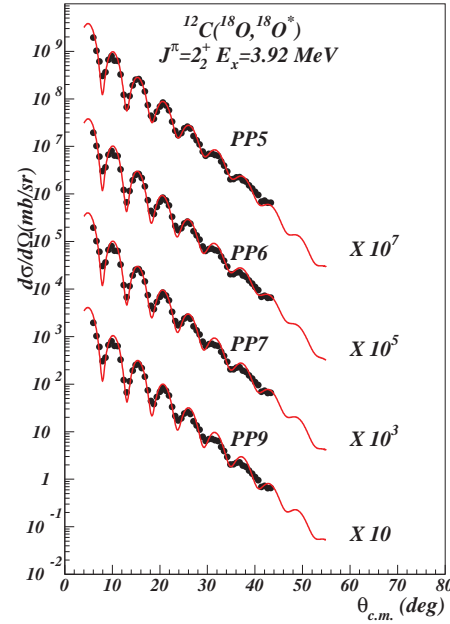


FIGURE 16. (Color online) Inelastic cross section to 2_2^+ (3.92 MeV) state in ^{18}O . The DWBA calculation is based on the potentials in Table 1.

A close examination of the results in Table 2 shows that we have obtained consistent results for all effective interactions used in the folding model. Our results confirm the conjecture that one can extract from the elastic scattering at best only the low momenta of the interaction (volume integrals and *rms* radii). Corrections in the range parameters are large especially for the imaginary component of the optical potential. We found substantial renormalization for the real part of the optical potential, on average $N_V = 0.36 \pm 0.05$ in line with the previous study [11]. This can be easily understood: the bare folding formfactor has a volume integral around $J_V \approx 450 \text{ MeV fm}^3$, while the data requires precise values around $160\text{--}190 \text{ MeV fm}^3$. Noteworthy, the renormalization of the imaginary component in the JLM model is again quite close to unity. Although the density dependence in the GOGNY and JLM effective interactions is very different, one cannot disentangle between the two models for the overlap density based on the present data, since both of them give identical results.

SEMICLASSICAL BARRIER AND INTERNAL BARRIER AMPLITUDES

Once we have established the main features of the average OM potential, we turn now to study the reaction mechanism using semiclassical methods.

The semiclassical uniform approximation for the scattering amplitude of Brink and Takigawa [26] is well adapted to describe situations in which the scattering is controlled by at most three active, isolated, complex turning points. An approximate multireflection series expansion of the scattering function can be obtained, the terms of which have the same simple physical meaning as in the exact Debye expansion for the scattering of light on a spherical well. The major interest in this theory comes from the fact that it can give precious information on the response of a nuclear system to the nuclear interior.

We take as an example the potential PP9 in Table 1 which is a WS phase equivalent to the JLM1 optical potential. We discard the absorptive term and define the effective potential as,

$$V_{eff}(r) = V(r) + \frac{\hbar^2}{2\mu} \frac{\lambda^2}{r^2}, \quad \lambda = \ell + \frac{1}{2} \quad (13)$$

where the Langer prescription has been used for the centrifugal term. This guarantees the correct behavior of the semiclassical wave function at the origin. Then we calculate the deflection function,

$$\Theta(\lambda) = \pi - 2 \int_{r_1}^{\infty} \frac{\sqrt{\frac{\hbar^2}{2\mu} \lambda dr}}{r^2 \sqrt{E_{c.m.} - V_{eff}}} \quad (14)$$

where r_1 is the outer zero of the square root, i.e. the radius of closest approach to the scatterer and μ is the reduced mass. Note that with the replacement $\hbar\lambda = b\sqrt{2\mu E}$, Eq. 14 becomes identical with the classical deflection function $\Theta(b)$, where b is the impact parameter. The result is shown in Fig. 9. The behavior of $\Theta(\lambda)$ is the one expected for an attractive nuclear potential. The nuclear rainbow angle is $\theta_R \approx 36^\circ$. All the measured angular range is classically illuminated and only a few points were measured in the dark side. This explains partially the ambiguities found with the WS formfactors.

However this simple calculation does not provide too much information about the interference effects of the corresponding semiclassical trajectories. Going into the complex r -plane we search for complex turning points, i.e. the complex roots of the quantity $E_{c.m.} - V_{eff} - iW$. This is an intricate numerical problem, because, for a WS optical potential, the turning points are located near the potential singularities and there are an infinite number of such poles. The situation for integer angular momenta is depicted in Fig. 10. Active turning points are located near the poles of the real formfactor. Inactive turning points are located quite far from the real axis and give negligible small contribution to the total S-matrix. We observe an ideal situation with three, well isolated, turning points for each partial wave. The multireflection expansion of the scattering function in the Brink-Takigawa approach reads,

$$S_{WKB}(\ell) = \sum_{q=0}^{\infty} S_q(\ell) \quad (15)$$

where,

$$S_0(\ell) = \frac{\exp(2i\delta_1^\ell)}{N(S_{21}/\pi)} \quad (16)$$

and for $q \neq 0$,

$$S_q(\ell) = (-)^{q+1} \frac{\exp[2i(qS_{32} + S_{21} + \delta_1^\ell)]}{N^{q+1}(S_{21}/\pi)} \quad (17)$$

In these equations δ_1^ℓ is the WKB (complex) phase shift corresponding to the turning point r_1 , $N(z)$ is the barrier penetrability factor,

$$N(z) = \frac{\sqrt{2\pi}}{\Gamma(z + \frac{1}{2})} \exp(z \ln z - z) \quad (18)$$

and S_{ij} is the action integral calculated between turning points r_i and r_j ,

$$S_{ij} = \int_{r_i}^{r_j} dr \left\{ \frac{2\mu}{\hbar^2} [E_{c.m.} - V_{eff} - iW] \right\}^{1/2} \quad (19)$$

S_{21} and S_{32} are independent of the integration path provided they lie on the first Riemann sheet and collision with potential poles is avoided. Each term in Eq. 15 has a simple physical interpretation. The first term (the barrier term, denoted also S_B) retains contributions from trajectories reflected at the barrier, not penetrating the internal region. The q th term corresponds to trajectories refracted q times in the nuclear interior with $q-1$ reflections at the barrier turning point r_2 . Summation of terms $q \geq 1$ can be recast into a single term,

$$S_I = \frac{\exp[2i(S_{32} + S_{21} + \delta_1^\ell)]}{N(S_{21}/\pi)^2} \frac{1}{1 + \exp[2iS_{32}]/N(S_{21}/\pi)} \quad (20)$$

and is known as the internal barrier scattering function. The last factor in Eq. 20, the enhancement factor, is responsible for the multiple reflections of the wave within the potential pocket. When the absorption in the nuclear interior is large, the enhancement factor reduces to unity. Since the semiclassical scattering function is decomposed additively, $S_{WKB} = S_B + S_I$, the corresponding total scattering amplitude is decomposed likewise as $f_{WKB} = f_B + f_I$ and conveniently the

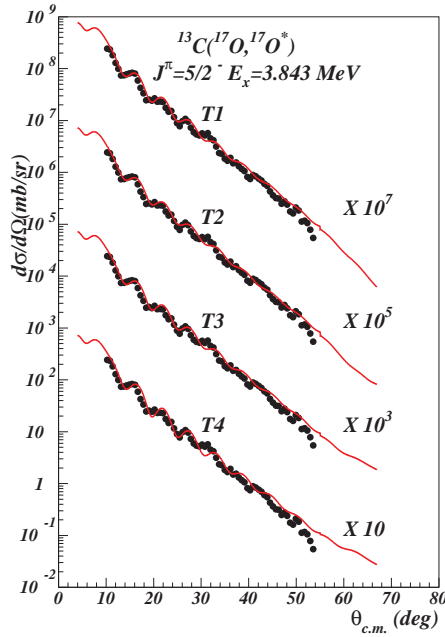


FIGURE 17. (Color online) Inelastic cross section to $5/2^-$ (3.84 MeV) state in ^{17}O . The DWBA calculation is based on the potentials in Table 1.

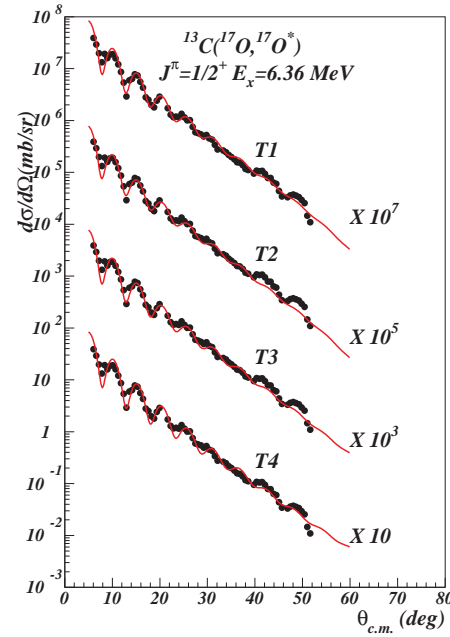


FIGURE 18. (Color online) Inelastic cross section to $1/2^+$ (6.36 MeV) state in ^{17}O . The DWBA calculation is based on the potentials in Table 1.

corresponding barrier and internal barrier angular distributions are calculated as $\sigma_{B,I} = |f_{B,I}|^2$, using the usual angular momentum expansion of the amplitudes.

The poles of the semiclassical S-matrix are given by,

$$N(i\varepsilon) + e^{2iS_{32}} = 0 ; \quad \varepsilon = -\frac{i}{\pi} S_{21} \quad (21)$$

Semiclassical Regge poles of Eq. 21 are too far from the real axis to have a noticeable influence on the total cross section. The accuracy of the semiclassical calculation has been checked by comparing the barrier and internal barrier absorption profiles with the exact quantum-mechanical result in Fig. 11. One observes that the semiclassical B/I expansion is an *exact* decomposition of the quantum result. They are virtually identical at the scale of the figure. The internal component gets significant values up to the grazing angular momentum ($\ell_g=36$) and is negligible small beyond this value. The barrier component resembles a strong absorption profile and this justifies the interpretation that it corresponds to that part of the flux not penetrating into the nuclear interior. Second, the B/I components are almost decoupled in the angular momentum space and therefore they will contribute in different angular ranges.

Semiclassical cross sections are compared with the data in Fig. 12. Better insight into this technique is obtained by further decomposing the B/I components into far and near (BF/BN and IF/IN) subcomponents. Clearly, the barrier component dominates the entire measured angular range. Fraunhofer diffractive oscillations appear as the result of BF and BN interference. At large angles, the internal contribution is negligible and the reaction is peripheral.

The Argand diagrams corresponding to the B/I decomposition is displayed in Fig. 13. The barrier amplitude (panel c) is almost identical with the exact quantum result (panel a) while the internal barrier component shows a nice orbiting effect, but the corresponding dynamical content ($S_I(\ell)$) is too small to have any sizeable effect in the total cross section.

A similar analysis was performed for the reaction $^{17}\text{O}+^{13}\text{C}$ based on the WS potential, parameter set T1 Table 1. Again we find that the WKB cross section is identical with the exact quantum result based on the same potential. The barrier component match perfectly the data in the entire angular range, while the internal barrier component gives negligible contribution, see Fig.14. Thus the peripherality character of our reactions is completely demonstrated.

INELASTIC TRANSITIONS

TABLE 3. Average deformation obtained from inelastic scattering.

Nucleus	J^π	β_λ
^{17}O	$5/2^-$	0.66 ± 0.03
^{17}O	$1/2^+$	0.19 ± 0.01
^{18}O	2_1^+	0.38 ± 0.04
^{18}O	2_2^+	0.52 ± 0.05

We examine in this section the ability of our optical potentials to describe the measured data for inelastic transitions to selected states in ^{18}O ($J^\pi = 2_1^+$, $E_x = 1.982$ MeV, Fig. 15 and $J^\pi = 2_2^+$, $E_x = 3.92$ MeV, Fig. 16) and two transitions in ^{17}O ($J^\pi = \frac{5}{2}^-$, $E_x = 3.843$ MeV, Fig. 17 and $J^\pi = \frac{1}{2}^+$, $E_x = 6.36$ MeV, Fig. 18).

The pattern of our data shows a clear diffractive character since they obey fairly well to the Blair phase rule [27] and therefore a standard DWBA should be an appropriate approach. The deformation table [28] indicates a quadrupole deformation $\beta_2 = 0.107$ for ^{18}O . The systematic by Raman *et al.*[29] gives a value of 0.355(8). Since the DWBA cross section scales with β_2^2 , we execute a number of calculations using $\beta_2 = 0.015 - 0.6$, chosen rather arbitrary in the range of suggested values. DWUCK4 and FRESKO give identical shapes for these values using the usual formfactor for inelastic transitions $V_\lambda = -\frac{\delta_\lambda}{\sqrt{4\pi}} \frac{dU}{dr}$ where δ_λ is the deformation length and U is the potential. Optimum deformation parameters were obtained by averaging over various optical potentials and different angular ranges in the angular distributions. The scaled calculations that match the data are shown in Fig. 15 and Fig. 16 and the optimum deformation parameters are given in Table 3.

The shape of the calculated cross section is virtually identical for all the potentials at the scale of the figure. This proves once again that our potentials are almost phase equivalent, small differences appearing only at large angles much beyond the measured angular range. Remarkably, the calculation with the PP9 parameter set, which is a WS potential phase equivalent to JLM1 folding potential describes the data as well as the other parameter sets. The situation is similar for the other folding potentials. Thus we have obtained a consistent description of both elastic and inelastic cross section using a large palette of optical potentials.

The pattern of the measured transitions in ^{17}O is quite different. The cross section decays almost exponentially at large angles with small amplitude wiggles. The experimental study by Cunsolo *et al.*[30] using three particle transfer reaction showed that the low-lying negative parity state in ^{17}O , $J^\pi = \frac{5}{2}^-$, $E_x = 3.843$ MeV is a member of ^{16}O K^+ α -rotational band coupled to $p_{1/2}$ neutron, and thus has a pure $4p - 3h$ configuration. The state $J^\pi = \frac{1}{2}^+$, $E_x = 6.36$ MeV, located only 3 keV bellow the α threshold in ^{17}O is weakly populated in the reaction $^{13}\text{C}(^6\text{Li},d)^{17}\text{O}$ [31]. This state is astrophysically important since it is considered the main source of the $^{13}\text{C}(\alpha,n)^{16}\text{O}$ reaction rate uncertainty. According to Cunsolo *et al.*[32] this state has a dominant $3p - 2h$ structure and belongs to a $(sd)^3$, $T=1/2$ ^{17}O rotational band. Repeating the procedure used for ^{18}O , we obtain a satisfactory description of our data with the deformation parameters given in Table III, see Figs. 17 and 18.

CONCLUSIONS

We have measured elastic scattering cross sections for $^{18}\text{O}+^{12}\text{C}$ and $^{17}\text{O}+^{13}\text{C}$ at 12 MeV/nucleon as well as inelastic transition to selected states in $^{18}\text{O}^*$ and $^{17}\text{O}^*$ in order to determine the optical potentials needed to study the one neutron pickup reaction $^{13}\text{C}(^{17}\text{O},^{18}\text{O})^{12}\text{C}$. Optical potentials in both incoming and outgoing channels were extracted from a standard analysis using Woods-Saxon formfactors. Analysis in terms of semimicroscopic double folding formfactors, using six different approximations for the NN effective interactions helped us to eliminate the ambiguities found with WS potentials. Thus a unique solution emerged from the analysis, which is quite surprising when the reaction mechanism is dominated by strong absorption. We found that the neutron excess over the closed d shell leads to a less refractive interaction as compared with the closed shell nucleus ^{16}O . We found that the absorptive component of the JLM is adequate for the d shell heavy ion interaction. The well known Gogny effective interaction, designed mainly for HFB calculations gives excellent results for scattering provided that the knockon exchange and isovector components are properly included. A detailed semiclassical analysis in terms of barrier and internal barrier amplitudes

of Brink and Takigawa demonstrated that the flux penetrating the barrier has negligible contribution to the total cross section, and thus the reactions are peripheral. This provides a complete justification for the use of ANC method to extract spectroscopic information from the transfer reaction.

ACKNOWLEDGMENTS

This work was supported by CNCSIS (Romania) Grant PN-II-PCE-55/2011. T. A-A. thanks the Hashemite University for support. We thanks V. Balanica for technical support and to dr. Vlad Avrigeanu for correspondence.

REFERENCES

1. A. Garcia, E. G. Adelberger, P. V. Magnus, D. M. Markoff, K. B. Swartz, M. S. Smith, K. I. Hahn, N. Bateman and P. D. Parker, *Phys. Rev.* **C43**, 2012 (1991).
2. R. K. Wallace and S. E. Woosley, *Astrophys. J. Suppl. Ser.* **45**, 389 (1981).
3. B. C. Robertson, J. T. Sample, D. R. Goosman, K. Nagatani and K. W. Jones, *Phys. Rev.* **C4**, 2176 (1971).
4. S. Szilner, M. P. Nicoli, Z. Basrak, R. M. Freeman, F. Haas, A. Morsad, M. E. Brandan, and G. R. Satchler, *Phys. Rev.* **C64**, 064614 (2001).
5. A. T. Rudchik *et al.*, *Eur. Phys. J.* **A44**, 221 (2010).
6. M. C. Mermaz, M. A. G. Fernandes, A. Greiner, B. T. Kim and N. Lisbona, *Phys. Rev.* **C19**, 794 (1979).
7. B. Heusch, C. Beck, J. P. Coffin, P. Engelstein, R. M. Freeman, G. Guillaume, F. Haas, and P. Wagner, *Phys. Rev.* **C26**, 542 (1982).
8. D. M. Pringle, W. N. Catford, J. S. Winfield, D. G. Lewis, N. A. Jelley, K. W. Allen and J. H. Coupland, *Nucl. Instrum. Methods Phys. Res.* **A245**, 230 (1986).
9. S. Kowalski and H. A. Enge, computer code RAYTRACE (unpublished), University of Oxford, England, UK, 1986.
10. A. M. Mukhamedzhanov, V. Burjan, F. Carstoiu, J. Cejpek, H. L. Clark, C. A. Gagliardi, Y.-W. Lui, V. Kroha, L. Trache, R. E. Tribble, H. M. Xu and X. G. Zhou, *Phys. Rev.* **C56**, 1302 (1997).
11. L. Trache, A. Azhari, H. L. Clark, C. A. Gagliardi, Y.-W. Lui, A. M. Mukhamedzhanov, X. Tang, N. Timofeyuk, R. E. Tribble and F. Carstoiu, *Phys. Rev.* **C61**, 024612 (2000).
12. Yu. A. Glukhov, S. A. Goncharov, A. S. Dem'yanova, A. A. Ogloblin, M. V. Rozhkov, V. P. Rudakov, V. Trashka, *J. Izv. Ross. Akad. Nauk, Ser. Fiz.* **65**, 647 (2001).
13. N. Anantaraman, H. Toki and G. F. Bertsch, *Nucl. Phys.* **A398**, 269 (1983).
14. J. P. Jeukenne, A. Lejeune and C. Mahaux, *Phys. Rev.* **C16**, 80 (1977).
15. M. Beiner and R. J. Lombard, *Ann. Phys. (N.Y.)* **86**, 262 (1974).
16. I. Angeli, *Heavy Ion Physics*, **8**, 23 (1998).
17. Dao T. Khoa, Hoang Sy Than, Tran Hoai Nam, Marcella Grasso, and Nguyen Van Giai *Phys. Rev. C* **69**, 044605 (2004).
18. F. Carstoiu and M. Lassaut, *Nucl. Phys.* **597**, 269 (1996).
19. Dao T. Khoa, *Phys. Rev.* **C63**, 034007 (2001).
20. X. Campi and A. Bouyssi, *Phys. Lett.* **73B**, 263 (1978).
21. J. W. Negele and K. Yazaki, *Phys. Rev. Lett.* **47**, 71 (1981).
22. D. Gogny, *Proc. Int. Conf. on Nucl. Physics, Munich 1973*, eds J. de Boer and H. J. Mang, Vol. 1, p. 48.
23. D. H. Youngblood, H. L. Clark and Y.-W. Lui, *Phys. Rev. Lett.* **82**, 691 (1999).
24. G. Colo, N. Van Giai, P. F. Bortignon and M. R. Quaglia, *Phys. Lett.* **B485**, 362 (2000).
25. J. P. Auger and R. J. Lombard, *Phys. Lett.* **90B**, 200 (1980).
26. D. M. Brink and N. Takigawa, *Nucl. Phys.* **A279**, 159 (1977).
27. J. S. Blair, *Phys. Rev.* **115**, 928 (1959).
28. P. Möller, J. R. Nix, W. D. Myers and W. J. Swiatecki, *At. Data Nucl. Data Tables* **59**, 185 (1995).
29. S. Raman, C. W. Nestor, Jr. and P. Tikkanen, *Atomic Data and Nuclear Data Tables* **78**, 1 (2001).
30. A. Cunsolo, A. Foti, G. Immé, G. Pappalardo, G. Raciti, N. Saunier, *Phys. Rev.* **C24**, 2127 (1981).
31. S. Kubono, K. Abe, S. Kato, T. Teranishi, M. Kurokawa, X. Liu, N. Imai, K. Kumagai, P. Strasser, M. H. Tanaka, Y. Fuchi, C. S. Lee, Y. K. Kwon, L. Lee, J. H. Ha and Y. K. Kim, *Phys. Rev. Lett.* **90**, 062501 (2003).
32. A. Cunsolo, A. Foti, G. Immé, G. Pappalardo and G. Raciti, *Phys. Lett.* **124B**, 439 (1983).

Investigating $^{13}\text{C} + ^{12}\text{C}$ reaction by the activation method. Sensitivity tests

Daniela Chesneanu, L. Trache, R. Margineanu, A. Pantelica, D. Ghita, M. Straticiuc, I. Burducea, A. M. Blebea-Apostu, C. M. Gomoiu, and X. Tang

Citation: [AIP Conference Proceedings](#) **1645**, 311 (2015); doi: 10.1063/1.4909592

View online: <http://dx.doi.org/10.1063/1.4909592>

View Table of Contents: <http://scitation.aip.org/content/aip/proceeding/aipcp/1645?ver=pdfcov>

Published by the [AIP Publishing](#)

Articles you may be interested in

[Oscillation rheometry – method for processing stability testing of high sensitive polymers](#)

[AIP Conf. Proc.](#) **1662**, 030009 (2015); 10.1063/1.4918884

[Testing the quasi-absolute method in photon activation analysis](#)

[AIP Conf. Proc.](#) **1525**, 412 (2013); 10.1063/1.4802360

[Fusion and Reaction Functions: a New Method to Investigate Reaction Mechanisms](#)

[AIP Conf. Proc.](#) **1245**, 86 (2010); 10.1063/1.3448018

[Sensitivity of Activation Cross Sections of Tungsten to Nuclear Reaction Mechanisms](#)

[AIP Conf. Proc.](#) **769**, 1501 (2005); 10.1063/1.1945289

[Investigation of the reliability of density functional methods: Reaction and activation energies for Si–Si bond cleavage and H₂ elimination from silanes](#)

[J. Chem. Phys.](#) **104**, 148 (1996); 10.1063/1.470885

Investigating $^{13}\text{C}+^{12}\text{C}$ Reaction by the Activation Method. Sensitivity Tests

D. Chesneanu^{a)}, L. Trache, R. Margineanu, A. Pantelica, D. Ghita, M. Straticiuc,

I. Burducea, A.M. Blebea-Apostu, C.M. Gomoiu

¹*Horia Hulubei National Institute for Physics and Nuclear Engineering, P.O. Box MG-6, 077125
Bucharest-Magurele, Romania*

X. Tang

²*Institute of Modern Physics, CAS, 509 NANCHANG ROAD, LANZHOU, GANSU, 730000, China.*

^{a)}Corresponding author: chesneanu@nipne.ro

Abstract. We have performed experiments to check the limits of sensitivity of the activation method using the new 3 MV Tandatron accelerator and the low and ultra-low background laboratories of the “Horia Hulubei” National Institute of Physics and Nuclear Engineering (IFIN-HH). We have used the $^{12}\text{C}+^{13}\text{C}$ reaction at beam energies $E_{\text{lab}} = 6, 7$ and 8 MeV. The knowledge of this fusion cross section at deep sub-barrier energies is of interest for astrophysical applications, as it provides an upper limit for the fusion cross section of $^{12}\text{C}+^{12}\text{C}$ over a wide energy range. A ^{13}C beam with intensities 0.5 – 2 particle/ μA was provided by the accelerator and used to bombard graphite targets, resulting in activation with ^{24}Na from the $^{12}\text{C}(^{13}\text{C}, p)$ reaction. The 1369 and 2754 keV gamma-rays from ^{24}Na de-activation were clearly observed in the spectra obtained in two different laboratories used for measurements at low and ultralow background: one at the surface and one located underground in the Unirea salt mine from Slanic Prahova, Romania. In the underground laboratory, for $E_{\text{lab}} = 6$ MeV we have measured an activity of 0.085 ± 0.011 Bq, corresponding to cross sections of 1 – 3 nb. This demonstrates that it is possible to measure ^{12}C targets irradiated at lower energies for at least 10 times lower cross sections than before. β – γ coincidences will lead us another factor of 10 lower, proving that this installations can be successfully used for nuclear astrophysics measurements.

INTRODUCTION

With the final goal of establishing a solid line of research in nuclear astrophysics (NA) at the Bucharest accelerators and laboratories of IFIN-HH, we have performed experiments to check the limits of one method that seems appropriate and for which the institute has or could acquire installations: the activation method. We used for irradiation one of the new tandem accelerators which can provide good intensities for light ions and the low and ultralow background laboratories, situated above ground and underground, respectively, for activation measurements. We have chosen the $^{13}\text{C}+^{12}\text{C}$ reaction, which leads to an activation appropriate for our tests: ^{24}Na , with a half-life of 15.0 hours, formed by one proton evaporation.

Nuclear astrophysics, or more precisely nuclear physics for astrophysics, is becoming more and more an explicit motivation for nuclear physics research, for European laboratories programs, in the USA, Japan and China, but also for the ones from Romania: through direct measurements (at low energies as in stars) or indirect methods (at the most common energies in nuclear physics laboratories). Direct measurements are very difficult because of the low cross sections involved and require dedicated facilities: proton or alpha particle accelerators of very high intensities at low energies and, if possible, low background and special detection systems. Such a facility did not exist in Romania and therefore, direct measurements were not made in Romania. The use of indirect methods involve typically radioactive beams, which were also not available locally. We wanted to prove that we can do direct measurements now, using newly available installations [1,2].

The reaction $^{12}\text{C} + ^{12}\text{C}$ in the low energy region is of great interest in astrophysics (see eg [3].) because of its essential role in studying a wide range of burning scenarios in carbon-rich stellar environments. It is important for understanding carbon burning nucleosynthesis that occurs in stars with more than 10 solar masses during late evolutionary periods [4], in intermediate mass stars (8-10 solar masses), which can lead a detonation wave and a supernova explosion [5], in binary systems, where a massive carbon-oxygen white dwarf exceeds the Chandrasekhar mass limit accumulating material from its partner star. The temperatures at which the carbon burnout occurs are found in the range of 0.5-1.2 GK corresponding to the center-of-mass energy range of 1 to 3 MeV. To verify all these scenarios and put constraints on models requires a detailed knowledge of the carbon fusion processes at these energies. Considerable efforts have been made to measure the cross section of $^{12}\text{C} + ^{12}\text{C}$ reaction at astrophysical energies, involving both the detection of charged particles and gamma-ray spectroscopy. However, previous measurements were made for $E_{\text{c.m.}} \geq 2.1$ MeV, the upper region of astrophysical interest. Also, as $E_{\text{c.m.}} = 3.0$ MeV cross sections reported are not consistent and are quite uncertain [6-8]. Moreover, the extrapolation procedure in the case of $^{12}\text{C} + ^{12}\text{C}$ from current experimental data at ultra-low energies is complicated by the presence of possible resonant structures even in the low energy excitation function. Measurements that could extend to below $E_{\text{c.m.}} = 2.1$ MeV would be extremely important. It was found, however, that the $^{13}\text{C} + ^{12}\text{C}$ and $^{13}\text{C} + ^{13}\text{C}$ reactions do not have such resonances and provide material for understanding fusion at low energies, and ways to determine the maximum cross section for the reaction $^{12}\text{C} + ^{12}\text{C}$.

A University of Notre Dame group [9] has proposed a $^{13}\text{C} + ^{12}\text{C}$ experiment in collaboration with us and a group of Lanzhou, China at 3 MV Tandem from IFIN-HH. It is the motivation for our choice of measurements here: irradiations with a ^{13}C beam followed by measurement of activities at both surface and underground laboratory characterized by an ultra-low background radiation.

EXPERIMENTAL METHODS FOR INVESTIGATION OF THE $^{12}\text{C} + ^{13}\text{C}$ REACTION BY THE ACTIVATION METHOD

The *HVEE Tandetron 3 MV electrostatic accelerator* - recently installed at IFIN-HH is dedicated to:

- 1) Ion Beam Analysis (IBA) - analytical techniques that use accelerated ion beams: Rutherford backscattering spectrometry (RBS), X-ray emission induced by charged particles (PIXE), nuclear reaction analysis (NRA), etc.
- 2) Testing the radiation resistance of the materials or implants.
- 3) Nuclear astrophysics.

For nuclear astrophysics we assess that this facility is suitable for direct measurements of cross sections induced by α particles (He-burning) and light ions (^6Li , ^{12}C , ^{13}C , ^{16}O ...), due to relatively low energies and high intensities and its stable functioning, as tested by us last year.

The *GammaSpec laboratory* is an above ground installation in IFIN-HH main campus, in the same location as the tandem accelerators, consisting of a HpGe detector very well shielded, and carefully calibrated with sources and international inter-laboratory comparisons [10, 11].

The *Underground Laboratory in the Unirea salt mine, Slanic Prahova (MicroBequerel or " μBq ")*, is located in a salt mine, about 2 hours drive North of Bucharest. Environmental conditions in the salt mine are very stable year round: temperature between 12 and 13° C, humidity 67-70% approximately, area of $\sim 70,000 \text{ m}^2$, height between 52 and 57 m, depth is 208 m below ground (approximately 600 m.w.e), the distance between the walls is between 32 and 36 m, volume is $2.9 \times 10^6 \text{ m}^3$ [12]. In this mine a laboratory was built to perform measurements using gamma-ray spectrometry in ultralow radiation background. The average dose underground was found $1.29 \pm 0.30 \text{ nSv/h}$, approximately 70-80 times lower than the dose at the surface. As ambient background radiation comes from: i) natural radioactivity (especially from the decay of ^{238}U , ^{232}Th and ^{222}Rn present in the atmosphere and ^{40}K); ii) cosmic rays (μ , ^1H , ^3H ; ^7Be , ^{14}C ...); and iii) neutrons from (α , n) reactions and fission, the i) and iii) sources are particularly low in this mine due to its thick and compact salt walls. Figure 1 compares γ -ray spectra measured above ground and underground. The top spectrum shows that the strongest component of the γ rays spectrum at $E_\gamma < 3\text{MeV}$ is associated with the natural environment radioactivity and exhibits intense characteristic lines. At higher energies, the background radiation originates mostly from cosmic rays. The natural radioactivity is significantly reduced for measurements in the underground laboratory (bottom spectrum). From Fig. 1 it can be seen that the measured background radiation (using a protection shield consisting of 15 cm Pb and 5 cm Cu produced by Canberra Ind.) is about 4000 times smaller compared to the background spectrum measured at the surface. This is the major advantage we want to test and use in the current measurements [13, 14].

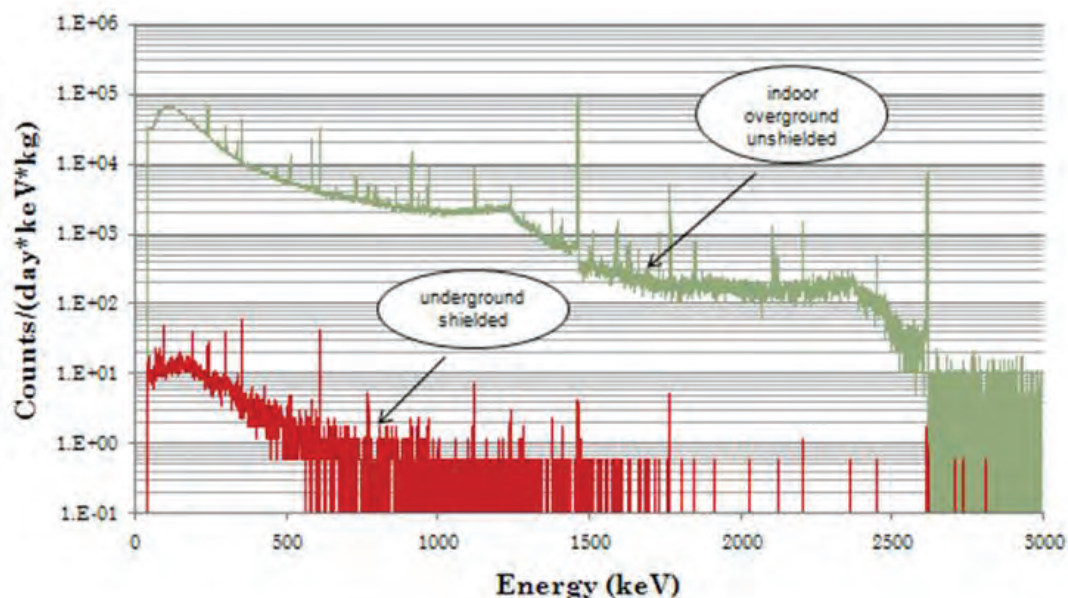


FIGURE 1. Typical spectrum of γ rays measured at the Earth's surface and underground

EXPERIMENTAL RESULTS

In this experimental phase we studied $^{12}\text{C} + ^{13}\text{C}$ fusion reaction in the laboratory energy range of 6 to 8 MeV. A $^{13}\text{C}^{+3}$ beam with intensity 0.5 μA , at the first irradiation ($E_{\text{lab}}=8$ MeV), and 1.9 μA , for the irradiations at energies $E_{\text{lab}}=6$ and 7 MeV, provided by the 3 MV Tandatron accelerator, impinging on a 1 mm thick natural carbon (graphite) target. A gas stripper system was used to increase the intensity of the $^{13}\text{C}^{+3}$ charge state.

Cross section of the $^{12}\text{C}(^{13}\text{C}, p)^{24}\text{Na}$ reaction can be determined by measuring the γ radiation corresponding to nucleus ^{24}Na ($T_{1/2} = 15.00$ h), using the activation method. The irradiated carbon targets were measured in the GammaSpec laboratory and in the underground laboratory. The cascading γ rays (1369 and 2754 keV) were detected with germanium detectors. The detection systems have been protected with lead castles to reduce ambient background radiation. The first case studied was a C target irradiated for 15 hours with an 8 MeV beam. γ rays were measured in the underground laboratory 4 times successively, 82.000 s each measurement (comparable to $T_{1/2}$ of ^{24}Na) using a germanium detector with 120% relative efficiency, in a protective castle as described before. We found an activity of 4.44 ± 0.19 Bq and evaluated the minimal detectable activity at 0.048 Bq. In the four the γ -ray spectra we could observe the decreasing activity of the irradiated target and the gradual relative increase of the background radiation.

The following two steps consisted of the activation of C targets at two different beam energies, 6 and 7 MeV, and from measuring them both in the underground laboratory and in the GammaSpec laboratory located at the surface. In this latter laboratory, the spectrometric system is based on an Ortec HPGe detector 30185 GEM, resolution 2.1 keV at 1332 keV of ^{60}Co , and relative efficiency 30% (compared to 3 "x 3" NaI (Tl) standard). This spectrometric system is protected by a lead cylindrical shield (10 cm thick), covered on the inside with tin (1 mm thick) and copper (1.5 mm thick) foils. Thus for γ rays of energies between 20 and 2750 keV in a 24 hours measurement one obtains a count rate of 1.2-1.8 events/sec (depends mainly on the concentration of ^{222}Rn in natural background).

For the target irradiated (23 hours) at $E_{\text{lab}} = 7$ MeV, and measured in the GammaSpec laboratory, the beam intensity was 1.87 μA , yielding an activity at the end of irradiation equal with 5.20 ± 0.40 Bq. This activity was calculated after corrections were made for the efficiency and the time needed to transport the target from the reaction chamber to the GammaSpec laboratory. For measurements made in the underground laboratory another C target was irradiated using the same parameters, but for a longer irradiation time of about 25 hours.

Activity values measured in the two laboratories are shown in Tables 1 and 2; the two sets of measurements gave comparable results, within the evaluated uncertainties. The incident ^{13}C beam energy (E_{lab}) in MeV, beam current (I) in μA , and counting time of the irradiated targets (t_c) in seconds are also given in these tables. Knowing the activated targets activity at the measurement moment and the background rate of accumulation we determined the limit of detection for the evaluation of the $^{12}\text{C} + ^{13}\text{C}$ fusion reaction cross sections. The minimum measurable cross section results to be about 3 nb using beam intensity around 0.6 μA (particle μA , $^{13}\text{C}^{+3}$ charge state), as in these cases. That is an order of magnitude below the lowest value measured until now in other laboratories. Increasing the beam intensity to approximately 6-10 μA , it is possible to decrease the limit of detection of 10 more times, so we can measure at the energies lower than those now existing in the literature.

Tests conducted at the lowest $E_{\text{lab}}(^{13}\text{C}) = 6$ MeV have revealed low activities of the activated targets, but to which the experimental setups are still sensitive. Barely in the surface lab, but clearly in the underground one (see Fig. 2) [15]. Reducing the limit by an order of magnitude is still possible by increasing the beam intensity. There will be, however, limitations on the extent to which the current intensity can be increased without damaging the targets. A high current beam raises problems with sputtering effect (some produced ^{24}Na 's are sputtered away from the target surface during irradiation) and with heating effects. In a test at 10 μA we had visible signs of carbon sputtering from the target. For future measurements it will be necessary to construct a target cooling system. But again there is a limitation on how heat can be dissipated in the target.

Another way to improve the signal-to-noise ratio in de-activation measurements is using the β - γ coincidence method. This method allows to suppress the ambient background γ rays from natural radioactive isotopes such as ^{40}K and ^{208}Tl . In the Notre Dame experiment the peaks at 1369 keV and 2754 keV of ^{24}Na could be observed only in the β gated γ -ray spectra. It is obvious that this experimental setup made now at IFIN-HH, will allow decreasing the total fusion cross section from this measurement with another order of magnitude.

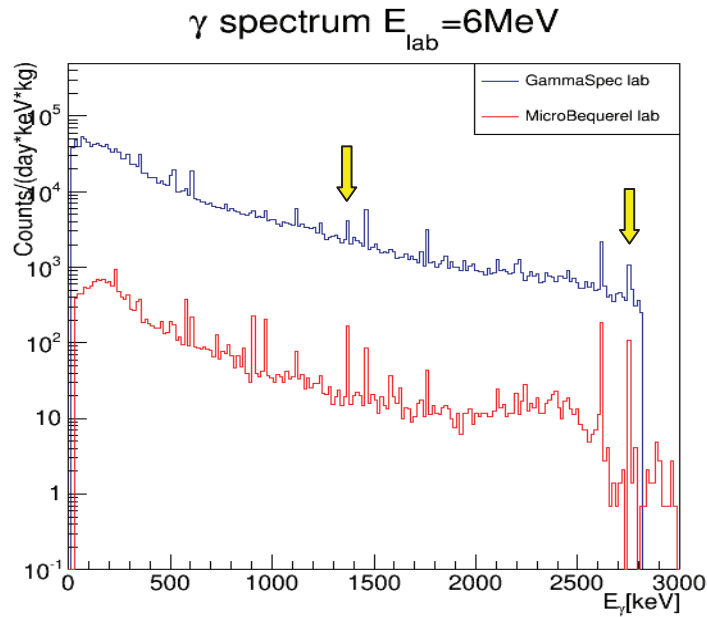


FIGURE 2. Comparison between γ spectra ($E_{\text{lab}} = 6$ MeV) measured in underground laboratory and GammaSpec laboratory (arrows-the cascading γ rays 1369 and 2754 keV)

TABLE 1. Experimental results obtained in GammaSpec laboratory

$E_{\text{lab}}(^{13}\text{C})$ (MeV)	$I(\mu\text{A})$	$t_c(\text{s})$	^{24}Na (Bq)
7.0	1.87	81000	5.20 ± 0.40
6.0	1.90	86400	0.115 ± 0.018

TABLE 2. Experimental results obtained in the underground laboratory

$E_{\text{lab}}(^{13}\text{C})$ (MeV)	$I(\mu\text{A})$	$t_c(\text{s})$	^{24}Na (Bq)
7.0	1.87	86400	5.23 ± 0.043
6.0	1.90	84480	0.085 ± 0.011

CONCLUSIONS

Study of carbon burning is an open question in nuclear astrophysics. This process represents the third stage of stellar evolution of massive stars with mass greater than 8 stellar masses that continue mainly through $^{12}\text{C} + ^{12}\text{C}$ fusion processes and to a lesser extent by $^{12}\text{C} + ^{16}\text{O}$. Direct measurement at the Gamow window energies are therefore essential, but are difficult to carry due to the background from the cosmic rays, terrestrial environment and/or accelerator beams. Major improvements can be achieved by using high intensity accelerators, advanced detection techniques and/or underground measurements. $^{12}\text{C} + ^{13}\text{C}$ fusion process gives information about the fusion mechanism at low energies and can be studied both in-beam γ spectroscopy and activation method using experimental setups that consists of an accelerator and detectors for γ spectroscopy.

To determine the optimum parameters of this experiment, stability and resolution tests of ^{12}C beam obtained at the 3 MV accelerator of IFIN-HH were conducted last year. Following these tests, it turns out that the accelerator has the characteristics required for nuclear astrophysics measurements, namely: allow the terminal voltage between 0.1-3.2 MV, stable while providing stability of incident beam energy used, the currents are stable over time, allowing precise measurements. In particular, the intensities of the order of 10 μA obtained for ^{12}C , an order of magnitude higher than those obtained from the University of Notre Dame FN tandem, make possible to carry the proposed experiments in collaboration with the group from there.

We studied the $^{12}\text{C} + ^{13}\text{C}$ fusion reaction in the energy range $E_{\text{c.m.}} = 2.9 - 3.8$ MeV using the activation method and gamma-ray spectroscopy. Activities of irradiated targets measured both in the underground and surface laboratories allowed to determine the limit of detection of cross sections of the order of 1-3 nb. By increasing the intensity it is possible to gain a factor of 10 in sensitivity and by using β - γ coincidences, another factor of 10. However, this will imply a good cooling of the graphite targets. We emphasize that the minimum value of the measurable cross sections in general, is dependent on the specific characteristics of the produced isotope and of the γ transition(s) used, but the order of magnitude set here (nanobarns) remains valid, as remains the possibility to reduce it by increasing the intensity and using β - γ coincidences. Calibrations and measurements performed in identical or similar conditions will also allow us to reduce the uncertainties associated with the experimental data corresponding with range $E_{\text{c.m.}} =$

2.6-5.0 MeV below 20%, and to determine the cross section for the $^{12}\text{C} + ^{13}\text{C}$ process at an energy lower than $E_{\text{c.m.}} = 2.6$ MeV.

In conclusion, the 3 MV accelerator is suitable for nuclear astrophysics measurements due to energies and intensities provided and stability in operation. Low (DFN) and ultralow ("µBq" Slanic) background laboratories of the institute can be successfully used for measurements by activation with lifetime greater than ten minutes and several hours, respectively, necessary to transport the probes. These facilities have been included recently in a European project proposal Horizon 2020 program, called the European Laboratory Astrophysics Network (ELAN) as TA (Transnational Access facility), in a select group of seven multi-disciplinary laboratories of atomic and molecular spectroscopy or radiation installations and of only two other nuclear astrophysics labs.

ACKNOWLEDGMENTS

This work was supported by the Romanian National Authority for Scientific Research Project No. PN-09-37-01-07 and Project No. PNII-IDEI 27/2013.

REFERENCES

1. D. G. Ghita et al., AIP Conf. Proc. 1525, 208 (2013); doi: 10.1063/1.4802321
2. D. G. Ghita et al., Proceedings of HIAT 2012, Chicago, IL USA
3. G. Wallerstein et. al. Rev. Mod. Phys, 69 998 (1997)
4. F. Kappeler et al., Ann. Rev. Nucl. Part. Sci. 48, 175 (1998).
5. E. Garcia-Berro et al., Astrophys. J. 286, 765 (1997).
6. K. U. Kettner et al., Phys. Rev. Lett. 38, 337 (1977).
7. H.W. Becker et al., Z. Phys. A 303, 305 (1981).
8. T. Spillane et al., Phys. Rev. Lett. 98, 122501 (2007).
9. <http://www.nipne.ro/facilities/laboratories/english/gamaspec.php>
10. A. Pantelica et al., Rad. Prot. Dosim. 97(2) 187-192 (2001).
11. V. Petrescu, "Monografie Slanic Prahova", (2002).
12. R. M. Margineanu et al., Applied Radiation and Isotopes 67 (2009) 759–761
13. R. M. Margineanu et al., J Radioanal Nucl Chem, DOI 10.1007/s10967-013-2545-4
14. D. Chesneanu et al., Carpathian Summer School of Physics 2014, Sinaia, Romania, (2014)
(<http://www.nipne.ro/indico/getFile.py/access?contribId=73&resId=0&materialId=slides&confId=141>).

HEAVY ION ORBITING AND REGGE POLES (I)

F. CARSTOIU¹, M. LASSAUT², L. TRACHE¹, V. BALANICA¹

¹National Institute for Nuclear Physics and Engineering,
P.O.Box MG-6, RO-077125 Bucharest-Magurele, Romania

²Institut de Physique Nucléaire, CNRS-IN2P3, Univ. Paris-Sud,
Université Paris-Saclay, 91406 Orsay Cedex, France

Received September 8, 2015

We review the semiclassical theory for heavy ion orbiting insisting on the connection with Regge poles and barrier-top resonances. Although the physical content of the phenomenon is well understood semiclassically, a clear signature is hard to be found because the relation between the observation angle and the deflection angle is not one to one.

Key words: G-matrix effective interactions, folding potentials, WKB, Regge poles.

PACS: 24.10.Ht, 25.55.Ci, 25.70.Ef.

1. INTRODUCTION

We have a long-term program to understand and describe nucleus-nucleus collisions in terms of one body interaction potential, the optical model potential (OMP). A good understanding of all phenomena occurring in the elastic nucleus-nucleus scattering, which are used typically to extract OMP, and the interpretation of the origin of different aspects, including the well known potential ambiguities, are of crucial importance for finding and justifying the procedures used for predicting nucleus-nucleus OMP in the era of radioactive nuclear beams (RNB), including ours based on double folding [1]. The reliability of these potentials is crucial for the correct description of a number of reactions involving RNBs, from elastic to transfer and breakup, at energies ranging from a few to a few hundred MeV/nucleon. Of particular interest for us is to support the absolute values of the calculated cross sections for reactions used in indirect methods for nuclear astrophysics, see [2] and [3] for the most recent results. In this framework, we treat here the case of heavy ion orbiting, one of the phenomena found over the years to occur in special cases of elastic scattering, well understood semi-classically, but not well documented by specific examples.

The anomalous large-angle scattering of α -particles at moderate energies from elements throughout the periodic table has been a subject of considerable experimental study and has evoked a wide range of novel theoretical explanations [4, 5]. The conventional nuclear optical potential can explain much, if not all, of the anomalous

scattering. The dominant physical parameter determining back-angle scattering is the strength, W , of the imaginary part of the optical potential. Lowering of W by a modest factor of two or three lead to changes in back-angle scattering by several orders of magnitude. This effect was dubbed in literature improperly as incomplete absorption. This severe sensitivity of back-angle scattering to the imaginary strength of the optical potential was explained as a sudden emergence of the giant resonances of the high-partial-wave strength functions, as W decreases [6]. A more popular explanation is the interference between the wave reflected at the internal angular momentum barrier with the wave reflected at the nuclear radius.

Analysis of several heavy ion elastic scattering angular distribution in the energy range of 4-10 MeV/A conclude that backward-angle structures are caused by very few partial waves close to grazing collision value $\ell = kR$. Consequently, all theoretical approaches have to strengthen the contribution from these partial waves relative to the normal optical or diffraction model. Cowley and Heymann [7] and McVoy [8] parametrize the scattering amplitude by a Regge pole expansion in angular momentum. The explanation in terms of a sequence of Regge poles suggests that the physical mechanism behind the large angle structures could be heavy ion orbiting.

Orbiting could be understood simply in terms of the classical equation of motion. Let a particle m in a strong attractive potential $V(r)$. Then the motion is given by

$$\frac{1}{2}m\dot{r}^2 + \frac{1}{2}\frac{L^2}{mr^2} + V(r) = E \quad (1)$$

Let the effective interaction $U(r, L) = \frac{1}{2}\frac{L^2}{mr^2} + V(r)$ and assume that for a certain angular momentum $L = L_{orb}$ the effective interaction has a maximum U_{max} and $U_{max} = E$. If this condition is satisfied then the radial velocity $\dot{r} = 0$ and the particle is orbiting indefinitely with a radius corresponding to the maximum. For E close to the critical energy the particle remains a finite time in this state.

In this paper we review the semiclassical theory of Brink and Takigawa [9] in relation with heavy ion orbiting, barrier-top resonances and Regge poles. In a second part of the paper we examine the ability of the double folding model of the optical potential to describe orbiting.

2. ORBITING AND REGGE POLES

We start from the radial Schrödinger equation for a real spherical potential

$$-\frac{\hbar^2}{2\mu} \left(\frac{\partial}{\partial r^2} - \frac{\ell(\ell+1)}{r^2} \right) \Psi + V(r)\Psi = E\Psi \quad (2)$$

and assume that the effective potential

$$V_{\text{eff}}(r) = V(r) + \frac{\hbar^2}{2\mu} \frac{\ell(\ell+1)}{r^2} \quad (3)$$

has a barrier at a finite radius say $r = r_B$. Then close to the barrier we may write:

$$V_{\text{eff}}(r) \approx V_B - \frac{1}{2} \mu \omega_B^2 (r - r_B)^2 \quad (4)$$

$$-\frac{\hbar^2}{2\mu} \frac{\partial^2 \Psi}{\partial r^2} - \frac{1}{2} \mu \omega_B^2 (r - r_B)^2 \Psi = (E - V_B) \Psi \quad (5)$$

In fact a Taylor series expansion of V_{eff} gives:

$$V_{\text{eff}}(r) = V_{\text{eff}}(r_B) + \frac{1}{2} (r - r_B)^2 V''_{\text{eff}} \Big|_{r_B} \quad (6)$$

$$V_B = V_{\text{eff}}(r_B) \quad (7)$$

$$\omega_B = \sqrt{-\frac{V''_{\text{eff}}(r_B)}{\mu}} \quad (8)$$

In Eq.(5) we change the variable

$$x = \sqrt{\frac{\mu \omega_B}{\hbar}} (r - r_B) \quad (9)$$

and Eq.(5) becomes

$$\frac{\partial^2 \Psi}{\partial x^2} + x^2 \Psi + 2\varepsilon \Psi = 0 \quad (10)$$

$$\text{with } \varepsilon = \frac{E - V_B}{\hbar \omega_B}$$

Friedman and Goebel [10] have shown that resonances (poles in complex energy plane) emerge when

$$\varepsilon_n = -\left(n + \frac{1}{2}\right) i \quad (11)$$

which is just the quantization of the inverted harmonic oscillator well. It results that

$$E_n = V_B - i \left(n + \frac{1}{2}\right) \hbar \omega_B \quad (12)$$

These are poles for fixed angular momentum in complex energy plane. The orbiting angular momentum is defined by

$$V_B(\ell_{\text{orb}}(E)) = E \quad (13)$$

For ℓ close to ℓ_{orb} we expand to first order

$$V_B(\ell) = V_B(\ell_{\text{orb}}) + \frac{\partial V_B}{\partial \ell}(\ell - \ell_{\text{orb}}) = E + \hbar\omega_{\text{orb}}(\ell - \ell_{\text{orb}}) \quad (14)$$

where

$$\begin{aligned} \hbar\omega_{\text{orb}} &= \left. \frac{\partial V_B}{\partial \ell} \right|_{\ell=\ell_{\text{orb}}} = \left. \frac{\partial}{\partial \ell} \left[\frac{\hbar^2}{2\mu} \frac{\ell(\ell+1)}{r_B^2} \right] \right|_{\ell=\ell_{\text{orb}}} \\ &= \frac{\hbar^2}{2\mu r_B^2} \frac{\partial}{\partial \ell}(\ell^2 + \ell) \Big|_{\ell=\ell_{\text{orb}}} = \frac{\hbar^2}{2\mu r_B^2} (2\ell_{\text{orb}} + 1) \end{aligned} \quad (15)$$

The orbiting frequency at the top of the barrier reads :

$$\omega_{\text{orb}} = \frac{\hbar}{\mu r_B^2} \left(\ell_{\text{orb}} + \frac{1}{2} \right) \quad (16)$$

We can write Eq.(14) in the form

$$E - V_B(\ell) = -\hbar\omega_{\text{orb}}(\ell - \ell_{\text{orb}}) \quad (17)$$

and continue with Eq.(10)

$$E - V_B(\ell) = \hbar\omega_B \varepsilon = -\hbar\omega_{\text{orb}}(\ell - \ell_{\text{orb}}) \quad (18)$$

The reduced momentum reads

$$\frac{E - V_B(\ell)}{\hbar\omega_B} = -\frac{\hbar\omega_{\text{orb}}}{\hbar\omega_B}(\ell - \ell_{\text{orb}}) \equiv -\lambda \quad (19)$$

Therefore we have $\lambda = -\varepsilon$ and the barrier-top resonances translate into Regge poles at

$$\lambda_n = \left(n + \frac{1}{2} \right) i \quad (20)$$

or

$$(\ell_n - \ell_{\text{orb}}) \frac{\omega_{\text{orb}}}{\omega_B} = \left(n + \frac{1}{2} \right) i \quad (21)$$

We get

$$\ell_n = \ell_{\text{orb}} + \frac{\omega_B}{\omega_{\text{orb}}} \left(n + \frac{1}{2} \right) i \quad (22)$$

or

$$\ell_n = \ell_{\text{orb}} + \Gamma_\ell \left(n + \frac{1}{2} \right) i \quad (23)$$

so the lowest pole is exactly at $\ell_0 = \ell_{\text{orb}} + i\frac{\Gamma_\ell}{2}$ with $\Gamma_\ell = \frac{\omega_B}{\omega_{\text{orb}}}$. Note that Γ_ℓ depends on ℓ_{orb} through relation (16)

$$\Gamma_\ell = \frac{\omega_B}{\omega_{\text{orb}}} = \frac{\sqrt{-\frac{V''_{\text{eff}}(r_B)}{\mu}}}{\frac{\hbar}{\mu r_B^2} \left(\ell_{\text{orb}} + \frac{1}{2} \right)} \quad (24)$$

where in Eq.(24) the primes denote the derivative with respect to r_B . We have

$$V_{\text{eff}}(r_B) = V(r_B) + \frac{\hbar^2}{2\mu} \frac{\ell(\ell+1)}{r_B^2} \quad (25)$$

$$V'_{\text{eff}}(r_B) = V'(r_B) - \frac{\hbar^2}{2\mu} \ell(\ell+1) \frac{2}{r_B^3} = V'(r_B) - \frac{\hbar^2}{\mu} \frac{\ell(\ell+1)}{r_B^3} \quad (26)$$

$$V''_{\text{eff}}(r_B) = V''(r_B) + \frac{\hbar^2}{\mu} \frac{3\ell(\ell+1)}{r_B^4} \quad (27)$$

In the presence of absorption, Friedman and Goebel [10] conjectured that the pole will be shifted by the quantity

$$\Delta\ell_n = i \frac{\omega(r_B)}{\omega_{\text{orb}}}. \quad (28)$$

3. SEMICLASSICAL ORBITING

We turn now to study the reaction mechanism governing orbiting using semiclassical methods. The far-side dominance observed in some heavy ion elastic scattering angular distributions is not able to explain the behavior of the S-matrix elements at low angular momentum. The reason is of course that the far/near (F/N) decomposition method does not perform a dynamic decomposition of the scattering function, but merely decomposes the scattering amplitude into traveling waves. The intermediate angle structures, have been repeatedly interpreted as arising from the interference of two ranges in angular momenta, $\ell_<$ and $\ell_>$, contributing to the same negative deflection angle. However, the corresponding cross sections, $\sigma_{F<}$ and $\sigma_{F>}$, cannot be isolated because their dynamic content (S -matrix) is not accessible.

The semiclassical uniform approximation for the scattering amplitude of Brink and Takigawa [9] is well adapted to describe situations in which the scattering is controlled by at most three active, isolated, complex turning points. An approximate multireflection series expansion of the scattering function can be obtained, the terms of which have the same simple physical meaning as in the exact Debye expansion for the scattering of light on a spherical well. The major interest in this theory comes from the fact that it can give precious information on the response of a nuclear system to the nuclear interior. An application [11] of this technique helped to clarify the controversial problem of the "Airy oscillation" seen in low energy $^{16}\text{O}+^{12}\text{C}$ scattering [13].

We discard the absorptive term in the optical potential and define the effective potential as,

$$V_{\text{eff}}(r) = V(r) + \frac{\hbar^2}{2\mu} \frac{\lambda^2}{r^2}, \quad \lambda = \ell + \frac{1}{2} \quad (29)$$

where the Langer prescription has been used for the centrifugal term. This guarantees the correct behavior of the semiclassical wave function at the origin [14]. Then we calculate the deflection function,

$$\Theta(\lambda) = \pi - 2 \int_{r_1}^{\infty} \frac{\sqrt{\frac{\hbar^2}{2\mu}} \lambda dr}{r^2 \sqrt{E_{\text{c.m.}} - V_{\text{eff}}(r)}} \quad (30)$$

where r_1 is the outer zero of the square root, i.e. the radius of closest approach to the scatterer and μ is the reduced mass. Note that with the replacement $\hbar\lambda = b\sqrt{2\mu E}$, Eq.(30) becomes identical with the classical deflection function $\Theta(b)$, where b is the impact parameter. The behavior of $\Theta(\lambda)$ is the one expected for a strong nuclear potential in a *near orbiting* kinematical situation in which the c.m. energy approximately equals that of the top of the barrier for some specific angular momentum. All the measured angular range is classically illuminated. The deflection function exhibit no genuine minima, but rather a pronounced cusp close to an orbiting logarithmic singularity. Therefore any interpretation of structures in angular distributions in terms of Airy oscillations can be discarded. Rather we need an interpretation appropriate for orbiting, a well documented situation in classical physics [15]. We identify the cusp angular momentum as orbiting momentum (λ_{orb}) since this is related to the coalescence of two (barrier) turning points and the innermost turning point given by the centrifugal barrier becomes classically accessible. There are two branches that can be distinguished, an internal branch for low active momenta $\lambda < \lambda_{\text{orb}}$ related to semiclassical trajectories which penetrate into the nuclear pocket and a less developed external (barrier) branch ($\lambda > \lambda_{\text{orb}}$) related to trajectories deflected at the diffuse edge of the potential.

However this simple calculation cannot determine the relative importance of these branches and provides no information about the interference effects of the corresponding semiclassical trajectories. To clarify these points it is best to go into the complex r -plane and look for complex turning points, i.e. the complex roots of the quantity $E_{\text{c.m.}} - V_{\text{eff}} - iW$. This is an intricate numerical problem, because, for a WS optical potential, the turning points are located near the potential singularities and there are an infinite number of such poles. We consider an ideal situation with three, well isolated, turning points for each partial wave.

The multireflection expansion of the scattering function in the Brink-Takigawa

approach reads,

$$S_{WKB}(\ell) = \sum_{q=0}^{\infty} S_q(\ell) \quad (31)$$

where,

$$S_0(\ell) = \frac{\exp(2i\delta_1^\ell)}{N(-i\varepsilon)} \quad (32)$$

and for $q \neq 0$,

$$S_q(\ell) = (-)^{q+1} \frac{\exp[2i(qS_{32} + S_{21} + \delta_1^\ell)]}{N^{q+1}(-i\varepsilon)} \quad (33)$$

In these equations, $\varepsilon = S_{21}/\pi$ and δ_1^ℓ is the WKB (complex) phase-shift corresponding to the turning point r_1 , $N(z)$ is the barrier penetrability factor,

$$N(z) = \frac{\sqrt{2\pi}}{\Gamma(z + \frac{1}{2})} \exp(z \ln z - z) \quad (34)$$

and S_{ij} is the action integral calculated between turning points r_i and r_j ,

$$S_{ij} = \int_{r_i}^{r_j} dr \left\{ \frac{2\mu}{\hbar^2} [E_{c.m.} - V_{\text{eff}}(r) - iW(r)] \right\}^{1/2} \quad (35)$$

S_{21} and S_{32} are independent of the integration path provided they lie on the first Riemann sheet and collision with potential poles is avoided. Each term in Eq.(31) has a simple physical interpretation. The first term (the barrier term, denoted also S_B) retains contributions from trajectories reflected at the barrier, not penetrating the internal region. The q -th term corresponds to trajectories refracted q times in the nuclear interior with $q - 1$ reflections at the barrier turning point r_2 . Summation of terms $q \geq 1$ can be recast into a single term,

$$S_I = \frac{\exp[2i(S_{32} + S_{21} + \delta_1^\ell)]}{N(-iS_{21}/\pi)^2} \frac{1}{1 + \exp[2iS_{32}]/N(-iS_{21}/\pi)} \quad (36)$$

and is known as the internal barrier scattering function. When the absorption in the nuclear interior is large, the second factor in the above equation reduces to one and we are left with the expression used in [16]. Since the semiclassical scattering function is decomposed additively, $S_{WKB} = S_B + S_I$, the corresponding total scattering amplitude is decomposed likewise as $f_{WKB} = f_B + f_I$ and conveniently the corresponding barrier and internal barrier angular distributions are calculated as $\sigma_{B,I} = |f_{B,I}|^2$, using the usual angular momentum expansion of the amplitudes.

The accuracy of the semiclassical calculation is usually checked by comparing the barrier and internal barrier absorption profiles with the exact quantum-mechanical

result. When the action integrals are calculated accurately, the semiclassical B/I expansion is an *exact* decomposition of the quantum result. The internal component gets significant values up to the grazing angular momentum ℓ_g and is negligibly small beyond this value. The barrier component resembles a strong absorption profile and this justifies the interpretation that it corresponds to that part of the flux not penetrating into the nuclear interior. For values near the orbiting angular momentum ℓ_{orb} , the two components interfere and a downward spike appears in the total profile, in complete agreement with the quantum result. This is the famous Grün-Wall spike [17] introduced phenomenologically to explain ALAS for α -particle scattering, and appears here as a strong interference between barrier and internal barrier amplitudes. Second, the B/I components are almost decoupled in the angular momentum space and therefore they will contribute in different angular ranges.

A better insight into this technique is obtained by further decomposing the B/I components into far and near (BF/BN and IF/IN) subcomponents. The barrier component dominates the forward angle region. Fraunhofer diffractive oscillations appear as the result of BF and BN interference. At large angles, the internal contribution accounts for the full cross section.

Thus, the intermediate angle exotic structure in angular distributions for the elastic scattering of ${}^6\text{Li}$ on ${}^{16}\text{O}$ [18] can be understood as a result of coherent interference of two far-side subamplitudes generated by different terms in the uniform multireflection expansion of the scattering function (terms $q=0$ and $q=1$ in Eq.(31)), corresponding to the scattering at the barrier and the internal barrier. This interference effect appears as a signature of a surprisingly transparent interaction potential for loosely bound nucleus ${}^6\text{Li}$ at this low energy which allows part of the incident flux to penetrate the nuclear interior and reemerge with significant probability.

The multireflection series (31) is the uniform approximation analogue of the Debye expansion of the scattering function. Anni [11] used Eq.(31) to interpret ${}^{16}\text{O}+{}^{12}\text{C}$ scattering data at 132 MeV assuming a surface transparent optical potentials and convincingly showed that medium angle structures are given by interference effects of the barrier/internal amplitudes and more precisely by interference between saddles appearing in the first and second term of multireflection expansion and therefore cannot be interpreted as a manifestation as a nuclear rainbow and associated Airy oscillation.

In the following we will provide a third interpretation by using explicitly the orbiting conditions and explicitly calculating Sommerfeld poles near the real axis.

We will make a totally different assumption on the physical nature of the phenomenon: the absorption is negligible near the barrier but strong in the nuclear interior. In such conditions, the scattering amplitude is described by the barrier component alone modified slightly by the barrier penetration factor :

$$S_n \approx \frac{e^{2i\delta_1(\lambda)}}{N(-i\frac{S_{21}}{\pi})} \quad (37)$$

which is slightly changed compared with the original Brink-Takigawa formulation. Since δ_1 describes trajectories reflected at outer turning point, the scattering amplitude $S \sim e^{2i\delta_1}$ will be very much similar to that given by the strong absorption model. The action S_{21} is given by

$$S_{21} = \int_{r_2}^{r_1} \left[\frac{2\mu}{\hbar^2} (E - V_{\text{eff}}(r)) \right]^{\frac{1}{2}} dr \quad (38)$$

with

$$V_{\text{eff}}(r) = V(r) + V_c(r) + \frac{\hbar^2 \lambda^2}{2\mu r^2}, \quad \lambda = \ell + \frac{1}{2} \quad (39)$$

where V_c is the Coulomb potential. Near the barrier, the absorption is small and the effective potential is almost real and

$$V_{\text{eff}}(r) = V_B + \frac{1}{2} \mu \omega_B^2 (r - r_B)^2 \quad (40)$$

with

$$\omega_B = \sqrt{-\frac{V_{\text{eff}}''(r)}{\mu}} \Big|_{r=r_B} \quad (41)$$

where in Eq.(41) the prime denote the derivative with respect to r . Eq.(38) becomes:

$$S_{21} = \int_{r_2}^{r_1} \left[\frac{2\mu}{\hbar^2} (E - V_B - \frac{1}{2} \mu \omega_B^2 (r - r_B)^2) \right]^{\frac{1}{2}} dr \quad (42)$$

With the variable change,

$$r - r_B = \frac{\hbar x}{\mu \omega_B}, \quad x = \frac{\mu \omega_B}{\hbar} (r - r_B), \quad dx = \frac{\mu \omega_B}{\hbar} dr \quad (43)$$

$$S_{21} = \frac{\hbar}{\mu \omega_B} \int_{x_2}^{x_1} \left[\frac{2\mu}{\hbar^2} (E - V_B) - x^2 \right]^{\frac{1}{2}} dx \quad (44)$$

$$x_2 = \frac{\mu \omega_B}{\hbar} (r_2 - r_B), \quad x_1 = \frac{\mu \omega_B}{\hbar} (r_1 - r_B) \quad (45)$$

the action integral S_{21} can be calculated exactly as,

$$S_{21} = \pi \frac{E - V_B}{\hbar \omega_B} \quad (46)$$

So that ε entering Eq.(32) is

$$\varepsilon = \frac{E - V_B}{\hbar \omega_B} \quad (47)$$

Eqs.(32) and (34) show that the poles in S -matrix are given by the poles of the Gamma function [12]. Taking $z = -i\varepsilon$ in Eq.(34)

$$\frac{1}{2} - i\varepsilon_n = -n \quad (48)$$

$$\varepsilon_n = -i \left(n + \frac{1}{2} \right) \quad (49)$$

$$\frac{E_n - V_B}{\hbar\omega} = -i \left(n + \frac{1}{2} \right) \quad (50)$$

$$E_n = V_B - i\hbar\omega_B \left(n + \frac{1}{2} \right) \quad (51)$$

Eq.(51) represents the Bohr-Sommerfeld quantization for the inverted oscillator well. These are precisely the barrier-top resonances (Regge poles) of Friedman and Goebel [10].

Now we use the orbiting condition

$$V_B(\ell_{\text{orb}}(E)) = E \quad (52)$$

to obtain poles in angular momentum. For ℓ close to orbiting momentum we expand the potential to first order

$$V_B(\ell) = V_B(\ell_{\text{orb}}) + \frac{\partial V_B}{\partial \ell}(\ell - \ell_{\text{orb}}) \equiv E + \hbar\omega_{\text{orb}}(\ell - \ell_{\text{orb}}) \quad (53)$$

where the orbiting frequency is

$$\hbar\omega_{\text{orb}} = \left. \frac{\partial V_B}{\partial \ell} \right|_{\ell_{\text{orb}}} = \frac{\hbar^2}{\mu r_B^2} \left(\ell_{\text{orb}} + \frac{1}{2} \right) \quad (54)$$

Taking in (53) $E = E_n$ and $\ell = \ell_n$ and then combining with (51) we obtain

$$\begin{cases} V_B - E_n &= \hbar\omega_{\text{orb}}(\ell_n - \ell_{\text{orb}}) \\ V_B - E_n &= i\hbar\omega_B \left(n + \frac{1}{2} \right) \end{cases} \quad (55)$$

We get

$$\hbar\omega_{\text{orb}}(\ell_n - \ell_{\text{orb}}) = i\hbar\omega_B \left(n + \frac{1}{2} \right) \quad (56)$$

so on

$$\ell_n = \ell_{\text{orb}} + i \frac{\omega_B}{\omega_{\text{orb}}} \left(n + \frac{1}{2} \right) \quad (57)$$

These are the barrier-top poles in angular momentum space. Eq.(57) shows that the nearest pole to real axis has a real part given precisely by the orbiting momentum and a width:

$$\Gamma_\ell = \frac{\omega_B}{\omega_{\text{orb}}} \Rightarrow \ell_n = \ell_{\text{orb}} + i\Gamma_\ell \left(n + \frac{1}{2} \right) \quad (58)$$

Going back to the amplitude (37), the phase shift reads :

$$2i\tilde{\delta}_1(\lambda) = 2i\delta_1(\lambda) + \ln \left[\Gamma \left(\frac{1}{2} - i\varepsilon \right) \right] - \frac{1}{2} \ln(2\pi) + (z - z \ln z)|_{z=-i\varepsilon} \quad (59)$$

Taking into account the equations (47,55) or (18) we have

$$\varepsilon_n = -\frac{\hbar\omega_{\text{orb}}}{\hbar\omega_B}(\ell_n - \ell_{\text{orb}}) = -\frac{\hbar\omega_{\text{orb}}}{\hbar\omega_B}(\lambda_n - \lambda_{\text{orb}}), \quad \lambda = \ell + \frac{1}{2} \quad (60)$$

At the vicinity of $\lambda = \lambda_{\text{orb}}$, where ε_0 is close to zero, the equation (59) is separated in a smooth part labeled $g(\lambda)$ and a part including the logarithmic singularity, namely:

$$2\tilde{\delta}_1(\lambda) = g(\lambda) + (\varepsilon_0 \ln(-i\varepsilon_0) - \varepsilon_0) \quad (61)$$

Here \ln denotes the principal determination of the complex logarithm. We have

$$\begin{aligned} \ln(-i\varepsilon_0) &= \ln|\varepsilon_0| - i\frac{\pi}{2} & \varepsilon_0 > 0 \\ \ln(-i\varepsilon_0) &= \ln|\varepsilon_0| + i\frac{\pi}{2} & \varepsilon_0 < 0 \end{aligned}$$

which implies that the imaginary part of $\varepsilon_0 \ln(-i\varepsilon_0) - \varepsilon_0$ has the same sign regardless of whether ε_0 is positive or negative. This smooth part of the singularity, namely $-i\frac{\pi}{2}|\lambda - \lambda_{\text{orb}}|$, is included in the function g and we are left with :

$$2\tilde{\delta}_1(\lambda) = g(\lambda) + (\varepsilon_0 \ln(|\varepsilon_0|) - \varepsilon_0) \quad (62)$$

Using Eq.(62) and the fact that

$$\frac{d}{d\varepsilon_0}(\varepsilon_0 \ln(|\varepsilon_0|) - \varepsilon_0) = \ln(|\varepsilon_0|) \quad (63)$$

we obtain the following semiclassical deflection function

$$\Theta(\lambda) = 2\tilde{\delta}'_1(\lambda) = g'(\lambda) + \frac{\omega_{\text{orb}}}{\omega_B} \ln \left[\frac{\omega_{\text{orb}}}{\omega_B} |\lambda - \lambda_{\text{orb}}| \right] \quad (64)$$

(the prime being taken with respect to λ) which displays the normal logarithmic singularity near the orbiting on angular momentum. Thus the main signature of the heavy ion orbiting will be a logarithmic singularity in the semiclassical deflection function.

The Equation (64) is valid for every $\lambda - \lambda_{\text{orb}}$ positive or negative. Note that we have neglected the weak dependence of orbiting frequency on angular momentum (54).

4. REGGE POLES

A long standing problem in the α -nucleus scattering at energies above the Coulomb barrier is the so called ALAS, a strong increase of the cross section at

large angles. It was observed by Grün and Wall [17] that a downward narrow spike superimposed on the smooth-cut-off model for ℓ values near grazing $\ell = kR$ aided materially to explain ALAS. The Grün and Wall dip is explained semiclassically as a strong destructive interference between the internal barrier and barrier components of the scattering amplitude near the orbiting momentum. Alternatively, the dip is explained as an interference pole-background components of the scattering amplitude for highly transparent potentials, such that the low absorption is not able to suppress the resonant effects in the low partial waves. Semiclassically, these effects appear as a consequence of multiple reflections of the internal amplitude between the most internal complex turning points of the potential. In fact a common property of the WS potentials which describe well the data, is that they possess several narrow shape (molecular) resonances located in the most active waves. In this section we examine this effect in terms of a purely phenomenological Regge pole approximation.

For this purpose we adopt the "product" representation of the S-matrix [8],

$$S(\ell) = S_{bkg}(\ell)S_{pole}(\ell) \quad (65)$$

where the background (*bkg*) component is borrowed from the strong absorption model of Ericson [19],

$$S_{bkg} = \left[1 + \beta \exp(-i\alpha) \exp\left(\frac{L-l}{\Delta}\right) \right]^{-1} \quad (66)$$

We note that an alternative description in terms of additive pole-background components is possible [7]. For the pole term we adopt the expression,

$$S_{pole}(\ell) = \prod_{j=1}^2 \left[1 + i \frac{D_j(\ell)}{l - L_j - i\hat{\Gamma}_j(\ell)/2} \right] \quad (67)$$

This term describes resonances in ℓ centered at L_j with total width $\hat{\Gamma}_j$. In line with McVoy [8] we assume the zeros and the widths slowly ℓ dependent and vanishing exponentially as $\ell \rightarrow \infty$,

$$D_j(\ell) = \frac{D_j}{1 + \exp(\frac{l-L}{\Delta_j})} \quad (68)$$

$$\hat{\Gamma}_j(\ell) = \frac{\Gamma_j}{1 + \exp(\frac{l-L}{\Delta_j})} \quad (69)$$

Clearly, D measures the distance between the pole ($p = 1/2\Gamma$) and the zero ($z = 1/2\Gamma - D$). The model has 12 parameters, twice as much as the WS model. The reason is that we were not able to find a single pole unitary solution for both background and pole components. Since the problem is highly nonlinear there is no guarantee for the uniqueness of the solution. We used a Monte Carlo procedure to

generate input parameters and then minimized the usual χ^2 objective function.

5. CONCLUSIONS

We have reviewed the semiclassical theory of Brink and Takigawa [9] in connection with heavy ion orbiting. The phenomenon is quite frequent for α -particle scattering on light targets in the energy range 5-10 MeV/A where significant increase in the cross section at large angles is found. A possible signature will be to find a logarithmic singularity in the semiclassical deflection function associated with a downward spike in the absorption profile near the grazing angular momentum $\ell = kR$.

Acknowledgements. This work was partly supported by CNCSIS Romania, under program PN-II-PCE-55/2011 and PN-II-ID-PCE-0299/2012, and partly by IN2P3, France.

REFERENCES

1. L. Trache, A. Azhari, H. L. Clark, C. A. Gagliardi, Y.-W. Lui, A. M. Mukhamedzhanov, R. E. Tribble, F. Carstoiu Phys. Rev. C **61**, 024612(2000).
2. T. Al-Abdullah, F. Carstoiu, X. Chen, H. L. Clarke, C. A. Gagliardi, Y.-W. Lui, A. Mukhamedzhanov, G. Tabacaru, Y. Takimoto, L. Trache, R.E.Tribble, Y. Zhai Phys. Rev. C **89**, 025809 (2014).
3. T. Al-Abdullah, F. Carstoiu, C. A. Gagliardi, G. Tabacaru, L. Trache and R. E. Tribble. Phys. Rev. C **89**, 064602 (2014).
4. G. Gaul, H. Lüdecke, R. Santo, H. Schmeing and R. Stock, Nucl. Phys. **A137**, 177 (1969).
5. H. Oeschler, H. Schröter, H. Fuchs, L. Baum, G. Gaul, H. Ludeke, R. Santo and R. Stock, Phys. Rev. Lett. **28**, 694 (1972).
6. D. M. Brink, J. Grotowski and E. Vogt, Nucl. Phys. **A309** 359(1978).
7. A. A. Cowley and G. Heymann, Nucl. Phys. **A146**, 465 (1970).
8. K. W. McVoy, Phys. Rev. C **3**, 1104 (1971).
9. D. M. Brink and N. Takigawa, Nucl. Phys. **A279**, 159 (1977).
10. W. A. Friedman and C. J. Goebel, Ann. Phys. **104**, 145 (1977).
11. R. Anni, Phys. Rev. C **63**, 031601R (2001).
12. A. Erdélyi, W. Magnus, F. Oberhettinger and F.G. Tricomi, "Higher Transcendental Functions" (vol II. McGraw-Hill, New York, 1953).
13. A. A. Ogloblin *et al.*, Phys. Rev. C **62**, 044601 (2000).
14. P. Fröbrich and R. Lipperheide, *Theory of Nuclear Reactions* (Clarendon Press, Oxford, 1996).
15. K. W. Ford and J. A. Wheeler, Ann. Phys. (N. Y.) **7**, 259 (1959).
16. F. Michel, G. Reidemeister and S. Ohkubo, Phys. Rev. Lett. **89**, 152701 (2002); *ibidem*, Phys. Rev. C **63**, 034620 (2001).
17. C. R. Grün and N. S. Wall, Nucl. Phys. **81**, 161 (1966).
18. F. Carstoiu and L. Trache, Phys. Rev. **C85**, 054606 (2012).
19. T. E. O. Ericson, "Preludes in Theoretical Physics" (eds. A. de-Shalit, L. Van Hove and H. Feshbach, North Holland, 1965).

Fusion cross section of $^{12}\text{C}+^{13}\text{C}$ at sub-barrier energies

N.T. Zhang^{1,a}, X.D. Tang¹, H. Chen¹, D. Chesneanu², M. Straticiuc², L. Trache², I. Burducea², K.A. Li¹, Y.J. Li³, D.G. Ghita², R. Margineanu², A. Pantelica² and C. Gomoiu²

¹*Institute of Modern Physics, Chinese Academy of Sciences, 730000 Lanzhou, China*

²*Horia Hulubei National Institute for R&D in Physics and Nuclear Engineering (IFIN-HH), P.O.B. MG-6, 077125 Bucharest-Magurele, Romania*

³*China Institute of Atomic Energy, 102413 Beijing, China*

Abstract. In the recent work at Notre Dame, correlations between three carbon isotope fusion systems have been studied and it is found that the fusion cross sections of $^{12}\text{C}+^{13}\text{C}$ and $^{13}\text{C}+^{13}\text{C}$ provide an upper limit on the fusion cross section of the astrophysically important $^{12}\text{C}+^{12}\text{C}$ reaction. The aim of this work is to continue such research by measuring the fusion cross section of the $^{12}\text{C}+^{13}\text{C}$ reaction to lower energies. In this experiment, the off-line activity measurement was performed in the ultra-low background laboratory and the fusion cross section for $^{12}\text{C}+^{13}\text{C}$ has been determined in the energy range of $E_{\text{c.m.}}=2.5\text{--}6.8$ MeV. Comparison between this work and several models is also presented.

1 Introduction

Heavy-ion fusion reactions between light nuclei such as carbon and oxygen isotopes have been intensively studied because of their importance in a wide variety of stellar burning scenarios. Among them, carbon burning driven by the $^{12}\text{C}+^{12}\text{C}$ fusion is a crucial process for the formation of white dwarfs, nucleosynthesis in massive stars, and ignition in type Ia supernovae and superbursts [1, 2]. The temperatures for the hydrostatic carbon burning process range from 0.8 to 1.2 GK, corresponding to $E_{\text{c.m.}}=1\text{--}3$ MeV. Unfortunately, because of the very low cross sections, this important energy range is only partially measured at energies above $E_{\text{c.m.}}=2.1$ MeV. For the unmeasured energy ranges, one has to rely on extrapolation methods. Moreover, the situation is further complicated by the existence of the strong, relatively narrow resonances in $^{12}\text{C}+^{12}\text{C}$ reactions. The large resonance reported at energies around $E_{\text{c.m.}}=2.1$ MeV has not been confirmed by following experiment [3].

In an attempt to learn about the resonance structures of the low-energy $^{12}\text{C}+^{12}\text{C}$ reaction, the carbon isotope fusion reactions were systematically studied at the University of Notre Dame (UND) [4]. It was found that the cross sections of the $^{12}\text{C}+^{12}\text{C}$ fusion reaction at resonant energies match with the cross sections in the $^{12}\text{C}+^{13}\text{C}$ and $^{13}\text{C}+^{13}\text{C}$ systems within their quoted uncertainties (see Fig. 1). The observed correlation is explained by the level density differences among the three carbon isotope systems [4, 5]. As a result, the $^{12}\text{C}+^{13}\text{C}$ and $^{13}\text{C}+^{13}\text{C}$ systems provide an upper limit for $^{12}\text{C}+^{12}\text{C}$ in a wide range from $E_{\text{c.m.}}=2.6$ MeV up to more than 20 MeV. Since the two carbon fusion cross sections are much easier to be modeled due to their smooth behaviors, such an upper limit could be predicted

^ae-mail: zhangningtao@impcas.ac.cn

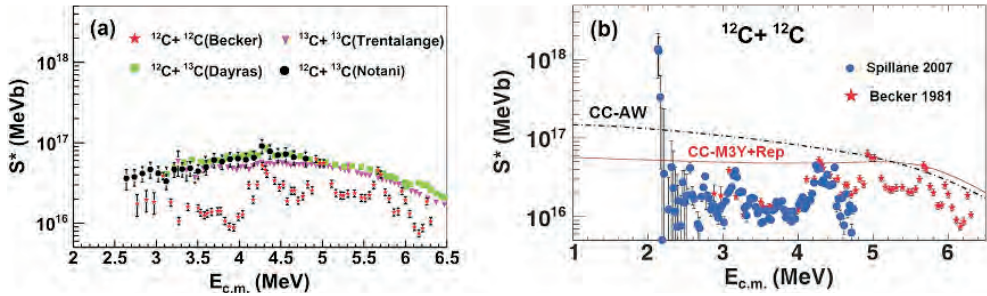


Figure 1. The experimental S^* factors for the carbon isotope fusion reactions: $^{12}\text{C}+^{12}\text{C}$ from Ref. [7] (red stars) and Ref. [3] (blue points) and $^{12}\text{C}+^{13}\text{C}$ from Ref. [4] (black points) and Ref. [8] (green squares), and $^{13}\text{C}+^{13}\text{C}$ [9] (magenta triangles). In Fig. 1(b), two coupled-channels calculations using Akyüz-Winther potential (CC-AW, dot-dashed line) and M3Y+Rep potential (CC-M3Y+Rep, red solid line), respectively, are shown for comparison. Here the modified S^* factor is defined as $S^*(E)=\sigma(E)\cdot E\cdot\exp(87.21/\sqrt{E+0.46E})$.

within the astrophysical energy range. The coupled-channel calculation with the M3Y+Rep potential was used to fit the $^{12}\text{C}+^{13}\text{C}$ and $^{13}\text{C}+^{13}\text{C}$ data and constrain the effective nuclear potential, which was then used for the prediction of the $^{12}\text{C}+^{12}\text{C}$ fusion cross sections [4, 6]. It was found that the coupled-channel calculation using the constrained M3Y+Rep potential provides an excellent upper limit for almost all the data except for the strong resonance at 2.14 MeV, which has not been confirmed [4].

Measurement of $^{12}\text{C}+^{13}\text{C}$ and $^{13}\text{C}+^{13}\text{C}$ at deep sub-barrier energies gives us not only an opportunity to model the resonance strengths in $^{12}\text{C}+^{12}\text{C}$ but also a test of the predictive powers of various theoretical models for the carbon fusion cross sections at deep sub-barrier energies. Lacking of experimental data within the energies of astrophysical interest, large discrepancies exist among different nuclear reaction models. Therefore, it is important to push the measurements of the fusion cross sections of $^{12}\text{C}+^{13}\text{C}$ and $^{13}\text{C}+^{13}\text{C}$ down towards lower energies.

2 $^{12}\text{C}+^{13}\text{C}$ experiment at IFIN-HH

We report an experiment to measure the cross section of $^{12}\text{C}+^{13}\text{C}$ reaction by detecting the residual nucleus ^{24}Na which β -decays with a half-life of 15.0 h. Similar measurements have been performed by Notani and Dayras [4, 8]. In the present experiment, the ^{13}C beam was produced by a cesium sputter ion source and injected into a HVEE Tandetron 3 MV electrostatic accelerator of IFIN-HH [10]. The ^{13}C beam impinges a natural graphite target with thickness of 1 mm. The reaction has been studied by varying the beam energies between 5.2 and 6.8 MeV in steps of 0.2 MeV. The ^{13}C beam current used in this experiment varies in the range of 2 to 8 μA .

After each irradiation, the target sample would be quickly transported to an underground counting station (μBq) in the Unirea salt mine for offline γ -ray measurement [11]. This salt mine is located in the vicinity of Slanic-Prahova city, about one hundred kilometers away from the Bucharest. In this salt mine, the μBq underground laboratory is situated at a depth of 208 m below surface (estimated to 560 m water equivalent). The total gamma background spectrum between 40 keV and 3 MeV was 100 times smaller at laboratory level with respect to the same spectrum recorded at surface in open field. In the μBq , a well shielded HPGe detector was used to detect two cascading γ rays (1369- and 2754-keV) emitted from the γ decay of ^{24}Na . One typical gamma spectrum is displayed in Fig. 2. In some cases, the measurement was performed in the Low Background Gamma-Ray Spectrometry

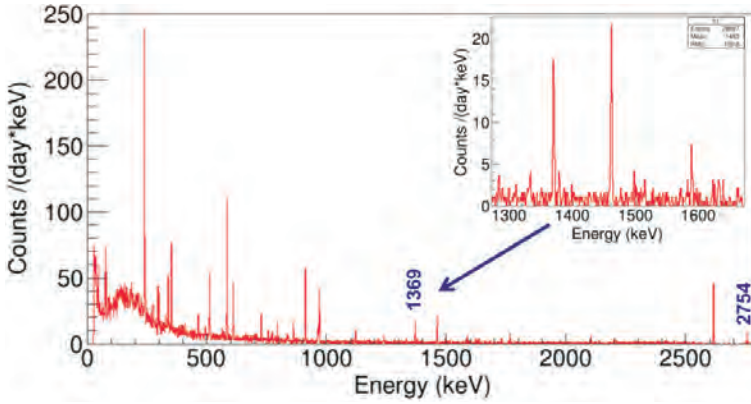


Figure 2. A typical gamma spectrum measured in the underground μBq lab within 46 hours. Beam energy for this spectrum is 5.2 MeV ($E_{\text{c.m.}}=2.5$ MeV), which is the lowest energy point in the experiment. The statistical error for 1369-keV γ peak is 11%, much lower than that in the Notani measurement [4].

Laboratory (GamaSpec) in a basement of IFIN-HH [12]. In this lab, limited by the background γ rays, only target samples irradiated at higher beam energies (>5.8 MeV) could be measured. Furthermore, this measurement was used to cross check the experimental setup in the two laboratories and validate our results.

The thick-target yield (Y) for $^{12}\text{C}(^{13}\text{C},\text{p})^{24}\text{Na}$ reaction was obtained by normalizing the observed yield to the total incident ^{13}C beam flux. From the thick-target yield excitation function, the differential yield dY/dE are determined and then the corresponding cross sections are calculated using the equation $\sigma(E)=dY/dE*dE/d(\rho X)/N_v$, where N_v is the number of atoms per unit of volume and $dE/d(\rho X)$ is the stopping power in the target material, given by the SRIM code. Finally, the total fusion cross sections of $^{12}\text{C}+^{13}\text{C}$ are deduced from the proton emission channel using the theoretical branching ratio given by Hauser-Feshbach model [8].

3 Preliminary results and summary

The preliminary results are shown in Fig. 3. In this work, the lowest cross section for $^{12}\text{C}(^{13}\text{C},\text{p})^{24}\text{Na}$ reaction has been measured down to 3 nb as shown in Fig. 3(a), representing the lowest energy reached for this reaction. This is the great advantage of the ultra-low background underground laboratory. Figure 3(b) shows the modified S factor (S^*) deduced from the total fusion cross section. The result agrees with that of the two previous measurements in the energy region from 2.6-3.3 MeV. Limited by the beam time, only one new data point ($E_{\text{c.m.}}=2.5$ MeV) is added in our first experiment. It has been observed that the optical model with Woods-Saxon type potential reproduces the experimental data only at energies above 4 MeV. At deep sub-barrier energies, it significantly overestimates the cross section, which is quoted as hindrance effect. The equivalent square-well (ESW) model and coupled-channels (CC) with M3Y+Rep potential can predict the experimental data very well. The hindrance model prediction obtained by fitting the Dayras data also shows a reasonable agreement to the experimental data above 2.7 MeV, but predicts a much sharper decrease at astrophysical energies [13]. In order to test the predictive power of the extrapolation models, we will continue our measurement towards lower energies.

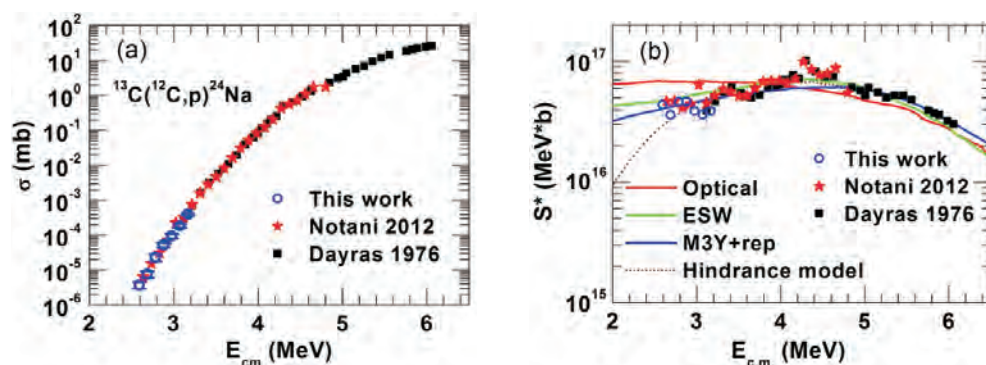


Figure 3. The preliminary fusion cross section of $^{12}\text{C}(^{13}\text{C},p)^{24}\text{Na}$ reaction obtained from the present work (a) and the deduced S^* factor for the $^{12}\text{C}+^{13}\text{C}$ reaction system (b). The results from the previous experiments are also shown.

4 Summary and acknowledgement

In summary, in our first-stage experiment performed in IFIN-HH, $^{12}\text{C}+^{13}\text{C}$ fusion cross section has been measured down to $E_{\text{c.m.}}=2.5$ MeV using thick target technique and activation method. It shows the 3 MV accelerator in IFIN-HH is very suitable for nuclear astrophysics measurements because of high beam intensities and stability in operation. Also, the ultralow background underground laboratory of the institute demonstrates a great potential for measurements of ultra-low activity with lifetime several hours. These facilities offer a new opportunity to measure $^{12}\text{C}+^{13}\text{C}$ fusion cross section at even lower energies.

This work is supported by the National Natural Sciences Foundation of China under Grants No. 11405226 and No. 11475228, the 100 Talents Program of the Chinese Academy of Sciences. It is also supported by the grants PN 09 37 01 07 and PN-II-ID-PCE-2012-4-0299 of the Romanian National Authority for Scientific Research and Innovation.

References

- [1] W. Hillebrandt and J. Niemeyer, *Annu. Rev. Astron. Astrophys.* **38**, 191 (2000)
- [2] L.R. Gasques et al., *Phys. Rev. C* **76**, 035802 (2007)
- [3] T. Spillane et al., M. Romano, J. Schweitzer, *Phys. Rev. Lett.* **98**, 122501 (2007)
- [4] M. Notani et al., *Phys. Rev. C* **85**, 014607 (2012)
- [5] C.L. Jiang, B.B. Back, H. Esbensen, R.V. F. Janssens, K.E. Rehm and R.J. Charity, *Phys. Rev. Lett.* **110**, 072701 (2013)
- [6] H. Esbensen, X. Tang and C.L. Jiang, *Phys. Rev. C* **84**, 064613 (2011)
- [7] H.W. Becker, K.U. Kettner, C. Rolfs, H.P. Trautvetter, *Z. Phys. A* **303**, 305 (1981)
- [8] R.A. Dayras, R.G. Stokstad, Z.E. Switkowski, R.M. Wieland, *Nucl. Phys. A* **265**, 153 (1976)
- [9] S. Trentalange, S.C. Wu, J.L. Osborne, C. A. Barnes, *Nucl. Phys. A* **483**, 406 (1988)
- [10] I. Burducea, M. Straticiuc, D.G. Ghiță, D.V. Moșu, C.I. Călinescu, N.C. Podaru, D.J.W. Mous, I. Ursu and N.V. Zamfir, *Nucl. Instr. and Meth. B* **359**, 12 (2015)
- [11] R. Margineanu, C. Simion, S. Bercea, O.G. Dului, D. Gheorghiu, A. Stochioiu and M. Matei, *Appl. Radiat. Isot.* **66**, 1501 (2008)

- [12] <https://www.nipne.ro/facilities/laboratories/english/gamaspec.php>
- [13] C.L. Jiang, K.E. Rehm, B.B. Back, and R.V.F. Janssens, Phys. Rev. C **79**, 044601 (2009)

Eur. Phys. J. A (2016) **52**: 24

DOI 10.1140/epja/i2016-16024-3

Trojan Horse measurement of the $^{18}\text{F}(\text{p}, \alpha)^{15}\text{O}$ astrophysical $S(E)$ -factor

R.G. Pizzone et al.



Società
Italiana
di Fisica



Springer

Trojan Horse measurement of the $^{18}\text{F}(\text{p}, \alpha)^{15}\text{O}$ astrophysical $S(E)$ -factor

R.G. Pizzone^{1,2,a}, B.T. Roeder¹, M. McCleskey¹, L. Trache^{1,3}, R.E. Tribble^{1,4}, C. Spitaleri^{2,5}, C.A. Bertulani⁶, S. Cherubini^{2,4}, M. Gulino^{2,7}, I. Indelicato^{2,5}, M. La Cognata², L. Lamia⁵, G.G. Rapisarda^{2,5}, and R. Spartá^{2,5}

¹ Cyclotron Institute, Texas A& M University, College Station, TX, USA

² Laboratori Nazionali del Sud - INFN, via S. Sofia 62, 95123 Catania, Italy

³ IFIN-HH, Bucharest-Magurele, Romania

⁴ Brookhaven National Laboratory, USA

⁵ Dipartimento di Fisica e Astronomia, Università degli Studi di Catania, Catania, Italy

⁶ Department of Physics and Astronomy, Texas A&M University-Commerce, Commerce, USA

⁷ KORE University, Enna, Italy

Received: 4 November 2015 / Revised: 11 December 2015

Published online: 12 February 2016 – © Società Italiana di Fisica / Springer-Verlag 2016

Communicated by C. Broggini

Abstract. Crucial information on novae nucleosynthesis is linked to the abundance of ^{18}F , which, due to great improvements in gamma-ray astronomy, can be detected in explosive environments. Therefore, the reaction network producing and destroying this radioactive isotope has been extensively studied in the last years. Among those reactions, the $^{18}\text{F}(\text{p}, \alpha)^{15}\text{O}$ cross section has been measured by means of several dedicated experiments, both using direct and indirect methods. The presence of resonances in the energy region of astrophysical interest has been reported by many authors. In the present work a report on a recent experiment performed via the Trojan Horse Method (THM) is presented and the results are given and compared with the ones known in the literature, both direct and indirect. Data arising from THM measurements are then averaged and the reaction rate calculated in the novae energy range.

1 Introduction

Gamma-ray emission from novae detected in dedicated satellite-borne experiments has become a probe for understanding novae explosions as well as the structure of such exotic stellar objects. In particular, it was noted [1] that electron-positron annihilation should occur in nova envelopes, since short-lived β^+ unstable radioactive nuclei (*i.e.*, positron emitters) are synthesized during the explosion, according to the present models. The 511 keV line might be one of the main observable features. Specifically, positrons emitted by ^{18}F may have the special feature to be emitted (and then quickly annihilated) at the moment (around 110 minutes, half-life of ^{18}F) when the novae envelope starts to be transparent to the γ -radiation [1–3].

^{18}F appears to be produced in the novae inner shells via the Hot-CNO cycle according to several authors [2]. In particular the production path goes through:

$$^{16}\text{O}(\text{p}, \gamma)^{17}\text{F}(\text{p}, \gamma)^{18}\text{Ne}(\beta^+)^{18}\text{F},$$

or

$$^{16}\text{O}(\text{p}, \gamma)^{17}\text{F}(\beta^+)^{17}\text{O}(\text{p}, \gamma)^{18}\text{F},$$

while its destruction is mainly connected with the following processes: $^{18}\text{F}(\text{p}, \alpha)^{15}\text{O}$ or $^{18}\text{F}(\text{p}, \gamma)^{19}\text{Ne}$. Thus the cross sections and the related reaction rates for all the cited reactions and in particular for the $^{18}\text{F}(\text{p}, \alpha)^{15}\text{O}$ reaction should be measured in the astrophysically relevant Gamow window [4], of the order of few hundreds keV (corresponding to $0.05 \leq T_9 \leq 0.5$).

In the last decade this reaction has been widely studied and, in particular, great efforts have been devoted to its study by means of direct measurements at the relevant astrophysical energies. Such a measurement appears to be very challenging not only for the involved energy range which leads to tiny cross sections but also because the ^{18}F is a radioactive isotope, so it requires dedicated techniques to be produced.

Starting from the beginning of this century many experimental groups have tried to measure the astrophysical $S(E)$ -factor for the $^{18}\text{F}(\text{p}, \alpha)^{15}\text{O}$ reaction. A first direct experiment was performed by [5] focusing on the resonance at $E_{\text{cm}} = 330$ keV and its strength. Other measurements were then performed in the following years by several groups with different methodologies, *e.g.*, [6–14]. Up to now many uncertainties are still present on the low-energy resonance and its width, thus affecting the determination

^a e-mail: rgpizzone@lns.infn.it

of the reaction rate at the temperatures relevant for astrophysics and, consequently, the novae nucleosynthesis. Therefore new experimental investigation, especially focused in the novae nucleosynthesis Gamow window, are mandatory.

2 Method

Alternative and challenging ways to obtain the bare nucleus cross section, σ_b , for charged-particles at sub-Coulomb energies have been provided by indirect methods. Among them, the Trojan Horse Method (THM) [15–19] is particularly suited to investigate binary reactions induced at astrophysical energies by neutrons or charged particles by using appropriate three-body reactions. The THM allows one to avoid both Coulomb barrier suppression and electron screening effects, thus preventing the use of extrapolations. The method has proven very helpful in the last two decades for application to several aspects of nuclear astrophysics research like primordial nucleosynthesis [20, 21], the lithium problem [22, 23], AGB nucleosynthesis [24], light elements depletion in stars [25]. In all those cases it has involved the interaction of stable nuclei with p , α or n . Thus, the method can be regarded as a powerful indirect technique to get information about bare nucleus cross section for reactions of astrophysical interest, which leads to new reaction rates determination.

The basic assumptions of the Trojan Horse Method (THM) have already been reviewed recently in [19]. Here we shall just recall that this method is based on the quasi-free (QF) breakup reaction mechanism, which allows us to derive indirectly the cross section of a two-body process from the measurement of a suitable three-body one. In particular, the QF reaction mechanism specializes in the THM approach, relevant for astrophysical applications, when the incident energy is chosen so as to overcome the Coulomb barrier of the interacting nuclei. The Trojan Horse nucleus breaks up into a participant particle and a spectator one. Most used candidates as a Trojan Horse nucleus are deuteron and ^6Li but also ^3He has been successfully used [26]. The breakup process can then be thought as occurring within the nuclear region, so that Coulomb repulsion effects are greatly reduced. As a consequence, the method also becomes insensitive to problems connected with the electron screening effect. The THM has been extensively applied to reactions of astrophysical interest induced by stable beams [27–31]. The first measurement with radioactive ion beams by means of THM was discussed in [32] where the $^{18}\text{F}(p, \alpha)^{15}\text{O}$ reaction was studied for the first time by means of the THM. In this paper we will apply the method to a new experimental run for the $^{18}\text{F}(d, \alpha n)^{15}\text{O}$ measurement in order to obtain relevant information on the $^{18}\text{F}(p, \alpha)^{15}\text{O}$ cross section at energies relevant for astrophysics (see fig. 1). This will help to confirm the indirect data already obtained in [32] and improve the statistics.

In the $^{18}\text{F}(d, \alpha n)^{15}\text{O}$ process, the QF break-up is identified and selected, with deuteron splitting into its constituents p and n , whereby n is regarded as the spectator

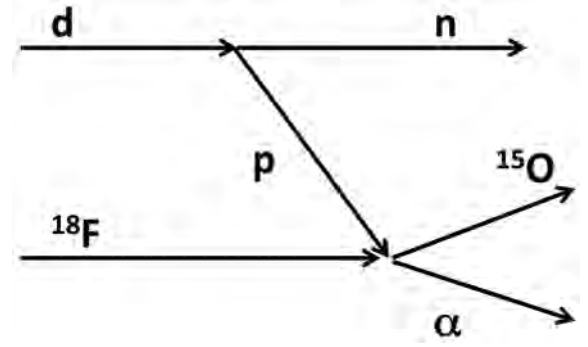


Fig. 1. Schematic representation of the quasi-free mechanism of interest in the three-body reaction used in the Trojan Horse method. The upper vertex marks the deuteron break-up while the lower vertex marks the half-off-energy shell process $^{18}\text{F}(p, \alpha)^{15}\text{O}$.

to the $^{18}\text{F}(p, \alpha)^{15}\text{O}$ virtual reaction. Moreover, appropriate kinematics conditions can be selected so that the $^{18}\text{F}(p, \alpha)^{15}\text{O}$ binary reaction can then take place at low interaction energies, in principle even negligible, according to the post collision prescription:

$$E_{\text{cm}} = E_{\alpha-^{15}\text{O}} - Q_{2b}, \quad (1)$$

where $E_{\alpha-^{15}\text{O}}$ is the relative energy between the detected α and ^{15}O while Q_{2b} ($= 2.88 \text{ MeV}$) is the Q -value for the $^{18}\text{F}(p, \alpha)^{15}\text{O}$ process.

According to the Plane Wave Impulse Approximation (PWIA), the three-body differential cross section measured in an α - ^{15}O coincidence experiment can be expressed in terms of the two-body one as

$$\frac{d^3\sigma}{dE_{\alpha} d\Omega_{\alpha} d\Omega_{\text{O}}} \propto (KF) |\Phi(\mathbf{p}_s)|^2 \left(\frac{d\sigma}{d\Omega} \right)^{\text{HOES}}, \quad (2)$$

where KF is a kinematical factor. The experimental spectator momentum distribution $|\Phi(\mathbf{p}_s)|^2$ is related to the p - n relative motion in the ^2H nucleus with $(d\sigma/d\Omega)^{\text{HOES}}$ the half-off-energy shell binary cross section of astrophysical interest.

Experimental evidence for a QF contribution in the $^{18}\text{F}(d, \alpha n)^{15}\text{O}$ process has been obtained in a different experimental run in a wide energy range [32].

Sequential decay processes (SD), which usually predominate in three-body reactions, have shown to be unimportant in large parts of the selected phase-space region at the present energy [32]. Since the ^2H momentum distribution is known (at least within a given range of the spectator momentum, see [33]), eq. (2) can be inverted to obtain the two-body cross section. For the target breakup, one expects a maximum in the QF contribution at the kinematical conditions where the spectator energy is zero, thus reflecting the neutron momentum distribution in ^2H , which shows a maximum at $p_s = 0$, since the relative p - n motion is mainly $l = 0$ [33]. This gives rise to the choice of the detection angles for the outgoing α and ^{15}O particles. They are calculated using three-body kinematics under the condition that the spectator energy, E_n ,

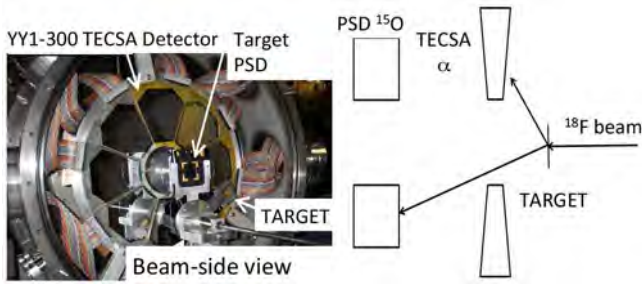


Fig. 2. Schematic view of the experimental setup used in the experiment as described in the text (right). A beam-side view of the experimental apparatus is portrayed on the left side of the picture.

is null and are referred to as the *quasi-free angles* in the standard prescriptions of the THM.

Since the Coulomb barrier is assumed to be overcome in the entrance channel, the obtained half-off-energy shell cross section, $(d\sigma/d\Omega)^{\text{HOES}}$, should be the nuclear part only of the cross section for bare-nuclei, without the Coulomb barrier and also without electron screening effects. Moreover, the nuclear cross section is obtained within an arbitrary normalization constant to be matched to direct measurements, so that direct data have to be available at energies suitable for the normalization procedure. The agreement between the two cross sections at higher energies and the subsequent normalization represents indeed a necessary requirement for the application of the THM to a reaction of astrophysical interest and constitutes a natural step also for reactions induced by radioactive ion beams.

3 Experiment

The experiment was performed at the Cyclotron Institute of the Texas A&M University where the K500 cyclotron provided a 9 A MeV ^{18}O primary beam. The MARS spectrometer [34, 35] was then used to produce a ^{18}F beam via the $p(^{18}\text{O}, ^{18}\text{F})n$ reaction, after energy degrading of the primary beam by means of an Al degrader (around $30\text{ }\mu\text{m}$ thick). After isotopic selection the obtained secondary beam was tuned through MARS with a final energy of 52 MeV on a position sensitive detector at the target location of TECSA (TEexas Edinbrough Catania Silicon Array) [36]. A beam spot of $3 \times 5\text{ mm}$ was obtained after the beam optimization procedure was completed. The energy spread of the beam was around 2.5%. The isotopic ^{18}F purity of the beam was checked during the tuning and it was found that the beam was 94% pure and the intensity of the beam was about $3\text{--}4 \times 10^5$ ions/s. All these features were verified during the data taking by inserting a dedicated PSD detector in the target position (clearly visible in fig. 2).

The beam impinged on an isotopically enriched deuterated polyethylene (CD_2) targets (98% purity). All the used targets were with a thickness in the range $400\text{--}800\text{ }\mu\text{g}/\text{cm}^2$. The experimental set-up consisted of

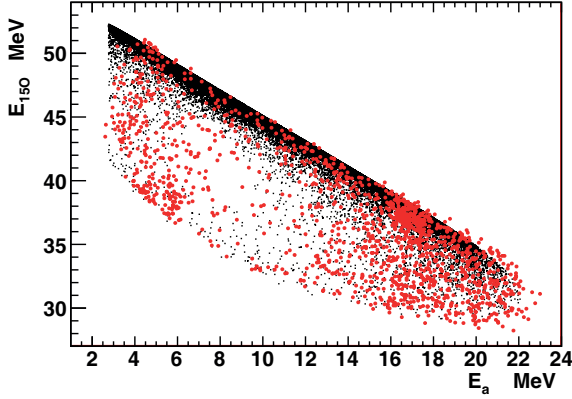
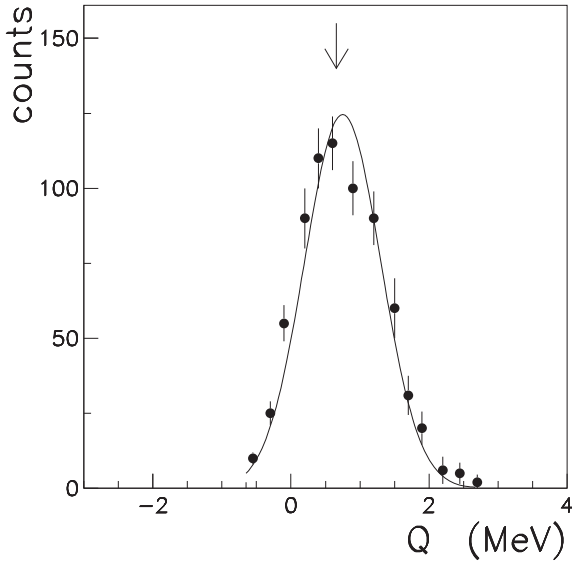
two silicon detector arrays working in coincidence. The TECSA array [36], made up of 8 YY1-300 Micron detectors (each one with 16 arch strips), was set at 190 mm from target covering angles in the range $\theta_\alpha = 15^\circ\text{--}40^\circ$. It was optimized for the α -particle detection. Closer to the beam axis a second detector system is placed, consisting of two position sensitive detectors (PSD's, type X1, 16 strips each), placed symmetrically at 340 mm and covering angles from $\theta_{^{15}\text{O}} = 3^\circ\text{--}12^\circ$ degrees. This one was aiming to the ^{15}O detection. The experimental set-up is sketched in fig. 2 and a summary of the geometrical features of the experimental set-up is reported in table 1. The disposition of the experimental setup was chosen to cover as much as possible of the QF angular range, known *a priori* from a Monte Carlo simulation. A plastic scintillator, put downstream at the very end of the experimental chamber, was used for monitoring and acquiring the overall beam current. Energy resolution of the cited detectors is around 0.8% while the angular one, in the present experimental set-up was about 0.7° for the PSD's and 1.1° for TECSA. The detectors were calibrated in energy by means of standard alpha sources and ^{18}F scattering off the CD_2 target. The position-sensitive detectors was also calibrated in position by means of a mask which was used during the calibration runs. The measurement of the energy and position of the two ejectiles gave the possibility to calculate all the kinematic variables regarding the third, undetected, particle as well as other variables of interest for the following data analysis (*e.g.*, Q -value, relative energy α - ^{15}O , spectator momentum).

4 Data analysis

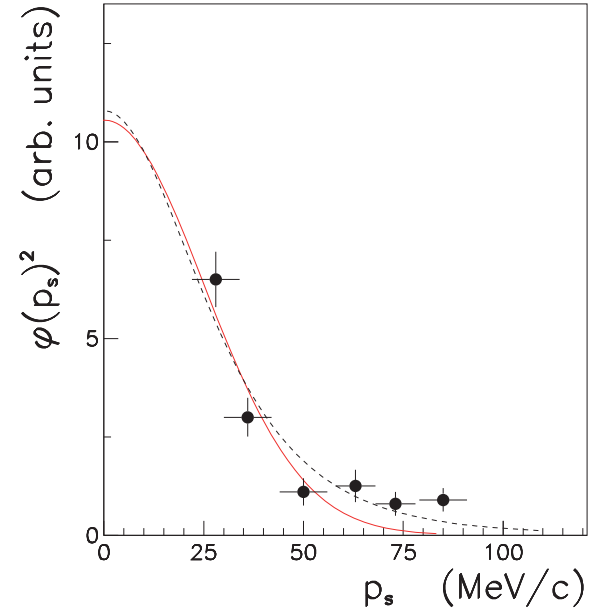
The first step in data-analysis was to identify the events related to the $^{18}\text{F}(d, \alpha n)^{15}\text{O}$ reaction from the other occurring in the target. This is accomplished by studying the kinematic locus related to the above reaction and the Q -value spectrum. Coincidences between each PSD and TECSA strips were examined and a typical plot of the particle energy detected in forward PSD detector *versus* the energy detected in TECSA is reported in fig. 3. A narrow angular range ($\approx \pm 2^\circ$) is selected on both detectors and events coming from an appropriate Monte Carlo simulation, taking into account the geometrical properties of the experimental set-up as well as the features of the detectors, are reported as black dots. A good agreement shows up, thus allowing us further studies. Using a graphical cut which selects only the events overlapping with the Monte Carlo simulation, the Q -value spectrum is plotted in fig. 4, showing a peak compatible, within the experimental errors, with the theoretical Q -value of 0.66 MeV. From now on only the events with the Q -value ranging from 0 to 1.5 and inside the graphical cut in the kinematic locus were used for further data analysis. Considering the good beam purity (contaminants less than 6%) and after tagging on the coincidence together, the kinematical selection and Q -value spectrum, we can assume that the studied events are arising from the 3-body reaction of interest, *i.e.* $^{18}\text{F}(d, \alpha n)^{15}\text{O}$. The first step after

Table 1. Geometrical and physical details of the detector system used in the present measurement and discussed in the text.

Detector	Particle	Angular coverage	Distance from target	Energy resolution	Angular resolution
TECSA	α	$15^\circ\text{--}40^\circ$	19 cm	0.08%	0.7°
X1-PSD	^{15}O	$3^\circ\text{--}12^\circ$	34 cm	0.08%	1.1°

**Fig. 3.** Energy in the PSD (aiming for ^{15}O detection) vs. energy detected in TECSA (aiming for α 's). Experimental events define a kinematic locus (red) that is compared with the one expected from the $^{18}\text{F}(d, \alpha n)^{15}\text{O}$ reaction, as calculated in an appropriate Monte Carlo simulation (black points) for the same.**Fig. 4.** Q -value spectrum for the data taken in the present experiment after selecting coincidences events in the kinematic locus defined in fig. 3. An arrow marks the expected value for the studied reaction ($Q = 0.66$ MeV).

identifying the 3-body process is to investigate the reaction mechanisms involved and to separate the quasi-free (QF) contribution from any other kind of reaction mechanism as required by the THM prescriptions. This can be done by studying, among all the available observables, the most sensitive to the reaction mechanism which is, by far, the shape of the momentum distribution, $|\varphi(\mathbf{p}_s)|^2$. According to the prescriptions in [37, 38], the momentum distribution of the third and un-detected particle is exam-

**Fig. 5.** Momentum distribution shape for the deuteron break-up. The comparison with a Hulthen function (dashed line) with parameters set according to [39]. The Gaussian fit to the present data is also reported (red solid line).

ined. This gives a major constraint for the presence of the QF mechanism and the possible application of the THM. In order to extract the experimental momentum distribution of the undetected particle (the spectator after the QF process is identified and selected) $|\varphi(\mathbf{p}_s)|_{\text{exp}}^2$, the energy sharing method can be applied to each pair of coincidence detectors, selecting energy intervals, ΔE_{cm} . Keeping in mind the factorization of eq. (2), since $[(d\sigma/d\Omega)_{\text{cm}}]^{\text{HOES}}$ is nearly constant in an adequate energy interval, one can get the shape of the momentum distribution of the undetected neutron directly from the coincidence yield divided by the kinematical factor, as calculated from a suitable Monte Carlo simulation. The obtained momentum distribution is reported in fig. 5. It is also compared with the theoretical distribution calculated from the Hulthen function (dashed line) with parameters taken from [39]. We can see how within the experimental errors the theoretical curve reproduces the experimental data, thus confirming the hypothesis that the neutron is acting as a spectator and that the process under investigation is a quasi-free mechanism. We only considered the s-wave since other contribution, *i.e.* the d -wave, were shown to be negligible [33]. According to the prescription adopted in [19] and in the standard THM approaches, only data in the $|p_s| < 55$ MeV/ c range were chosen and used in the further analysis.

An experimental full width at half maximum (FWHM) $\Gamma \approx 55 \pm 7$ MeV/ c was obtained after fitting the

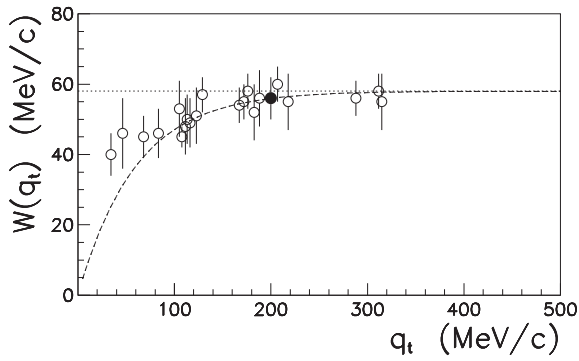


Fig. 6. Full width of the deuteron momentum distribution measured by means of the deuteron break-up as a function of the transferred momentum q_t . The full black dot marks the values obtained for the present experiment. Empty circles represent the data (table 2 of ref. [38]) and the fit (dashed line) is the same as shown in that paper. The asymptotic value is also shown as a dotted line.

experimental distribution reported in fig. 5 with a Gaussian function, and has to be compared with the asymptotic theoretical value of about 58 MeV/c. The comparison, for the present results (black circle) and data published on [38] (empty dots) as a function of the transferred momentum, q_t , is reported in fig. 6. This is coherent with results observed for other cases of deuteron break-up as well as for other isotopes. After this test we can stress the role of the neutron as a spectator to the QF process, which constitutes a solid base for the further THM application to the $^{18}\text{F}(\text{d}, \alpha\text{n})^{15}\text{O}$ reaction for retrieving information on the $^{18}\text{F}(\text{p}, \alpha)^{15}\text{O}$ bare nucleus cross section at astrophysical energies.

5 Results

In the standard THM analysis, the two body cross section is derived by dividing the experimental three-body one by the product of the kinematic factor modulated by the momentum distribution of the spectator inside the Trojan Horse nucleus [19], *i.e.*

$$\left(\frac{d\sigma}{d\Omega}\right)^{\text{HOES}} \propto \frac{d^3\sigma}{dE_{\alpha_1} d\Omega_{\alpha_1} d\Omega_{\alpha_2}} / (KF \cdot |\varphi_{\text{exp}}(\mathbf{p}_s)|^2). \quad (3)$$

Usually the factors $KF \cdot |\varphi_{\text{exp}}(\mathbf{p}_s)|^2$ are calculated by means of a Monte Carlo simulation, taking into account the geometrical position of the detectors. The width of the momentum distribution is set to the experimentally measured value in order to account for the distortion effects arising at low transferred momenta as discussed in [37].

The extracted $[d\sigma/d\Omega]^{\text{HOES}}$ as a function of E_{cm} , was then compared to a previous THM run performed in CNS at the CRIB facility whose details are reported extensively in [32]. In fig. 7, the comparison between present data and those extracted in [32] are reported. We can notice a good agreement between the two THM measurements,

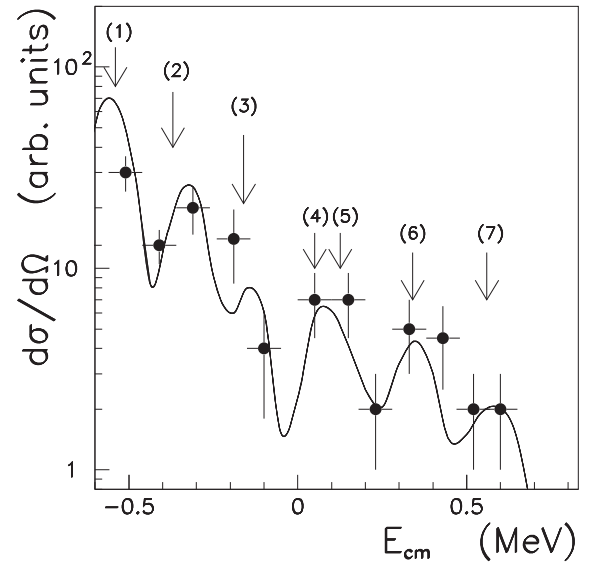


Fig. 7. Comparison of the data extracted in this experimental run (circles) with a line fitting the data from [32] (black solid line). Arrows mark the observed levels in ^{19}Ne , labeled according to table 2.

Table 2. Energy levels of ^{19}Ne in the energy range explored by the present experiment. Progressive numbers in first column correspond to energy levels in fig. 7. The $^{19}\text{Ne}^*$ energy values are taken from [32].

Number	E_{cm} (MeV)	Energy $^{19}\text{Ne}^*$ (keV)	$J(\pi)$	Ref.
1	-0.57	5837	—	[41]
2	-0.34	6070	$3/2^+, 5/2^-$	[10]
3	-0.16	6255	$11/2^-$	[10]
4	0.05	6460	$3/2^+, 5/2^-$	[10, 40]
5	0.13	6537	$5/2^+, 9/2^+$	[40]
6	0.33	6755	$3/2^-$	[10, 12, 40]
7	0.56	6967	$5/2^+$	[40]

within the experimental uncertainties. The observed levels, marked by arrows, correspond to levels in ^{19}Ne which are reported in table 2, taken from [40] or [10]. Although the energy resolution is poorer than in the previous run (mainly due to the poorer angular resolution of the present experimental apparatus), the agreement between the two data sets confirms once again the applicability of the THM to the present reaction. The first validity check that standard THM prescriptions do recommend is to reproduce the direct excitation function. This is done by comparing the distributions measured with direct methods to the one measured by means of THM. The latter should be normalized to the direct data. The THM cross section extracted above is corrected for the penetrability factor (below the Coulomb barrier) which also makes the comparison of half-off-energy shell and on-energy shell data [19] possible. The penetrability factor is, as usual, described in terms of the regular and irregular Coulomb functions [17].

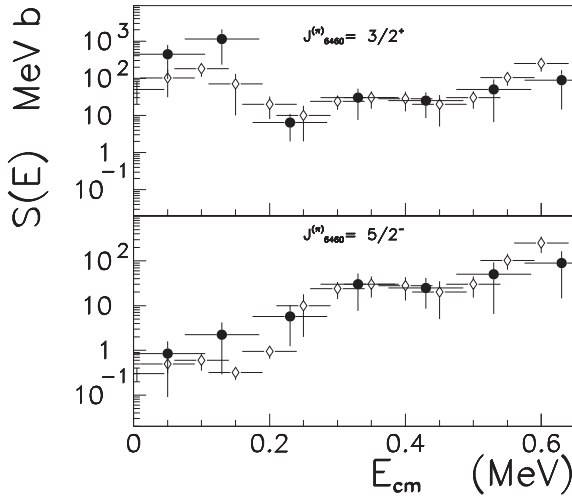


Fig. 8. Comparison of the data extracted in this experimental run (black circles) with data from Cherubini *et al.* [32] (empty diamonds). Lower panel: $S(E)$ -factor extracted with the choice of $J^{(\pi)} = 5/2^-$ for the 6460 keV state in ^{19}Ne normalized to direct data from [32]. Upper panel: $S(E)$ -factor for $J^{(\pi)} = 3/2^+$.

THM data are also not affected by suppression effects coming from the centrifugal barrier. Assuming the J^π values of the populated ^{19}Ne excited states as in table 2, the data of each resonance have been integrated over the full angular range by means the corresponding Legendre polynomial. Finally, the data have been corrected also for the penetrability of the centrifugal barriers.

It is then possible to normalize to the direct data (after comparison with the data from [32]) at the higher possible energies (0.5–0.65 MeV) in the present case. The comparison is reported in fig. 8, where present data are represented by solid circles while the ones from [32] by diamonds. Energy states reported in table 2 were investigated in the present work; in particular the explored energy range makes relevant the contribution from the 6255 (sub threshold state), 6460, 6537, 6755, 6967 keV states of ^{19}Ne . The respective J^π were assigned accordingly as reported in table 2. A specific discussion should be done for the resonance at $E_{\text{cm}} = 0.05$ MeV (corresponding to the 6460 keV state in ^{19}Ne) where two possible values of J^π were taken into account. This is clear in fig. 8. In the upper panel the black circles correspond to the choice of $J^\pi = 3/2^+$ for the 6460 keV state in ^{19}Ne following [40]. Direct data from [5, 6] are reported for comparison and normalization purposes. In the lower panel the full dots represents the results for a $J^\pi = 5/2^-$ assumption for the same level as discussed in [10]. This uncertainty leads therefore to an uncertainty between the $S(E)$ lower limit (corresponding to $J^\pi = 5/2^-$ for the 6460 keV state in ^{19}Ne) and an upper limit assuming $J^\pi = 3/2^+$. Further studies (both with direct and indirect methods) and in particular the angular distribution will be necessary to improve the data quality in the low energy range. It was possible, with the present experimental run, to confirm the possibility of application of the THM to the $^{18}\text{F}(d, \alpha)^{15}\text{O}$ reaction for studying the $^{18}\text{F}(p, \alpha)^{15}\text{O}$ (as reported in [32]) within the

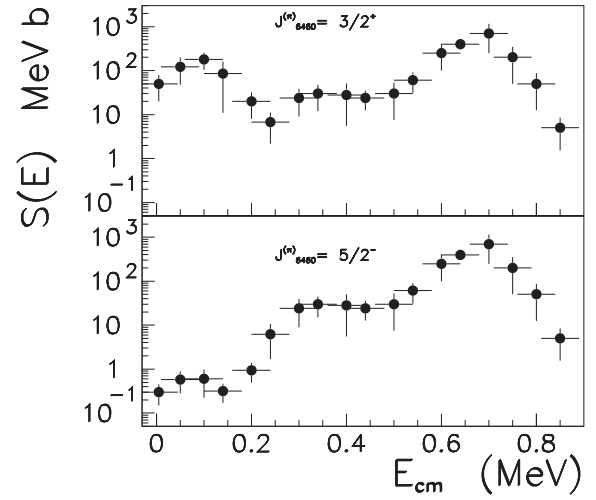


Fig. 9. Average of the present data and those from Cherubini *et al.* (2015) [32]. Lower panel: $S(E)$ -factor extracted with the choice of $J^{(\pi)} = 5/2^-$ for the 6460 keV state in ^{19}Ne . Upper panel: $S(E)$ -factor for $J^{(\pi)} = 3/2^+$.

experimental errors. This was also possible in the present case where the experimental set-up and the beam production line is much simpler than the ones used in [32] (*e.g.*, simpler detection system and no beam-tracking available in the present case). This also strengthen the role of the THM which may play a leading role in the field of radioactive beams in the further years, even in cases where the experimental setup is quite simple, like the present one. However, it was possible to extract the astrophysical $S(E)$ -factor by means of the THM for a reaction induced by an unstable beam, thus confirming results from [32] in all the energy range relevant for astrophysics. Further efforts are necessary to improve the energy and angular resolution of the detection system and therefore reduce the statistical error on the $S(E)$ -factor. The extraction of the angular distribution will also be crucial to assign the J^π of the involved levels and will be the aim of a future, dedicated experiment, to be performed in the future with the optimized version of the detection system adopted in [32].

Data from the present experiment and the ones reported in [32] were then averaged, weighting over the respective errors. The results are reported in fig. 9 where $J^{(\pi)}$ assignment is coherent with the assumption stated above.

6 Reaction rate

The reaction rate for the $^{18}\text{F}(p, \alpha)^{15}\text{O}$ reaction is calculated using the standard expression [4]:

$$R_{ij} = \frac{N_i N_j}{1 + \delta_{ij}} \langle \sigma v \rangle = \frac{N_i N_j}{1 + \delta_{ij}} \left(\frac{8}{\pi A} \right)^{\frac{1}{2}} \left(\frac{1}{k_B T} \right)^{\frac{3}{2}} \cdot \int_0^\infty S(E) \exp \left[- \left(\frac{E}{k_B T} + 2\pi \eta(E) \right) \right] dE, \quad (4)$$

where $S(E)$ is the $^{18}\text{F}(p, \alpha)^{15}\text{O}$ reaction astrophysical factor and $N_{i(j)}$ is the number of nuclei of species $i(j)$.

Table 3. Reaction rate for the $^{18}\text{F}(\text{p}, \alpha)^{15}\text{O}$ as a function of temperature. The cases of $J^{(\pi)} = 3/2^+$ and $J^{(\pi)} = 1/2^-, 3/2^-$ or $5/2^-$ are considered and reported as discussed in the text.

T_9	$R_{ij} (J^{(\pi)} = 3/2^+) [\text{cm}^3 \text{ mol}^{-1} \text{ s}^{-1}]$	$R_{ij} (J^{(\pi)} = 5/2^-) [\text{cm}^3 \text{ mol}^{-1} \text{ s}^{-1}]$
0.05	4.82×10^{-11}	9.13×10^{-9}
0.06	7.19×10^{-10}	1.51×10^{-7}
0.07	5.44×10^{-9}	1.37×10^{-6}
0.08	2.83×10^{-8}	8.01×10^{-6}
0.09	1.19×10^{-7}	3.50×10^{-5}
0.10	4.40×10^{-7}	1.20×10^{-4}
0.11	1.48×10^{-6}	3.46×10^{-4}
0.12	4.67×10^{-6}	8.61×10^{-4}
0.13	1.39×10^{-5}	1.92×10^{-3}
0.14	3.93×10^{-4}	3.88×10^{-3}
0.16	2.66×10^{-4}	1.23×10^{-2}
0.18	1.44×10^{-3}	3.43×10^{-2}
0.20	6.19×10^{-3}	7.85×10^{-2}
0.22	2.17×10^{-2}	1.65×10^{-2}
0.24	6.51×10^{-2}	3.08×10^{-1}
0.26	1.69×10^{-1}	5.58×10^{-1}
0.28	3.90×10^{-1}	9.75×10^{-1}
0.30	8.23×10^{-1}	1.65×10^0
0.325	1.89×10^0	3.09×10^0
0.35	3.97×10^0	5.61×10^0
0.375	7.75×10^0	9.90×10^0
0.40	1.43×10^1	1.76×10^1
0.45	4.40×10^1	4.79×10^1
0.50	1.21×10^2	1.26×10^2
0.60	6.80×10^2	6.88×10^2
0.70	2.67×10^3	2.68×10^3
0.8	7.76×10^3	7.77×10^3
0.9	1.80×10^4	1.80×10^4
1.0	3.52×10^4	3.52×10^4
1.1	6.06×10^4	6.06×10^4
1.15	7.66×10^4	7.66×10^4

We will express our reaction rates in the form $N_A \langle \sigma v \rangle$ (in units of $\text{cm}^3 \text{ mol}^{-1} \text{ s}^{-1}$), where N_A is the Avogadro number and $\langle \sigma v \rangle$ involves the integral in eq. (4) with the Maxwell distribution.

The factor $1 + \delta_{ij}$ in the denominator of eq. (4) corrects for the double counting when $i = j$. The reaction rate was evaluated for both choices of J^π discussed above thus giving rise to a lower and upper limit of its value.

The calculated value corresponding to the present data is reported in table 3 and then compared with the rate extracted by [42]. Both for the case of $J^{(\pi)} = 3/2^+$ and for $J^{(\pi)} = 5/2^-$ a significant enhancement with respect to the reference data is evident; the ratio in fact ranges between 10^2 and 10^5 in the temperature window relevant for the novae nucleosynthesis ($T_9 = 0.05\text{--}0.25$). An analytic expression for the reaction rate was fitted using the

Table 4. Coefficients for the best fit of expression (5) for the reaction rate of the $^{18}\text{F}(\text{p}, \alpha)^{15}\text{O}$. The choice of different $J^{(\pi)}$ is indicated.

a_i	$R_{ij} (J^{(\pi)} = 3/2^+)$	$R_{ij} (J^{(\pi)} = 5/2^-)$
a_1	-0.357147×10^3	0.465126×10^3
a_2	0.259556	-0.229640
a_3	-0.859008×10^2	0.496752×10^2
a_4	0.569710×10^3	-0.660878×10^3
a_5	-0.153842×10^3	0.220031×10^3
a_6	0.372533×10^2	-0.631201×10^2
a_7	-0.119559×10^3	0.127164×10^3

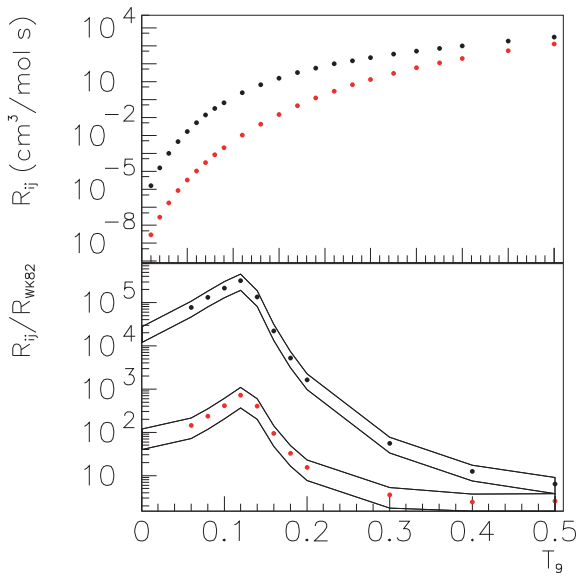


Fig. 10. Reaction rate (upper panel) as a function of T_9 calculated from the presently extracted $S(E)$ as described in the text. Red symbols mark the case of $J^{(\pi)} = 5/2^-$ while black ones the $J^{(\pi)} = 3/2^+$ one. In the lower panel it is reported its respective ratio divided by the [42] value. The error on the present calculation is represented by the solid lines.

expression

$$R_{ij} = \exp \left(a_1 + a_2/T_9 + a_3/T_9^{1/3} + a_4 T_9^{1/3} + a_5 T_9 + a_6 T_9^{5/3} + a_7 \log(T_9) \right) \quad (5)$$

and the resulting parameters a_i are reported in table 4.

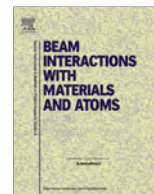
The extracted reaction rate (see fig. 10) has significant astrophysical implications especially in the novae temperature range, where a larger rate with respect to [42] is reported. As regards the upper value ($J^{(\pi)} = 5/2^-$) results are coherent with the reaction rate calculation from [2] while the lower limit ($J^{(\pi)} = 3/2^+$) is much closer to the behavior of [42]. Further astrophysical applications will be investigated in a forthcoming paper.

The authors would like to thank the Cyclotron Institute accelerator division for the smooth operation of the machine. The authors also thank the mechanical workshop for the extensive work in preparation of the experiment and the INFN-LNS target laboratory and C. Marchetta for the isotopically enriched deuterated polyethylene targets and continuous assistance during the whole measurement. This work was supported by the Italian Ministry of the University under Grant No. RBFR082838 and “LNS Astrofisica Nucleare (fondi premiali)”. This work was partially supported by the US-DOE grant number DE-FG02-13ER42025; the U.S. NSF Grant No. 1415656, the U.S. DOE grant No. DE-FG02-08ER41533 and the NNSA grant.

References

1. J. Jose, M. Hernanz, J. Phys. G: Nucl. Part. Phys. **34**, R431 (2007).
2. A. Coc, M. Hernanz, J. Jose, J.P. Thibaud, Astron. Astrophys. **357**, 561 (2000).
3. R. Diehl, AIP Conf. Proc. **1269**, 144 (2010).
4. C. Iliadis, *Nuclear Physics of Stars* (Wiley, 2007).
5. D.W. Bardayan, J.C. Batchelder, J.C. Blackmon, A.E. Champagne *et al.*, Phys. Rev. Lett. **89**, 262501 (2002).
6. C.E. Beer, A.M. Laird, A.St.J. Murphy, M.A. Bentley *et al.*, Phys. Rev. C **83**, 042801(R) (2011).
7. N. DeSereville, C. Angulo, A. Coc, N.L. Achouri *et al.*, Phys. Rev. C **79**, 015801 (2009).
8. J.S. Graulich, S. Cherubini, R. Coszach, S. El Hajjaji *et al.*, Nucl. Phys. A **688**, 138C (2001).
9. J.S. Graulich, S. Cherubini, R. Coszach, El Hajjaji *et al.*, Phys. Rev. C **63**, 011302(R) (2000).
10. A. Laird, A. Parikh, A.St.J. Murphy, K. Wimmer *et al.*, Phys. Rev. Lett. **110**, 032502 (2013).
11. Murphy *et al.*, Phys. Rev. C **79**, 058801 (2009).
12. Adekola *et al.*, Phys. Rev. C **83**, 052801 (2011).
13. Adekola *et al.*, Phys. Rev. C **84**, 054611 (2011).
14. Mountford *et al.*, Phys. Rev. C **85**, 022801(R) (2012).
15. G. Baur, C.A. Bertulani, H. Rebel, Nucl. Phys. A **458**, 188 (1986).
16. C. Spitaleri, Prob. Fund. Phys. **II**, 21 (1991).
17. C. Spitaleri, S. Typel, R.G. Pizzone, M.L. Aliotta *et al.*, Phys. Rev. C **63**, 055801 (2001).
18. C. Spitaleri, A.M. Mukhamedzhanov, L.D. Blokhintsev, M. La Cognata *et al.*, Phys. At. Nucl. **74**, 1725 (2011).
19. R.E. Tribble *et al.*, Rep. Progr. Phys. **77**, 106901 (2014).
20. R.G. Pizzone, R. Sparta, C.A. Bertulani, C. Spitaleri *et al.*, Astrophys. J. **786**, 112 (2014).
21. A. Rinollo *et al.*, Nucl. Phys. A **758**, 146c (2005).
22. R.G. Pizzone, A. Tumino, S. Degl’Innocenti, C. Spitaleri *et al.*, Astron. Astrophys. **438**, 779 (2005).
23. L. Lamia *et al.*, Astron. Astrophys. **541**, 158 (2012).
24. S. Palmerini, M.L. Sergi, M. La Cognata, L. Lamia *et al.*, Astrophys. J. **764**, 128 (2013).
25. S. Romano *et al.*, Eur. Phys. J. A **27**, 221 (2006).
26. R.G. Pizzone, C. Spitaleri, L. Lamia, C. Bertulani *et al.*, Phys. Rev. C **83**, 045801 (2011).
27. M. Lattuada, R.G. Pizzone, S. Typel, P. Figuera *et al.*, Astrophys. J. **562**, 1076 (2001).
28. C. Spitaleri, L. Lamia, S.M.R. Puglia, S. Romano *et al.*, Phys. Rev. C **90**, 035801 (2014).
29. R.G. Pizzone *et al.*, Phys. Rev. C **87**, 025805 (2013).

30. A. Tumino *et al.*, Phys. Lett. B **700**, 111 (2011).
31. A. Tumino *et al.*, Phys. Rev. C **78**, 064001 (2008).
32. S. Cherubini, M. Gulino, C. Spitaleri, M. La Cognata *et al.*, Phys. Rev. C **92**, 015805 (2015).
33. L. Lamia, M. La Cognata, C. Spitaleri, B. Irgaziev, R.G. Pizzone, Phys. Rev. C **85**, 025805 (2012).
34. R.E. Tribble, R.H. Burch, C.A. Gagliardi, Nucl. Instrum. Methods A **285**, 441 (1989).
35. R.E. Tribble, C.A. Gagliardi, W. Liu, Nucl. Instrum. Methods B **56/57**, 956 (1991).
36. B.T. Roeder, M. McCleskey, L. Trache, A.A. Alharbi *et al.*, Nucl. Instrum. Methods A **634**, 71 (2011).
37. R.G. Pizzone, C. Spitaleri, S. Cherubini, M. La Cognata *et al.*, Phys. Rev. C **71**, 058801 (2005).
38. R.G. Pizzone, C. Spitaleri, A.M. Mukhamedzhanov, L.D. Blokhintsev *et al.*, Phys. Rev. C **80**, 025807 (2009).
39. M. Zadro, D. Miljanic, C. Spitaleri, G. Calvi *et al.*, Phys. Rev. C **40**, 181 (1989).
40. C.D. Nesaraja, N. Shu, D.W. Bardayan, J.C. Blackmon *et al.*, Phys. Rev. C **75**, 055809 (2007).
41. D.R. Tilley, H.R. Weller, C.M. Cheves, R.M. Chasteler, Nucl. Phys. A **595**, 1 (1995).
42. M. Wiescher, K. Kettner, Astrophys. J. **263**, 891 (1982).



AstroBox2 – Detector for low-energy β -delayed particle detection



A. Saastamoinen^{a,*}, E. Pollacco^b, B.T. Roeder^a, A. Spiridon^a, M. Daq^a, L. Trache^c, G. Pascovici^c,
R. De Oliveira^d, M.R.D. Rodrigues^e, R.E. Tribble^a

^a Cyclotron Institute, Texas A&M University, College Station, TX 77843, USA

^b IRFU, CEA Saclay, Gif-sur-Yvette, France

^c National Institute of Physics and Nuclear Engineering, Bucharest-Magurele RO-077125, Romania

^d CERN, Geneva, Switzerland

^e Instituto de Física, Universidade de São Paulo, Caixa Postal 66318, CEP 05314-970, São Paulo, SP, Brazil

ARTICLE INFO

Article history:

Received 2 September 2015

Received in revised form 4 February 2016

Accepted 4 February 2016

Available online 12 March 2016

Keywords:

Radioactive ion beams

Micro pattern gas amplifier detector

MPGAD

Implantation

$\beta\beta$ $\beta\gamma$

ABSTRACT

Efficient suppression of β -background is essential for studies of low-energy β -delayed charged particle decays of astrophysical interest. A promising method for such studies has been a micro pattern gas amplifier detector where the sample is implanted into the gas volume and the decays that follow are observed with high gain and signal to noise ratio. An upgraded version of the original AstroBox detector has been built and commissioned at Texas A&M University. Here a description of the new AstroBox2 detector is given, selected results from the commissioning tests are presented, and future perspectives discussed.

© 2016 Elsevier B.V. All rights reserved.

1. Introduction

Resonant reactions are important in many explosive hydrogen-burning scenarios. The key parameters in understanding the aforementioned astrophysical reaction rates are the energies and decay widths of the associated nuclear states along the reaction paths. The relevant states for particle capture reactions are located in the Gamow window, just above the associated particle separation threshold (e.g. proton separation energy, S_p). The properties of these states can be probed by using indirect methods, which include β -decay studies.

Over the past years we have studied the decay of several beta-delayed proton emitters of astrophysical interest by implanting the nuclei of interest into Si detectors of various segmentations [1–5]. In these studies it was realized that shrinking the physical detection volume of elements in a Si detector does not reduce the beta-background to allow unambiguous interpretation of the proton data originating from weak decay branches in the typical energy range of astrophysically interesting decays ($E_p \sim$ few hundred keV). To further reduce the β -background a novel gas detector, AstroBox was developed [6]. The Astrobox detector is based

on Micro Pattern Gas Amplifier Detector (MPGAD) technology [7] and was proven to work in operating conditions required for low energy β -delayed charged particle detection.

We have built an upgraded version of this detector, AstroBox2. The major change to the first version [6] is the overall size and change of the segmentation geometry of the MPGAD anode. The earlier cylindrical symmetry with only five segments has been replaced by a set of 29 rectangular anode pads that are arranged into a symmetric geometry along the beam axis. The new configuration allows better control of the source implantation and gives more refined possibilities for decay studies. The new custom made detector chamber has several technical improvements that enhance the overall usability of the setup. In this article we give a description of the AstroBox2 detector and results from the first commissioning tests.

2. Description of the detector

The general operating principle of the detector and associated components is similar to the description in Ref. [6]. In short, AstroBox2 detector, shown in Fig. 1, is a rectangular-shaped gas detector, operated in a mode in which the ions of interest are stopped inside the gas volume and let decay. The electrons created by the decay radiation ionizing the gas are drifted towards a gas

* Corresponding author. Tel.: +1 979 845 1411; fax: +1 979 845 1899.

E-mail address: ajsaasta@comp.tamu.edu (A. Saastamoinen).

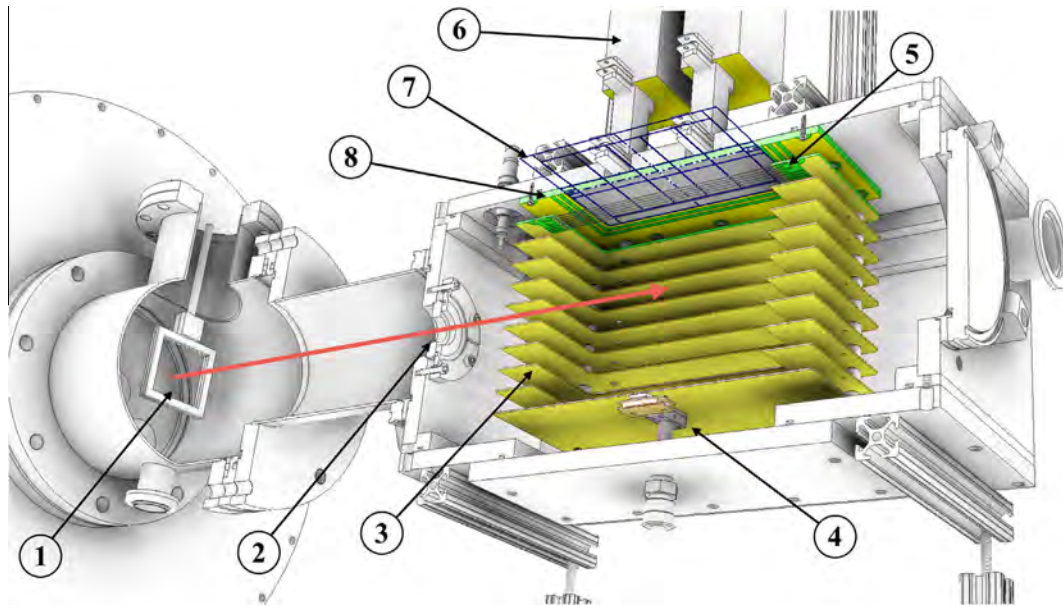


Fig. 1. An illustration of the AstroBox2 detector setup. The red arrow indicates secondary beam direction from the MARS spectrometer. (1) Rotatable degrader frame. (2) Aramica window (50 μm) separating gas volume from separator vacuum. (3) Field cage equipotential rings. (4) Cathode with a source holder that can be masked while the detector remains under operating conditions. (5) Gating grid. (6) Preamplifiers. (7) An overlaid grid highlighting the Micromegas detector anode pad structure, cf. Fig. 4. (8) The PCB onto which the Micromegas is mounted. See text for more details. (For interpretation of the references to color in this figure legend, the reader is referred to the web version of this article.)

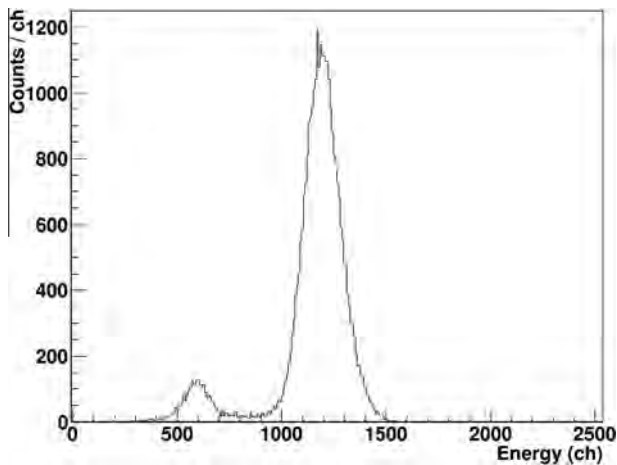


Fig. 2. Detector response to ^{55}Fe X-ray source. Typical resolution of 14–16% is achieved for the 5.9 keV X-ray when taking into account the weaker 6.5 keV X-ray distorting the shape. The small peak on left is the Ar X-ray escape peak.

amplifier based on Micromegas technology [7]. The Micromegas detector element with active area of $100\text{ mm} \times 145\text{ mm}$ is divided into 29 rectangular anode pads of various sizes arranged symmetrically along the beam axis. At the moment only a detector with a 128- μm amplification gap has been tested, but we have acquired also detectors with 256 μm and 64 μm gaps. The pad layout is shown in Figs. 1 and 4. The detector printed circuit board (PCB) doubles as a sub-flange which allows the signals to be transmitted directly to the readout electronics and the detector element voltages to be applied without any feed-throughs.

The signals from the 29 anode pads are read out with two Mesytec MPR16-100 16 channel preamplifiers coupled to Mesytec MSCF16 shaper/discriminator modules. The detector is triggered as a logic OR of any of the pads. The data acquisition consists of one Mesytec 32 channel MADC32 ADC in 8 k hi-res mode for energy

information, a CAEN V1190A TDC for timing information, and two of Struck Innovative Systeme SIS3820 scalers for rate monitoring and decay time measurements.

The field cage with spacing of 16.5 mm is mounted on the detector PCB. The rest of the chamber was designed around the detector assembly by keeping the size as small as possible, while taking into account the minimal safe distance to run the cathode at a potential of -3.3 kV to achieve a uniform electric field of about 200 V/cm across the whole active gas volume. The equipotential

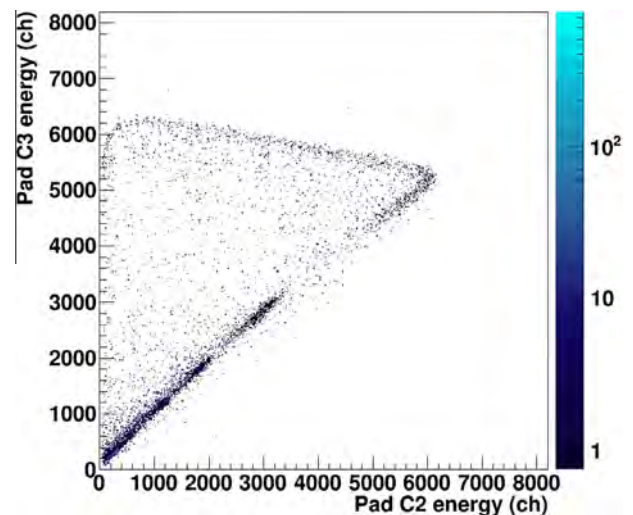


Fig. 3. Measured energy losses in two pads (labeled C2,C3) along the beam path versus each other when the ^{25}Si beam is stopped on the pad C3 (the centermost pad of the detector). The diagonal has the ions with same magnetic rigidity and $Z < 14$ punching through these two pads. The almost horizontal line indicates the energy loss of ^{25}Si particles stopping in different locations within the pad C3. The fraction of ^{25}Si ions punching through the following pad (C4, not shown) are located in the corner formed by the diagonal and the horizontal line.

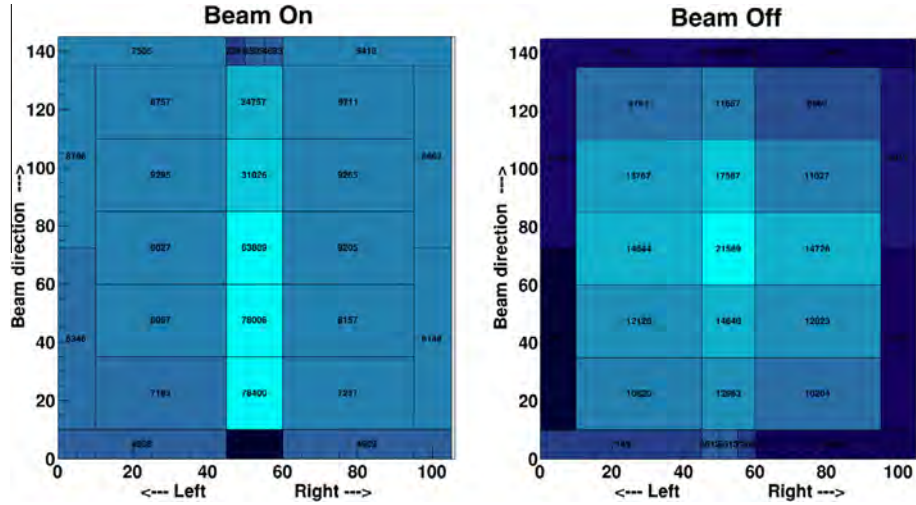


Fig. 4. Event display showing the anode pads with signal above set threshold. Data from same run as in Fig. 3. The axis units are in mm, corresponding to the physical detector layout, cf. Fig. 1. When the beam is on (left panel), the majority of signal is collected from the centermost pad, and from the pads along the beam axis. When beam is switched off (right panel) the most intense counts (brighter color) are confined into the centermost pad where the beam has stopped and where majority of decays occur.

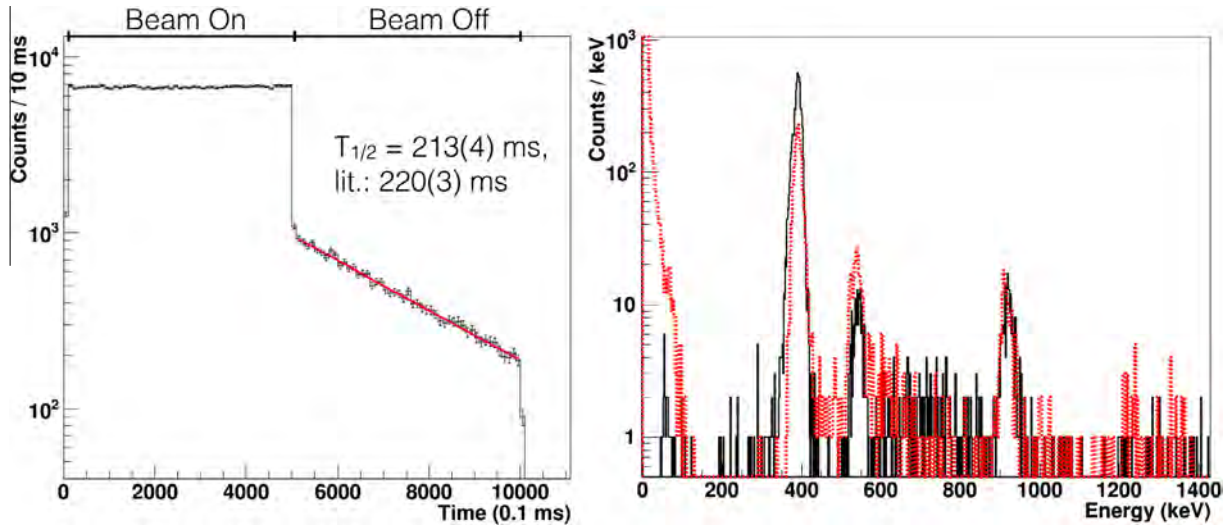


Fig. 5. Left: Decay time spectrum of ^{25}Si gated by the decay energies of the 401, 555, and 943 keV proton peaks. The data was collected during beam off period of a pulsed beam with a cycle of 500 ms on and 500 ms off. Right: Measured β -delayed proton spectrum of ^{25}Si (black, solid) compared to a GEANT4 simulation (red, dashed) when decays are confined into one pad active volume. The experimental data is cut at about 100 keV due to the discriminator threshold, whereas the simulation shows the expected background without electronics threshold. Resolution of the 401 keV proton group is $\sim 4\%$. (For interpretation of the references to color in this figure legend, the reader is referred to the web version of this article.)

ring closest to the Micromegas is a PCB having a set of 50 μm thick wires, forming a gating grid that can be used to limit the transmission of the drifting electrons. All high voltages for the anode pads and for the gating grid were taken from Ortec 710 bias supply (0–1 kV) or Mesytec MHV4 (0–400 V), and the cathode voltage was provided from Ortec 549 bias supply (0–5 kV).

The overall construction of the chamber is modular, allowing easy customization for different experimental needs. All materials inside the gas volume are chosen to be minimally outgassing, and all hardware inside the gas volume is of vented design by default. At the moment the gas handling system is the same as in AstroBox [6]. There are two variants of the cathode. The first is solid construction with a source holder in which the test source can be masked without breaking the vacuum. The second cathode is a thin copper mesh soldered on a spare field cage element. This transparent construction allows scanning of the whole active detector area by a movable source holder.

3. Source tests

The first detector element with 128 μm amplification gap has been tested off-line in various conditions to determine operational parameters for optimal performance. All tests were carried out using a P5 gas mixture (5% CH_4 + 95% Ar) at 800 torr pressure, which is a typical pressure required for β -delayed proton decay studies. In all off-line and on-line tests the cathode was run at -3.3 kV, the mesh was kept at ground potential, and the anode voltage was varied to adjust the gas gain.

The detector response for α sources was tested with a mixed source containing ^{148}Gd , ^{239}Pu , ^{241}Am , and ^{244}Cm . The source is housed in a tightly collimated holder (two 1 mm holes 3 mm apart) over the centermost anode pad. Typical resolution of 3% is achieved for the 5.486 MeV ^{241}Am α line.

An extensive set of tests was carried out with an ^{55}Fe X-ray source by utilizing the transparent cathode. The collimated X-ray

source was mounted on a steel ring sitting on a plexiglass window at the bottom of the chamber. This configuration allows moving the source with a magnet outside the window, while keeping the detector under operational conditions (magnet can be removed to avoid distortion of the field inside the detector). The response of the centermost pad to the 5.9 keV X-ray is shown in Fig. 2. Typical resolution of 14–16% is achieved across the whole detector.

4. In-beam test with β p-decay of ^{25}Si

The in-beam test was conducted at the Cyclotron Institute of Texas A&M University. A secondary beam of ^{25}Si was produced through fragmentation by bombarding a 254 μm thick Al foil with a 40-MeV/u ^{28}Si beam from the K500 cyclotron. The reaction products were separated with the Momentum Achromat Recoil Spectrometer (MARS) [8], yielding a beam of ^{25}Si with 25% purity at 34 MeV/u and $\delta p/p = 0.25\%$. During the testing, a typical implantation rate was about 50 pps for ^{25}Si .

To implant the sample into the detector, the beam was passed through a rotatable 21 mil (533 μm) thick Al degrader and through a 50 μm thick aramica window. The combination of small initial momentum distribution and adjustable degrader thickness allows precise control of implantation of the sample over the desired pad. As all species in the beam from MARS have same magnetic rigidity, the relatively low density of the stopping medium lets the impurities with lower Z pass through the active volume of the detector, whereas impurities with higher Z are stopped before reaching the active volume. The beam energy loss of two pads versus each other along the beam path is shown in Fig. 3 for the case when the beam stops over the centermost pad of the detector. For more detailed description of the implantation procedure, see Ref. [6]. In this configuration the gating grid was kept at the corresponding field cage potential of -330 V , whereas the anode voltage was at $+300\text{ V}$ to limit amplification of the large signal induced by the beam.

In the measurement configuration, the gating grid was pulsed between ground (beam on) and the corresponding field cage potential of about -330 V (beam off). The high voltage pulsing was done by using a Behlke HTS-31-03-GSM switch that was synchronized to the cyclotron beam pulsing. The beam on and off periods were both 500 ms with 5 ms wait period in-between to allow settling of the gating grid voltage transition induced noise. The anode was run at $+450\text{ V}$.

Fig. 4 illustrates event display for both beam on and off cases when the beam is stopped into the centermost pad and following decays observed. A sample of the observed β -delayed proton spectrum and associated time spectrum is shown in Fig. 5. The energy

spectrum shown is generated by vetoing all the surrounding pads around the pad where the beam was stopped on. In this way, the β -background of the measured data is suppressed below the used discriminator threshold of about 100 keV (simulated spectrum shows the expected background without electronics threshold). A comparison of the measured data to a GEANT4 [9] simulation, based on the energies and branching ratios of the latest decay study of Thomas et al. [10] shows a reasonably good agreement. The difference in intensities is likely due to fact that these proton groups were on top of large β -background in Ref. [10].

5. Future developments and outlook

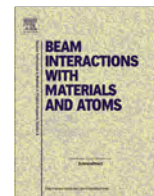
So far the very first detector element with 128 μm amplification gap has been thoroughly tested. We have recently acquired two new detector elements using a more uniform, electroformed mesh with amplification gaps of 64 and 128 μm . These will be tested during fall 2015 and spring 2016. Future improvements of the detector under consideration include replacing the old gas handling system with an improved new system including fully electropolished stainless steel tubing, added filters, and fully oil free pumping for more reliable and faster gas handling. Other future additions for the setup will include HPGe detectors for identifying possible particle- γ -coincidences to distinguish whether the observed particles populate the ground state or some excited state in the proton daughter. In addition, an implementation of digital GET (General Electronics for TPCs) electronics for the data readout is under consideration. The first physics runs are foreseen to be conducted during spring 2016.

Acknowledgements

This work has been supported in part by the US DOE under Grants DE-FG02-93ER40773 and DE-NA0001786, and by the grant PN2-ID-27-2013 from ANCSI Bucharest, Romania. Authors thank Praveen Schidling for lending the Behlke HV switch for the test run.

References

- [1] A. Saastamoinen et al., *Phys. Rev. C* 83 (4) (2011) 045808.
- [2] L. Trache, et al., *PoS(NIC X)* (2008) 163.
- [3] A. Saastamoinen et al., *AIP Conf. Proc.* 1409 (4) (2011) 71.
- [4] J. Wallace et al., *Phys. Lett. B* 712 (1–2) (2012) 59–62.
- [5] M. McCleskey et al., *Nucl. Instr. Meth. Phys. Res. A* 700 (2013) 124.
- [6] E. Pollacco et al., *Nucl. Instr. Meth. Phys. Res. A* 723 (2013) 102.
- [7] Y. Giomataris et al., *Nucl. Instr. Meth. Phys. Res. A* 376 (1) (1996) 29–35.
- [8] R. Tribble et al., *Nucl. Phys. A* 701 (1–4) (2002) 278–281.
- [9] S. Agostinelli et al., *Nucl. Instr. Meth. Phys. Res. A* 506 (3) (2003) 250–303.
- [10] J.-C. Thomas et al., *Eur. Phys. J. A* 21 (2004) 419–435.



Upgrade of the TAMU MDM-focal plane detector with MicroMegas technology



A. Spiridon^{a,*}, E. Pollacco^b, B.T. Roeder^a, A. Saastamoinen^a, R. Chyzh^a, M. Dag^a, R.E. Tribble^a, L. Trache^c, G. Pascovici^c, R. De Oliveira^d

^a Cyclotron Institute, Texas A&M University, College Station, TX 77843, USA

^b IRFU, CEA Saclay, Gif-sur-Yvette, France

^c National Institute of Physics and Nuclear Engineering, Bucharest-Magurele RO-077125, Romania

^d CERN, Geneva, Switzerland

ARTICLE INFO

Article history:

Received 2 September 2015

Received in revised form 10 December 2015

Accepted 1 February 2016

Available online 19 February 2016

Keywords:

Radioactive ion beams

Micro pattern gas amplifier detector

MPGAD

Spectrometers

ABSTRACT

A gridded ionization chamber used as a focal plane detector at the back of the TAMU-MDM spectrometer was modified to use MicroMegas technology for the purpose of improving energy resolution and particle identification. The upgraded system was tested in experimental conditions with several heavy-ion beams at 12 MeV/u and found to achieve resolutions between 3.2% and 4.8%. This is a significant improvement over the previous performance of 10–15% obtained using the existing, conventional ionization chambers.

© 2016 Elsevier B.V. All rights reserved.

1. Introduction

X-ray bursts are the most frequent thermonuclear explosion occurring in the universe and represent one type of phenomena responsible for heavier element nucleosynthesis. For this reason and others, a number of powerful X-ray observatories have been used to take large amounts of data on these bursts. The interpretation of these observations, however, is problematic due to the lack of a complete understanding of the nuclear physics at the base of these phenomena [1]. Among the various processes occurring in X-ray bursts, the most important is the rp-process. It is dominated by (p, γ), (α , p) reactions and β -decays. Critical nuclear data is needed related to these processes such as: nuclear masses, β -decay rates and reaction rates. Of the three, reaction rates are the most difficult to determine with direct methods due to the fact that most of the nuclei involved in these reactions are unstable [2].

At Cyclotron Institute, Texas A&M University, we have measured various proton capture reactions indirectly using the Asymptotic Normalization Coefficient (ANC) method [3] and experiments involving proton and neutron transfer reactions. These experiments were done primarily with the Multipole-Dipole-Multipole (MDM) spectrometer [4]. The Oxford focal plane detector sitting

at the back was used to identify particles and measure their positions along the dispersive x-direction. Using raytrace reconstruction we could determine the scattering angle at the target as a function of the angle of the particle path in the detector [5]. The reactions studied so far involved nuclei with $A \leq 26$. For masses in that region, we found that we were having significant difficulties with the particle identification (PID) due to the insufficient resolution of both the ΔE (energy lost in the gas) and E_{res} (residual energy, deposited in the stopping material) signals (see Fig. 1). Specifically, we needed to analyze isotopes of masses A and $A + 1$ separately but could not gate on each exclusively due to overlap.

In order to improve ΔE , we decided to use a MicroMegas detector. This is a relatively new detector technology that we have successfully used in a different system, called Astrobox [6], which is built specifically for low noise and is used to detect very low-energy protons from beta-delayed proton emitters.

The MicroMegas detector operates as a two-stage parallel-plate avalanche chamber. It consists of a small amplification gap (50–300 μm) and a much larger drift gap (on the order of cm) separated by a thin electroformed micromesh. It has been shown to provide gains of up to 10^5 [7].

In the course of testing and using the Astrobox, we observed that the MicroMegas also detected the incoming energetic heavier ions with good resolution for particle identification. In light of that,

* Corresponding author. Tel.: +1 979 845 1411.

E-mail address: aspiridon@comp.tamu.edu (A. Spiridon).

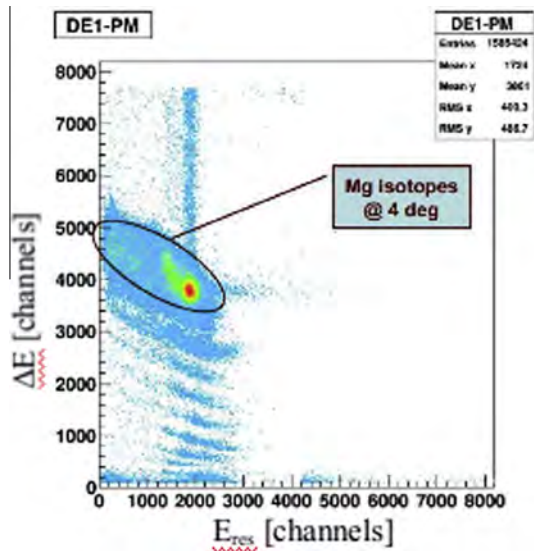


Fig. 1. Standard 2D ΔE - E_{res} spectrum produced by the Oxford detector and used for PID.



Fig. 3. (Top) The MicroMegas anode. (Bottom) Oxford detector with the new Anode mounted.

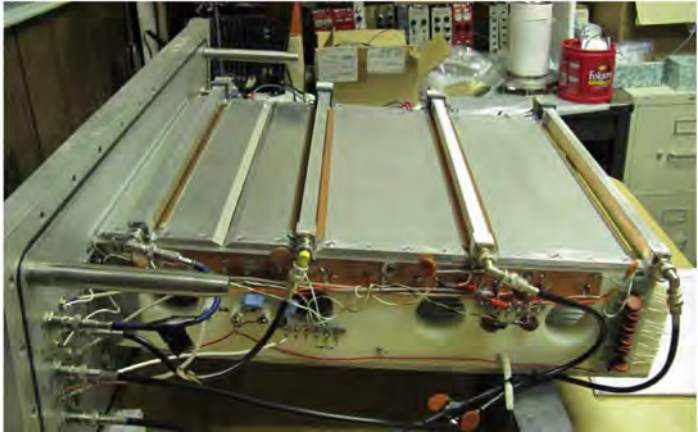
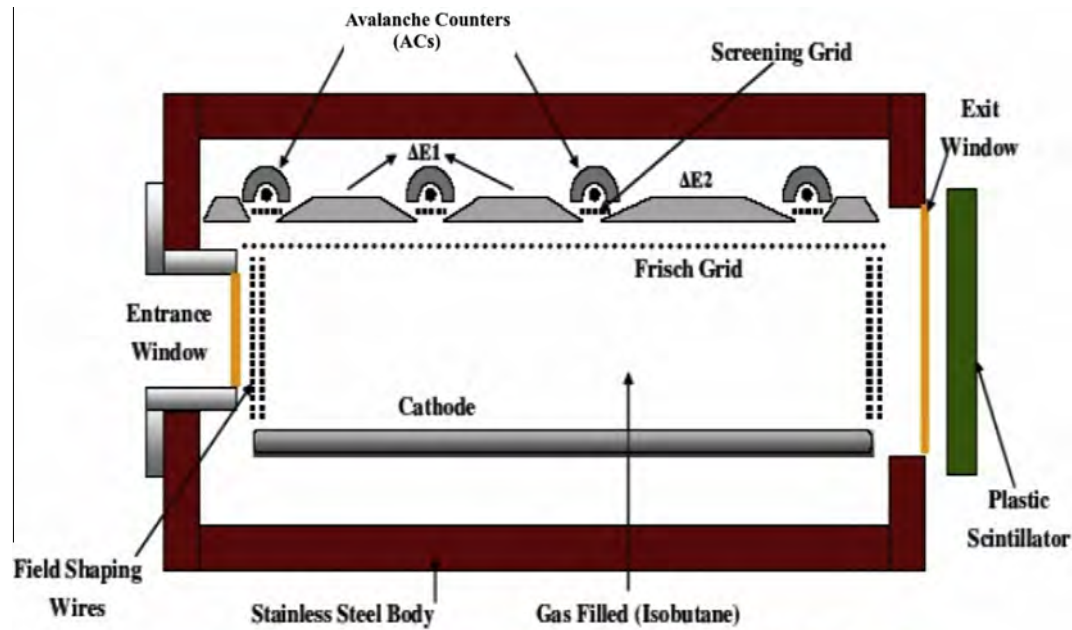


Fig. 2. (Top) Schematic drawing of the Oxford. (Bottom) Photo showing the Oxford detector.

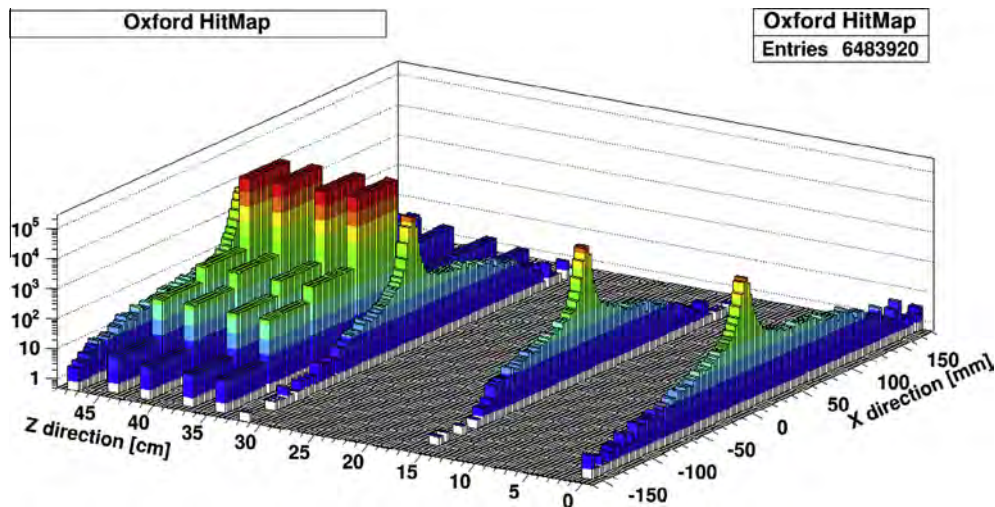


Fig. 4. A map of the Oxford detector showing the 4 position-sensitive avalanche counters and the MicroMegas pads. The peaks show that the beam is passing through the center of the detector highlighting predominantly column 4 (central) of the MicroMegas anode. X-axis is along the wires (ACs). Positive direction corresponds to higher reaction angles and higher energy particles. Z-axis is along the beam. Positive direction is downstream. The position of the first AC is taken as the 0 of the axis.

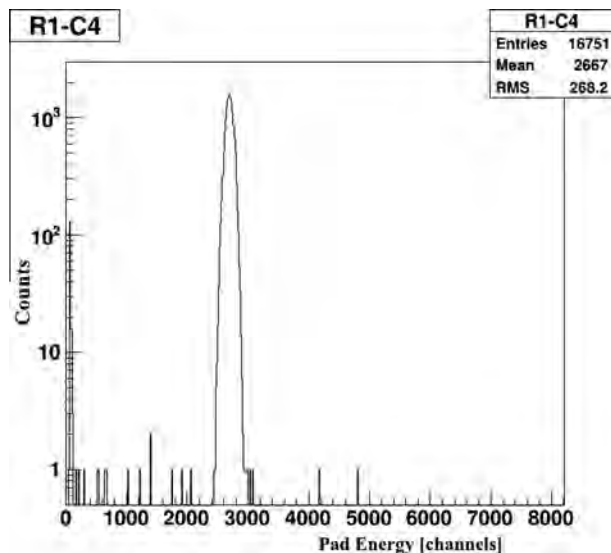


Fig. 5. Energy spectrum for pad R1-C4 of the MicroMegas anode.

we decided that this technology was exactly what we needed to upgrade the Oxford focal plane detector.

2. The TAMU-focal plane detector

The Oxford detector is a gridded ionization chamber with a plastic scintillator at the back. Fig. 2 (top) shows a schematic side view of the detector and its components. Fig. 2 (bottom) shows a photograph, similarly oriented for comparison. In both pictures, the beam of particles would come from the left. Four resistive wires working in avalanche conditions (AC) allow for position determination at four different depths in the detector and therefore permit raytrace reconstruction. Energy lost in the ionization gas, ΔE , is measured by the three anode plates at the top. Particles are stopped in the scintillator at the back, and the residual energy, E_{res} , is measured with two phototubes. A more detailed description of the detector, its components and its operation can be found in ref [8]. Currently, with only the first two plates connected to produce a signal we call $\Delta E1$, we obtain energy resolutions of 10–

15%, depending on voltage settings, gas pressure, particle Z and energy.

The third plate, $\Delta E2$, gave a signal with similar or poorer resolution and was never shown to improve particle identification. For this reason, we replaced the $\Delta E2$ anode with a MicroMegas plate (type Bulk) of identical size, 14.6 cm by 42.6 cm (Fig. 3, top).

The detection area consisted of 28 pads, 3.25 cm by 4.4 cm, each giving an individual ΔE signal corresponding to the energy lost in the respective gas region. The mesh was made of nickel and created an amplification gap of 256 μm with the anode. The drift region, between this mesh and the cathode was 12 cm. The detector was filled with isobutane gas and was operated at different pressures, between 30 and 100 Torr.

The 28 signals were read out through two DSub-25 connectors (Fig. 3, bottom), two rows of pads to each. Short flat cables routed the signals to two DSub-25 feedthroughs in the detector chamber. The electronics used to process them were: 2 Mesytec MPR-16 preamplifiers, 2 Mesytec MSCF-16 amplifiers and one VME-ADC module. The acquisition trigger was given by the coincidence between the phototube signals.

3. Results

We tested the upgraded detector with 3 beams: ^{16}O , ^{22}Ne and ^{28}Si . Each beam had an energy of 12 MeV/u. We used mainly elastic scattering on ^{197}Au . The heavy target allowed for a relatively pure beam (with some inelastic contributions). We also used ^{27}Al (only for ^{16}O) and ^{13}C targets in order to produce a cocktail of nuclei and observe the resulting PID spectra.

The purpose of these test experiments was to determine the MicroMegas response to different settings. We looked at the detector behavior for different bias voltages, different gas pressures and particles of different N and Z.

In studies done by other groups and also in our AstroBox tests, MicroMegas were only used with gases around atmospheric pressure. With the Oxford, we are limited by the entrance and exit windows so we had to start at 100 Torr, the maximum pressure we could safely have inside the detector without breaking the windows. However, this pressure is problematic at larger reaction angles where particles stop before triggering the data acquisition. In order to test the detector under the conditions of an ANC study

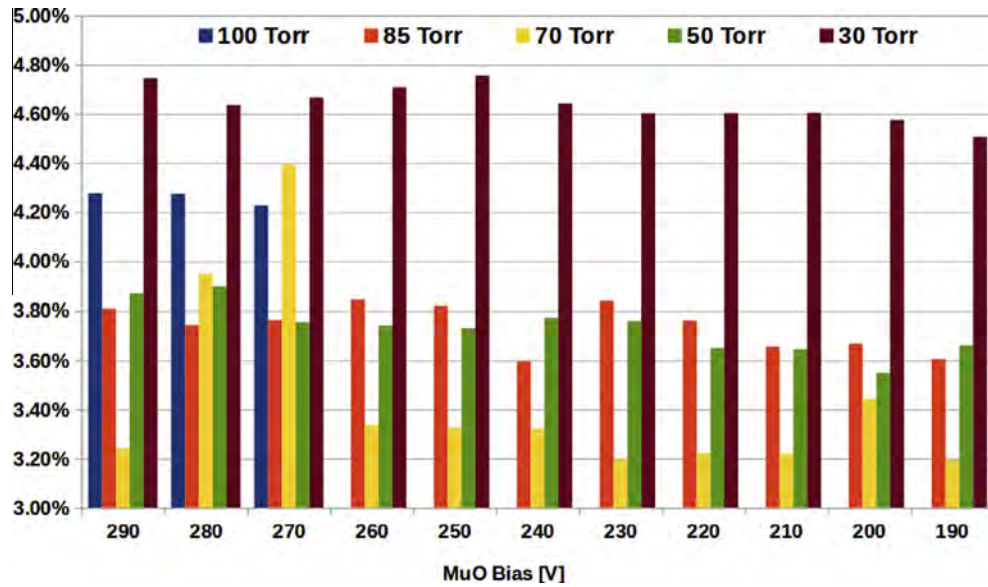


Fig. 6. Plot showing the energy loss resolution for the MicroMegas anode (averaged over the 28 pads) for different bias voltages of the MicroMegas and different gas pressures when detecting $^{22}\text{Ne} + ^{197}\text{Au}$ elastic scattering.

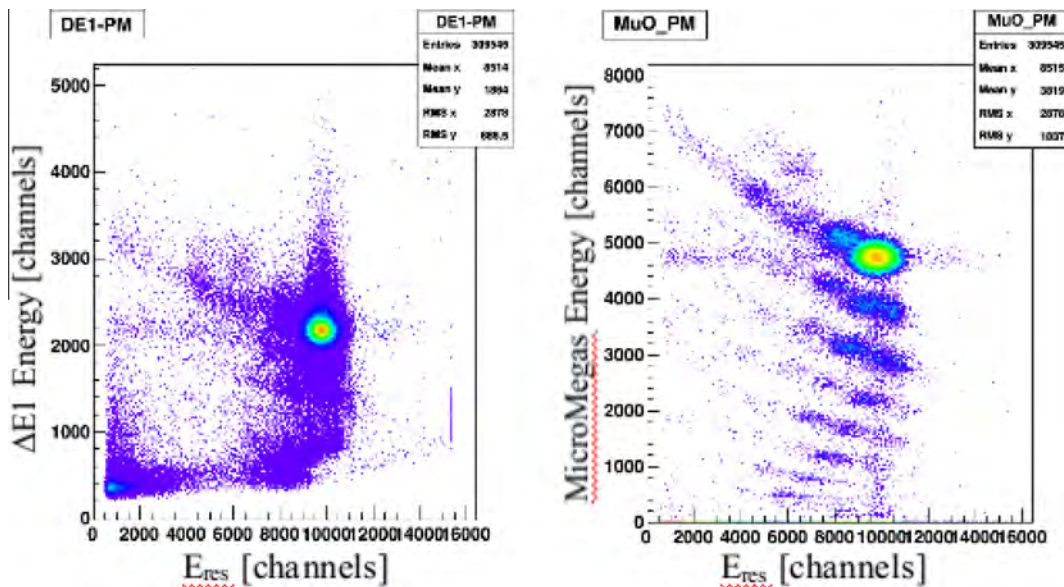


Fig. 7. Spectrum on left shows energy detected by the ionization chamber, $\Delta E1$, versus E_{res} . Spectrum on right shows energy detected by the MicroMegas versus same E_{res} . The data in both cases is from ^{22}Ne on ^{13}C at 5 degrees.

we had to cover the lower pressure range as well, especially 30 Torr which is what we typically use for such studies.

For each beam, we focused on elastic scattering off the gold foil. The reaction products were collimated with a narrow slit before going into the spectrometer. This allowed us to test each column of 4 pads in the MicroMegas anode with the same beam energy distribution. As an example, Fig. 4 shows the beam passing through the center of the Oxford detector, highlighting column 4 of the MicroMegas anode. The 4 position spectra detected by the ACs confirm this. Under these conditions, we observed the detector behavior for different bias voltages, gas pressures, and electronic gains.

An example of energy spectrum for an individual pad is shown in Fig. 5. The label 'R1-C4' denotes that it corresponds to the center pad in the first row to meet the beam. The resolution of the peak is $\sim 5.5\%$. For all three test beams, we obtained energy resolutions for

the individual pads in the range of 5.5–6.5% for 100 Torr and 85 Torr, 5.5–6% for 70 Torr, 6.5–7% for 50 Torr, and 8–9% for 30 Torr. Averaging the energy over all the pads gave us significantly better resolution (Fig. 6).

Last but not least, we looked at a cocktail of reaction products using the ^{27}Al and ^{13}C targets for different MDM angles and compared the PID spectra we obtained with the spectra that were obtained before the modification. Fig. 7 shows one such comparison for ^{22}Ne at 5 degrees and 30 Torr. It can be easily seen that the better resolution of the MicroMegas translates into improved separation between the various particles detected.

The $\Delta E1$ signal comes solely from the ionization electrons collected in the corresponding section of gas. However, the charge is small and requires significant electronic amplification using

preamplifiers and amplifiers. This has the dual effect of worsening the resolution and increasing the noise.

On the other hand, a smaller amount of electrons is produced in the section of gas under the MicroMegas but each electron creates an avalanche in the amplification gap. As such the charge collected is large enough to require little, if any, electronic gain leading to less noise and better resolution.

4. Conclusions

Using the MicroMegas to detect energy lost in the gas section of the Oxford detector led to energy resolutions 2–3 times better than with the ionization chamber. As such, the upgrade was considered successful and meets the requirements for particle identification in ANC studies so the modified detector is now being used in nuclear physics experiments. However, for a wider range of applications we would like to do further testing, with higher energy beams (20–40 MeV/u), heavier particles (^{32}S , ^{40}Ar . .), as well as different

gas mixtures. In particular, the improved Oxford is also intended for future use in studies with re-accelerated unstable beams from the T-Rex upgrade of our facility [9].

Acknowledgements

This work has been supported in part by the US DOE under Grants DE-FG02-93ER40773 and DE-NA0001785.

References

- [1] C.E. Rolfs, W.S. Rodney, *Cauldrons in Cosmos*, University of Chicago Press, 1988.
- [2] H. Schatz, *Nucl. Phys. A* 827 (2009) 26c–33c.
- [3] A.M. Mukhamedzhanov et al., *Nucl. Phys. A* 631 (1998) 788c–792c.
- [4] D.M. Pringle et al., *Nucl. Instr. Meth. Phys. Res. A* 245 (1986) 230–247.
- [5] D. Youngblood et al., *Nucl. Instr. Meth. Phys. Res. A* 361 (1995) 359.
- [6] E. Pollacco et al., *Nucl. Instr. Meth. Phys. Res. A* 723 (2013) 102.
- [7] Y. Giomataris et al., *Nucl. Instr. Meth. Phys. Res. A* 376 (1996) 29–35.
- [8] T. Al-Abdullah, Ph.D. thesis, Texas A&M University, 2007.
- [9] R.E. Tribble et al., *Eur. Phys. J. Spec. Top.* 150 (2007) 225.

Nuclear Astrophysics at IFIN-HH

This content has been downloaded from IOPscience. Please scroll down to see the full text.

2016 J. Phys.: Conf. Ser. 703 012011

(<http://iopscience.iop.org/1742-6596/703/1/012011>)

View [the table of contents for this issue](#), or go to the [journal homepage](#) for more

Download details:

IP Address: 194.102.58.6

This content was downloaded on 16/09/2016 at 13:05

Please note that [terms and conditions apply](#).

You may also be interested in:

[Measurements of the atmospheric muon flux using a mobile detector based on plastic scintillators read-out by optical fibers and PMTs](#)

D I Stanca, B Mitrica, M Petcu et al.

[The ELI-Nuclear Physics Project](#)

N V Zamfir

[Fractional exclusion statistics in systems with localized states](#)

G A Nemnes and D V Anghel

[The measuring of the absorbed dose in human tissue that underwent irradiation with ionizing radiation](#)

S. Bercea, A. Nikolic, C. Cenus et al.

Nuclear Astrophysics at IFIN-HH

Livius Trache

“Horia Hulubei” National Institute for Physics and Nuclear Engineering (IFIN-HH)
Bucharest-Magurele, RO-077125, Romania

livius.trache@nipne.ro

Abstract. I will present the possibilities and some results of doing nuclear astrophysics research in IFIN-HH Bucharest-Magurele. There are basically two lines of experimental activities: (1) direct measurements with beams from the local accelerators, in particular with the new 3 MV Tandatron accelerator. This facility turns out to be competitive for reactions induced by α -particles and light ions. Extra capabilities are given by the ultra-low background laboratory we have in a salt mine about 2.5 hrs. driving north of Bucharest; (2) indirect measurements done with beams at international facilities, in particular at those providing Rare Ion Beams. Completely new and unique opportunities will be provided by ELI-NP, under construction in our institute.

1. Introduction

I am glad to be again at this school! It is one of the three pillars of the European Network of Nuclear Astrophysics (ENNAS) and together with the Russbach, Austria, winter school and the Carpathian summer school in Sinaia, Romania, does an excellent service to the community. I did not want to miss coming and lecturing here. This time I did not chose the title, the organizers chose it for me. And I was glad to oblige! I will, therefore, talk about research in nuclear astrophysics (NA) at my home institute IFIN-HH, a home that I re-joined 3 years ago after a two decades absence. Besides my own group that I try to organize, there are groups with at least part of their activity motivated by NA at the accelerators the institute has. That is when we refer to experimental work. There are theoretical activities motivated by NA and I will briefly mention those, but not insist.

You (students) have learned already at this school, and I am sure you did know already, that, *grosso modo*, in experimental nuclear astrophysics we use:

- 1) direct measurements, that is, we measure the reactions that happen in stars at exactly the energies they happen, or as close to them as possible and
- 2) indirect measurements.

The first type of measurements are difficult mostly due to the very low cross sections which are typical for the very low energies available in stars. Only cases where the reactions are possible with the available projectile-target combinations (stable nuclei) can be studied so far. Particular care must be taken to get accelerators with high currents, good targets, high detection efficiencies and conditions to maintain good signal/background ratios. I will show in the next section that we can do competitively a few types of these measurements in Bucharest. The indirect methods are those methods in which we make studies using nuclear reactions at much higher energies than those available/important in the stars, typical nuclear laboratory energies 100-1000 times larger, seeking information which is later used to evaluate reaction rates at very low energies. Here there are advantages related firstly to the larger cross sections of the reactions employed and secondly to the

fact that by using Radioactive Nuclear Beams (RNB), available lately in several laboratories, we can extend our measurements to stellar reactions which involve unstable partner(s). In IFIN-HH we do not have RNB so far, therefore this type of measurements we can only pursue at outside facilities. Important to notice is that good, reliable theoretical support is crucial in all indirect methods; I will briefly argue on that later.

2. Direct measurements

The goal of these type of measurements is to measure cross sections in the Gamow window. This means very low energies and consequently very low cross sections, a fact easily understandable for the case of reactions between charged particles (as for example (p, γ), (α , γ) or ion-ion fusion), as due to the Coulomb barrier. As such, it is no wonder that the first measurements in the Gamow window are only about one decade old! That could be done in an underground lab like that in the National Laboratory Gran Sasso and several other labs are now working with very light projectiles like p, d, or ^3He and different detection techniques.

In Bucharest we do not have a proton accelerator and conditions to compete in the study of proton induced reactions. But it turns out we have good conditions to study α -induced reactions and reactions between light ions important in NA. Let me elaborate on that. IFIN-HH has now 3 tandem accelerators:

- an old, but fully refurbished, 9 MV FN tandem pelletron, which is used mostly for gamma-ray spectroscopy;
- a 3 MV tandetron, installed in 2012 and which works since mid 2013 for applications like Ion Beam Analyses, ion implantation and cross section measurements [1];
- a 1 MV tandetron completely dedicated to Accelerator mass Spectrometry, used for ^{14}C dating and other such applications (like geological dating).

Since the beginning of its operation we tested the capabilities of the 3 MV tandetron for direct measurements for nuclear astrophysics. The conditions necessary for this are: appropriate energy range, stability, diversity of projectiles, high currents. We tested all of the above and found the it will be competitive. The energies are given by the terminal voltage range which is $V=0.3 - 3.3$ MV. It was tested to be stable over weeks of operation. It has two ion sources: a duoplasmatron and a sputter source. Na, Cs and Li charge exchange are used preferentially. These allow a diversity of beams to be provided. Table 1 shows the intensities of the beams analyzed.

2.1. Nuclear Astrophysics Group (NAG)

An extra opportunity is provided by the ultra-low background laboratory the institute has in a salt mine located at about 100 km north of Bucharest-Magurele, in Slanic-Prahova [2]. We call it microBequerel. While at about 260 m below surface this is not a particularly deep mine, it has the property of being very low in natural radioactivity, due to a large distance from rocks and its compact walls. With a well shielded Ge detector a background reduction factor up to 4000 was obtained (relative to the surface background of the same unshielded detector).

Projectile	Intensity	Source
$^1\text{H}^+$	$>25 \mu\text{A}$	duoplasmatron
$^4\text{He}/^3\text{He}^+$	$>3 \mu\text{A}$	
$^{11}\text{B}^{3+}$	$>50 \text{ e}\mu\text{A}$	sputter
$^{12}\text{C}^{3+}$	$>80 \text{ e}\mu\text{A}$	
$^{16}\text{O}^{3+}$	$>80 \text{ e}\mu\text{A}$	
$^{28}\text{Si}^{3+}$	$>70 \text{ e}\mu\text{A}$	
$^{31}\text{P}^{3+}$	$>70 \text{ e}\mu\text{A}$	
$^{58}\text{Ni}^{3+}$	$>20 \text{ e}\mu\text{A}$	
$^{63}\text{Cu}^{2+}$	$>20 \text{ e}\mu\text{A}$	
$^{75}\text{As}^{2+}$	$>10 \text{ e}\mu\text{A}$	
$^{197}\text{Au}^{2+}$	$>80 \text{ e}\mu\text{A}$	

Table 1. Beam intensities from the 3 MV tandetron [1].

We have, therefore, tested a procedure in which we irradiate targets in Magurele, then transfer them in Slanic and measure them [3]. Obviously this procedure will not work for cases where the resulting activity after irradiation has half-lives much shorter than the transfer time of about 2.5 hrs.

One case ideal for the test of the procedure we proposed together with colleagues from China (IMP Lanzhou and CIAE Beijing): the reaction $^{13}\text{C}+^{12}\text{C}$. The motivation of the experiment, the setup of 2014 and its preliminary results were presented at this school by one of our students and is included in this volume [4], please see it for details. You can see there pictures of the accelerator and of the salt mine. I will only mention here that only one reaction channel leads to radioactivity (one-proton evaporation), ^{24}Na which has $T_{1/2}=15.0$ h, excellent for the procedure we used: one day of irradiation, transfer to Slanic in 2.5 hrs and about one day de-activation measurement there, during the irradiation of the next target, and so on... With these we could reach (measurements in Sept.-Oct. 2014 and Oct. 2015) cross sections of the order of tens of picobarns, about 100 times more sensitive than any measurement done before. In the latter experiment we also measured prompt gamma-rays (as far down in projectile energy as we could) to assess the contribution of the other open reaction channels. Another condition, which did I not mention so far, is the availability of good detection devices. We have several high resolution, high efficiency HpGe detectors (100-120 % relative efficiency), many large Si detectors and we are building a large (80 cm diameter) reaction chamber. I mention that the tandems accelerators are internationally open facilities, with PAC meeting annually and are transnational access facilities under the ENSAR2 project.

2.2. Other activities in nuclear astrophysics

There are also groups in the Department of Nuclear Physics (DFN) of IFIN-HH using beams from the 9 MV tandem for nuclear astrophysics. They measured (α,γ) reactions at relatively low bombarding energies on medium mass targets, having in mind to obtain data for modeling the nucleosynthesis of the *p-nuclei*. One such example is presented at this school by Andreea Oprea [5]. Detailed measurements, down to energies close to the Gamow window, can provide data to determine optical potentials for α -particles at low energies and radiation strength functions. The experiments typically measure prompt or activation gamma-rays as the department is rich in gamma-ray detectors and in experience in using them. Experimental measurements are complemented by theory efforts to provide systematics of α -particle optical potentials at low and very low energies by Vlad and Marilena Avrigeanu of the same department (see for example [6] and references therein).

3. Indirect measurements at outside facilities

This type of measurements involve radioactive nuclear beams, as I said before, and they are planned or actually done at outside facilities. I will not talk generally about indirect methods in NA here, I was doing it at earlier editions of the school, they were discussed by prof. Carlos Bertulani a few days ago. I will only mention two of them, pursued by my NAG group.

3.1. Coulomb and nuclear breakup of ^9C at RIBF of RIKEN

We have proposed earlier to use breakup reactions to extract Asymptotic Normalization Coefficients and from there radiative proton-capture rates [7]. We were talking about nuclear breakup. Coulomb breakup was proposed long before and used as a reliable indirect method in NA [8, 9]. The current knowledge of the rate of the $^8\text{B}(p,\gamma)^9\text{C}$ reaction in stellar conditions is contradictory at best and there is no hope to determine it, now or ever, by other means than by indirect methods. This reaction gives a possible path to the hot *pp* chain *pp-IV* at high temperatures and away from it toward a rapid alpha process *rap I* at high temperatures and densities and therefore is important in understanding nucleosynthesis in super-massive hot stars in the early universe, including possible bypasses of the 3α -process. Our best hope at the determination of the astrophysical factor S_{18} at low energies is by using the $^9\text{C}\rightarrow^8\text{B}+p$ breakup. We proposed to use a combination of nuclear and Coulomb dissociation measurements using the SAMURAI spectrograph of RIBF at RIKEN (on a light target – Be or C and on a heavy target – Pb, respectively) at two energies (100 and 300 MeV/nucleon) to extract structure information which will allow to evaluate the radiative proton capture cross section at low energies and from there the reaction rate. We proposed an exclusive study of the reaction, which may allow a better

understanding of the reaction mechanism (proposal NP1412-SAMURAI29R1, approved by PAC Dec. 2014). The high probability of two-proton breakup ${}^9\text{C} \rightarrow {}^7\text{Be} + 2\text{p}$ for this projectile makes it a good case to learn about the complex reaction mechanisms involved. Such an understanding may allow for a better theoretical description of the reactions and more accurate calculations of the momentum and angular distributions, a crucial step in using indirect methods for nuclear astrophysics.

Not negligibly, the reaction proposed is the easiest among the p-HI experiments being planned at this point with SAMURAI and will be a good start for the use of the Si detector system in front of SAMURAI as it results in a smaller dynamical range and an easier particle identification and less kinematic focus. Part of the preparations for these experiment, actually for a whole set of proton breakup experiments proposed at SAMURAI was to build the detection system in front of the spectrograph which involves many channels (upward of 1024) and with the capability to measure energies on a very broad dynamic range (from 200 keV to 600 MeV). An approach based on ASICs was proposed, developed and tested at the HIMAC medical facility in Chiba, Japan. I do not detail that multi-year work here.

3.2. β -delayed proton decay with AstroBox2 at Texas A&M University

Last edition of the school I discussed the design of a new type of detector to measure β -delayed proton emission, using a detection scheme that involved the stopping of the p-emitting nuclei in the middle of a gas detector after their production and separation with the MARS recoil separator of the Cyclotron Institute at Texas A&M University. The β -delayed protons emitted produce ionization in gas and the resulting charges are directed and then amplified with very efficient and good resolution devices called micromegas. The detector was called Astrobox1 [10] and we have shown its use for measuring very low energy protons, as well as the connection between these measurements and the determination of astrophysical reaction rates for proton induced reaction rates dominated by resonances. Its main advantage over very thin Si detectors (45-65 μm) we have used in the first stage of this project is that it is less sensitive to betas emitted always in the first stage of the decay, which gave a large continuous background in Si at low energies, exactly in the energy range of interest for us (protons of 150-500 keV). The sensitivity is down to around 10^{-4} (p-branching ratios). Since, we have worked, with our colleagues at CEA/IRFU Saclay, TAMU and CERN on an improved version of this detection scheme. The detector, dubbed Astrobox2, was built in this transcontinental collaboration and the first test measurements were done at the Cyclotron Institute, Texas A&M University, in College Station, TX in April 2015. The active part of the detector, the micromegas was built for us by a group at CERN, the inventors of such devices. The body of the detector was designed in Texas by dr. A. Saastamoinen. Its design and realization was actively pursued by us and by our collaborator from CEA/IRFU Saclay, France, dr. E. Pollacco. Schematically is shown in Figure 1. The main difference from AstroBox1 is that it does not have anymore a cylindrical symmetry (on an axis perpendicular to the beam), but is more appropriate to the geometry of the beam and its stopping in the gas of the detector. Another difference is that it has 29 separated pads and correspondingly 29 signals, compared with 3 (or 5) only for AstroBox1 (AB1).

The tests that were done, were:

- Off-beam tests using ${}^{55}\text{Fe}$ and ${}^{241}\text{Am}$ sources
- In-beam commissioning of the detector using a ${}^{25}\text{Si}$ radioactive beam separated by the MARS spectrometer. The radioactive specie we used, ${}^{25}\text{Si}$, is very appropriate for a test of a new proton detector, as it is a good, well known, β -delayed proton emitter with a large βp -branching. It was produced at a reasonable rate from a primary beam of ${}^{28}\text{Si}$ at 40 MeV/nucleon on a ${}^{27}\text{Al}$ solid target. The result was actually a cocktail of secondary beams, a benefit for the identification of the beam in AB2.
- In-beam measurements for the ${}^{23}\text{Al}$ secondary beam, which is the main focus of the physics for these measurements.

The same scheme of measurements was used in 2012 on a test of AB1. The first two parts of the tests went very well, and the commissioning of the AB2 detector was a success. So appeared to be the

last measurement, for which we reserved the last 4 days of the experiment. The primary beam of ^{24}Mg at 45 MeV/nucleon was delivered successfully to us on Friday April 24, and the next day the secondary beam of ^{23}Al was selected and was stopped in the middle of the AB2. The data need still be fully analyzed to see if the reconstruction of all signals from adding the adjacent pads improved the statistics to the point we need.

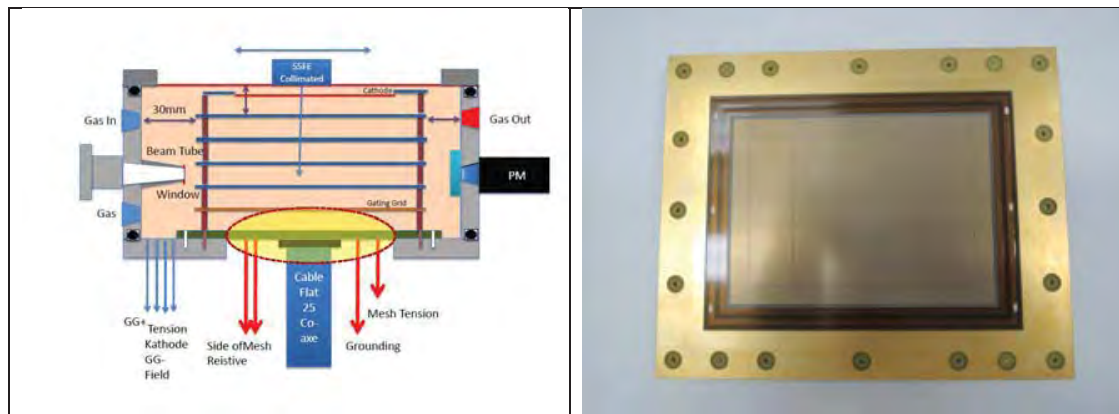


Figure 1. AstroBox2: left - schematic view of the detector, parallel to the beam entering from left; right - photo of the micromegas plate.

3.3. Theory for indirect methods in NA

We have a long-term program to understand and describe nucleus-nucleus collisions in terms of one interaction potential, the optical model potential (OMP). A good understanding of all phenomena occurring in the elastic nucleus-nucleus scattering, which are used typically to extract OMP, and the interpretation of the origin of different aspects, including the well known potential ambiguities, are of crucial importance for finding and justifying the procedures used for predicting nucleus-nucleus OMP in the era of radioactive nuclear beams (RNB), including ours based on double folding [11]. The reliability of these potentials is crucial in the correct description of a number of reactions involving RNBs, from elastic to transfer, to breakup, at energies ranging from a few to a few hundred MeV/nucleon. Of particular interest for us is to support the absolute values of the calculated cross sections for reactions used in indirect methods for nuclear astrophysics [13]. In this framework, we paid and pay particular attention to obtain OMP using double folding and to finding systematics for the re-normalization coefficients that appear as needed in quasi-all cases. It is extremely important for the use of indirect methods to be able to obtain and rightfully claim good absolute values for the calculated cross sections for various phenomena (including ^9C breakup, e.g.), see Refs. 12-14 for the most recent results.

4. ELI-NP

The most important and the most notable news from IFIN-HH in the last 3 years is ELI-NP. This is a large European project being built by our institute, in our institute and is designed to be an independent European institution in a few years. It consists of two 10 PW lasers and a gamma-beam system capable of delivering brilliant and mono-energetic gamma beams up to 19-20 MeV. These powerful lasers will make possible a nuclear physics program that has many potentially unique capabilities. Is being described in the talk by dr. O. Tesileanu here, including its program in nuclear astrophysics, which is developed in collaboration with scientists from Europe and the whole world, including many from LNS Catania. I will list here only one idea that may not have been included in that talk. It is expected that at ELI-NP stellar plasma conditions will be produced for long enough

periods of time to have nuclear reactions in equilibrium at large temperatures T . There will be many problems, like how to realize those stellar plasmas, how to characterize them, how to obtain and measure the signals, but among other things, they may provide the unique opportunity to measure reaction rates for capture reactions on excited states and without electron screening [15]. Impossible to realize otherwise in any current laboratory!

And, by the way: one of the best things for the future users of ELI-NP is that there is already a 1 PW laser running on our campus, not in IFIN-HH, but in the laser institute nearby (INFLPR).

Acknowledgements

This work was supported by Romanian National Authority for Scientific Research and Innovation under grants PNII-ID-PCE-2012-4-0299 and PN-09-37-01-07.

References

- [1] I. Burducea, M. Straticiuc, D.G. Ghita, D.V. Mosu, C.I. Calinescu, N.C. Podaru, D.J.W. Mous, I. Ursu, N.V. Zamfir, **Nuclear Instruments and Methods in Physics Research B** **359**, 1219, 2015.
- [2] R. Margineanu, C. Simion, S. Bercea, O.G. Dului, D. Gheorghiu, A. Stochioiu, M. Matei, **Applied Radiation and Isotopes** **66**, 1501-1506, 2008.
- [3] D. Chesneanu et al. in "Exotic Nuclei and Nuclear/Particle Astrophysics (V). From Nuclei to Stars", *Proceedings CSSP14*, L. Trache, D. Chesneanu and C.A. Ur (eds.), **AIP Conf. Proc. Series**, **1645**, 311 (2015).
- [4] D. Tudor et al., these Proceedings
- [5] A. Oprea et al., these Proceedings
- [6] V. Avrigeanu and M. Avrigeanu, **Phys. Rev. C** **91**, 064611 (2015)
- [7] L. Trache, F. Carstoiu, C.A. Gagliardi and R.E. Tribble, **Phys. Rev. Lett.** **87**, 271102 (2001).
- [8] G. Baur, C.A. Bertulani and H. Rebel, **Nucl. Phys. A** **458**, 188 (1986).
- [9] T. Motobayashi et al., see for example **Nucl. Phys. A** **682**, 345c (2001).
- [10] E. Pollacco, L. Trache et al., **Nucl. Instr. Meth. Phys. Res. A** **723**, 102 (2013).
- [11] L. Trache, A. Azhari, H. L. Clark, C. A. Gagliardi, Y.-W. Lui, A. M. Mukhamedzhanov, R. E. Tribble, F. Carstoiu **Phys. Rev. C** **61**, 024612(2000).
- [12] T. Al-Abdullah, F. Carstoiu, X. Chen, H. L. Clark, C. A. Gagliardi, Y.-W. Lui, A. Mukhamedzhanov, G. Tabacaru, Y. Tokimoto, L. Trache, R. E. Tribble, and Y. Zhai, **Phys. Rev. C** **89**, 025809 (2014).
- [13] M. McCleskey, A. M. Mukhamedzhanov, L. Trache, R. E. Tribble, A. Banu, V. Eremenko, V. Z. Goldberg, Y.-W. Lui, E. McCleskey, B. T. Roeder, A. Spiridon, F. Carstoiu, V. Burjan, Z. Hons, and I. J. Thompson, **Phys. Rev. C** **89**, 044605 (2014).
- [14] T. Al-Abdullah, F. Carstoiu, C. A. Gagliardi, G. Tabacaru, L. Trache, and R. E. Tribble, **Phys. Rev. C** **89**, 064602 (2014).
- [15] L. Trache in http://eurisol.ifj.edu.pl/eurisol_krakow_proceedings.pdf, pp. 101-104.

Experimental study of the $^{13}\text{C}+^{12}\text{C}$ fusion reaction at deep sub-barrier energies

This content has been downloaded from IOPscience. Please scroll down to see the full text.

2016 J. Phys.: Conf. Ser. 703 012028

(<http://iopscience.iop.org/1742-6596/703/1/012028>)

View [the table of contents for this issue](#), or go to the [journal homepage](#) for more

Download details:

IP Address: 194.102.58.23

This content was downloaded on 20/10/2016 at 23:49

Please note that [terms and conditions apply](#).

You may also be interested in:

[Modelling of local carbon deposition on a rough test limiter exposed to the edge plasma of TEXTOR](#)
Shuyu Dai, A Kirschner, D Matveev et al.

Experimental study of the $^{13}\text{C}+^{12}\text{C}$ fusion reaction at deep sub-barrier energies

D. Tudor¹, A.I. Chilug¹, M. Straticiuc¹, L. Trache¹, D. Chesneanu¹,
S. Toma¹, D. G. Ghita¹, I. Burducea¹, R. Margineanu¹, A. Pantelica¹,
C. Gomoiu¹, N.T. Zhang², X. Tang³, Y.J. Li³

¹ IFIN-HH, Bucharest-Magurele, Romania

² N.T. Zhang, X. Tang - Institute of Modern Physics, Lanzhou, China

³ Y.J. Li - CIAE, Beijing, China

Abstract. Heavy-ion fusion reactions between light nuclei such as carbon and oxygen isotopes have been studied because of their significance for a wide variety of stellar burning scenarios. One important stellar reaction is $^{12}\text{C}+^{12}\text{C}$, but it is difficult to measure it in the Gamow window because of very low cross sections and several resonances occurring. Hints can be obtained from the study of $^{13}\text{C}+^{12}\text{C}$ reaction. We have measured this process by an activation method for energies down to $E_{cm}=2.5$ MeV using ^{13}C beams from the Bucharest 3 MV tandetron and gamma-ray deactivation measurements in our low and ultralow background laboratories, the latter located in a salt mine about 100 km north of Bucharest. Results obtained so far are shown and discussed in connection with the possibility to go even further down in energy and with the interpretation of the reaction mechanism at such deep sub-barrier energies.

1. Introduction

One of the important questions in nuclear astrophysics is the carbon burning scenario. This process represents the third stage of stellar evolution of massive stars. Until now fusion reaction have only been measured at energies well above the region of astrophysical interest because of the extremely low cross section and signal/background ratio. In stellar environments the reaction rates are estimated by extrapolating measurements done at higher energies, extrapolations that imply a certain degree of uncertainty. For the $^{12}\text{C}+^{12}\text{C}$ fusion reaction the situation is more complicated because of the resonances occurring below the Coulomb barrier. Therefore direct measurements at the Gamow window energies are essential, but very difficult to carry out due to the background from the cosmic rays, terrestrial environment etc.

We have established a program at IFIN-HH Bucharest-Magurele to test the possibility to make direct measurements for nuclear astrophysics using the new 3 MV tandetron accelerator [1] and an ultra-low background laboratory [2] situated in a salt mine at about 2.5 hours drive north of Bucharest. Therefore improvements can be made using irradiation de-activation sequences: we irradiate probes at the new 3 MV tandetron accelerator and move the probes for de-activation measurements in the ultra-low background laboratory in the salt mine. The preliminary results are presented here. The measurement we report in this paper has been performed in collaboration with the IMP Lanzhou.



2. $^{13}\text{C}+^{12}\text{C}$ Experiment

The resonances from the $^{12}\text{C}+^{12}\text{C}$ fusion reaction make it very difficult to measure, so to be able to test the predictive power of various models and establish a reliable upper limit for the cross section, we studied the $^{13}\text{C}+^{12}\text{C}$ fusion cross section at deep sub-barrier energies. After initial tests of accelerator performances, we have proven that it has high and stable beam current in the range of tens of μA for negative ions (^{12}C , ^{13}C , ^{28}Si , ^{197}Au). The machine has a maximum voltage of 3.2 MV, and it can run as low as 200 kV. We concluded that we could be competitive to perform the study of reactions induced by alphas and light ions (0.2-1 MeV per nucleon).

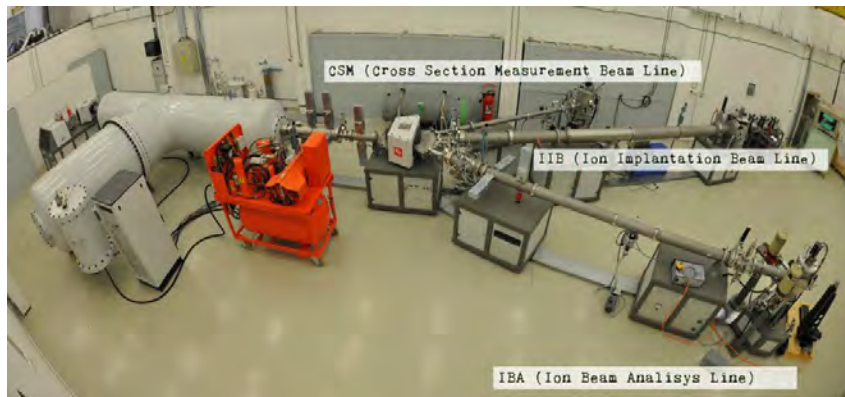


Figure 1. 3 MV Tandatron Accelerator at IFIN-HH [4].

The reaction we chose $^{13}\text{C}+^{12}\text{C}$ has the advantage that leads to an activation product with a half-life allowing for the transportation and efficient de-activation measurement. Therefore, our interest was focused on the proton evaporation channel $^{12}\text{C}(^{13}\text{C},\text{p})^{24}\text{Na}$. The experiment had been performed in October 2014. The ^{13}C beam at laboratory energy range of $E_{\text{lab}} = 6.8 - 5.2$ MeV ($E_{\text{cm}} = 3.2 - 2.5$ MeV), with steps of 0.2 MeV, impinged on 1 mm thick natural carbon targets. Intensities in the range of 2-8 μA were used in different runs. The irradiation chamber was electrically isolated, acting as a Faraday cup for current integration.

Thick target yield for the $^{12}\text{C}(^{13}\text{C},\text{p})^{24}\text{Na}$ fusion reaction was determined through the measurement of the gamma-ray yield following the beta-decay of ^{24}Na ($T_{1/2}=15$ h) at the GammaSpec laboratory at the ground level (in IFIN-HH) and the ultra-low background laboratory μBq (in the salt mine at Slanic). At the μBq the background decreased almost 4000 times (Fig. 2). In these laboratories the cascading gamma rays (1369 and 2754 keV) were detected with HPGe detectors with 30% relative efficiency (at GammaSpec) and 120% (at μBq in the salt mine) [2]. Their calibration is well known.

The $^{12}\text{C}(^{13}\text{C},\text{p})^{24}\text{Na}$ cross sections was calculated from the extracted thick target yield $Y(E)$, using the following equation:

$$\sigma(E) = \frac{1}{N_{\nu}} \frac{dY(E)}{dE} \frac{dE}{dx}, \quad (1)$$

where N_{ν} is the number density of target nuclei present in the target and dE/dx is the stopping power.

As you can see (Fig. 3) we went down to the lowest energy ever reached $E_{\text{cm}}=2.5$ MeV and have obtained a good agreement with the past experiments [3-5]. Proton-evaporation cross section were determined and statistical model calculations were used to evaluate the total reaction cross section.

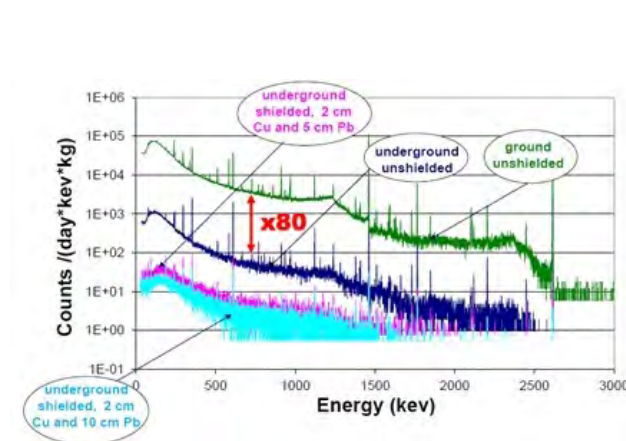


Figure 2. Background from the salt mine (μBq laboratory)[2].

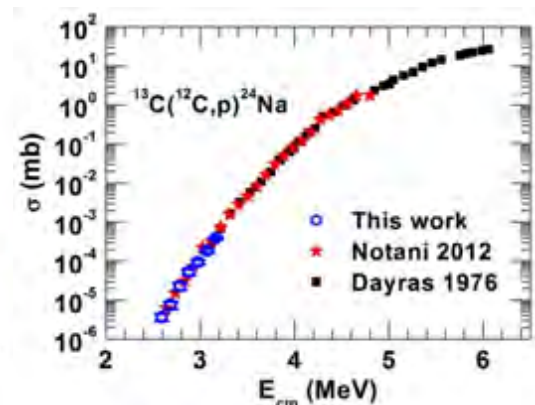


Figure 3. Preliminary cross section of $^{12}\text{C}(^{13}\text{C},p)^{24}\text{Na}$ from our experiment and results from the previous experiments.

3. Summary

We have made a number of irradiations at the 3 MV tandetron and measured the $^{12}\text{C}(^{13}\text{C},p)^{24}\text{Na}$ thick-target yield. The activation measurements were done at the low background laboratory GammaSpec and the ultra-low background laboratory μBq in the Slanic-Prahova salt mine. We went down to the lowest energy ever reached for this reaction ($E_{\text{cm}}=2.5$ MeV), where the cross section was of 4 nb. We have obtained a good agreement with the past experiments and for this year experiment (October 2015) we plan to go to even lower energies. For the ground level measurements (at IFIN-HH) we plan to perform beta-gamma coincidences to further clean the background.

Acknowledgments

Part of this work was supported by the Romanian National Authority for Scientific Research under the project Nuclear astrophysics studies at IFIN-HH, PNII-ID-PCE-2012-4-0299.

References

- [1] I. Burducea, M. Straticiuc, D.G. Ghita, D.V. Mosu, C.I. Calinescu, N.C. Podaru, D.J.W. Mous, I. Ursu, N.V. Zamfir, Nuclear Instruments and Methods in Physics Research B 359, 1219, 2015.
- [2] R. Margineanu, C. Simion, S. Bercea, O.G. Dului, D. Gheorghiu, A. Stochioiu, M. Matei, Applied Radiation and Isotopes 66, 1501-1506, 2008.
- [3] R.A. Dayras, R.G. Stokstad, Z.E. Switkowski and R.M. Wieland, Nuclear Physics A 625, 152-188, 1976.
- [4] X. Fang et al., Journal of Physics: Conference Series 420, 012151, 2013.
- [5] M. Notani, X.D. Tang et al., Physical Review C 85, 014607, 2012.

HEAVY ION ORBITING AND REGGE POLES (II)

F. CARSTOIU¹, M. LASSAUT², L. TRACHE¹, V. BALANICA¹

¹National Institute for Nuclear Physics and Engineering,
P.O.Box MG-6, RO-077125 Bucharest-Magurele, Romania

²Institut de Physique Nucléaire, CNRS-IN2P3, Univ. Paris-Sud,
Université Paris-Saclay, 91406 Orsay Cedex, France

Received September 8, 2015

We discuss two specific examples of heavy ion orbiting. A first example, $\alpha+^{16}\text{O}$ at 54.1 MeV reaction dominated by strong optical potentials shows all characteristics of a strongly refractive scattering: Fraunhofer cross over at very forward angles, deep Airy oscillation, rainbow bump, significant increase of the cross section at large angles. We demonstrate semiclassically that this in fact is a typical orbiting reaction. In a second example, $\alpha+^{28}\text{Si}$ at 18.0 MeV, we describe a special kind of heavy ion orbiting-butterfly scattering, with diffractive oscillations in the entire physical angular range, determined by Regge pole dominance.

Key words: G-matrix effective interactions, folding potentials, WKB, Regge poles.

PACS: 24.10.Ht, 25.55.Ci, 25.70.Ef.

1. INTRODUCTION

Significant progress has been achieved during the last decades in our understanding of the optical potential between light heavy-ions as a consequence of the measurement of accurate and extensive elastic differential cross sections. In many cases angular distributions have been measured to sufficiently large angles and thus the reaction mechanism governing the interaction could be identified with precision, ranging from diffraction due to strong absorption to refractive effects (rainbows). A good understanding of all phenomena occurring in the elastic nucleus-nucleus scattering, which are used typically to extract OMP, and the interpretation of the origin of different aspects, including the well known potential ambiguities, are of crucial importance for finding and justifying the procedures used for predicting nucleus-nucleus OMP in the era of radioactive nuclear beams (RNB) see e.g. [1]. The reliability of these potentials is essential for the correct description of a number of reactions involving RNBs, from elastic to nucleon transfer and nucleon removal, at energies ranging from a few to a few hundred MeV/nucleon. The folding model is central to this understanding, coupled with increased insight into the nature of realistic effective nucleon-nucleon interactions. Of particular interest for us is to support the absolute values of the calculated cross sections for reactions used in indirect methods for nuclear astrophysics, see [2] and [3] for the most recent results. In this

framework, we treat here the case of heavy ion orbiting, one of the phenomena found over the years to occur in special cases of elastic scattering, well understood semi-classically, but not well documented by specific examples.

In Sect. 2 we remind the basic ingredients of the double folding model. Sect. 3 is devoted to the analysis of $^4\text{He}+^{16}\text{O}$ at 54.1 MeV. In Sect. 4 the reaction $^4\text{He}+^{28}\text{Si}$ at 18 MeV is discussed. Our conclusions are presented in Sect. 5.

2. FOLDING FORMFACTORS

In the following we discuss the ability of the folding model to describe orbiting/resonant elastic scattering. We start by a quite simple model in which the spin-isospin independent formfactor of the OMP is given by the double folding integral,

$$V_{fold}(R) = \int d\vec{r}_1 d\vec{r}_2 \rho_1(r_1) \rho_2(r_2) v_{M3Y}(s) \quad (1)$$

where v_{M3Y} is the M3Y parametrization of the G-matrix obtained from the Paris NN interaction [4], and $\vec{s} = \vec{r}_1 + \vec{R} - \vec{r}_2$ is the NN separation distance. A small isovector component arising from a nonnegligible neutron skin is added if necessary. The Coulomb component of the optical potential is calculated by replacing the nuclear s.p. densities with proton densities and using $v_{coul}(s) = e^2/s$ as effective interaction. The small effect arising from finite proton size is ignored. In the simplest version of this model, dubbed here as M3YZR, the knockon exchange component is simulated by a zero range potential with a slightly energy dependent strength,

$$J_{00}(E) = -276(1 - 0.005E/A) \quad (2)$$

We keep the number of fitting parameters at the minimum level and take the OMP in the form,

$$U(R) = N_V V(R, t_V) + i N_W V(R, t_W) \quad (3)$$

where $N_{V,W}$ are normalization constants and $t_{V,W}$ are range parameters defined by the scaling transformation,

$$V(R, t) \rightarrow t^3 V_{fold}(tR) \quad (4)$$

This transformation conserves the volume integral of the folding potential and modifies the radius as,

$$\langle R^2 \rangle_V = \frac{1}{t^2} \langle R^2 \rangle_{fold} \quad (5)$$

Thus the strength of the formfactor is controlled by the parameters $N_{V,W}$. Note that the transformation in Eq. (4) ensures that only the *rms* radius of the bare folding potential is changed. This is in line with the original prescription of [5] which proposed a smearing procedure in terms of a normalized Gaussian function. We found that the

transformation in Eq. (4) is more efficient and less time consuming. Based on Eq. (5) one may estimate in an average way the importance of the dynamic polarization potential (DPP) and finite range effects. Throughout this paper we use single particle densities obtained from a spherical Hartree-Fock (HF+BCS) calculation based on the density functional of Beiner and Lombard [6]. The obtained *rms* charge radii are very close to the experimental values [7]. A more elaborate calculation leads to a nonlocal knockon exchange kernel [8],

$$U_{ex}(\vec{R}^+, \vec{R}^-) = \mu^3 v_{ex}(\mu R^-) \int d\vec{X}_1 \rho_1(X_1) \hat{j}_1 \left(k_{f1}(X_1) \frac{(A_1 - 1)A_2}{A_1 + A_2} R^- \right) \quad (6)$$

$$\times \rho_2(|\vec{R}^+ - \vec{X}_1|) \hat{j}_1 \left(k_{f2}(|\vec{R}^+ - \vec{X}_1|) \frac{(A_2 - 1)A_1}{A_1 + A_2} R^- \right)$$

where $A_{1,2}$ are mass numbers, μ is the reduced mass of the system, $k_{f1,2}$ are Fermi momenta, $R^{+,-}$ are the usual nonlocal coordinates and v_{ex} is the exchange component of the interaction including the long range OPEP tail. Eq. (6) already shows that the nonlocality is small and behaves as $\sim \mu^{-1}$. In the lowest order of the Perey-Saxon approximation, the local equivalent of the nonlocal kernel is obtained by solving the nonlinear equation,

$$U_L(R) = 4\pi \int d\vec{r}_1 d\vec{r}_2 \rho_1(r_1) \rho_2(r_2) \quad (7)$$

$$\times \int s^2 ds v_{ex}(s) \hat{j}_1(k_{f1}(r_1) \beta_1 s) \hat{j}_1(k_{f2}(r_2) \beta_2 s)$$

$$\times j_0 \left(\frac{1}{\mu} K(R) s \right) \delta(\vec{r}_2 - \vec{r}_1 + \vec{R})$$

Above $\beta_i = (A_i - 1)/A_i$ are recoil corrections, $\hat{j}_1(x) = 3j_1(x)/x$ and $j_{0,1}$ are spherical Bessel functions. The local Fermi momenta k_f are evaluated in an extended Thomas-Fermi approximation [9]. We have explored also the extended Slater approximation for the mixed densities of Campi and Bouyssy [10] but did not obtained substantial improvements over the usual Slater approximation. The local momentum for the relative motion is given by,

$$K^2(R) = \frac{2\mu}{\hbar^2} (E_{c.m.} - U_D(R) - U_L(R)) \quad (8)$$

where U_D is the total direct component of the potential including the Coulomb term. In Eq. (8) we assumed a purely real local momentum of the relative motion since the absorptive component of the OMP is small compared with the real part. The effective mass correction [11], $\frac{\mu^*}{\mu} = 1 - \frac{\partial U}{\partial E}$ is of the order of a few percent for our systems and is absorbed in the renormalization parameter N_W . Some tens of iterations are needed to solve the coupled Eq. (7) and (8) in order to obtain a precision of 10^{-7} in the entire radial range ($R_{max} = 25\text{fm}$). We start the iteration process by using

$U_L^{(0)} = U_D$. Calculations with finite range model are dubbed M3YFR. Neglecting the spin-orbit component, the Gogny NN effective interaction can be expressed as a sum of a central, finite range term and a zero range density dependent term,

$$v(\vec{r}_{12}) = \sum_{i=1}^2 (W_i + B_i P_\sigma - H_i P_\tau - M_i P_\sigma P_\tau) e^{-\frac{r_{12}^2}{\mu_i^2}} + t_3 (1 + P_\sigma) \rho^\alpha(\vec{R}_{12}) \delta(\vec{r}_{12}) \quad (9)$$

where $\vec{r}_{12} = \vec{r}_1 - \vec{r}_2$, $\vec{R}_{12} = (\vec{r}_1 + \vec{r}_2)/2$ and standard notations have been used for parameter strengths and spin-isospin exchange operators. The strengths parameters and the ranges are taken from [12]. The isoscalar and isovector components of the effective interaction are constructed in the standard way. The interest in this interaction resides in its excellent description (at the HF level) of the saturation properties of the nuclear matter in line with modern estimation from the isoscalar giant monopole [13] or dipole resonance [14] studies. Antisymmetrization of the density dependent term is trivial, so that the sum of direct and exchange term reads,

$$v_D^\rho(r_{12}) + v_{ex}^\rho(r_{12}) = \frac{3t_3}{4} \rho^\alpha \delta(\vec{r}_{12}) \quad (10)$$

The local equivalent of the finite range knockon exchange is calculated with Eq. (7). Two approximations were used for the overlap density,

$$\rho = (\rho_1(r_1)\rho_2(r_2))^{1/2} \quad (11)$$

and

$$\rho = \frac{1}{2}(\rho_1(r_1) + \rho_2(r_2)) \quad (12)$$

The first approximation Eq. (11) has the merit that the overlap density goes to zero when one of the interacting nucleons is far from the bulk. In Eq. (12) a factor 1/2 was introduced such as the overlap density does not exceeds the equilibrium density for normal nuclear matter. At large density overlaps, the fusion and other inelastic processes are dominant and the elastic scattering amplitude is negligible small. The calculated OM potentials are dubbed GOGNY1 (11) and GOGNY3 (12). Both definitions represent crude approximations of the overlap density but are widely used in the estimation of the density dependence effects in the folding model. We further examine the density dependence effects by using the nuclear matter approach of Jeukenne, Lejeune and Mahaux (JLM) [5] which incorporates a complex, energy and density dependent parametrization of the NN effective interaction obtained in a Brueckner Hartree-Fock approximation from the Reid soft core NN potential. The systematic study [1] of the elastic scattering between *p*-shell nuclei at energies around 10 MeV/nucleon leads to the surprising result that on average, the imaginary part of the folded JLM potential was perfectly adequate to describe such reactions and

did not need any renormalization ($N_W = 1.00 \pm 0.09$), while the real component needed a substantial renormalization, in line with other effective interactions used in folding models. We examine here to which extent this feature is conserved for tightly bound nuclei. Exchange effects are included in this model at the level of N-target interaction. Calculations with this model are dubbed JLM1 and JLM3, depending on which definition we use for the overlap density (Eqs.(11) and (12) respectively).

3. ${}^4\text{He}+{}^{16}\text{O}$ AT 54.1 MeV

The reaction ${}^4\text{He}+{}^{16}\text{O}$ at $E_{lab}=54.1$ MeV was measured by Abele *et al.* [15] and discussed extensively within the folding model in [16]. An optical potential description of both $\alpha+{}^{16}\text{O}$ elastic scattering and α -cluster states in ${}^{20}\text{Ne}$ was given by Michel *et al.* [17]. The corresponding global potential $\alpha+{}^{16}\text{O}$ gives a reasonable description of the α -structure in ${}^{20}\text{Ne}$. However such a global approach cannot be used to reveal a delicate phenomenon such as orbiting. A more detailed analysis is necessary.

Table 1

Discrete solutions with WS^1 form factors for the reaction ${}^4\text{He}+{}^{16}\text{O}$ at 54.1 MeV.

V	W	r_V	r_W	r_c	a_V	a_W	χ^2	σ_R	J_V	R_V	J_W	R_W
135.	10.57	0.7231	1.0741	1.0	0.8022	0.6867	8.72	1050.	399.	3.7646	74.	4.2654
160.	18.17	0.8773	0.9618	1.0	0.5993	0.5083	7.87	999.	624.	3.5712	85.	3.5963
214.	24.42	0.9104	0.9553	1.0	0.5066	0.1188	7.72	986.	865.	3.4548	97.	3.0712

Table 2

Unique solution with WS^2 form factors for the reaction ${}^4\text{He}+{}^{16}\text{O}$ at 54.1 MeV.

V	W	r_V	r_W	r_c	a_V	a_W	χ^2	σ_R	J_V	R_V	J_W	R_W
155.	14.75	0.9088	1.1628	1.0	1.2026	1.0812	4.19	1028.	393.	3.6687	75.	4.0902

A grid search using standard WS^1 formfactors for the optical potential revealed a number of discrete solutions, see Table 1 and Figure 1a. Although almost all physical angular range was measured the data are not able to fix uniquely the potential of a WS shape. The members of the potential family are very strong, reaching high values of the normalized real volume integral. The *rms* radii of the real and imaginary component get smaller as the potential is stronger. However the reaction cross section is almost constant which suggests that the members of the potential sequence are almost phase equivalent. Examination of the Figure 2a shows quite similar cross section with the exception of the solution with $J_v = 399$ MeV fm³ which show a very deep Airy oscillation near $\theta = 60^\circ$ just at the end of the Fraunhofer sector. This structure which is followed by a wide bump together with the far side dominance is

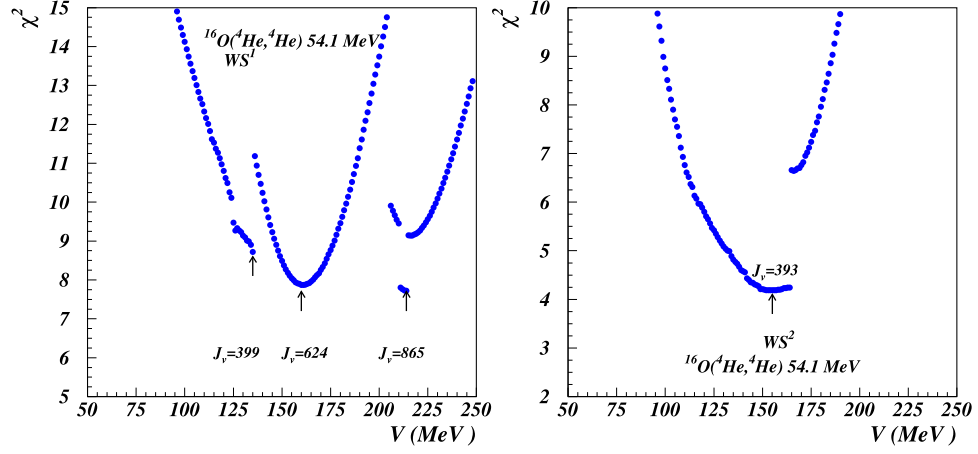


Fig. 1 – (Color online) Grid search with WS^1 (a) and WS^2 (b) form factors for the reaction ${}^4\text{He}+{}^{16}\text{O}$ at 54.1 MeV, Table 1.

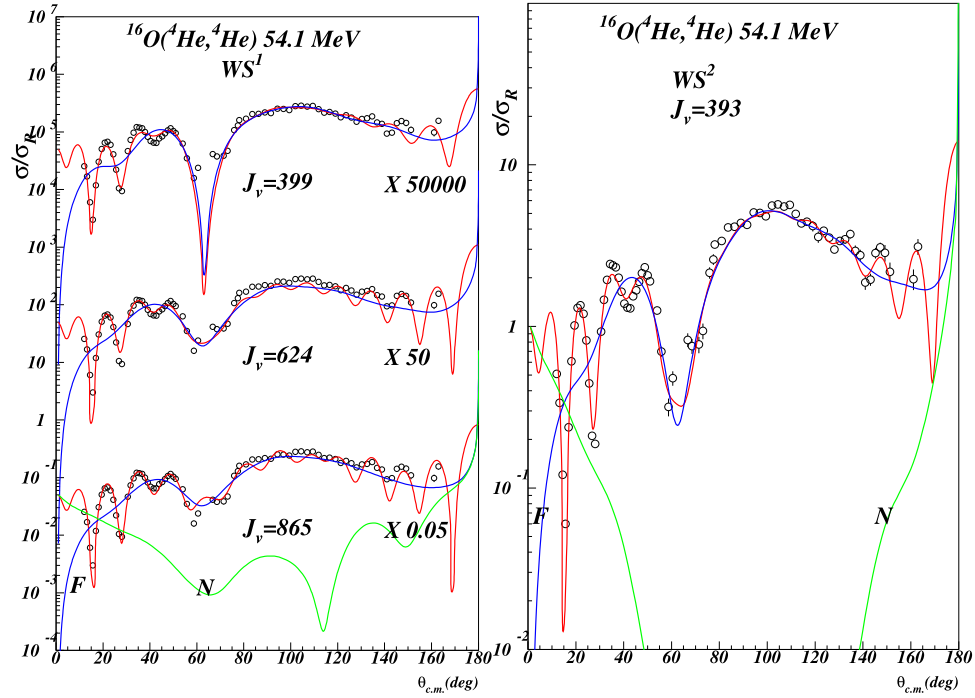


Fig. 2 – (Color online) F/N decomposition for the WS^1 (a) and WS^2 (b) potentials.

usually interpreted as a strong refractive effect of a quite transparent potential. This picture has been already challenged by Anni [18] for the simple reason that the far side amplitude has never been decomposed into subamplitudes which would explain the interference. A subsequent analysis in terms of WS^2 formfactors (squared WS) revealed a single solution in the range $J_v < 1000 \text{ MeV fm}^3$, see Table 2 and Figure 1b. The uniqueness of the solution cannot be guaranteed by our search procedure. Remarkably, the WS^2 solution and the first WS^1 solution in Table 1 have almost identical bulk average parameters (volume integrals, rms radii and reaction cross section) which suggests that this is the physical solution. The far and near side (F and N) amplitudes have the same structure with a deep Airy oscillation carried entirely by the far side component. We shall use later this solution for our semiclassical analysis.

Table 3
Unique solutions obtained with folding form factors for the reaction $^4\text{He}+^{16}\text{O}$ at 54.1 MeV

pot	N_V	N_W	t_V	t_W	χ^2	σ_R	J_V	R_V	J_W	R_W
M3YZR	0.8400	0.1718	1.0178	0.8536	4.63	1083.	374.10	3.603	75.61	4.286
M3YFR	0.8250	0.1689	1.0020	0.8887	4.94	1069.	397.46	3.661	80.70	4.120
GOGNY1	0.6850	0.1420	1.0143	0.9147	5.81	1057.	401.73	3.657	82.67	4.049
GOGNY3	0.8800	0.1830	1.0278	0.9340	6.05	1058.	406.87	3.666	84.06	4.029
JLM1	0.6750	0.5947	0.9620	0.8801	4.23	1037.	391.99	3.626	77.48	4.076
JLM3	0.7250	0.6736	0.9577	0.8773	4.27	1042.	388.28	3.619	76.96	4.107

In the folding model we use three different effective interactions, namely the density independent M3Y, and two density dependent GOGNY and JLM in six different versions. A grid search using the strength N_v as a control parameter revealed a unique solution for all model interactions. We have obtained an almost unique shape for the function $\chi^2(J_v)$ see Table 3 and Figure 3. The folding solutions are fully consistent with the WS model. The average real volume integral is $J_v = 392 \pm 18 \text{ MeV fm}^3$ and the real rms radius $R_v = 3.65 \pm 0.02 \text{ fm}$. The normalization for the real component ranges from $N_v \approx 0.7$ to $N_v \approx 0.9$ strengthen once again the conjecture that the true physical parameter is the volume integral and not the normalization parameter. A standard far side/near side decomposition is plotted in Figures 4a and 4b showing the same far side dominance and an Airy minimum forward to a "rainbow" bump. There are some glories at very large angles due to a strong F/N interference since both amplitudes become large in this sector. We start a WKB analysis [19] by searching the turning point trajectories in the complex r plane. We use the WS^1 potential with real volume integral $J_v = 399 \text{ MeV fm}^3$. We observe an ideal situation with three active well separated turning points close to the real axis, Figure 5a. The active points, which give the essential contribution to the action integrals are correlated with the poles of the real component of the optical potential (left hand stars in

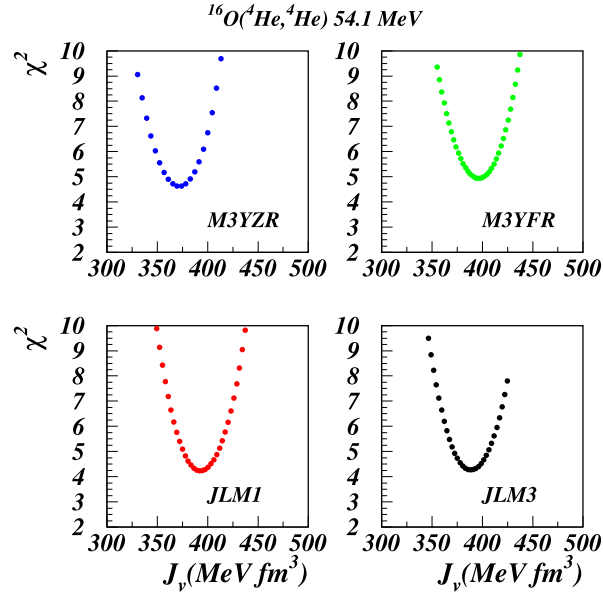


Fig. 3 – (Color online) Grid search with folding form factors. Unique solution, Table 3

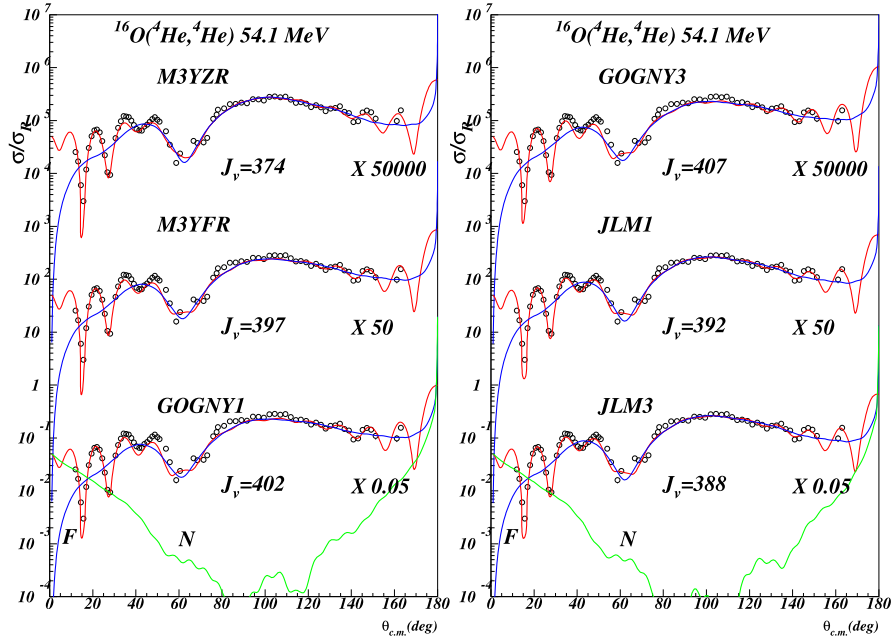


Fig. 4 – (Color online) F/N decomposition for the folding potentials from Table 3.

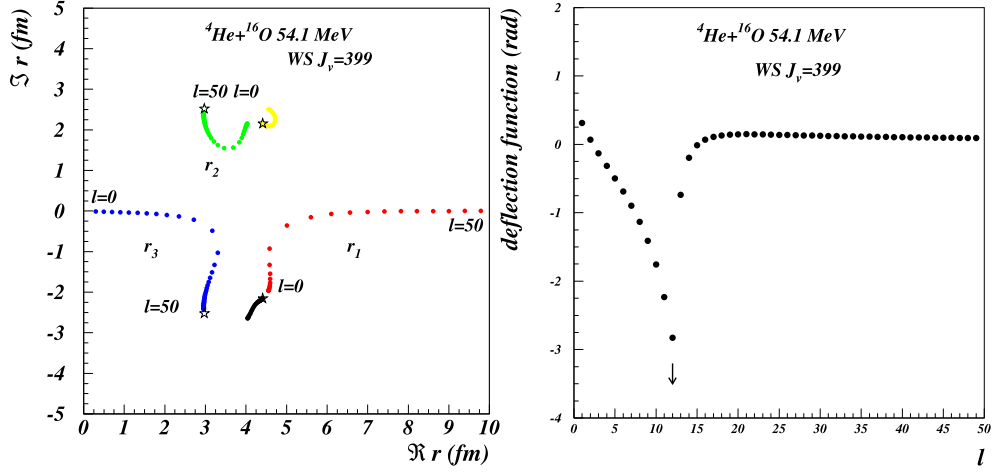


Fig. 5 – (Color online) (a) Complex turning points for the WS potential with $J_V = 399 \text{ MeV fm}^3$. (b) Semiclassical deflection function for the WS potential with $J_V = 399 \text{ MeV fm}^3$. The pattern is close to a near orbiting situation with the orbiting momentum $\ell \sim 12$.

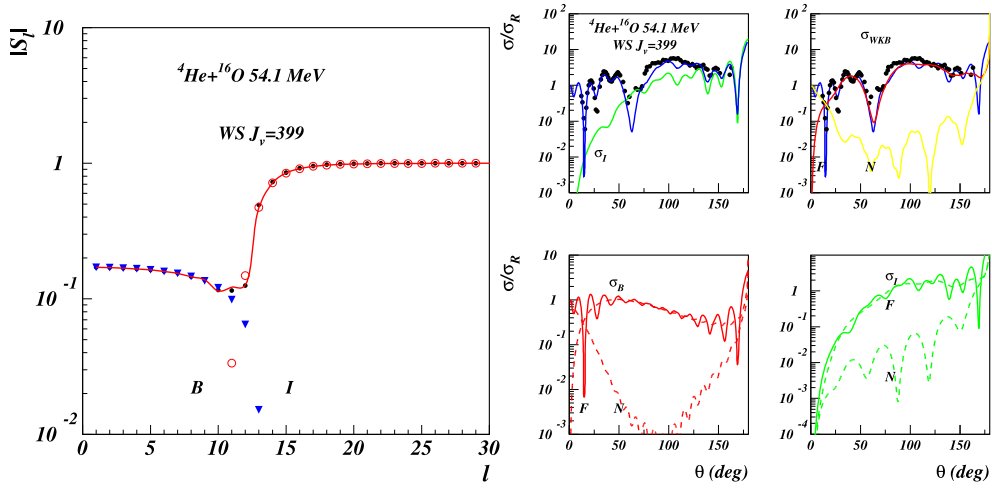


Fig. 6 – (Color online) (a) Absorption profile for the WS potential with $J_V = 399 \text{ MeV fm}^3$ (see text). (b) Semiclassical (WKB) analysis of the reaction $^4\text{He}+^{16}\text{O}$ at 54.1 MeV based on the WS potential with $J_V = 399 \text{ MeV fm}^3$ (see text).

the figure). The inactive turning points are correlated with the poles of the imaginary potential and give negligible small contribution to the action integrals. The semiclassical deflection function is shown in Figure 5b. There are at most 20 partial waves which contribute significantly to the scattering. The Coulomb rainbow is embedded

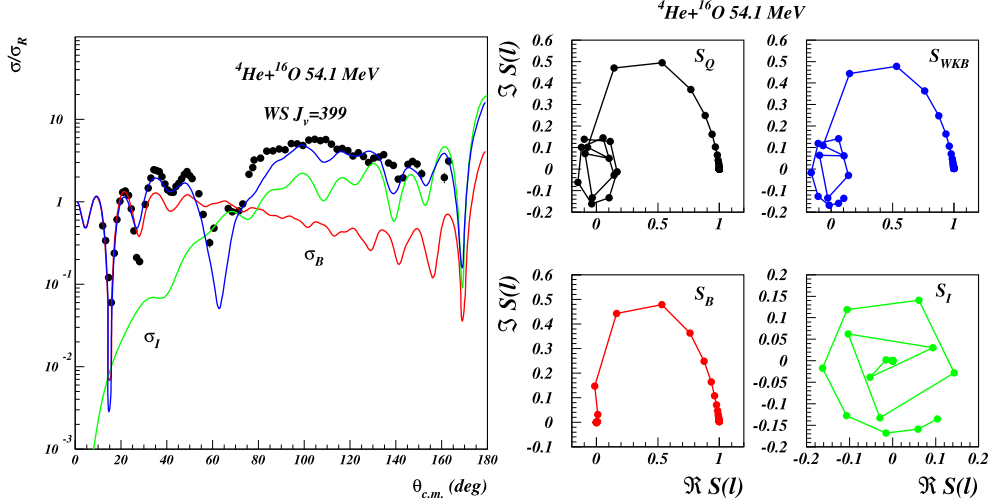


Fig. 7 – (Color online) (a) The semiclassical (WKB) cross section is decomposed into barrier (B, red line) and internal barrier (I, green line). The deep Airy minimum appears as a strong interference of the B/I components. The internal barrier component dominates at large angles, reaching exceptionally large values ($\sigma_I/\sigma_R \sim 20$ at $\theta \sim 180^\circ$). (b) Argand diagram for the semiclassical S-matrix based on the WS potential with $J_V = 399 \text{ MeV fm}^3$. The trajectory for the S_{WKB} matches perfectly the exact quantum result S_Q . The internal barrier component, which reaches exceptionally large values, rotates several times around the origin suggesting the orbiting.

in the Fraunhofer sector. Clearly there is a logarithmic singularity near $l_{orb} = 12$ and therefore the reaction is dominated by orbiting. The semiclassical absorption profile (modulus of the scattering amplitude as a function of the angular momentum) is shown in Figure 6a. The semiclassical profile (curve) is identical with the exact quantum-mechanically result (black dots) which strengthen the conjecture that the WKB decomposition of the scattering amplitude is exact, at least for this reaction. The internal barrier component (I) is quite large, characteristic for strongly refractive reactions [20] and is negligibly small beyond the orbiting momentum. The barrier (B) and internal barrier (I) components of the scattering amplitude interfere destructively giving rise to a shallow Grünh-Wall dip near the orbiting momentum. The semiclassical (WKB), barrier (B) and internal barrier (I) cross sections as well as their far side/near side subcomponents are shown in Figures 6b and 7a. The barrier component (left lower panel) is responsible for the diffractive Fraunhofer sector and becomes again significant near $\theta = 180^\circ$. The internal barrier component (right lower panel) is significant at all intermediate angles and the destructive interference with the barrier component explains the Airy minimum near $\theta = 60^\circ$. The internal barrier cross section is exceptionally large near $\theta = 180^\circ$ where $\sigma_I/\sigma_R = 20$. Finally, the Argand diagram for the semiclassical (WKB) S-matrix is shown in Figure 7b.

The exact quantum result (Q) is shown for comparison. The WKB S-matrix is decomposed into barrier (B) and internal barrier (I) components. The orbiting/resonant effect is evident in the low partial waves sector. The barrier component is free for resonances. The entire resonant effect is isolated into the internal barrier component (right lower panel) where the S-matrix rotates anti-clockwise several times around the origin. These are resonances /Regge poles of the orbiting mechanism.

Table 4
Discrete solutions with folding form factors for the reaction ${}^4\text{He}+{}^{28}\text{Si}$ at 18.0 MeV.

pot	N_V	N_W	t_V	t_W	χ^2	σ_R	J_V	R_V	J_W	R_W
M3YZR	0.4900	0.0673	0.8469	0.9997	4.47	1183.	220.80	4.649	30.63	3.946
	0.7450	0.0581	0.8675	1.2983	6.58	1287.	336.18	4.540	27.00	3.051
M3YFR	0.4300	0.0647	0.8750	1.1067	4.49	1141.	210.15	4.572	32.09	3.627
	0.6650	0.0539	0.8971	1.1402	6.13	1233.	325.48	4.461	26.78	3.522
GOGNY1	0.3600	0.0564	0.8900	1.1525	4.69	1138.	208.14	4.541	33.18	3.520
	0.5550	0.0432	0.9126	1.2495	5.64	1215.	321.34	4.430	25.58	3.251
JLM1	0.3550	0.2354	0.8367	1.1387	4.19	1143.	212.48	4.568	30.92	3.629
	0.5450	0.1889	0.8560	1.3226	5.92	1242.	326.64	4.466	25.09	3.133
JLM3	0.3900	0.3019	0.8321	1.1436	4.20	1138.	212.10	4.572	30.29	3.642
	0.6000	0.2502	0.8527	1.3011	6.10	1241.	326.77	4.463	25.35	3.209

Table 5
Discrete solutions with WS^1 form factors for the reaction ${}^4\text{He}+{}^{28}\text{Si}$ at 18.0 MeV.

V	W	r_V	r_W	r_c	a_V	a_W	χ^2	σ_R	J_V	R_V	J_W	R_W
53.	3.44	0.9174	1.2304	1.0	0.9271	0.2423	4.43	1089.	223.	4.7611	24.	4.4982
88.	4.70	0.8756	1.2234	1.0	0.8542	0.2368	5.08	1140.	314.	4.4623	32.	4.4693
128.	5.70	0.8550	1.2244	1.0	0.7962	0.2270	5.45	1159.	414.	4.2585	39.	4.4659

Table 6
Unitary solutions with Regge pole amplitudes for the reaction ${}^4\text{He}+{}^{28}\text{Si}$ at 18.0 MeV.

Set	L	Δ	α	β	L_1	Δ_1	D_1	Γ_1	L_2	Δ_2	D_2	Γ_2	χ^2	σ_R
R1	8.14	4.00	-1.66	2.13	7.73	0.415	10.3	20.6	8.68	0.204	10.9	2.61	2.64	1680
R2	7.85	4.16	-1.67	2.37	7.98	0.421	13.6	27.4	8.06	0.413	11.3	1.38	2.69	1703

4. ${}^4\text{He}+{}^{28}\text{Si}$ AT 18 MEV

We discuss here another reaction, ${}^4\text{He}+{}^{28}\text{Si}$ at $E_{lab} = 18$ MeV measured by Ahlfeld *et al.* [21]. The incident energy is quite low, just at the limit where the reaction mechanism starts to be dominated by direct interactions over compound elastic. The interest in this reaction resides in the fact that it displays a special kind

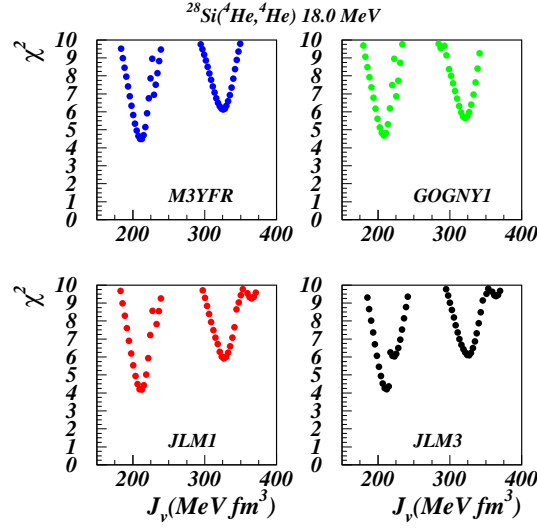


Fig. 8 – (Color online) Search for discrete solutions with folding form factors.

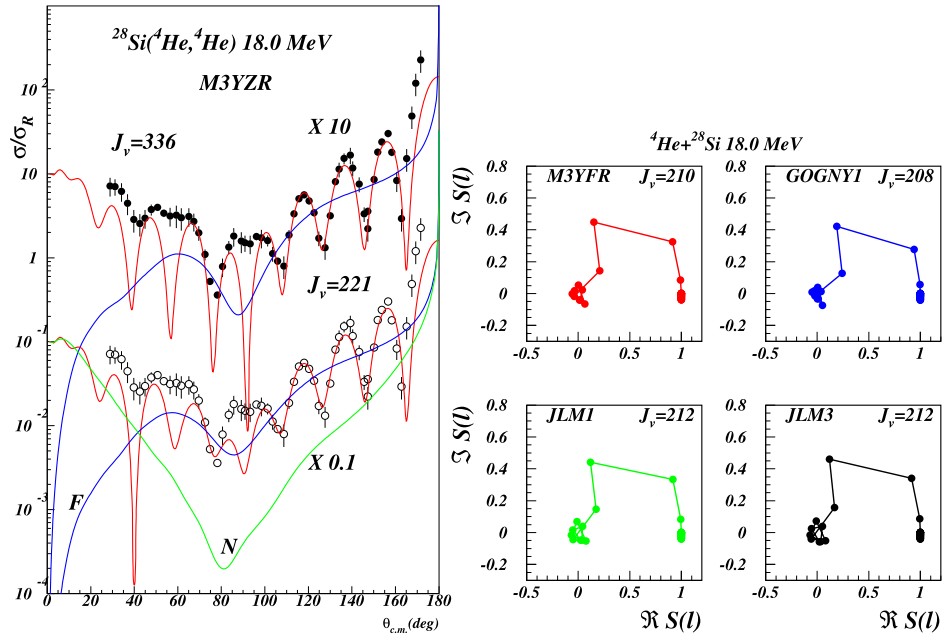


Fig. 9 – (Color online) (a) F/N decomposition with M3YZR. There are normalization problems at forward angles. (b) Argand diagram for the S-matrix calculated with several folding solutions with real volume integral $J_V \sim 210 \text{ MeV fm}^3$.

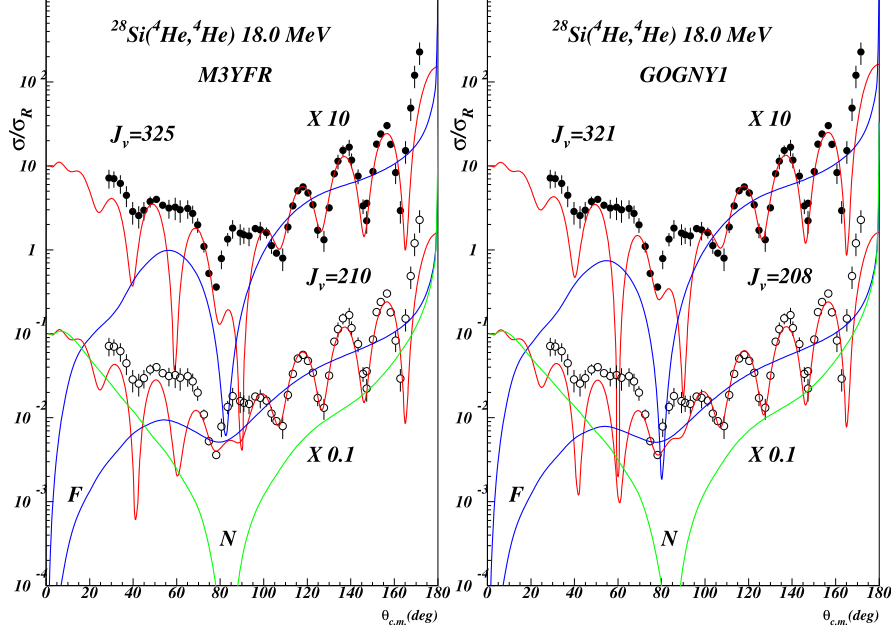


Fig. 10 – (Color online) (a) F/N decomposition with M3YFR. (b) F/N decomposition with GOGNY1.

of orbiting-butterfly scattering. The angular distribution is almost symmetric with respect to $\theta = 90^\circ$ and displays diffractive oscillations in the entire physical angular range. Our analysis goes through the same steps as for the preceding reaction. Since the energy is quite low, we expect a significant number of discrete solutions with both WS and folding optical potentials see Tables 4 and 5. The χ^2 landscape is explored in Figures 8 and 12b. Remarkably two solutions with $J_v \approx 200 \text{ MeV fm}^3$ and $J_v \approx 300 \text{ MeV fm}^3$ appear in all six model calculations. The far side/near side decomposition is shown in Figures 9a-11b and 13a. For all solutions there is a clear far side dominance and a particularly deep Airy minimum near $\theta = 80^\circ$ for the solution with $J_v \approx 300 \text{ MeV fm}^3$. This should in principle indicate a strongly refractive reaction mechanism. But we shall see that is not the case. The first hint is given by the large angle oscillations which can be fitted by a renormalized $P_8^2(\theta)$ amplitude which suggests the presence of a Regge pole near $\ell = 8$. For the moment we are interested if there are other traces of resonant scattering in our reaction. We show the Argand diagram for the folding S-matrix in Figure 9b. The figure shows convincingly that the corresponding folding potentials are phase equivalent since the S-matrix trajectories in angular momentum space are identical. Second, there is a cluster of points in the low angular momentum sector which in fact is a signature of the orbiting. The absorption profile for the same S-matrix is shown in Figure 12a. There is a signif-

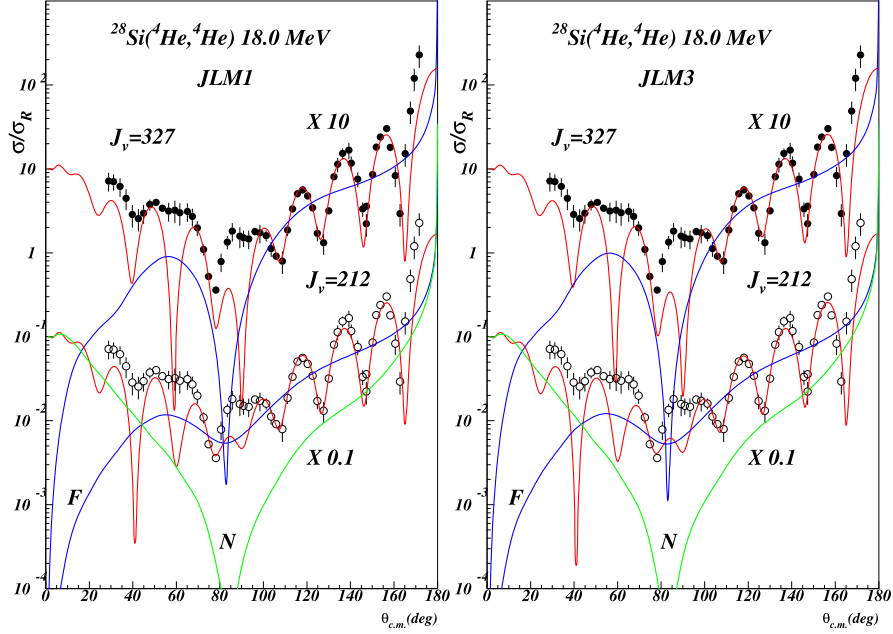


Fig. 11 – (Color online) F/N decomposition with JLM1(a) and JLM3(b).

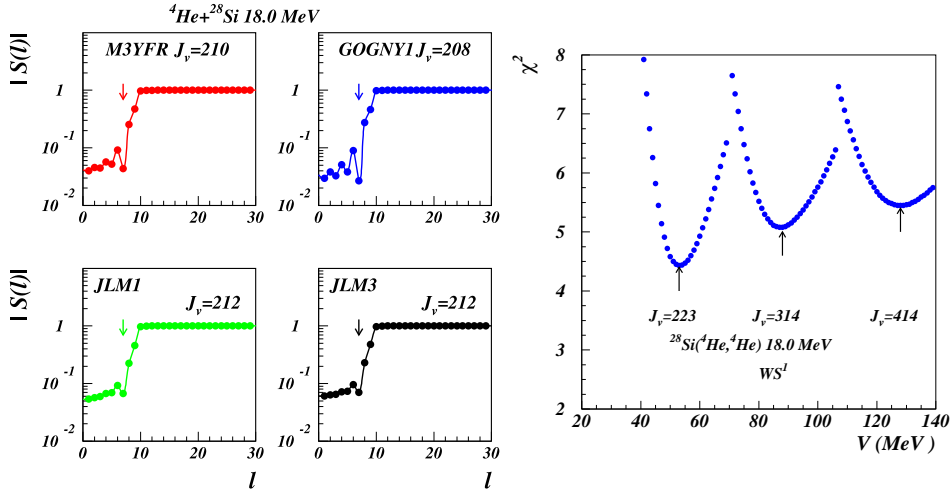


Fig. 12 – (Color online) (a) Absorption profile calculated with several folding solutions. The arrows indicate the position of the Regge pole. (b) Search for discrete solutions with WS^1 form factors.

icant odd-even staggering at low partial waves (multiple Regge poles). The arrow indicates the location of the main Regge pole near $\ell = 8$. The trajectories of the

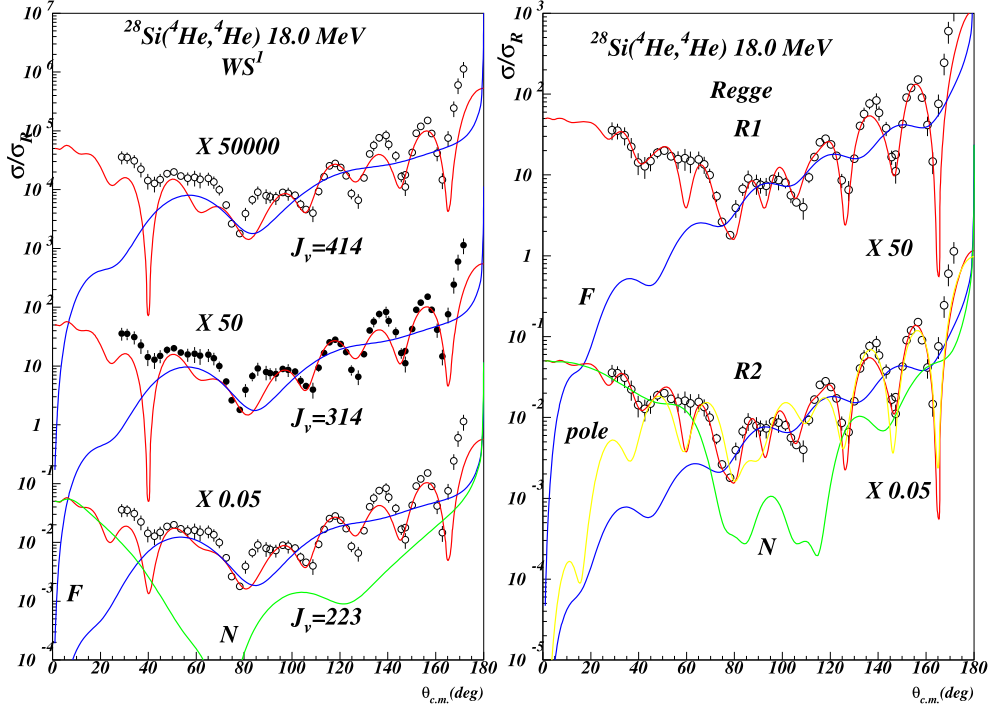


Fig. 13 – (Color online) (a) F/N decomposition with WS^1 . This calculation did not solved the normalization problem at forward angles. (b) F/N decomposition using Regge pole amplitudes. The pole components dominate the cross section in the entire angular range.

complex turning points for the WS^1 potential with $J_v = 223 \text{ MeV fm}^3$ are shown in Figure 14b. The barrier turning point r_2 and the outer point r_1 have an unusual trajectory shape due to the fact that the imaginary component of the optical potential has complex poles located close to the real axis (right hand stars), see in Table 5 potentials with very small a_w . The calculation of the action integrals requires a careful numerical evaluation since the poles should be avoided. Figure 15a displays the semiclassical deflection function with a typical orbiting singularity near $\lambda = 9.5$. The semiclassical absorption profile, shown in Figure 15b, indicate a quite strong internal barrier component. The semiclassical profile do not reproduce the exact Grün-Wall spike (black dots) but still appears as a B/I interference near the orbiting momentum. The internal barrier component (I) is negligibly small beyond the orbiting momentum. The semiclassical cross section are calculated and displayed in Figure 16a. The barrier component, typical for strong absorption, follows quite well the experimental cross section, though it is the internal barrier component which dominates the cross section at large angles. The Argand diagram shown in Figure 16b shows a strong

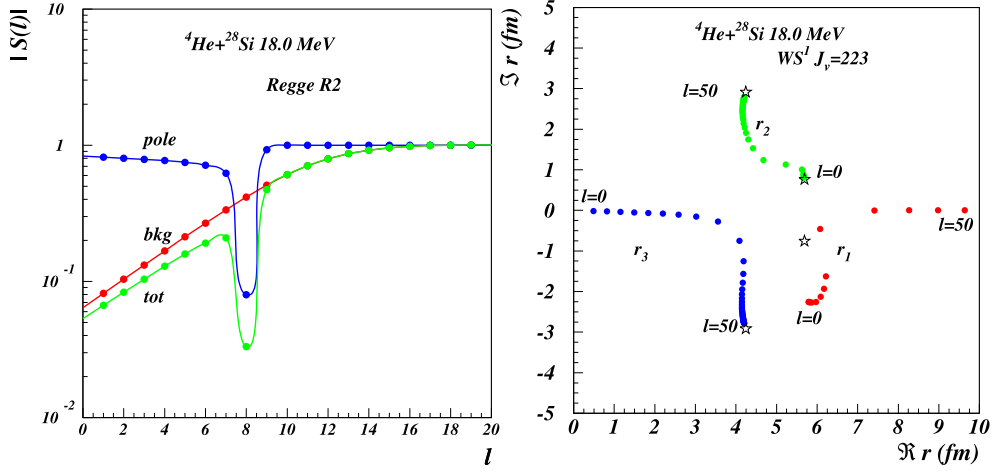


Fig. 14 – (Color online) (a) Absorption profile using Regge pole amplitude R2. The main pole located near $\ell = 8$ produced a deep Grün-Wall spike in the total S-matrix. (b) Complex turning point trajectory for the WS^1 potential with real volume integral $J_V = 223 \text{ MeV fm}^3$.

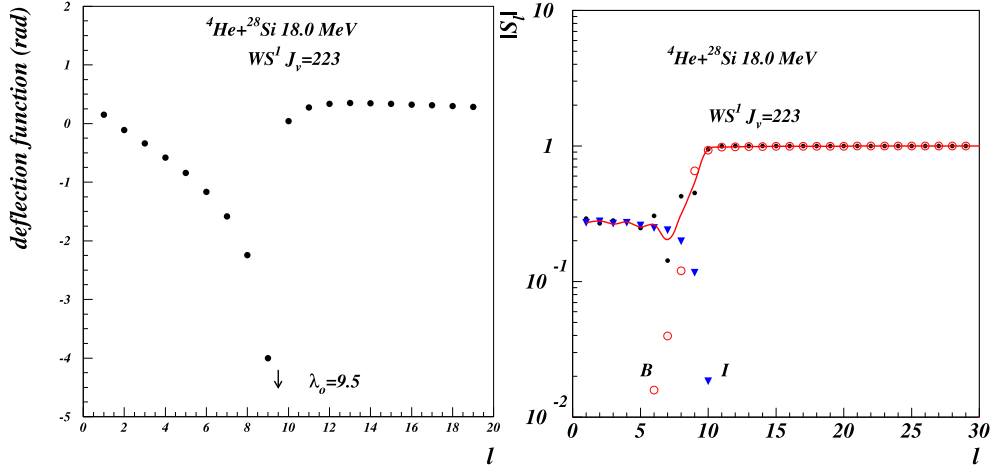


Fig. 15 – (Color online) (a) Deflection function. The orbiting angular momentum is $\lambda_0 = 9.5$. (b) Semiclassical (WKB) absorption profile red curve. The quantum mechanical solution (black dots) is shown for comparison. The WKB solution is decomposed into barrier (B) and internal barrier (I) components.

orbiting effect in both semiclassical (WKB) and quantum (Q) S-matrix. The entire resonant effect is isolated into the internal barrier component (I). Finally we search the Regge poles directly from the data. We proceed as follows: we guess a reasonable background-two pole solution, as described in the preceding paper and then generate

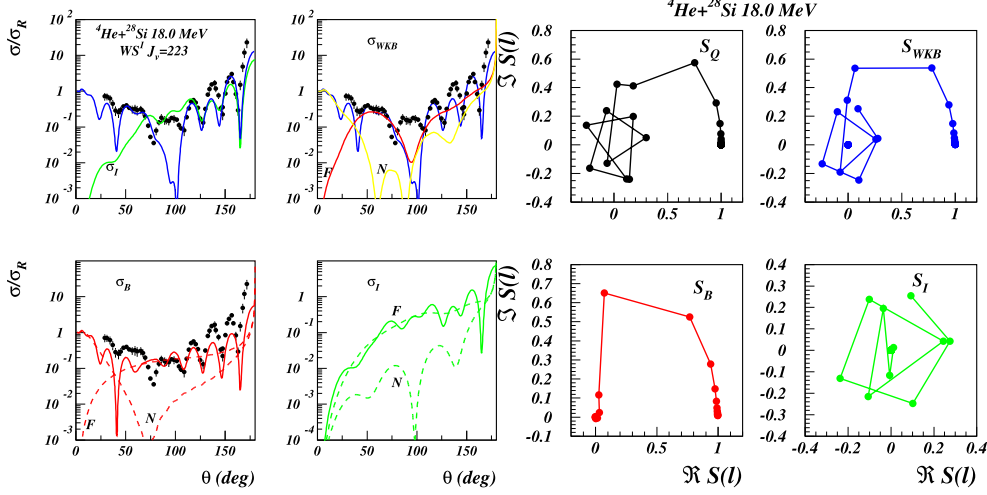


Fig. 16 – (Color online) (a) Semiclassical (WKB) cross section compared with the data. The regular oscillations at large angles are triggered by the barrier component. But their amplitude is determined by the internal barrier component (green curve). The B/I components are further decomposed into F/N subcomponents. (b) Argand diagram for the semiclassical (WKB) S-matrix is compared with the exact quantum mechanical result (Q). The orbiting effect is isolated into the internal barrier component (I).

about 10^6 input solution by Monte Carlo for our searching code which minimizes a standard χ^2 function. We are looking for solutions for which both the background and the pole component are unitary, since we want to isolate the pole contribution to the cross section. Two fully unitary solutions are given in Table 6 and confirms the preceding analysis with a main pole located near $\lambda = 8$. The cross sections obtained with this model are plotted in Fig.13b. The butterfly effect is even more evident in this calculation. The background component is important only at forward angles, while the pole component contributes significantly at all angles. The background absorption profile shown in Fig. 14a is typical for strong absorption regime while the Grün-Wall spike of exceptional amplitude appears here as carried out by the pole component alone.

5. CONCLUSION

We have analyzed here two apparently obscure angular distribution for heavy ion scattering which proved to be extremely rich in information about the reaction mechanism. The first example $\alpha+^{16}\text{O}$ at 54.1 MeV show all characteristics of a strongly refractive reaction but proves to be in fact a typical example of heavy ion orbiting. A second example, $\alpha+^{28}\text{Si}$ at 18.0 MeV taken at the limit where the direct interaction starts to dominate over the compound elastic, show a special case of heavy

ion orbiting, butterfly scattering with diffractive oscillations in the entire physical angular range due to Regge pole dominance. In the light of our analysis it is evident that a lot of reactions dubbed improperly as ALAS (strong increase of the cross section at large angles) should be reanalyzed since most if not all of them could be in fact cases of nuclear orbiting.

Acknowledgements. This work was partly supported by CNCSIS Romania, under program PN-II-PCE-55/2011 and PN-II-ID-PCE-0299/2012, and partly by IN2P3, France.

REFERENCES

1. L. Trache, A. Azhari, H. L. Clark, C. A. Gagliardi, Y.-W. Lui, A. M. Mukhamedzhanov, X. Tang, N. Timofeyuk, R. E. Tribble and F. Carstoiu, Phys. Rev. **C61**, 024612 (2000).
2. T. Al-Abdullah, F. Carstoiu, X. Chen, H. L. Clarke, C. A. Gagliardi, Y.-W. Lui, A. Mukhamedzhanov, G. Tabacaru, Y. Takimoto, L. Trache, R.E.Tribble, Y. Zhai Phys. Rev. C **89**, 025809 (2014).
3. T. Al-Abdullah, F. Carstoiu, C. A. Gagliardi, G. Tabacaru, L. Trache and R. E. Tribble. Phys. Rev. C **89**, 064602 (2014).
4. N. Anantaraman, H. Toki and G. F. Bertsch, Nucl. Phys. **A398**, 269 (1983).
5. J. P. Jeukenne, A. Lejeune and C. Mahaux, Phys. Rev. **C16**, 80 (1977).
6. M. Beiner and R. J. Lombard, Ann. Phys. (N.Y.) **86**, 262 (1974).
7. I. Angeli, Heavy Ion Physics, **8**, 23 (1998).
8. F. Carstoiu and M. Lassaut, Nucl. Phys. **597**, 269 (1996).
9. Dao T. Khoa, Phys. Rev. **C63**, 034007 (2001).
10. X. Campi and A. Bouyssy, Phys. Lett. **73B**, 263 (1978).
11. J. W. Negele and K. Yazaki, Phys. Rev. Lett. **47**, 71 (1981).
12. D. Gogny, *Proc. Int. Conf. on Nucl. Physics, Munich 1973*, eds J. de Boer and H. J. Mang, Vol. 1, p. 48.
13. D. H. Youngblood, H. L. Clark and Y.-W. Lui, Phys. Rev. Lett. **82**, 691 (1999).
14. G. Colo, N. Van Giai, P. F. Bortignon and M. R. Quaglia, Phys. Lett. **B485**, 362 (2000).
15. H. Abele, H.J. Hauser, A. Korber, W. Leitner, R. Neu, H. Plappert, T. Rohwer, G. Staudt, M. Strasser, S. Welte, M. Walz, P.D. Eversheim, F. Hinterberger, Z. Physik **A326** 373, 1987.
16. H. Abele and G. Staudt, Phys. Rev. **C47**, 742 (1993).
17. F. Michel, J. Albinski, P. Belery, Th. Delbar, Gh. Gregoire, B. Tasiaux and G. Reidemeister Phys. Rev. **C28**, 1904 (1983).
18. R. Anni, Phys. Rev. C **63**, 031601R (2001).
19. D. M. Brink and N. Takigawa, Nucl. Phys. **A279**, 159 (1977).
20. Florin Carstoiu, Livius Trache, Robert E. Tribble, Carl A. Gagliardi Phys. Rev. **C70** 054610, (2004)
21. C. E. Ahlfeld, G. E. Assousa, R. A. Lasalle, W. J. Thompson, H. A. Van Rinsvelt, N. P. Heydenburg, Nucl. Phys **A191** 137(1972).

HEAVY ION ORBITING AND REGGE POLES (III)

F. CARSTOIU¹, M. LASSAUT², L. TRACHE¹, V. BALANICA¹

¹Horia Hulubei National Institute for Nuclear Physics and Engineering,
P.O.B. MG-6, RO-077125, Bucharest-Magurele, Romania

²Institut de Physique Nucléaire, CNRS-IN2P3, Univ. Paris-Sud,
Université Paris-Saclay, 91406 Orsay Cedex, France

Received March 8, 2016

We discuss two reactions initiated by the loosely bounded ${}^6\text{Li}$ in an energy window where the interaction with light targets is strongly refractive and moderately absorbing. The surface transparency of the optical potential allows a considerable internal barrier component of the scattering amplitude which leads to significant refractive effects and diffractive scattering at large angles due to Regge poles located near the real axis, close to the orbiting momentum. The folding potentials based on realistic effective NN interactions revealed a number of phase equivalent discrete solutions with real volume integrals close to the bare potential values ($N_v \approx 1$). This suggests that the real part of the dynamic polarization potential arising from the coupling to the breakup channel is small.

Key words: G-matrix effective interactions, folding potentials, WKB, Regge poles, orbiting.

PACS: 24.10.Ht, 25.55.Ci, 25.70.Ef.

1. INTRODUCTION

We discuss here two reactions initiated by ${}^6\text{Li}$ in an energy window where the interaction with light targets is strong and moderately absorptive. The interaction shows sufficient surface transparency to allow strong refractive effects superimposed on diffractive effects due to strong absorption at forward angles and Regge poles at large angles. Our basic approach for analysis is the folding potential as a first order approximation of the mean field in the sense of the reaction theory of Feshbach [1]. We adhere to the empirical finding that the complex second order potential, the so called Dynamic Polarization Potential (DPP), which arise from the coupling to inelastic channels is dominantly imaginary and has a large effect mostly on the range of total potential. Indeed, all phenomenological analyzes of the heavy ion elastic scattering found that $R_v < R_w$, where $R_{v,w}$ are the radii of the real and imaginary component of the optical potential. We use folding form factors for both real and imaginary components of the optical potential,

$$U(R) = N_v V(R, t_v) + i N_w V(R, t_w) \quad (1)$$

where $N_{v,w}$ are normalization constants and $t_{v,w}$ are range parameters defined by the scaling transformation,

$$V(R, t) \rightarrow t^3 V_{fold}(tR) \quad (2)$$

This transformation conserves the volume integral of the folding potential and modifies the radius as,

$$\langle R^2 \rangle_V = \frac{1}{t^2} \langle R^2 \rangle_{fold} \quad (3)$$

If our approximation has a physical meaning then we should find $t_v \approx 1$ and large corrections for t_w . Besides a huge computing time saving, the scaling transformation defined above allowed a full exploration of the parameter space N_v, N_w, t_v, t_w . In this way we found for each reaction a sequence of phase equivalent solutions, common to all effective interaction used, and with real normalization $N_v \rightarrow 1$. In the particular case of the loosely bound ${}^6\text{Li}$, for which the coupling to the breakup channel could be important, the existence of solutions with volume integrals close to the bare potential values ($N_v \approx 1$), some care should be taken in obtaining the DPP from a CCDC calculation [2].

On a theoretical point of view, the discrete ambiguities have been investigated for complex potentials by Sabatier [3] and Cuet [4] in the framework of the WKB method. A physical interpretation has been given by Leeb and Schmid [5], in which the occurrence of discrete ambiguities is linked to the existence of partly Pauli forbidden states. For real potentials, Loeffel [6] has obtained theorems ensuring a unique potential from the knowledge of the phase-shifts δ_ℓ for all (non-discrete) non negative values of $\lambda = \ell + 1/2$. If the data set reduces to discrete values of $\lambda = \ell + 1/2$ for non-negative integer ℓ , the Carlson's theorem [7] predicts a unique potential $V(r)$, provided it belongs to a suitable class [6, 8]. In this case the ambiguities are due to the fact that we have at our disposition only a finite number of phase-shifts $\delta_\ell, \ell = 0, 1, \dots, N$. A class of real phase-equivalent potentials reproducing the phase-shifts $\delta_\ell, \ell = 0, 1, \dots, N$ has been constructed in [9].

As remarked by Brandan and Satchler [10] the knock-on exchange contribution to the folding potential is far from negligible when realistic nucleon-nucleon interactions are used. The relative sizes of the direct and exchange terms are sensitive to the effective interaction chosen between two nucleons in odd states of relative motion. This occurs because the odd-state components yield direct and exchange terms of opposite sign. A typical example is the well known G-matrix effective interaction in his Reid or Paris variants. The older Reid-based interaction results in an attractive direct component, and an attractive exchange component of similar magnitude. On the other hand, the more realistic Paris-based interaction results in a repulsive direct potential. This is compensated for by a much more attractive exchange term, such that the summed direct plus exchange potentials from the two interactions are almost identical. This points to a proper manipulation of the exchange kernels.

Finally, we show that the high surface transparency of the potential allows a strong internal barrier component of the scattering amplitude with repeated reflections between the most internal (centrifugal) turning point and the barrier turning point, and thus important refractive/resonant effects such as orbiting to be identified.

2. ${}^6\text{Li}+{}^{12}\text{C}$ AT 30.6 MeV

Table 1

A standard WS¹ solution for the reaction ${}^6\text{Li}+{}^{12}\text{C}$ at 30.6 MeV. The reduced radii are defined in the heavy ion convention. $J_{v,w}$ are volume integrals per interacting nucleon pair and $R_{v,w}$ are the *rms* radii of the potential.

V	W	r_v	r_w	r_c	a_v	a_w	χ^2	σ_R	J_v	R_v	J_w	R_w
204.	7.53	0.5842	1.2594	1.0	0.8844	0.5851	5.06	1189.	387.	3.7710	68.	4.5583

Table 2

Discrete folding solutions for the reaction ${}^6\text{Li}+{}^{12}\text{C}$ at 30.6 MeV. $N_{v,w}$ are normalization parameters, $t_{v,w}$ are scaling range parameters [16], $J_{v,w}$ are normalized volume integrals and $R_{v,w}$ are *rms* radii.

pot	N_v	N_w	t_v	t_w	χ^2	σ_R	J_v	R_v	J_w	R_w
M3YZR	0.5700	0.1305	1.0075	0.7328	6.03	1340.	260.53	3.741	58.48	5.125
	0.8100	0.1332	1.0460	0.8126	3.30	1246.	371.27	3.605	60.04	4.627
	1.0550	0.1432	1.0806	0.8547	3.48	1223.	484.78	3.491	64.74	4.401
M3YFR	0.5000	0.1094	1.0077	0.7759	8.77	1285.	275.03	3.791	59.21	4.908
	0.7000	0.1131	1.0512	0.8456	5.18	1213.	386.23	3.636	61.49	4.508
	0.9100	0.1227	1.0876	0.8801	5.89	1197.	503.39	3.516	66.88	4.333
GOGNY1	0.4300	0.0925	1.0092	0.7915	10.24	1265.	280.70	3.808	59.47	4.840
	0.6050	0.0970	1.0503	0.8568	7.70	1204.	396.07	3.661	62.62	4.476
	0.7900	0.1071	1.0871	0.8831	8.64	1198.	518.51	3.539	69.33	4.344
JLM1	0.4150	0.3745	0.9644	0.8066	6.99	1237.	271.45	3.775	58.18	4.826
	0.5900	0.4002	1.0000	0.8695	5.22	1191.	386.94	3.643	62.44	4.481
	0.7750	0.4385	1.0272	0.9062	6.58	1181.	509.30	3.547	68.59	4.303
JLM3	0.4500	0.4597	0.9571	0.7990	5.18	1249.	269.30	3.769	57.27	4.853
	0.6350	0.4860	0.9942	0.8620	3.92	1199.	381.08	3.630	60.81	4.502
	0.8250	0.5329	1.0264	0.8915	5.39	1191.	496.30	3.518	66.81	4.355

The elastic scattering of ${}^6\text{Li}$ on ${}^{12}\text{C}$ at 30.6 MeV was measured by Chuev *et al.* [11] and analyzed by Bassani *et al.* [12] in terms of standard optical potentials using volume Woods-Saxon form factors. The major interest in these data lie in an exotic pattern with deep Airy oscillations at intermediate angles and a substantial increase of the cross section at large angles. Similar features were observed by Vineyard *et al.* [13] in the scattering of ${}^6\text{Li}$ on ${}^{12}\text{C}$ at 24 and 30 MeV, ${}^6\text{Li}$ on ${}^{16}\text{O}$ at 25.7 MeV and ${}^7\text{Li}$ on ${}^{12}\text{C}$ at 34 MeV. The similarity with ALAS phenomenon is striking. Enhanced contributions to backward scattering could occur by means of exchange or heavy-particle stripping mechanisms which provides large momentum transfer in

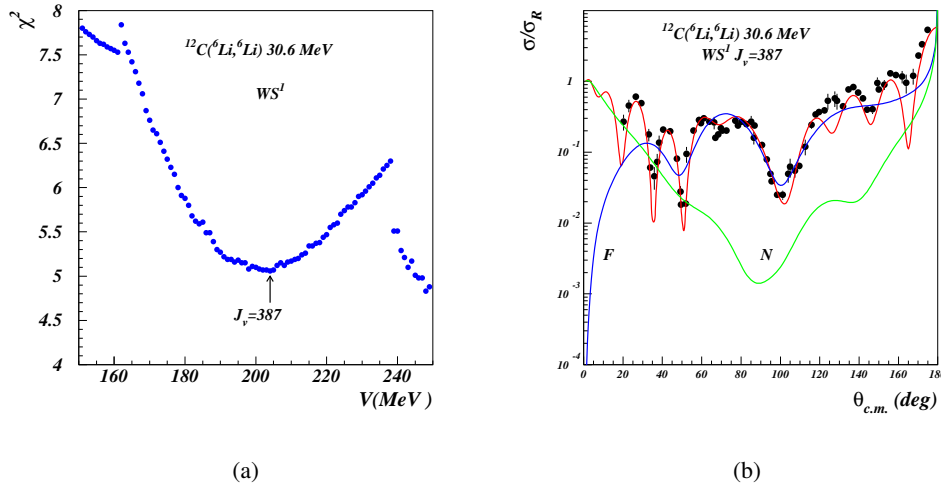


Fig. 1 – (Color on-line)(a) Grid search with WS^1 form factors. At least one well defined solution. (b) F/N decomposition with WS^1 form factors. This calculation confirms the structure of the F/N components found with folding form factors.

a single scattering process. Besides the well known ^{40}Ca case, for α scattering the phenomenon was observed at the ^{16}O shell closure: $^{12,14}\text{C}$, $^{14,15}\text{N}$ and ^{16}O all show enhanced cross section, whereas the neutron excess in ^{18}O drastically suppressed the backward scattering. According to Brink [14] the simplest explanation of ALAS could be given in terms of ordinary optical model by using strong real potentials and weak absorption. Oeschler *et al.* [15] proposed an explanation in terms of single particle resonances of potential scattering which are not damped out due to reduced absorption. Using a detailed semi-classical analysis we show that at least in this particular case the reaction mechanism is dominated by heavy ion orbiting. We start by executing a standard optical model analysis using volume Woods-Saxon form factors. The potential radii are defined in the heavy ion convention. The Coulomb component is included in the hard sphere approximation. A detailed grid search using the strength of the real potential as a control parameter revealed a single solution with real volume integral $J_v < 400 \text{ MeV fm}^3$, see Table 1 and Figure 1a. There are hints for many other solutions at larger J_v values. Though the χ^2 pattern is quite large, the absolute minimum could be identified unambiguously. The corresponding real potential is very strong and absorption is weak, suggesting that the coupling with inelastic channels including breakup is quite small. The far side/near side decomposition of the scattering amplitude is shown in Figure 1b. The dominant far side component is heavy structured with a remarkable deep Airy oscillation near $\theta = 100^\circ$

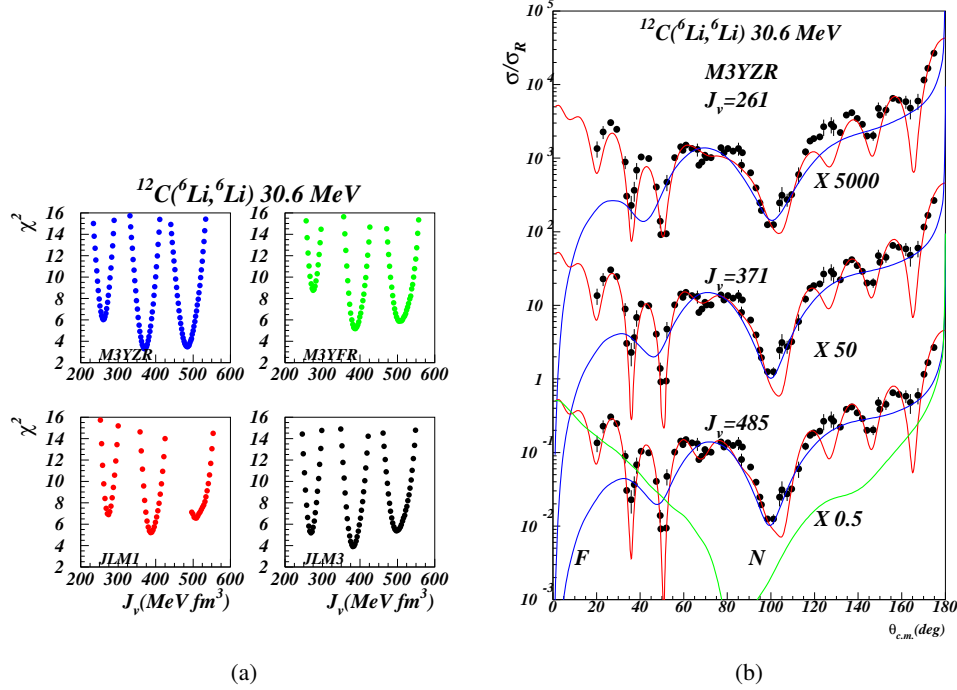


Fig. 2 – (Color on-line)(a) Grid search with selected folding form factors. At least three well defined solutions for each model. (b) F/N decomposition with M3YZR. Strong refractive effects. Heavy structured far side component. Two deep Airy oscillations.

followed by oscillations of increased amplitude at larger angles.

The folding model analysis is executed using effective interactions described in our preceding paper [16] including the well known M3Y [17] in two versions (zero range and finite range knock-on exchange) as well as density dependent effective interactions GOGNY [18] and JLM [19]. The single particle densities were obtained from a standard spherical Hartree-Fock calculation using the density functional of Beiner and Lombard [20]. The obtained charge *rms* radii agree quite well with the systematics of Angeli [21]. Using a grid search analysis we found a number of discrete solutions see Table 2 and Figure 2a. The minima are very narrow and thus the discrete solutions are precisely defined. Examination of cross sections plotted in Figs. 2b-4b shows that these potentials are almost phase equivalent. Such equivalence was suggested to be due to the modulo π uncertainty inherent to phase determinations [9]. For deep potentials another half wavelength can accommodate in the potential well. Moreover, examination of the Table 2 shows that all folding models predict the same sequence of discrete solutions. Real volume integrals are consistent within 2%

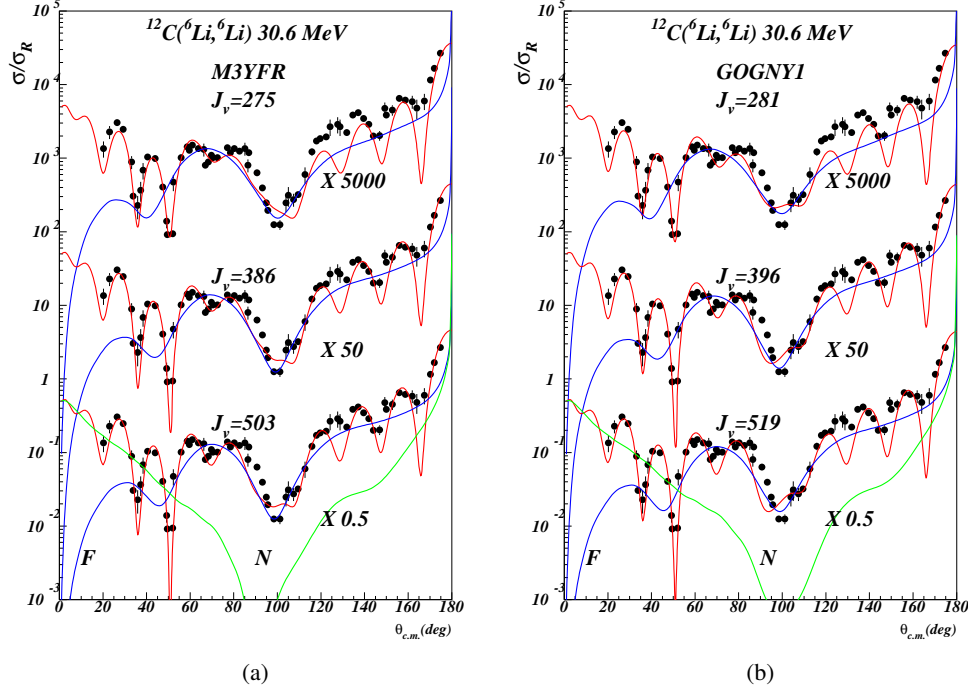


Fig. 3 – (Color on-line)(a) F/N decomposition with M3YFR. (b) F/N decomposition with GOGNY1.

precision. The reaction cross section is well defined and has little variation from one calculation to another $\sigma_R = 1228 \pm 50$ mb. Although we are far from the saturation (≈ 15 MeV/A), the constant reaction cross section means simply that all important inelastic channels are already open and therefore σ_R is independent of the strength of the real potential. The major correction is needed for the imaginary range parameter t_w (of the order of 20%) in line with the Feshbach's theory of the dynamical polarization potential (DPP). At this point a remark concerning the DPP is in order. Using a CCDC calculation, Sakuragi [2] conjectured that the DPP arising from the coupling with ${}^6\text{Li} \rightarrow \alpha + d$ breakup states is independent of target and energy and has a huge repulsive real component of the order of 40% from the bare optical potential and thus there is no need for the renormalization of the folding potential obtained from the M3Y effective interaction. However the existence of many phase equivalent discrete folding solutions with normalizations $N_v \sim 0.6 - 1$ invalidates this conjecture at least for the reaction discussed here.

The semi-classical (WKB) analysis for the decomposition of the scattering amplitude into barrier and internal barrier components starts by executing the main steps outlined in [22]. We use the WS^1 potential tabulated in Table 1 as a representative

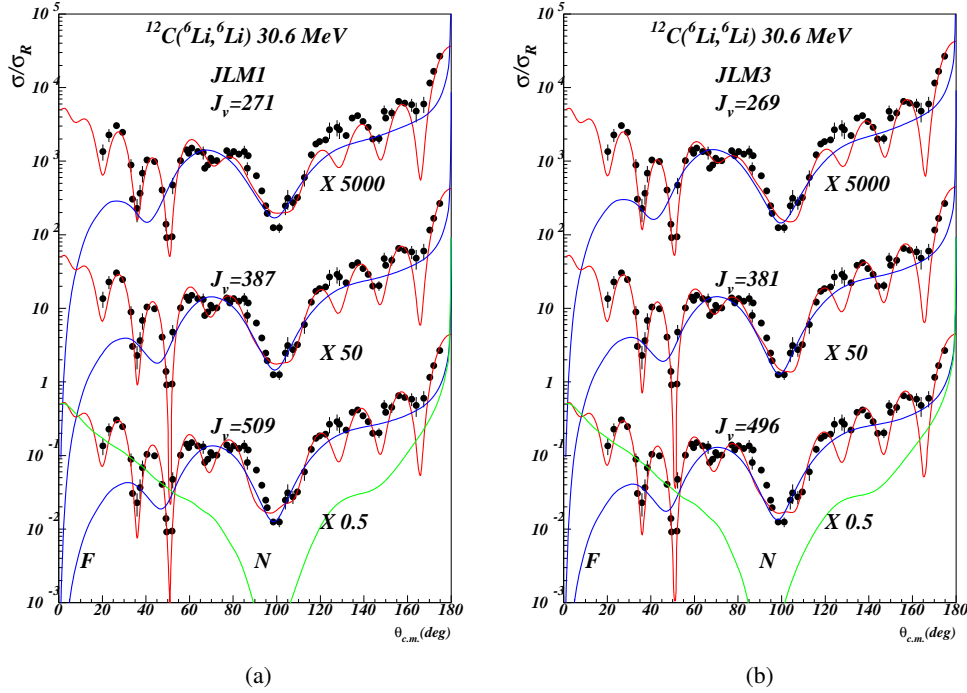


Fig. 4 – (Color on-line)(a) F/N decomposition with JLM1. (b) F/N decomposition with JLM3.

potential for this reaction. The complex turning point trajectories are depicted in Fig. 5. The picture is characteristic for strong optical potentials and moderate absorption with three turning points well separated in complex plane. The inactive turning points plotted in black, are correlated with the poles of the imaginary component of the optical potential (right hand complex conjugate stars). These give negligible small contribution to the scattering amplitude. The semi-classical deflection function Fig. 6a indicates an orbiting singularity near $\ell_o = 11$ typical for strong real potentials. This is the first hint that the reaction mechanism is dominated by heavy ion orbiting. The survival elastic probability Fig. 6b shows a very large internal barrier component for all partial waves $\ell < \ell_o$ and negligible small beyond this value. Destructive interference with the barrier component produces a small Grün-Wall spike near the orbiting momentum. The same feature is present in the exact quantum mechanical calculation (black dots in the figure). In fact we may remark that accurate calculation of the complex turning points and action integrals make the semi-classical result almost identical with the quantum mechanical result. The semi-classical scattering amplitude, decomposed into barrier and internal barrier components leads to the cross sections depicted in Fig. 7a. The barrier component which corresponds

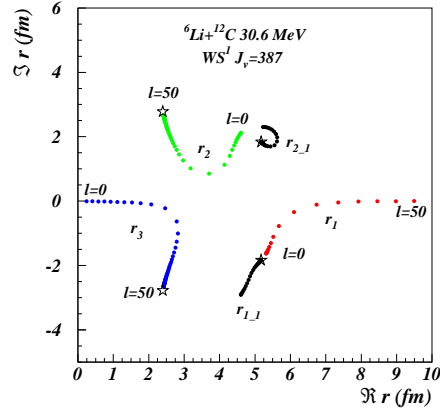
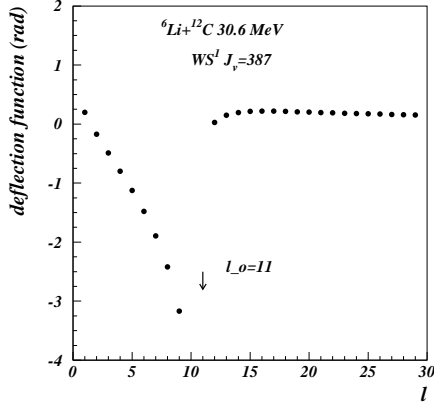
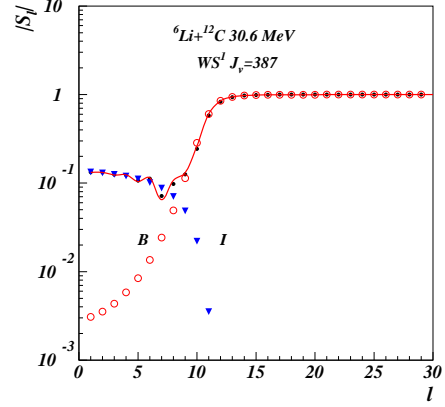


Fig. 5 – (Color on-line) Complex turning point trajectories for the WS^1 potential with the real volume integral $J_v = 387 \text{ MeV fm}^3$. The inactive turning points (black) are correlated with the poles of the imaginary potential. The active turning points (blue and green) are correlated with the poles of the real potential (stars).



(a)



(b)

Fig. 6 – (Color on-line)(a) Semiclassical deflection function. The orbiting momentum is $\ell_o = 11$. (b) The semiclassical absorption profile (red curve) is compared with the exact quantum result (black dots). The semiclassical S-matrix is decomposed into barrier (B) and internal barrier (I) components. The B/I interference produces a Grün-Wall spike near $\ell = 8$.

to the flux reflected at the barrier has a typical diffraction pattern due to strong ab-

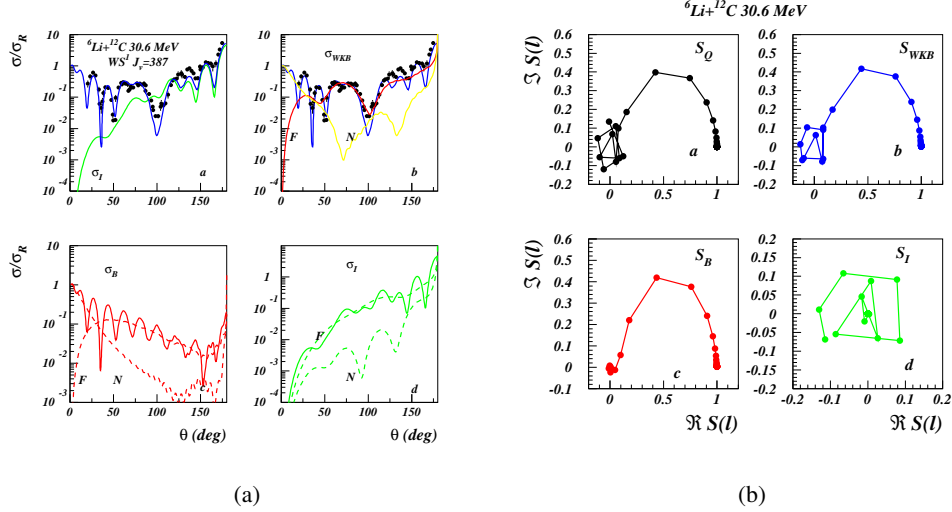


Fig. 7 – (Color on-line)(a) The semiclassical (WKB) cross section is decomposed into barrier (B) and internal barrier (I) components. Each component is further decomposed into F/N subcomponents. The internal barrier component is exceptionally large and dominates the large angles. The strong B/I interference produces the deep minimum near $\theta = 100^\circ$. (b) Argand diagram for the semiclassical S-matrix. The exact quantum result (Q) is shown for comparison. The orbiting (resonant) effect is isolated into the internal barrier component (I).

sorption with large Fraunhofer oscillations at forward angles. The internal barrier component which corresponds to repeated reflections between the turning points r_3 and r_2 (Fig. 5) is responsible for the behavior of the cross section at large angles. Destructive interference of two far side components of the barrier and internal barrier amplitudes (BF and IF) leads to the deep Airy oscillation near $\theta = 100^\circ$. The Argand diagram, Fig. 7b, shows clearly the resonant effect in the low partial waves due to orbiting which is present in both total WKB and quantum S-matrix. The entire resonant effect is isolated into the internal barrier component (lower right panel). The S-matrix trajectory rotates anticlockwise around the origin several times, suggesting the presence of multiple Regge poles.

3. ${}^6\text{Li}+{}^{13}\text{C}$ AT 54 MeV

The reaction ${}^6\text{Li}+{}^{13}\text{C}$ at 54 MeV was measured [23] as a part of our long term program to find reliable ways to predict optical model potentials for reactions with radioactive beams (RNBs). In particular our interest focuses on finding reliable descriptions for transfer reactions involving relatively light, loosely bound nuclei, which are used as indirect methods in nuclear astrophysics. The stable ${}^6\text{Li}$ is

Table 3

Discrete solutions with WS¹ form factors for the reaction ${}^6\text{Li}+{}^{13}\text{C}$ at 54 MeV.

V	W	r_v	r_w	r_c	a_v	a_w	χ^2	σ_R	J_v	R_v	J_w	R_w
210.	15.79	0.5308	1.1474	1.0	0.8991	0.7486	3.91	1343.	325.	3.7485	115.	4.6333
306.	19.37	0.5233	1.0727	1.0	0.8268	0.8063	3.32	1365.	416.	3.5017	123.	4.5800

Table 4

Discrete solutions with folding form factors for the reaction ${}^6\text{Li}+{}^{13}\text{C}$ at 54 MeV.

pot	N_v	N_w	t_v	t_w	χ^2	σ_R	J_v	R_v	J_w	R_w
M3YZR	0.6750	0.2491	1.0796	0.7735	7.24	1503.	305.75	3.560	110.41	4.949
	0.9100	0.2591	1.1300	0.8078	4.86	1444.	413.68	3.403	115.10	4.741
	1.1450	0.2690	1.1736	0.8313	5.55	1408.	522.13	3.279	119.68	4.609
M3YFR	0.6100	0.2129	1.0751	0.7978	5.52	1454.	325.93	3.607	111.59	4.842
	0.8200	0.2228	1.1275	0.8243	5.46	1414.	439.74	3.442	116.96	4.689
	1.0450	0.2358	1.1616	0.8443	7.04	1395.	561.73	3.342	123.98	4.578
GOGNY1	0.5200	0.1773	1.0810	0.8076	5.68	1435.	333.31	3.615	111.52	4.820
	0.7000	0.1849	1.1317	0.8314	7.05	1400.	450.25	3.456	116.48	4.684
JLM1	0.5050	0.7103	1.0383	0.8094	6.04	1405.	322.18	3.575	108.71	4.810
	0.6750	0.7357	1.0867	0.8228	8.76	1389.	432.17	3.418	112.71	4.733

Table 5

Unitary solutions with Regge pole amplitudes for the reaction ${}^6\text{Li}+{}^{13}\text{C}$ at 54 MeV.

Set	L	Δ	α	β	L_1	Δ_1	D_1	Γ_1	L_2	Δ_2	D_2	Γ_2	χ^2	σ_R
R1	14.2	1.97	-2.80	-1.99	11.3	0.791	2.02	3.08	11.2	2.09	0.64	0.227	6.12	1446
R2	14.2	1.95	-2.73	-2.13	11.4	0.639	1.45	2.73	11.1	1.24	1.14	0.431	6.08	1440
R3	14.6	2.06	-2.55	-1.59	11.2	0.497	2.56	5.33	12.2	15.9	-0.78	0.0168	5.36	1427

an archetype of fragile nuclei, and produced in laboratory with sufficient intensity to allow high precision angular distributions to be measured. At energies around 10 MeV/A, the ${}^6\text{Li}$ interaction with light targets is moderately absorptive to allow strong refractive/resonant effects to be identified in elastic angular distribution [24]. We present here a new and dedicated analysis of these data underlying the hints for heavy ion orbiting.

A standard optical model analysis in terms of WS¹ volume potentials revealed at least two discrete solutions with real volume integrals $J_v < 450 \text{ MeV fm}^3$, Table 3 and Fig. 8a. The far side/near side decomposition of the scattering amplitude is shown in Fig. 8b. The data show complex forms with characteristic rapid oscillations at forward angles (Fraunhofer) and a marked change in shape at intermediate angles: a kind of plateau followed by a very deep minimum. This feature is common for several other reactions involving ${}^7\text{Li}$ at similar energies [23]. Assuming pure Fraunhofer scattering at forward angles, we extract a grazing angular momentum $\ell_g = 15$ from the angular spacing $\Delta\theta = \pi(\ell_g + 1/2)$. Examination of potentials in Table 3 shows a strongly refractive core surrounded by a weakly absorptive halo. In fact the

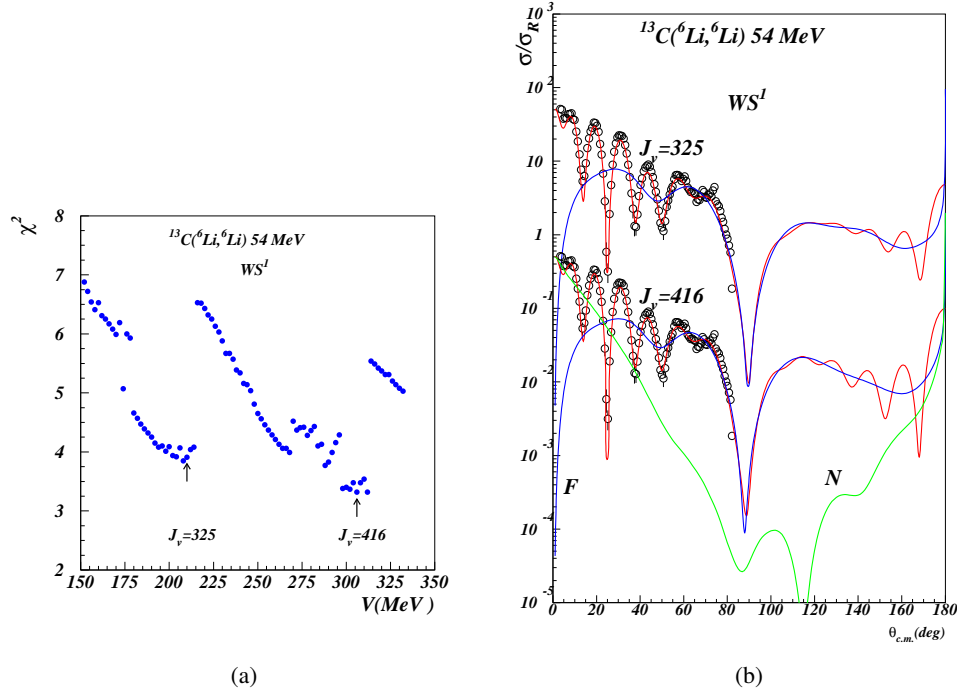


Fig. 8 – (Color on-line)(a) Search for discrete solutions with WS^1 form factors. (b) F/N decomposition with WS^1 form factors. The potentials are very deep. The reaction mechanism is strongly refractive. The far side component shows a deep Airy oscillation due to a strong destructive interference barrier/internal barrier components of the scattering amplitude.

transparency parameter $w = W(r)/V(r)$ calculated at the grazing distance $\ell_g = kR_g$ is of the order of 0.1 allowing the cross section to be fully dominated by the far side component. Beyond the deep minimum near $\theta = 80^\circ$ the far side component shows a rainbow bump. Diffractive oscillations of increased amplitude due to N/F interference at very large angles are modulated by the normal increase of the far side component in this sector.

A grid search using the well known M3Y effective interaction supplemented with the one nucleon zero range knock-on exchange revealed a number of discrete solutions corresponding to normalizations $N_v = 0.7 - 1.1$ see Fig. 9. These fully equivalent solutions reflect the usual uncertainty in the phase shift determination using angular distribution taken at fixed energy. Solutions with normalizations close to unity and consistent real volume integrals are found for all effective interactions. This strengthens the conjecture that one can extract from an elastic angular distribution at best only the low rank moments of the interaction (volume integrals and *rms* radii).

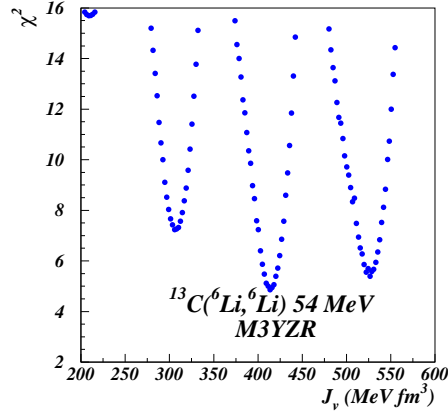


Fig. 9 – (Color on-line) Search for discrete solutions with M3YZR.

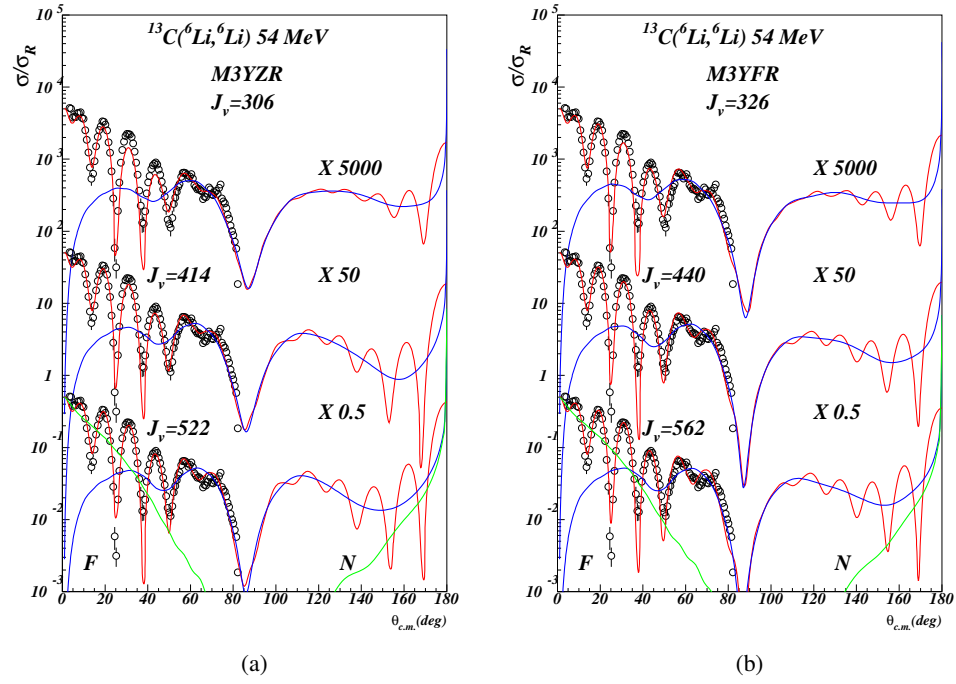


Fig. 10 – (Color on-line)(a) F/N decomposition with M3YZR. The larger real volume integral, the better agreement with the data. (b) F/N decomposition with M3YFR.

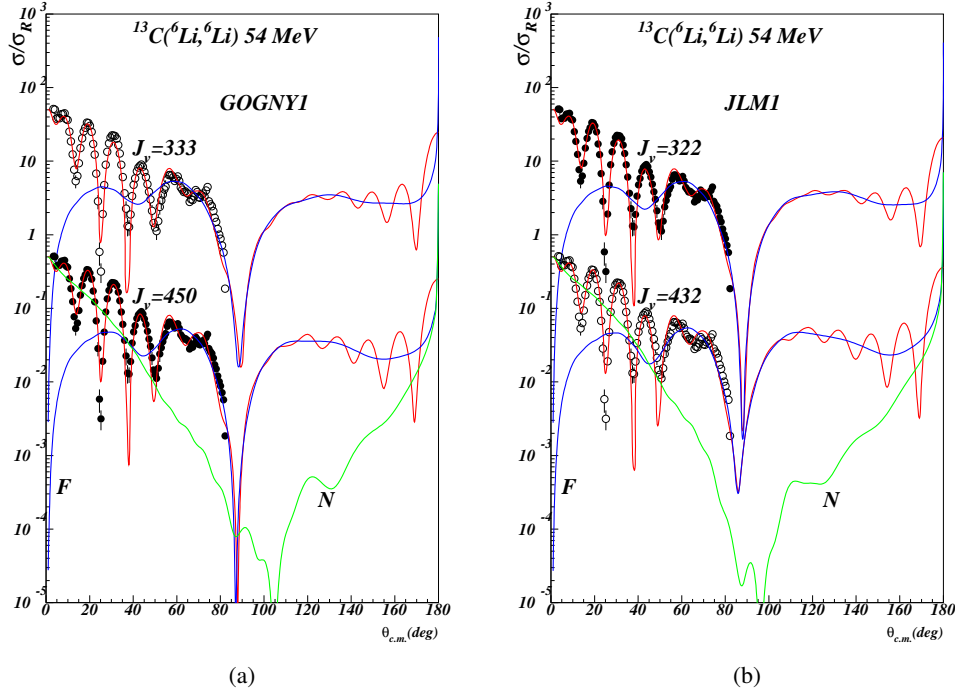


Fig. 11 – (Color on-line)(a) F/N decomposition with GOGNY1. Extremely deep Airy oscillation. (b) F/N decomposition with JLM1.

This imply that one cannot determine the DPP from a coupled channel calculation by forcing a normalization $N_v = 1$. Owing to the force of circumstances (real volume integrals of the order of $\sim 400 \text{ MeV fm}^3$ for the bare interaction) the data analysis will lead normally to $N_v = 1$ without invoking a complicated repulsive DPP if such a solution is compatible with the data. The far side/near side analysis displayed in Figs. 10a-11b shows the same heavy structure of the F/N components with deep Airy oscillations and rainbow bumps. The density dependence (pseudo zero range for GOGNY and approximately polynomial for JLM) cannot be disentangled based on the present calculation since both effective interactions GOGNY and JLM predict almost identical results, Figs. 11a and 11b. Also calculations with M3Y using a zero range knock-on exchange or exact finite range exchange give identical results. This justifies to some extent the popular use of pseudo-delta folding for exchange which avoids the tedious manipulation of nonlocal kernels.

A semi-classical (WKB) analysis based on the WS^1 potential with $J_v = 325 \text{ MeV fm}^3$ is performed in order to clarify the mechanism behind the deep minimum near $\theta = 80^\circ$ and the oscillations near $\theta = 180^\circ$. The complex turning point trajec-

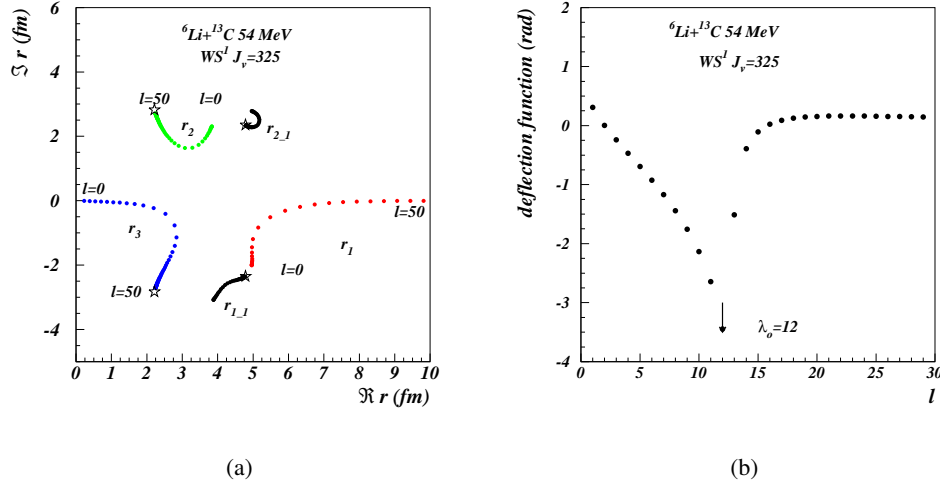


Fig. 12 – (Color on-line)(a) Complex turning point trajectories for the WS^1 potential with the real volume integral $J_v = 325$ MeV fm³. The inactive points are plotted in black. The stars are the poles of the real and imaginary components of the optical potential. (b) Semi-classical deflection function. The pattern is close to orbiting with a singularity near the orbiting momentum $\lambda_o = 12$.

tories plotted in Fig. 12a show the usual pattern with three well isolated points, an essential condition for the applicability of the Brink-Takigawa theory [25]. Since the potential is very strong, there is no surprise that the semi-classical deflection function Fig. 12b shows the usual singularity near the orbiting momentum $\lambda_o = 12$. The internal barrier component of the elastic survival probability, Fig. 13a is large for angular momenta $\lambda < \lambda_o$ and negligibly small in the rest. Practically all the essential features of the reaction are decided by the angular momentum components in this range. The strong destructive B/I interference near the λ_o produces the well known Grün-Wall spike [26] often invoked for the increase of the cross section at backward angles. Semi-classical cross section and barrier/internal barrier decomposition are shown in Fig. 13b. The deep minimum near $\theta = 80^\circ$ appears as a destructive interference of two far side components of the barrier and internal barrier amplitudes. The forward angle sector (Fraunhofer diffraction) is entirely explained by the barrier component. This justifies the picture that the barrier component is determined by the flux reflected at the most external turning point, not penetrating the barrier. High frequency oscillations at large angles are numerical instabilities in the calculation of the corresponding action integrals. Argand diagram are presented in Fig. 14. The semi-classical (WKB) and the exact quantum result (Q) are identical. The entire orbiting/resonant effect is isolated into the internal barrier component (d) which rotates

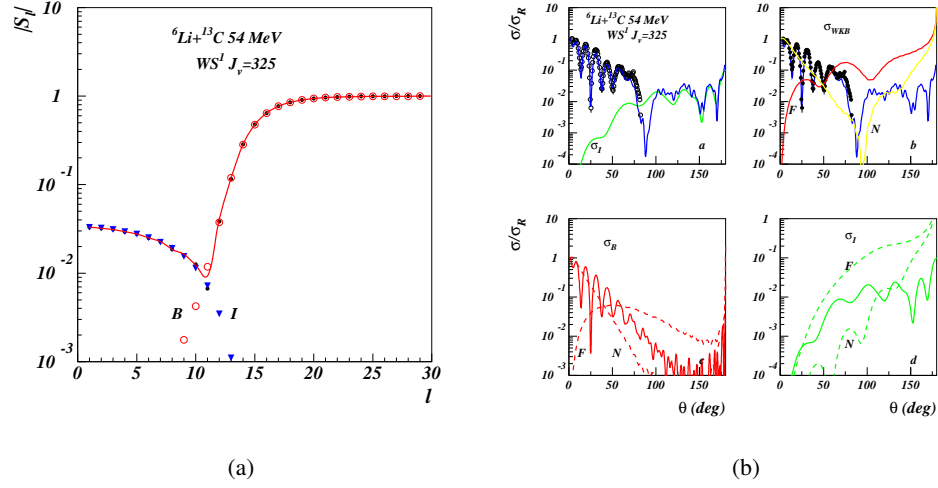


Fig. 13 – (Color on-line)(a) Absorption profile. The semi-classical (WKB) profile (curve) reproduces exactly the exact quantum result (black dots). The strong B/I interference near the orbiting momentum produces a deep Grün-Wall spike. The internal barrier component (triangles) is large as a manifestation of the refractive/resonant effects. (b) Semi-classical (WKB) cross sections F/N and B/I decomposition. The deep minimum near $\theta = 80^\circ$ appears as a strong B/I interference. As opposite to the quantum (WS) description, the rainbow bump appears here with some oscillatory structures since the internal barrier expansion of the scattering amplitude is not very reliable at large angles.

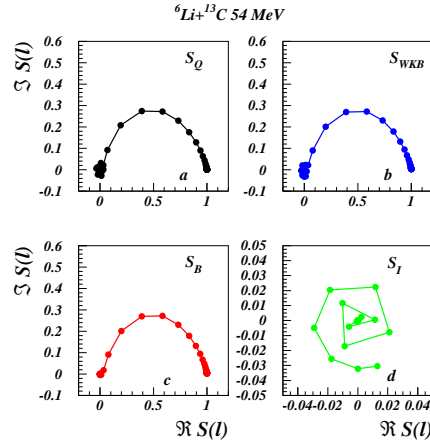


Fig. 14 – (Color on-line) Argand diagram for the semi-classical (WKB) S-matrix. The WKB pattern is identical with the exact quantum result (Q). The resonance effect is isolated into the internal barrier component (I) which rotates anti-clockwise several times around the origin.

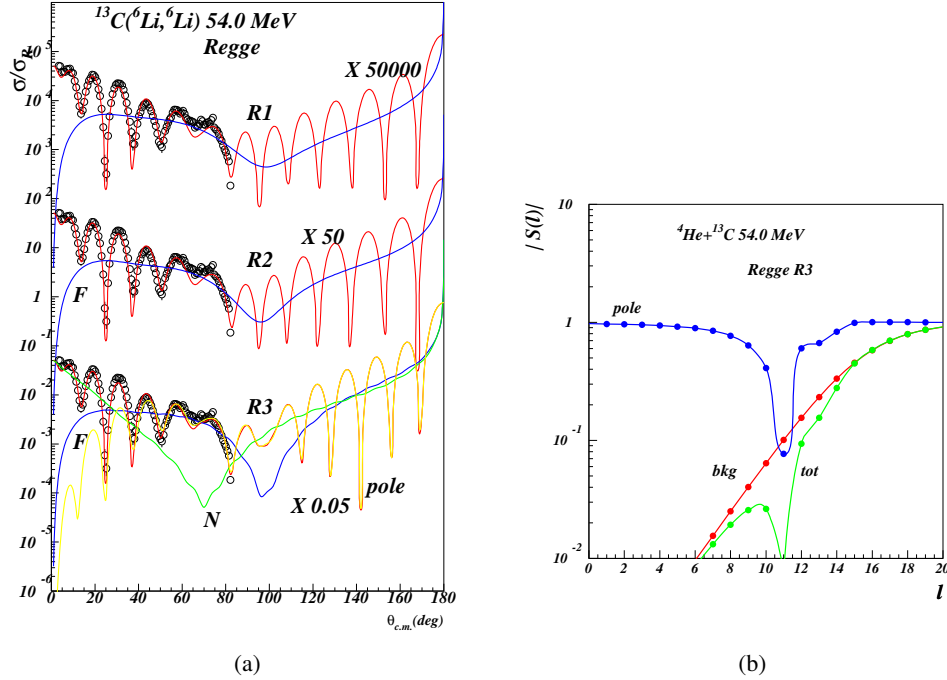


Fig. 15 – (Color on-line)(a) F/N decomposition using Regge pole amplitudes. The drop in the cross section near $\theta = 80^\circ$ appears as a F/N interference. At large angles the dominant pole component shows a pattern similar to P_L^2 with angular momentum close to the orbiting momentum $\lambda_o = 12$. (b) Absorption profile using Regge pole amplitude R3. The pole component modifies dramatically the total profile. In this case the Grün-Wall deep is carried entirely by the pole component.

anti-clockwise several times around the origin.

Three fully unitary solutions obtained with the McVoy parametrization [27] of the Regge pole scattering amplitude are tabulated in Table 5. These are obtained by constraining the background component to reproduce the reaction cross section given by the ordinary optical potential. Note that the pole component gives a small contribution to the total reaction cross section since it represents only a small (but essential) perturbation in the total scattering amplitude. In practice it is quite easy to obtain excellent non-unitary solutions, but these are rejected from obvious reasons. We also reject solutions with very large pole widths $\Gamma_{1,2}$ which exceed more than few units of angular momentum. We believe that in fact we have a unique solution in the table, the variation in the parameters reflecting merely the unavoidable parameter correlations in the highly nonlinear χ^2 minimization problem. The cross sections calculated in this approximation are depicted in Fig.15a. The pole component (yellow curve) dominates the cross section in almost all the angular range. The

background component gives an excellent description of the forward angle sector, thus confirming that the corresponding oscillations are a manifestation of diffraction due to strong absorption. At large angles the dominant pole component produces regular oscillations of the form P_{11}^2 , with angular momentum close to the orbiting value $\lambda_o = 12$. The far side component of the total amplitude has the same structure as in the ordinary optical model calculation. Although the Airy oscillation is much damped, a clear signal that the mechanism is governed by diffraction due to Regge pole. The elastic survival probability is displayed in Fig. 15b for the R3 parametrization. A spectacular spike appear in the total S-matrix due to the main Regge pole localized near the real axis. Thus the legendary Grün-Wall deep appears here as a natural effect of the Regge pole presence.

4. CONCLUSION

We have analyzed two reactions initiated by the fragile ${}^6\text{Li}$ on light targets in an energy window (5-9 MeV/A) in which the interaction is sufficiently strong and moderate absorptive in such a way that refractive and resonant effects are not damped by the absorption. A dedicated semi-classical and Regge pole analysis revealed typical characteristics of heavy ion orbiting. The standard optical model analysis with double folding form factors in the scaling approximation revealed a number of discrete solutions fully phase equivalent, encompassing normalization of the real form factors close to unity. This suggests that the usual calculation of the dynamic polarization potential by including coupling to the breakup channel should be revised.

Acknowledgements. This work was partly supported by CNCSIS Romania, under program PN-II-PCE-55/2011 and PN-II-ID-PCE-0299/2012, and partly by IN2P3, France.

REFERENCES

1. H. Feshbach, *Theoretical Nuclear Physics* (Wiley, New York, 1992).
2. Y. Sakuragi, Phys. Rev. **C35**, 2161 (1987).
3. P. C. Sabatier, Phys. Rev. A **8**, 589 (1973).
4. M. Cuet, Ann. Physics **120**, 1 (1979).
5. H. Leeb and E.W. Schmid, Z. Physik **A296**, 51 (1980).
6. J.J. Loeffel, Ann. Inst. Henri Poincaré **8**, 339 (1968).
7. R. Ph. Boas, *Entire Functions* (Academic Press, New York, 1954).
8. K. Chadan and P.C. Sabatier, *Inverse Problems in Quantum Scattering Theory* (2nd edn., Springer, Berlin, 1989).
9. M. Lassaut, R. J. Lombard, J. Phys. A: Math. Theor. **43**, 445210 (2010).
10. M. E. Brandan and G. R. Satchler, Phys. Rep. **285**, 143 (1997).
11. V. I. Chuev, V. V. Davidov, B. G. Novatskii, A. A. Ogloblin, S. B. Sakuta and D. N. Stepanov, Symp. on heavy-ion reactions and many-particle excitations, Saclay, 1971, contributed papers.

12. G. Bassani *et al.*, Nucl. Phys. **A189**, p.353 (1972).
13. M. F. Vineyard, J. Cook, K. W. Kemper, and M. N. Stephens, Phys. Rev. **C30**, 916 (1984).
14. D. Brink, J. Grabowski and E. Vogt, Nucl. Phys. **A309**, 359 (1978).
15. H. Oeschler, H. Fuchs and H. Schröter, Nucl. Phys. **A202**, 513 (1973).
16. F. Carstoiu, M. Lassaut, L. Trache, V. Balanica, Rom. J. Phys. **61**, 400-412 (2016).
17. N. Anantaraman, H. Toki and G. F. Bertsch, Nucl. Phys. **A398**, 269 (1983).
18. D. Gogny, Proc. Int. Conf. on Nucl. Physics, Munich 1973, eds J. de Boer and H. J. Mang, Vol. 1, p. 48.
19. J. P. Jeukenne, A. Lejeune and C. Mahaux, Phys. Rev. **C16**, 80 (1977).
20. M. Beiner and R. J. Lombard, Ann. Phys. (N.Y.) **86**, 262 (1974).
21. I. Angeli, Heavy Ion Physics **8**, 23 (1998).
22. T. Al-Abdullah, F. Carstoiu, C. A. Gagliardi, G. Tabacaru, L. Trache and R. E. Tribble, Phys. Rev. **C89**, 064602 (2014).
23. Florin Carstoiu, Livius Trache, Robert E. Tribble, and Carl A. Gagliardi, Phys. Rev. **C70**, 054610 (2004).
24. Florin Carstoiu, Livius Trache, Phys. Rev. **C85**, 054606 (2012).
25. D. M. Brink and N. Takigawa, Nucl. Phys. **A279**, 159 (1977).
26. C. R. Grün and N. S. Wall, Nucl. Phys. **81**, 161 (1966).
27. K. W. McVoy, Phys. Rev. **C3**, 1104 (1971).

New generation of experiments for the investigation of stellar (p, γ) reaction rates using SAMURAI *

V. Panin¹, K. Yoneda¹ M. Kurokawa¹, J. Blackmon² Z. Elekes³ D. Kim⁴ T. Motobayashi¹

H. Otsu¹ B. C. Rasco² A. Saastamoinen⁵ L. Sobotka⁶ L. Trache⁷ T. Uesaka¹

1. *RIKEN Nishina Center, 2-1 Hirosawa, Wako, Saitama 351-0198, Japan;*

2. *Louisiana State University, 211-A Nicholson Hal, Tower Dr., Baton Rouge, LA 708030-4001, USA;*

3. *MTA Atomki, Bem tér 18/c H-4026 Debrecen, Hungary;*

4. *Ewha Womans University, Seoul, South Korea;*

5. *Texas A&M University, USA;*

6. *Department of Chemistry, Washington University, Saint Louis, MO, 63130, USA;*

7. *IFIN-HH, str. Reactorului 30, Bucharest-Magurele RO-77125, Romania;*

Abstract

The future experimental campaign with the SAMURAI setup at RIKEN will explore a wide range of neutron-deficient nuclei with a particular focus on the most critical (p, γ) reaction rates relevant to the astrophysical rp -process in type I X-ray bursts (XRB). Intense radioactive-ion (RI) beams at an energy of a few hundred MeV/nucleon will be deployed to populate proton-unbound states in the nuclei of interest through the Coulomb excitation or nucleon-removal processes. The decay of these states into a proton and a heavy residue will be measured using complete kinematics and the information about time reversal proton-capture process will be obtained. This method will provide the vital experimental data on the resonances, which dominate the stellar (p, γ) reaction rates, as well as on the direct proton-capture process for some other cases. The experimental setup will utilize for the first time the High-Resolution 90°-mode of the SAMURAI spectrometer in combination with the existing detection systems, including custom-designed Si-strip detectors for simultaneous detection and tracking of heavy ions and protons emitted from the target. The details of the experimental method and the utilized apparatus are discussed in this paper.

Key words: type I X-ray bursts, rp -process, (p, γ) reaction rates, neutron-deficient RI beams

1 Subject and Motivation

Explosive hydrogen burning at extreme temperature and density conditions is one of the most fascinating topics in modern nuclear astrophysics, which only in the last decades became accessible for detailed experimental studies due to availability of intense neutron-deficient RI beams. Such exotic nuclear species in the proximity of the proton drip-line play an important role in the astrophysical rp -process - a dominating nucleosynthesis path in type-I X-ray bursts (XRB) which are often referred as the most frequent type of thermonuclear explosions in the Galaxy ^[1-3]

XRBs are recurrent events originating from close binary star systems due to thermonuclear runaway at the surface of a neutron star which accretes H/He-rich matter from an adjacent low-mass donor star ^[1]. When

Received date:

Revised date:

* **Foundation item:** This work is supported by the OTKA project number 114454.

Biography: Valerii Panin (1985), male (Ukraine), Alchevsk, PhD, Experimental Nuclear Physics; E-mail: valerii.panin@riken.jp

critical temperature ($T \approx 1\text{--}2$ GK) and density ($\rho \approx 10^6$ g/cm³) are reached in the hot envelope of the neutron star, the explosive process is triggered by 3α -reaction followed by a sequence of (p, γ) and (α, p) reactions (αp -process) promoting the burning material into the $A=40$ region [4]. After that, a rapid sequence of (p, γ) reactions and β -decays occurs (rp -process), thus processing the abundance flow further along the proton dripline with an extension all the way into $A \approx 100$ region [5, 6] where the nucleosynthesis is believed to stop in the closed SnSbTe cycle due to disintegration of α -unbound isotopes $^{106-108}\text{Te}$. The entire process lasts typically 10-100 s and results in an excessive yield (factor of about 10) of X-ray photons emanated from the neutron star's surface. This phenomenon is usually observed as a fast X-ray flash with a characteristic shape of the light curve. A wealth of information about properties of a neutron star such as mass, radius, spinning frequency etc., can be extracted from the XRB light curves [3, 7], if the underlying nuclear process is correctly described in the framework of an accurate fluid dynamics model.

The main difficulty in studying XRB nucleosynthesis arises from its complexity - several hundreds isotopes and thousands nuclear interactions can be involved in a single XRB event. However, experimental information is very scarce for most of them and theoretical calculations may yield uncertainties of a factor of 10-100 for some reaction rates that, in turn, leads to significant discrepancies in the predicted XRB properties such as energy generation rates, light curves and resulting final chemical abundances [8, 9]. The final chemical abundances can be essential, in particular, for the cooling of the neutron star surface as well as for the consecutive bursts which develop on the preceding nuclear ashes [10]. It was found in the recent state-of-the-art sensitivity studies [3, 8, 9], based on large (over 600 isotopes) network calculations and on various hydrodynamic models with different XRB conditions (accretion rate, temperature and density profiles, etc.), that about less than 50 reactions may have any significant effect on the XRB properties such as overall energy output and final chemical yields. Such reactions can be identified in the vicinity of the so called waiting point (WP) nuclei (^{30}S , ^{60}Zn , ^{64}Ge , ^{68}Se , etc.) for which successive adding of another proton is inhibited by negative or very low proton-capture Q -values (a few hundreds keV). In such case (p, γ) reactions are hampered by either proton decay or reverse photodisintegration (γ, p) establishing (p, γ) -(γ, p) equilibrium. In both situations the process must “wait” until the relatively slow β^+ decay to process towards heavier nuclei via adjacent isotonic chains. This may lead to accumulation of the material in the region of the WP-nucleus (Z, N) and thus define the resulting composition of the burned ashes as well as nuclear energy generation rates and profiles of the XRB light curves. Investigation of the identified most critical (p, γ) reaction rates is of primary importance for the experimental studies in the next years. It will also become the main focus of the future experimental campaign with the large-acceptance spectrometer SAMURAI, taking advantage of the most intense RI-beams in the world available at RI-beam Factory in RIKEN [11]

2 Reactions in focus and the experimental method

Based on the previous theoretical sensitivity studies and XRB model predictions, the following set of reactions has been selected for future experiments at SAMURAI.

2.1 Breakout from WP-nuclei ^{64}Ge and ^{56}Ni

- $^{65}\text{As}(p, \gamma)^{66}\text{Se}$

The reaction rate is found amongst the most influential for the final chemical yields of XRB [3, 9]. This is mainly due to its bridging effect on WP-nuclei ^{64}Ge , which, in most of the studied models, is a starting point towards production of heavier elements but is also a limiting factor of the rp -process due to its

β -decay life-time of 92 s being comparable to the typical time scale of the entire XRB process. A possible breakout can occur at certain density and temperature conditions even through the proton unbound nucleus ^{65}As due to its finite lifetime. Hence, sequential two-proton capture on the WP-nucleus can be much faster than the associated β -decay ^[12]. In this case, decay constant of the ^{64}Ge via two-proton capture can be expressed as follows ^[3]:

$$\lambda_{^{64}\text{Ge} \rightarrow ^{65}\text{As} \rightarrow ^{66}\text{Se}} = F(N_p, T, j_i, G_i) \times \exp\left(\frac{Q_{^{64}\text{Ge} \rightarrow ^{65}\text{As}}}{kT}\right) \times \lambda_{^{65}\text{As} \rightarrow ^{66}\text{Se}} \quad (1)$$

where $F(N_p, T, j_i, G_i)$ is a function depending on proton density N_p , temperature T , nuclear spins j_i and normalized partition functions G_i (for $i = ^{64}\text{Ge}$, ^{65}As and proton); $Q_{^{64}\text{Ge} \rightarrow ^{65}\text{As}}$ is a Q value for proton capture on ^{64}Ge and $\lambda_{^{65}\text{As} \rightarrow ^{66}\text{Se}}$ is a decay constant of ^{65}As with respect to subsequent proton capture. It can be seen that the breakout is not governed by the rate of $^{64}\text{Ge}(p, \gamma)^{65}\text{As}$ reaction, but by its Q-value, and by the rate of $^{65}\text{As}(p, \gamma)^{66}\text{Se}$ reaction.

- $^{57}\text{Cu}(p, \gamma)^{58}\text{Zn}$

Similarly to the previous case, the reaction can lead to the breakout from doubly-magic WP-nucleus ^{56}Ni via sequential proton capture ^[13]. Early network calculations assumed that the rp-process stops at ^{56}Ni due to its low proton capture Q-value of 695 keV and comparatively long β -decay lifetime ($\tau = 2.3 \times 10^4$ s). However, later calculations ^[4, 14] employing larger networks show that the rp-process may process well beyond ^{56}Ni region. Influence of this reaction rate on the final chemical yields, nuclear energy generation rates and on the XBR light curves is also discussed in the recent state-of-the-art sensitivity studies ^[3, 9]

In the experiment, proton unbound states of ^{66}Se and ^{58}Zn will be populated by neutron removal reactions from ^{67}Se and ^{59}Zn beams, respectively, incident on the Be target at an energy 250 MeV/u. Proton decay spectroscopy of these states will be performed in-flight using the SAMURAI setup as explained in section 3.

2.2 Resonant reaction rates around WP-nucleus ^{34}Ar

- $^{34}\text{Ar}(p, \gamma)^{35}\text{K}$

Together with ^{30}S , the WP-nucleus ^{34}Ar was theoretically linked to the phenomenon of the multiple-peaked structure observed in some X-ray bursts ^[15]. Since the rates near the proton drip line can be significantly affected by isolated resonances ^[16], the identification of these states are important together with the determination of resonance energies (E_R) and strengths ($\omega\gamma$), which are the only nuclear physics inputs into the resonant part of thermonuclear reaction rate. There is no experimental information on the resonance strengths, only shell model calculations are available to evaluate this reaction rate.

- $^{35}\text{Ar}(p, \gamma)^{36}\text{K}$

When varied by a factor greater than 3, the reaction rate was found to significantly affect the calculated nuclear energy generation rate in the theoretical models ^[17]. The dramatic impact of $^{35}\text{Ar}(p, \gamma)^{36}\text{K}$ rate on XRB light curves had also been previously demonstrated by Thielemann ^[18]. Resonance strengths are not measured for this reaction yet.

- $^{35}\text{K}(p, \gamma)^{36}\text{Ca}$

The reaction rate was identified by Amthor ^[19] as one of the 12 proton capture rates with an impact on predicted light curves. This rate was also found to affect predicted nuclear energy generation rates in the study of ^[17]. Presently, only the energy of one excited state is known in ^{36}Ca ^[20], and this state with tentative spin-parity assignment is the sole input considered in rate evaluations to date. so far.

The above three reactions will be studied via coulomb dissociation of ^{35}K , ^{36}K and ^{36}Ca beams inside lead target at 200 MeV/u beam energy. One- and two-proton decays in-flight of these nuclei will be measured to extract energies and strengths of the resonances relevant to the rp-process.

2.3 Direct proton capture reaction rates $^{27}\text{P}(p, \gamma)^{28}\text{S}$ and $^{31}\text{Cl}(p, \gamma)^{32}\text{Ar}$

These reactions are predicted to be among 10 most important reaction ^[19] with the strong influence on the calculated XRB light curves. Both reactions rates are expected to be dominated by a direct proton capture, because no excited states at astrophysically relevant energies are known for ^{32}Ar and ^{28}S . Coulomb dissociation cross section of time-reversal processes $^{32}\text{Ar} \rightarrow ^{31}\text{Cl} + p$ and $^{28}\text{S} \rightarrow ^{27}\text{P} + p$ will be measured with lead target and 250 MeV/u beam energies to extract direct-capture components of the reaction rates. Complementary measurements of proton-removal reactions in the nuclear field (e. g. using ^{12}C target) will be additionally performed to extract Asymptotic Normalization Coefficients, which can be directly related to the direct-capture cross section. Combining the information from the both type of measurements would help to constrain the model uncertainties and to determine the reaction rates with higher accuracy

2.4 Direct proton capture reaction rate $^8\text{B}(p, \gamma)^9\text{C}$

The current knowledge of the rate of the $^8\text{B}(p, \gamma)^9\text{C}$ reaction in stellar conditions is contradictory at the best and there is no hope to determine it by other means than by indirect methods. This reaction gives a possible path to the hot pp chain pp-IV at high temperatures and away from it toward a rapid alpha process *rap* I at high temperatures and densities and therefore is important in understanding nucleosynthesis in super-massive hot stars in the early universe, including possible bypasses of the 3α -process ^[21]. Similar to the method described in subsection 2.3, breakup in nuclear and Coulomb fields at a beam energy of 300 MeV/u will be employed to estimate the direct-capture reaction rate.

3 Experimental apparatus

3.1 SAMURAI setup

An overview of the intended experimental setup is shown in Fig.1. Radioactive secondary beams will be produced by the fragmentation of primary stable beams (e. g. ^{78}Kr , ^{40}Ca or ^{16}O) at a few hundreds MeV/u energy in beryllium target and separated by BigRIPS fragment separator ^[11]. The particle identification of the beam will be then performed event-by-event using the $B\rho$ - ΔE -ToF method. A secondary reaction target will be placed at the target position of the Superconducting Analyzer for MUlti-particles from RAdioIsotope Beams (SAMURAI) ^[22] and the incident beam will be focused on the target via superconducting quadrupole magnet STQ. Incident secondary beams will be measured in the tracking systems before the target with two scintillating detectors, SBT1 and SBT2, for time-of-flight measurements. The position of hit on the target and incoming angle of the secondary beams will be measured by two drift chambers (BDC1,2) placed upstream of the target. An ionization chamber ICB will be used for charge identification of the incident ions. After traversing this pre-

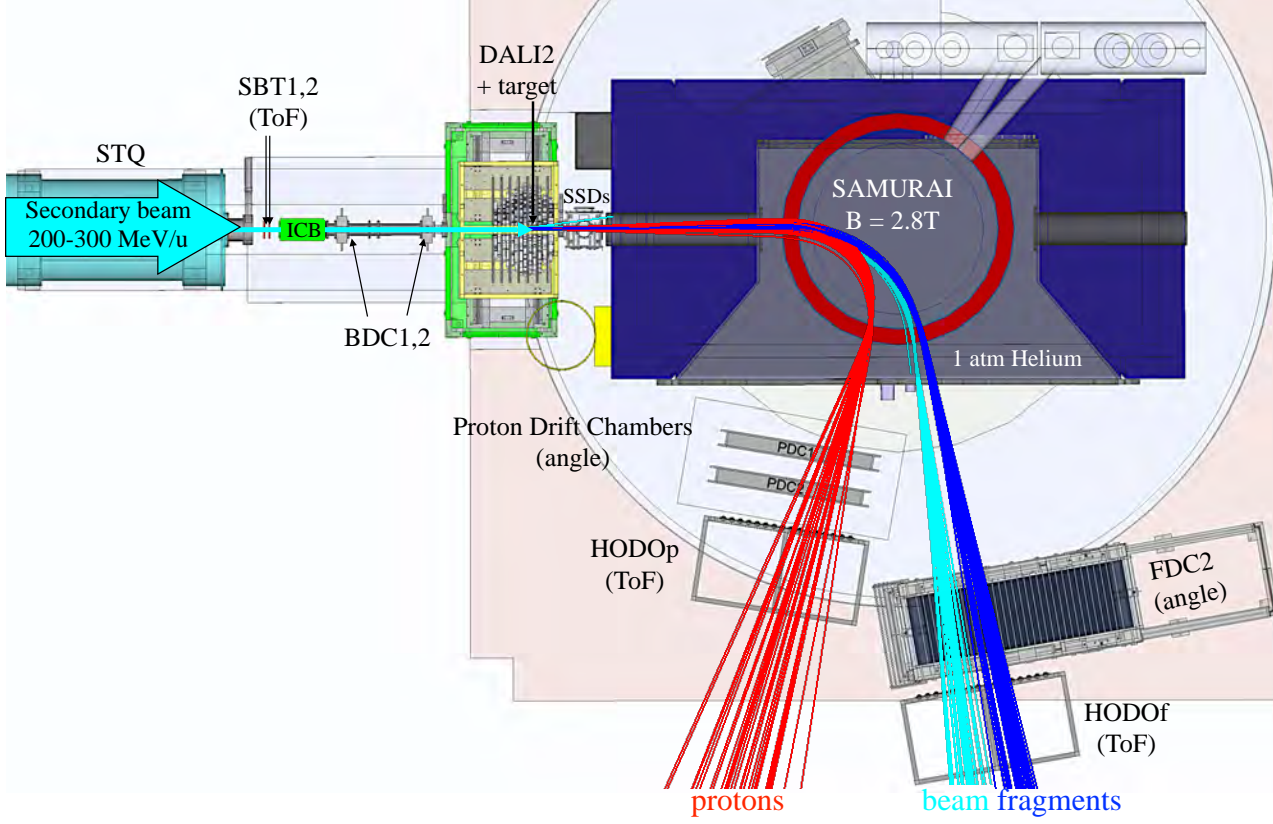


Fig. 1 High-Resolution (90°) mode of the SAMURAI setup will be used to measure heavy-ion-proton breakup reactions. Shown particle trajectories were simulated with Geant4 for the case of $^{28}\text{S} \rightarrow ^{27}\text{P} + p$ breakup. See text for more details.

target section the beam is incident on the reaction target (beryllium, carbon or lead) inside the DALI2 γ -ray detector that will measure gamma-rays in coincidence with charged fragments. Directly after the target an array of Silicon Strip Detectors (SSDs) will be used to measure trajectories of outgoing protons and fragments. Due to the wide dynamic range of these detectors ($\sim 10^4$), simultaneous detection and tracking of a proton and a heavy ion is possible. The SSDs will provide vital information about relative angles between the fragment and the proton with a resolution of a few mrad, which determines to a large extent the invariant mass reconstruction and the corresponding relative energy resolution. Next, the SAMURAI spectrometer, rotated 90 degrees with respect to the beam (High-Resolution mode) will separate the unreacted beam, breakup fragments and protons. The magnetic field will be set at around 2.8 Tesla in the center of the spectrometer filled with helium gas at 1 atmosphere pressure. After the magnet, the protons are tracked by the two proton drift chambers, PDC1 and PDC2. The heavy fragments and the unreacted beam are measured in a separate drift chamber, FDC2. The time of flight and ΔE of the decay products are measured in two hodoscopes, labeled HODP and HODF, for the protons and the heavy fragments, respectively. Hence, identification and momentum measurement of every traversing particle will be performed and the invariant-mass analysis of the reaction products will be applied to reconstruct the decay energy of the initial system.

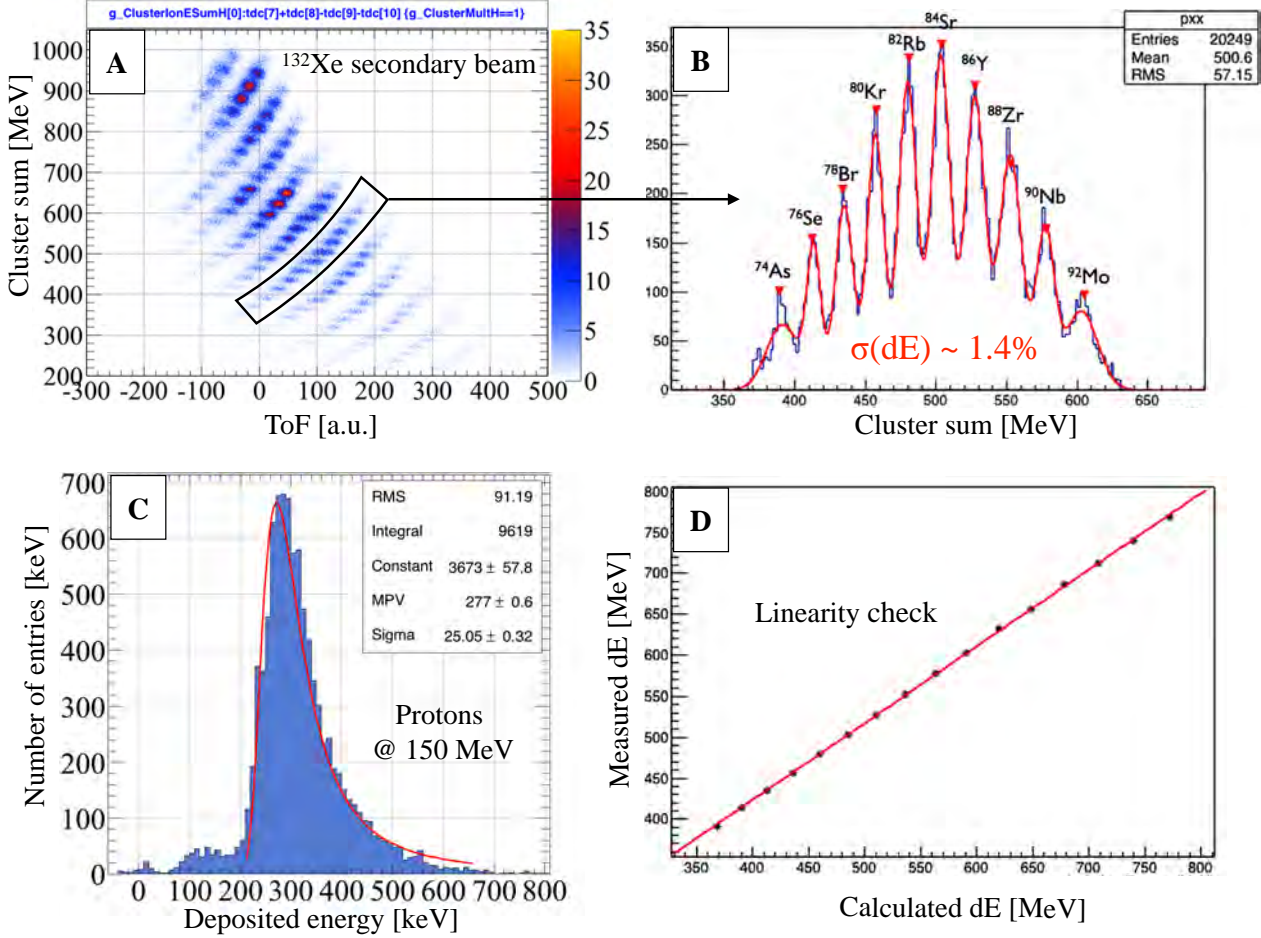


Fig. 2 Results of the performance test of the SSDs. Figure A shows the particle identification of ^{132}Xe secondary beam, using the deposited energy (strip-cluster sum) measured by low-gain readout of the SSD as a function of the ToF. Figure B shows the energy response in the SSD with the graphical cut indicated in Figure A, while Figure D displays the linearity check for this energy range by plotting measured energies against the calculated ones. A signal from 150 MeV proton in high-gain readout of the same SSD is shown in Figure C together with the Landau function fit.

3.2 Silicon Strip Detectors

An essential component of the setup will be an array of GLAST-type ^[23] single-sided Silicon Strip Detectors (SSDs) situated downstream of the target. Each detector is $325 \mu\text{m}$ thick and has dimensions of $87.6 \times 87.6 \text{ cm}^2$ with $864 \mu\text{m}$ readout pitch size. Outgoing protons and heavy residues will be measured in the SSDs in order to reconstruct their relative angles with the precision of a few mrad. A key feature of the detectors is their wide dynamic range, which allows for simultaneous detection of protons and heavy ions, depositing in a single SSD a few hundred keV and up to 1 GeV energy, respectively. This is achieved via custom-designed ASIC dual-gain preamplifiers coupled to the high-density processing circuit HINP ^[24].

A performance test of the SSDs was conducted at the HIMAC facility in Japan, using irradiation of the detectors by proton beams at different energies (from 150 to 230 MeV/u) as well as by heavy-ion beams at a few hundred MeV/u in order to confirm the designed dynamic range. The results of the performance test are summarized in Fig.2. Good linearity of the low-gain readout was observed together with the deposited-energy (dE) resolution of $\sim 1.4\%$. The performance of the high-gain readout with respect to proton beams

was also confirmed, yielding a proton-detection efficiency of $>97\%$ and the cross-talk ratio of $\sim 1\%$. Thus, it was confirmed that the dynamic range of the SSDs spans from $\sim 100\text{keV}$ up to $\sim 1\text{ GeV}$, which would allow simultaneous detection of protons and $Z \approx 50$ heavy ions in SAMURAI experiments.

3.3 Parameters of the experimental setup

Based on detailed Geant4 simulations of the particle transmission through the magnetic field of the SAMURAI spectrometer, and taking into account realistic detector responses, the following parameters of the setup can be estimated:

- Momentum resolutions: $P/\sigma_P \approx 1300$ for heavy ions and $P/\sigma_P \approx 500$ for protons;
- Angular resolutions: $\sim 3\text{ mrad}$ for protons and $\sim 2\text{ mrad}$ for heavy ions;
- Total detection efficiency: $\sim 100\%$ for heavy ions and $\sim 20\%$ for protons at relative energy $E_{rel}=1\text{ MeV}$;
- E_{rel} resolution $\sim 100\text{ keV}$ (sigma) at $E_{rel}=1\text{ MeV}$.

4 Summary and Outlook

The future experimental setup using SAMURAI spectrometer will serve as a powerful tool for systematic experimental studies of the most important (p, γ) reactions in the region of the astrophysical interest, using inverse and complete kinematics measurements of the heavy-ion-proton breakup reactions at relativistic energies. With the combination of the SAMURAI tracking detectors and the newly designed SSD trackers, possessing an extremely wide dynamic range, several neutron-deficient nuclei up to ^{100}Sn region can be potentially studied. The first experimental campaign will be ready to run in 2016, focusing on the proton decay of such exotic species as ^{66}Se , ^{58}Zn , ^{35}K , ^{36}K , ^{36}Ca , ^{28}S , ^{32}Ar and ^9C .

References

- [1] W. H. G. Lewin, J. van Paradijs, and R. E. Taam, *Space Science Rev.*, 1993, **62**:223.
- [2] S. E. Woosley and R. E. Taam, *Nature*, 1976 **263**:101.
- [3] A. Parikh, J. Jose, G. Sala, and C. Iliadis, *Prog. Part. Nucl. Phys.*, 2013, **69**:225.
- [4] H. Schatz et al, *Phys. Rep.*, 1998, **294**:167.
- [5] H. Schatz et al., *Phys. Rev. Lett.*, 2001, **86**:3471.
- [6] O. Koike et al., *Astrophys. Jour.*, 2004, **603**:242.
- [7] W. H. G. Lewin et al., *Cambridge Univ. Press*, 1995, p. 175.
- [8] A. Parikh et al., *Phys. Rev. C*, 2009, **79**:045802.
- [9] A. Parikh et al., *New Astron. Rev.*, 2008, **52**:409.
- [10] H. Schatz, *Int. Symp. Nucl. Astrophys., Nuclei in the Cosmos IX*, 2006.
- [11] <http://www.nishina.riken.jp/RIBF/>
- [12] J. Görres, M. Wiescher, and F.-K. Thielemann, *Phys. Rev. C*, 1995, **51**:392.
- [13] O. Forstner, H. Herndl, H. Oberhummer, H. Schatz, and B. A. Brown, *Phys. Rev. C*, 2001, **64**:045801.

- [14] L. van Wormer, J. Gorres, C. Iliadis, M. Wiescher, and F.-K. Thielemann, *Astrophys. Jour.*, 1994, **432**:326.
- [15] J. L. Fisker et al. *Astr. J.*, 2004 **608**:L61.
- [16] H. Schatz et al. *Nucl. Phys. A*, 1999, **654**:924c.
- [17] A. Parikh et al. *Astr. J. Suppl.*, 2008, **178**:110.
- [18] F. K. Thielemann et al. *Prog. Part. Nucl. Phys.*, 2001, **46**:5.
- [19] A. M. Amthor. PhD thesis, Michigan State University, 2008.
- [20] A. Bürger et al. *Phys. Rev. C*, 2012, **86**:064609.
- [21] M. Wiescher et al., *Astrophys. Jour.*, 1989, **343**:352
- [22] T. Kobayashi et al., *Nucl. Instr. Meth. Phys. Res.*, 2013 **B317**:294
- [23] R. Bellazzini, *Nucl. Instr. Meth. Phys. Res.*, 2003 **A512**:136.
- [24] G. L. Engel, *Nucl. Instr. Meth. Phys. Res.*, 2007, **A573**:418.

Beta-decay of ^{31}Cl : an indirect probe of the $^{30}\text{P}(\text{p}, \gamma)^{31}\text{S}$ reaction. Present status and future perspectives^{*}

Antti Saastamoinen^{1,a}, Anu Kankainen^{2,b}, and Livius Trache³

¹ Cyclotron Institute, Texas A&M University, College Station, TX, 77843-3366, USA

² University of Edinburgh, Edinburgh EH9 3JZ, UK

³ National Institute for Physics and Nuclear Engineering, P.O.Box MG-6, Bucharest-Magurele, Romania

Received: 6 June 2015 / Revised: 7 June 2016

Published online: 11 August 2016 – © Società Italiana di Fisica / Springer-Verlag 2016

Abstract. β -decay of ^{31}Cl can be used as a selective tool for studying astrophysically relevant states in ^{31}S . In this article we review the present status of the decay data. The implications for the $^{30}\text{P}(\text{p}, \gamma)^{31}\text{S}$ reaction rate at novae temperatures, and future experimental ideas are discussed.

1 Introduction

Novae explosions are frequent and bright phenomena resulting from a binary system where a white dwarf accretes hydrogen-rich material from its companion star [1]. Observations from optical, ultraviolet and infrared spectra have given evidence that novae produce enhanced amounts of carbon, nitrogen and oxygen with respect to solar abundances. Heavier so-called ONe novae have shown an enhancement in the abundances of heavier elements. In ONe novae, the $^{30}\text{P}(\text{p}, \gamma)^{31}\text{S}$ is a bottle-neck reaction, affecting the production of heavier elements. If the reaction is not fast enough, the beta-decay of ^{30}P ($T_{1/2} = 2.498(4)$ min [2]) takes over and proton capture fails to produce heavier elements.

At typical nova peak temperatures of about 0.2–0.4 GK, the proton capture reaction $^{30}\text{P}(\text{p}, \gamma)^{31}\text{S}$ proceeds mostly via resonant capture through narrow and isolated resonances. For such reactions, and in the absence of interference, the reaction rate may be written

$$N_a \langle \sigma v \rangle = 1.5399 \cdot 10^{11} (\mu T_9)^{-3/2} \times \sum_i (\omega \gamma)_i e^{(-11.605 E_i / T_9)}, \quad (1)$$

in units of $\text{cm}^3 \text{mol}^{-1} \text{s}^{-1}$, where μ is the reduced mass of the colliding nuclei in atomic mass units, T_9 the temperature in GK, and E_i and $\omega \gamma_i$ are the center-of-mass energy and the resonance strength of the i -th resonance in MeV, respectively [3, 4]. Due to the exponential nature of the energy dependence, it is crucial to determine the resonance energies to a reasonably good precision: Uncertainty of few keV is usually enough. However, sometimes better resolution is needed to distinguish densely packed states. In addition, proper identification of the spins and parities, as well as the proton and γ -widths of the states affects the rate directly via the resonance strength $(\omega \gamma)_i$. Typically for low resonance energies when $\Gamma_p \ll \Gamma_\gamma$, the resonance strength depends only on the proton width, *i.e.* $\omega \gamma \approx \omega \Gamma_p$.

Given the short half-life of ^{30}P no such targets can be manufactured. So far direct experimental studies of the reaction have not been possible due to low intensities of available ^{30}P radioactive ion beams. On the other hand, ^{31}Cl has a high β -decay Q value ($Q_{EC} = 11976(50)$ keV [5]), allowing it to populate states above the proton separation energy in ^{31}S ($S_p = 6130.9(4)$ keV [5]).

Nuclear β -decay is a very selective process: allowed decays populate only states where the spin changes maximum by one unit, and the parity remains unchanged. If the spin changes by more than one unit, or the parity changes, the decays are strongly suppressed (forbidden decays). Thus β -decay of ^{31}Cl ($J_{g.s.}^\pi = \frac{3}{2}^+$) populates levels in ^{31}S that most likely have $J^\pi = \frac{1}{2}^+$, $\frac{3}{2}^+$, or $\frac{5}{2}^+$.

^{*} Contribution to the Focus Point on “Evaluation of the ^{30}P proton capture reaction rate in classical novae” edited by C. Wrede.

^a e-mail: ajsaasta@comp.tamu.edu

^b *Present address:* Department of Physics, P.O. Box 35 (YFL), FI-40014 University of Jyväskylä, Finland.

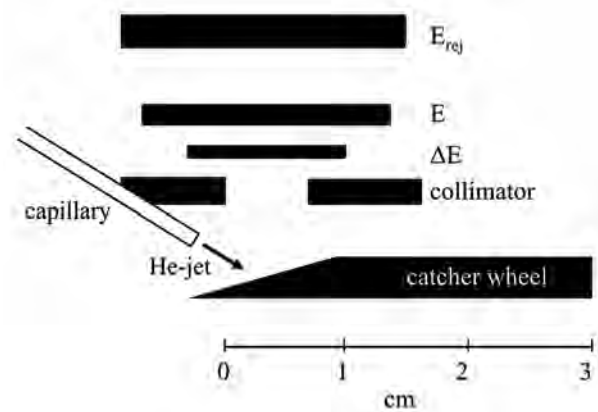


Fig. 1. The experimental setup at Berkeley, adapted from fig. 1 of ref. [8].

In the case of $^{30}\text{P}(p, \gamma)^{31}\text{S}$, the proton is captured by a ^{30}P nucleus with $J^\pi = 1^+$ and thus the s -wave ($l = 0$) captures will go to states with $J^\pi = \frac{1}{2}^+$ or $\frac{3}{2}^+$ which may be populated in the β -decay of ^{31}Cl . As mentioned earlier, allowed β -decay may also populate $J^\pi = \frac{5}{2}^+$ states, corresponding to d -wave ($l = 2$) capture.

In this article we review the known experimental data of β -decay of ^{31}Cl , concentrating on the states relevant for the $^{30}\text{P}(p, \gamma)^{31}\text{S}$ reaction: *i.e.* we focus on the existing data above $S_p(^{31}\text{S})$. Since the early 1980s, β -decay of ^{31}Cl has been studied with several different techniques. We group here the experiments by the sample production method used. Experimental setups for experiments where samples were produced with different ISOL (Isotope Separation On-Line) techniques are discussed in sect. 2, and with samples produced with in-flight technique in sect. 3. In sect. 4 we summarize the known β -decay data that are relevant for the $^{30}\text{P}(p, \gamma)^{31}\text{S}$ reaction rate evaluation presented elsewhere in this Focus Point.

2 Samples produced with ISOL techniques

2.1 Studies in Oslo

The first studies on the beta-decay of ^{31}Cl were performed at the MC-35 cyclotron of the University of Oslo in 1982 [6, 7]. The $^{31}\text{Cl}^+$ ions were produced using a 34 MeV proton beam impinging on a ZnS target and transported from the target region via He-jet technique. The ^{31}Cl beam was implanted on an aluminized mylar tape surrounded by a single $31.1\ \mu\text{m}$ thick surface-barrier detector and a detector telescope consisting of a $10.8\ \mu\text{m}$, $25\ \text{mm}^2$ ΔE and a $300\ \mu\text{m}$ E , $100\ \text{mm}^2$ E detector. The two most intense beta-delayed proton groups of ^{31}Cl at 989(10) and 1528(20) keV were observed and a half-life of 150_{-20}^{+25} ms determined based on those groups.

2.2 Studies in Berkeley

The next beta-decay studies on ^{31}Cl were performed at the Lawrence Berkeley Laboratory 88 inch Cyclotron [8] with a 45 MeV proton beam on a ZnS target. The reaction products were swept away from the target region using the He-jet technique and implanted on a rotating wheel in front of a ΔE ($8.3\ \mu\text{m}$, $50\ \text{mm}^2$) - E ($68\ \mu\text{m}$, $100\ \text{mm}^2$) - E_{rej} ($20\ \mu\text{m}$, $300\ \text{mm}^2$) setup as illustrated in fig. 1. The E_{rej} detector was used to reject the events due to positrons but also to detect higher-energy protons. An overall resolution for protons of 75 keV was achieved with this setup. Altogether eight proton peaks in the energy range of 845 to 2204 keV were observed [8]. ^{31}Cl was restudied at Lawrence Berkeley in the 1990s using two gas ΔE (CF_4 , $30\ \mu\text{g}/\text{cm}^2$) - gas ΔE (CF_4 , $30\ \mu\text{g}/\text{cm}^2$) - E (Si $300\ \mu\text{m}$, $380\ \text{mm}^2$) detectors. However, this latter experiment suffered from contamination by beta-delayed protons of ^{25}Si resulting from the aluminum backing discs of the ZnS target. As a result, only the two strongest proton peaks of [8] were confirmed although the total proton beam charge was 220 mC [9] compared to 90 mC in the previous Berkeley experiment [8] and 15 mC at the Oslo MC-35 cyclotron [7].

2.3 Studies in Jyväskylä

In 2004, the first experiment on ^{31}Cl employing a mass-separator was performed at the IGISOL3 (Ion Guide Isotope Separator On Line) facility [10] at the Accelerator Laboratory of the University of Jyväskylä (JYFL). There, 40 and 45 MeV proton beams impinging on a thin ZnS target at the entrance of the ion guide cell were employed. The reaction

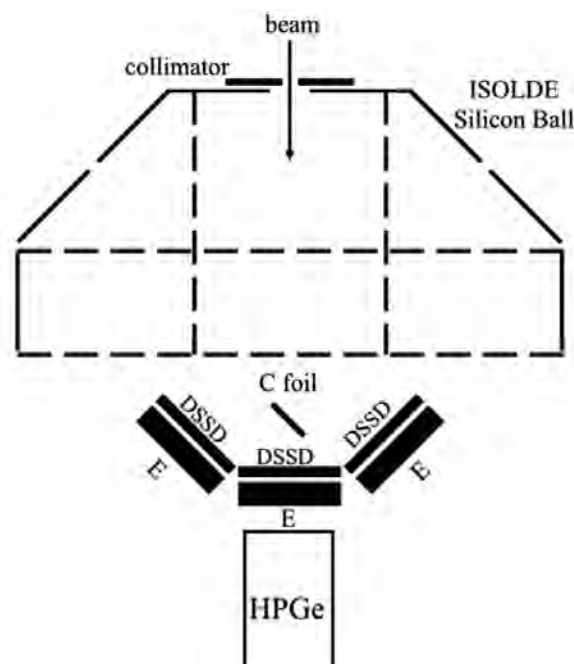


Fig. 2. An illustration of the experimental setup for the beta-decay of ^{31}Cl at IGISOL. Not in scale, adapted from fig. 2 of ref. [11].

products were stopped and thermalized in the helium gas of the ion guide ($p = 200$ mbar) and extracted from the gas cell through use of a differential pumping system and application of an electric field. The ions were accelerated to $40q$ keV and further mass-separated with a 55° dipole magnet. As a result, a pure beam of $A/q = 31$ reaction products was delivered to the spectroscopy setup. This was an advantage since the previous experiments had to collect data also at lower energy below the ^{31}Cl production threshold in order to distinguish the proton peaks belonging to other reaction products, such as ^{32}Cl . The yield of ^{31}Cl at IGISOL was about around 14 ions/s which was about 1000 times less than the yield of ^{31}S [11].

New double-sided silicon strip detectors (DSSDs), offering much better energy resolution and reduced summing of the events due to pixelated readout structure, became available in the beginning of the millennium [12, 13]. At IGISOL, the $^{31}\text{Cl}^+$ beam was implanted into a $30 \mu\text{g}/\text{cm}^2$ thick carbon foil surrounded by three DSSDs and the ISOLDE Silicon Ball detector [14]. The DSSDs were about $60 \mu\text{m}$ thick and had sixteen 50 mm long and 3 mm wide front strips and similar but orthogonal back strips. One of the DSSDs was a Micron Semiconductor Ltd. (MSL) W1 detector with a dead layer of 600 nm [12] and two others were of a newer design with a dead layer of 100 nm [13]. Each DSSD was backed with a thick silicon detector in order to detect positrons and higher energy protons. A hemisphere of the ISOLDE Silicon Ball detector [14] consisting of 144 individual $25.5 \times 25.5 \text{ mm}^2$ Si detectors was useful for covering a larger solid angle for detecting beta particles. For the first time in these types of experiment, a HPGe detector (70%) was used to detect beta-delayed gamma-rays from ^{31}Cl . The detector setup of the experiment is shown in fig. 2.

The peaks observed in ref. [8] were confirmed together with 5 new peaks. The experiment suffered from electronic noise at lower energies, as well as strong isobaric background, from ^{31}S , and no proton peaks below 700 keV could be distinguished. Some of the observed proton peaks were uncertain. Total of four γ -lines were attributed to ^{31}Cl decay. One of the lines, at 4045(2) keV, was deduced to originate from the isobaric analogue state (IAS) at 6280(2) keV.

3 Samples produced with an in-flight technique

3.1 Studies in Texas A&M

In a series of experiments at Texas A&M University (TAMU) [15–17], a ^{31}Cl beam was produced by bombarding a $2.5 \text{ mg}/\text{cm}^2$ thick liquid-nitrogen-cooled H_2 target at 1.6 atm pressure with a ^{32}S beam at 40 MeV/u. The reaction products from inverse-kinematics reaction $^1\text{H}(^{32}\text{S}, ^{31}\text{Cl})2\text{n}$ were separated with the Momentum Achromat Recoil Spectrometer (MARS) [18]. The production method and the energy used allowed, for the first time, the separation of ^{31}Cl from its isobars. The resulting ^{31}Cl beam had intensity of 3000 pps at 90% purity, the major impurity stopped in the

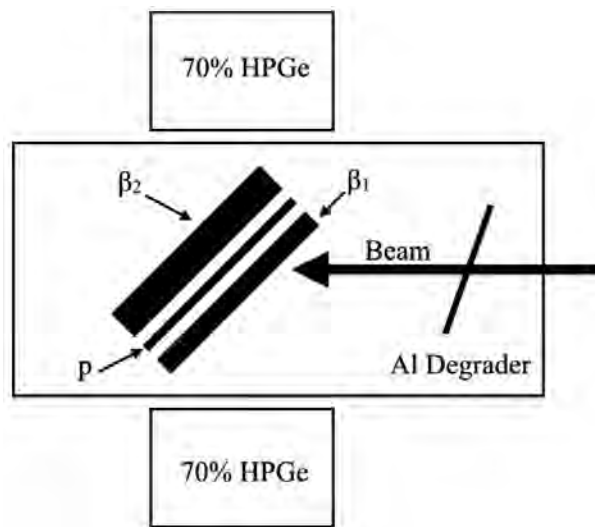


Fig. 3. A schematic presentation of the experimental setup at Texas A&M, not to scale. Label “p” refers to a DSSSD used, “ β_1 ” to Si detector added for the second experiment, and “ β_2 ” for a thick Si-pad detector. In the first experiment, only one HPGe was used. See text for more details.

setup being ^{29}S . During the implantation into the setup the beam momentum spread was restricted to $\Delta p/p = 0.25\%$ and the rate to about 800 pps.

In the first of the experiments, the produced ^{31}Cl ions were implanted into a detector setup consisting of a $65\text{ }\mu\text{m}$ thick MSL W1 type DSSSD with $16 + 16\text{ } 3.1 \times 50\text{ mm}^2$ strips (labeled “p” in fig. 3), a 1 mm thick Si-pad detector ($50 \times 50\text{ mm}^2$, “ β_2 ” in fig. 3), and a 70% HPGe detector facing the front side of the Si detector stack [15, 16]. In the second experiment, the DSSSD was changed to a $45\text{ }\mu\text{m}$ thick MSL BB2 type detector with $24 + 24\text{ } 1 \times 24\text{ mm}^2$ strips, an additional $300\text{ }\mu\text{m}$ thick Si $50 \times 50\text{ mm}^2$ detector was added before the DSSSD “ β_1 ” in fig. 3, and another 70% HPGe detector was added on the opposite side [17, 19]. During the second experiment, data were taken also in a configuration consisting of only the two HPGe detectors and the thick Si detector, while the other Si detectors (β_1 , p) were replaced by an $125\text{ }\mu\text{m}$ thick Al plate. This configuration allowed maximum beam to be used for higher statistics of β - γ - γ coincidences. In addition, to measure a more precise half-life, the standard tape transport - gas counter setup for high-precision β -decay half-life measurements was used. See, *e.g.*, ref. [20] and references therein for a detailed description of the half-life setup.

The TAMU experiments [15–17] confirmed the results of the JYFL experiment [11] for the proton spectrum up to about 2 MeV, while suffering from ^{29}S impurities and the fact that the higher-energy protons escaped the implantation detector. In addition to proton data, an extensive set of γ -lines was collected. The results include first direct measurement of the IAS through direct four different decay paths, including coincident cascades through the excited states. The comparison of the datasets is discussed further in sect. 4.

3.2 Studies at the NSCL

Very recently, β -decay of ^{31}Cl has been studied at the National Superconducting Cyclotron Laboratory (NSCL) by using coupled K500 and K1200 cyclotrons and the A1900 separator to produce an about 88% pure beam of ^{31}Cl with intensity of more than 6000 pps. In this experiment, 50 MeV/u ^{31}Cl ions were implanted into a plastic scintillator, surrounded by an array of Yale Clovershare “Clover” type HPGe detectors. At the time of writing this contribution, the resulting $\beta\gamma(\gamma)$ -coincidence data are under analysis [21, 22].

4 Summary of the ^{31}Cl β -decay data above $S_p(^{31}\text{S})$

The proton spectra of the experiments in JYFL and in TAMU are compared in fig. 4. It is worth noting that in the JYFL experiment the ^{31}Cl source was implanted into a C foil, whereas the TAMU spectrum has been collected by implanting the ^{31}Cl ions inside the detector. The latter method thus measures not only the proton energy, but also the energy of the recoiling proton daughter and the preceding β -particle. The TAMU spectrum has several peaks from ^{29}S contamination. The JYFL data have large backgrounds from the whole $A = 31$ isobar present in the beam (mainly ^{31}S). The extracted proton energies of both the aforementioned experiments, along with all other known data are given in table 1. All the known experimental proton energies agree within the uncertainties of each experiment.

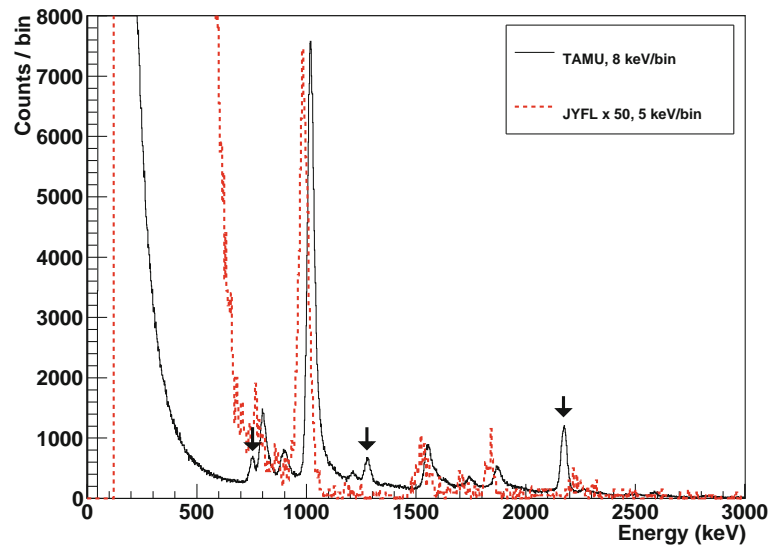


Fig. 4. A comparison between the proton spectra of the experiments in JYFL (red, dashed) and in TAMU (black, solid). The JYFL data has been multiplied by factor of 50 to match the statistics of the 996 keV proton line in TAMU spectrum. The arrows point out ^{29}S contamination in the TAMU data. Note that in the JYFL experiment the ^{31}Cl source was implanted into a C foil, whereas the TAMU spectrum was collected by implanting the ^{31}Cl ions inside the detector, measuring the total decay energy. See text for details.

Table 1. A comparison of known proton energies from ^{31}Cl decay. All energies are given as E_{lab} in keV. The average value is the weighted average of all the works presented in this table. The corresponding level energy is determined by assuming decay to the ground state of ^{30}P and using the calculated average proton energy with $S_p(^{31}\text{S}) = 6130.9(4)$ keV [5].

Refs. [6, 7]	Ref. [8]	Ref. [9]	Ref. [11]	Ref. [17]	Average	E_{lev}
			762(14)	780(2)	780(2)	6936(2)
	845(30)		853(18)	877(2)	876(2)	7036(2)
989(15)	986(10)	986(10)	978(15)	993(2)	993(2)	7157(2)
	1173(30)		1175(19)	1185(3)	1185(3)	7355(3)
				1345(17)	1345(17)	7521(17)
1528(20)	1520(15)	1524(10)	1521(20)	1520(3)	1521(3)	7702(3)
				1594(17)	1594(17)	7778(17)
	1695(20)		1688(22)	1706(3)	1706(3)	7894(3)
	1827(20)		1825(23)	1830(3)	1830(3)	8022(3)
				1927(17)	1927(17)	8122(17)
	2113(30)		2075(30)	2070(17)	2079(13)	8279(13)
	2204(30)		2217(30)	2224(3)	2224(3)	8429(3)
			2299(30)	2286(17)	2289(15)	8496(15)
			2454(40)	2489(17)	2484(16)	8697(16)
			2601(40)	2641(17)	2635(16)	8854(16)
			2751(40)	2807(17)	2799(16)	9023(16)

Table 1 gives these proton energies as ^{31}S excitation energies, assuming that the proton decays populate the ground state of ^{30}P . It is worth noting that there is some evidence for some of these decays populating excited states in ^{30}P as shown in ref. [17]. However, so far known levels populated by β -delayed proton emission from ^{31}Cl are too high in energy to yield information about the states inside the Gamow window of $^{30}\text{P}(p, \gamma)^{31}\text{S}$ in typical novae temperatures as illustrated in the partial decay scheme in fig. 5.

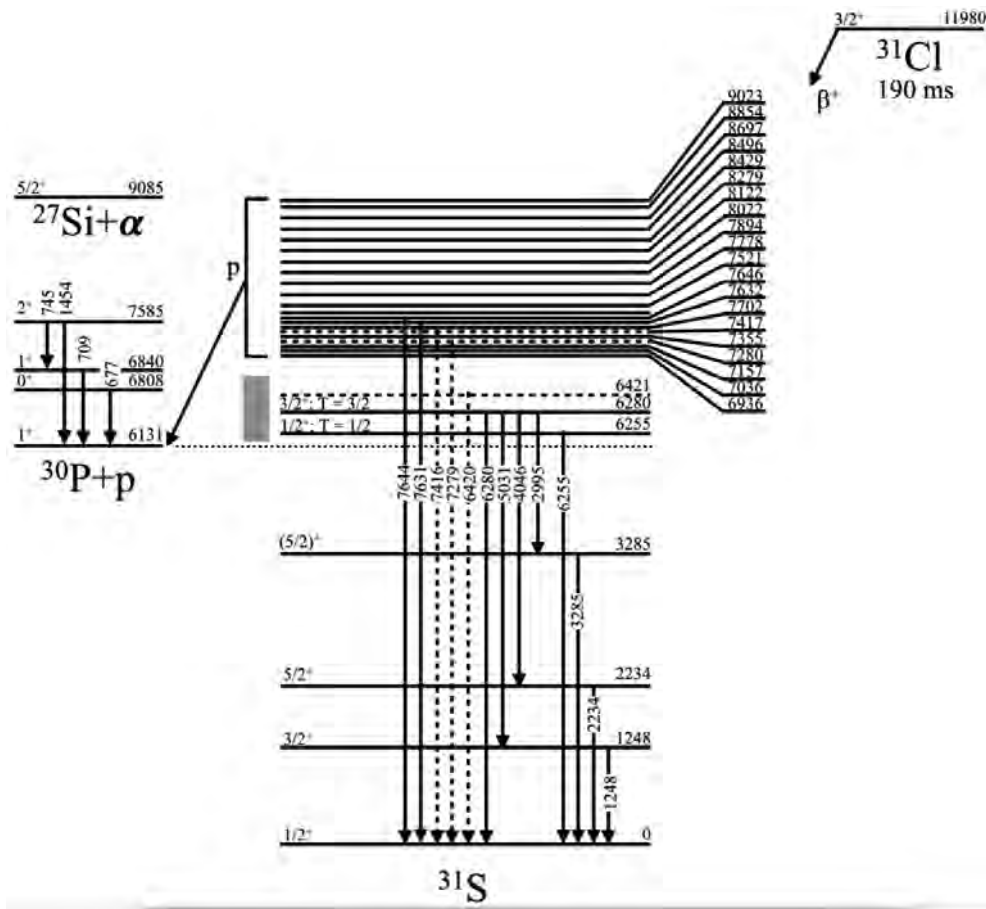


Fig. 5. Partial and simplified decay scheme of ^{31}Cl illustrating levels above $S_p(^{31}\text{S})$. See tables 1 and 2 for more detailed energies. The definitive spin-parities are from ref. [23]. Most of the proton unbound levels have $J^\pi = (1/2, 3/2, 5/2)^+$. The dashed lines and γ -transitions are tentative assignments of ref. [17] without known literature counterpart. The gray band denotes the Gamow window at typical novae temperatures (0.2–0.4 GK).

The presently known β -delayed γ -data have more information to offer about states inside the Gamow window. Table 2 lists the known β -delayed γ -lines beyond the proton threshold, with comparison to other known states that can be populated in β -decay. In the JYFL data, ref. [11], one γ -line was assumed to originate from beyond the proton threshold: the 4045(2) keV was deduced to be transition from the IAS to the 2234 keV second excited state in ^{31}S , and thus a level energy of 6280(2) keV was deduced. However, no coincidence data were collected. The TAMU dataset, refs. [15–17], has a direct transition from the IAS, along with three transitions that are in coincidence with γ -lines from the lower levels. One direct transition corresponding to a previously known level at 6259 keV was measured with improved precision. In addition, two transitions without previously known matching levels at 6420 and 7280 keV were observed and tentatively assigned to corresponding levels. Two high-energy γ -lines matching previously known 7600(30) and 7660(30) keV levels were observed and tentatively assigned to originate from these levels. None of these four transitions could be attributed to originate from any other species in the beam cocktail, nor escape or sum peaks. Their nature needs to be confirmed with an independent measurement. In the TAMU dataset, there is a γ -line at 6389.7(11) keV, but this overlaps with an escape peak of a higher-energy γ -ray.

An increase in the number of counts at 5030 and 6420 keV was also seen in the JYFL data set, although statistics was not enough to assign them as peaks. In addition, peaks at around 7630 and 7640 keV were observed at IGISOL as seen in fig. 6. Since they were located at the very end of the gamma-ray energy spectrum, they were treated as possible overflow peaks and not taken into account in the data analysis. However, also a peak located at the position of the first escape peak at around 7130 keV is seen in the JYFL data set supporting that the peaks at around 7630 keV are real. This is supported also by the fact that there are no known γ -rays at these energies originating from any nuclei at $A = 31$, $A = 62$, or $A = 15, 16$ regions.

Table 2. The γ -transitions from ^{31}Cl decay above $S_p(^{31}\text{S}) = 6130.9(4)$ keV [5]. The level energies are calculated from the observed E_γ by taking into account the energy of the recoiling nucleus. For comparison, known levels by other techniques from the literature. All energies are given in keV.

Ref. [11] $E_\gamma; E_{\text{final}}$	Ref. [17] $E_\gamma; E_{\text{final}}$	E_{level}	Literature $E_{\text{level}}; J^\pi$	Remarks
	6254.6(5); 0	6255.3(5)	6259(2); $\frac{1}{2}^+, T = \frac{1}{2}$	Refs. [24, 25]
	2995.6(2); 3284.8(3)	6280.2(3)	6281.2(14); $\frac{3}{2}^+, T = \frac{3}{2}$	Ref. [25]: Average of refs. [11, 25–28]
4045(2); 2235.6(4)	4046.2(2); 2234.3(2)			
	5031.5(3); 1247.6(3)			
	6279.5(3); 0			
	6420.0(6); 0	6420.7(6)		
	7279(1); 0	7280(1)		
	7415.8(9); 0	7416.8(9)		
	7630.8(6); 0	7631.8(6)	7600(30)	Ref. [26]
	7643.6(8); 0	7644.6(8)	7660(30)	Ref. [26], Ref. [25]: $7641(3), (\frac{5}{2} - \frac{13}{2})^-$

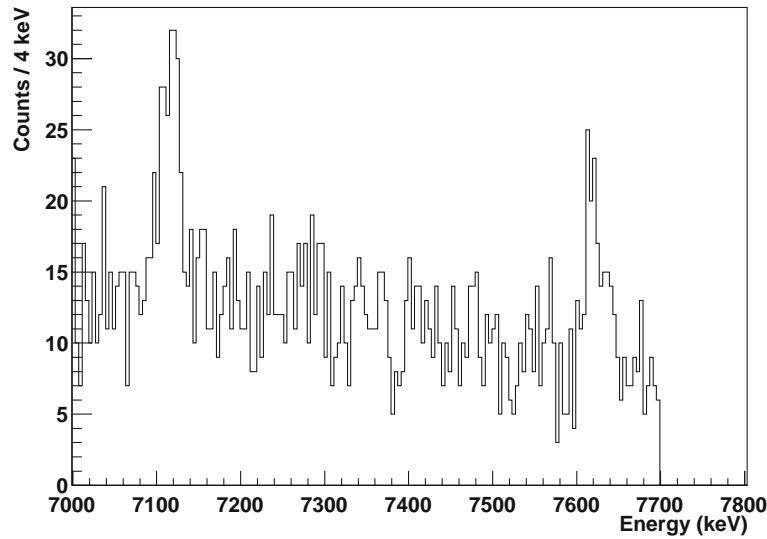


Fig. 6. Previously unpublished high-energy part of the γ -spectrum from the JYFL experiment. The double peak at around 7630 keV and matching line 511 keV below suggest this being a real transition rather than overflow. See text for more details.

5 Conclusions and future perspectives

The main contributions of the present β -decay data to the $^{30}\text{P}(p, \gamma)^{31}\text{S}$ rate at novae temperatures are the precise energies of the resonances at 6255.3(5) and 6280.2(3) keV. The latter of these has been observed in two independent β -decay studies [11, 17]. These energies are in reasonable agreement with the known energies from other known data as seen in table 2. There is a few keV discrepancy to some of the known reaction measurements in refs. [24, 25, 28, 29], but agreement within the uncertainties of ref. [27]. The tentative 6420.7(6) keV state of ref. [17] needs to be confirmed by other study. Some of the dataset of ref. [17] is still under analysis, and the very recent study of refs. [21, 22] may offer some new insights on some of the states above the proton threshold in ^{31}S . It is worth noting that the improved IAS energy yields a more precise prediction for the ^{31}Cl ground-state mass excess through the Isobaric Multiplet Mass Equation (IMME). The determined value of $-7056.8(3.3)$ keV agrees with the known value $-7070(50)$ keV [5] and reduces the uncertainties related to the $^{30}\text{S}(p, \gamma)^{31}\text{Cl}$ reaction.

It is clear that, so far, in-flight methods provide a cleaner source of ^{31}Cl than ISOL methods. However, if one can acquire high enough production of ^{31}Cl through ISOL methods, then it may be possible to utilize a Penning trap to produce a 100% clean source [30]. In addition, replacing the traditional catcher foil with a Paul trap [31] should allow mitigation against the deleterious features introduced by use of a catcher foil, thus making the dead-layer of used Si detectors the only limitation for the low energy. Such configurations would also allow the nature of the low-energy β -delayed particles to be distinguished, which in principle can be either protons or alphas.

The limitations of silicon detectors make measuring of β -delayed protons of astrophysical interest rather difficult, if not impossible. Even when implanting ions inside a Si detector, which allows the complications due to energy loss in dead layers or catcher material to be ignored, the low-energy region is usually dominated by a large background contribution from the betas originating from decay channels without protons, or even worse, from impurities. In some cases low-energy proton peaks can be extracted by using background subtraction [32]. However, recent advances using Micro-MESH-Gaseous-Structures (MicroMEGAS) based detectors are a promising new tool for measuring low-energy β -delayed particles essentially background free down to 100 keV or even lower [33]. Using such detector, in combination with efficient γ -detection capability, will offer access to the ^{31}Cl β -delayed protons of astrophysical interest.

References

1. J. Jose, M. Hernanz, J. Phys. G **34**, R431 (2007).
2. M.S. Basunia, Nucl. Data Sheets **111**, 2331 (2010).
3. C. Rolfs, W. Rodney, *Cauldrons in the Cosmos* (The University of Chicago Press, Chicago, USA, 1988).
4. C. Iliadis, *Nuclear Physics of Stars* (Wiley-VCH, Weinheim, 2007) ISBN: 978-3-527-40602-9.
5. M. Wang *et al.*, Chin. Phys. C **36**, 1603 (2012).
6. J. Äystö *et al.*, Phys. Lett. B **110**, 437 (1982).
7. J. Äystö *et al.*, Phys. Scr. **T5**, 193 (1983).
8. J. Äystö *et al.*, Phys. Rev. C **32**, 1700 (1985).
9. T. Ognibene *et al.*, Phys. Rev. C **54**, 1098 (1996).
10. P. Karvonen *et al.*, Nucl. Instrum. Methods Phys. Res. B **266**, 4454 (2008).
11. A. Kankainen *et al.*, Eur. Phys. J. A **27**, 67 (2006).
12. U.C. Bergmann, H.O.U. Fynbo, O. Tengblad, Nucl. Instrum. Methods Phys. Res. A **515**, 657 (2003).
13. O. Tengblad *et al.*, Nucl. Instrum. Methods Phys. Res. A **525**, 458 (2004).
14. L.M. Fraile, J. Äystö, Nucl. Instrum. Methods Phys. Res. A **513**, 287 (2003).
15. L. Trache *et al.*, PoS (NIC X), 163 (2008).
16. A. Saastamoinen *et al.*, AIP Conf. Proc. **1409**, 71 (2011).
17. A. Saastamoinen, PhD thesis, University of Jyväskylä (2011).
18. R. Tribble *et al.*, Nucl. Phys. A **701**, 278 (2002).
19. M. McCleskey *et al.*, Nucl. Instrum. Methods Phys. Res. A **700**, 124 (2013).
20. V.E. Iacob *et al.*, Phys. Rev. C **82**, 035502 (2010).
21. C. Wrede *et al.*, Phys. Proc. **66**, 532 (2015).
22. M. Bennett, C. Wrede, private communication.
23. C. Ouellet, B. Singh, Nucl. Data Sheets **114**, 209 (2013).
24. C. Wrede *et al.*, Phys. Rev. C **76**, 052802(R) (2007).
25. C. Wrede *et al.*, Phys. Rev. C **79**, 045803 (2009).
26. P. Endt, Nucl. Phys. A **633**, 1 (1998).
27. J. Vernotte *et al.*, Nucl. Phys. A **655**, 415 (1999).
28. Z. Ma *et al.*, Phys. Rev. C **76**, 015803 (2007).
29. A. Parikh *et al.*, Phys. Rev. C **83**, 045806 (2011).
30. T. Eronen *et al.*, Eur. Phys. J. A **48**, 46 (2012).
31. N. Scielzo *et al.*, Nucl. Instrum. Methods Phys. Res. A **681**, 94 (2012).
32. A. Saastamoinen *et al.*, Phys. Rev. C **83**, 045808 (2011).
33. E. Pollacco *et al.*, Nucl. Instrum. Methods Phys. Res. A **723**, 102 (2013).

Study of $^{16}\text{O}(^{12}\text{C},\alpha)^{20}\text{Ne}$ for the investigation of carbon-carbon fusion reaction via the Trojan Horse Method

This content has been downloaded from IOPscience. Please scroll down to see the full text.

2016 J. Phys.: Conf. Ser. 703 012024

(<http://iopscience.iop.org/1742-6596/703/1/012024>)

View [the table of contents for this issue](#), or go to the [journal homepage](#) for more

Download details:

IP Address: 194.102.58.6

This content was downloaded on 16/09/2016 at 13:02

Please note that [terms and conditions apply](#).

Study of $^{16}\text{O}(^{12}\text{C},\alpha^{20}\text{Ne})\alpha$ for the investigation of carbon-carbon fusion reaction via the Trojan Horse Method.

G.G. Rapisarda^{1,2}, C. Spitaleri^{1,2}, C. Bordeanu³, Z. Hons⁴, G.G. Kiss¹, M. La Cognata¹, J. Mrazek⁴, C. Nita³, D. Pantelica³, H. Petrascu³, R.G. Pizzone¹, S. Romano^{1,2}, T. Szücs⁵, L. Trache^{3,6}, A. Tumino^{1,7}, G. Velisa³.

¹ INFN Laboratori Nazionali del Sud, Catania, Italy

² Dipartimento di Fisica e Astronomia Università di Catania, Italy

³ NIPNE, Bucharest, Romania

⁴ Nuclear Physics Institute of ASCR, Rez near Prague, Czech Republic

⁵ ATOMKI, Debrecen, Hungary

⁶ Cyclotron Institute Texas A&M University, College Station, TX, USA

⁷ Università degli studi di Enna Kore Enna, Italy

E-mail: grapisarda@lns.infn.it

Abstract. Carbon-carbon fusion reaction represents a nuclear process of great interest in astrophysics, since the carbon burning is connected with the third phase of massive stars ($M > 8 M_{\odot}$) evolution. In spite of several experimental works, carbon-carbon cross section has been measured at energy still above the Gamow window moreover data at low energy present big uncertainty. In this paper we report the results about the study of the reaction $^{16}\text{O}(^{12}\text{C},\alpha^{20}\text{Ne})\alpha$ as a possible three-body process to investigate $^{12}\text{C}(^{12}\text{C},\alpha)^{20}\text{Ne}$ at astrophysical energy via Trojan Horse Method (THM). This study represent the first step of a program of experiments aimed to measure the $^{12}\text{C}+^{12}\text{C}$ cross section at astrophysical energy using the THM.

1. Introduction

The $^{12}\text{C}+^{12}\text{C}$ reaction is of great interest both in nuclear physics, producing the first evidence of nuclear molecular phenomena, as well as in astrophysics. In particular in this last field Carbon burning is connected with the third phase of massive star evolution in stars with $M > 8 M_{\odot}$ [1]. $^{12}\text{C}+^{12}\text{C}$ reaction rate is a fundamental parameter to determine the so-called M_{up} , that is, the minimum mass of a star for carbon ignition. Stars with M_{up} evolve into CO White dwarf, while stars with $M > M_{up}$ conclude their life as core-collapse Supernovae [2]. The core carbon burning takes place in a temperature range of $T = 0.5 - 1.0$ GK. For a temperature of 0.5 GK, the corresponding Gamow energy for the $^{12}\text{C}+^{12}\text{C}$ fusion is $E_G = 1.5 \pm 0.3$ MeV. Accurate determination of the carbon burning reaction rate requires very precise measurement of the $^{12}\text{C}+^{12}\text{C}$ cross section down to this energy, well below the Coulomb barrier. In spite of the key role of carbon fusion reactions in understanding stellar evolution, experimental data available ([3] and references therein) cover down to carbon-carbon center of mass energy $E_{cm} = 2$ MeV, that is at the higher edge of the Gamow peak. Moreover experimental data below $E_{cm} = 3$ MeV are rather uncertain [2]. Up to now people calculate the reaction rate by means of the from data at higher energy, but this procedure can lead to wrong result since the $^{12}\text{C}+^{12}\text{C}$ excitation function is characterized by resonant structures also at the low energy of astrophysical interest



[3] . In this framework new and accurate experimental data, down to the astrophysical energies, are strongly required.

A possible way to measure $^{12}\text{C}+^{12}\text{C}$ excitation function down to astrophysical energies, overcoming the problems connected to the direct measurement, mainly the strong suppression of the cross section due to the Coulomb barrier, is by using indirect methods. Among of them the Trojan Horse Method (THM) [5, 6, 7] is a consolidated method applied successfully for the study of nuclear reaction of astrophysical interest. In this paper we report on the measurement of the $^{16}\text{O}(^{12}\text{C}, \alpha^{20}\text{Ne})\alpha$ in quasi-free kinematic condition to study the possibility to apply the THM to this three-body reaction for the indirect study of the $^{12}\text{C}(^{12}\text{C}, ^{20}\text{Ne})\alpha$ reaction, that is the alpha channel of the carbon-carbon fusion. This represent the first measurement of a experimental program devoted to the study of the carbon-carbon fusion reaction via THM.

2. The Trojan Horse Method

The THM is a powerful technique that allows to extract a two-body reaction cross section, $A + x \rightarrow c + C$, down to the low energies of astrophysical interest by selecting the quasi-free break-up channel of a suitable three-body reaction $A + a \rightarrow c + C + s$. Nucleus a is selected to have an high probability for a cluster configuration $x \oplus s$. The $A + a$ interaction induces the nucleus a breakup into x and s . Selecting the quasi-free kinematic condition it is assumed that s acts as a spectator while x interacts with the nucleus A leading to the astrophysically relevant two-body reaction. The $A + a$ reaction is induced at energies higher than the Coulomb barrier, in this way the breakup can take place inside the nuclear field and accordingly the $A + x$ interaction takes place without suffering the Coulomb barrier suppression and the electron screening. Moreover thanks to $x \oplus s$ inter-cluster motion, the THM allows to measure the two-body cross section in a wide energy using a single beam energy.

THM has been widely applied to study nuclear reaction involved in several astrophysical scenario including reactions induced by unstable nuclei and by neutrons [8, 9, 10, 11, 13, 14].

3. Experimental set-up

In the present case $^{16}\text{O}(^{12}\text{C}, \alpha^{20}\text{Ne})\alpha$ had been selected as possible three-body reaction for the indirect study of the $^{12}\text{C}(^{12}\text{C}, ^{20}\text{Ne})\alpha$ reaction via THM. For the first time ^{16}O has been selected as Trojan Horse nucleus for is possible $^{12}\text{C} \oplus \alpha$ configuration. The experiment took place at the Horia Hulubei National Institute of Physics and Nuclear Engineering (IFIN-HH) Bucharest, Romania. The 9 MV Tandem accelerator provided a 25 MeV ^{16}O beam with a spot size on the target of about 2 mm and an intensity of about 8 nA. A natural carbon target, 100 $\mu\text{g}/\text{cm}^2$ thick, was used to induce the $^{16}\text{O}+^{12}\text{C}$ reaction. Energy and position of the outgoing particles were detected using six charge-partition position sensitive silicon detectors (PSD) in a symmetric configuration to double the number of collected events. PSDs 1,2,3 covered the angular rages 13° - 26° , 41° - 55° and 65° - 80° respectively; PSDs 4,5,6 were placed on the other side with respect to the beam axis, covering the same angular ranges. Particle identification was carried out with ΔE - E technique. In particular two ionization chambers (IC) filled by P10 (average pressure 23 mb) placed in front of PSD1 and PSD4. The two telescopes (IC-PSD) were devoted to the neon detection and identification. The experimental set-up described above had been set to measure the $^{12}\text{C}(^{12}\text{C}, \alpha^{20}\text{Ne})$ excitation function in a wide range 0-3 MeV, including the Gamov region.

Signals produced by detectors were processed through standard electronic. The trigger signal was produced by the coincidence between PSD1 (PSD4) and the total OR between PSD4-5-6 (PSD1-2-3). For the energy calibration we used a ^{12}C beam on Au target to get carbon from elastic scattering, ^{12}C beam on carbon target to get alphas for the $^{20}\text{Ne}+\alpha$ exit channel and a standard alpha source.

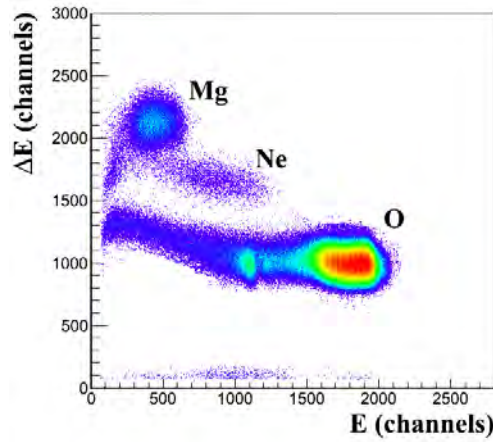


Figure 1. ΔE -E matrix for neon identification.

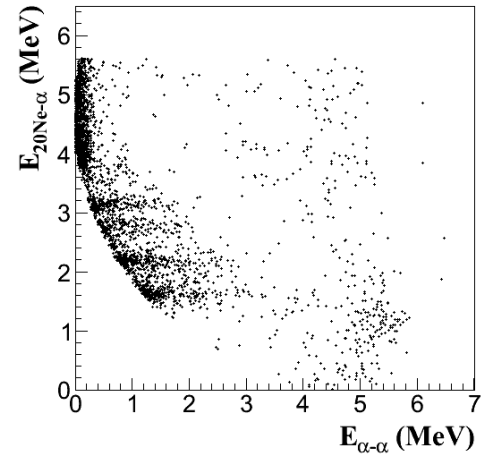


Figure 2. ^{20}Ne - α relative energy $E_{20\text{Ne}\alpha}$ versus α - α relative energy $E_{\alpha\alpha}$

4. Data Analysis

To identify the reaction channel $^{16}\text{O}(^{12}\text{C}, \alpha^{20}\text{Ne})\alpha$ of our interest we performed the study of ΔE -E matrices. In fig.1 typical experimental result is shown.

We can identify three loci related to oxygen (mainly due to the beam scattering) neon and magnesium. To select data of our interest a graphical cut was made around the neon locus. The experimental q -value for the three-body process was reconstructed considering alpha particles detected on PSD5-6 (PSD2-3) and assuming that the third undetected particle is an alpha particle. The experimental values obtained -2.66 MeV, -4.23 MeV, corresponds with good approximation to the theoretical q -value of the $^{16}\text{O}(^{12}\text{C}, \alpha^{20}\text{Ne})\alpha$ reaction with ^{20}Ne at g.s and 1^{st} excited state respectively. This result confirms the correct selection of the reaction channel. For the following analysis we selected events related to ^{20}Ne at g.s. In fig.1 we can observe also that magnesium partially overlaps the neon locus. This is partially due to the resolution of the detection system, on the other hand the loci are overlapped since we are in a energy range corresponding to the Bragg peak region. In particular the contamination is evident for events corresponding to a kinematic region with high probability for the quasi-free process. For this reason we applied a procedure in order to remove spurious events avoiding to put sharp cuts.

In order to study the reaction mechanism populating our three-body channel, we reconstructed the relative energy matrices. In particular in fig.2 we have ^{20}Ne -alpha relative energy ($E_{20\text{Ne}\alpha}$) versus alpha-alpha relative energy ($E_{\alpha\alpha}$). The vertical locus for a fix alpha-alpha relative energy corresponds to the formation of the ^8Be g.s. It means that our exit channel is populated by a sequential process $^{16}\text{O} + ^{12}\text{C} \rightarrow ^{20}\text{Ne} + ^8\text{Be}^* \rightarrow ^{20}\text{Ne} + \alpha + \alpha$. The horizontal loci for fix $E_{20\text{Ne}\alpha}$ energy correspond to the population of ^{24}Mg excited states. Due to the $l = 0$ ^{12}C - α intercluster motion inside the ^{16}O , the region where we expect to have the highest probability for the quasi-free process corresponds to low values for momentum of the alpha particle spectator (p_s) (less than 100 MeV/c.) The study of the ^{20}Ne -alpha relative energy as function of p_s indicates that the quasi-free region shows a very low statistic, moreover there is no evidence of ^{24}Mg excited states. We have to say that this region corresponds to low-energy ^{20}Ne area where we had the strong contamination of spurious events. So the low-statistic could be due to wrong selection of the events in this region. On the other hand the ^{24}Mg excited states are populated in correspondence of high momenta. This result indicates that these levels are populated by a sequential mechanism $^{16}\text{O} + ^{12}\text{C} \rightarrow ^{24}\text{Mg}^* + \alpha \rightarrow ^{20}\text{Ne} + \alpha + \alpha$. In fig.3 the spectrum of the ^{24}Mg excited states populated is shown. We can see five levels. The experimental data did not

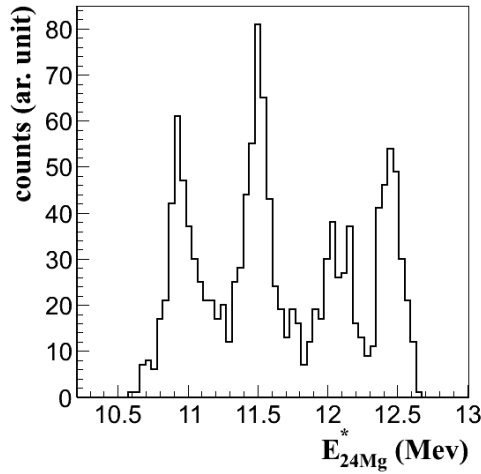


Figure 3. ^{24}Mg excited states populated in the present work.

E_{24Mg}^* MeV	E_{24Mg}^* MeV	J^π
present work	E. Goldberg et al.	
10.94		
11.50	11.52	2^+
12.03	11.96	2^+
12.16		
12.45	12.46	1^-

Table 1. ^{24}Mg excited states energy obtained in the present work compared with the excited levels measured in E. Goldberg *et al.* [15]

allow to make J^π assignment, on the other hand this energy range shows a very high density of ^{24}Mg levels. In tab.1 we report a comparison between our data and the results obtained by E. Goldberg *et al.* [15] where the ^{24}Mg levels were observed via ^{20}Ne -alpha resonant scattering.

5. Conclusion

In the framework of the study carbon-carbon fusion reaction at astrophysical energy via THM, we have studied the $^{16}\text{O}(^{12}\text{C}, \alpha ^{20}\text{Ne})\alpha$ using for the first time the ^{16}O as Trojan Horse nucleus. Experimental results obtained, in the experimental conditions described, have shown that three-body exit channel is mainly populated by sequential decay mechanism while no clear evidence of quasi-free process has been observed. The strong contamination of spurious events in the quasi-free energy region could be the reason of wrong selection of quasi-free events. ^{24}Mg excited states have been populated and compared with data present in literature. On the basis of this results a new experimental run has been performed with a different experimental set-up in order to increase the resolution and avoid the contaminations problems. Moreover we performed a experimental run where THM have been applied to the $^{14}\text{N}(^{12}\text{C}, \alpha ^{20}\text{Ne})^2\text{H}$ three-body reaction using for the first time ^{14}N ($^{12}\text{C} \oplus d$ cluster configuration) as Trojan Horse nucleus.

References

- [1] C.E. Rolfs and W.S. Rodney, *Cauldrons in the Cosmos* (University of Chicago Press, 1998)
- [2] F. Strieder, J. Phys.: Conf. Ser. **202**, (2010) 012025.
- [3] T. Spillane et al., Phys. Rev. Lett. **98**, (2007) 122501-4.
- [4] R.L. Cooper, A.W. Steiner and E.F. Brown, Astroph. J. **702**, (2009) 660-671.
- [5] G. Baur et al., Nucl. Phys. A **458**, (2007) 188.
- [6] C. Spitaleri et al. Phys. of Atomic Nuclei **74**, (2011) 1725.
- [7] R. Tribble et al., Rep. Prog. Phys. **77**, (2014) 106901.
- [8] G. Calvi et al. Nucl. Phys. A **621** (1997) 139.
- [9] A. Tumino et al., Phys. Rev. Lett. **98**, (2007) 252502.
- [10] C. Spitaleri et al. Phys. Rev. C **90**, (2014) 035801.
- [11] A. Tumino et al. Astrophys. J. **785**, (2014) 96.
- [12] M.L. Sergi et al. Phys. Rev. C **91**, (2015) 065803.
- [13] S. Cherubini et al. Phys. Rev. C **92**, (2015) 015805.
- [14] M. Gulino et al. Phys. Rev. C **87**, (2013) 012801.
- [15] E. Goldberg Phys. Rev. **93**, (1954) 799.